

**Virtual screening and molecular
modeling studies applied to discover
novel sirtuin modulators and
cholinesterase inhibitors**

Dissertation

Zur Erlangung des akademischen Grades

Doctor rerum naturalium (Dr. rer. nat.)

der Naturwissenschaftlichen Fakultät I - Biowissenschaften
der Martin-Luther-Universität Halle-Wittenberg

vorgelegt von

M.Sc. Zayan Alhalabi

geboren am 15.01.1982

Gutachter:

1. Prof. Dr. Wolfgang Sippl
2. Prof. Dr. Mike Schutkowski
3. Prof. Dr. Gerhard Wolber

Datum der Disputation: 11.12.2020

Abstract

The current thesis focuses on the application of computer-aided drug design methods in the context of discovering new enzyme inhibitors and rationalizing the interactions with their target proteins. Two classes of vital protein targets, sirtuins and cholinesterases, were studied in this work. In order to discover novel inhibitors and to support the chemical optimization of compounds for these challenging protein targets, computer-aided drug design methods have been applied. The computational methods used in this work comprise homology modeling, docking, molecular dynamics simulations, virtual screening, and protein-ligand interactions analysis. The combination of information from computational studies with synthetic chemistry as well as enzymatic testing aided the discovery of novel inhibitors of some of the seven sirtuin isoforms. More specifically, the first reported small-molecule Sirt4 inhibitors were identified using structure-based virtual screening. In case of Sirt1, a novel inhibitor chemotype, which is thiocyanates, was discovered. This type of inhibitors could be biologically characterized as NAD⁺-competitive and reversible inhibitors. In case of Sirt5, selective peptidic inhibitors were found to be active in the low nanomolar range. These peptides were analyzed by docking and molecular dynamics simulations to rationalize the binding mode. The obtained results could explain the selectivity and the structure-activity relationship for this class of Sirt5 inhibitors.

Upon virtual screening of a natural product library, several potent novel compounds that inhibit Sirt1 and Sirt2 were identified. Additionally, several Sirt2 inhibitors with improved solubility in biological systems were discovered with the support of docking and binding free energy calculations.

In the second part of the thesis, new selective inhibitors for acetylcholinesterase (AChE) and butyrylcholinesterase (BChE) were analyzed using computational methods. Molecular docking studies were able to predict the binding modes of the active compounds. Hence, (2E) α , β -unsaturated fatty acids, as well as ursolic and oleanolic acid derivatives, were discovered as novel cholinesterase inhibitors.

Keywords: Computer-aided drug design methods, virtual screening, docking, sirtuins, cholinesterases, selective inhibitors, Sirt1, Sirt2, Sirt4, Sirt5, AChE, BChE.

Kurzfassung

Diese Dissertation konzentriert sich auf die Anwendung von Methoden des computergestützten Wirkstoffdesigns im Kontext der Entdeckung neuer Enzyminhibitoren und der Rationalisierung von Interaktionen mit deren Zielproteinen. Die untersuchten Inhibitoren sind in der Lage lebenswichtige Proteinstrukturen wie Sirtuine und Cholinesterasen zu hemmen. Um neue Inhibitoren für herausfordernde Zielstrukturen zu entdecken, wurden Methoden des computergestützten Wirkstoffdesigns angewandt. Die verwendeten rechnergestützten Methoden kombinieren Homologiemodellierung, Docking, Molekulardynamiksimulationen, virtuelles Screening und die Analyse von Protein-Ligand-Interaktionen. Die Kombination von Informationen aus computergestützten Studien mit synthetischer Chemie und enzymatischen Tests half bei der Entdeckung neuer Inhibitoren für mehrere der sieben Sirtuin-Isoformen. Genauer gesagt, wurden die ersten niedermolekularen Sirt4-Inhibitoren durch virtuelles Screening identifiziert. Im Falle von Sirt1 konnte ein neuartiger Inhibitor-Chemotyp entdeckt werden, die Thiocyanate, die biologisch als NAD⁺-kompetitive reversible Inhibitoren charakterisiert werden konnten. Im Fall von Sirt5 wurden selektive peptidische Inhibitoren, die im niedernanomolaren Bereich aktiv sind, mittels Docking und Molekulardynamiksimulationen analysiert, um den Bindungsmodus und die Struktur-Aktivitäts-Beziehungen abzuleiten. Die erhaltenen Ergebnisse konnten die Selektivität und die Struktur-Aktivitäts-Beziehung für diese Klasse von Sirt5-Inhibitoren erklären.

Beim virtuellen Screening einer Naturstoff-Bibliothek wurden mehrere potente neue Verbindungen identifiziert, die Sirt1 und Sirt2 hemmen. Darüber hinaus wurden mehrere Sirt2-Inhibitoren mit verbesserter Löslichkeit in biologischen Systemen durch Unterstützung von Docking und Berechnungen freier Bindungsenergien entwickelt.

In dem zweiten Teil der Arbeit wurden neue selektive Inhibitoren für Acetylcholinesterase (AChE) und Butyrylcholinesterase (BChE) mit Hilfe von verschiedenen Berechnungsmethoden analysiert. Molekulare Dockingstudien waren in der Lage, die Bindungsmodi der Wirkstoffe vorherzusagen. Es wurden (2E) α , β -ungesättigte Fettsäuren, zusätzlich zu Ursol- und Oleanolsäurederivaten als neue Cholinesterase-Inhibitoren untersucht.

Schlagwörter: Methoden des computergestützten Wirkstoffdesign, virtuelles Screening, Docking, Sirtuine, Cholinesterasen, selektive Inhibitoren, Sirt1, Sirt2, Sirt4, Sirt5, AChE, BChE.

Acknowledgments

First of all, I would like to thank my supervisor Prof. Wolfgang Sippl for giving me the opportunity to work on this project, for supporting me, for his patience, and the encouraging thoughts he gave me over the years.

I am also truly thankful to my Ph.D thesis committee Prof. Mike Schutkowski and Prof. Gerhard Wolber for their great interest in theoretical and complicated scientific matters and their supportive comments and encouragement during my Ph.D work.

I would like to thank our collaborators Prof. Dr. Manfred Jung, Prof. Dr. Mike Schutkowski, and Prof. Dr. Clemens Steegborn, and their research groups for their contributions to our projects.

I am grateful to my colleague Dr. Dina Robaa for many valuable, encouraging ideas and discussions. Her advice and experience have always been of great help to my project progress. In addition, I would like to thank Dr. Jelena Melesina for her advice and her patience and for her useful comments she gave me during my work.

My truthful thanks also go to Prof. Dr. René Csuk, who gave me a chance to join his team during the publication.

I also want to extend my warm thanks to all the friends that I met during my Ph.D in Germany, especially Conrad Simoben, Anas Msouti, Lucas Praetorius, and Chiara Luise. Moreover, I would especially like to thank Dr. Fidele Ntie-Kang for his efforts during my Ph.D work.

Furthermore, I want to thank my husband Haytham for the encouragement and support he gave me. I am thankful to my brother and sisters. Many thanks to my father, who raised me with the love of science and motivation in all steps of my life.

At last, I want to thank my loving, supportive, encouraging, and patient mother, Jihan, whose faithful support is so appreciated during my Ph.D time.

Dedication

I dedicate this dissertation to my beloved parents, my husband, my mother-in-law, and my unborn child "Adam"

CONTENT

Abstract.....	III
Kurzfassung	V
Acknowledgments	VII
List of Figures.....	XII
List of Abbreviations	XIII
1. Introduction.....	1
1.1. Sirtuins	1
1.1.1. Sirtuins as epigenetics targets and its role in cancer	1
1.1.2. The activity and mechanisms of sirtuins	2
1.1.3. Crystal structure of sirtuins	3
1.1.4. The role of sirtuin modulators in cancer	7
1.2. Cholinesterase	11
1.2.1. The crystal structure of cholinesterases.....	11
1.2.2. Cholinesterase inhibitors	14
1.3. Cholinesterases and sirtuins are reported targets for Alzheimer’s disease	15
1.4. Computer-aided drug design of sirtuin and cholinesterase inhibitors.....	16
1.5. Sirtuins and cholinesterase inhibitors derived from natural products.....	17
2. Aim of the Work.....	19
3. Methods and Materials	21
3.1. Computer-aided drug design (CADD).....	21
3.1.1. Virtual screening	21
3.1.2. Molecular docking.....	22
3.1.3. Homology modeling.....	23
3.1.4. Molecular Dynamics (MD) simulations.....	24
3.2. <i>In vitro</i> assay	25

3.2.1. Sirtuins assay.....	25
3.2.2. Cholinesterase assay.....	26
3.3. Cellular assay used for Sirt1 inhibitors.....	27
4. Results and Discussion.....	29
4.1. Manuscript 1: KATching-Up on Small Molecule Modulators of Lysine Acetyltransferases.....	31
4.2. Manuscript 2: Sirtuin 1 Inhibiting Thiocyanates (S1th)—A New Class of Isozyme Selective Inhibitors of NAD ⁺ Dependent Lysine Deacetylases.....	33
4.3. Manuscript 3: Potent and Selective Inhibitors of Human Sirtuin 5.....	35
4.4. Manuscript 4: Identification of Bichalcones as Sirtuin Inhibitors by Virtual Screening and <i>In Vitro</i> Testing.....	37
4.5. Manuscript 5: Three-Component Aminoalkylations Yielding Dihydronaphthoxazine-Based Sirtuin Inhibitors: Scaffold Modification and Exploration of Space for Polar Side-Chains.....	39
4.6. Manuscript 6: Virtual screening and identification of specific inhibitors for the mitochondrial deacylase Sirtuin 4.....	41
4.7. Manuscript 7: Unexpected AChE inhibitory activity of (2E) α , β unsaturated fatty acids.....	43
4.8. Manuscript 8: Ursolic and oleanolic acid derivatives with cholinesterase inhibiting potential.....	45
5. Summary of the Results.....	47
5.1. Developing selective Sirt1 inhibitors and investigating their inhibition in some cancer cell lines.....	49
5.2. Identification of potent and selective Sirt5 inhibitors.....	51
5.3. Identification of sirtuin inhibitors from natural products using virtual screening of the p-ANAPL library.....	52
5.4. Hit identification and lead optimization for Sirt2.....	54
5.5. Virtual screening and identification of specific inhibitors for the mitochondrial deacylase Sirtuin 4.....	55
5.6. Discovering novel acetylcholinesterase (AChE) and butyrylcholinesterase (BChE) inhibitors.....	57

6. Conclusion	61
7. References.....	65
8. Appendix.....	79

List of Figures

Figure 1: Modification of histones and DNA in epigenetic regulation of gene expression.

Figure 2: The mechanism of sirtuins.

Figure 3: The crystal structure of Sirt2, the figure shows the binding pockets, NAD⁺, and SirReal2.

Figure 4: Three-dimensional structure of sirtuins. The Rossmann domain and the zinc-binding domain are shown in the figure.

Figure 5: The sequence of the seven full-length human sirtuins.

Figure 6: Examples of reported sirtuin inhibitors.

Figure 7: The overall structure and the binding pocket of AChE with donepezil.

Figure 8: Cholinesterase inhibitors

Figure 9: 2D structure of the compounds **S1th3**, **S1th13**.

Figure 10: Docking poses obtained for **S1th3** and **S1th13** in Sirt1.

Figure 11: The binding modes of compounds **33** and **15**, the crystal structure of zSirt5 with **33** was overlaid with the crystal structure of zSirt5 and **15**.

Figure 12: 2D structure of Rhuschalcone IV and Rhuschalcone I.

Figure 13: The possible binding modes of the natural product inhibitors in Sirt1 peptide pocket and Sirt2 extended C-pocket

Figure 14: The crystal structure of hSirt2 with the compound **8b**.

Figure 15: 2D structure of the compounds **OSSK_979070** and **OSSK_671780**.

Figure 16: Predicted docking pose of the VS hits **OSSK_671780** in the peptide-binding pocket of hSirt4 homology model.

Figure 17: Predicted common binding mode of AChE inhibitors from fatty acids (compounds **13**, **14**, and **23**) with the crystal structure of AChE.

Figure 18: The 2D chemical structures of the cholinesterase inhibitors (compounds **18**, **10**).

List of Abbreviations

2D	Two-dimensional
3D	Three-dimensional
ACh	Acetylcholine
AChE	Acetylcholinesterase
AD	Alzheimer's disease
ADMET	Absorption, Distribution, Metabolism, Excretion and Toxicity
ADP	Adenosine-Diphosphate
ADPr	Adenosine Diphosphate Ribose
AMBER	Assisted Model Building with Energy Refinement
Amber12: EHT	Amber12: Extended Hueckel Theory
aMD	Accelerated Molecular Dynamics
BBB	Blood-Brain Barrier
BChE	Butyrylcholinesterase
CADD	Computer-aided Drug Design
ChE	Cholinesterase
cMD	Conventional Molecular Dynamics
CNS	Central Nervous System
CPS1	Carbamoyl Phosphate Synthetase 1
CR	Calorie Restriction
CTR	C-Terminal regulatory segment
DDB1	DNA Damage-Binding Protein 1
DOPE	Discrete Optimized Protein Energy
FDA	Food and Drug Administration
FOXO3	Forkhead Box P3
H2AX	Histone Family Member X
HEK293T cells	Human embryonic kidney 293 cells
HELa cells	cervical cancer cells
HM	Homology modeling
HTVS	High throughput virtual screening

HMG	Hydroxymethylglutaryl
H bond	Hydrogen bond
KATs	Lysine Acetyltransferases
KDACs	Lysine Deacetylases
MEF	Mouse Embryonic Fibroblast
MMFF94	Merck Molecular Forcefield 94 version
MOE	Molecular Operating Environment
MW	Molecular Weight
NAD ⁺	Nicotinamide Adenine Dinucleotide
NPs	Natural Products
OPLS	Optimized Potentials for Liquid Simulations
PAINS	Pan Assay Interference Compounds
p-ANAPL	pan-African Natural Products Library
PAS	Peripheral Anionic Site
PDB	Protein Data Bank
PTMs	Post-Translational Modifications
R&D	Research and Development
Sirt	Sirtuins
UniProt	Universal protein resource
VS	Virtual screening
XSirt4	<i>Xenopus tropicalis</i> Sirt4

"A scientist is happy, not in resting on his attainments, but in the steady acquisition of fresh knowledge."

Max Planck

1. Introduction

1.1. Sirtuins

1.1.1. Sirtuins as epigenetics targets and its role in cancer

DNA is packaged by wrapping around histone proteins to form a nucleosome. Nucleosomes are, in turn, compacted to form chromatin. The degree of compactness depends on the types of post-translation modifications present on the histones, in particular on their terminal residues protruding from the nucleosome particle. Thus, methylated histones tend to be repressive or activating; this depends on the position and the degree of methylation, whereas acetylated histone is less compacted (1).

Gene expression can be regulated by post-translational modifications of histones, changing the structure of the chromatin, and chemical modification of the DNA. All these elements are necessary to maintain the chromatin structure and the cellular phenotype (1, 2). Hence, chromatin is controlled by post-translational modifications (PTMs) of the core histone proteins (3).

The proteins that add groups of acetyl, methyl, or other PTMs to the histone code, such as lysine acetyltransferases (KATs) and histone methyltransferases, are called writers. The proteins that recognize and bind to histone modifications are named readers of the code, such as bromodomains that bind specifically to acetylated lysines. The enzymes that remove histone marks are termed erasers such as lysine deacetylases (KDACs) and lysine demethylases (1, 4, 5). **Figure 1** explains the modifications of histones in the epigenetic regulation of gene expression.

Sirtuins are class III histone deacetylases. Sirtuins consist of seven sirtuins (Sirt1-7) that are localized in different locations, like cytoplasm (Sirt1 and Sirt2), nucleus (Sirt1, Sirt2, Sirt6, and Sirt7), and mitochondria (Sirt3, Sirt4, and Sirt5) (6). They are divided into four diverse classes: class I contains Sirt1, Sirt2, and Sirt3, Sirt4 is class II, Sirt5 is class III, and Sirt6 and Sirt7 are class IV (7). In the last decade, numerous additional acetylated substrate proteins have been found for the different sirtuin isoforms (8). It is nowadays evident that sirtuins are more promiscuous as previously expected.

Sirtuins are considered as key regulators for several cellular signaling pathways. They are potential epigenetic targets that are involved in multiple diseases, including cancer and neurodegenerative diseases such as Alzheimer’s disease (AD) and Parkinson’s disease. Sirtuins control several biological processes, including transcription, cell survival, DNA repair, and longevity (9, 10). Thus, the modulation of sirtuins activity could provide interesting and novel therapeutic possibilities (11–13). On the other site, the promiscuity of sirtuins makes it challenging to understand their biological role in detail.

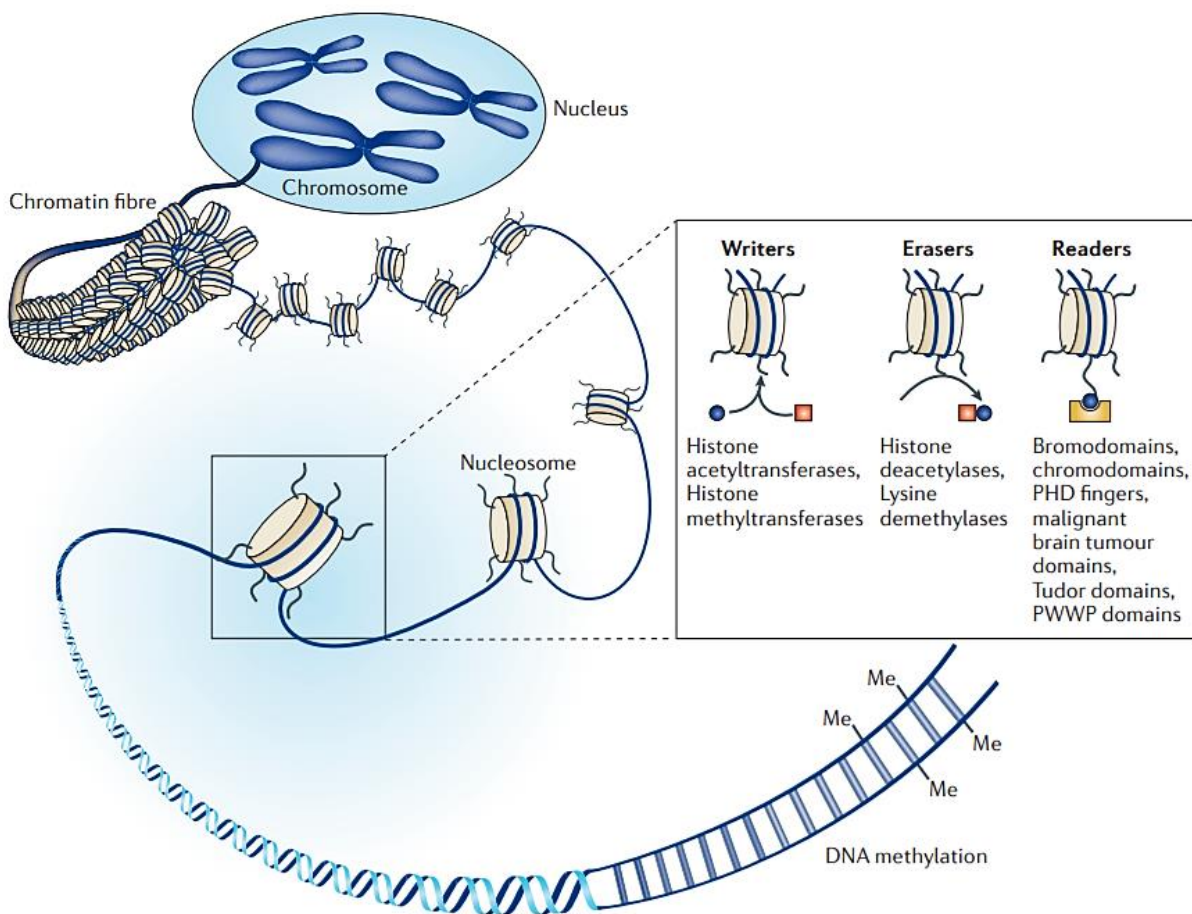


Figure1: Modification of histones and DNA in epigenetic regulation of gene expression (1).

1.1.2. The activity and mechanisms of sirtuins

Sirtuins are nicotinamide adenine dinucleotide (NAD⁺)-dependent histone deacetylases protein targets (14). They transfer the acetyl group from the lysine side chain of a substrate to the cofactor NAD⁺. As a result, nicotinamide, 2'-O-acetyl-ADP-ribose, and a

deacetylated substrate are generated (15–17). The mechanism of action is described in **Figure 2**.

The other catalytic activities of sirtuins are the mono-ADP-ribosyltransferase activity of Sirt4 and Sirt6 (18, 19). Moreover, Sirt4 catalyzes the removal of 3-hydroxy-3-methylglutaryl (HMG) from lysine residues of target proteins (20). In addition, Sirt5 has demalonylase and desuccinylase activities (21). Sirt6 was also found to be active in removing long-chain fatty-acyl groups, including myristoyl and palmitoyl groups (22). Interestingly, recent studies have identified the activity of Sirt2 as demyristoylase (23). Additionally, Sirt2 can remove 4-oxononanoyl from histones and non-histone proteins (24).

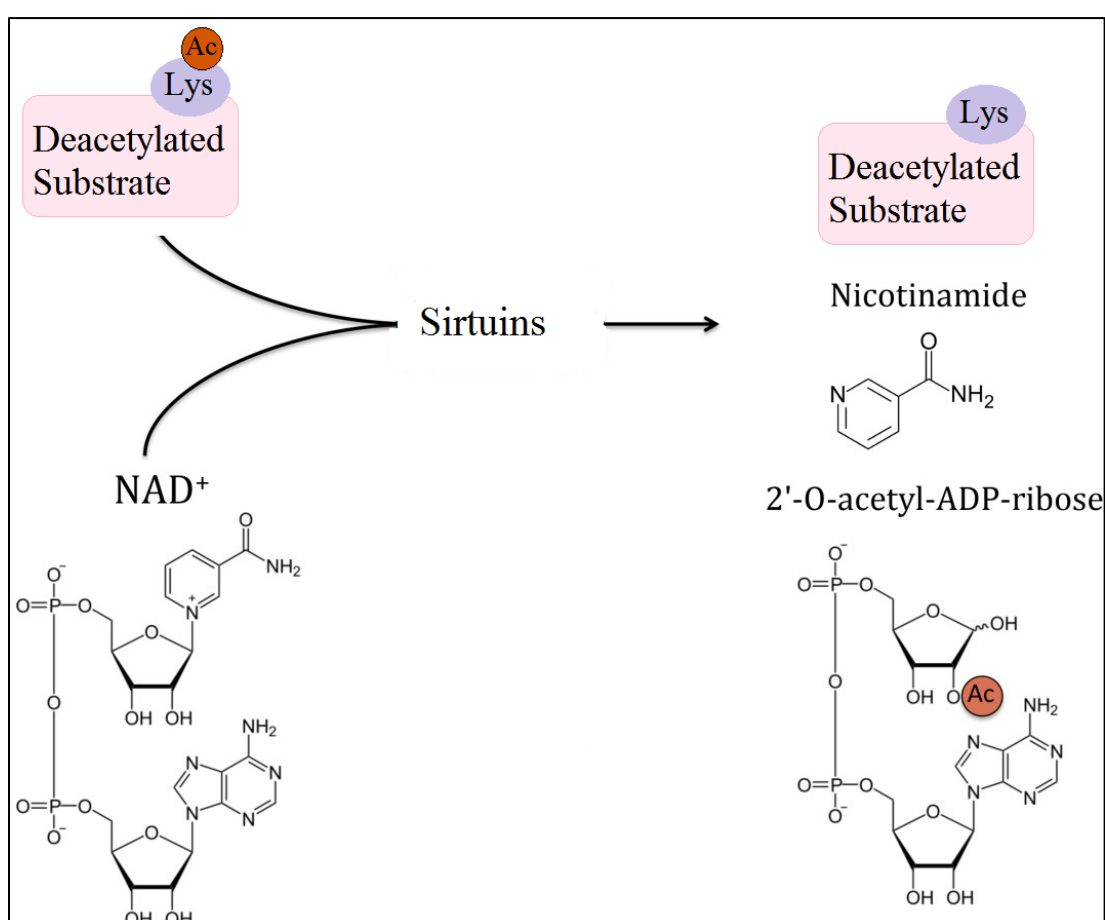


Figure 2: The mechanism of sirtuins, adapted from (15).

1.1.3. Crystal structure of sirtuins

Sirtuins are a conserved catalytic core family of 275 amino acids (7). The sirtuins core consists of a Rossmann-fold domain and a small zinc-binding domain, which is the most diverse region between sirtuins types. The cofactor NAD⁺ or ADPr (Adenosine

Diphosphate Ribose) and the acylated substrate are bound to a cleft between these two domains (25). The loops which connect the small and large domains form a cleft that acts as the enzyme active site. In this cleft, NAD^+ and acyl-lysine substrates bind in opposite sides. The sirtuins sequence alignment shows high sequence conservation and high identity of the cofactor binding sites and the residues of the catalytic pocket (7, 25).

The NAD^+ binding pocket is divided into three subpockets, pocket A, comprises the adenine-ribose binding site, pocket B, refers to the nicotinamide-ribose binding site, and pocket C indicates to the nicotinamide moiety binding site (**Figure 3**) (26). The pocket nearby the C-pocket is called the extended C-site (EC-site); this hydrophobic pocket is close to the zinc-binding domain; it is known as the selectivity pocket. Occupation of this selectivity pocket is observed in the crystal structures of Sirt2 by the selective inhibitor SirReal2 (27).

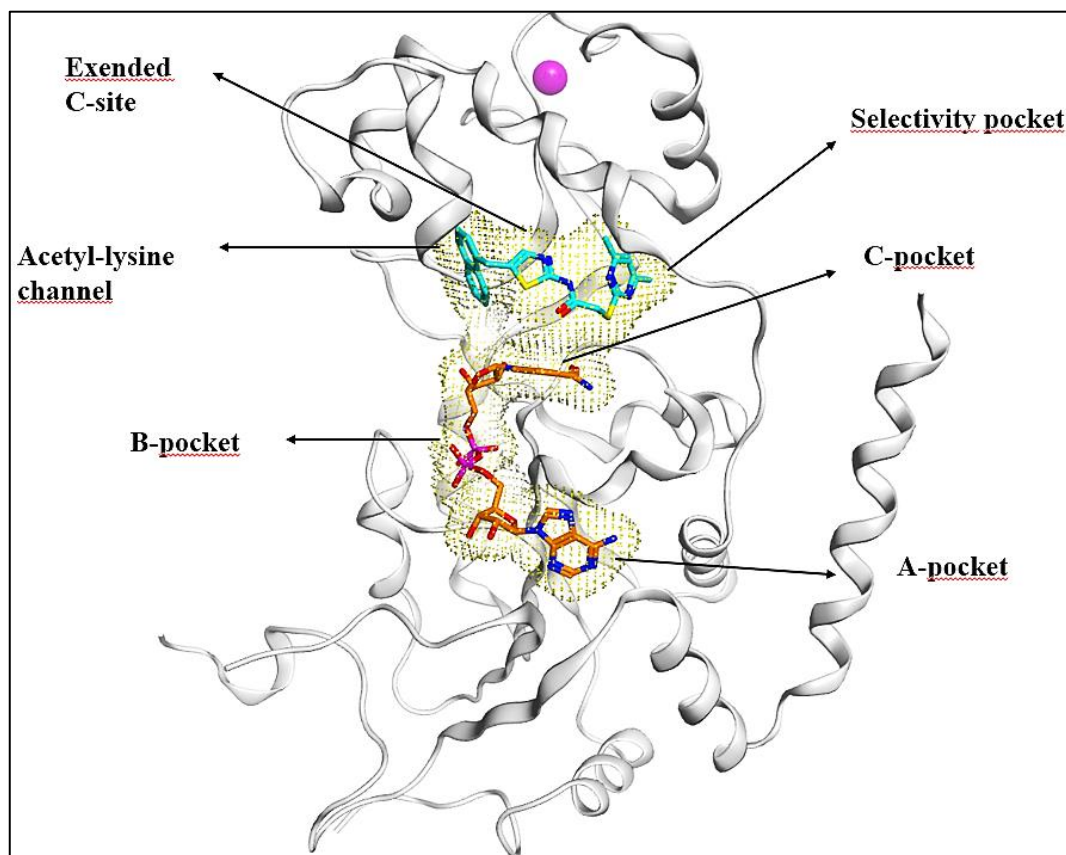


Figure 3: The crystal structure of Sirt2 (PDB code: 4RMG), the pockets are colored with yellow, NAD^+ in orange, SirReal2 in cyan, zinc atom in magenta.

The crystal structures of sirtuins were resolved and deposited in Protein data bank (PDB) (28). Importantly, mitochondrial sirtuins Sirt4 and Sirt5 reveal a unique insertion in the small zinc-binding domain consist of a short helix and an extended loop, which may be important in the mitochondrial localization (7, 29). This additional loop was shown in the crystal structure of *Xenopus tropicalis* Sirt4 (XSirt4), which was resolved in 2017 (no human crystal structure for Sirt4 was reported so far). It reveals an unusual acyl binding site and a Sirt4-specific loop (30). This extended loop (**Figure 4**) consists of 12 residues (residues 195–206) and exists in the Zn²⁺ binding module. The loop is oriented deep into the catalytic core and contributes to the active site lining (30–32). Likewise, the crystal structure of Sirt5 shows an additional loop and helix (helix α 9) inserted in the zinc-binding domain.

Interestingly, sirtuins could adopt different conformational states (33). Namely, Sirt2 (PDB entry: 3ZGV) moves from an open conformation to a closed conformation after ADPr binding (33). Moreover, the apo form of Sirt1 adopts a wide-open conformation when compared to the substrate- and cofactor-bound state or closed conformation. Thus, the binding of a substrate leads to a closure of Rossmann and zinc-binding domains around the substrate. Notably, in the closed state, the smaller domain forms an interface with the larger domain; this results in the formation of a substrate pocket (34). Similar behavior was observed in Sirt3 and Sirt5 subtypes (35, 36). The crystal structures of sirtuins are shown in **Figure 4**.

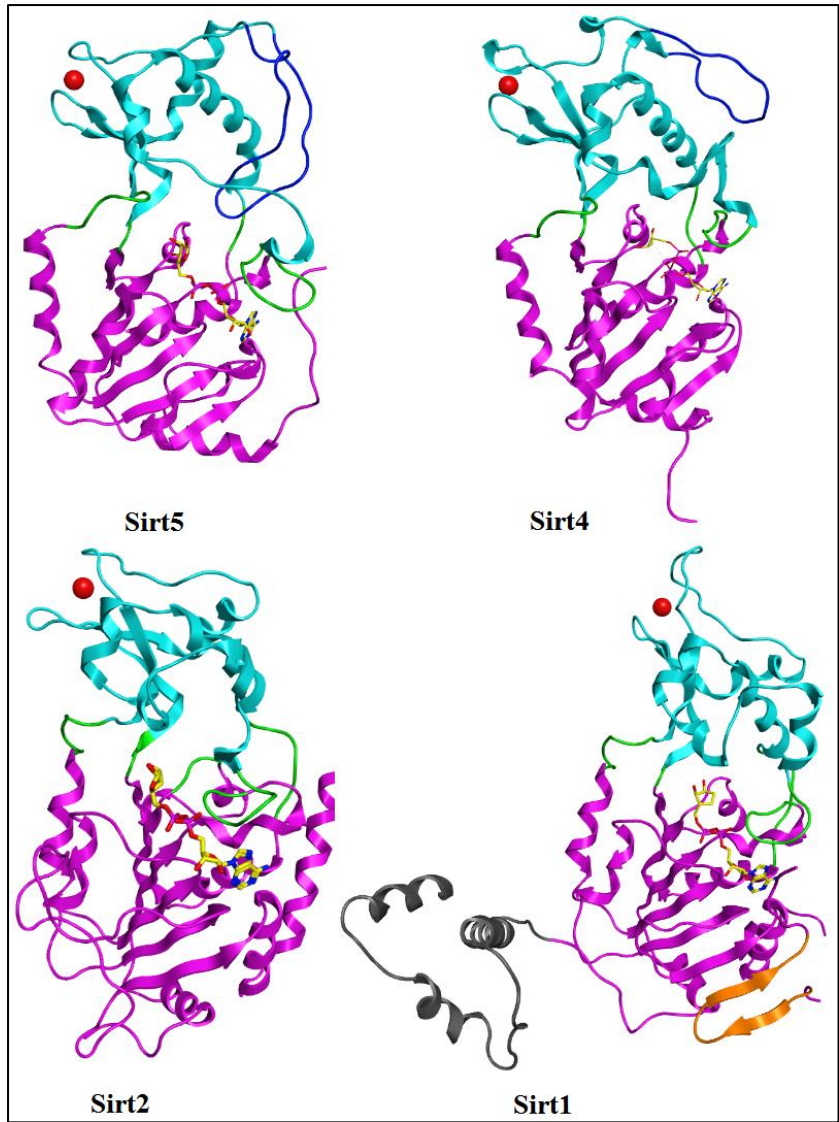


Figure 4: Three-dimensional structure of sirtuins. Sirt1 (PDB: 4ZZJ), Sirt2 (PDB: 5D7O), Sirt4 (PDB: 5OJ7), Sirt5 (PDB: 3RIY). The Rossmann-fold domain is shown in magenta. The zinc-binding domain is in cyan. The extended loops are in dark blue, the connecting loops are in green, and the zinc ion is in red, NAD⁺ in yellow, N terminus in grey, C-terminal regulatory segment (CTR) is in orange.

Unlike the conserved catalytic core, the N- and C-termini of sirtuins are relatively variable in length, chemical composition, and sensitivity to post-translational modifications (37). It was shown that Sirt1 protein contains the most extended N- and C-terminal parts (38). Interestingly, XSirt4 crystal structure has no C-terminus, rather only a short N-terminus of ~28 residues (30). The specific N-terminal and C-terminal domains may contribute to the localization of sirtuins in cells (37). Remarkably, the crystal structure of Sirt1 contains a C-terminal regulatory segment (CTR), which could control the activity of Sirt1 uniquely

(34). The conserved catalytic core and the variable N-/C- termini of the seven human sirtuins are shown in **Figure 5**.

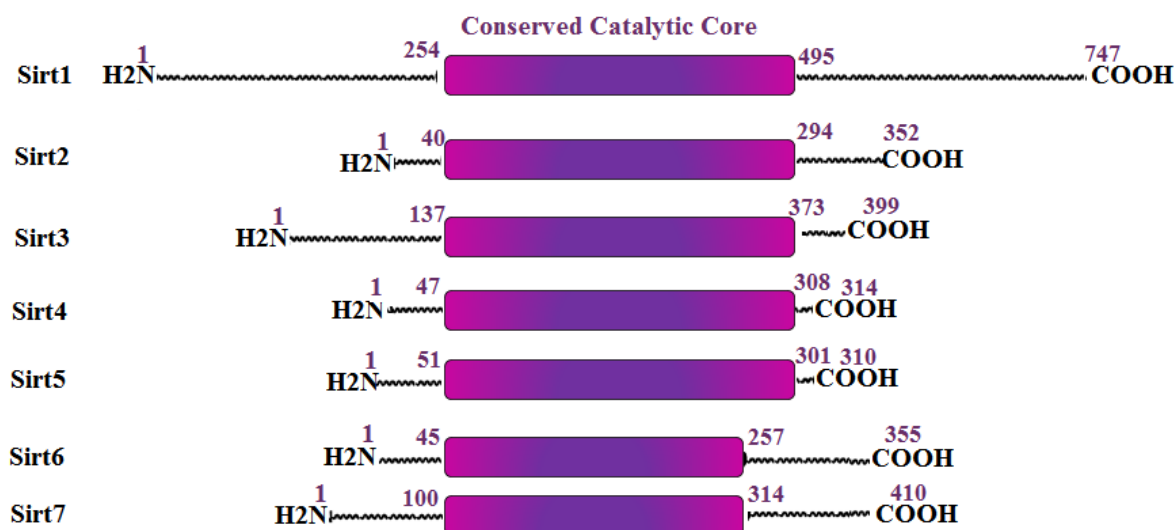


Figure 5: The sequence of the seven full-length human sirtuins. The magenta bar in each sequence refers to the conserved catalytic core, adapted from (37).

1.1.4. The role of sirtuin modulators in cancer

Cancer is the main public health problem in the world (39). It is a class of diseases with a common feature of abnormal cell growth. Most cancers are associated with genomic instability (40). Sirtuins are overexpressed in many human cancers (41, 42). They are targets for cancer therapy. Sirtuins play contradictory roles in cancer. Some sirtuins help to prevent DNA from damage, maintain genomic stability, and restrict replicative life span. Thus, they have a protective effect against cancer. On the other hand, some data indicate that sirtuins may be involved in tumorigenesis since they promote cell survival under stress conditions (43).

The potential contribution of sirtuins in the pathogenesis of several diseases has motivated the efforts to identify small molecules that can modify the activity of sirtuins (44). Remarkably, several sirtuin inhibitors have been identified and developed as anti-cancer drug candidates (45, 46). Hence, the development of modulators of sirtuin might offer therapeutic opportunities for various types of cancer (42).

Many sirtuin inhibitors in the low nanomolar range have been reported, such as peptide inhibitors that inhibit Sirt5. These inhibitors can be used as good starting points for the design of small-molecule selective inhibitors (47–49). Furthermore, compound GW5074 (**Figure 6**) was identified as a weak Sirt5 inhibitor; it inhibits Sirt5's desuccinylase activity (50). Another Sirt5 inhibitor is suramin (**Figure 6**), which inhibits the deacetylase activity of Sirt5 with an IC₅₀ value of 22 μM. It was studied for its potential anti-cancer activity (51). However, the low bioavailability as well as the promiscuity of suramin makes this class of inhibitors difficult to further optimize.

Sirt1 is the most studied protein among all sirtuins; it acts as a tumor suppressor and as an oncoprotein; this depends on the type and stage of cancer (42). Interestingly, Sirt1 maintains genomic stability and constrains the metabolism of cancer, thereby preventing cancer development. Furthermore, Sirt1 inhibition increases the acetylation of p53, promotes cell survival, and induces apoptosis in cancer cells. Also, Sirt1 limits oncolysis in prostate cancer cells (52).

Several compounds have been shown to inhibit the deacetylase activity of Sirt1 like tenovin-6 (**Figure 6**), which also inhibits Sirt2, Sirt3. Tenovin-6 has a potential effect in decreasing tumor growth by activating p53 (53, 54). Another small molecule, Ex-527 (**Figure 6**), was discovered as a potent and selective Sirt1 inhibitor (IC₅₀ =98 nM) (55).

Numerous Sirt2 inhibitors, such as AGK2 and MIND4 (**Figure 6**), have been developed in recent years. AGK2 has protective effects in Parkinson's disease; it activates the apoptosis of glioma cells (56, 57); compound MIND4 has neuroprotective effects; it was studied in the therapy of Huntington's disease (57, 58). Another inhibitor for Sirt2 is splitomicin (**Figure 6**); it has IC₅₀ of 60 μM (59). Its derivatives showed antiproliferative effects and tubulin hyperacetylation in MCF7 breast cancer cells (60). One of the most selective Sirt2 inhibitors so far is SirReal2, which binds to the extended C-site and induces a rearrangement of the active site of Sirt2. This binding mode was shown by solved co-crystal structures. (27).

Some compounds are inhibitors of both Sirt1 and Sirt2 like sirtinol (**Figure 6**), which also inhibits yeast Sirt2 and human Sirt1 with relative high IC₅₀ values of 70 μM and 40 μM, respectively (61). Interestingly, sirtinol reduces the expression of Sirt1 in MCF-7 breast cancer cells. It causes autophagic cell death in MCF-7 cells (62). Cambinol (**Figure 6**) is a β-naphthol compound that inhibits human Sirt2 in addition to human Sirt1 with IC₅₀

values of 56 μM for Sirt1 and 59 μM for Sirt2 (63). Cambinol showed antitumor activity in lymphoma cells (63). Besides, salermide (**Figure 6**) is a reversed amide based on the structure of sirtinol; it has a stronger inhibition effect on Sirt1 and Sirt2 than sirtinol (64).

Recent research suggests that mitochondrial sirtuins, Sirt 3, 4, 5, act as tumor suppressors by controlling the cell's metabolic state (65, 66). Therefore, regulating these enzymes may have important effects on cancer management (65). It was shown that LC-0296 inhibits Sirt3 (**Figure 6**) (67), whereas no inhibitors were discovered until now for Sirt4. In case of Sirt5 only peptides have been reported as potent inhibitors.

Sirt6 also has a tumor-suppressive role by inhibiting cancer metabolism and elevating genomic stability (68). Some quercetin derivatives were shown to inhibit Sirt6 (69).

Additionally, Sirt7 can deacetylate key cell signaling molecules, such as FOXO3 and DDB1 (**Figure 6**), and therefore regulates the progression of apoptosis in response to DNA damage and oxidative stress (70, 71). Cyclic tripeptides inhibitors were found to inhibit Sirt7 (72).

It was shown that nicotinamide (**Figure 6**) inhibits Sirt1, Sirt2, Sirt3, Sirt5, and Sirt6 with IC_{50} values differing from 50 to 184 μM (44). Notably, sirtuin activators were mostly developed for Sirt1, such as resveratrol (**Figure 6**), which inhibits human Sirt3 and stimulates Sirt5 and Sirt1 (73).

In conclusion, several sirtuin inhibitors have shown anti-cancer activities; however, more selective and effective sirtuin modulators with anti-cancer effects need to be developed to clearly show the therapeutic potential of these targets and inhibitors (74).

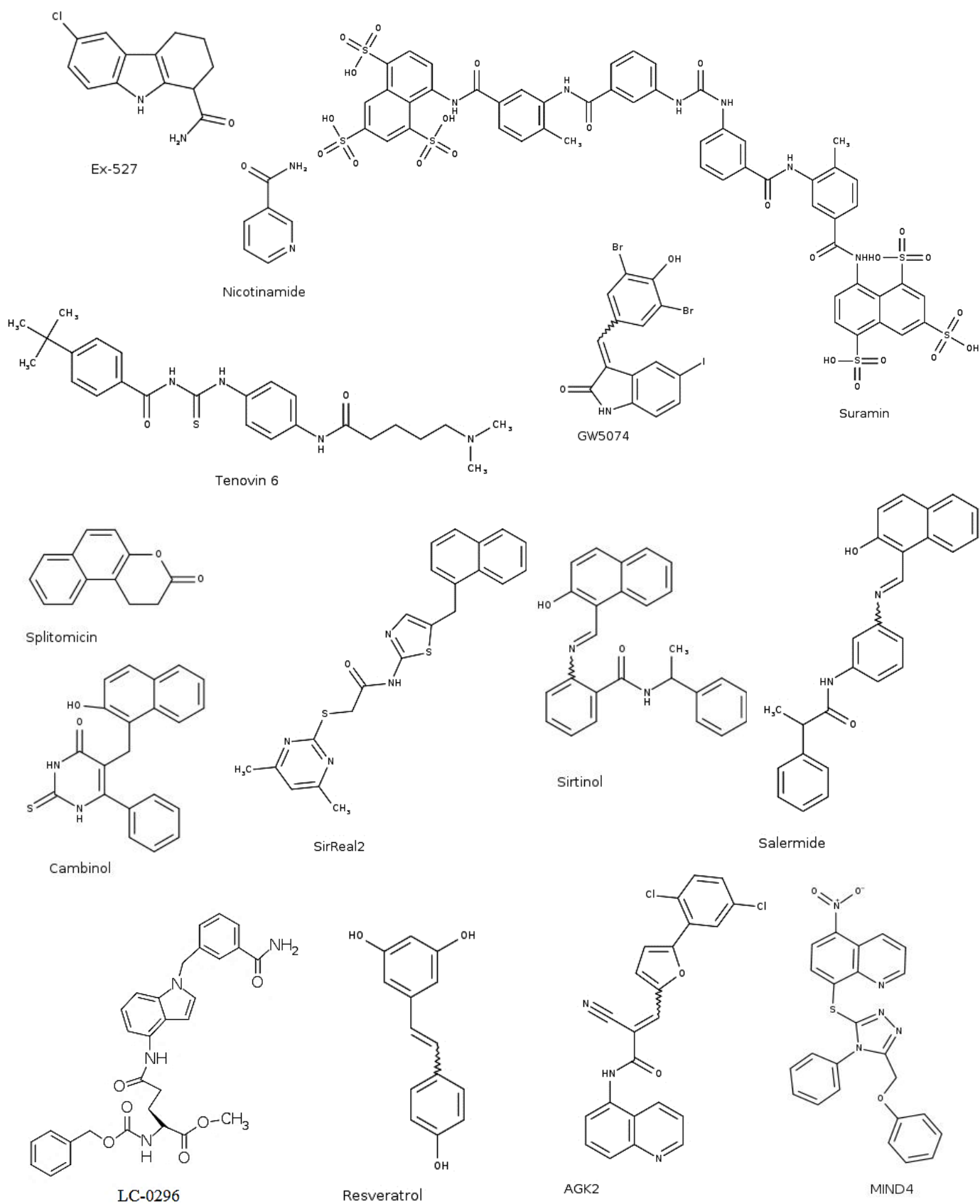


Figure 6: Examples of reported sirtuin inhibitors.

1.2. Cholinesterase

Cholinesterase (ChE) is an enzyme that catalyzes the hydrolysis of acetylcholine (ACh), which is a neurotransmitter responsible for the transfer of electrical impulses in nerve cells (75, 76). Basically, every living cell synthesizes ACh, which plays a mediator role in the interactions of nonneuronal cells with the external environment, the neural system, cytokines, and hormones. (75).

ACh binds to its receptors after being released into the synaptic cleft. The ACh receptors consist of two different types; the first type is muscarinic acetylcholine receptors (mAChR); the second type is nicotinic acetylcholine receptors (nAChR). Muscarinic ACh receptors (mAChRs) mediate the neurotransmission in neurons and organs like the heart, smooth muscle fiber, and glands. Whereas, nicotinic ACh receptors (nAChRs) mediate chemical neurotransmission at neurons, ganglia, and interneurons (75).

The CNS contains two forms of cholinesterase (ChE) enzymes: acetylcholinesterase (AChE) and butyrylcholinesterase (BChE), both enzymes are capable of hydrolyzing ACh in the central and peripheral nervous systems (77, 78).

1.2.1. The crystal structure of cholinesterases

The structures of BChE and AChE are almost similar (79). The active site of AChE or BChE is not on the surface of the protein; instead, it is in a 20 Å deep gorge (79, 80). The active site is categorized into two sub-sites: The first one is at the entrance of the gorge, it is called the peripheral anionic site (PAS), and the second one is the catalytic area at the bottom of the gorge. The catalytic active anionic site of AChE contains two subsites, named the “esteratic” site, which is responsible for the catalytic enzyme activity, and the “anionic” site, which is known as a choline-binding pocket (80).

The esteratic site in AChE includes three essential amino acids, Ser200, His440, and Glu327, which form a catalytic triad. The AChE anionic site consists of Trp84, Tyr130, Phe330, and Phe331. In this site, the substrate quaternary ammonium group bind with cation- π interactions. The AChE peripheral anionic site (PAS), which is located at the entry to the active gorge, consists of five amino acids Asp72, Tyr70, Tyr121, Trp279, and Tyr334. This site is important for the interaction with β -amyloid. Two aromatic amino acids Phe288 and Phe290 in AChE, define the acyl pocket (**Figure 7**) (81).

It was shown that the serine and histidine residues, which are located in the esteratic active site, are essential for the activity of AChE (80). The “anionic” subsite performs the interaction with the positively charged quaternary ammonium group of acetylcholine. Thus, it is the binding site for some quaternary ligands that act as inhibitors of AChE. It was shown that the “peripheral” anionic site PAS is involved in substrate inhibition of AChE (82–84).

Notably, some aromatic amino acids from the active site of AChE are substituted by aliphatic ones in BChE (80, 85, 86). AChE has three conserved aromatic residues (Tyr70, Tyr121, and Trp279); they form the aromatic peripheral binding site. None of these aromatic residues is conserved in BChE. Moreover, Phe330 in AChE is substituted by the non-aromatic residue Ala328 in BChE (87).

Figure 7 shows the binding pocket and the crystal structure of acetylcholinesterase of *Torpedo californica* (TcAChE), which was crystallized with the inhibitor N-benzylpiperidine (**E2020**: Donepezil). This compound has a unique orientation along the active-site pocket, expanding from the anionic area of the active site near Trp84 to the anionic site near Trp279 (**Figure 7**) (88–90).

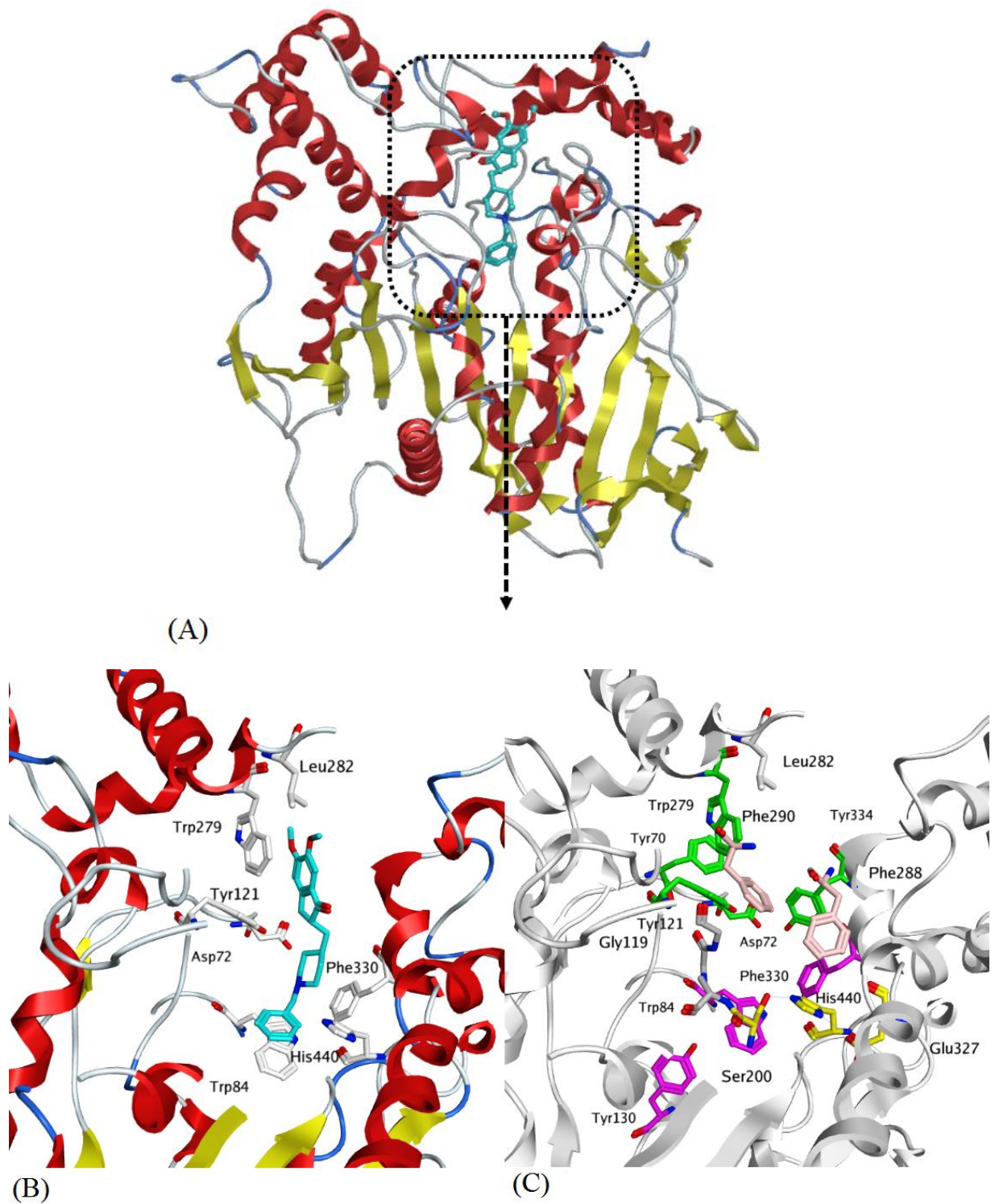


Figure 7: (A): The overall structure of TcAChE, (B): The binding pocket of TcAChE with donepezil (cyan color), β strands are shown in yellow color, α helices are shown in red color, (C): The binding pocket showing the PAS site in green residues, the magenta residues represent the anionic site, whereas the yellow residues reflect the catalytic site, the pink residues represent the acyl site.

1.2.2. Cholinesterase inhibitors

Cholinesterase inhibitors inhibit the cholinesterase enzyme; thereby, the level and duration of ACh action will be increased (77, 91). Consequently, inhibitors of AChE and BChE are essential in managing diseases that exhibit weak neurotransmission mediated by low concentrations of ACh (92, 93).

Several ChE inhibitors have been discovered, such as donepezil, galantamine, rivastigmine, and memantine (**Figure 8**); they are currently available in the market; and used as drugs to treat AD (94).

Physostigmine (**Figure 8**) is the first studied AChE inhibitor in the treatment of AD; it was isolated from the *Calabar bean* (*Physostigma venenosum*) (95). Rivastigmine (**Figure 8**) is a pseudo-irreversible dual AChE and BChE inhibitor. It has a good blood-brain barrier BBB permeability. Furthermore, rivastigmine was approved for the treatment of mild-to-moderate AD and has gained approval for Parkinson's related dementia (94, 96).

Tacrine (**Figure 8**) is an inhibitor for both AChE and BChE (97). Another inhibitor for AChE is donepezil; it was approved to treat mild to moderate AD in 1996 (98). Meanwhile, it increases the Sirt1 enzyme activity (99). Also, galantamine (**Figure 8**) that exists in *Amaryllidaceae* plant family is used as an AChE inhibitor (100). Most of the old discovered traditional inhibitors such as physostigmine, tacrine, donepezil, rivastigmine, and galantamine were mainly obtained from natural products (92).

Phenserine (**Figure 8**), which is derived from physostigmine, is also an AChE inhibitor. It decreases the beta-amyloid peptide formation and has a rapid absorption rate (92, 101). Ganstigmine (**Figure 8**) is the N-oxide of physostigmine. It is 115 times more effective against AChE than against BChE (102). Huperzine-A (HupA) (**Figure 8**) is a highly selective, reversible, and active AChE inhibitor. It is a lycopodium alkaloid derived from a Chinese medicinal plant *Huperzia serrata* (103).

Indeed, the cholinesterase inhibitors, which were derived from traditional compounds like phenserine, and the compounds extracted from natural sources, such as huperzine, have lesser side effects, better CNS permeability, and potency than the old inhibitors.

Importantly, all the inhibitors cannot cure diseases, but they are necessary to stop AD disease from becoming worse (92).

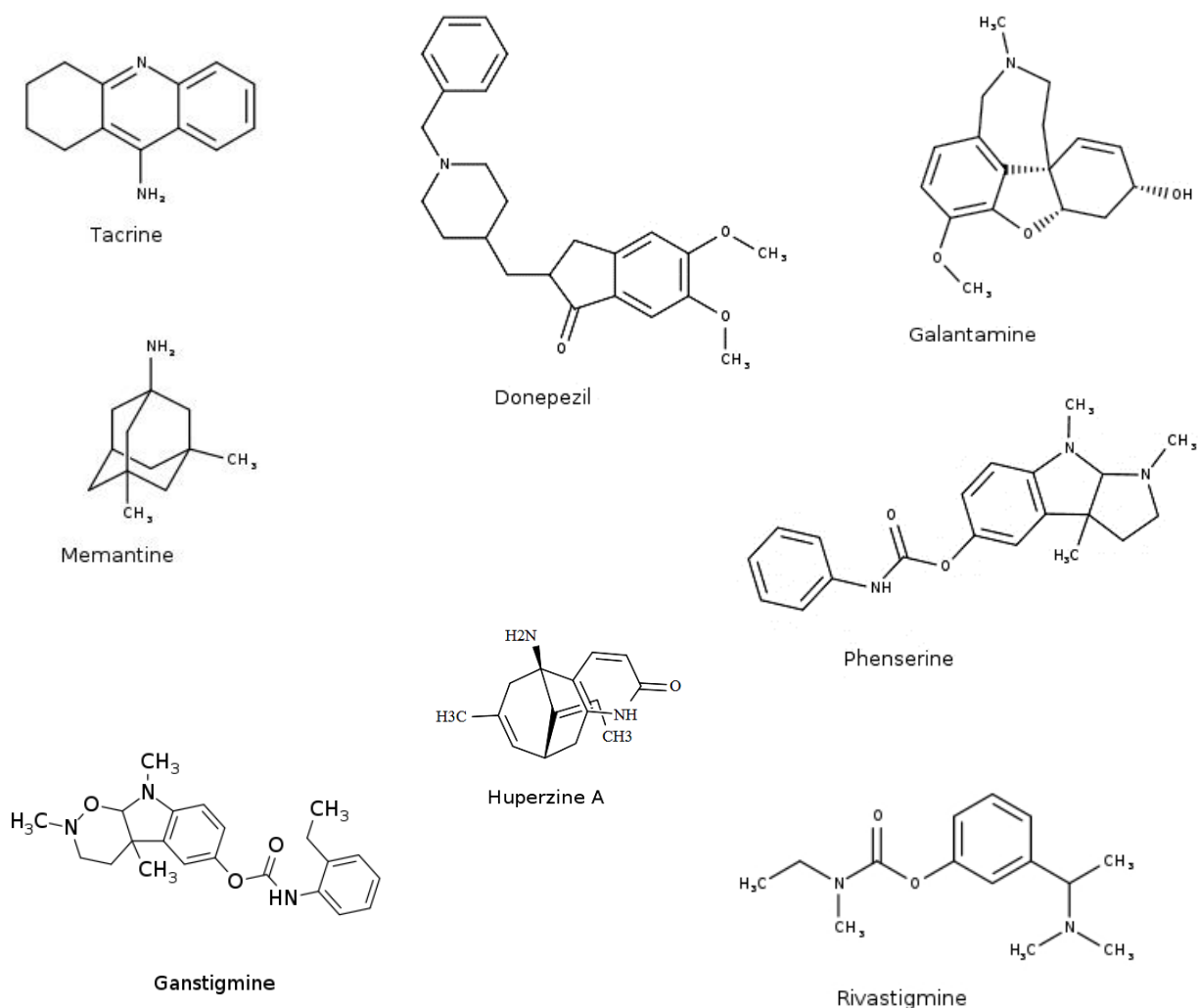


Figure 8: Cholinesterase inhibitors.

1.3. Cholinesterases and sirtuins are reported targets for Alzheimer's disease

Alzheimer's disease is one of the most important diseases of the 21st century besides cancer, strokes, and heart attacks (11). The pathophysiological processes described for AD involve degeneration of the neurons and synapses associated with cholinergic deficiency (104). Also, cholinergic signaling, which is vital in cognition, is gradually lost in AD. Therefore, increasing the levels of acetylcholine is of great importance (105). Alzheimer's disease is a neurodegenerative disorder characterized by the precipitation of amyloid- β peptide ($A\beta$) in the type of amyloid plaques and neurofibrillary tangles in the brain of the patient (76, 106). Interestingly, AChE interacts with the amyloid- β peptide ($A\beta$) and

supports the formation of the amyloid fibril. This interaction between the $A\beta$ peptide and AChE is located close to the peripheral anionic binding site (PAS) of the enzyme (107). Hence, the inhibition of AChE is useful to treat AD (108).

Additionally, the selective inhibition of BChE could considerably raise ACh levels and improve the cognitive functioning of aged rats without any adverse parasympathetic side effects. Consequently, the selective inhibition of BChE could represent a promising clinical treatment strategy for AD (109, 110).

In conclusion, the inhibition of AChE and BChE represents a promising strategy for the development of novel therapeutics for AD because they increase the availability of acetylcholine in the brain regions (76). Thus, both AChE and BChE enzymes represent promising targets for AD and important tools for a deeper explanation into AD's pathology (105).

Several AChE inhibitors are already FDA-approved for treating AD, these drugs can reduce and slow the symptoms of AD, but they cannot stop the destruction of the brain cells (111). Interestingly, many approved drugs have restricted therapeutic capabilities such as poor bioavailability, hepato-toxicity, or non-selectivity, that contribute to side effects like dizziness, diarrhea, nausea, and vomiting. Therefore, discovering new AD drugs is of great importance (112).

On the other hand, the effects of sirtuins on AD were also investigated. Sirt1 has a protective effect in AD and is considered as an essential target in the field of AD (113). Several studies have shown that Sirt1 mediates the adaptive response to calorie restriction; through the calorie restriction, Sirt1 is involved in AD neuropathology (113). Besides, the activation of Sirt1 was shown to be involved in the prevention of amyloid neuropathology. Accordingly, designing drugs that can modulate Sirt1 activity could be significant in AD therapy (114).

1.4. Computer-aided drug design of sirtuin and cholinesterase inhibitors

Great advances in genomics led to a significant increase in the possible therapeutic protein targets available for investigation. These potential targets have increased the demand for

technologies that can rapidly identify several lead drug candidates to fight the common diseases of aging, such as cancer and Alzheimer's disease (AD) (115).

The design of novel drug candidates with high therapeutic properties remains a challenge for the pharmaceutical industry. Traditionally, the drug discovery pipeline for a safe drug requires enormous money and time (116). Thus, identifying new chemical compounds with a high probability of binding to the target protein combined with the desired biological response is one of the main objectives in drug discovery (117). However, the emergence of computer-aided drug design techniques has facilitated the drug discovery process.

Computer-aided drug design methods use the structural information of either the target (structure-based) or known active ligand (ligand-based) to promote the identification of promising candidate drugs. Complementing these computational methods with wet-lab procedures has a powerful impact on rational drug design (118).

Many efforts and multiple computational methods have been applied to identify novel sirtuin and AChE modulators, such as fragment-based screening, focused library screening, and computer-based screening in combination with *in vitro* tests (119–121).

Notably, computer-aided drug design techniques were also used to discover new drugs from compounds of natural origin. Hence, natural products derived scaffolds can serve as additional starting points for lead optimization and drug design (122).

1.5. Sirtuins and cholinesterase inhibitors derived from natural products

Natural products (NPs) play a significant role in drug discovery. Besides the often reported bioavailability issues, some of the natural products also have acceptable absorption, distribution, metabolism excretion, and toxicology properties (ADMET) (123). Moreover, they have exhibited a therapeutic effect in fighting cancer for over 40 years (124). NPs tend to be more hydrophilic. This property makes them substrates for transporter systems as they need to be transferred into the cell to begin their mechanism of action. Furthermore, statistical analysis of the structural properties of NPs and synthetic compounds has proved that NPs occupy a big, diverse, and drug-like chemical space (122, 123, 125, 126). Besides, drugs derived from natural products can serve as drug leads for anti-cancer, anti-microbial, and anti-inflammatory drugs (127).

It was shown that the chemotherapeutic drugs used to treat cancer are generally associated with high toxicity, resistance, and undesirable side-effects. Therefore the demand for novel drugs that have fewer side-effects and greater therapeutic efficiency in fighting cancer has increased; (124). Importantly, the compounds derived from plant and natural products have been a significant source of several clinically anti-cancer compounds (128).

Several NPs and their derivatives act as sirtuin or AChE inhibitors; some of them could be used in cancer and neurodegenerative diseases treatment. Thus, several natural products show promising effects for AD treatment (129). The most studied natural product from polyphenols is resveratrol, which is an activator of Sirt1; it is found in grape seed as well as in red wine. Resveratrol has neuroprotective effects; it reduces the insulin-like growth factor-1 expression. It can also be used in AD treatment (69, 130–132). Likewise, a natural compound (3,2',3',4'-tetrahydroxychalcone) was shown to have deacetylase inhibitory properties against Sirt1. It inhibits cell growth in HEK293T (human embryonic kidney cell) cells (133). Curcumin is a natural bioactive phytochemical compound that has antioxidant and anti-inflammatory characteristics. Additionally, curcumin increases Sirt1 activity; it has anti-cancer activity and anti-inflammatory properties. Importantly, curcumin prevents the development of colon cancer by decreasing Sirt1. (134).

Remarkably, several plant extracts exhibit inhibitory activity against acetylcholinesterase, especially the species which belong to *Amaryllidaceae*, *Apiaceae*, *Asteraceae*, *Fabaceae*, and *Fumariaceae*. The main isolated compounds from this species are alkaloids (135). Furthermore, the AChE inhibitor galantamine, which is one of the most used drugs for AD treatment today, is an alkaloid extracted from *Galanthus woronowii*, *Narcissus spp.* (82, 136). Likewise, rosmarinic acid is a natural product identified as a cholinesterase inhibitor (137). Also, different compounds derived from traditional Chinese medicine and several plant-derived flavonoids have been discovered as AChE inhibitors (138, 139).

2. Aim of the Work

This work aimed to design novel inhibitors of the two protein classes, sirtuin and acetylcholinesterases. The discovered compounds can be used to further analyze the biological role of the individual target proteins for several diseases and disorders such as Alzheimer's disease and cancer. In addition, molecular docking and structural analysis are helpful in rationalizing the binding mode and structure-activity relationship of newly developed inhibitors series.

Despite many biological studies on Sirt1, few compounds have been found to inhibit Sirt1, and only one small molecule compound, EX-527 (Selisistat), is currently in clinical trials for the treatment of Huntington disease; it has reached phase III clinical trials. Therefore, the goal was to find new Sirt1 inhibitors using computational methods and to test them using cellular assay.

Due to the highly conserved amino acids sequence and the high similarity of the structure of the catalytic core among the members of the sirtuins family, it is challenging to find selective sirtuin inhibitors. Most of the Sirt5 inhibitors have weak potency or lack isoform selectivity. Therefore, discovering new effective and selective Sirt5 inhibitors with the support of computational studies represents a promising strategy.

Natural products are additional sources for new lead compounds. They are useful for further modification in drug development and the lead optimization process, so computational methods are applied in the current work in order to identify compounds from natural products that can inhibit sirtuins.

Sirt2 is another promising target of the sirtuins family that was investigated in this work. We use computational methods to identify selective Sirt2 inhibitors with improved solubility, and the binding mode of the inhibitors is studied to provide a potential explanation of the activity.

Sirt4 has been shown to be a tumor-suppressive agent and therefore represents a promising therapeutic target for cancer treatment. However, until now, there are no reported inhibitors for this enzyme. Consequently, this study aimed to develop small molecule Sirt4 inhibitors. At the beginning of the project, there was no X-ray structure available for Sirt4, and therefore Sirt4 homology models were initially used to set up virtual screening experiments. Later the first crystal structure of *Xenopus tropicalis* Sirt4 was solved by our collaborator and was subsequently applied to find novel lead structures.

Another group of targets that are addressed in this study is cholinesterases. Several inhibitors of cholinesterase are available on the market. However, most of them have low bioavailability, limited therapeutic power, side effects, hepato-toxicity, or non-selectivity. Thus, part of this research aimed to develop selective inhibitors that target AChE and BChE in order to treat Alzheimer's disease.

All of the computer-based studies in the current work were carried out in close collaborations with research groups to perform the chemical optimization together with X-ray crystallography and the *in vitro* and cellular testing. Thus, the applied computational methods and the obtained results were continuously validated and adapted in order to increase the accuracy and success of *in silico* studies.

3. Methods and Materials

3.1. Computer-aided drug design (CADD)

The use of computer programs in pharmaceutical research is typically referred to as computer-aided drug design (CADD). CADD approaches are effective tools for drug discovery. Therefore a trend towards the use of CADD has gained considerable prominence in the drug discovery process. Besides, CADD methods have several benefits, such as cost savings and the predictive power that supports the selection of promising candidates for chemical optimization (140). Hence, CADD approaches were applied in the current work, which includes the following methods:

3.1.1. Virtual screening

Virtual screening (VS) is a cost-effective strategy employed in lead discovery programs to identify potential drug candidates (141, 142). It is a promising tool for hit identification. Recent studies have demonstrated its successful application in drug discovery (141). VS involves the computational evaluation of databases of many candidate compounds that have to be docked and scored into the protein binding site of interest.

The virtual screening methods can be divided into two procedures:

- **Ligand-based virtual screening:** In this screening procedure, the 2D or 3D chemical structures of known active compounds are applied to retrieve other compounds of interest within large databases of compounds. This screening can be carried out using a similarity search with different metrics or simple substructure search (143).
- **Structure-based virtual screening:** In this procedure, the 3D structure of the target protein is important, and compounds from databases can be docked into the active site of the protein structure using a docking program. Docking scores can then be used to rank the molecules based on how well they fit and interact with the residues within the binding pocket of the protein of interest (144). When the 3D structure of the target is not available, a virtual model can be generated using homology modeling of the closest reported protein target for which the 3D structure is known and available (143, 145–147).

The initial stage of any virtual screening typically includes a pre-filtering of the database. One of these filters is Pan Assay Interference Compounds (PAINS) filter, which identifies chemically reactive and assay interfering compounds (148, 149). The best-known filter for the studied compounds is Lipinski's rule of five, which identifies four physicochemical parameter ranges ($\log P \leq 5$, H bond donors ≤ 5 , H bond acceptors ≤ 10 , MW ≤ 500) (150). These parameters are associated with acceptable aqueous solubility and intestinal permeability criteria of the studied compounds (151). Furthermore, filters that predict *in vitro* properties of the molecules like absorption, distribution, metabolism, excretion, and toxicity (ADMET) are often used to prepare focused libraries; in order to eliminate the compounds with undesirable pharmacokinetics and focus on potential drug candidates with good bioavailability (152).

In our work, the virtual screening of hSirt4 inhibitors was done, and a total of 1.3 million compounds from Princeton Bio Molecular Research, Inc. were docked into hSirt4. Likewise, in the virtual screening of Sirt1 inhibitors, we screened a collected library of commercially available compounds and identified thiocyanates as novel Sirt1 inhibitors. While a library of 3-substituted succinyl CPS1 peptides was studied to analyze the binding mode of peptidic Sirt5 inhibitors. Next, removal of the compounds forming unfavorable conformations within the binding sites in all targets was done.

3.1.2. Molecular docking

Molecular docking represents an *in silico* structure-based method. It is widely used in drug discovery for predicting the pose of a ligand and its ligand-protein interaction. A small molecule (ligand) can adopt different conformations within the active site of a large molecule (protein). It is also an essential tool to understand how chemical compounds interact with their targets (153).

One of the commonly used software for docking is Glide, which identifies the binding mode of the compound by Monte Carlo sampling method (154). The other software is GOLD (155), which is based on the genetic algorithm for protein-ligand docking. It calculates the energy functions using different scoring functions: GoldScore, ChemScore, ASP, and PLP Score (156).

In this work, all protein X-ray structures were downloaded from the PDB (28). The structures of the proteins were prepared by using the structure preparation module implemented in Molecular Operating Environment (MOE) software. Additionally, the

protonation states of the structures were determined using the protonate 3D module in MOE (157–159). Protein structures were energy minimized using Amber12: EHT force field or Amber 99, tethering of 0.5 Å for all the atoms during the minimization step was done (160).

The ligands in the docking sites were removed from the structures before the docking process. The docking was carried out using the scoring functions Gold score, PLP Score within the GOLD 5.2 (155, 161), or Glide SP and Glide XP scores implemented in Schrödinger Suite 2012-5.8. The position of the native ligand or selected residue in the binding site were used to define the binding site. The resulting docking poses were rescored using the Amber12: EHT force field and the MM-GB/SA approach (162–165).

The preparation of the ligands was done using LigPrep tool in Maestro (Schrödinger, LLC, New York, NY, USA, 2014) (166) or using the MMFF94x force field implemented in MOE (Molecular Operating Environment, Version 2014.09; Chemical Computing Group Inc., Montreal, Canada). The preparation process implicated 3D protonation at $\text{pH} = 7.3 \pm 0.2$ using Epik module. After that, an energy minimization step was done using the MMFF94 force field (167). The conformer generation module of OMEGA implemented in OpenEye Scientific Software was used to generate twenty conformers for each ligand molecule (168). Importantly, pan-Assay Interference (PAINS) filters were applied in this work using Schrodinger's Canvas tool to remove unwanted compounds before *in vitro* testing.

3.1.3. Homology modeling

Homology modeling is the development process of a structural model of a target protein from a known template structure. The final template of the protein is chosen based on sequence similarity; one or more structural templates can be selected. A pairwise or, in some cases, multiple-sequence alignment between the target and the template is generated. Several methods are employed to generate 3D models from the sequence of the target based on its templates. There are several methods for model building; one method is the rigid-body assembly method. In this method, the structure of the protein is divided into basic conserved core regions, loops, and side chains. Thus, the building of the 3D structure of the protein is done by putting the rigid bodies together, which are taken from the aligned template protein structures. Another method is the spatial restraint method; in this method, the model is built by meeting restraints from the template structure. The restraints are placed on the target structure, depending on the alignment. Such restraints are defined by

stereochemical restraints on the bond angle, dihedral angles, bond length, and van der waals contact distances. This method can be done with Modeller program. Finally, a refining and validation stage of the models should be done (169–172).

Modeller program is found to be a good tool in homology modeling besides MOE (172, 173). One basic requirement in the homology modeling process is the study of the model's stereochemistry; this analysis is carried out using parameters such as the length of the bond and angle of torsion. Procheck (174) is a common tool used to provides a comprehensive analysis of protein structure stereochemistry of the model. Ramachandran plot is also a powerful defining factor of protein structure quality. Residues with a problem of stereochemistry will fall out of the acceptable regions of the Ramachandran plot (170).

In the current work, the sequence of the protein was taken from UniProt database and saved as a FASTA file (175). A following protein BLAST search was performed to identify the proteins that reveal a sequence similarity with known structures (templates) (176).

The target-template alignment was done in MOE. Homology models were then generated using MOE (Molecular Operating Environment, Version 2014.09; Chemical Computing Group Inc., Montreal, Canada) and Modeller program version 9.11 (172). Consequently, five homology models of protein structures were generated. The model with the most favorable DOPE (Discrete Optimized Protein Energy) score was selected (177). The stereochemical quality of the models was analyzed using Procheck program.

3.1.4. Molecular Dynamics (MD) simulations

MD simulations have been applied successfully in drug discovery; MD simulations are valuable tools for investigating the structure of the protein. The ligand causes conformational changes upon binding. These changes are not usually sampled when the ligand is absent.

There are several types of MD simulations; one is the conventional MD simulations (cMD), which describe small conformational fluctuations of the protein structure. The other type of MD simulations is the accelerated molecular dynamics (aMD). It is an enhanced sampling method that improves the sampling of conformational space by reducing energy barriers separating different system states. Thus, the sampling of conformational space that cannot be easily obtained in a conventional (cMD) simulation can be done using aMD. (178, 179).

In the presented work, cMD and aMD simulations were performed using the program AMBER 12 and AMBER 2003 force field (160). The atom types of the ligand and AM1-BCC atomic charges were generated using the Antechamber module. Ligand parameters were obtained from the general AMBER force field GAFF (180). The LEaP module in AMBER, was used to prepare the ligand-protein complex, add counter ions, solvate, and prepare the parameter, topology, and coordinate data. The system was solvated using the water model TIP3BOX with a space of 10 Å. The steps of minimization were done. The temperature of the system was then equilibrated at 300 K. The protein-ligand complex was submitted to 20 ns cMD simulations and 80 ns aMD simulations.

3.2. *In vitro* assay

3.2.1. Sirtuins assay

Several enzymatic *in vitro* assays were used by the collaborators in the different projects (Prof. Dr. Manfred Jung: Albert-Ludwigs University, Prof. Dr. Clemens Steegborn: University of Bayreuth, Prof. Dr. Mike Schutkowski: MLU Halle-Wittenberg).

For Sirt1 and Sirt2, a fluorescence-based assay was used (181). Human Sirt1 or Sirt2 were first treated with the assay buffer, NAD⁺, and substrate Z-(Ac) Lys-AMC called ZMAL. The inhibitors were solved in DMSO. The enzyme concentration was adjusted to a final substrate conversion of 15–30%. The incubation time was four hours at 37°C and 150 rpm. The catalytic reaction deacetylation was stopped by adding a developer solution containing trypsin and nicotinamide and incubated almost 20 min at 37°C and 150 rpm.

The fluorescence intensity was calculated in a microplate reader (BMG Polarstar, λ_{ex} 390nm, λ_{em} 460nm). All compounds were tested with autofluorescence, quenching of amino methyl coumarin (AMC), and inhibition of trypsin under conditions of the assay. The inhibitory effect was determined by using the DMSO-controls as a reference. The GraphPad Prism program was used to determine the values of IC₅₀.

In case of Sirt4, peptide- and FdL-based activity assays were done. The coupled continuous assay was performed (182). The assays were performed with hSirt4 or XSirt4 in sodium phosphate buffer pH 7.8, DMSO, and α -ketoglutarate, NADPH, nicotinamidase, GDH, and the substrate peptide and NAD⁺. The reactions were incubated at room temperature, and the absorption at 340 nm was monitored in a LAMBDA Scan plate reader (MWG Biotech).

The fluorescence-based “FdL” assay was done in Tris/HCl and NaCl using hSirt4, fluo-HMG-Lys substrate, and NAD⁺. After 20 min NAM, and trypsin in assay buffer was added. Fluorescence was detected with excitation wavelength 365 nm and emission wavelength 465 nm using a FluoDia T70 (PTI Technologies).

For Sirt5, a fluorescence-based assay was used. The inhibitory activity of the compounds was tested in black low-binding 96-well microtiter plates, and each well-contained substrate AbzGVLK(glutaryl)AY(NO₂)GV-NH₂, NAD⁺, trypsin, Sirt5, DMSO, and inhibitor in assay buffer. The assay buffer contained Tris, NaCl, and MgCl₂ at pH 7.8. The reaction mixture without enzymes was incubated for 5 min at 37 °C, followed by pipetting trypsin. Sirt5 was added, the fluorescence was measured at a wavelength of 320 nm and an emission wavelength of 420 nm. The measurements were carried out in a plate reader (TECAN).

3.2.2. Cholinesterase assay

This work was done by our collaborators at Martin Luther University (Institute of chemistry- Prof. Dr. René Csuk)

The compounds and the standard inhibitor galantamine hydrobromide were applied to Ellman’s assays to measure their ability to inhibit the AChE and BChE (183). Thus, a mixture of different compounds solutions, DTNB solution and enzyme solution (AChE or BChE), were prepared. The reaction of the enzyme was started by adding the substrate. The assays employed a TECAN SpectraFluorPlus working in kinetic mode. The absorbance was calculated at $\lambda = 415$ nm at 30 °C. The inhibition mode and K_i were calculated using Dixon, Lineweaver-Burk, and CornishBowden plots. The IC_{50} values were calculated using GraphPad Prism 5 software.

3.3. Cellular assay used for Sirt1 inhibitors

This work was done by the group of Prof. Dr. Manfred Jung, University of Freiburg, using several cellular assays.

Since the level of phosphorylation of H2AX in mice embryonic fibroblasts (MEFs) decreases if Sirt1 is inhibited (184), γ H2AX level determination assay was performed. In this assay, the inhibitors reduced the phosphorylation level of the DNA damage sensor Histone Family Member X (H2AX). Thereby DNA damage will be reduced. The same reduction of γ H2AX/H2AX levels is observed in Sirt1 knockout cells and after the treatment of wild type MEFs with the selective Sirt1 inhibitor EX-527.

Another kind of assay is the cell proliferation assay with HeLa or MCF7 cells. In these assays, Sirt1 thiocyanate inhibitors were evaluated for their antiproliferative activity against different human cancer cells.

Additionally, since the deubiquitinases target (DUBs) could also be inhibited by thiocyanates, therefore, DUB Labeling on HEK293T Cell Lysate assay was done using HEK293T cell lysate (human embryonic kidney cells, human) to test the selectivity of the inhibitors against deubiquitinases (DUBs) (185).

For further cellular assay details, please see the publications provided in results and discussion.

4. Results and Discussion

4.1. Manuscript 1: KATching-Up on Small Molecule Modulators of Lysine Acetyltransferases.

R. P., Simon, D., Robaa, Z., Alhalabi, W., Sippl, M., Jung.

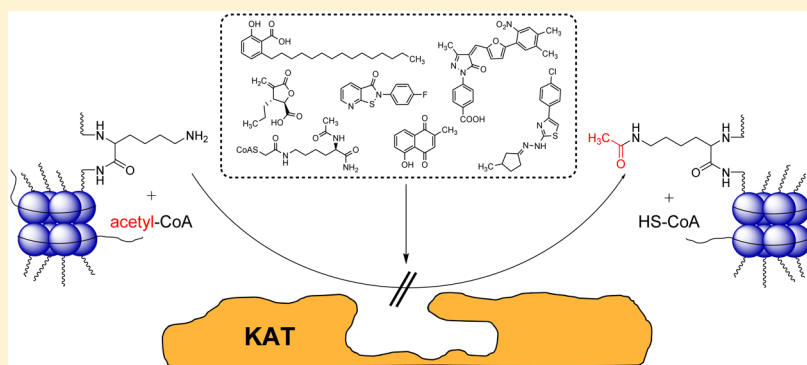
Journal of medicinal chemistry. 59, 1249–1270 (2016).

KATching-Up on Small Molecule Modulators of Lysine Acetyltransferases

Roman P. Simon,[†] Dina Robaa,[‡] Zayan Alhalabi,[‡] Wolfgang Sippl,[‡] and Manfred Jung^{*,†}

[†]Institute of Pharmaceutical Sciences, University of Freiburg, Albertstraße 25, Freiburg 79104, Germany

[‡]Department of Pharmaceutical Chemistry, University Halle-Wittenberg, Halle/Saale 06120, Germany



ABSTRACT: The reversible acetylation of lysines is one of the best characterized epigenetic modifications. Its involvement in many key physiological and pathological processes has been documented in numerous studies. Lysine deacetylases (KDACs) and acetyltransferases (KATs) maintain the acetylation equilibrium at histones but also many other proteins. Besides acetylation, also other acyl groups are reversibly installed at the side chain of lysines in proteins. Because of their involvement in disease, KDACs and KATs were proposed to be promising drug targets, and for KDACs, indeed, five inhibitors are now approved for human use. While there is a similar level of evidence for the potential of KATs as drug targets, no inhibitor is in clinical trials. Here, we review the evidence for the diverse roles of KATs in disease pathology, provide an overview of structural features and the available modulators, including those targeting the bromodomains of KATs, and present an outlook.

INTRODUCTION

For more than 50 years, the enzymatic acetylation of histones and other proteins and the functional consequences have been topics of scientific interest. A wide range of experimental efforts identified protein acetylation to be one of the key mechanisms in the regulation of biological functions.

The transfer or removal of acetyl groups to ϵ -amino group of lysine residues is mediated by two classes of enzymes. Histone acetyltransferases (HATs) catalyze the covalent attachment of acetyl groups to lysine residues of histones and other proteins by using acetyl-coenzyme A (acetyl-CoA) as a cofactor. Histone deacetylases (HDACs) conversely catalyze the amide hydrolysis of acetylated lysine. The attachment of acetyl groups to lysine residues goes along with two functional consequences. First, the positive charge of physiologically protonated ϵ -amino groups is abolished, resulting in altered electrostatic as well as steric properties of the affected protein region. Second, acetylation serves as a mark for distinct “reader” domains, which comprise specialized tertiary structures (e.g., bromodomains) in proteins that undergo a selective interaction with acetylated lysines.¹

The most studied targets of HATs are histone proteins. Together with other epigenetic posttranslational modifications (PTMs) (e.g., phosphorylation, methylation, ubiquitinylation, sumoylation, ADP ribosylation), acetylation serves as a

regulating tool to control transcriptional activity of specific chromatin loci.² Upon acetylation, local affinity of the modified histone protein to negatively charged DNA is decreased, resulting in a less condensed chromatin structure and in exposure of promoter sites. As a consequence of the increased accessibility, the DNA globally becomes more prone to access of the transcriptional machinery.³ In addition, transcription factors and other regulatory elements are recruited in a modification-specific manner to the relaxed promoter locus by interaction of specialized reader domains with acetyl lysine moieties.^{1,4} Thus, HATs and histone acetylation are functionally linked with the control of transcription activation, replication, and DNA damage repair.⁵ Mass spectrometry-based proteomics targeting the acetylome revealed that this kind of PTM occurs not just on histones but on thousands of other acetylation sites in more than 1500 proteins. Affected proteins play vital roles in fundamental cellular processes like cell division, signaling, apoptosis, and metabolism.^{6,7} Because of the broad acceptance of substrates, histone acetyltransferases and deacetylases are hence often referred to as lysine

Special Issue: Epigenetics

Received: September 28, 2015

Published: December 23, 2015

Table 1. Type A Lysine Acetyltransferases (KATs)

KAT	synonym	organism	physiological histone substrates	associated complexes/proteins
GNAT Family				
Gcn5	KAT2	<i>S. cerevisiae</i> , <i>D. melanogaster</i>	H3K9,14,18,23,36/H2B	SAGA, SLIK, ADA, HAT-A2, ATAC
hGcn5	KAT2A	<i>H. sapiens</i>	H3K9,14,18/H2B	STAGA, TFTC
PCAF	KAT2B	<i>H. sapiens</i>	H3K9,14,18/H2B	PCAF
Elp3	KAT9	<i>H. sapiens</i> , <i>S. cerevisiae</i> , <i>D. melanogaster</i>	H3	elongator
Hpa2	KAT10	<i>S. cerevisiae</i>	H3K14/H4K5,12	Hpa2
Hpa3		<i>S. cerevisiae</i>	H4K8	
Nut1		<i>S. cerevisiae</i>	H3 > H4	mediator
p300/CBP Family				
dCBP	KAT3	<i>D. melanogaster</i>	H4K5,8/H3K14,18	
CBP	KAT3A	<i>H. sapiens</i>	H2AK5/H2BK12,15	
p300	KAT3B	<i>H. sapiens</i>	H2AK5/H2BK12,15	
MYST Family				
Tip60	KAT5	<i>H. sapiens</i> , <i>D. melanogaster</i>	H4K5,8,12,16	TIP60
Esa1	KAT5	<i>S. cerevisiae</i>	H4K5,8,12,16/H2BK4,7	NuA4, Pic. NuA4
Sas3	KAT6	<i>S. cerevisiae</i>	H3K14,23	NuA3
MOZ/MYST3	KAT6A	<i>H. sapiens</i>	H3K14	MOZ/MORF
MORF/MYST4	KAT6B	<i>H. sapiens</i>	H3K14	MOZ/MORF
HBO1/MYST2	KAT7	<i>H. sapiens</i>	H4K5,8,12 > H3	HBO1
MOF/MYST1	KAT8	<i>H. sapiens</i> , <i>D. melanogaster</i>	H4K16	MSL
Sas2	KAT8	<i>S. cerevisiae</i>	H4K16	SAS
Transcription Factors Containing KAT Activity				
TAF1/TBP	KAT4	<i>H. sapiens</i> , <i>S. cerevisiae</i> , <i>D. melanogaster</i>	H3 > H4	TFIID
TFIIIC90	KAT12	<i>H. sapiens</i>	H3K9,14,18	TFIIIC
Nuclear Receptor Coactivators				
SRC1	KAT13A	<i>H. sapiens</i>	H3/H4	
AIB1/ACTR/SRC3	KAT13B	<i>H. sapiens</i>	H3/H4	
p160	KAT13C	<i>H. sapiens</i>	H3/H4	
CLOCK	KAT13D	<i>H. sapiens</i>	H3K9,14	
Other				
Rtt109	KAT11	<i>S. cerevisiae</i>	H3K9,27,56	
CMLO3		<i>X. levis</i>	H4	

acetyltransferases (KATs) and lysine deacetylases (KDACs), respectively.⁸ In concert, these enzymes dynamically regulate the lysine acetylation levels within the cellular proteome. This acetylation equilibrium is adjusted in response to cellular stimuli like autoacetylation, protein–protein interactions, phosphorylation, or the cellular acetyl-CoA level, leading to altered gene transcription and subsequently to phenotype adaption.⁹

Aberrant acetylation levels have been connected with a diversity of disease phenotypes including cancer, neurological disorders, and cardiovascular and metabolic malignancies.^{10–14} Hence, KAT enzymes seem to be deeply involved in the manifestation and progression of such diseases and therefore the elucidation of their precise mechanism is required to assess their potential as possible drug targets and small molecule modulators are of high interest for probing these pathways and as potential drugs.

■ FIFTY YEARS OF LYSINE ACETYLATION

In 1964, Allfrey and colleagues proposed an innovative hypothesis of reversible posttranslational histone modifications being a dynamic regulatory mechanism for RNA synthesis after they reported the incorporation of acetyl and methyl groups into histone proteins as a result of treating isolated nuclei with radiolabeled acetate (acetate-2-¹⁴C) and methionine (methionine-methyl-¹⁴C), respectively. The incorporation of these modifications was found to happen independently of the

transcription process, as they were still detected in nuclei pretreated with the transcription inhibitor puromycin. Moreover, the modifications decreased the histone-mediated repression of RNA synthesis.¹⁵ In consecutive work, they showed that the ϵ -amino group of lysine residues is the target of acetylation.¹⁶ During the following years, histone acetylation was linked to gene activation by a number of different studies. In 1978, sodium butyrate was described as a histone deacetylase inhibitor by Davie and co-workers.¹⁷ This was a milestone, as for the first time it was shown that epigenetic regulators could be targeted by small molecules. It took about 20 years until the first KAT enzyme Gcn5 (general control nonderepressible 5, p55) was identified by Brownell and Allis in 1995. In their studies, an acetyltransferase activity gel assay was employed, which detects the incorporation of ³H-acetate into histone substrates after electrophoretic separation of nuclear extracts in a SDS/polyacrylamide gel matrix.¹⁸ One year later, the Gottschling group reported the isolation and cloning of Hat1 from *Saccharomyces cerevisiae* lysates as the first KAT exhibiting cytosolic localization.¹⁹ The identification of distinct enzymes, which catalyze the transfer of acetyl groups from acetyl-CoA to histone protein substrates, formed the starting point for extensive studies about the precise mechanism and functional consequence of this PTM. New insights into structural aspects of chromatin organization and histone function were provided when Luger et al. solved the nucleosome particle crystal structure in 1997.²⁰ It was the same year that Grant et al.

identified and partially characterized the first KAT-containing protein complex SAGA (Spt-Ada-Gcn5-acetyltransferase) from *Saccharomyces cerevisiae* with its catalytic subunit Gcn5.²¹ Their findings added another level of complexity to the field of acetyltransferases because it demonstrated that their regulatory activity in a cellular context depends on multidomain protein complexes with a specific composition. The starting point of KAT inhibitor discovery was set two years later when Marmorstein and Allis published the crystal structure of Gcn5 as a nascent acetyltransferase as well as in a context with the cofactor acetyl-CoA and the physiologic ligand histone H3.²² Following these discoveries, Cole and colleagues synthesized the first KAT inhibitors. Inspired by earlier observations on serotonin *N*-acetyltransferases, they covalently linked lysine residues to CoA to generate pseudo bisubstrates of the addressed enzymes.²³ In 2006, Kim et al. performed the first proteomic screen targeting lysine acetylation and identified 388 acetylation sites in 195 proteins.⁷ Over the past few years, advances in assay technology and in computational methods have led to an increased understanding of acetylation biology and pathology.^{6,24} Furthermore, a growing number of other acyl groups are identified to be the subject of reversible attachment and cleavage on lysines in proteins. Examples are formyl, propionyl, butyryl, crotonyl, malonyl, succinyl, or long chain fatty acids.²⁵ There is no doubt that expanding on these observations will elucidate the full potential of the field of lysine acylation.

■ ENZYMES AND ENZYME FAMILIES

After the initial discovery of Hat1 and Gcn5, biological experiments led to the identification of additional KAT activity-containing enzymes that are classified according to their preferred cellular localization. Type B KATs share cytoplasmic localization and acetylate nascent histones to facilitate translocation into the nucleus, where the histone proteins are deacetylated and subsequently incorporated into chromatin fibers. Hat1 (KAT1) is one of two members of type B KATs. It is highly conserved through evolution in eukaryotes and acetylates free (not in a nucleosome) H4 protein on lysine residues 5 and 12, in humans also on H2A lysine residue 5. Together with the WD40 protein Hat2, Hat1 forms the Hat1/2 complex, which exhibits 10-fold increased activity compared to native Hat1. The intriguing observation that Hat1 is not solely found in the cytoplasm but also in the nucleus suggests that the enzyme activity shuttles between different cell compartments.²⁶ The second member of type B KATs is Hat4, which is located in the Golgi apparatus where it catalyzes the acetylation of H4 protein on position 79 and 91.²⁷ Type A KATs comprise a number of heterogenic enzymes that share nuclear localization. On the basis of their structural homology and catalytic mechanism, these enzymes are grouped into distinct families (Table 1).

The GNAT (Gcn5 related *N*-acetyltransferase) family includes the enzymes Gcn5,¹⁸ PCAF (p300/CBP associated factor),²⁸ Elp3,²⁹ Hpa2/3,³⁰ and Nut1.³¹ A characteristic feature of this enzyme family is the presence of up to four sequence motifs (A–D) with motif C being almost exclusively found in GNAT family enzymes. The A motif is the most highly conserved region, and it contains an acetyl-CoA binding domain that is defined by an Arg/Gln-X-X-Gly-X-Gly/Ala segment.³² This segment is not limited to GNAT enzymes, but also found in other KAT families. While the catalytic domains of KATs show high structural homology within a certain family,

enzymes differ in their N- and C-terminal regions, which are responsible for recognition, positioning, and binding of substrates. Structural motifs within these regions, like bromo- and chromodomains, zinc binding moieties, and cysteine/histidine rich modules (PHD, TAZ, ZZ) promote the target structure diversity.³³ One example for substrate discrimination by such structural motifs is Gcn5. Human Gcn5 can be distinguished from its yeast homologue by a 400-residue N-terminal region. Under in vitro conditions, recombinant human Gcn5 acetylates free histone H3 on lysine 14 and, to a minor degree, histone H4 on lysine 8 and 16. It is remarkable that in contrast to yeast Gcn5, which targets the same substrate residues, the human homologue is capable of acetylating histones in a nucleosomal context, indicating the role of the N-terminal region in substrate recognition.⁵ PCAF and human Gcn5 share about 80% sequence similarity and both exhibit site preference for in vitro H3K14 acetylation within free or nucleosomal histones. On the cellular level, the substrate pattern is shifted toward multiple H3 and H2B acetylation sites, stating that recombinant enzymes may differ in substrate specificity and turnover comparing in vitro and in vivo conditions.³⁴ Like the most KAT enzymes, Gcn5 and PCAF natively occur as part of multiprotein complexes. Functional interaction between subunits, as well as different PTMs on substrate or protein structures, direct affinity pattern to the more physiological substrates. Together, GNAT family enzymes and their multiprotein complexes are generally involved in transcriptional activation, elongation and DNA damage repair.³⁵

The ubiquitously expressed and metazoan specific KATs p300 and CBP (CREB-binding protein) form the p300/CBP family. Both enzymes share close structural and functional homology and are competent to acetylate all four histone proteins under in vitro conditions. The p300/CBP-mediated transfer of acetyl groups comprises a Theorell–Chance mechanism, which is characterized by stable binding of the cofactor acetyl-CoA followed by transient and rather weak association of the lysine substrate to the enzyme. This catalytic mechanism is distinct from the GNAT and MYST KAT families and may contribute to the broad substrate acceptance of p300/CBP. On molecular level, p300 and CBP interact with a variety of transcription factors and coactivators to form regulatory complexes at promoter regions. In this way, they stimulate transcription of specific genes and serve as inciting regulatory elements. About 100 protein substrates have been described for p300/CBP so far.³⁶ Interestingly, while being intensively studied in mammals, plant orthologues of p300/CBP have also been found and characterized, suggesting a fundamental functional implication of this enzyme family in all metazoan organisms.³⁷

The MYST family is named after the initially identified members (MOZ (monocytic leukemia zinc finger protein), Ybf2 (Sas3), Sas2 (something about silencing), and Tip60 (Tat-interactive protein)).³⁸ These enzymes show sequence similarities, which reaches a remarkable high degree in a particular MYST homology region within the catalytic domain. Like in the GNAT enzymes discussed above, the highly conserved cofactor-binding motif A is also present in the structure of MYST family members.³⁹ The acetyltransferase MOZ targets histone H3 lysine residue 14 and is correlated with transcription activation.⁸ Sas2 and Sas3 are involved in transcriptional silencing processes in *S. cerevisiae*.⁴⁰ Tip60 was the first reported human member of the MYST family with

preference for H4 acetylation. Transcriptional activation and DNA damage response are mediated by the acetylase activity of this enzyme.⁴¹ Following the founding members, more MYST family enzymes were identified and characterized. The yeast enzyme Esa1 is a homologue of human Tip60 and the catalytic subunit of the NuA4 complex. This complex promotes H4 acetylation and subsequently stimulates transcription of genes that are essential for cell cycle progression.⁴² The *in vivo* activity and specificity of almost all MYST family enzymes is highly determined by the composition of their protein complexes. HBO1 (HAT bound to ORC1) interacts with subunits of the origin of replication complex, consequently playing a functional role in DNA replication.⁴³ The isolated HBO1 complex acetylates histones H4 at position 5, 8, and 12 and less effectively H3, whereas recombinant HBO1 shows no significant acetylase activity, implicating protein–protein interactions and *in vivo* modifications in efficient substrate recognition and turn over.^{8,43} A close homologue to the MYST family founding member MOZ is the transcription activator MORF (MOZ related factor). While recombinant and full-length MORF catalyzes acetylation of H4 and H3 protein, under physiological condition solely histone H3 is targeted.^{8,44} The product of the *mof* (males absent on the first) gene represents one more member of this KAT family. The enzyme was identified in the course of studies targeting dosage-compensation of the X-chromosome in *D. melanogaster*.⁴⁵ MOF is related to the yeast enzyme Sas2 but targets different acetylation sites on H4, H3, and H2A proteins *in vitro*. In the native MSL complex, MOF catalyzes the acetylation of nucleosomal histone H4 exclusively on lysine residue 16, emphasizing the influence of the associated MSL proteins on MOF activity and substrate specificity.

KAT activity was also found in protein components of transcription factor complexes like TAF1/TBP and TFIIC90. These protein complexes affect transcription directly and form a separate KAT family.^{46,47} There are a few coactivators of nuclear hormone receptors, which exhibit ligand-dependent KAT activity. They serve as regulatory elements in hormone related transcriptional processes and are grouped in a unique KAT family.^{48,49} The global regulator of circadian gene expression CLOCK was shown to be a member of this family.⁵⁰

The fungal specific lysine acetyltransferase Rtt109 shows very little sequence homology to any of the other KAT family members, but its tertiary fold adopts a structure that is surprisingly similar to p300. However, the catalytic mechanism of Rtt109 involves a ternary intermediate complex and therefore differs significantly from the one of p300. Because of these differences, the enzyme is not assigned to any of the known KAT families. Isolated Rtt109 is not competent to efficiently acetylate lysine substrates, but its activity is stimulated by association with either of two different histone chaperones, Asf1 and Vps75. Upon formation of the enzyme–chaperone complex, the activity of the catalytic domain is dramatically increased and the substrate specificity is directed toward distinct lysine residues (H3K56 for Asf1 and H3K9,23 for Vps75).⁵¹ Bioinformatic analysis of the zebrafish genome led to the identification of the Camello protein family member CMLO3, for which lysine acetyltransferase activity on histone protein H4 was demonstrated. Their structural divergence and their perinuclear localization distinguish Camello proteins from other KATs and place them outside of any of the other KAT families.⁵²

Considering the vast number of identified nonhistone acetylation sites on a constantly growing number of proteins, covering a wide functional spectrum, it should be noted that for many of these acetylation reactions the responsible enzymes have not been identified yet.⁶ While several histone acetyltransferases were shown to also accept nonhistone substrates, the implications of specific nonhistone acetyltransferases, such as the α -tubulin acetyltransferase α TAT1⁵³ and the cohesin acetyltransferase Eco1/ESCO1,⁵⁴ still need to be determined.

■ KATS IN DISEASES

Lysine acetylation of histone and nonhistone proteins is generally linked to activation of transcriptional activity and therefore affects pivotal physiological processes within an organism. As a consequence of misregulated acetylase activity, the manifestation and progression of certain malignancy phenotypes correlates with pathological aberrations of the acetylation equilibrium. This could be either due to altered activity of the responsible enzymes or because of changes in their expression levels. The role of distinct KAT subtypes in diseases like cancer, neurodegenerative disorders, viral and parasitic infections, inflammation, and metabolic and cardiovascular malignancies have been extensively investigated.^{55,56}

p300 and CBP are global coactivators of gene transcription and involved in multiple cellular processes. Point mutation and microdeletion of the CBP gene result in Rubinstein–Taybi syndrome (RTS), which is characterized by physical abnormalities and mental retardation.⁵⁵ Elevated p300 expression levels have been associated with several types of cancer, including esophageal squamous cell carcinoma (ESCC),⁵⁷ hepatocellular carcinoma (HCC),⁵⁸ and melanoma. In the latter case, downregulation of p300 activity retards cell cycle progression in human melanocytes by activating replicative senescence.⁵⁹ It is reported that p300/CBP interaction with c-Myb facilitates myeloid differentiation block and is required for acute myeloid leukemia (AML) induction.⁶⁰ A characteristic feature of this hematologic malignancy is the presence of KAT activity-containing fusion proteins in consequence of chromosomal translocations. Fusion products of p300/CBP with MOZ, MORF, or MLL exhibit aberrant KAT activity and substrate specificity and hence lead to abnormal transcription activation.¹¹ The AML1-ETO oncogene is acetylated by and colocalized with p300 at specific promoter regions, which was found to be pivotal for leukemogenesis.⁶¹ After infection of a cell with the human immunodeficiency virus (HIV), p300-mediated acetylation of the viral protein integrase is crucial for incorporation of virus DNA into the cells' genome.⁶² Upon integration, p300/CBP interaction with the HIV-1-Tat protein promotes transcription of the HI provirus.⁶³ In patients with elevated glucose levels, binding of p300 to promoter sites is increased, which leads to upregulation of vasoactive factors and extracellular matrix proteins, suggesting a possible role of p300 in chronic diabetes related complications.⁶⁴ p300 and CBP stimulate cardiac growth and p300 activity is increased in agonist induced hypertrophy of cardiomyocytes. Recruitment and acetylation of specific transcription factors, such as GATA4 and MEF2, mediate elevated transcription levels of hypertrophy related effector proteins.¹³ The acetylation of NF- κ B by p300/CBP is associated with a loss of affinity for I κ B, leading to enhanced expression of proinflammatory downstream genes products. In neurodegenerative diseases, reduced CBP activity is associated

with loss of neuronal plasticity and destabilization of short-term memory, implicating CBP as an antitarget in this context.¹²

Like p300 and CBP, the GNAT family KATs serve as regulators of transcriptional activity and are similarly implicated in fundamental physiological processes. Their activity and specificity highly depend on protein–protein interactions, as these enzymes are usually part of multienzyme complexes. It was shown that Gcn5 activity is crucial for cell cycle progression.⁶⁵ While Gcn5 and PCAF play important roles in the activation and stabilization of the tumor suppressor p53, PCAF-mediated acetylation of the cyclin-dependent kinase inhibitor p27 facilitates its degradation and further leads to uncontrolled cell cycle progression.⁶⁶ The invasive potential and growth rate of urothelial cancer cells is hampered by PCAF knockout.⁶⁷ Drug resistant cancer cells exhibit elevated levels of PCAF and Gcn5-mediated H3K9 acetylation in promoter regions of the *MDR1* (multidrug resistant protein 1) gene.⁶⁸ Alongside p300, Gcn5 is competent to acetylate and thus activate HIV integrase and Tat proteins with essential impact on the HIV replication cycle.⁶⁹ A *Plasmodium falciparum* homologue of Gcn5 (PfGcn5) was found to play a key role in antigenic switching and expression of plasmodial proteins.⁷⁰ Interestingly, despite some evidence on an antitarget role of p300 in neurodegenerative diseases, knockout of PCAF promotes insensitivity to β -amyloid peptide toxicity in mice, suggesting PCAF to be a possible target for the treatment of Alzheimer disease.⁷¹ It was also shown that PCAF is involved in the extinction process of conditioned fear and that PCAF-mediated acetylation of connexin 43 is implicated in cardiac dystrophy.^{72,73} In type 2 diabetes, Gcn5 and PCAF were found to acetylate PGC-1 α (peroxisome proliferator-activated receptor gamma coactivator 1-alpha), a key coactivators in energy metabolism, thereby regulating its transcriptional activity.⁷⁴

MYST family KATs are more diverse in domain organization and complex formation than p300/CBP and GNAT family proteins. Aberrant activity of this KAT family has predominantly been implicated in manifestation and progression of cancer. The aforementioned fusion proteins of MOZ and MORF with other KAT family members in AML inductions are complemented by the MOZ-TIF2 fusion protein, which is yielded after chromosomal inversion. In AML, MOZ-TIF2 interacts with CBP and disrupts normal CBP-dependent transcriptional activation.⁷⁵ In addition, mutation in MOZ was associated with esophageal adenocarcinoma.⁷⁶ Altered activity of the MYST family member MORF has been linked to breast cancer, prostate cancer, and leiomyoma. Furthermore, these KATs are involved in developmental processes and mutation in their encoding genes have been found in several developmental disorders.⁷⁷ The acetyltransferase Tip60 plays an important role in hormone receptor signaling and DNA damage repair. The androgen receptor is activated in an androgen-independent manner upon Tip60-mediated acetylation. Related to this, the proliferation of prostate cancer has been correlated to aberrant Tip60 activity.⁷⁸ Moreover, resistance to apoptotic signaling cascades in cancer cells after DNA damage was associated with Tip60 mutations.⁷⁹ HBO1 is a key regulator of DNA replication and proliferation. Overexpression of HBO1 has been reported in a specific subset of human primary cancers.⁸⁰ Together, this emphasizes the role of mistargeted acetylation in oncogenesis and other malignancy phenotypes. The field of lysine acetylation in cell function and its involvement in diseases goes beyond the examples listed in this article. For more detailed information,

the reader is referred to more specific reviews regarding this topic.^{11,36,55,81}

■ STRUCTURAL ASPECTS OF KATS

KAT modules, which typically occur alongside other conserved protein modules as a part of much larger proteins, show different sizes between the various KAT families. A high sequence similarity is shared between members of the same family, whereas poor to no sequence homology is found between the families.⁸² Despite the poor sequence homology, all KATs adopt a globular α/β fold where the central core is structurally conserved. This central core is associated with the binding and catalysis of the cofactor acetyl-CoA. Meanwhile, the N- and C-terminal protein regions flanking the central core are structurally divergent and are believed to contribute to the substrate specificity of these enzymes. It is however questionable if substrate specificity of KATs can be solely attributed to the divergence of the N- and C-terminal domains. As previously mentioned, KATs are often found as subunits in large protein complexes, and their interacting protein partners were found to play a role in regulating their substrate selectivity as well as enhance their acetylase activity.⁸³ It should hence be noted that further biochemical and structural investigations are necessary to decipher the exact role of protein partners on the activity and substrate specificity of KATs. The GNAT, p300/CBP, and MYST families are the most extensively studied KATs, and crystal structures of several members of these families are available in apo form and/or in various ligand-bound forms. The overall structures of representative members for each family are shown in Figure 1.

Crystal structures of the KAT domain of Gcn5 (human, yeast and *Tetrahymena*) and PCAF have provided valuable information on the mechanism of catalysis as well as cofactor and substrate-binding of these enzymes. Acetyl-CoA is bound to the central core cleft via numerous hydrogen-bond interactions, mostly between the pantothenic and pyrophosphate moieties of the cofactor and the neighboring amino acid residues.⁸⁴ Meanwhile, the adenosine base shows no contacts with the protein, and it was found to adopt different orientations in various crystal structures.^{85,86} An insight into the binding of the peptide substrates to GNAT family KATs was attained by determining the crystal structures of *Tetrahymena* Gcn5 (tGcn5) with H3, H4, and p53 peptides (PDB IDs: 1q2c, 1q2d, 1pu9, 1pua, and 1qsn). The central core and the flanking N- and C-terminal residues create an L-shaped binding cleft, which accommodates acetyl-CoA and the peptide substrate. The active lysine residue is in contact with the conserved core region, showing van-der-Waals (vdW) interactions with Val123, Leu126, and Phe169 and a hydrogen-bond interaction between its backbone-NH and the backbone carbonyl group of Ala124. The rest of the histone tail occupies a large cleft formed by the flanking, less conserved N- and C-terminal regions. Interestingly, most of the interactions are mediated through hydrogen bonds between the backbone of the histone peptide and the protein, in addition to vdW contacts between the peptide side chains and some protein residues in the binding cleft.^{22,86} It was hypothesized that residues C-terminal to the reactive lysine of the peptide substrates play an important role in substrate selectivity.⁸⁶ Of particular importance are residues at the +2 and +4 position, which show strong vdW interactions with the protein. The N-terminal residues of the peptide seem to mainly contribute to the substrate affinity; only substrates with high affinities (H3

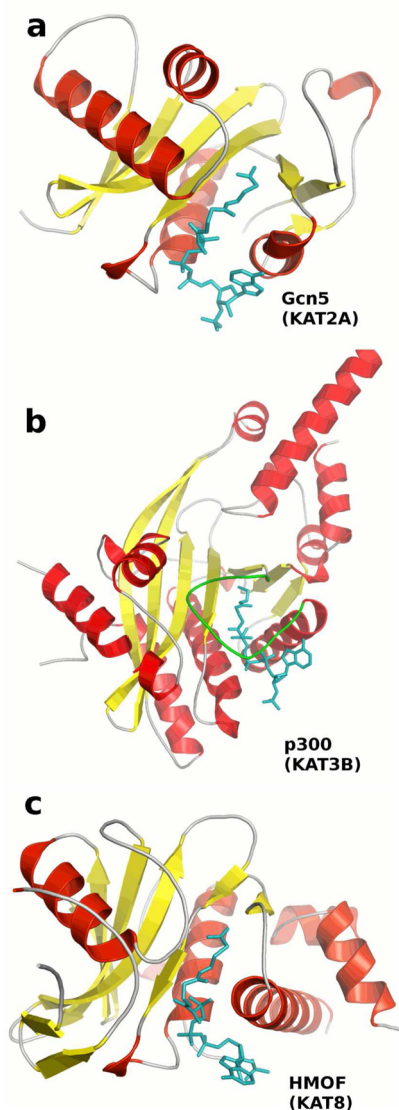


Figure 1. Overall structure of nuclear KATs. Acetyl-CoA (cyan sticks) is shown in complex with (a) hGcn5 (PDB ID 1zr4), (b) p300 (PDB ID 4pzt) with the L1 loop depicted as green ribbon, and (c) hMOF (PDB ID 2giv) as a representative of the MYST family.

peptide) display interactions between their N-terminal residues and the protein.^{86,87} It is noteworthy, that a loop region (aa 184–188 tGcn5), which constitutes a part of the substrate binding pocket, shows a considerable flexibility and a 9 Å outward movement is observed upon peptide binding.^{22,86} A similar conformational change is not observed in the crystal structure of Gcn5 in complex with the bisubstrate inhibitor Lys-CoA (PDB ID 1m1d).⁸⁵

As previously noted, p300 and CBP share a structural conservation of the central core with members of the Gcn5/PCAF and MYST family KATs and a structural divergence of the N- and C-terminal regions.^{88–90} However, p300/CBP show a unique feature among KATs, namely a ~25 residues long loop (L1 loop), which constitutes a part of the cofactor and lysine-binding pockets.⁸⁹ A salt bridge between Asp1399 with His1415 is essential for holding the L1 loop in the right conformation to allow for the acetyl-CoA binding. The crystal structure of p300 in complex with the bisubstrate inhibitor Lys-CoA (3biy.pdb) demonstrates that the lysine moiety is

surrounded by the hydrophobic residues Tyr1397, Trp1436, Cys1438 (L1 loop), and Tyr1446 (L1 loop). The ϵ -NH of the lysine moiety undergoes H-bond interactions with the backbone carbonyl of Trp1436. A common feature of all p300/CBP substrates is the presence of a basic residue (lysine or arginine) at the –3 or +4 position of the active lysine residue.^{89,91} This is consistent with the highly electronegative surface area of the crystallized p300 KAT domain (Figure 2),

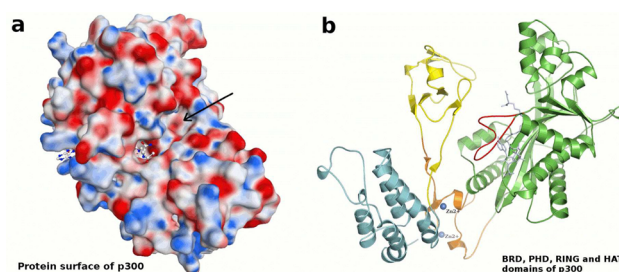


Figure 2. (a) Electrostatic surface of p300 (PDB ID 3biy) in complex with Lys-CoA (white sticks). Red color indicates electronegative regions, blue electropositive, and white regions having a neutral potential. The arrow points to the electronegative subpocket, which accommodates the Lys/Arg residue at –3 or +4 position of the peptidic substrate. Lys-CoA can be partly seen as white sticks. (b) the structure of p300 protein containing the bromo- (cyan), PHD (orange), RING (yellow), and KAT (green) domains (4bhw.pdb). The L1 loop is shown as red ribbon, and the zinc ions as violet spheres.

which distinguishes this family from other KATs. In particular, a highly electronegative pocket, formed of Thr1357, Glu1505, Asp1625, and Asp1628 and located 10 Å away from the active lysine pocket, is responsible for accommodating the basic residue at the –3 or +4 position. Mutations of these residues showed a significant decrease in p300 KAT activity.⁸⁹ In addition, the p300 KAT activity is regulated by a lysine-rich loop (aa 1520–1560; activation loop) that is hyperacetylated in the active form.⁹² It was suggested that the activation loop, in its deacetylated form, folds into the highly electronegative surface, thereby occluding the substrate binding pocket. Upon acetylation, this loop flips outward and allows substrate binding. Owing to its high proteolytic sensitivity, all crystal structures of p300 have been determined without the activation loop. Recently, a crystal structure of the KAT, RING, PHD, and BRD domains of the p300 protein has been determined.⁸⁸ These domains form a compact module, where the RING domain is in direct contact with the L1 loop and hence in close proximity of the KAT substrate pocket (Figure 2). The RING domain was found to have an inhibitory function on the acetylase activity of the KAT domain. Indeed, mutations which disrupt the integrity of the RING domain or the attachment between the RING and KAT domains resulted in an increase in the autoacetylation of the p300 activation loop and the p300 acetylase activity. Similar mutations were correlated with the pathology of some diseases; C1204R mutation is found in B-cell lymphomas, while deletion of the RING domain (1198–1234) occurs in breast cancer tissues.⁸⁸

The overall structure of the yeast MYST member Esa1 (PDB ID 1fy7)⁹³ and the later disclosed human homologue hMOF^{94–97} reveal, as expected, structural homology of the central core with other KATs. Meanwhile, the flanking N- and C-terminal segments show a structural divergence to other N-acetyltransferases. A distinctive feature of the MYST family is

the regulation of its acetylase activity by intramolecular autoacetylation of a conserved lysine residue proximal to the substrate binding site (K274 in hMOF).^{96,97} K274 autoacetylation was demonstrated to be essential for the *in vitro* and *in vivo* KAT catalytic activity.⁹⁷ The acetylated lysine residue (K274, hMOF) is buried into a side pocket of the enzyme active site, where it is stabilized by H-bond interactions with the conserved residues Tyr3012 and Ser303. The terminal methyl group displays vdW contacts with the conserved residues Phe283 and Phe285 (Figure 3).⁹⁶ In the deacetylated form, the

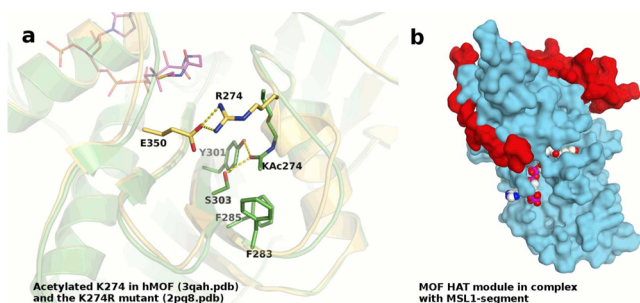


Figure 3. (a) Comparison of the interactions of the autoacetylated lysine (K274) in hMOF (green ribbons and sticks, PDB ID 3qah), with those of the deacetylated form as seen in the K274R mutant (yellow ribbons and sticks, PDB ID 2pq8). Only side chains of the involved residues are shown for clarity. Acetyl-CoA is shown as magenta sticks. (b) Structure of hMOF KAT domain (surface depiction in cyan) in complex with MSL1 segment (surface depiction in red); 4dnc.pdb. Lys-CoA is shown as white spheres.

lysine residue flips out of the side pocket and consequently blocks the substrate binding site, as observed in the crystal structure with the K274R mutant (Figure 3) (PDB ID 2pq8). The flipped-out form is stabilized by salt bridge interactions with the catalytically important Glu350, thus quenching its proton abstraction ability. The activity and substrate specificity of hMOF is regulated by its association with other proteins to form larger protein complexes.^{98,99} hMOF association with MSL1 and MSL3 in the MSL (male-specific lethal) complex leads to a pronounced enhancement of its enzymatic activity and a refinement of its substrate specificity to selectively target the nucleosomal H4K16.⁹⁹ Meanwhile, the complex of hMOF with NSL1, as found in the NSL (nonspecific lethal) complex, is more efficient in specifically acetylating K20 on p53 than hMOF alone.⁹⁸ The crystal structure of hMOF with MSL1470–540 has been recently revealed (PDB IDs 4dnc and 2y0m). The MSL1 segment interacts extensively with the N-terminal part of hMOF, mainly through H-bond and salt-bridge interactions. A depiction of the MOF–MSL1 complex is shown in Figure 3. The MSL1 segment is believed to act as a tether between MOF and MSL3, which is another essential member in the MSL complex.^{94,95} Although the determined crystal structures provide some basic structural insights into the nature of the interplay between the subunits in these complexes, further structural investigations are necessary to fully understand how the activity and substrate specificity of MOF is regulated by the complex subunits. Despite the availability of structural information on numerous KATs, so far only very few studies have reported on the use of *in silico* screening approaches for the identification of KAT inhibitors.

KAT MODULATORS

The multifold implication of lysine acetylation in physiologic pathways as well as manifestation and progression of diseases emphasizes the potential of KAT modulators as therapeutic strategy or versatile mechanistic tools. However, the identification of such compounds has proven to be challenging and the development of potent and selective KAT inhibitors lags far behind modulators of other epigenetic enzymes, like KDACs. Despite different approaches to find small molecule inhibitors of KAT enzymes, only few potent substances have been obtained so far. With the aid of computational methods and advanced assay technologies, recently progress was made toward compounds with improved KAT modulatory properties and *in vivo* characterization. According to their origin and mode of action, the known KAT modulators can be assigned to four distinct classes: bisubstrate inhibitors, natural compounds and their analogues and derivatives, synthetic small molecules, and bromodomain inhibitors.

Bisubstrate Inhibitors. The first published KAT inhibitors were bisubstrate analogues mimicking the ternary complex of cofactor acetyl-CoA and lysine substrate in spatial proximity during the catalytic process (Figure 4). Cole and colleagues

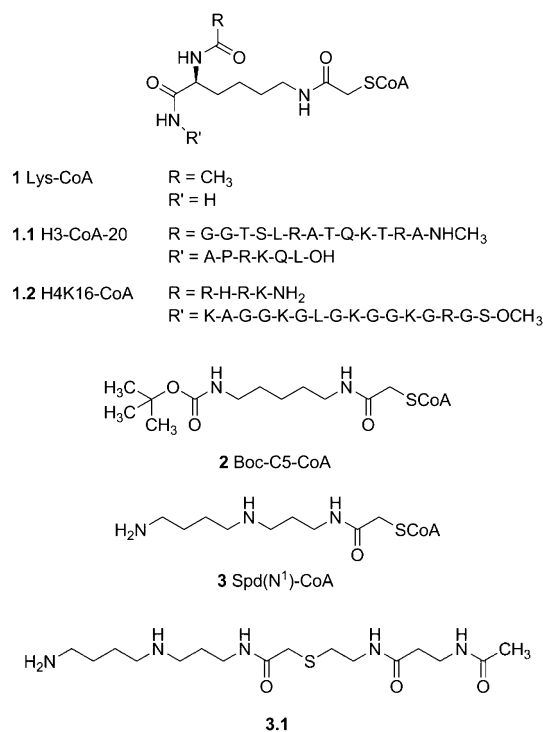


Figure 4. Structures of bisubstrate KAT inhibitors.

covalently linked CoA to the lysine residue of a substrate peptide of various chain lengths. The bisubstrates concept was adopted by several other groups to generate specific KAT inhibitors. Compound 1 (Lys-CoA) is yielded by connecting CoA and a single lysine residue via a methylene linker.²³ The compound is a potent inhibitor of p300 with an IC₅₀ value of 0.5 μM and pronounced selectivity toward p300 compared to PCAF. The particular potency of 1 results from the Theorell–Chance kinetic mechanism of p300/CBP catalysis, which is characterized by a strong cofactor-binding and a weak transient interaction with the histone substrate.²³ The selectivity pattern of bisubstrate inhibitors can efficiently be altered by modifying

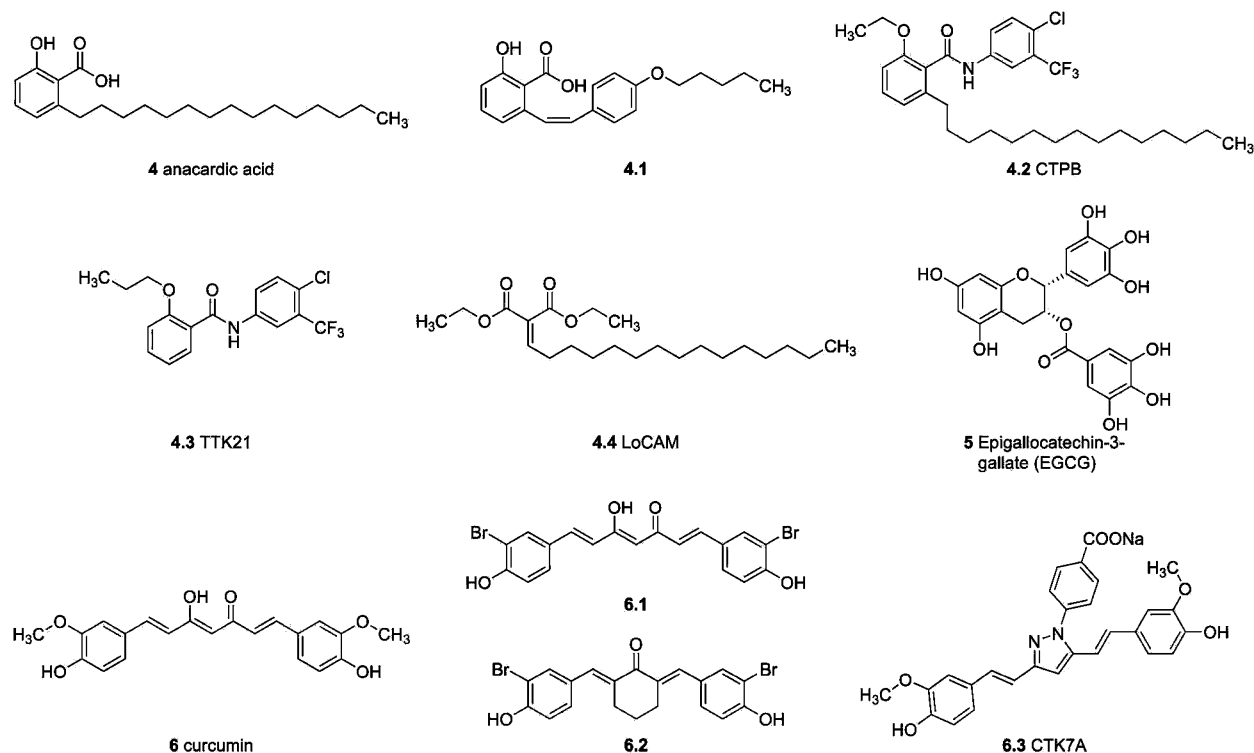


Figure 5. Structures of natural KAT modulators, synthetic analogues, and derivatives.

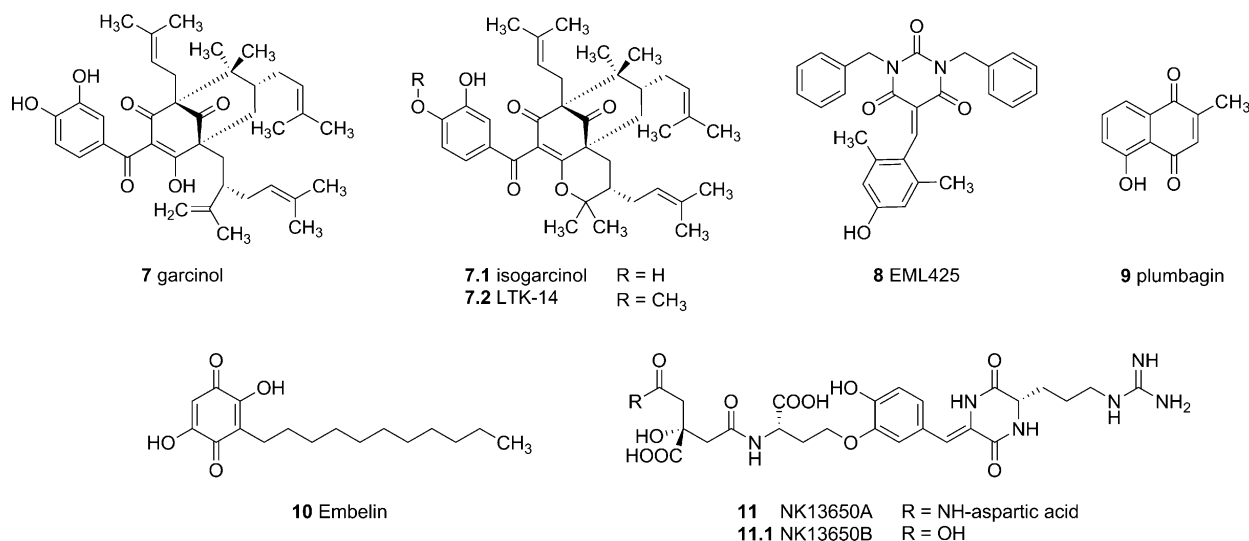


Figure 6. Structures of selected natural KAT inhibitors, their derivatives, and structural analogues.

the length and composition of the peptide chain that comprises the lysine-CoA construct. Derivative **1.1** (H3-CoA-20) mimics the native substrate H3K14 of PCAF and therefore inhibits the enzyme selectively with an IC_{50} value of $0.3 \mu M$.²³ To address MYST family enzymes, a series of H4 peptide-containing bisubstrates analogues was designed and structure **1.2** (H4K16-CoA) was reported as an acetyl-CoA competitive and potent Tip60 inhibitor with an IC_{50} value in the low micromolar range.¹⁰⁰ It should be noted that the mentioned bisubstrate analogues also inhibit the Tip60 yeast homologue Esa1 at low micromolar concentrations and therefore special caution in yeast studies is advised. Deduced from the crystal structure of p300, compound **2** (Boc-C5-CoA) was reported as p300 inhibitor (IC_{50} $0.07 \mu M$) with an optimized linker length that is

capable to occupy two binding pockets (P1, P2) within the enzyme active site.¹⁰¹ Attributed to the polar phosphate moieties and the partially peptidic structure, bisubstrate inhibitors generally suffer from poor cell permeability and metabolic instability, which limits their use to in vitro applications or requires membrane penetrating techniques like micro injection or lipid permeabilization. Different approaches have been applied to circumvent this limitation. Truncation of the CoA moiety in 3' position led to a significant reduction of inhibitory activity.¹⁰² Coupling of the inhibitors' amino acid backbone to the Tat protein transduction domain or to arginine rich peptides succeeded in facilitating cellular uptake and activity.^{103,104} However, the application of such inhibitor/peptide constructs is rather limited due to their

Table 2. KAT Modulators Listed with Their Results from Biochemical Evaluation: IC₅₀ Values or Percentage Enzyme Inhibition at a Specified Concentration (n.i. = No Inhibition)

compd	name/code	approach	results from biochemical testing					assay system	ref
			p300/CBP	Gcn5	PCAF	Tip60	other		
1	Lys-CoA	lead structure-based	0.5 μM		200 μM			radiometric gel	23
			0.98 μM		108.3 μM	29.8 μM	7 μM [Esa1]	radiometric filter-binding	100
			0.05 μM					radiometric gel	104
			30 μM					radiometric gel	121
			0.0032 μM [GST-p300C]					radiometric filter-binding	132
			200 μM		0.3 μM			radiometric gel	23
I.1	H3-CoA20	lead structure-based	6.62 μM		58.47 μM	17.59 μM	5.51 μM [Esa1]	radiometric filter-binding	100
I.2	H4K16-CoA	lead structure-based	0.07 μM					radiometric	101
2	Boc-CS-CoA	lead structure-based	8.5 μM		5 μM			radiometric filter-binding	107
4	anacardic acid	focused library screen	>1000 μM		667.1 μM	347.6 μM	297.2 μM [Esa1]	radiometric filter-binding	100
			>200 μM		>200 μM	64 μM	43 μM [MOF]	radiometric filter-binding	108
			4.15 μM, max 60%		1–2 mM		K _i = 64 μM [MOF]	colorimetric CoA-scavenging	112
					33.9 μM			immunosorbent ELISA-like	111
4.1		lead structure-based			662 μM			radiometric filter-binding	115
			n.i. (200 μM)		100% (200 μM)	65% (200 μM)		colorimetric CoA-scavenging	148
4.2	CTPB	lead structure-based	~400% (275 μM)		n.i.			immunosorbent ELISA-like	111
4.4	LoCAM	lead structure-based	74% (50 μM)	n.i.	~40% (50 μM)			radiometric filter-binding	107
			81.2% (100 μM)					immunosorbent ELISA-like	114
5	EGCG	focused library screen	30 μM/50 μM		37.5% (100 μM)	70 μM		radiometric filter-binding	115
6	curcumin	focused library screen	25 μM		60 μM			colorimetric	116
			6.5 μM		n.i. (100 μM)			radiometric filter-binding	118
			>40 μM					radiometric filter-binding	115
			>400 μM					radiometric filter-binding	100
			6.5 μM					radiometric gel	121
6.3	CTK7A	synthetic optimization	>50% (50 μM)		>50% (50 μM)	n.i. (100 μM)		AlphaLisa proximity immunoassay	127
7	garcinol	focused library screen	7 μM		5 μM			radiometric filter-binding	122
7.2	LTK-14	synthetic optimization	5–7 μM	n.i. (50 μM)	n.i. (50 μM)			radiometric filter-binding	124
			K _i = 5.1 μM		n.i. (80 μM)			radiometric filter-binding	126
								radiometric gel	125

Table 2. continued

compd	name/code	approach	results from biochemical testing						assay system	ref
			p300/CBP	Gcm5	PCAF	Tip60	other			
8	EML425	lead structure-based	2.9 μM [p300]/1.1 μM [CBP]	n.i.	n.i.			AlphaLisa proximity immunoassay	127	
9	plumbagin	focused library screen	20–25 μM [full length]; 2 μM [cat. domain]		50 μM			radiometric filter-binding	129	
10	Embelin	HTS	75% (25 μM)		7.2 μM	75% (25 μM)		radiometric filter-binding	131	
11	NK13650A	HTS	0.011 μM [GST-p300C]			n.i. (9 μM)		radiometric filter-binding	132	
11.1	NK13650B	HTS	0.022 μM [GST-p300C]			n.i. (9 μM)		radiometric filter-binding	132	
12.2	PUI139	virtual screen			1.64 μM			time-resolved fluorescence immunosorbent	136	
12.3	PUI141	virtual screen	5.35 μM [p300]/2.49 μM [CBP]	8.39 μM	9.74 μM		53% (5 μM) [MOF]	time-resolved fluorescence immunosorbent	137	
13	MC1823	phenotypic screen	5.92 μM [p300]/2.85 μM [CBP]	87.36 μM	130 μM		60% (5 μM) [MOF]	time-resolved fluorescence immunosorbent	136	
14.2	CPTH6	phenotypic screen			130 μM			time-resolved fluorescence immunosorbent	137	
15	MB-3	rational design	500 μM CBP	~40% (800 μM)	~40% (800 μM)		24% (25 μM); 30% (50 μM) [U937 nuclear extracts]	immunosorbent ELISA-like	140	
16	C646	virtual screen	1.6 μM , $K_i = 0.4 \mu\text{M}$, 86% (10 μM)	<10% (10 μM)	<10% (10 μM)		< 10% (10 μM) [Rtt109, Sas2, MOZ]	radiometric filter-binding	142	
17	L002	phenotypic screen	0.32 μM	33.9 μM	34.7 μM	2% (100 μM)	1% (100 μM) [HBO1]; ~28% (100 μM) [MORF]	colorimetric CoA-scavenging	112	
18	NU9056	virtual screen	1.98 μM , 128 μM [p300]/32% (100 μM) [CBP]		>100 μM	149 μM	190 μM [Esa1]	colorimetric CoA-scavenging/radiometric filter-binding	148	
19	TH1834	HTS	~58 μM		~35 μM	2 μM		radiometric filter-binding	149	
20	TH1834	rational design				60% (500 μM)		radiometric filter-binding immunosorbent gel	150	
21		HTS		n.i.			0.56 μM [Rtt109]	immunosorbent gel	151	

complex handling and elaborate production. Bandyopadhyay et al. fused CoA to the polyamine spermidine to generate compound **3** (Spd(N¹)-CoA), which is internalized into cells via polyamine transporter uptake.^{105,106} They further truncated the CoA moiety to the cysteamine- β -alanine core structure to achieve structure **3.1** and reported cellular activity comparable to **3**.¹⁰⁵ Both polyamine conjugates impeded histone acetylation-dependent repair and synthesis of DNA and consequently led to radio- and chemosensitization.

Natural Products and Synthetic Analogues and Derivatives. Screening of plant or microbial extracts has proven to be one of the most successful strategies in the discovery of KAT modulators. Several structures have been identified comprising micromolar activity (Figures 5 and 6 and Table 2). Common structural scaffolds of natural compounds, such as Michael reaction acceptors and polyphenols, are reflected in their frequent lack of selectivity and hence often pleiotropic effects in cellular systems. In addition, natural compounds usually comprise unfavorable physicochemical properties, which limit their further development. Synthetic and semisynthetic approaches have been carried out in order to determine structure–activity relationships and to optimize compound properties. Interestingly, in the course of biological evaluation, alongside with KAT inhibitors, compounds with enzyme activating capacity and mixed activities have been found. In this way, natural compounds are useful templates for further development into modulators of KAT activity, yet more druglike structures are still desirable.

The natural product **4** (anacardic acid), rich in the liquid of cashew nut shells, emerged from a screening of plant extracts with anticancer activity.¹⁰⁷ The substance was described in 2003 as a nonselective, noncompetitive inhibitor of p300/CBP and PCAF, but following studies also reported activity in Tip60 inhibition under similar experimental conditions.¹⁰⁸ The inhibitory potency of **4** varies between different studies and IC₅₀ values between 5 μ M and 1000 μ M were obtained for p300 inhibition, depending on assay conditions and enzyme source. On the cellular level, repression of the NF- κ B signaling pathway by KAT-dependent acetylation of the p65 subunit has been found. However, the application of compound **4** in numerous pharmacological studies is attributed to its pleiotropic affinity that affects multiple enzyme targets.¹⁰⁹ A limiting factor for further development of this natural product as a therapeutic tool is its unfavorable physicochemical properties, especially its high lipophilicity. The 6-alkyl salicylic acid structure has extensively been mined in order to generate compounds with increased solubility, cell permeability, and inhibitory efficacy. Our group probed a set of phenoxyacetic acid analogues (structures not shown) for their inhibitory capacity against KAT activity in nuclear extracts. We demonstrated that the position and length of the alkyl chain are pivotal for enzyme inhibition and that substitution of the phenolic hydroxyl group is well tolerated.¹¹⁰ Deduced from the co-crystal structure of PCAF with acetyl-CoA, Ghizzoni et al. proposed a binding model for **4** and synthesized a set of compounds with variations in the alkyl chain and the salicylic acid residue. Esterification of the carboxyl group diminished inhibitory activity, whereas modulation of the alkyl chain or hydroxylation in C4 position caused a shift of specificity toward MYST family KATs. This structure–activity relationship is supported by a recent study on alkyl salicylic acid derivatives in MOF inhibition, with **4** as a reference inhibitor.¹¹¹ Among the compounds tested by Ghizzoni et al., derivative **4.1** showed

inhibitory potency superior to **4** in PCAF inhibition.¹¹² Interestingly, in a subsequent publication, compound **4.1** was identified as an activator of PCAF with no effect on p300 and inhibitory activity on Tip60.¹⁰⁸ The activation of KAT enzymes by small molecules is consistent with observations of other groups. In an inhibitor screen of substituted benzamide analogues of **4**, derivative **4.2** (CTPB) promoted activation of p300 but not of PCAF and increased p300-dependent transcription activation.¹⁰⁷ An interesting attempt was followed by Chatterjee et al., which included binding of the small molecule p300/CBP activator **4.3** (TTK21) to glucose-based carbon nanospheres.¹¹³ The resulting particles readily penetrated the cell membrane to increase histone acetylation without causing apparent toxicity. Treatment with **4.3**-loaded nanospheres was further correlated with beneficial neurologic effects in a mouse xenograft model. Sbardella, Mai, and colleagues published the long chain alkylidenmalonate **4.4** (LoCAM) as a selective activator of PCAF while inhibiting p300/CBP in a comparable degree to the parent structure **4**.¹¹⁴ Structure–activity relationship studies on the LoCAM scaffold revealed that the replacement of one or both of the ester moieties with keto- or carboxylic acid groups greatly alters the modulation profile of the resulting analogues, ranging from selective activation to unselective inhibition. In terms of the aliphatic chain, it was shown that the introduction of a heteroatom is detrimental for binding efficiency and variations in alkyl chain length result in abrogated modulatory activity.¹¹⁵ The precise underlying mechanism of this activator/inhibitor ambivalence is still under investigation. Similar to compound **4**, disruption of NF- κ B signaling due to repression of KAT activity was demonstrated for some polyphenols like **5** (epigallocatechin-3-gallate (EGCG)).¹¹⁶ However, these compounds interact with a wide range of other protein targets and their structural optimization to achieve selectivity seems to be challenging.¹¹⁷

Compound **6** (curcumin) is a major component of *Curcuma longa* rhizome that is commonly used in Indian and Chinese traditional medicine.¹¹⁸ The compound was reported in 2004 as a p300 inhibitor (IC₅₀ 25 μ M) with no effect on PCAF. Treatment with **6** represses p300-dependent H3, H4, and p53 acetylation in different cell lines. Kinetic studies revealed a covalent mode of action at a binding site apart from the substrate and cofactor-binding pocket. The double bonds in the cinnamoyl structure serve potentially as Michael reaction acceptors, and their presence is crucial for binding with p300.¹¹⁹ Although certain selectivity between different KAT enzymes was demonstrated, the compounds' inhibitory activity is rather promiscuous as it also inhibits other epigenetic targets (e.g., KDACs, DNMT1, LSD1) as well as a multitude of nonepigenetic related proteins.¹²⁰ Still, **6** is under clinical investigation for several indications. Open-chain and cyclic cinnamoyl analogues (**6.1**–**6.2**) have been shown to inhibit p300 activity with similar potency as the lead structure.¹²¹ The sodium salt of the hydrazinocurcumin **6.3** (CTK7A) is more water-soluble while maintaining inhibitory potency.¹²² It should be noted that, like the parent structure, the described analogues interact with multiple target proteins aside from p300.¹¹⁷ Such promiscuous effects generally complicate the correlation of in vitro with in vivo observations. In addition, curcumin is known to be a membrane disruptor and therefore it is likely that some of its activities could be attributed to nondrug-like modes of action.¹²³

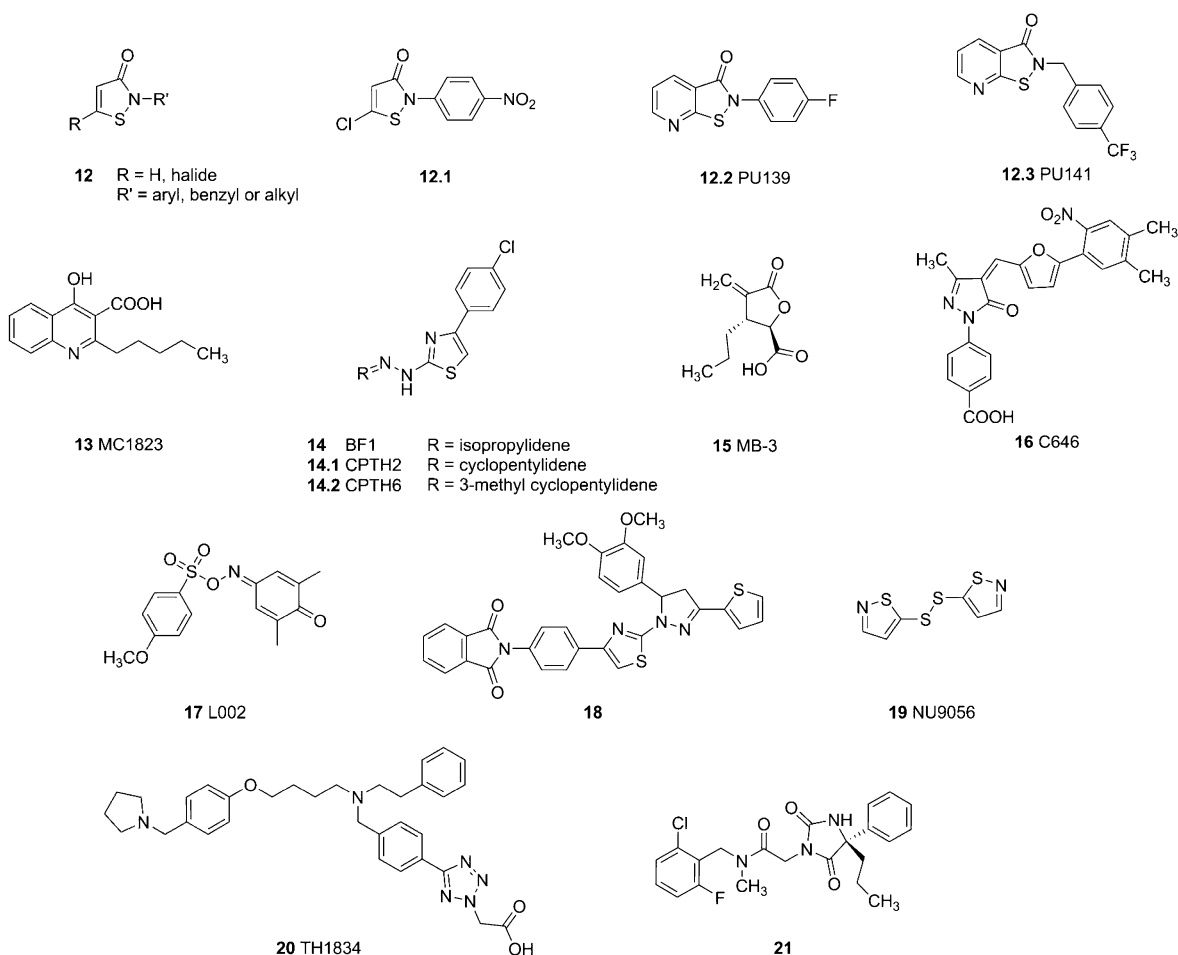


Figure 7. Structures of synthetic KAT inhibitors.

The polyisoprenylated benzophenone **7** (garcinol) was isolated from *Garcinia indica* and identified as a micromolar inhibitor of p300 (IC_{50} 7 μ M) and PCAF (IC_{50} 5 μ M) KAT activity.¹²⁴ Repression of histone acetylation and induction of apoptosis were found in human cancer cell lines upon treatment with this natural product. Isothermal calorimetric titration data proposed a two centered binding mode with the catechol hydroxyl groups interacting with the acetyl-CoA binding pocket, while the isoprenoid moieties are placed into the substrate binding domain of the enzyme.¹²⁵ Monomethylation of the intramolecular cyclization product **7.1** (isogarcinol) in C14-position led to derivative **7.2** (LTK-14), which provides a shifted inhibition pattern toward p300 activity and an attenuated T-cell cytotoxicity.¹²⁶ Human HeLa cells that are treated with **7.1** or one of its analogues develop concentration-dependent histone hypoacetylation and repression of gene transcription. The binding mode of **7.2** was proposed to be different from the parent compound, with a single unique binding side within the enzymes KAT domain.¹²⁵ Sbardella and colleagues recently published the benzylidene barbituric acid derivative **8** (EML425) as a selective and reversible inhibitor of p300/CBP with an inhibitory potency in the low micromolar range (IC_{50} 2.9 μ M for p300 and 1.1 μ M for CBP).¹²⁷ The compound resulted from a molecular pruning approach of structure **7** with isosteric replacement of the benzophenone core. Compound **8** was found to promote cell cycle arrest in G0/G1 phase accompanied by H3K9 and H4K5 hypoacetylation in U937 cells. Molecular modeling studies of this derivative

proposed high affinity for the same alternative binding site as for **7.2**. The suggested noncovalent manner of this binding mode is intriguing, as the benzylidene barbituric acid scaffold is potentially prone to Michael addition reactions and has been exploited in targeting enzyme structures apart from p300/CBP.¹²⁸

The hydroxynaphthoquinone **9** (plumbagin), isolated from *Plumbago rosea*, has been shown to attenuate p300-dependent acetylation of histones H3, H4, and p53 in HepG2 liver cancer cells without causing any effect on PCAF activity.¹²⁹ Structure–activity studies suggested the hydroxyl group in C5 position to be pivotal for forming hydrogen-bond interactions with Lys1358 in the active site of the enzyme. In consequence, derivatization of the naphthochinone in this position diminishes the inhibitory effect. Methylation in C3 position abrogated the thiol reactivity and therefore cytotoxicity of **9** while maintaining its function as a p300 inhibitor.¹³⁰ The 3-alkyl dihydroxybenzoquinone **10** (Embelin) is isolated from *Embelia ribes* and displays a similar scaffold.¹³¹ Compound **10** has been shown to inhibit KAT activity of recombinant PCAF and to promote H3K9 hypoacetylation in treated mice. The compound also attenuated PCAF-mediated MyoD acetylation in HEK239T cells, which was correlated to a block of differentiation in C2C12 cells. Chemical variation revealed that the 11-carbon alkyl chain in structure **10** is crucial for the inhibitory capacity as an analogue with one carbon less was reported to be completely inactive.

Two compounds have been identified during a micro-organism broth library screen. **11** (NK13650A) and **11.1** (NK13650B) are fungal metabolites of a *Penicillium* strain with a peptidic structure that contains a citric acid moiety.¹³² The evaluation of their inhibitory capacity revealed high selectivity for p300 KAT activity over Tip60, and IC₅₀ values were determined to be 11 and 22 nM, respectively. It was further demonstrated that these compounds were competent to repress androgen- and estrogen receptor-dependent activation of gene transcription and to be cytotoxic to different cancer cell lines. Owing to their peptidic nature, these compounds suffer from poor cell permeability and metabolic instability, which requires structural optimization. Nevertheless, the identification of secondary metabolites comprising KAT inhibitory activity supplies a promising strategy in lead structure discovery as such approaches were successfully applied on other biological targets, like KDACs.¹³³

Synthetic Compounds. Different approaches, such as high-throughput-strategies, rational design, and in silico screenings have been applied in order to find new potent small molecule KAT modulators. Derivatization of initial hits and investigations on the structure–activity relationships gained new insights into the characteristics of KAT enzymes. With the aid of computational methods, it was possible to identify and develop new compounds with pronounced inhibitory activity (Figure 7 and Table 2). Only few of these modulators are fully characterized in vitro and in vivo so far.

The inhibition of p300 and PCAF enzymes in biochemical and cell-based assays with concomitant repression of growth and histone acetylation by compounds comprising an isothiazolone structure (**12**) was first reported in 2005 by Aherne and colleagues.¹³⁴ An irreversible binding mode was suggested that involves disulfide bond formation between the isothiazolone sulfur and a cysteine residue in the enzyme. Consistent with this, addition of DTT to the reaction abolished inhibitory activity. Because the general reactivity of these substances is a major drawback, several efforts have been dedicated to developing derivatives with reduced promiscuity while maintaining inhibitory potency. Furdas et al. identified pyridoisothiazolones as novel PCAF inhibitors by applying a computational screening approach.¹³⁵ The NCI database was screened for compounds which contain an isothiazolone or isothiazolidinone substructure as found in the PCAF inhibitor **12.1**.¹³⁴ A subsequently carried out similarity search retrieved 51 related compounds from commercial databases, which were docked into the substrate binding site observed in the crystal structure of PCAF. Only compounds, which showed a reactive S–N moiety in close proximity to PCAF Cys574 in the docking results, were considered for further biological testing. By this means, different pyridoisothiazolones were discovered as novel KAT inhibitors with low micromolar IC₅₀ values and reduced general bioreactivity.¹³⁶ Structure–activity studies revealed a crucial role of the substituent in 2-position for inhibitory activity. *N*-Aryl substituted compounds were shown to cause pan-KAT inhibition on a series of enzymes (PCAF, Gcn5, p300, CBP, and MOF), while *N*-benzyl or *N*-alkyl substituents led to defined subtype selectivity patterns.¹³⁷ The Fantappie group incubated *Schistosoma mansoni* parasites with the compound **12.2** (PU139) and reported impaired promoter activity of the egg shell protein Smp14, probably evidently as a result of diminished SmGCN5 and SmCBP1 activity.¹³⁸ The repression of Smp14 controlled gene products led to production of abnormal and defective eggs, implying KAT

inhibition as novel strategy in the control of schistosomiasis. In a recent publication, Gajer et al. demonstrated two selected pyridoisothiazolones (**12.2** and **12.3** (PU141)) to trigger growth inhibition and histone hypoacetylation in multiple cancer cell lines and to block neuroblastoma cell growth in a SK-N-SH xenograft model in vivo.¹³⁹ The compounds were previously screened against a cysteine protease panel to assess their off-target selectivity, and no significant in vitro activity on these enzymes was observed. Thus, the inhibitors do not have a general reactivity toward all cysteine dependent enzymes. For **12.2**, the authors also reported reduction of histone acetylation in healthy mice and synergistic effects with the DNA-intercalating drug doxorubicin in the xenografts. This is one of very few examples for the demonstration of hypoacetylation in vivo after inhibitor treatment.

Yeast phenotypic screenings have yielded quinoline and hydrazone derivatives with KAT inhibiting activity. Structural optimization of the quinolone structure resulted in compound **13** (MC1823), which comprises a scaffold similar to that of **4**.¹⁴⁰ The reduction in cell viability of *S. cerevisiae* was correlated to a histone H3 and α -tubulin hypoacetylation as a result of Gcn5 inhibition. The same effect has been observed for the hydrazones **14–14.2**.^{141–143} In addition, p300 and PCAF activities are repressed by **14** (BF1) and **14.2** (CPTH6), respectively, and both compounds are competent to cause histone protein hypoacetylation in different human cancer cell lines.

In 2004, the α -methylene- γ -butyrolactone **15** (MB-3) was published as an inhibitor of Gcn5, selective over CBP.¹⁴⁴ Biel et al. followed a rational design strategy based on the electrostatic interaction fields within the active site of Gcn5. The assessed IC₅₀ value of 100 μ M is comparable with the K_D value of the H3 substrate and despite the apparent Michael reaction acceptor scaffold, the binding mode of MB-3 was reported to follow a noncovalent fashion.

The pyrazolone-containing inhibitor **16** (C646), was identified as a potent, selective, and reversible p300/CBP KAT inhibitor by means of a virtual screening approach.¹⁴⁵ Bowers et al. docked a database of ~500000 commercially available compounds into the same binding pocket as occupied by the bisubstrate inhibitor **1** in the p300 KAT enzyme and selected 194 compounds for biological testing. Three compounds were found to inhibit p300 KAT activity in the micromolar and submicromolar range, where **16** showed the highest inhibitory activity ($K_i = 460$ nM). The compound was predicted to be a bisubstrate inhibitor of p300, and the proposed binding mode shows numerous H-bond and salt bridge interactions of **16**, with the side chains of the binding pocket similar to those observed with the CoA moiety of the cocrystallized inhibitor **1**. Chemical modifications of functional groups indicated that the free carboxylic acid, as well as certain interactions mediated by the nitro group, are essential for inhibitory activity, although replacement of the nitro group with more metabolically favorable functionalities resulted in only minor loss of potency. Further, a reduced derivative demonstrated that the conjugated pyrazolone structure is pivotal for binding to the p300 active site, indicating that a certain level of planarity of the molecule is required for efficient active-site targeting. However, this structural entity is potentially prone to nucleophilic attack. Despite it being shown in the original publication that binding of **16** to p300 happens in a nontime dependent manner and is not abrogated by DTT or β -mercaptoethanol, the formation of covalent

conjugates with a number of different cellular cysteine containing proteins was observed in a recent publication.¹⁴⁶ The large conjugated system in structure **16** causes intrinsic fluorescence of the compound, which is an obstacle for its use in fluorescent-based assay methods. Cole and colleagues circumvented this hurdle by replacing the furan group with a phenyl ring.¹⁴⁷ The resultant derivative was absent of intrinsic fluorescence while mostly maintaining its inhibitory capacity (IC_{50} 9 μ M (p300)). In melanoma and lung cancer cell lines, treatment with **16** led to inhibition of cell growth and concomitant histone H3 and H4 hypoacetylation. Cell cycle arrest and induction of apoptosis upon administration was also observed in AML1-ETO positive leukemia cells.¹⁴⁸

The small molecule inhibitor **17** (L002) has been reported as a result of a large high-throughput screening approach of more than 600000 substances for their cytotoxic activity against the triple-negative breast cancer cell line MDA-MB-231.¹⁴⁹ Radioactive filter binding assays revealed inhibitory activity against p300 (IC_{50} 128 μ M) and GNAT family KATs (IC_{50} 34.7 μ M for PCAF and 33.9 μ M for Gcn5) but no inhibition of MYST family members. The IC_{50} value of **17** against p300 was determined to be 1.98 μ M in an orthogonal fluorescence assay. The sulfonyl-coupled iminoquinone structure was placed in silico into the acetyl-CoA domain of the p300 enzyme. In cellular experiments, the compound has been found to promote histone and p53 hypoacetylation and to suppress STAT3 activation in lymphoma, leukemia, and breast cancer cell lines. Reduction of tumor growth and decreased histone acetylation were correlated to in vivo administration in a MDA-MB-468 xenograft model.

Different scaffolds have been identified and tested in order to find inhibitors for the Tip60 histone acetyltransferase as a potential therapeutic strategy in correlated malignancies. The Zheng group published the phthalimide analogue **18** in 2011 as the result of a virtual screening campaign based on the Tip60 yeast homologue Esa1 crystal structure.¹⁵⁰ KAT inhibition efficacy was assessed in a radiometric in vitro assay for different KAT family members (Tip60, Esa1, p300, PCAF) and IC_{50} values between 100 and 190 μ M were determined, stating an unselective inhibitory activity. Computational docking and kinetic studies suggested that **18** targets the acetyl-CoA binding site of Tip60. One year later, Coffey et al. performed a high-throughput screening for Tip60 inhibitors of ~80000 substances. Structure **19** (NU9056), a derivative of an initial hit, bearing an isothiazole scaffold, was demonstrated to specifically inhibit Tip60 activity (IC_{50} 2 μ M).¹⁵¹ It was further shown that the derivative blocks acetylation of histone proteins in a concentration-dependent manner and induces apoptosis via caspase activation in prostate cancer cell lines. In 2014, **20** (TH1834) was developed during a rational design approach in accordance with the electrostatic surface potential of a Tip60 active site model.¹⁵² Under physiological conditions, the structure comprises two oppositely charged ends, which were predicted to interact with amino acid side chains on different sides of the Tip60 binding pocket. The ethylbenzene side chain was introduced as an isosteric replacement of acetyl-CoAs' adenine residue. Throughout the biological evaluation, compound **20** was tested at high concentration (500 μ M), promoting induction of apoptosis and radiosensitization in MCF7, DU-145, and PC-3 cancer cell lines.

An inhibitor (**21**) of the fungal KAT Rtt109 was published in 2013 as the result of a high-throughput screening campaign.⁵¹ The authors reported specific and noncompetitive in vitro

inhibition of enzyme-mediated H3K56 acetylation in presence of histone chaperone cofactor protein Vps75 or Asf1, respectively. Compound **21** did not show any apparent effect on p300 and Gcn5 activity but inhibited Rtt109 potently (IC_{50} 0.56 μ M) in a sulfhydryl scavenging assay. Kinetic measurements proposed a tight or irreversible binding mode as inhibitory activity increased over time and was not diminished by dialysis of the inhibitor from the reaction mixture. Inhibitors of the fungal specific acetyltransferase Rtt109 are proposed to be promising drug candidates against pathogenic fungal species, such as *Candida albicans*. The further development of compound **21** is limited by its inability to induce cellular effects, presumably due to drug efflux or rapid metabolism. Structure–activity studies need to be conducted to assess the overall potential of this scaffold.

Bromodomain Inhibitors. In addition to modulators targeting the catalytic domain of KATs, a more recent approach concentrates on the identification and development of small molecule inhibitors of KAT protein–protein interaction domains.^{153,154} One of the most thoroughly investigated interaction domains is the bromodomain, which recognizes and binds to acetylated lysine residues. The disruption of acetylation-dependent protein–protein interactions by small molecule inhibitors abrogates the assembly of transcriptional regulator complexes and subsequently represses the phenotypic consequences of acetylation signaling. The successful implementation of BET bromodomain ligands has evoked a growing interest in the identification of potent and selective small molecule inhibitors of non-BET bromodomains, as they are structural entities of several KATs. Mostly structure-guided approaches have yielded a set of KAT bromodomain ligands whose structures are depicted in Figure 8.

The *N*-aryl-propane-1,3-diamine **22** has been identified as an inhibitor of the PCAF bromodomain.¹⁵⁵ Binding of this bromodomain to the acetylated K50 moiety of the HIV-1-Tat protein is required to induce transcription of the integrated HIV-1 provirus. **22** successfully inhibited the transactivation of the HIV-1 promoter by blocking the PCAF bromodomain in C1866 cells with an IC_{50} value of 0.6 μ M. Higher concentrations of the inhibitor were shown to be cytotoxic, which is a drawback for further development of this scaffold.

Acetylation of the effector protein p53 at lysine residue 382 facilitates interaction with the CBP bromodomain. Upon binding, a coactivator complex is formed, which is recruited to p53 controlled promoter sites. Zhou et al. performed a cell-based compound screen against the p53-dependent expression of p21 in response to doxorubicin-mediated DNA damage. Structural optimization of initial hits yielded the azobenzene **23** (ischemin), which was demonstrated to inhibit the p53-CBP bromodomain interaction with an IC_{50} value of 5 μ M and a 5-fold selectivity over other bromodomains (PCAF, BRD4, BAZ2B).¹⁵⁶ Compound **23** was shown to be competent in protecting rat cardiomyocytes from p53-induced apoptosis in consequence of doxorubicin treatment.

Rooney et al. employed a fragment-based approach combined with chemical expansion of the initial hits to develop a series of dihydroquinoxalinones as the first submicromolar ligands for the CBP bromodomain. The most potent compound **24** was shown to bind to the bromodomain via an induced fit pocket, which is occupied by the tetrahydroquinoline side chain and stabilized by a cation– π interaction of this residue with R1173 of the protein.¹⁵⁷ The K_D of **24** was assessed in an isothermal titration calorimetry assay to be 390

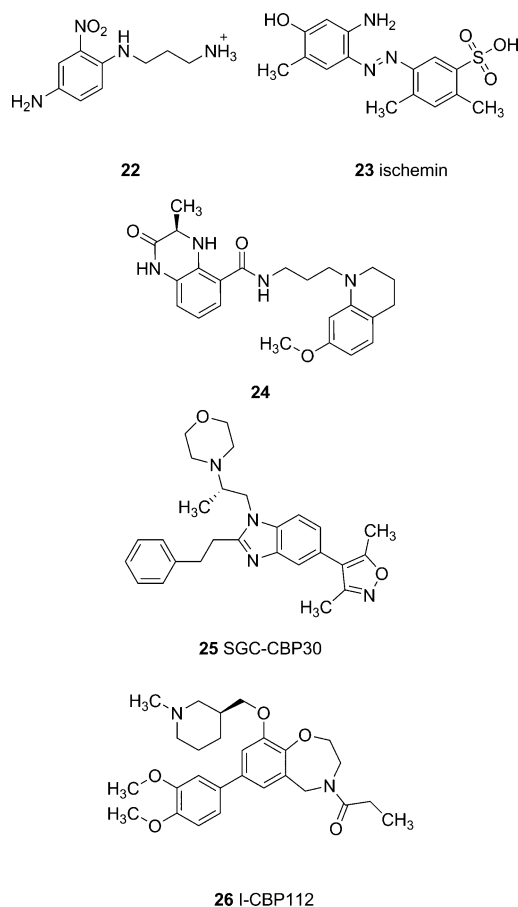


Figure 8. Structures of PCAF and CBP/p300 bromodomain inhibitors.

nM, and the selectivity for the CBP bromodomain over BRD4 (K_D 1.4 μ M) was stated to be modest.

Mining of the 3,5-dimethylisoxazole scaffold resulted in the identification of **25** (SGC-CBP30).¹⁵⁸ The aryl substituent of the isoxazole core forms a cation- π interaction with R1173 in the bromodomain binding site. The compound binds to the CBP bromodomain with a K_D value of 21 nM, and the achieved inhibition is highly selective over BRD4. In a luciferase-based reporter assay, the authors observed diminished expression of CBP-dependent p53 downstream genes as a result of SGC-CBP30 incubation.

SGC and GSK developed the CBP bromodomain inhibitor **26** (I-CBP112) on the basis of a benzoxazepine scaffold.¹⁵⁹ The acyl group in this structure mimics the acetyl residue of the native recognition motive, thereby forming hydrogen bonds to the binding site, while the aryl substituent interacts with the arginine moiety in position 1173 of the CBP bromodomain. The K_D values of **26** for binding to p300 and CBP bromodomains were determined to be 167 and 151 nM, respectively, with selectivity over a number of other bromodomains (e.g., BRD2, BRD4, PCAF, TIF1 α). The compound proved cellular activity in a FRAP assay on U2OS cells. Further studies revealed that **26** is capable to impair p53 interaction, which results in reduced p21 expression. Treatment of leukemia cell lines with the bromodomain inhibitor led to cell cycle arrest in G₁-phase and morphological differentiation.

DISCUSSION AND CONCLUSIONS

Altogether, epigenetic modifiers have emerged in the last 20 years as one of the most promising class of new targets for a variety of diseases. The majority of findings points to a pivotal role in cancer, but also for metabolic diseases, CNS disorders, and infectious pathologies promising data is available.¹⁶⁰ The evidence for the roles of different KAT enzymes in these indications was mostly gathered with the aid of molecular biology methods like gene knockdown or gene knockout. To distinguish whether the resultant phenotypic changes upon enzyme depletion can be assigned to the repression of either the acetyltransferase activity or protein-protein interactions, small molecule inhibitors are needed that specifically target either of these features. There is no doubt that new approaches in molecular biology will help to further elucidate the field of lysine acetylation to give a more rounded picture of their specific implication in pathological and physiological processes.¹⁶¹ Among the histone modifiers, inhibitors of histone deacetylases have gained approval for use in patients and five drugs are now on the market.¹⁶² For some epigenetic regulators, e.g., the bromodomains, the time span from first reports as druggable targets¹⁶³ to first clinical trials was about four to five years only.¹⁶⁴ KATs were among the first epigenetic modifiers to be discovered,¹⁸ yet, strangely, almost 20 years later, there is still no drug in advanced development. This is true despite numerous studies showing the involvement of KATs in disease and rich structural data. Structural reasons for the rather difficult development of potent and selective inhibitors are the structurally conserved cofactor binding site, which makes it difficult to achieve pronounced selectivity for a specific enzyme subtype and the relatively shallow substrate binding cleft where the histone substrate is placed.¹⁶⁰ Another problem in the identification of active compounds seems to be the variation in the different assay formats. Various assay strategies have been employed in the biochemical characterization of KAT enzymes (Table 2). Radiometric measurements have emerged as one of the standard procedures, allowing robust and sensitive readouts, but their application requires special hazard precautions and waste disposal. Colorimetric assays are susceptible for quenching effects and interference of the tested compound with the assay components. The need for time-consuming washing steps is the biggest disadvantage of heterogeneous immunosorbent methods, which complicates their application in high-throughput approaches. In comparison, the data generated by different biochemical assays for published compounds is very inconsistent. For example, for compound **4**, the measured potencies in p300 inhibition vary between IC₅₀ values of 8.5 and >1000 μ M in three radiometric filter-binding assays. The huge discrepancy may be explained by differences in enzyme source, type of substrate, substrate and cofactor concentration, buffer composition, and incubation time. Therefore, direct comparison of IC₅₀ values, even for similar assay types, can be misleading. Standardized assay protocols and reliable reference compounds would be valuable tools to achieve comparability of biochemical data. The implementation of new assay methods, like thermal shift¹⁶⁵ or microscale thermophoresis,¹⁶⁶ could prove beneficial for the identification and characterization of new substances and detection of promiscuous inhibition mechanisms. To avoid misinterpretation of compound hits from initial screens, it is important to confirm such observations in orthogonal assays that rely on a different type of readout. In addition, a panel of

counter screens against possible off-targets should be carried out to ensure target selectivity. The field of modulator development is further complicated by the fact that activity and substrate specificity of enzymes in biochemical assays can significantly differ from a cellular environment. This holds especially true for KATs as they natively occur in multiprotein complexes. Therefore, profound evaluation of cellular activity is needed to complement biochemical data.

A number of inhibitors have been discovered by various approaches but many of them suffer from several drawbacks, such as low *in vivo* potency, metabolic instability, or poor selectivity (Table 2). Among the different subtypes of KAT enzymes, p300/CBP seems to be the preferred target of most modulators. This is presumably due to the structural features of these isoenzymes that distinguish them from the other families. Although bisubstrate inhibitors of KAT activity excel in potency and selectivity, their further development into more druglike small molecules is largely prevented by their complex structure. The simple rationale of covalently linking ligands of both the cofactor and the substrate binding site is contradicted in terms of selectivity by the high structural conservation of KAT isoforms in these regions. The incorporation of large peptidic groups into the inhibitor structure is needed to achieve subtype selectivity, and the resulting compounds suffer from poor *in vivo* efficacy. However, analogues and derivatives of **1** might serve as a starting point for fragment-based approaches in future inhibitor discovery. Natural products have been investigated deeply as a class of KAT modulators. Extensive structure–activity studies have been carried out to assess their full potential, and a multifold of derivatives have been generated with the aim to improve physicochemical and modulatory properties. A lot of them feature structural motifs that are suspicious in terms of promiscuous behavior, such as Michael acceptors, phenolic or quinone moieties.¹⁶⁷ While for some of them selectivity and target engagement among the KATs has been shown, clearly data for the analysis on other targets is missing for most of these compounds. Or, like in the case of curcumin, inhibition of many other targets has been shown already. Despite large efforts that have been put into the characterization of natural KAT modulators and the development of improved derivatives, no compound with pronounced potency and especially high selectivity, for KAT enzymes and distinct KAT isoforms, has been obtained. The identification of structural analogues of known inhibitors with reversed inhibitory potency, actually increasing enzyme activity, as well as the isolation of highly potent peptidic natural products, are interesting findings. Crystal structures of these modulators in complex with the KAT enzyme would provide valuable information for further development. The class of synthetic compounds comprises a structurally heterogeneous set of molecules, which were identified by different approaches. Although some of these compounds were shown to be potent KAT inhibitors, only few of them feature subtype selectivity and have been characterized profoundly in a cellular setting. Screening and designing of small molecules with the aid of computational methods has proven to be useful in the targeting of specific interaction fields. In this way, it becomes much more likely to achieve subtype selectivity, like in the case of compound **16**. Another possibility for direct enzyme inhibition is targeting cysteines involved in the catalysis or present at the active site of the enzyme. The use of covalent inhibitors has emerged as a highly promising strategy in kinase inhibitors that has already culminated in the approval of ibrutinib¹⁶⁸ for the

treatment of mantle cell lymphoma and is pursued with high intensity. Thus, starting out from covalent modifiers of cysteines in KATs, affinity and selectivity could be built in subsequently, resulting potentially in highly potent and selective KAT inhibitors. For inhibitors that rely on the covalent targeting of cysteine residues, as it is the case with compounds **12.2** and **12.3**, further structural development of these lead structures is needed to direct their general reactivity further toward specific targets only. Because even for well characterized compounds, like **16**, covalent interaction with off-target protein structures has been demonstrated. Hence, such molecules are placed at the intersection of PAINS and covalent modifiers. Therefore, at the moment, maybe not a single KAT inhibitor does satisfy the rigid rules demanded for high quality chemical probes.¹⁶⁹ As most of the known KAT modulators were identified due to screenings of large compound libraries or in the course of chemical optimization or derivatization of such initial hits, it becomes more and more evident that this might not be the ideal way to find highly potent and specific ligands for KAT enzymes. Approaches like rational-design, fragment-based design, or virtual ligand screening could provide better suitable methods to deal with the KAT specific challenges concerning druggability. On the other hand, for therapeutic endeavors compounds with a more pleiotropic profile may still be useful, as a drug needs to be safe and effective and knowledge on the mode of action is not a prerequisite for successful treatment. The problem is of course that optimization toward an assumed target may then not be successful in terms of efficacy and needs to be performed with phenotypic cellular and animal models. A big problem is the widespread use of published KAT inhibitors in mechanistic studies with a danger of overinterpretation of the link of histone acetyltransferase inhibition and the studied mechanism in question, but on the other hand, it may still be informative to use these inhibitors to potentially gain insight in KAT biology. Therefore, for both drug discovery but especially chemical epigenetics, there is clearly still a big demand for high quality KAT inhibitors. Many points need to be addressed such as the relevance of nonhistone acetylation,^{170–172} the question of the relevance of acyl groups other than acetyl,¹⁷³ or the role of nonenzymatic versus enzymatic acetylation.^{174,175} The big question is whether after 20 years a new way can be discovered to reach that goal. As bromodomains have emerged as druggable and promising targets, one strategy is to target those domains that are part of KATs rather than the enzymatic activity. As there is no crystal structure of any KAT catalytic domain in context with a small molecule inhibitor aside from **1**, more structural data of KAT enzymes in complex with small molecule ligands and in context of their native multidomain protein complexes is needed to guide further development. Combined with new approaches in modulator discovery and optimization, computational methods using such information will largely improve the chances of developing potent and selective modulators of KAT enzymes. These will be highly useful as chemical probes and will show whether we can KATch up in terms of drug development with this difficult, yet still promising class of epigenetic targets.

■ AUTHOR INFORMATION

Corresponding Author

* Phone: +497612034896. Fax: +497612036321. E-mail: manfred.jung@pharmazie.uni-freiburg.de.

Author Contributions

The manuscript was written through contributions of all authors. All authors have given approval to the final version of the manuscript.

Notes

The authors declare no competing financial interest.

Biographies

Roman P. Simon holds a diploma degree in Pharmaceutical Sciences at the Institute of Pharmaceutical Sciences of the Albert-Ludwigs University Freiburg and works as a Ph.D. candidate in the group of Prof. M. Jung. He studied Pharmacy (state examination) at the University of Freiburg from 2008 to 2013. After a six months research stay in the group of Prof. Ganesan at the University of East Anglia in 2014, he returned to Freiburg. Since the beginning of 2015, he is a doctoral student, with his research focusing on development and characterization of novel small molecule KAT inhibitors.

Dina Robaa studied Pharmacy at the University of Alexandria in Egypt. She obtained her Ph.D. in Pharmaceutical Chemistry at the University of Jena in the group of Jochen Lehmann. Since 2011, she has been working as a postdoctoral fellow in the research group of Wolfgang Sippl. Her research focuses on structure-based drug design of several epigenetic modulators.

Zayan Alhalabi studied Pharmacy at the University of Damascus in Syria. She finished her diploma in Pharmaceutical Science. She obtained her master's degree in Pharmaceutical Chemistry at the University of Damascus 2012. In 2013, she started her Ph.D. at the Department of Medicinal Chemistry in the research group of Prof. Wolfgang Sippl. Her research focuses on structure-based drug design for epigenetic targets (Sirtuins).

Wolfgang Sippl is Professor for Medicinal Chemistry and Director of the Institute of Pharmacy at the Martin-Luther-University of Halle-Wittenberg (Germany). He obtained a Ph.D. in Pharmaceutical Chemistry at the University of Düsseldorf in the group of Hans-Dieter Höltje and was a postdoctoral fellow at the Université Louis-Pasteur in Strasbourg (France) where he worked with Camille G. Wermuth. Since 2003, he is Full Professor at the Institute of Pharmacy in Halle. His main interests are focussed on computational chemistry and structure-based drug design of novel epigenetic modulators for the therapy of cancer and parasitic diseases.

Manfred Jung did his Ph.D. with W. Hanefeld on the synthesis of aromatic retinoids at the University of Marburg. In 1993/94, he did a postdoc with T. Durst (University of Ottawa, Canada). From 1994 to 2003 he was a group leader at the University of Münster and obtained his habilitation in Pharmaceutical Chemistry (2000). Since 2003, he is a Professor of Pharmaceutical Chemistry at the University of Freiburg. In 2010, he declined an offer for a full professorship to the University of Mainz and is a Full Professor in Freiburg since 2011. The topic of his research is Chemical Epigenetics. His group is working on inhibitor synthesis, assay development, and screening for inhibitors of reversible histone acetylation and methylation but also histone readers.

ACKNOWLEDGMENTS

R.P.S and M.J. thank the Deutsche Forschungsgemeinschaft for funding (Ju 295/9-2 within SPP1463).

ABBREVIATIONS USED

BRD, bromodomain; H3K9, histone H3 lysine residue 9; HAT, histone acetyltransferase; KAT, lysine acetyltransferase; K_D , dissociation constant; KDAC, lysine desacetylase; MSL, male

specific lethal; PTM, posttranslational modification; vdW, van-der-Waals

REFERENCES

- (1) Zeng, L.; Zhou, M. M. Bromodomain: an acetyl-lysine binding domain. *FEBS Lett.* **2002**, *513*, 124–128.
- (2) Kouzarides, T. Chromatin modifications and their function. *Cell* **2007**, *128*, 693–705.
- (3) Smith, B. C.; Denu, J. M. Chemical mechanisms of histone lysine and arginine modifications. *Biochim. Biophys. Acta, Gene Regul. Mech.* **2009**, *1789*, 45–57.
- (4) Marmorstein, R.; Zhou, M. M. Writers and readers of histone acetylation: structure, mechanism, and inhibition. *Cold Spring Harbor Perspect. Biol.* **2014**, *6*, a018762.
- (5) Sterner, D. E.; Berger, S. L. Acetylation of histones and transcription-related factors. *Microbiol. Mol. Biol. Rev.* **2000**, *64*, 435–459.
- (6) Choudhary, C.; Kumar, C.; Gnäd, F.; Nielsen, M. L.; Rehman, M.; Walther, T. C.; Olsen, J. V.; Mann, M. Lysine acetylation targets protein complexes and co-regulates major cellular functions. *Science* **2009**, *325*, 834–840.
- (7) Kim, S. C.; Sprung, R.; Chen, Y.; Xu, Y.; Ball, H.; Pei, J.; Cheng, T.; Kho, Y.; Xiao, H.; Xiao, L.; Grishin, N. V.; White, M.; Yang, X. J.; Zhao, Y. Substrate and functional diversity of lysine acetylation revealed by a proteomics survey. *Mol. Cell* **2006**, *23*, 607–618.
- (8) Allis, C. D.; Berger, S. L.; Cote, J.; Dent, S.; Jenuwein, T.; Kouzarides, T.; Pillus, L.; Reinberg, D.; Shi, Y.; Shiekhhattar, R.; Shilatifard, A.; Workman, J.; Zhang, Y. New nomenclature for chromatin-modifying enzymes. *Cell* **2007**, *131*, 633–636.
- (9) Mellert, H. S.; McMahon, S. B. Biochemical pathways that regulate acetyltransferase and deacetylase activity in mammalian cells. *Trends Biochem. Sci.* **2009**, *34*, 571–578.
- (10) Feinberg, A. P. Phenotypic plasticity and the epigenetics of human disease. *Nature* **2007**, *447*, 433–440.
- (11) Sun, X. J.; Man, N.; Tan, Y.; Nimer, S. D.; Wang, L. The role of histone acetyltransferases in normal and malignant hematopoiesis. *Front. Oncol.* **2015**, *5*, 108.
- (12) Schneider, A.; Chatterjee, S.; Bousiges, O.; Selvi, B. R.; Swaminathan, A.; Cassel, R.; Blanc, F.; Kundu, T. K.; Bouillier, A. L. Acetyltransferases (HATs) as targets for neurological therapeutics. *Neurotherapeutics* **2013**, *10*, 568–588.
- (13) Wang, Y.; Miao, X.; Liu, Y.; Li, F.; Liu, Q.; Sun, J.; Cai, L. Dysregulation of histone acetyltransferases and deacetylases in cardiovascular diseases. *Oxid. Med. Cell. Longevity* **2014**, *2014*, 641979.
- (14) Caton, P. W.; Nayuni, N. K.; Kieswich, J.; Khan, N. Q.; Yaqoob, M. M.; Corder, R. Metformin suppresses hepatic gluconeogenesis through induction of SIRT1 and GCN5. *J. Endocrinol.* **2010**, *205*, 97–106.
- (15) Allfrey, V. G.; Faulkner, R.; Mirsky, A. E. Acetylation and methylation of histones and their possible role in the regulation of RNA synthesis. *Proc. Natl. Acad. Sci. U. S. A.* **1964**, *51*, 786–794.
- (16) Gershey, E. L.; Vidali, G.; Allfrey, V. G. Chemical studies of histone acetylation. The occurrence of epsilon-N-acetyllysine in the f2a1 histone. *J. Biol. Chem.* **1968**, *243*, 5018–5022.
- (17) Candido, E. P.; Reeves, R.; Davie, J. R. Sodium butyrate inhibits histone deacetylation in cultured cells. *Cell* **1978**, *14*, 105–113.
- (18) Brownell, J. E.; Allis, C. D. An activity gel assay detects a single, catalytically active histone acetyltransferase subunit in *Tetrahymena* macronuclei. *Proc. Natl. Acad. Sci. U. S. A.* **1995**, *92*, 6364–6368.
- (19) Parthun, M. R.; Widom, J.; Gottschling, D. E. The major cytoplasmic histone acetyltransferase in yeast: links to chromatin replication and histone metabolism. *Cell* **1996**, *87*, 85–94.
- (20) Luger, K.; Mader, A. W.; Richmond, R. K.; Sargent, D. F.; Richmond, T. J. Crystal structure of the nucleosome core particle at 2.8 Å resolution. *Nature* **1997**, *389*, 251–260.
- (21) Grant, P. A.; Duggan, L.; Cote, J.; Roberts, S. M.; Brownell, J. E.; Candau, R.; Ohba, R.; Owen-Hughes, T.; Allis, C. D.; Winston, F.; Berger, S. L.; Workman, J. L. Yeast Gcn5 functions in two multisubunit complexes to acetylate nucleosomal histones: characterization of an

Ada complex and the SAGA (Spt/Ada) complex. *Genes Dev.* **1997**, *11*, 1640–1650.

(22) Rojas, J. R.; Trievel, R. C.; Zhou, J.; Mo, Y.; Li, X.; Berger, S. L.; Allis, C. D.; Marmorstein, R. Structure of Tetrahymena GCN5 bound to coenzyme A and a histone H3 peptide. *Nature* **1999**, *401*, 93–98.

(23) Lau, O. D.; Kundu, T. K.; Soccio, R. E.; Ait-Si-Ali, S.; Khalil, E. M.; Vassilev, A.; Wolffe, A. P.; Nakatani, Y.; Roeder, R. G.; Cole, P. A. HATs off: selective synthetic inhibitors of the histone acetyltransferases p300 and PCAF. *Mol. Cell* **2000**, *5*, 589–595.

(24) Choudhary, C.; Weinert, B. T.; Nishida, Y.; Verdin, E.; Mann, M. The growing landscape of lysine acetylation links metabolism and cell signalling. *Nat. Rev. Mol. Cell Biol.* **2014**, *15*, 536–550.

(25) Lin, H.; Su, X.; He, B. Protein lysine acylation and cysteine succination by intermediates of energy metabolism. *ACS Chem. Biol.* **2012**, *7*, 947–960.

(26) Parthun, M. R. Hat1: the emerging cellular roles of a type B histone acetyltransferase. *Oncogene* **2007**, *26*, 5319–5328.

(27) Yang, X.; Yu, W.; Shi, L.; Sun, L.; Liang, J.; Yi, X.; Li, Q.; Zhang, Y.; Yang, F.; Han, X.; Zhang, D.; Yang, J.; Yao, Z.; Shang, Y. HAT4, a Golgi apparatus-anchored B-type histone acetyltransferase, acetylates free histone H4 and facilitates chromatin assembly. *Mol. Cell* **2011**, *44*, 39–50.

(28) Yang, X. J.; Ogryzko, V. V.; Nishikawa, J.; Howard, B. H.; Nakatani, Y. A p300/CBP-associated factor that competes with the adenoviral oncoprotein E1A. *Nature* **1996**, *382*, 319–324.

(29) Wittschleben, B. O.; Otero, G.; de Bizemont, T.; Fellows, J.; Erdjument-Bromage, H.; Ohba, R.; Li, Y.; Allis, C. D.; Tempst, P.; Svejstrup, J. Q. A novel histone acetyltransferase is an integral subunit of elongating RNA polymerase II holoenzyme. *Mol. Cell* **1999**, *4*, 123–128.

(30) Sampath, V.; Liu, B.; Tafrov, S.; Srinivasan, M.; Rieger, R.; Chen, E. I.; Sternglanz, R. Biochemical characterization of Hpa2 and Hpa3, two small closely related acetyltransferases from *Saccharomyces cerevisiae*. *J. Biol. Chem.* **2013**, *288*, 21506–21513.

(31) Lorch, Y.; Beve, J.; Gustafsson, C. M.; Myers, L. C.; Kornberg, R. D. Mediator-nucleosome interaction. *Mol. Cell* **2000**, *6*, 197–201.

(32) Dyda, F.; Klein, D. C.; Hickman, A. B. GCN5-related N-acetyltransferases: a structural overview. *Annu. Rev. Biophys. Biomol. Struct.* **2000**, *29*, 81–103.

(33) Marmorstein, R. Protein modules that manipulate histone tails for chromatin regulation. *Nat. Rev. Mol. Cell Biol.* **2001**, *2*, 422–432.

(34) Roth, S. Y.; Denu, J. M.; Allis, C. D. Histone acetyltransferases. *Annu. Rev. Biochem.* **2001**, *70*, 81–120.

(35) Kimura, A.; Matsubara, K.; Horikoshi, M. A decade of histone acetylation: marking eukaryotic chromosomes with specific codes. *J. Biochem.* **2005**, *138*, 647–662.

(36) Dancy, B. M.; Cole, P. A. Protein lysine acetylation by p300/CBP. *Chem. Rev.* **2015**, *115*, 2419–2452.

(37) Bordoli, L.; Netsch, M.; Luthi, U.; Lutz, W.; Eckner, R. Plant orthologs of p300/CBP: conservation of a core domain in metazoan p300/CBP acetyltransferase-related proteins. *Nucleic Acids Res.* **2001**, *29*, 589–597.

(38) Borrow, J.; Stanton, V. P., Jr.; Andresen, J. M.; Becher, R.; Behm, F. G.; Chaganti, R. S.; Civin, C. I.; Distcheche, C.; Dube, I.; Frischauf, A. M.; Horsman, D.; Mitelman, F.; Volinia, S.; Watmore, A. E.; Housman, D. E. The translocation t(8;16)(p11;p13) of acute myeloid leukaemia fuses a putative acetyltransferase to the CREB-binding protein. *Nat. Genet.* **1996**, *14*, 33–41.

(39) Neuwald, A. F.; Landsman, D. GCN5-related histone N-acetyltransferases belong to a diverse superfamily that includes the yeast SPT10 protein. *Trends Biochem. Sci.* **1997**, *22*, 154–155.

(40) Reifnyder, C.; Lowell, J.; Clarke, A.; Pillus, L. Yeast SAS silencing genes and human genes associated with AML and HIV-1 Tat interactions are homologous with acetyltransferases. *Nat. Genet.* **1997**, *16*, 109.

(41) Sapountzi, V.; Logan, I. R.; Robson, C. N. Cellular functions of TIP60. *Int. J. Biochem. Cell Biol.* **2006**, *38*, 1496–1509.

(42) Smith, E. R.; Eisen, A.; Gu, W.; Sattah, M.; Pannuti, A.; Zhou, J.; Cook, R. G.; Lucchesi, J. C.; Allis, C. D. ESA1 is a histone

acetyltransferase that is essential for growth in yeast. *Proc. Natl. Acad. Sci. U. S. A.* **1998**, *95*, 3561–3565.

(43) Iizuka, M.; Stillman, B. Histone acetyltransferase HBO1 interacts with the ORC1 subunit of the human initiator protein. *J. Biol. Chem.* **1999**, *274*, 23027–23034.

(44) Champagne, N.; Bertos, N. R.; Pelletier, N.; Wang, A. H.; Vezmar, M.; Yang, Y.; Heng, H. H.; Yang, X. J. Identification of a human histone acetyltransferase related to monocytic leukemia zinc finger protein. *J. Biol. Chem.* **1999**, *274*, 28528–28536.

(45) Smith, E. R.; Pannuti, A.; Gu, W.; Steurnagel, A.; Cook, R. G.; Allis, C. D.; Lucchesi, J. C. The drosophila MSL complex acetylates histone H4 at lysine 16, a chromatin modification linked to dosage compensation. *Mol. Cell Biol.* **2000**, *20*, 312–318.

(46) Mizzen, C. A.; Yang, X. J.; Kokubo, T.; Brownell, J. E.; Bannister, A. J.; Owen-Hughes, T.; Workman, J.; Wang, L.; Berger, S. L.; Kouzarides, T.; Nakatani, Y.; Allis, C. D. The TAF(II)250 subunit of TFIID has histone acetyltransferase activity. *Cell* **1996**, *87*, 1261–1270.

(47) Hsieh, Y. J.; Kundu, T. K.; Wang, Z.; Kovelman, R.; Roeder, R. G. The TFIIC90 subunit of TFIIC interacts with multiple components of the RNA polymerase III machinery and contains a histone-specific acetyltransferase activity. *Mol. Cell Biol.* **1999**, *19*, 7697–7704.

(48) York, B.; O'Malley, B. W. Steroid receptor coactivator (SRC) family: masters of systems biology. *J. Biol. Chem.* **2010**, *285*, 38743–38750.

(49) Spencer, T. E.; Jenster, G.; Burcin, M. M.; Allis, C. D.; Zhou, J.; Mizzen, C. A.; McKenna, N. J.; Onate, S. A.; Tsai, S. Y.; Tsai, M. J.; O'Malley, B. W. Steroid receptor coactivator-1 is a histone acetyltransferase. *Nature* **1997**, *389*, 194–198.

(50) Doi, M.; Hirayama, J.; Sassone-Corsi, P. Circadian regulator CLOCK is a histone acetyltransferase. *Cell* **2006**, *125*, 497–508.

(51) Lopes da Rosa, J.; Bajaj, V.; Spoonamore, J.; Kaufman, P. D. A small molecule inhibitor of fungal histone acetyltransferase Rtt109. *Bioorg. Med. Chem. Lett.* **2013**, *23*, 2853–2859.

(52) Karmodiya, K.; Anamika, K.; Muley, V.; Pradhan, S. J.; Bhide, Y.; Galande, S. Camello, a novel family of Histone Acetyltransferases that acetylate histone H4 and is essential for zebrafish development. *Sci. Rep.* **2014**, *4*, 6076.

(53) Friedmann, D. R.; Aguilar, A.; Fan, J.; Nachury, M. V.; Marmorstein, R. Structure of the alpha-tubulin acetyltransferase, alphaTAT1, and implications for tubulin-specific acetylation. *Proc. Natl. Acad. Sci. U. S. A.* **2012**, *109*, 19655–19660.

(54) Hou, F.; Zou, H. Two human orthologues of Eco1/Ctf7 acetyltransferases are both required for proper sister-chromatid cohesion. *Mol. Biol. Cell* **2005**, *16*, 3908–3918.

(55) Portela, A.; Esteller, M. Epigenetic modifications and human disease. *Nat. Biotechnol.* **2010**, *28*, 1057–1068.

(56) Selvi, B. R.; Chatterjee, S.; Modak, R.; Eswaramoorthy, M.; Kundu, T. K. Histone acetylation as a therapeutic target. *Subcell. Biochem.* **2013**, *61*, 567–596.

(57) Li, Y.; Yang, H. X.; Luo, R. Z.; Zhang, Y.; Li, M.; Wang, X.; Jia, W. H. High expression of p300 has an unfavorable impact on survival in resectable esophageal squamous cell carcinoma. *Ann. Thorac. Surg.* **2011**, *91*, 1531–1538.

(58) Li, M.; Luo, R. Z.; Chen, J. W.; Cao, Y.; Lu, J. B.; He, J. H.; Wu, Q. L.; Cai, M. Y. High expression of transcriptional coactivator p300 correlates with aggressive features and poor prognosis of hepatocellular carcinoma. *J. Transl. Med.* **2011**, *9*, 5.

(59) Bandyopadhyay, D.; Okan, N. A.; Bales, E.; Nascimento, L.; Cole, P. A.; Medrano, E. E. Down-regulation of p300/CBP histone acetyltransferase activates a senescence checkpoint in human melanocytes. *Cancer Res.* **2002**, *62*, 6231–6239.

(60) Pattabiraman, D. R.; McGirr, C.; Shakhbazov, K.; Barbier, V.; Krishnan, K.; Mukhopadhyay, P.; Hawthorne, P.; Trezise, A.; Ding, J.; Grimmond, S. M.; Papathanasiou, P.; Alexander, W. S.; Perkins, A. C.; Levesque, J. P.; Winkler, I. G.; Gonda, T. J. Interaction of c-Myb with p300 is required for the induction of acute myeloid leukemia (AML) by human AML oncogenes. *Blood* **2014**, *123*, 2682–2690.

- (61) Sun, X. J.; Wang, Z.; Wang, L.; Jiang, Y.; Kost, N.; Soong, T. D.; Chen, W. Y.; Tang, Z.; Nakadai, T.; Elemento, O.; Fischle, W.; Melnick, A.; Patel, D. J.; Nimer, S. D.; Roeder, R. G. A stable transcription factor complex nucleated by oligomeric AML1-ETO controls leukaemogenesis. *Nature* **2013**, *500*, 93–97.
- (62) Cereseto, A.; Manganaro, L.; Gutierrez, M. I.; Terreni, M.; Fittipaldi, A.; Lusic, M.; Marcello, A.; Giacca, M. Acetylation of HIV-1 integrase by p300 regulates viral integration. *EMBO J.* **2005**, *24*, 3070–3081.
- (63) Deng, L.; de la Fuente, C.; Fu, P.; Wang, L.; Donnelly, R.; Wade, J. D.; Lambert, P.; Li, H.; Lee, C. G.; Kashanchi, F. Acetylation of HIV-1 Tat by CBP/P300 increases transcription of integrated HIV-1 genome and enhances binding to core histones. *Virology* **2000**, *277*, 278–295.
- (64) Chen, S.; Feng, B.; George, B.; Chakrabarti, R.; Chen, M.; Chakrabarti, S. Transcriptional coactivator p300 regulates glucose-induced gene expression in endothelial cells. *Am. J. Physiol. Endocrinol. Metab.* **2010**, *298*, E127–E137.
- (65) Kikuchi, H.; Takami, Y.; Nakayama, T. GCN5: a supervisor in all-inclusive control of vertebrate cell cycle progression through transcription regulation of various cell cycle-related genes. *Gene* **2005**, *347*, 83–97.
- (66) Perez-Luna, M.; Aguasca, M.; Perearnau, A.; Serratos, J.; Martinez-Balbas, M.; Jesus Pujol, M.; Bachs, O. PCAF regulates the stability of the transcriptional regulator and cyclin-dependent kinase inhibitor p27 Kip1. *Nucleic Acids Res.* **2012**, *40*, 6520–6533.
- (67) Shiota, M.; Yokomizo, A.; Tada, Y.; Uchiumi, T.; Inokuchi, J.; Tatsugami, K.; Kuroiwa, K.; Yamamoto, K.; Seki, N.; Naito, S. P300/CBP-associated factor regulates Y-box binding protein-1 expression and promotes cancer cell growth, cancer invasion and drug resistance. *Cancer Sci.* **2010**, *101*, 1797–1806.
- (68) Toth, M.; Boros, I. M.; Balint, E. Elevated level of lysine 9-acetylated histone H3 at the MDR1 promoter in multidrug-resistant cells. *Cancer Sci.* **2012**, *103*, 659–669.
- (69) Terreni, M.; Valentini, P.; Liverani, V.; Gutierrez, M. I.; Di Primio, C.; Di Fenza, A.; Tozzini, V.; Allouch, A.; Albanese, A.; Giacca, M.; Cereseto, A. GCN5-dependent acetylation of HIV-1 integrase enhances viral integration. *Retrovirology* **2010**, *7*, 18.
- (70) Miao, J.; Fan, Q.; Cui, L.; Li, J.; Li, J.; Cui, L. The malaria parasite *Plasmodium falciparum* histones: organization, expression, and acetylation. *Gene* **2006**, *369*, 53–65.
- (71) Duclot, F.; Meffre, J.; Jacquet, C.; Gongora, C.; Maurice, T. Mice knock out for the histone acetyltransferase p300/CREB binding protein-associated factor develop a resistance to amyloid toxicity. *Neuroscience* **2010**, *167*, 850–863.
- (72) Wei, W.; Coelho, C. M.; Li, X.; Marek, R.; Yan, S.; Anderson, S.; Meyers, D.; Mukherjee, C.; Sbardella, G.; Castellano, S.; Milite, C.; Rotili, D.; Mai, A.; Cole, P. A.; Sah, P.; Kobor, M. S.; Bredy, T. W. p300/CBP-associated factor selectively regulates the extinction of conditioned fear. *J. Neurosci.* **2012**, *32*, 11930–11941.
- (73) Colussi, C.; Rosati, J.; Straino, S.; Spallotta, F.; Berni, R.; Stilli, D.; Rossi, S.; Musso, E.; Macchi, E.; Mai, A.; Sbardella, G.; Castellano, S.; Chimenti, C.; Frustaci, A.; Nebbioso, A.; Altucci, L.; Capogrossi, M. C.; Gaetano, C. Nepsilon-lysine acetylation determines dissociation from GAP junctions and lateralization of connexin 43 in normal and dystrophic heart. *Proc. Natl. Acad. Sci. U. S. A.* **2011**, *108*, 2795–2800.
- (74) Sun, C.; Wang, M.; Liu, X.; Luo, L.; Li, K.; Zhang, S.; Wang, Y.; Yang, Y.; Ding, F.; Gu, X. PCAF improves glucose homeostasis by suppressing the gluconeogenic activity of PGC-1alpha. *Cell Rep.* **2014**, *9*, 2250–2262.
- (75) Kindle, K. B.; Troke, P. J.; Collins, H. M.; Matsuda, S.; Bossi, D.; Bellodi, C.; Kalkhoven, E.; Salomoni, P.; Pelicci, P. G.; Minucci, S.; Heery, D. M. MOZ-TIF2 inhibits transcription by nuclear receptors and p53 by impairment of CBP function. *Mol. Cell. Biol.* **2005**, *25*, 988–1002.
- (76) Dulak, A. M.; Stojanov, P.; Peng, S.; Lawrence, M. S.; Fox, C.; Stewart, C.; Bandla, S.; Imamura, Y.; Schumacher, S. E.; Shefler, E.; McKenna, A.; Carter, S. L.; Cibulskis, K.; Sivachenko, A.; Saksena, G.; Voet, D.; Ramos, A. H.; Auclair, D.; Thompson, K.; Sougnez, C.; Onofrio, R. C.; Guiducci, C.; Beroukhi, R.; Zhou, Z.; Lin, L.; Lin, J.; Reddy, R.; Chang, A.; Landrenau, R.; Pennathur, A.; Ogino, S.; Luketich, J. D.; Golub, T. R.; Gabriel, S. B.; Lander, E. S.; Beer, D. G.; Godfrey, T. E.; Getz, G.; Bass, A. J. Exome and whole-genome sequencing of esophageal adenocarcinoma identifies recurrent driver events and mutational complexity. *Nat. Genet.* **2013**, *45*, 478–486.
- (77) Yang, X. J. MOZ and MORF acetyltransferases: molecular interaction, animal development and human disease. *Biochim. Biophys. Acta, Mol. Cell Res.* **2015**, *1853*, 1818–1826.
- (78) Shiota, M.; Yokomizo, A.; Masubuchi, D.; Tada, Y.; Inokuchi, J.; Eto, M.; Uchiumi, T.; Fujimoto, N.; Naito, S. Tip60 promotes prostate cancer cell proliferation by translocation of androgen receptor into the nucleus. *Prostate* **2010**, *70*, 540–554.
- (79) Ikura, T.; Ogryzko, V. V.; Grigoriev, M.; Groisman, R.; Wang, J.; Horikoshi, M.; Scully, R.; Qin, J.; Nakatani, Y. Involvement of the TIP60 histone acetylase complex in DNA repair and apoptosis. *Cell* **2000**, *102*, 463–473.
- (80) Iizuka, M.; Takahashi, Y.; Mizzen, C. A.; Cook, R. G.; Fujita, M.; Allis, C. D.; Frierson, H. F., Jr.; Fukusato, T.; Smith, M. M. Histone acetyltransferase Hbo1: catalytic activity, cellular abundance, and links to primary cancers. *Gene* **2009**, *436*, 108–114.
- (81) Dekker, F. J.; van den Bosch, T.; Martin, N. I. Small molecule inhibitors of histone acetyltransferases and deacetylases are potential drugs for inflammatory diseases. *Drug Discovery Today* **2014**, *19*, 654–660.
- (82) Kuo, M. H.; Allis, C. D. Roles of histone acetyltransferases and deacetylases in gene regulation. *BioEssays* **1998**, *20*, 615–626.
- (83) Lee, K. K.; Workman, J. L. Histone acetyltransferase complexes: one size doesn't fit all. *Nat. Rev. Mol. Cell Biol.* **2007**, *8*, 284–295.
- (84) Schuetz, A.; Bernstein, G.; Dong, A.; Antoshenko, T.; Wu, H.; Loppnau, P.; Bochkarev, A.; Plotnikov, A. N. Crystal structure of a binary complex between human GCN5 histone acetyltransferase domain and acetyl coenzyme A. *Proteins: Struct., Funct., Genet.* **2007**, *68*, 403–407.
- (85) Poux, A. N.; Cebrat, M.; Kim, C. M.; Cole, P. A.; Marmorstein, R. Structure of the GCN5 histone acetyltransferase bound to a bisubstrate inhibitor. *Proc. Natl. Acad. Sci. U. S. A.* **2002**, *99*, 14065–14070.
- (86) Poux, A. N.; Marmorstein, R. Molecular basis for Gcn5/PCAF histone acetyltransferase selectivity for histone and nonhistone substrates. *Biochemistry* **2003**, *42*, 14366–14374.
- (87) Clements, A.; Poux, A. N.; Lo, W. S.; Pillus, L.; Berger, S. L.; Marmorstein, R. Structural basis for histone and phosphohistone binding by the GCN5 histone acetyltransferase. *Mol. Cell* **2003**, *12*, 461–473.
- (88) Delvecchio, M.; Gaucher, J.; Aguilar-Gurreri, C.; Ortega, E.; Panne, D. Structure of the p300 catalytic core and implications for chromatin targeting and HAT regulation. *Nat. Struct. Mol. Biol.* **2013**, *20*, 1040–1046.
- (89) Liu, X.; Wang, L.; Zhao, K.; Thompson, P. R.; Hwang, Y.; Marmorstein, R.; Cole, P. A. The structural basis of protein acetylation by the p300/CBP transcriptional coactivator. *Nature* **2008**, *451*, 846–850.
- (90) Maksimoska, J.; Segura-Pena, D.; Cole, P. A.; Marmorstein, R. Structure of the p300 histone acetyltransferase bound to acetyl-coenzyme A and its analogues. *Biochemistry* **2014**, *53*, 3415–3422.
- (91) Thompson, P. R.; Kurooka, H.; Nakatani, Y.; Cole, P. A. Transcriptional coactivator protein p300. Kinetic characterization of its histone acetyltransferase activity. *J. Biol. Chem.* **2001**, *276*, 33721–33729.
- (92) Thompson, P. R.; Wang, D.; Wang, L.; Fulco, M.; Pediconi, N.; Zhang, D.; An, W.; Ge, Q.; Roeder, R. G.; Wong, J.; Levrero, M.; Sartorelli, V.; Cotter, R. J.; Cole, P. A. Regulation of the p300 HAT domain via a novel activation loop. *Nat. Struct. Mol. Biol.* **2004**, *11*, 308–315.
- (93) Yan, Y.; Barlev, N. A.; Haley, R. H.; Berger, S. L.; Marmorstein, R. Crystal structure of yeast Esa1 suggests a unified mechanism for catalysis and substrate binding by histone acetyltransferases. *Mol. Cell* **2000**, *6*, 1195–1205.

- (94) Huang, J.; Wan, B.; Wu, L.; Yang, Y.; Dou, Y.; Lei, M. Structural insight into the regulation of MOF in the male-specific lethal complex and the non-specific lethal complex. *Cell Res.* **2012**, *22*, 1078–1081.
- (95) Kadlec, J.; Hallacsi, E.; Lipp, M.; Holz, H.; Sanchez-Weatherby, J.; Cusack, S.; Akhtar, A. Structural basis for MOF and MSL3 recruitment into the dosage compensation complex by MSL1. *Nat. Struct. Mol. Biol.* **2011**, *18*, 142–149.
- (96) Sun, B.; Guo, S.; Tang, Q.; Li, C.; Zeng, R.; Xiong, Z.; Zhong, C.; Ding, J. Regulation of the histone acetyltransferase activity of hMOF via autoacetylation of Lys274. *Cell Res.* **2011**, *21*, 1262–1266.
- (97) Yuan, H.; Rossetto, D.; Mellert, H.; Dang, W.; Srinivasan, M.; Johnson, J.; Hodawadekar, S.; Ding, E. C.; Speicher, K.; Abshiru, N.; Perry, R.; Wu, J.; Yang, C.; Zheng, Y. G.; Speicher, D. W.; Thibault, P.; Verreault, A.; Johnson, F. B.; Berger, S. L.; Sternglanz, R.; McMahon, S. B.; Cote, J.; Marmorstein, R. MYST protein acetyltransferase activity requires active site lysine autoacetylation. *EMBO J.* **2012**, *31*, 58–70.
- (98) Li, X.; Wu, L.; Corsa, C. A.; Kunkel, S.; Dou, Y. Two mammalian MOF complexes regulate transcription activation by distinct mechanisms. *Mol. Cell* **2009**, *36*, 290–301.
- (99) Morales, V.; Straub, T.; Neumann, M. F.; Mengus, G.; Akhtar, A.; Becker, P. B. Functional integration of the histone acetyltransferase MOF into the dosage compensation complex. *EMBO J.* **2004**, *23*, 2258–2268.
- (100) Wu, J.; Xie, N.; Wu, Z.; Zhang, Y.; Zheng, Y. G. Bisubstrate inhibitors of the MYST HATs Esal and Tip60. *Bioorg. Med. Chem.* **2009**, *17*, 1381–1386.
- (101) Kwie, F. H.; Briet, M.; Soupaya, D.; Hoffmann, P.; Maturano, M.; Rodriguez, F.; Blonski, C.; Lherbet, C.; Baudoin-Dehoux, C. New potent bisubstrate inhibitors of histone acetyltransferase p300: design, synthesis and biological evaluation. *Chem. Biol. Drug Des.* **2011**, *77*, 86–92.
- (102) Cebrat, M.; Kim, C. M.; Thompson, P. R.; Daugherty, M.; Cole, P. A. Synthesis and analysis of potential prodrugs of coenzyme A analogues for the inhibition of the histone acetyltransferase p300. *Bioorg. Med. Chem.* **2003**, *11*, 3307–3313.
- (103) Wadia, J. S.; Dowdy, S. F. Transmembrane delivery of protein and peptide drugs by TAT-mediated transduction in the treatment of cancer. *Adv. Drug Delivery Rev.* **2005**, *57*, 579–596.
- (104) Zheng, Y.; Balasubramanyam, K.; Cebrat, M.; Buck, D.; Guidez, F.; Zelent, A.; Alani, R. M.; Cole, P. A. Synthesis and evaluation of a potent and selective cell-permeable p300 histone acetyltransferase inhibitor. *J. Am. Chem. Soc.* **2005**, *127*, 17182–17183.
- (105) Bandyopadhyay, K.; Baneres, J. L.; Martin, A.; Blonski, C.; Parello, J.; Gjerset, R. A. Spermidinyl-CoA-based HAT inhibitors block DNA repair and provide cancer-specific chemo- and radiosensitization. *Cell Cycle* **2009**, *8*, 2779–2788.
- (106) Cullis, P. M.; Wolfenden, R.; Cousens, L. S.; Alberts, B. M. Inhibition of histone acetylation by *N*-[2-(*S*-coenzyme A)acetyl] spermidine amide, a multisubstrate analog. *J. Biol. Chem.* **1982**, *257*, 12165–12169.
- (107) Balasubramanyam, K.; Swaminathan, V.; Ranganathan, A.; Kundu, T. K. Small molecule modulators of histone acetyltransferase p300. *J. Biol. Chem.* **2003**, *278*, 19134–19140.
- (108) Ghizzoni, M.; Wu, J.; Gao, T.; Haisma, H. J.; Dekker, F. J.; George Zheng, Y. 6-alkylsalicylates are selective Tip60 inhibitors and target the acetyl-CoA binding site. *Eur. J. Med. Chem.* **2012**, *47*, 337–344.
- (109) Hemshekhar, M.; Sebastin Santhosh, M.; Kemparaju, K.; Girish, K. S. Emerging roles of anacardic acid and its derivatives: a pharmacological overview. *Basic Clin. Pharmacol. Toxicol.* **2012**, *110*, 122–132.
- (110) Eliseeva, E. D.; Valkov, V.; Jung, M.; Jung, M. O. Characterization of novel inhibitors of histone acetyltransferases. *Mol. Cancer Ther.* **2007**, *6*, 2391–2398.
- (111) Wapenaar, H.; van der Wouden, P. E.; Groves, M. R.; Rotili, D.; Mai, A.; Dekker, F. J. Enzyme kinetics and inhibition of histone acetyltransferase KAT8. *Eur. J. Med. Chem.* **2015**, *105*, 289–296.
- (112) Ghizzoni, M.; Boltjes, A.; Graaf, C.; Haisma, H. J.; Dekker, F. J. Improved inhibition of the histone acetyltransferase PCAF by an anacardic acid derivative. *Bioorg. Med. Chem.* **2010**, *18*, 5826–5834.
- (113) Chatterjee, S.; Mizar, P.; Cassel, R.; Neidl, R.; Selvi, B. R.; Mohankrishna, D. V.; Vedamurthy, B. M.; Schneider, A.; Bousiges, O.; Mathis, C.; Cassel, J. C.; Eswaramoorthy, M.; Kundu, T. K.; Boutillier, A. L. A novel activator of CBP/p300 acetyltransferases promotes neurogenesis and extends memory duration in adult mice. *J. Neurosci.* **2013**, *33*, 10698–10712.
- (114) Sbardella, G.; Castellano, S.; Vicidomini, C.; Rotili, D.; Nebbioso, A.; Miceli, M.; Altucci, L.; Mai, A. Identification of long chain alkylidenemalonates as novel small molecule modulators of histone acetyltransferases. *Bioorg. Med. Chem. Lett.* **2008**, *18*, 2788–2792.
- (115) Castellano, S.; Milite, C.; Feoli, A.; Viviano, M.; Mai, A.; Novellino, E.; Tosco, A.; Sbardella, G. Identification of structural features of 2-alkylidene-1,3-dicarbonyl derivatives that induce inhibition and/or activation of histone acetyltransferases KAT3B/p300 and KAT2B/PCAF. *ChemMedChem* **2015**, *10*, 144–157.
- (116) Choi, K. C.; Jung, M. G.; Lee, Y. H.; Yoon, J. C.; Kwon, S. H.; Kang, H. B.; Kim, M. J.; Cha, J. H.; Kim, Y. J.; Jun, W. J.; Lee, J. M.; Yoon, H. G. Epigallocatechin-3-gallate, a histone acetyltransferase inhibitor, inhibits EBV-induced B lymphocyte transformation via suppression of RelA acetylation. *Cancer Res.* **2009**, *69*, 583–592.
- (117) Mai, A.; Cheng, D.; Bedford, M. T.; Valente, S.; Nebbioso, A.; Perrone, A.; Brosch, G.; Sbardella, G.; De Bellis, F.; Miceli, M.; Altucci, L. Epigenetic multiple ligands: mixed histone/protein methyltransferase, acetyltransferase, and class III deacetylase (sirtuin) inhibitors. *J. Med. Chem.* **2008**, *51*, 2279–2290.
- (118) Balasubramanyam, K.; Varier, R. A.; Altaf, M.; Swaminathan, V.; Siddappa, N. B.; Ranga, U.; Kundu, T. K. Curcumin, a novel p300/CREB-binding protein-specific inhibitor of acetyltransferase, represses the acetylation of histone/nonhistone proteins and histone acetyltransferase-dependent chromatin transcription. *J. Biol. Chem.* **2004**, *279*, 51163–51171.
- (119) Neckers, L.; Trepel, J.; Lee, S.; Chung, E. J.; Lee, M.-J.; Jung, Y.-J.; Marcu, M. G. Curcumin is an inhibitor of p300 histone acetyltransferase. *Med. Chem.* **2006**, *2*, 169–174.
- (120) Fu, S.; Kurzrock, R. Development of curcumin as an epigenetic agent. *Cancer* **2010**, *116*, 4670–4676.
- (121) Costi, R.; Di Santo, R.; Artico, M.; Miele, G.; Valentini, P.; Novellino, E.; Cereseto, A. Cinnamoyl compounds as simple molecules that inhibit p300 histone acetyltransferase. *J. Med. Chem.* **2007**, *50*, 1973–1977.
- (122) Arif, M.; Vedamurthy, B. M.; Choudhari, R.; Ostwal, Y. B.; Mantelingu, K.; Kodaganur, G. S.; Kundu, T. K. Nitric oxide-mediated histone hyperacetylation in oral cancer: target for a water-soluble HAT inhibitor, CTK7A. *Chem. Biol.* **2010**, *17*, 903–913.
- (123) Ingolfsson, H. I.; Thakur, P.; Herold, K. F.; Hobart, E. A.; Ramsey, N. B.; Periole, X.; de Jong, D. H.; Zwama, M.; Yilmaz, D.; Hall, K.; Maretzky, T.; Hemmings, H. C., Jr.; Blobel, C.; Marrink, S. J.; Kocer, A.; Sack, J. T.; Andersen, O. S. Phytochemicals perturb membranes and promiscuously alter protein function. *ACS Chem. Biol.* **2014**, *9*, 1788–1798.
- (124) Balasubramanyam, K.; Altaf, M.; Varier, R. A.; Swaminathan, V.; Ravindran, A.; Sadhale, P. P.; Kundu, T. K. Polyisoprenylated benzophenone, garcinol, a natural histone acetyltransferase inhibitor, represses chromatin transcription and alters global gene expression. *J. Biol. Chem.* **2004**, *279*, 33716–33726.
- (125) Arif, M.; Pradhan, S. K.; G R, T.; Vedamurthy, B. M.; Agrawal, S.; Dasgupta, D.; Kundu, T. K. Mechanism of p300 specific histone acetyltransferase inhibition by small molecules. *J. Med. Chem.* **2009**, *52*, 267–277.
- (126) Mantelingu, K.; Reddy, B. A.; Swaminathan, V.; Kishore, A. H.; Siddappa, N. B.; Kumar, G. V.; Nagashankar, G.; Natesh, N.; Roy, S.; Sadhale, P. P.; Ranga, U.; Narayana, C.; Kundu, T. K. Specific inhibition of p300-HAT alters global gene expression and represses HIV replication. *Chem. Biol.* **2007**, *14*, 645–657.

- (127) Milite, C.; Feoli, A.; Sasaki, K.; La Pietra, V.; Balzano, A. L.; Marinelli, L.; Mai, A.; Novellino, E.; Castellano, S.; Tosco, A.; Sbardella, G. A novel cell-permeable, selective, and noncompetitive inhibitor of KAT3 histone acetyltransferases from a combined molecular pruning/classical isosterism approach. *J. Med. Chem.* **2015**, *58*, 2779–2798.
- (128) Maurer, B.; Rumpf, T.; Scharfe, M.; Stolfa, D. A.; Schmitt, M. L.; He, W.; Verdin, E.; Sippl, W.; Jung, M. Inhibitors of the NAD(+)-dependent protein desuccinylase and demalonylase Sirt5. *ACS Med. Chem. Lett.* **2012**, *3*, 1050–1053.
- (129) Ravindra, K. C.; Selvi, B. R.; Arif, M.; Reddy, B. A.; Thanuja, G. R.; Agrawal, S.; Pradhan, S. K.; Nagashayana, N.; Dasgupta, D.; Kundu, T. K. Inhibition of lysine acetyltransferase KAT3B/p300 activity by a naturally occurring hydroxynaphthoquinone, plumbagin. *J. Biol. Chem.* **2009**, *284*, 24453–24464.
- (130) Vasudevarao, M. D.; Mizar, P.; Kumari, S.; Mandal, S.; Siddhanta, S.; Swamy, M. M.; Kaypee, S.; Kodihalli, R. C.; Banerjee, A.; Naryana, C.; Dasgupta, D.; Kundu, T. K. Naphthoquinone-mediated inhibition of lysine acetyltransferase KAT3B/p300, basis for non-toxic inhibitor synthesis. *J. Biol. Chem.* **2014**, *289*, 7702–7717.
- (131) Modak, R.; Basha, J.; Bharathy, N.; Maity, K.; Mizar, P.; Bhat, A. V.; Vasudevan, M.; Rao, V. K.; Kok, W. K.; Natesh, N.; Taneja, R.; Kundu, T. K. Probing p300/CBP associated factor (PCAF)-dependent pathways with a small molecule inhibitor. *ACS Chem. Biol.* **2013**, *8*, 1311–1323.
- (132) Tohyama, S.; Tomura, A.; Ikeda, N.; Hatano, M.; Odanaka, J.; Kubota, Y.; Umekita, M.; Igarashi, M.; Sawa, R.; Morino, T. Discovery and characterization of NK13650s, naturally occurring p300-selective histone acetyltransferase inhibitors. *J. Org. Chem.* **2012**, *77*, 9044–9052.
- (133) Furumai, R.; Komatsu, Y.; Nishino, N.; Khochbin, S.; Yoshida, M.; Horinouchi, S. Potent histone deacetylase inhibitors built from trichostatin A and cyclic tetrapeptide antibiotics including trapoxin. *Proc. Natl. Acad. Sci. U. S. A.* **2001**, *98*, 87–92.
- (134) Stimson, L.; Rowlands, M. G.; Newbatt, Y. M.; Smith, N. F.; Raynaud, F. L.; Rogers, P.; Bavetsias, V.; Gorsuch, S.; Jarman, M.; Bannister, A.; Kouzarides, T.; McDonald, E.; Workman, P.; Aherne, G. W. Isothiazolones as inhibitors of PCAF and p300 histone acetyltransferase activity. *Mol. Cancer Ther.* **2005**, *4*, 1521–1532.
- (135) Furdas, S. D.; Kannan, S.; Sippl, W.; Jung, M. Small molecule inhibitors of histone acetyltransferases as epigenetic tools and drug candidates. *Arch. Pharm. (Weinheim, Ger.)* **2012**, *345*, 7–21.
- (136) Furdas, S. D.; Shekfeh, S.; Bissinger, E. M.; Wagner, J. M.; Schlimme, S.; Valkov, V.; Hendzel, M.; Jung, M.; Sippl, W. Synthesis and biological testing of novel pyridoisothiazolones as histone acetyltransferase inhibitors. *Bioorg. Med. Chem.* **2011**, *19*, 3678–3689.
- (137) Furdas, S. D.; Hoffmann, I.; Robaa, D.; Herquel, B.; Malinka, W.; Świątek, P.; Akhtar, A.; Sippl, W.; Jung, M. Pyrido- and benzisothiazolones as inhibitors of histone acetyltransferases (HATs). *MedChemComm* **2014**, *5*, 1856–1862.
- (138) Carneiro, V. C.; de Abreu da Silva, I. C.; Torres, E. J.; Caby, S.; Lancelot, J.; Vanderstraete, M.; Furdas, S. D.; Jung, M.; Pierce, R. J.; Fantappie, M. R. Epigenetic changes modulate schistosome egg formation and are a novel target for reducing transmission of schistosomiasis. *PLoS Pathog.* **2014**, *10*, e1004116.
- (139) Gajer, J. M.; Furdas, S. D.; Grunder, A.; Gothwal, M.; Heinicke, U.; Keller, K.; Colland, F.; Fulda, S.; Pahl, H. L.; Fichtner, I.; Sippl, W.; Jung, M. Histone acetyltransferase inhibitors block neuroblastoma cell growth in vivo. *Oncogenesis* **2015**, *4*, e137.
- (140) Mai, A.; Rotili, D.; Tarantino, D.; Ornaghi, P.; Tosi, F.; Vicidomini, C.; Sbardella, G.; Nebbioso, A.; Miceli, M.; Altucci, L.; Filetici, P. Small-molecule inhibitors of histone acetyltransferase activity: identification and biological properties. *J. Med. Chem.* **2006**, *49*, 6897–6907.
- (141) Secci, D.; Carradori, S.; Bizzarri, B.; Bolasco, A.; Ballario, P.; Patramani, Z.; Fragapane, P.; Vernarecci, S.; Canzonetta, C.; Filetici, P. Synthesis of a novel series of thiazole-based histone acetyltransferase inhibitors. *Bioorg. Med. Chem.* **2014**, *22*, 1680–1689.
- (142) Trisciuglio, D.; Ragazzoni, Y.; Pelosi, A.; Desideri, M.; Carradori, S.; Gabellini, C.; Maresca, G.; Nescatelli, R.; Secci, D.; Bolasco, A.; Bizzarri, B.; Cavaliere, C.; D'Agnano, I.; Filetici, P.; Ricci-Vitiani, L.; Rizzo, M. G.; Del Bufalo, D. CPTH6, a thiazole derivative, induces histone hypoacetylation and apoptosis in human leukemia cells. *Clin. Cancer Res.* **2012**, *18*, 475–486.
- (143) Chimenti, F.; Bizzarri, B.; Maccioni, E.; Secci, D.; Bolasco, A.; Chimenti, P.; Fioravanti, R.; Granese, A.; Carradori, S.; Tosi, F.; Ballario, P.; Vernarecci, S.; Filetici, P. A novel histone acetyltransferase inhibitor modulating Gcn5 network: cyclopentylidene-[4-(4'-chlorophenyl)thiazol-2-yl]hydrazone. *J. Med. Chem.* **2009**, *52*, 530–536.
- (144) Biel, M.; Kretsovali, A.; Karatzali, E.; Papamatheakis, J.; Giannini, A. Design, synthesis, and biological evaluation of a small-molecule inhibitor of the histone acetyltransferase Gcn5. *Angew. Chem., Int. Ed.* **2004**, *43*, 3974–3976.
- (145) Bowers, E. M.; Yan, G.; Mukherjee, C.; Orry, A.; Wang, L.; Holbert, M. A.; Crump, N. T.; Hazzalin, C. A.; Liszczak, G.; Yuan, H.; Larocca, C.; Saldanha, S. A.; Abagyan, R.; Sun, Y.; Meyers, D. J.; Marmorstein, R.; Mahadevan, L. C.; Alani, R. M.; Cole, P. A. Virtual ligand screening of the p300/CBP histone acetyltransferase: identification of a selective small molecule inhibitor. *Chem. Biol.* **2010**, *17*, 471–482.
- (146) Shrimp, J. H.; Sorum, A. W.; Garlick, J. M.; Guasch, L.; Nicklaus, M. C.; Meier, J. L. Characterizing the Covalent Targets of a Small Molecule Inhibitor of the Lysine Acetyltransferase P300. *ACS Med. Chem. Lett.* **2015**, DOI: 10.1021/acsmedchemlett.5b00385.
- (147) Dancy, B. M.; Crump, N. T.; Peterson, D. J.; Mukherjee, C.; Bowers, E. M.; Ahn, Y. H.; Yoshida, M.; Zhang, J.; Mahadevan, L. C.; Meyers, D. J.; Boeke, J. D.; Cole, P. A. Live-cell studies of p300/CBP histone acetyltransferase activity and inhibition. *ChemBioChem* **2012**, *13*, 2113–2121.
- (148) Gao, X. N.; Lin, J.; Ning, Q. Y.; Gao, L.; Yao, Y. S.; Zhou, J. H.; Li, Y. H.; Wang, L. L.; Yu, L. A histone acetyltransferase p300 inhibitor C646 induces cell cycle arrest and apoptosis selectively in AML1-ETO-positive AML cells. *PLoS One* **2013**, *8*, e55481.
- (149) Yang, H.; Pinello, C. E.; Luo, J.; Li, D.; Wang, Y.; Zhao, L. Y.; Jahn, S. C.; Saldanha, S. A.; Planck, J.; Geary, K. R.; Ma, H.; Law, B. K.; Roush, W. R.; Hodder, P.; Liao, D. Small-molecule inhibitors of acetyltransferase p300 identified by high-throughput screening are potent anticancer agents. *Mol. Cancer Ther.* **2013**, *12*, 610–620.
- (150) Wu, J.; Wang, J.; Li, M.; Yang, Y.; Wang, B.; Zheng, Y. G. Small molecule inhibitors of histone acetyltransferase Tip60. *Bioorg. Chem.* **2011**, *39*, 53–58.
- (151) Coffey, K.; Blackburn, T. J.; Cook, S.; Golding, B. T.; Griffin, R. J.; Hardcastle, I. R.; Hewitt, L.; Huberman, K.; McNeill, H. V.; Newell, D. R.; Roche, C.; Ryan-Munden, C. A.; Watson, A.; Robson, C. N. Characterisation of a Tip60 specific inhibitor, NU9056, in prostate cancer. *PLoS One* **2012**, *7*, e45539.
- (152) Gao, C.; Bourke, E.; Scobie, M.; Famme, M. A.; Koolmeister, T.; Helleday, T.; Eriksson, L. A.; Lowndes, N. F.; Brown, J. A. Rational design and validation of a Tip60 histone acetyltransferase inhibitor. *Sci. Rep.* **2014**, *4*, 5372.
- (153) Majmudar, C. Y.; Hojfeldt, J. W.; Arevang, C. J.; Pomerantz, W. C.; Gagnon, J. K.; Schultz, P. J.; Cesa, L. C.; Doss, C. H.; Rowe, S. P.; Vasquez, V.; Tamayo-Castillo, G.; Cierpicki, T.; Brooks, C. L., 3rd; Sherman, D. H.; Mapp, A. K. Sekikaic acid and lobaric acid target a dynamic interface of the coactivator CBP/p300. *Angew. Chem., Int. Ed.* **2012**, *51*, 11258–11262.
- (154) Sachchidanand; Resnick-Silverman, L.; Yan, S.; Mutjaba, S.; Liu, W. J.; Zeng, L.; Manfredi, J. J.; Zhou, M. M. Target structure-based discovery of small molecules that block human p53 and CREB binding protein association. *Chem. Biol.* **2006**, *13*, 81–90.
- (155) Wang, Q.; Wang, R.; Zhang, B.; Zhang, S.; Zheng, Y.; Wang, Z. Small organic molecules targeting PCAF bromodomain as potent inhibitors of HIV-1 replication. *MedChemComm* **2013**, *4*, 737–740.
- (156) Borah, J. C.; Mujtaba, S.; Karakikes, I.; Zeng, L.; Muller, M.; Patel, J.; Moshkina, N.; Morohashi, K.; Zhang, W.; Gerona-Navarro, G.; Hajjar, R. J.; Zhou, M. M. A small molecule binding to the

coactivator CREB-binding protein blocks apoptosis in cardiomyocytes. *Chem. Biol.* **2011**, *18*, 531–541.

(157) Rooney, T. P.; Filippakopoulos, P.; Fedorov, O.; Picaud, S.; Cortopassi, W. A.; Hay, D. A.; Martin, S.; Tumber, A.; Rogers, C. M.; Philpott, M.; Wang, M.; Thompson, A. L.; Heightman, T. D.; Pryde, D. C.; Cook, A.; Paton, R. S.; Muller, S.; Knapp, S.; Brennan, P. E.; Conway, S. J. A series of potent CREBBP bromodomain ligands reveals an induced-fit pocket stabilized by a cation- π interaction. *Angew. Chem., Int. Ed.* **2014**, *53*, 6126–6130.

(158) Hay, D. A.; Fedorov, O.; Martin, S.; Singleton, D. C.; Tallant, C.; Wells, C.; Picaud, S.; Philpott, M.; Monteiro, O. P.; Rogers, C. M.; Conway, S. J.; Rooney, T. P.; Tumber, A.; Yapp, C.; Filippakopoulos, P.; Bunnage, M. E.; Muller, S.; Knapp, S.; Schofield, C. J.; Brennan, P. E. Discovery and optimization of small-molecule ligands for the CBP/p300 bromodomains. *J. Am. Chem. Soc.* **2014**, *136*, 9308–9319.

(159) Picaud, S.; Fedorov, O.; Thanasopoulou, A.; Leonards, K.; Jones, K.; Meier, J.; Olzscha, H.; Monteiro, O.; Martin, S.; Philpott, M.; Tumber, A.; Filippakopoulos, P.; Yapp, C.; Wells, C.; Che, K. H.; Bannister, A.; Robson, S.; Kumar, U.; Parr, N.; Lee, K.; Lugo, D.; Jeffrey, P.; Taylor, S.; Vecellio, M. L.; Bountra, C.; Brennan, P. E.; O'Mahony, A.; Velichko, S.; Muller, S.; Hay, D.; Daniels, D. L.; Urh, M.; La Thangue, N. B.; Kouzarides, T.; Prinjha, R.; Schwaller, J.; Knapp, S. Generation of a selective small molecule inhibitor of the CBP/p300 bromodomain for leukemia therapy. *Cancer Res.* **2015**, *75*, 5106–5119.

(160) Arrowsmith, C. H.; Bountra, C.; Fish, P. V.; Lee, K.; Schapira, M. Epigenetic protein families: a new frontier for drug discovery. *Nat. Rev. Drug Discovery* **2012**, *11*, 384–400.

(161) Hilton, I. B.; D'Ippolito, A. M.; Vockley, C. M.; Thakore, P. I.; Crawford, G. E.; Reddy, T. E.; Gersbach, C. A. Epigenome editing by a CRISPR-Cas9-based acetyltransferase activates genes from promoters and enhancers. *Nat. Biotechnol.* **2015**, *33*, 510–517.

(162) Mottamal, M.; Zheng, S.; Huang, T. L.; Wang, G. Histone deacetylase inhibitors in clinical studies as templates for new anticancer agents. *Molecules* **2015**, *20*, 3898–3941.

(163) Filippakopoulos, P.; Qi, J.; Picaud, S.; Shen, Y.; Smith, W. B.; Fedorov, O.; Morse, E. M.; Keates, T.; Hickman, T. T.; Felletar, L.; Philpott, M.; Munro, S.; McKeown, M. R.; Wang, Y.; Christie, A. L.; West, N.; Cameron, M. J.; Schwartz, B.; Heightman, T. D.; La Thangue, N.; French, C. A.; Wiest, O.; Kung, A. L.; Knapp, S.; Bradner, J. E. Selective inhibition of BET bromodomains. *Nature* **2010**, *468*, 1067–1073.

(164) Brand, M.; Measures, A. M.; Wilson, B. G.; Cortopassi, W. A.; Alexander, R.; Hoss, M.; Hewings, D. S.; Rooney, T. P.; Paton, R. S.; Conway, S. J. Small molecule inhibitors of bromodomain-acetyl-lysine interactions. *ACS Chem. Biol.* **2015**, *10*, 22–39.

(165) Andreotti, G.; Monticelli, M.; Cubellis, M. V. Looking for protein stabilizing drugs with thermal shift assay. *Drug Test. Anal.* **2015**, *7*, 831–834.

(166) Jerabek-Willemsen, M.; Andre, T.; Wanner, R.; Roth, H. M.; Duhr, S.; Baaske, P.; Breitsprecher, D. MicroScale Thermophoresis: Interaction analysis and beyond. *J. Mol. Struct.* **2014**, *1077*, 101–113.

(167) Baell, J. B.; Holloway, G. A. New substructure filters for removal of pan assay interference compounds (PAINS) from screening libraries and for their exclusion in bioassays. *J. Med. Chem.* **2010**, *53*, 2719–2740.

(168) Pan, Z.; Scheerens, H.; Li, S. J.; Schultz, B. E.; Sprengeler, P. A.; Burrill, L. C.; Mendonca, R. V.; Sweeney, M. D.; Scott, K. C.; Grothaus, P. G.; Jeffery, D. A.; Spoerke, J. M.; Honigberg, L. A.; Young, P. R.; Dalrymple, S. A.; Palmer, J. T. Discovery of selective irreversible inhibitors for Bruton's tyrosine kinase. *ChemMedChem* **2007**, *2*, 58–61.

(169) Arrowsmith, C. H.; Audia, J. E.; Austin, C.; Baell, J.; Bennett, J.; Blagg, J.; Bountra, C.; Brennan, P. E.; Brown, P. J.; Bunnage, M. E.; Buser-Doepner, C.; Campbell, R. M.; Carter, A. J.; Cohen, P.; Copeland, R. A.; Cravatt, B.; Dahlin, J. L.; Dhanak, D.; Edwards, A. M.; Frederiksen, M.; Frye, S. V.; Gray, N.; Grimshaw, C. E.; Hepworth, D.; Howe, T.; Huber, K. V.; Jin, J.; Knapp, S.; Kotz, J. D.; Kruger, R. G.; Lowe, D.; Mader, M. M.; Marsden, B.; Mueller-Fahrnow, A.; Muller,

S.; O'Hagan, R. C.; Overington, J. P.; Owen, D. R.; Rosenberg, S. H.; Roth, B.; Ross, R.; Schapira, M.; Schreiber, S. L.; Shoichet, B.; Sundstrom, M.; Superti-Furga, G.; Taunton, J.; Toledo-Sherman, L.; Walpole, C.; Walters, M. A.; Willson, T. M.; Workman, P.; Young, R. N.; Zuercher, W. J. The promise and peril of chemical probes. *Nat. Chem. Biol.* **2015**, *11*, 536–541.

(170) Scholz, C.; Weinert, B. T.; Wagner, S. A.; Beli, P.; Miyake, Y.; Qi, J.; Jensen, L. J.; Streicher, W.; McCarthy, A. R.; Westwood, N. J.; Lain, S.; Cox, J.; Matthias, P.; Mann, M.; Bradner, J. E.; Choudhary, C. Acetylation site specificities of lysine deacetylase inhibitors in human cells. *Nat. Biotechnol.* **2015**, *33*, 415–423.

(171) Glozak, M. A.; Sengupta, N.; Zhang, X.; Seto, E. Acetylation and deacetylation of non-histone proteins. *Gene* **2005**, *363*, 15–23.

(172) Singh, B. N.; Zhang, G. H.; Hwa, Y. L.; Li, J. P.; Dowdy, S. C.; Jiang, S. W. Nonhistone protein acetylation as cancer therapy targets. *Expert Rev. Anticancer Ther.* **2010**, *10*, 935–954.

(173) Weinert, B. T.; Scholz, C.; Wagner, S. A.; Iesmantavicius, V.; Su, D.; Daniel, J. A.; Choudhary, C. Lysine succinylation is a frequently occurring modification in prokaryotes and eukaryotes and extensively overlaps with acetylation. *Cell Rep.* **2013**, *4*, 842–851.

(174) Baeza, J.; Smallegan, M. J.; Denu, J. M. Site-specific reactivity of nonenzymatic lysine acetylation. *ACS Chem. Biol.* **2015**, *10*, 122–128.

(175) Weinert, B. T.; Moustafa, T.; Iesmantavicius, V.; Zechner, R.; Choudhary, C. Analysis of acetylation stoichiometry suggests that SIRT3 repairs nonenzymatic acetylation lesions. *EMBO J.* **2015**, *34*, 2620–2632.

4.2. Manuscript 2: Sirtuin 1 Inhibiting Thiocyanates (S1th)—A New Class of Isotype Selective Inhibitors of NAD⁺ Dependent Lysine Deacetylases.

N., Wössner, Z., Alhalabi, J., Nieto, S., Swyter, J., Gan, K., Schmidtkunz, L., Zhang, A., Vaquero, H., Ovaa, O., Einsle., W., Sippl, M., Jung.

Frontiers in oncology. 10, 657, (2020).



Sirtuin 1 Inhibiting Thiocyanates (S1th)—A New Class of Isotype Selective Inhibitors of NAD⁺ Dependent Lysine Deacetylases

Nathalie Wössner¹, Zayan Alhalabi², Jessica González³, Sören Swyter¹, Jin Gan⁴, Karin Schmidtkunz¹, Lin Zhang⁵, Alejandro Vaquero³, Huib Ovaa⁴, Oliver Einsle⁵, Wolfgang Sippl² and Manfred Jung^{1*}

¹ Department of Pharmaceutical and Medicinal Chemistry, Institute of Pharmaceutical Sciences, University of Freiburg, Freiburg im Breisgau, Germany, ² Department of Medicinal Chemistry, Institute of Pharmacy, University of Halle-Wittenberg, Halle, Germany, ³ Chromatin Biology Laboratory, Josep Carreras Leukaemia Research Institute (IJC), Badalona, Barcelona, Spain, ⁴ Department of Cell and Chemical Biology, Oncode Institute, Leiden University Medical Center, Leiden, Netherlands, ⁵ Department of Protein Crystallography, Institute of Biochemistry, University of Freiburg, Freiburg im Breisgau, Germany

OPEN ACCESS

Edited by:

Cristian Scatena,
University of Pisa, Italy

Reviewed by:

Sumit Sahni,
Kolling Institute of Medical
Research, Australia
Sujit Kumar Bhutia,
National Institute of Technology
Rourkela, India

*Correspondence:

Manfred Jung
manfred.jung@
pharmazie.uni-freiburg.de

Specialty section:

This article was submitted to
Cancer Metabolism,
a section of the journal
Frontiers in Oncology

Received: 09 December 2019

Accepted: 08 April 2020

Published: 30 April 2020

Citation:

Wössner N, Alhalabi Z, González J, Swyter S, Gan J, Schmidtkunz K, Zhang L, Vaquero A, Ovaa H, Einsle O, Sippl W and Jung M (2020) Sirtuin 1 Inhibiting Thiocyanates (S1th)—A New Class of Isotype Selective Inhibitors of NAD⁺ Dependent Lysine Deacetylases. *Front. Oncol.* 10:657. doi: 10.3389/fonc.2020.00657

Sirtuin 1 (Sirt1) is a NAD⁺ dependent lysine deacetylase associated with the pathogenesis of various diseases including cancer. In many cancer types Sirt1 expression is increased and higher levels have been associated with metastasis and poor prognosis. However, it was also shown, that Sirt1 can have tumor suppressing properties and in some instances even a dual role for the same cancer type has been reported. Increased Sirt1 activity has been linked to extension of the life span of cells, respectively, organisms by promoting DNA repair processes and downregulation of tumor suppressor proteins. This may have the downside of enhancing tumor growth and metastasis. In mice embryonic fibroblasts depletion of Sirt1 was shown to decrease levels of the DNA damage sensor histone H2AX. Impairment of DNA repair mechanisms by Sirt1 can promote tumorigenesis but also lower chemoresistance toward DNA targeting therapies. Despite many biological studies, there is currently just one small molecule Sirt1 inhibitor in clinical trials. Selisistat (EX-527) reached phase III clinical trials for treatment of Huntington's Disease. New small molecule Sirt1 modulators are crucial for further investigation of the contradicting roles of Sirt1 in cancer. We tested a small library of commercially available compounds that were proposed by virtual screening and docking studies against Sirt1, 2 and 3. A thienopyrimidone featuring a phenyl thiocyanate moiety was found to selectively inhibit Sirt1 with an IC₅₀ of 13 μM. Structural analogs lacking the thiocyanate function did not show inhibition of Sirt1 revealing this group as key for the selectivity and affinity toward Sirt1. Further analogs with higher solubility were identified through iterative docking studies and *in vitro* testing. The most active compounds (down to 5 μM IC₅₀) were further studied in cells. The ratio of phosphorylated γH2AX to unmodified H2AX is lower when Sirt1 is depleted or inhibited. Our new Sirtuin 1 inhibiting thiocyanates (S1th) lead to similarly lowered γH2AX/H2AX ratios in mouse embryonic fibroblasts as Sirt1 knockout and treatment with the reference inhibitor EX-527. In

addition to that we were able to show antiproliferative activity, inhibition of migration and colony forming as well as hyperacetylation of Sirt1 targets p53 and H3 by the S1th in cervical cancer cells (HeLa). These results reveal thiocyanates as a promising new class of selective Sirt1 inhibitors.

Keywords: sirtuins, lysine deacetylase, thiocyanate, DNA damage, histone, H2AX, p53

INTRODUCTION

Sirtuins are deacetylases able to cleave off acetyl and also longer chain acyl groups from the ϵ -amino residue of lysines in histones and non-histone proteins in a NAD⁺-dependent manner. For their activity on histones they have been designated to form class III of the histone deacetylases (HDACs). Generally, HDACs are known to deacetylate resp. deacetylate various protein substrates and for sirtuins many findings actually focus on non-histone substrates (1). The human genome contains seven sirtuins isotypes (Sirt1-7) that differ in substrate spectrum and localization (2). With regard to drug discovery the majority of efforts has focused on Sirt2 where many small molecule inhibitors are now present. Other isotypes have been addressed as well but only for Sirt1 a drug is currently in clinical trials (see below) (3, 4). Due to conflicting evidence of roles of sirtuin isotypes in different diseases both activators and inhibitors have been investigated (5–7).

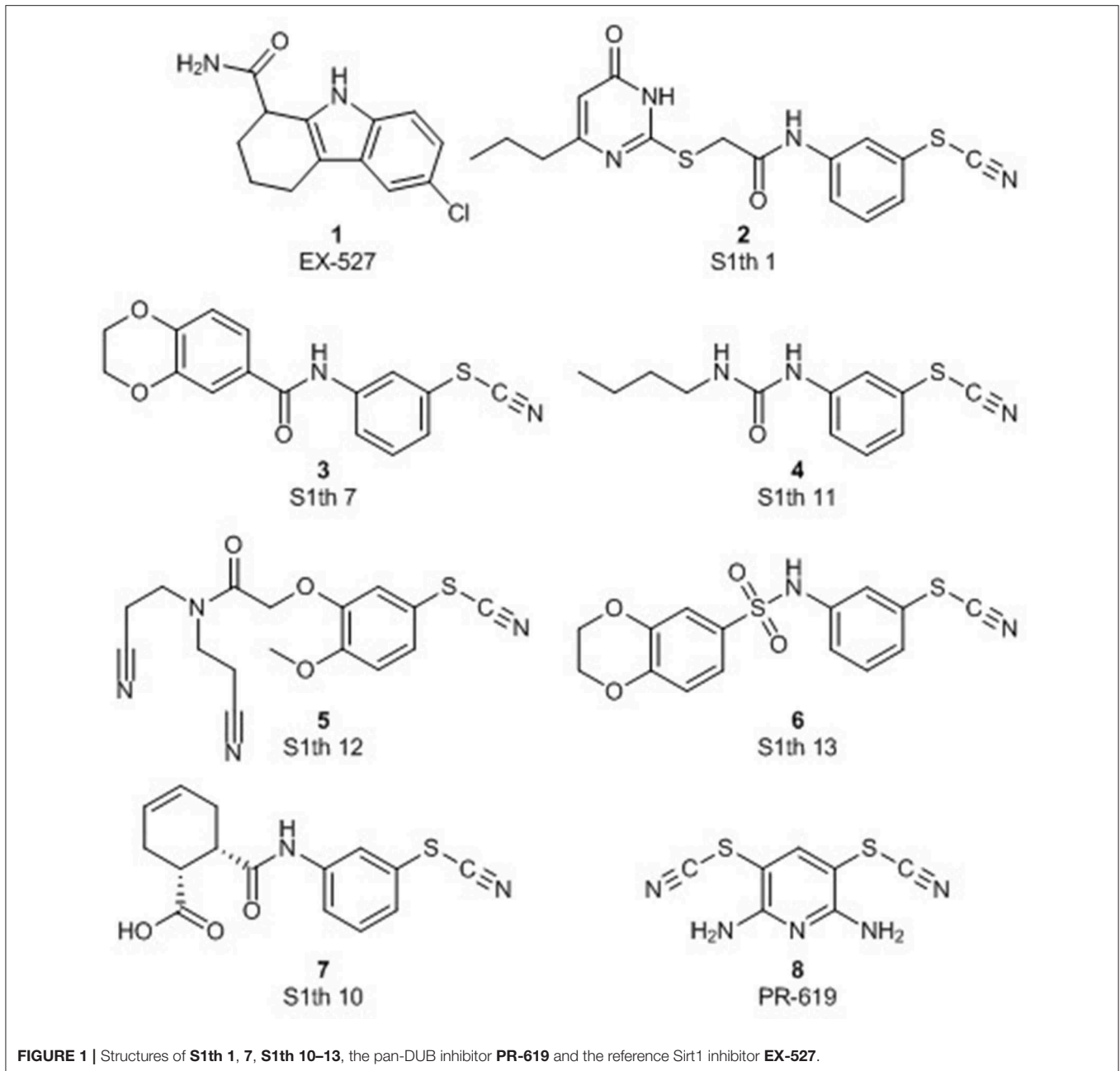
Sirt2 has been discussed as an anticancer target but also tumor suppressive activities of Sirt2 have been mentioned (8–15). These effects might be tissue or organ specific which complicates drug development and no Sirt2 inhibitor has reached clinical trials yet. Sirt6 has been identified as a tumor suppressor and hence Sirt6 activators are the focus of drug discovery efforts regarding this phenotype (16, 17). But also tumor promoting effects of Sirt6 have been described (18). In addition, Sirt6 inhibition might be a way to increase the efficacy of cytostatic drugs with DNA-damaging mode of action (19).

Regarding Sirt1, it has been studied strongly in the context of neurodegenerative diseases and Selisistat [EX-527 (1), **Figure 1**] is a potent and selective Sirt1 inhibitor that was undergoing clinical testing in Huntington's disease (20). A strong focus attention was dedicated to potentially lifespan extending Sirt1 activators. The initial studies mostly dealt with resveratrol, a natural product with pleiotropic activities which makes mechanistic studies difficult. Later, drug-like sirtuin activating compounds (STACs) were identified and went into clinical trials. While the discussion on the relevance and robustness of activation of deacetylation by Sirt1 has been very controversial, some effects of resveratrol have indeed been linked to Sirt1 in animal models and depending on the deacetylation substrate, activation has been proven in reliable biochemical assays (21). With regard to cancer, Sirt1 was postulated as an anticancer target, e.g., promoting epithelial-to-mesenchymal transition (EMT) in many cancer types (22) but it was also reported to suppress EMT in types like ovarian cancer. Yang et al. postulated that the conflicting behavior of Sirt1 in cancer cells may depend on its subcellular localization (23). In some cancer

types both tumor promoting and suppressing actions have been described, for example in prostate cancer. In Sirt1 knockout mice increased cell proliferation of prostatic intraepithelial neoplasia was observed, implicating Sirt1 as a tumor suppressor (24). However, via global transcriptome analysis increased levels of Sirt1 were identified as a key biomarker for prostate cancer suggesting a tumor promoting influence of Sirt1 (25). Several important tumor suppressors like p53, FOXO3a, or E2F1 that induce apoptosis in malignant cells (e.g., in breast cancer) are deacetylated by Sirt1, and thereby inactivated, promoting cell survival (26–29). In breast cancer tissue elevated Sirt1 expression correlates with tumor size, high histological grades and lymph node metastasis (30). Nevertheless, Sirt1 can still act as a tumor suppressor in breast cancer cells as well. It is crucial for DNA damage response, regulates several DNA repair enzymes like Ku70 and thereby enables stable, efficient DNA repair (31, 32). Some known oncogenes like NF- κ B are directly deacetylated by Sirt1 promoting downregulation of the NF- κ B-dependent cell survival pathway (33).

In some cancer types (e.g., glioma, bladder, or ovarian cancer) lower expression levels of Sirt1 have been detected, although in most cancer types an increased expression was observed (34). A meta-analysis showed that Sirt1 overexpression significantly correlates with poor prognosis in solid tumors (35). Anticancer effects of sirtuin inhibitors have been described on a cellular level. In cervical cancer cells EX-527 induced cell death while inhibition of the isotype Sirt2 led to cell cycle arrest. In the breast carcinoma cell line MCF-7 though, the opposite effect was observed, Sirt1 inhibition by EX-527 led to cell cycle arrest while treatment with Sirtinol or Salermide (Sirt1/2 inhibitors with a stronger effect on Sirt2) resulted in cell death (36, 37). In melanoma, chronic lymphocytic leukemia as well as hepatocellular carcinoma cell lines both Sirt1 inhibitors (EX-527) and Sirt2 inhibitors impaired cell growth and viability (38–40).

As already mentioned, Sirt1 plays a pivotal role in DNA damage response (DDR). For example, phosphorylation of the DNA damage sensor H2AX which gets phosphorylated to γ H2AX upon double strand breaks (DSBs) in healthy cells is significantly downregulated when Sirt1 is inhibited or depleted (41, 42). DDR can be regulated through Sirt1 either by direct histone deacetylation which changes chromatin compaction or by activation and inactivation of non-histone proteins that are involved in the major DNA repair mechanisms: homologous recombination (HR), non-homologous end joining (NHEJ), nucleotide excision repair (NER), mismatch repair (MMR), and base excision repair (BER) (43–47). Due to Sirt1s implications in DNA damage sensing and recruitment of repair proteins it can alter resistance toward some cancer



therapies targeting DNA stability. Application of EX-527 reduced chemoresistance in endometrial carcinoma cells (48).

EX-527 is widely used for studies on the effects of Sirt1 inhibition in cells and living organisms, partially due to a lack of other selective Sirt1 inhibitors. The only two compounds that show similar potency toward Sirt1 are its analog CHIC-35 and the Suramin analog NF675 (49, 50). However, both of them show slightly less selectivity over Sirt2 (51) and Suramins are usually poorly cell permeable. Other than that, only few specific Sirt1 inhibitors have been identified. Several examples with low micro molar affinity exist, like certain Splitomicin derivatives or the so-called spiro series (52, 53). To get more insights into

the role of Sirt1 in different cancer types and to better examine its therapeutic potential in cancer further Sirt1 inhibitors are needed. Here we present a new class of sirtuin 1 inhibitors based on a specific interaction with a thiocyanate moiety that lead to altered γ H2AX/H2AX ratios in mouse embryonic fibroblast cells.

MATERIALS AND METHODS

All test compounds are commercially available and were purchased from Princeton BioMolecular Research, Sigma Aldrich, Enamine, or Chembridge and used as received.

Enzyme Expression and Purification

Recombinant human Sirt5_{37–310} was purchased readily in Tris Buffer [25 mM Tris, 100 mM NaCl, 5 mM DTT, 10% glycerol (v/v)] from Enzo Life Sciences (NY, USA). Human Sirt3_{118–395} was expressed and purified as described previously (54). For expression of human Sirt1_{134–747} and Sirt2_{56–356} chemically competent cells of *E. coli* BL21 Star (DE3) were transformed with the expression vectors pET30S-hSirt1_{134–747} or pET30S-hSirt2_{56–356}. Bacteria were grown at 37°C in 2×YT medium supplemented with 50 μg·mL⁻¹ of kanamycin to an OD₆₀₀ of 0.6. Then isopropyl-β-D-1-thiogalactopyranoside (IPTG) was added to a final concentration of 1 mM to induce gene expression. After further cultivation at 20°C for 12 h, the cells were harvested by centrifugation for 15 min at 5,000 g. The cells were resuspended in lysis buffer [100 mM Tris/HCl buffer at pH 8.0, 150 mM NaCl and 10% (v/v) glycerol] and disrupted by ultrasonication (Branson Digital Sonifier 250) at 70% amplitude for 10 min (3 s working, 10 s pause). The crude extract was cleared by centrifugation at 100,000 g for 1 h, and the supernatant was loaded onto a Strep-Tactin Superflow cartridge (5 ml bed volume, IBA Lifescience, Germany). Target proteins were eluted with lysis buffer containing 5 mM D-Desthiobiotin (IBA Lifescience, Germany) and further separated by size-exclusion chromatography (Superdex S200 26/60, GE Healthcare, IL, USA) equilibrated in Tris/HCl buffer (20 mM, 150 mM NaCl, pH 8.0). Pure protein was concentrated by ultrafiltration, flash-frozen in liquid nitrogen and stored at -80°C until further use. Identity as well as purity were verified by SDS-PAGE (55) and protein concentration was determined by the bicinchoninic acid (BCA) method, using bovine serum albumin (BSA) as a standard (56). Deacetylase activity was confirmed to be NAD⁺-dependent and could be inhibited with the physiological sirtuin inhibitor nicotinamide.

In vitro Characterization

Homogeneous ZMAL-Based Fluorescence Assay for Class I Sirtuins

All compounds were tested in the trypsin-coupled high-throughput ZMAL-assay in black 96-well plates (OptiPlate™-96F, black, 96 well, Pinch bar design, PerkinElmer, USA), using ZMAL (Z-Lys(acetyl)-AMC) as a substrate (57). Sirt1_{134–747}, Sirt2_{56–356}, and Sirt3_{118–395} were mixed with 5 μL substrate (10.5 μM final assay concentration, diluted from a 12.6 mM stock in DMSO) and 3 μL Inhibitor in DMSO at various concentrations or DMSO as a control [final DMSO concentration 5% (v/v)]. The mixture was supplemented with assay buffer (50 mM Tris/HCl, 137 mM NaCl, 2.7 mM KCl, 1 mM MgCl₂, pH 8.0) to a total volume of 55 μL. Enzyme concentration was adjusted to get a final conversion of 20–30%. Addition of 5 μL NAD⁺ (6 mM in assay buffer, final assay concentration of 500 μM) initiated the catalytic reaction and the plates were incubated at 37°C for 4 h with agitation at 140 rpm. The catalytic reaction was stopped by addition of 60 μL stop solution [50 mM Tris, 100 mM NaCl, 6.7% (V/V) DMSO, 5.5 U/μL trypsin, 8 μM nicotinamide, pH 8.0]. The plate was again incubated at 37°C and 140 rpm for 20 min to release free AMC from the deacetylated substrate by trypsin digestion. Afterwards,

fluorescence intensity was measured in a microplate reader (λ_{Ex} = 390 nm, λ_{Em} = 460 nm, BMG POLARstar Optima, BMG Labtech, Germany). An enzyme-free blank control and a 100% conversion control containing AMC instead of ZMAL were measured in addition. Inhibition was calculated in % in relation to a DMSO control after blank signal subtraction and IC₅₀ values were determined using a non-linear regression to fit the dose-response curve with OriginPro 9G (OriginLab, USA). Pre-tests as well as IC₅₀ determination was carried out at least twice in duplicates.

Homogeneous ZKsA-Based Fluorescence Assay for Sirt5

Inhibition of Sirt5 was measured using a general procedure described before with small modifications (58). Sirt5 was purchased from Enzo Life Science (NY, USA) and used as received. Z-Lys(succ)-aminomethyl coumarin (ZKsA) was used as a substrate for Sirt5 mediated desuccinylation. In black 384-well non-binding plates (Greiner Bio-One, Monroe, NC) Sirt5 was mixed with 2 μL of ZKsA (1 mM stock solution in assay buffer [(50 mM Tris-HCl, 137 mM NaCl, 2.7 mM KCl, 1 mM MgCl₂, pH 8.0, and 0.1% PEG8000), 100 μM final assay concentration], 1 μL of Inhibitor dissolved in DMSO or DMSO as a control [final DMSO concentration 5% (v/v)], 2 μL NAD⁺ (5 mM stock solution in assay buffer, final assay concentration 500 μM) and filled up to a total volume of 20 μL with assay buffer. The mixture was incubated for 1 h at 37°C and 140 rpm before 4 μL of trypsin solution (50 mM Tris, 100 mM NaCl, pH 8.0, 6 mg/mL trypsin buffer, 1 mg/mL final assay concentration) was added to stop the enzymatic reaction. After 2 min of incubation at 37°C and 140 rpm fluorescence intensity was detected as described above. Sirt5 concentration was adjusted to 15–30% substrate conversion. A negative control without enzyme and a positive control containing AMC instead of ZKsA were performed as well. Inhibition was calculated in % in relation to a DMSO control and was determined in triplicates.

Homogeneous ZMAL-Based Fluorescence Assay for HDAC1 and 6

The inhibition of HDAC1 and 6 by the S1th and PR-619 was determined via the ZMAL-assay according to the same general procedure described for sirtuins (2.2.1). 5 μL substrate (10.5 μM final assay concentration) were mixed with 3 μL of inhibitor in DMSO or DMSO and 10 μL of HDAC solution (concentration adjusted to 15–30% conversion) and filled up to 60 μL with assay buffer (50 mM Tris, 137 mM NaCl, 1 mM MgCl₂, 2.7 mM KCl, 1 mg/ml BSA, pH = 8.0). The mixture was incubated at 37°C and 140 rpm for 1.5 h. For the stop solution Trichostatin A (3.3 μM) was used instead of nicotinamide. Fluorescence intensity was measured as described above. An enzyme free blank control and an AMC containing 100% control were performed as well and inhibition was calculated in % in relation to a DMSO control.

Jump Dilution Assay

To test the compounds for reversibility a jump dilution assay based on the trypsin-coupled ZMAL assay described above was used. In black 96 well plates (OptiPlate™-96F, black, 96 well,

Pinch bar design, PerkinElmer, USA) 1 μL Sirt1_{134–747} in assay buffer (50 mM Tris/HCl, 137 mM NaCl, 2.7 mM KCl, 1 mM MgCl₂, Sirt1 concentration 100-fold higher than normally used) with 1 μL inhibitor in a concentration 10-fold higher than the IC₅₀ were preincubated at room temperature for 10 min before the mixture was rapidly diluted 100-fold with assay mix [assay buffer, ZMAL (final assay concentration 500 μM), DMSO (final assay concentration 5% (v/v), NAD⁺ (final assay concentration 500 μM), pH 8.0] to a total volume of 200 μL . The reaction was stopped after 2.5, 5, 7.5, 10, 12.5, 15, 20, 25, and 30 min by addition of 60 μL stop solution [50 mM Tris, 100 mM NaCl, 6.7% (V/V) DMSO, trypsin 5.5 U/ μL , 8 μM nicotinamide, pH 8.0]. The plate was again incubated at 37°C and 140 rpm for 20 min to get the free AMC from the deacetylated substrate by trypsin digest. Afterwards fluorescence intensity was measured in a microplate reader ($\lambda_{\text{Ex}} = 390 \text{ nm}$, $\lambda_{\text{Em}} = 460 \text{ nm}$, BMG POLARstar Optima, BMG Labtech, Germany). An enzyme-free blank control and a 100% conversion control containing AMC instead of ZMAL were performed additionally. Conversion was calculated in % in relation to the 100% control after subtraction of the blank fluorescence signal. Conversion in % was plotted against time with OriginPro 9G (OriginLab, USA) and an exponential fit was performed to fit the curves.

NAD⁺ Competition Assay

NAD⁺ competition was determined using the trypsin coupled ZMAL assay. Sirt1_{134–747}, the ZMAL substrate and the inhibitors or DMSO were mixed and filled up to 55 μL in black 96-well plates as described above. The reaction was initiated by the addition of 5 μL of NAD⁺ in concentrations ranging from 62.5 to 2,000 μM final assay concentration. After 4 h of incubation at 37°C and 140 rpm the reaction was stopped by addition of the trypsin containing 60 μL stop solution, incubated again for 20 min at 37°C and 140 rpm and fluorescence was detected with a BMG POLARstar ($\lambda_{\text{Ex}} = 390 \text{ nm}$, $\lambda_{\text{Em}} = 460 \text{ nm}$, BMG POLARstar Optima, BMG Labtech, Germany). An enzyme-free blank control and a control containing AMC instead of ZMAL were measured additionally. Conversion was calculated in % in relation to the 100% control (AMC) after subtraction of the blank fluorescence signal. Conversion in % was plotted against NAD⁺ concentration with OriginPro 9G (OriginLab, USA) and an exponential fit was performed to fit the curves.

FOXO3a Substrate Competition Assay

Peptide substrate competition was measured using a homogeneous fluorescence-based fluorescamine assay similar to that previously reported as an activity assay for Sirt2 and Sirt3 with Ac- α -tubulin as a substrate (59). For Sirt1 a partial sequence of the physiological Sirt1 substrate FOXO3a [Ac-DSPQLSK(Ac)WPPGTSS-NH₂, custom synthesized by PSL, Heidelberg, Germany], hereafter called FOXO3a-ac, was used as substrate. Substrates were stored as 1 mM stocks in assay buffer [HEPES 25 mM, NaCl 137 mM, KCl 2.7 mM, MgCl₂ 1 mM, Triton-X 100 0.015% (v/v), pH 8.0] and diluted with assay buffer to 240 μM FOXO3a-ac peptide (20 μM final assay concentration). In black 96-well plates (OptiPlate™–96F, black, 96 well, Pinch bar design, PerkinElmer, USA) 0.05 μL

Sirt1_{134–747} (3 mg/mL, final assay conversion 20–30%) was mixed with 5 μL of the diluted peptide and 3 μL of inhibitor dissolved in DMSO in various concentrations or DMSO as a control [final DMSO concentration 5% (v/v)] and filled up to 55 μL with assay buffer. After addition of 5 μL NAD⁺ (6 mM, final assay concentration 500 μM) to start the enzymatic reaction the plate was incubated for 1 h at 37°C and 140 rpm. Afterwards pH was adjusted with 5 μL of 0.1 M NaOH and the enzymatic reaction was stopped with stopping solution [8.73 mM nicotinamide (final assay concentration 4 mM), 0.455 mM fluorescamine (final assay concentration 62.5 μM) in acetone]. The fluorescence signal was measured using a microplate reader ($\lambda_{\text{Ex}} = 390 \text{ nm}$, $\lambda_{\text{Em}} = 485 \text{ nm}$, BMG POLARstar Optima, BMG Labtech, Germany). Additionally, a 100% inhibition control containing the physiological sirtuin inhibitor nicotinamide (6 mM final assay concentration) and a control simulating 100% conversion containing the deacetylated FOXO3a peptide (Ac-DSPQLSKWPPGTSS-NH₂, custom synthesized by PSL, Heidelberg, Germany) in equivalent concentration as the substrate were performed. Inhibition was calculated in % in relation to DMSO control after subtraction of the 100% inhibition fluorescence signal. IC₅₀ values were determined using a non-linear regression to fit the dose-response curve with OriginPro 9G (OriginLab, USA).

Fluorescent Thermal Shift Assay (FTSA)

In a 96-well plate (Hard-Shell® PCR-plates, 96-well, thin-wall, BioRAD, USA) 14 μL Sirt1_{134–747} in assay buffer (0.3 mg/mL final assay concentration, 50 mM Tris/HCl, 137 mM NaCl, 2.7 mM KCl, 1 mM MgCl₂, pH 8.0) were mixed with 1 μL inhibitor in DMSO (100 μM) or DMSO [final assay concentration 5% (v/v)] as a control and 5 μL SyproOrange (1:100 in assay buffer). The fluorescence intensity was monitored during a constant increase of temperature from 20 to 95°C, 1 K per 20 s, using a real-time-PCR-machine (C1000 Touch™ Thermal Cycler, CFX96™ Real-Time System, BioRAD, USA). Melting temperatures were calculated via GraphPad Prism according to a published procedure (60).

Cellular Assays

DUB Labeling on HEK293T Cell Lysate

Pan-inhibition of deubiquitinases (DUBs) was tested using HEK293T cell lysate (human embryonic kidney cells, human). Cells were harvested and resuspended in HR buffer (50 mM Tris, 5 mM MgCl₂, 250 mM sucrose, 1 mM DTT, pH 7.4). Cell lysis was achieved by sonication (Bioruptor, Diagenode, high intensity for 10 min with an ON/OFF cycle of 30 s) at 4°C and the cell debris was removed by centrifugation at 13,500 rpm for 15 min. Cell lysate protein concentration was determined with a NanoDrop spectrophotometer (NanoDrop One™ Spektrophotometer, Thermo Fisher, MA, USA) by measuring absorbance at 280 nm. Nineteen microliter of the lysate (2 $\mu\text{g}/\mu\text{L}$) were incubated with inhibitors dissolved in DMSO at various concentrations or DMSO as a control for 30 min at 37°C. Afterwards 1 μL of Rhodamine-Ub-PA (1 μM final assay concentration) was added to each sample, followed by further incubation for 40 min at 37°C (61). The labeling reaction

was stopped by addition of NuPAGE 4× LDS sample buffer (Invitrogen Life Technologies, Carlsbad, CA, USA) containing β -mercaptoethanol and boiling for 7 min at 95°C. The proteins of the samples as well as protein marker (PageRuler™ Pre-stained Protein Ladder, 10–250 kDa, Thermo Fisher, MA, USA) were resolved by a 4–12% SDS-PAGE using the NuPAGE system with MOPS running buffer (Invitrogen Life Technologies, Carlsbad, CA, USA). The resulting gel was scanned with a Typhoon imager (GE Healthcare Life Sciences, USA) to visualize the Rhodamine-Ub-PA probe and Cy5 (marker). Subsequently the gel was stained with InstantBlue™ Protein Stain (Expedeon, UK) and scanned on a Amersham scanner (Amersham Typhoon gel and blot imaging system, GE Healthcare Life Sciences, USA).

γ H2AX Level Determination

Sirt1 WT and KO MEFS cells were treated with 10 μ M EX-527, 12 μ M **S1th 13** (6), 20 μ M **S1th 12** (5), 30 μ M **S1th 10** (7) and 30 μ M SirReal2 [Sirt2 inhibitor, synthesized according to (62)] for 48 h. Oxidative stress was induced using 10 μ M Camptothecin 2 h. Whole-cell extracts were performed according to the Dignam protocol (63). Primary antibodies used for the western blot were anti-H2AX and anti- γ H2AX (ab11175 and ab2893 resp., Abcam, UK). Densitometric analysis of the western blots was performed with Quantity One software (Bio-Rad Laboratories, Inc., USA).

Cell Proliferation Assay With HeLa or MCF7 Cells

1.5×10^4 cells/well were seeded in 24-well plates and grown in DMEM 10% in presence of DMSO, 20 μ M EX-527, 12 μ M **S1th 13**, 20 μ M **S1th 12**, or 30 μ M **S1th 10**. The growth media containing the drugs was replaced every 48 h. Cells were collected and counted at the indicated times starting 24 h after seeding (0, 24, 48, 72, 96, and 120 h). The experiment was performed twice in duplicates.

Wound Healing Assay With HeLa Cells

For wound healing assay 6×10^5 cells per well were seeded in 6-well plates and grown for 24 h in DMEM containing 10% FBS. After 24 h, a lineal gap between cells was created in the middle of the plate by scratching the cell monolayer with a 1 mL pipette tip in the same position in each well. Once the scratching is done, plates were washed twice with PBS and then grown in DMEM containing 1% FBS and the drugs in the same concentrations as for the proliferation assay. As described previously, the growth media 1% FBS containing the drugs was replaced every 48 h. Images were acquired in an Optimal microscope (Leica microscopes, DE) using Leica Application Suite X (LAS X) every 24 h (0, 24, 48, and 72 h) until the gap closed. The quantification of the area of the gap at the indicated times was performed with Image J-MRI Wound Healing Tool. The experiment was performed only once.

Colony Forming Assay With HeLa or MCF7 Cells

For colony assays, 50 cells per well were seeded in 6-well plates and grown in the same conditions with the same drug concentrations as for the proliferation assays. In this case, the growth media containing the drugs was replaced every 48 h. After 7–10 days, when isolated colonies were formed, wells were

washed with PBS, and cells were fixed with cold methanol for 5 min at RT. Cells were stained with crystal violet for 10 min at RT and washed with H₂O. Images were acquired using iBright (Thermo Fisher Scientific, MA, USA). For quantification, cells of each well were resuspended in 10% glacial acetic acid to dissolve crystal violet whose levels were monitored by measuring absorbance at 590 nm. The experiment was performed in duplicates.

Analysis of Acetylation Status in HeLa Cells by Western Blotting

5×10^4 cells were plated in 6-well plates and grown with the conditions and drug concentrations as described for the proliferation assay. Cells were harvested at 48 h and resuspended in protein loading buffer. After sonication the samples were centrifuged at 14,000 rpm in an Eppendorf microcentrifuge (Eppendorf, DE) and the supernatants were analyzed by western-blot. The following antibodies were used: histone H3 (Cell Signaling #9715), histone H3K9ac (Cell Signaling # C5B11), GAPDH (Cell Signaling #D16H11), p53 (ThermoFisher #PA527822), and p53K382ac (Abcam 75754). Quantification was carried out using imageJ.

Computational Methods

3D structures of all compounds under study were generated from SMILES strings, and a subsequent energy minimization was carried out using the MMFF94x force field implemented in Molecular Operating Environment System (MOE) 2014.10 (Chemical Computing Group, Montreal, Canada). All compounds were used in their neutral form. A maximum of 100 conformations were generated for each ligand using the Conformational Search module implemented in MOE.

The structure of Sirt1 protein in complex with NAD⁺ and the small molecule inhibitor EX-527 was downloaded from the Protein Data Bank (PDB ID 4I5I) (64). In addition, crystal structures of Sirt2 in complex with the EX-527 analog CHIC35 and ADPR (PDB ID 5D7Q) and Sirt3 in complex with EX-527 and NAD⁺ (PDB ID 4BV3) were investigated. The protein structures were prepared by using the Structure Preparation module in MOE. Hydrogen atoms were added, for titratable amino acids the protonation state was calculated using the Protonate 3D module in MOE. Protein structures were energy minimized using the AMBER99 force field with a tethering force constant of (3/2) kT/2 ($\sigma = 0.5$ Å) for all atoms during the minimization (65). AM1-BCC charges were used for the studied ligands (66). All molecules except the zinc ion were removed from the structures.

Protein-ligand docking was performed using GOLD5.6 (67). For Sirt1, Ser442 was used to define the size of the grid box (15 Å radius). In case of Sirt2 and Sirt3, the corresponding Ser263 and Ser321 were used, respectively. Ten docking poses were calculated for each inhibitor. All other options were left at their default values. Using the docking setup, the cocrystallized inhibitors EX-527 and CHIC35 could be correctly docked with RMSD values below 0.6 Å. Virtual screening was carried out using program GOLD5.6 and the settings described above. To decrease calculation time, the Virtual Screening setup was used

within GOLD5.6 and only the top-ranked pose was stored for further evaluation. In total 16 compounds were purchased and submitted to biochemical testing (eleven compounds from Princeton Biomolecular Research, one from Sigma-Aldrich and four from Enamine, **Supplementary Table 1**). All docking scores displayed in **Supplementary Table 1**.

RESULTS

Docking

Based on a previously collected library of putative sirtuin inhibitors we carried out a virtual screening using the GOLD5.6 docking software and the available crystal structure of Sirt1 in complex with the inhibitor EX-527 and NAD⁺ (64). A first *in vitro* screening (for primary *in vitro* screening data see **Supplementary Table 2**) on the three class I sirtuins indicated a thienopyrimidone carrying a thiocyanate moiety which we termed **S1th 1 (2)** (structure **Figure 1**) as a promising hit for Sirt1 inhibition. Two structural analogs of **S1th 1** with the same heterocyclic system but different functional groups were docked to the NAD⁺ binding site of Sirt1 and were submitted to a second round of biochemical testing (**Table 1**). Among the three selected thienopyrimidones only **S1th 1** was able to inhibit Sirt1 in the micro molar range (IC₅₀ 13 μM). The docking pose of the active analog showed that the phenyl thiocyanate moiety is located in the adenine pocket, engaging in a hydrogen bond to Cys482 (backbone NH, **Figure 2A**). The pyrimidine ring is located in the polar phosphate pocket of Sirt1 and shows a hydrogen bond to Ser442. A third hydrogen bond was observed between the amide group of the inhibitor and Gln445. The two inactive analogs (**OSSK_338451** and **OSSK_531963**, structures **Supplementary Figure 1**) showed a similar binding mode lacking an interaction in the adenine pocket. Due to the close proximity of the potentially reactive thiocyanate group of **S1th 1** and Cys482 we speculated that an irreversible binding might occur. Therefore, we tested the reversibility of enzyme inhibition as well as NAD⁺ competition and competition toward a peptide analog of the physiological Sirt1 substrate FOXO3a to confirm the proposed binding mode. *In vitro* results showed that the inhibitors are reversible binders and NAD⁺ competitive but not substrate competitive which is in agreement with the predicted binding mode of the thiocyanates (**Figure 3**).

To confirm the importance of the thiocyanate group we screened the whole Princeton BioMol. Res. Compound collection

virtually (considering only phenyl thiocyanates) and docked the resulting 113 thiocyanates to Sirt1. Eight promising hits were cherry picked, purchased and submitted to a third round of biochemical testing (**Table 2**). Among the eight compounds, **S1th 7 (3)** showed increased inhibition compared to **S1th 1** with an IC₅₀ of 6.34 μM (**Table 2**) which is also supported by the best docking score. The predicted binding pose of **S1th 7** shows two hydrogen bonds to Asp272 and Asn465 (**Figure 2B**). Since we encountered solubility problems of the active hits in cellular testing at higher concentrations, we purchased six more polar compounds and submitted them to a fourth round of biochemical testing. **S1th 11 (4)**, **12 (5)**, and **13 (6)** (from Enamine) were found to be better soluble and equally active as **S1th 7**. The binding mode of the active hit **S1th 13** (IC₅₀ of 5.2 μM, **Table 3**) is similar to that observed for the previous hits showing interactions with Cys482, Asn465 and in addition to Asp272 (**Figure 2C**).

All active inhibitors, both from the 3rd and the 4th round, retained the extremely high selectivity of the initial hit for Sirt1 over the isotypes Sirt2 and 3. Docking to Sirt2 and Sirt3 was subsequently carried out for the active hits in order to rationalize the observed selectivity. In case of Sirt2, there are three different amino acid residues in the putative thiocyanate binding pocket that affect the docking results (**Figure 2D**): Val266, Arg466, and Asp481 of Sirt1 are substituted by Thr89, Lys287, and Glu323 in the Sirt2 structure, respectively. The inhibitors could be docked in a similar orientation to the Sirt2 binding pocket, however with less favorable docking scores. Especially the interaction of the thiocyanate phenyl ring with Arg466 is lost in case of Sirt2, which might explain the lower docking scores. In case of Sirt3, there are four amino acid residues substituted in the putative binding pocket. Val266, Ser267, Cys482, and Asp483 of Sirt1 are substituted by Thr150, Pro151, Val366, and Val367 in the Sirt3 structure (**Figure 2E**). Val366, Val367, and Pro151 are restricting the size of the putative thiocyanate binding pocket and consequently the thiocyanate moiety is not able to interact with the protein as observed for Sirt1.

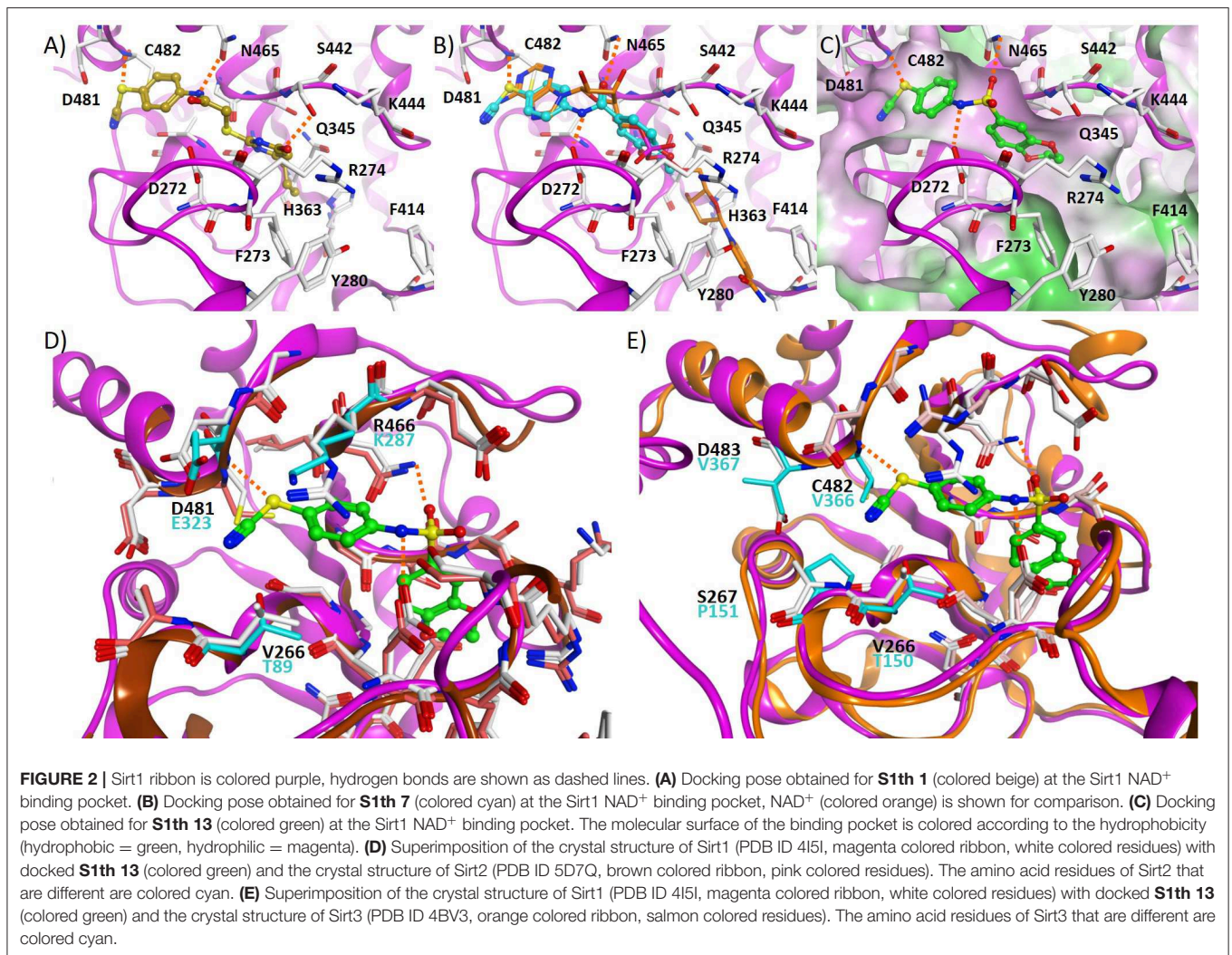
In vitro Characterization of S1th

We wanted to further elucidate the binding mode and selectivity of the S1th. Apart from the closely related class I sirtuins (Sirt2 and 3) also inhibition of Sirt5 as a representative of other sirtuin classes was tested. Although Sirt5 sequence and structure in general shows less overlap with Sirt1 than the class I sirtuins, the active side residue Cys482 which is explicitly important for S1th binding is conserved in Sirt5. Yet, no inhibition of Sirt5 by **S1th 10–13** at 10 μM was observed. In general, thiocyanates are known to act as chelating groups making them candidates for inhibition of ion-dependent enzymes like classical HDACs which feature a zinc ion in their active site. It has been shown that cruciferous vegetable isothiocyanates like sulforaphane can act as potent pan-HDAC inhibitors (68). Consequently, to further investigate the selectivity of our new thiocyanate Sirt1 inhibitors, they were tested against two representative zinc dependent HDACs, HDAC1 (Class I) and HDAC6 (Class II). HDAC1 was not inhibited by the tested thiocyanates at 100 μM at all. For HDAC6 a very weak inhibition by **S1th 10 (7)**, **12** and **13**

TABLE 1 | Inhibition of class I sirtuins by **S1th 1** and its two structural analogs **OSSK_338451** and **OSSK_531963** (2nd round of *in vitro* screening).

Compound	IC ₅₀ [μM] or % inhibition @ 50 μM		
	Sirt1	Sirt2	Sirt3
S1th 1	13 ± 0.6	23%	n.i.*
OSSK_33845	n.i.	n.i.	n.i.
OSSK_531963	n.i.	n.i.	n.i.

*n.i., no inhibition (<10%).



(19, 36, and 29% at 100 μ M) was observed (Table 4). Another likely off-target effect of thiocyanates could be the inhibition of deubiquitinases (DUBs). Deubiquitination activity of these enzymes relies on a cysteine residue in the catalytic core which acts as a nucleophile (69). Most known DUB inhibitors therefore feature a functional group that can form specific interactions with this cysteine. PR-619 (8), a compound featuring two aromatic thiocyanate moieties, was shown to inhibit more than twenty DUBs with IC₅₀ values ranging from 5 to 20 μ M and, as we could show, is also able to inhibit Sirt1 with an IC₅₀ of $2.7 \pm 0.2 \mu$ M (70, 71). HDAC1 and 6 are inhibited to ~50% residual activity by PR-619 as well. The S1th however did not show inhibition of DUBs which we could show in a fluorescence based activity assay using HEK-293 cell lysate and a Rhodamine-Ub-PA probe (Supplementary Figure 2). These results support the excellent selectivity of the S1th not only amongst sirtuins but also over other possible off-targets.

To better understand the binding of the S1th a series of fluorescent thermal shift assay (FTSA) experiments was

performed. Binding of a ligand usually results in a stabilization of the protein which can be observed as an increase of the melting temperature (T_m) in FTSA. For example, binding of the NAD⁺ metabolite adenosine diphosphate ribose (ADPR), which is formed during the catalytic reaction of the sirtuins, leads to a stabilization up to 4 K. The known Sirt1 binders EX-527 and SRT1720 (72) only cause a very small shift or no shift at all (Supplementary Figure 3a). For the S1th however we observed a strong left shift of the T_m from 5.9 up to 9.6 K for the most potent inhibitors of the fourth round at 100 μ M (Figure 3). The decrease of T_m is concentration dependent for all tested compounds (S1th 10–13), resulting in a smaller ΔT at lower concentrations (Supplementary Figure 3c). Shifts of T_m to decreased temperatures have been associated with an apparent destabilization of the protein by covalent binding compounds, detergent-like compounds or compounds that extract stabilizing ions from the structure in several cases (73). This could be a hint toward a covalent interaction of the thiocyanate moiety with Cys482. However, another widely recognized explanation

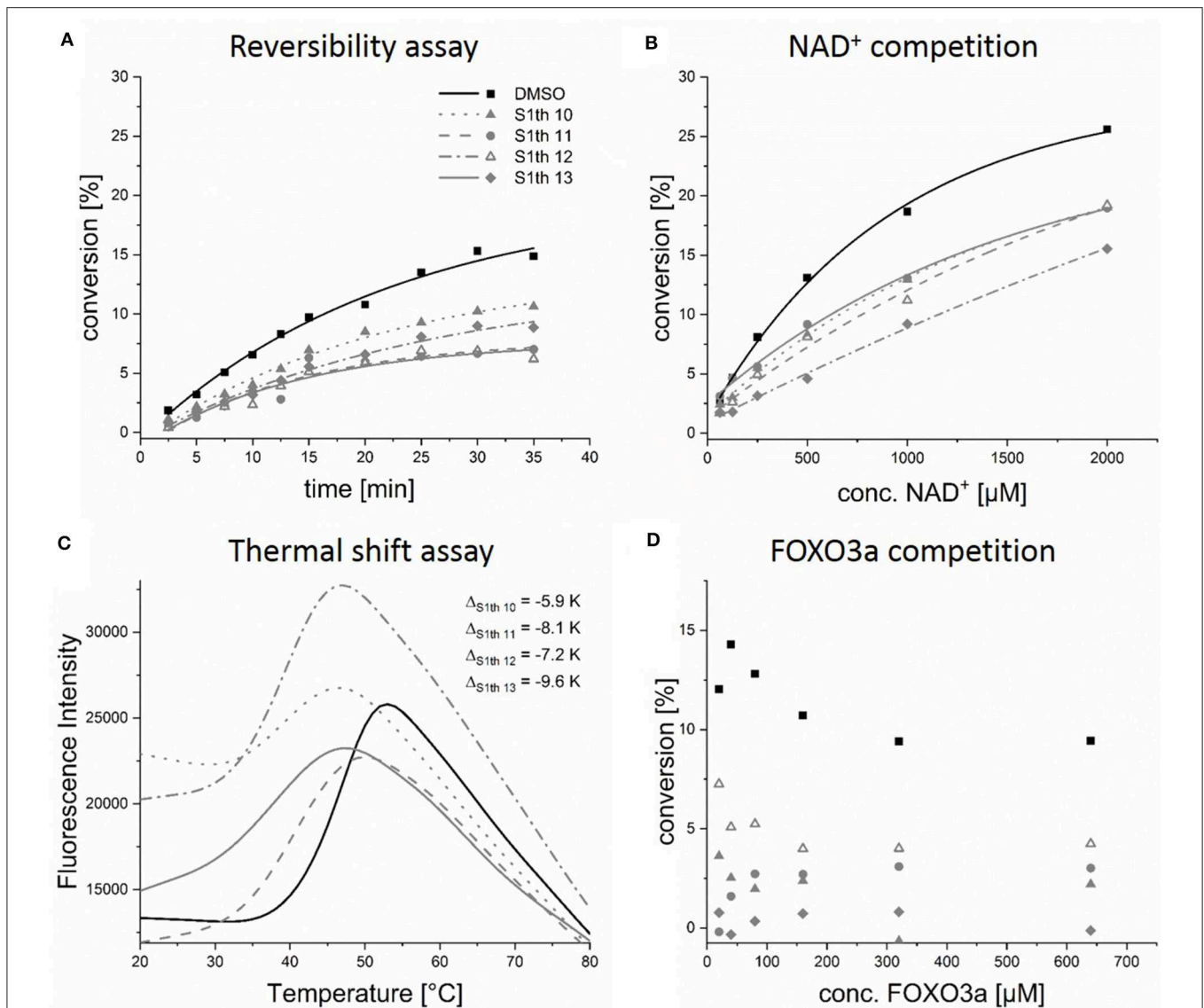


FIGURE 3 | *In vitro* characterization of the thiocyanates. Evaluation of reversibility, competition with NAD⁺ or the peptide substrate FOXO3a and enzyme stabilization; **(A)** Sirt1 and the respective thiocyanate inhibitor (50 µM) were preincubated for 10 min and then rapidly diluted 1:100 with assay solution (buffer, ZMAL, NAD⁺), activity of Sirt1 was measured at different time points. Increasing activity can be observed for non-covalent inhibitors; **(B)** thiocyanate inhibitors (100 µM) were incubated with increasing concentrations of NAD⁺, showing that the inhibitors can be replaced by NAD⁺; **(C)** binding of **S1th 10–13** (100 µM) to Sirt1 leads to a strong decrease of T_m ; **(D)** S1th (100 µM) were incubated with increasing concentrations of the peptide substrate FOXO3a, the inhibitors are not competitive toward FOXO3a. All biochemical assays were performed at least twice in duplicates.

for left shifts is that these compounds bind more strongly to a conformation different from the native one (74, 75). In regard to this, one has to take into account that T_m is considerably more affected by entropy than by enthalpy. Consequently, enthalpy-driven binding to the native state can be outnumbered by weaker entropy-driven binding to a different conformation or even the denatured state resulting in a left shift (76). The shift of T_m induced by **S1th 10–13** can be reversed through addition of ADPR. As the thiocyanates are binding to the NAD⁺ pocket they are also competitive toward the physiological NAD⁺

metabolite ADPR. Simultaneous application of ADPR and the S1th resulted in a significantly smaller decrease of T_m (Sirt1) than treatment with S1th alone (**Supplementary Figure 3b**). To ensure that the observation of a left shift is specific for Sirt1 the compounds were also tested in an FTSA using Sirt2. There was no decrease of T_m observed, in fact binding of the thiocyanates leads to a very small positive shift (0.2–0.5 K) of T_m for Sirt2 (**Supplementary Figure 3d**). As the Cys482 residue is conserved in five out of the seven human sirtuin isotypes including Sirt2 and 5, this data shows a unique and specific binding mode of the

TABLE 2 | Inhibition of class I sirtuins by thiocyanate analogs of 3rd round of virtual screening (**S1th 2–9**).

Compound	IC ₅₀ [μM] or % inhibition @ 50 μM		
	Sirt1	Sirt2	Sirt3
S1th 2	6.4 ± 0.7	n.i.*	n.i.
S1th 3	2.8 ± 0.5	n.i.	n.i.
S1th 4	5.3 ± 0.5	n.i.	n.i.
S1th 5	9.4 ± 1.4	n.i.	n.i.
S1th 6	5.1 ± 0.6	n.i.	n.i.
S1th 7	6.3 ± 0.5	n.i.	n.i.
S1th 8	40%	n.i.	n.i.
S1th 9	n.i.	n.i.	n.i.

*n.i., no inhibition (<10%).

TABLE 3 | Inhibition of sirtuins 1, 2, 3 and 5 by thiocyanate analogs of 4th round of virtual screening (**S1th 10–13**) and **PR-619**.

Compound	IC ₅₀ [μM] or % inhibition @ 50 μM			
	Sirt1	Sirt2	Sirt3	Sirt5**
S1th 10	23 ± 6.0	n.i.*	n.i.	n.i.
S1th 11	6.3 ± 0.8	n.i.	n.i.	n.i.
S1th 12	5.9 ± 1.4	n.i.	n.i.	n.i.
S1th 13	5.2 ± 1.0	n.i.	n.i.	n.i.
PR-619	2.7 ± 0.2	36%	n.i.	28%

*n.i., no inhibition (<10%), **inhibition tested @ 10 μM.

TABLE 4 | Selectivity over histone deacetylases and deubiquitinases compared to pan-DUB inhibitor PR-619.

Compound	% inhibition @ 100 μM		Qualitative pan-DUB inhibition	
	HDAC1	HDAC6	@ 10 μM	@ 50 μM
S1th 10	n.i.*	29%	n.i.	n.i.
S1th 11	n.i.	n.i.	n.i.	n.i.
S1th 12	n.i.	36%	n.i.	n.i.
S1th 13	n.i.	19%	n.i.	n.i.
PR-619	54%	49%	+	+++

*n.i., no inhibition (<10%), + low inhibition, +++ full inhibition.

thiocyanates to the Sirt1 structure that was already proposed by the docking to Sirt1, 2 and 3 (77).

Effects of S1th in Cellular Systems

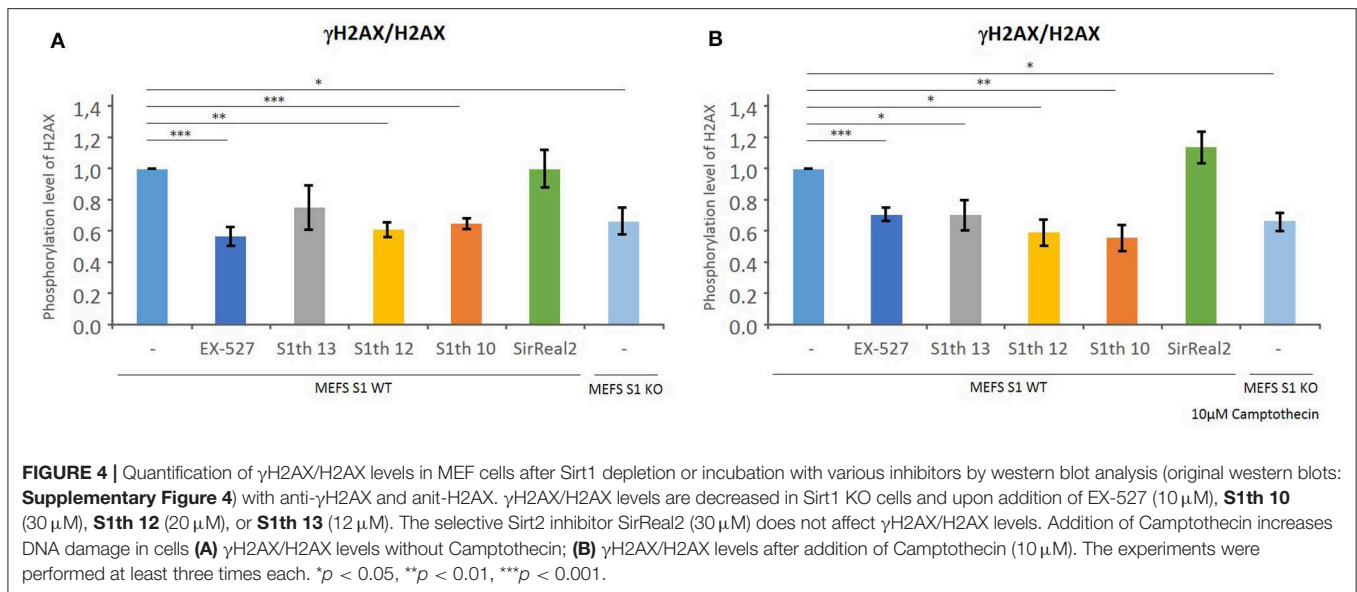
Sirt1 Dependent Effects in Mice Embryonic Fibroblasts (MEFs)

As described previously by Wang et al., the phosphorylation level of H2AX in mice embryonic fibroblasts (MEFs) is decreased if Sirt1 is depleted or inhibited (42). Phosphorylation of H2AX is a key step in DNA damage sensing. Determination of γH2AX/H2AX levels in MEFs via western blotting was employed to show target engagement in cells of our new class

of Sirt1 inhibitors. To demonstrate the maximum change in phosphorylation possible, the γH2AX/H2AX levels of wild type MEFs and Sirt1 KO MEFs were determined. The effect of **S1th 10**, **12**, and **13** (30, 20, and 12 μM, respectively) was compared to that of EX-527 (10 μM) as a positive control and to the specific Sirt2 inhibitor SirReal2 (30 μM) as a negative control (**Figure 4**, for western blots see **Supplementary Figure 4**). All three inhibitors showed a reduction of γH2AX/H2AX levels and the observed effect is similar to that of EX-527. The effect of the sirtuin 1 inhibitors becomes even more apparent when the topoisomerase I inhibitor Camptothecin is added to the cells (78). Treatment with Camptothecin induces DNA damage which in functional cells leads to elevated phosphorylation levels of H2AX. When EX-527 or the S1th were administered to these cells again a strong decrease of γH2AX/H2AX was detected. This shows that in cells with higher stress levels through DNA damage, the S1th can significantly alter DDR.

Impact of S1th on Cervical Cancer Cells (HeLa)

After showing Sirt1 dependent effects in non-cancerous mouse cells we wanted to investigate whether our new inhibitors have an impact on proliferation, migration and colony forming properties of human cancer cells. As already mentioned Sirt1 can play very contradictory roles in different tissues and even within one cancer type. Still, cases have been reported where Sirt1 inhibition impairs cell growth. For cervical cancer cells (HeLa) effects on cell proliferation upon administration of EX-527 have been reported (79). Based on these findings we chose HeLa cells for further examination of the S1th. The three best characterized inhibitors **S1th 10**, **12**, and **13** as well as EX-527 were administered to HeLa cells and the effects on cell proliferation, migration and colony forming were observed (**Figure 5**). EX-527, **S1th 10** and **S1th 13** significantly decreased cell proliferation, with EX-527 being slightly more effective than the S1th. **S1th12** only showed a mild effect on proliferation. Interestingly, even though having the most impact on cell proliferation, EX-527 failed to impair migration of HeLa cells in a wound healing assay within the first 24 h. A monolayer of HeLa cells was plated and a “wound” was introduced by scratching. Through cell migration the cells grow back together to heal the wound in the monolayer. Other than EX-527, the S1th all showed good inhibition of cell migration already after 24 h. **S1th 13** appeared to be most effective showing an ~50% lower reduction of total wound area compared to a control where no drug was applied. After 72 h also EX-527 showed a mild effect on wound healing and the inhibition by the S1th that could already be observed after 24 h became more apparent. In consistency with the results on proliferation and migration also a colony forming assay proved **S1th 13** to be the most potent drug of our new class. EX-527 completely suppressed colony forming of HeLa cells. **S1th 13** proved to be almost as potent as EX-527 while for **S1th 10** and **12** only mild effects were observed. Effects of the S1th on proliferation and colony forming were also confirmed in initial studies in the breast cancer cell line MCF7 (**Supplementary Figure 5**). In addition, we performed western blot analysis of the Sirt1 substrates H3K9ac and p53K382ac (**Figure 6**). To determine the acetylation status

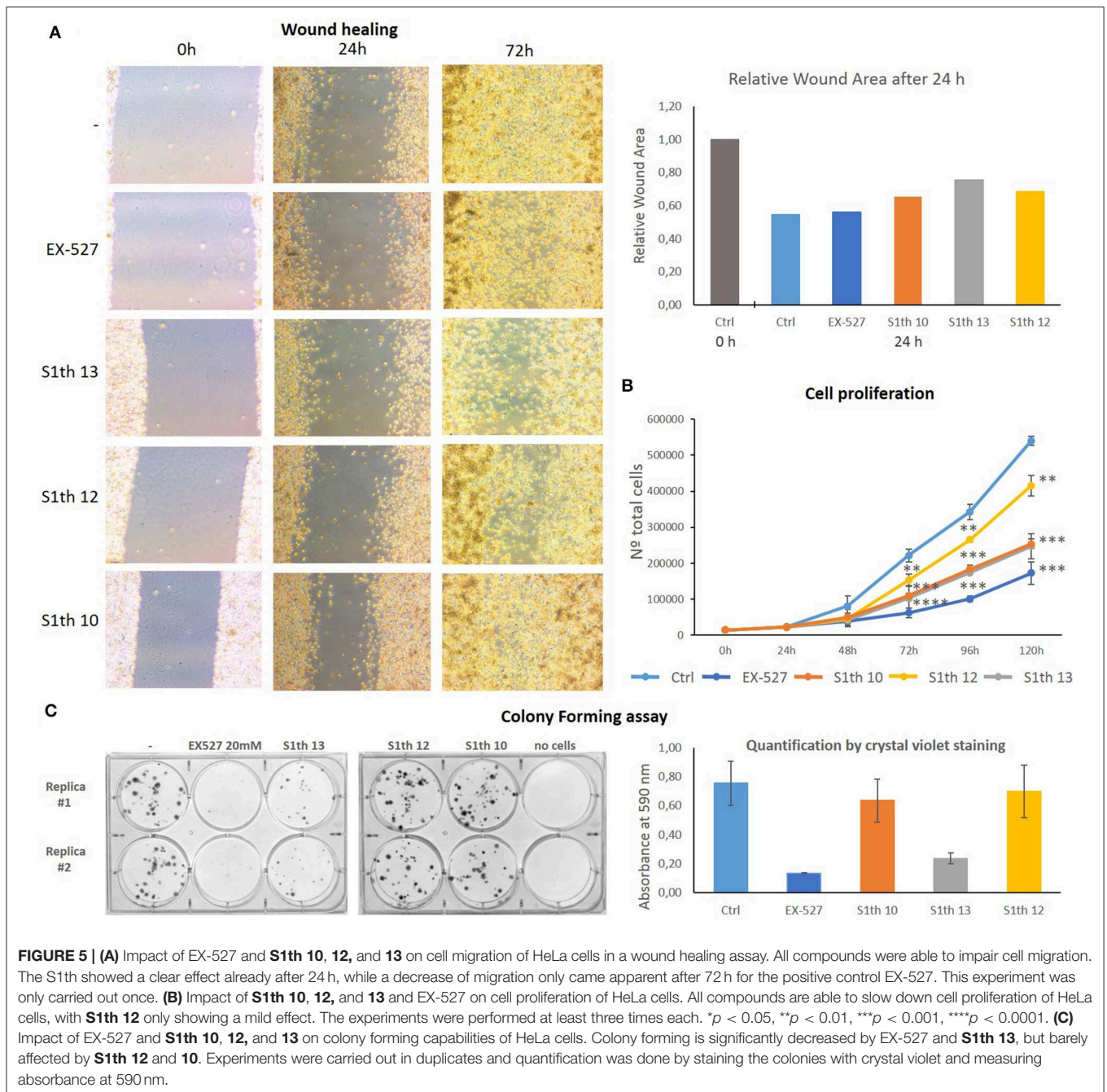


binding of α -H3K9ac and α -p53K382ac were compared to α -H3 and α -p53 binding, respectively. Thereby stable expression of H3 and p53 in all samples was ensured and additionally α -GAPDH was used as a loading control. All three S1th tested were able to significantly increase H3K9 and p53K382 acetylation and thereby affirm selective Sirt1 inhibition in HeLa cells. For EX-527 no hyperacetylation of H3K9 but increased acetylation levels of p53K382 were observed.

DISCUSSION

To further investigate the role of Sirt1 in cancer, new selective inhibitors for this isotype will be of great value. However, so far only few such inhibitors have been reported. In this study we identified a new class of selective and potent Sirt1 inhibitors, the Sirtuin 1 inhibiting Thiocyanates (S1th) by an iterative process of virtual screening and biochemical testing. Molecular docking of the S1th to the crystal structure of Sirt1 in complex with its cofactor NAD⁺ revealed their putative binding mode. In general, the inhibitors are proposed to bind to the NAD⁺ binding pocket of Sirt1. This could be confirmed in a competition assay, showing competition between the inhibitors and the cofactor NAD⁺ but not toward a peptide substrate analog. The most potent inhibitor of this class **S1th 13** is thought to engage in two hydrogen bonds with Asn465 and Asp272 and a potentially covalent interaction with Cys482. As indicated by competition assays binding of the S1th is reversible leading to the conclusion that even though the interaction with Cys482 could be covalent it is also fully reversible. Fast reversible covalent inhibitors have been reported before e.g., for kinases (80). In thermal shift assays covalent inhibitors often show a characteristic left shift, as they can destabilize the thermodynamically most stable conformation of an enzyme or can stabilize a different confirmation. S1th binding resulted in a strong left shift of Sirt1 melting temperature.

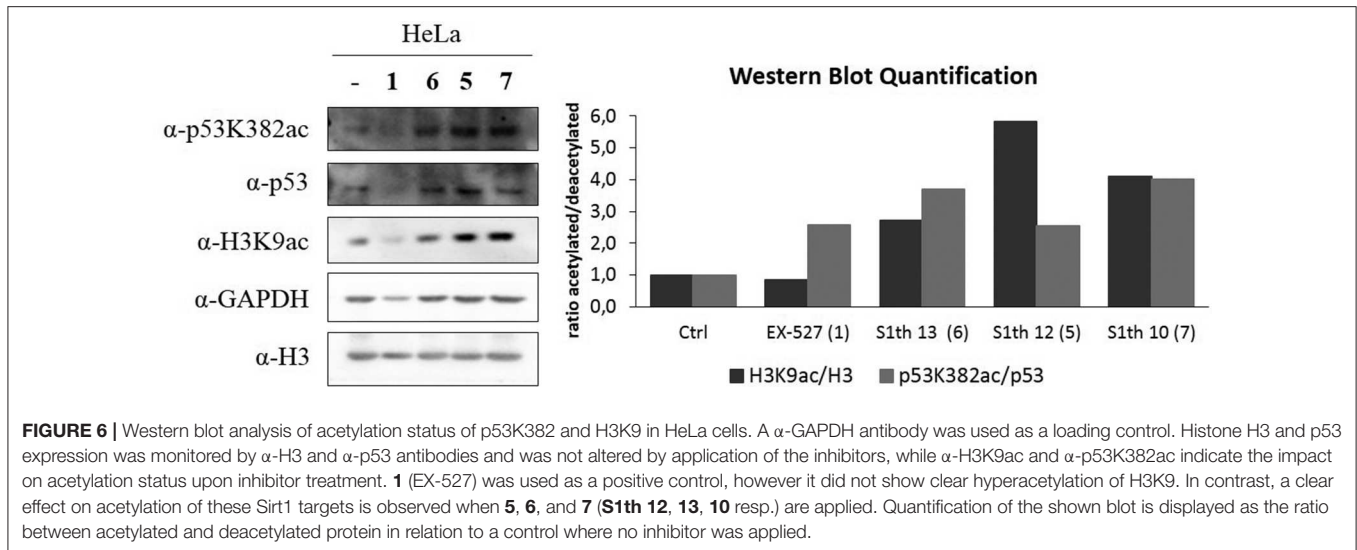
Interestingly, the Sirt2 melting temperature was not affected at all by the S1th, although the respective cysteine residue is conserved in Sirt2 (Cys324). These results indicate that no unspecific binding of the S1th's thiocyanate moiety occurs and the interaction between the thiocyanate and Cys482 in Sirt1 is highly selective. Further we could demonstrate that S1th are selective over sirtuin isotypes 3 and 5, representatives of HDAC class I and II (HDAC 1 and 6) as well as a set of deubiquitinases (DUBs). Selectivity over DUBs is especially remarkable since they are known to be inhibited by thiocyanates through binding of a catalytically relevant cysteine residue in the active site of DUBs. The thiocyanate PR-619 for example is a pan-DUB inhibitor and as we showed also inhibits Sirt1 with a low micro molar IC₅₀. After ensuring high selectivity and potency of our new inhibitor class we wanted to prove target engagement in cells. **S1th 10**, **12**, and **13** were applied to MEF cells and the effect on H2AX phosphorylation was detected. H2AX is a DNA damage sensor that gets phosphorylated upon DNA damage. Phosphorylation of H2AX was significantly decreased by **S1th 10**, **12**, and **13** as well as by the positive control EX-527 while a selective Sirt2 inhibitor (SirReal2) did not show any effect. The reduction of γ H2AX/H2AX levels observed after application of Sirt1 inhibitors was similar as in Sirt1 KO MEFs. Additional treatment with camptothecin, a drug that induces DNA damage through inhibition of topoisomerase I and thereby increases γ H2AX/H2AX levels, didn't surpass the inhibitory effect of the S1th or the positive control but even seemed to increase the efficacy especially for **S1th 13**. Finally, we tested the effects of S1th on proliferation, migration and colony forming capabilities of human cervical cancer cells. The cervical cancer cell line HeLa was treated with **S1th 10**, **12**, **13** and EX-527 as a positive control. **S1th 13** showed significant inhibition of proliferation, migration and colony forming while **S1th 10** and **12** only had moderate effects. EX-527 also showed robust inhibition of cell proliferation



and colony forming, however for migration a clear effect became apparent only 72 h after treatment but not already after 24 h, as observed for the S1th. Finally, western blot analysis confirmed that the effect of S1th in HeLa cells is associated with concomitant hyperacetylation of H3K9 and p53K382.

Although the *in vitro* potency of the S1th is yet lower than that of the reference EX-527, their discovery, especially their very high selectivity, still opens up new possibilities. Remarkably, unlike EX-527 that has strongly decreased potency in the cellular setting as compared to the biochemical assay, they show similar

potencies in cells as *in vitro*. This demonstrates their high potential to further study the role of Sirt1 in cellular model systems for cancer research but also in other diseases. The structural knowledge obtained from available crystal structures of Sirt1 and our docking studies can be utilized for future inhibitor optimization. Knowing that thiocyanates are able to engage in a specific interaction right in the catalytic core of the enzyme, new structures can be designed and synthesized. Already now the S1th present a valid alternative to EX-527 for cellular studies.



DATA AVAILABILITY STATEMENT

All datasets generated for this study are included in the article/**Supplementary Material**.

AUTHOR CONTRIBUTIONS

MJ and WS contributed conception and design of the study. ZA performed the computational studies. HO and JGa performed selectivity testing on DUBs. KS performed selectivity testing on HDACs. SS performed initial *in vitro* testing. Cellular tests were planned by AV and JGo and performed by JGo. OE and LZ designed and executed expression and purification of enzymes for *in vitro* testing. NW performed *in vitro* studies and wrote major parts of the manuscript. MJ, ZA, and WS wrote sections of the manuscript. All authors contributed to manuscript revision, read and approved the submitted version.

REFERENCES

- Houtkooper RH, Pirinen E, Auwerx J. Sirtuins as regulators of metabolism and healthspan. *Nat Rev Mol Cell Biol.* (2012) 13:225–38. doi: 10.1038/nrm3293
- Schiedel M, Robaa D, Rumpf T, Sippl W, Jung M. The current state of NAD⁺-dependent histone deacetylases (sirtuins) as novel therapeutic targets. *Med Res Rev.* (2018) 38:147–200. doi: 10.1002/med.21436
- Carafa V, Rotili D, Forgione M, Cuomo F, Serrettiello E, Hailu GS, et al. Sirtuin functions and modulation: from chemistry to the clinic. *Clin Epigenetics.* (2016) 8:61. doi: 10.1186/s13148-016-0224-3
- Robaa D, Monaldi D, Wössner N, Norio K, Rumpf T, Schiedel M, et al. Opening the selectivity pocket in the human lysine deacetylase Sirtuin2 - new opportunities, new questions. *Chem Rec.* (2018) 18:1701–7. doi: 10.1002/tcr.201800044
- Dang W. The controversial world of sirtuins. *Drug Discov Today Technol.* (2014) 12:e9–e17. doi: 10.1016/j.ddtec.2012.08.003
- Dai H, Sinclair DA, Ellis JL, Steegborn C. Sirtuin activators and inhibitors: promises, achievements, and challenges. *Pharmacol Ther.* (2018) 188:140–54. doi: 10.1016/j.pharmthera.2018.03.004
- Lee S-H, Lee J-H, Lee H-Y, Min K-J. Sirtuin signaling in cellular senescence and aging. *BMB Rep.* (2019) 52:24–34. doi: 10.5483/BMBRep.2019.52.1.290
- Park S-H, Zhu Y, Ozden O, Kim H-S, Jiang H, Deng C-X, et al. SIRT2 is a tumor suppressor that connects aging, acetylome, cell cycle signaling, and carcinogenesis. *Transl Cancer Res.* (2012) 1:15–21.
- Serrano L, Martínez-Redondo P, Marazuela-Duque A, Vazquez BN, Dooley SJ, Voigt P, et al. The tumor suppressor SirT2 regulates cell cycle progression and genome stability by modulating the mitotic deposition of H4K20 methylation. *Genes Dev.* (2013) 27:639–53. doi: 10.1101/gad.211342.112
- Jing H, Hu J, He B, Negrón Abril YL, Stupinski J, Weiser K, et al. A SIRT2-selective inhibitor promotes c-Myc oncoprotein degradation and exhibits broad anticancer activity. *Cancer Cell.* (2016) 29:297–310. doi: 10.1016/j.ccell.2016.02.007
- Schiedel M, Rumpf T, Karaman B, Lehoczky A, Oláh J, Gerhardt S, et al. Aminothiazoles as potent and selective Sirt2 inhibitors: a structure-activity relationship study. *J Med Chem.* (2016) 59:1599–612. doi: 10.1021/acs.jmedchem.5b01517
- Shah AA, Ito A, Nakata A, Yoshida M. Identification of a selective sIRT2 inhibitor and its anti-breast cancer activity. *Biol Pharm Bull.* (2016) 39:1739–42. doi: 10.1248/bpb.b16-00520

FUNDING

MJ, WS, and NW thank the DFG (Ju295/14-1, Si868/15-1; MJ and NW additionally thank 235777276/GRK1976 and CRC992) for funding. AV thanks the Spanish Ministry of Economy and Competitiveness - MINECO SAF2017-88975R (AV) cofunded by FEDER funds/European Regional Development Fund (ERDF) - A Way to Build Europe and the Catalan government agency AGAUR 2017-SGR148 (AV) and the CERCA Programme/Generalitat de Catalunya and the Josep Carreras Foundation for institutional support.

SUPPLEMENTARY MATERIAL

The Supplementary Material for this article can be found online at: <https://www.frontiersin.org/articles/10.3389/fonc.2020.00657/full#supplementary-material>

13. Moniot S, Forgione M, Lucidi A, Hailu GS, Nebbioso A, Carafa V, et al. Development of 1,2,4-oxadiazoles as potent and selective inhibitors of the human deacetylase Sirtuin 2: structure-activity relationship, X-ray crystal structure, and anticancer activity. *J Med Chem.* (2017) 60:2344–60. doi: 10.1021/acs.jmedchem.6b01609
14. Kozako T, Mellini P, Ohsugi T, Aikawa A, Uchida Y-I, Honda S-I, et al. Novel small molecule SIRT2 inhibitors induce cell death in leukemic cell lines. *BMC Cancer.* (2018) 18:791. doi: 10.1186/s12885-018-4710-1
15. Spiegelman NA, Price IR, Jing H, Wang M, Yang M, Cao J, et al. Direct comparison of SIRT2 inhibitors: potency, specificity, activity-dependent inhibition, and on-target anticancer activities. *ChemMedChem.* (2018) 13:1890–4. doi: 10.1002/cmdc.201800391
16. Desantis V, Lamanuzzi A, Vacca A. The role of SIRT6 in tumors. *Haematologica.* (2018) 103:1–4. doi: 10.3324/haematol.2017.182675
17. Huang Z, Zhao J, Deng W, Chen Y, Shang J, Song K, et al. Identification of a cellularly active SIRT6 allosteric activator. *Nat Chem Biol.* (2018) 14:1118–26. doi: 10.1038/s41589-018-0150-0
18. Ran L-K, Chen Y, Zhang Z-Z, Tao N-N, Ren J-H, Zhou L, et al. SIRT6 overexpression potentiates apoptosis evasion in hepatocellular carcinoma via BCL2-associated X protein-dependent apoptotic pathway. *Clin Cancer Res.* (2016) 22:3372–82. doi: 10.1158/1078-0432.CCR-15-1638
19. Cagnetta A, Soncini D, Orecchioni S, Talarico G, Minetto P, Guolo F, et al. Depletion of SIRT6 enzymatic activity increases acute myeloid leukemia cells' vulnerability to DNA-damaging agents. *Haematologica.* (2018) 103:80–90. doi: 10.3324/haematol.2017.176248
20. Süßmuth SD, Haider S, Landwehrmeyer GB, Farmer R, Frost C, Tripepi G, et al. An exploratory double-blind, randomized clinical trial with selisistat, a SirT1 inhibitor, in patients with Huntington's disease. *Br J Clin Pharmacol.* (2015) 79:465–76. doi: 10.1111/bcp.12512
21. Borra MT, Smith BC, Denu JM. Mechanism of human SIRT1 activation by resveratrol. *J Biol Chem.* (2005) 280:17187–95. doi: 10.1074/jbc.M501250200
22. Choupani J, Mansoori Derakhshan S, Bayat S, Alivand MR, Shekari Khaniani M. Narrower insight to SIRT1 role in cancer: a potential therapeutic target to control epithelial-mesenchymal transition in cancer cells. *J Cell Physiol.* (2018) 233:4443–57. doi: 10.1002/jcp.26302
23. Yang T, Zhou R, Yu S, Yu S, Cui Z, Hu P, et al. Cytoplasmic SIRT1 inhibits cell migration and invasion by impeding epithelial-mesenchymal transition in ovarian carcinoma. *Mol Cell Biochem.* (2019) 459:157–69. doi: 10.1007/s11010-019-03559-y
24. Di Sante G, Pestell TG, Casimiro MC, Bisetto S, Powell MJ, Lisanti MP, et al. Loss of Sirt1 promotes prostatic intraepithelial neoplasia, reduces mitophagy, and delays PARK2 translocation to mitochondria. *Am J Pathol.* (2015) 185:266–79. doi: 10.1016/j.ajpath.2014.09.014
25. Long Q, Xu J, Osunkoya AO, Sannigrahi S, Johnson BA, Zhou W, et al. Global transcriptome analysis of formalin-fixed prostate cancer specimens identifies biomarkers of disease recurrence. *Cancer Res.* (2014) 74:3228–37. doi: 10.1158/0008-5472.CAN-13-2699
26. Vaziri H, Dessain SK, Ng Eaton E, Imai SI, Frye RA, Pandita TK, et al. hSIR2(SIRT1) functions as an NAD-dependent p53 deacetylase. *Cell.* (2001) 107:149–59. doi: 10.1016/S0092-8674(01)00527-X
27. Wang C, Chen L, Hou X, Li Z, Kabra N, Ma Y, et al. Interactions between E2F1 and SirT1 regulate apoptotic response to DNA damage. *Nat Cell Biol.* (2006) 8:1025–31. doi: 10.1038/ncb1468
28. Abdelmawgoud H, El Awady RR. Effect of Sirtuin 1 inhibition on matrix metalloproteinase 2 and Forkhead box O3a expression in breast cancer cells. *Genes Dis.* (2017) 4:240–6. doi: 10.1016/j.gendis.2017.11.001
29. Rifai K, Idrissou M, Penault-Llorca F, Bignon Y-J, Bernard-Gallon D. Breaking down the contradictory roles of histone deacetylase SIRT1 in human breast cancer. *Cancers.* (2018) 10:409. doi: 10.3390/cancers10110409
30. Jin X, Wei Y, Xu F, Zhao M, Dai K, Shen R, et al. SIRT1 promotes formation of breast cancer through modulating Akt activity. *J Cancer.* (2018) 9:2012–23. doi: 10.7150/jca.24275
31. Jeong J, Juhn K, Lee H, Kim S-H, Min B-H, Lee K-M, et al. SIRT1 promotes DNA repair activity and deacetylation of Ku70. *Exp Mol Med.* (2007) 39:8–13. doi: 10.1038/emmm.2007.2
32. Oberdoerffer P, Michan S, McVay M, Mostoslavsky R, Vann J, Park S-K, et al. SIRT1 redistribution on chromatin promotes genomic stability but alters gene expression during aging. *Cell.* (2008) 135:907–18. doi: 10.1016/j.cell.2008.10.025
33. Yeung F, Hoberg JE, Ramsey CS, Keller MD, Jones DR, Frye RA, et al. Modulation of NF- κ B-dependent transcription and cell survival by the SIRT1 deacetylase. *EMBO J.* (2004) 23:2369–80. doi: 10.1038/sj.emboj.7600244
34. Wilking MJ, Ahmad N. The role of SIRT1 in cancer: the saga continues. *Am J Pathol.* (2015) 185:26–8. doi: 10.1016/j.ajpath.2014.10.002
35. Wang C, Yang W, Dong F, Guo Y, Tan J, Ruan S, et al. The prognostic role of Sirt1 expression in solid malignancies: a meta-analysis. *Oncotarget.* (2017) 8:66343–51. doi: 10.18632/oncotarget.18494
36. Peck B, Chen CY, Ho KK, Di Fruscia P, Myatt SS, Coombes RC, et al. SIRT inhibitors induce cell death and p53 acetylation through targeting both SIRT1 and SIRT2. *Mol Cancer Ther.* (2010) 9:844–55. doi: 10.1158/1535-7163.MCT-09-0971
37. Singh S, Kumar PU, Thakur S, Kiran S, Sen B, Sharma S, et al. Expression/localization patterns of sirtuins (SIRT1, SIRT2, and SIRT7) during progression of cervical cancer and effects of sirtuin inhibitors on growth of cervical cancer cells. *Tumor Biol.* (2015) 36:6159–71. doi: 10.1007/s13277-015-3300-y
38. Wilking MJ, Singh CK, Nihal M, Ndiaye MA, Ahmad N. Sirtuin deacetylases: a new target for melanoma management. *Cell Cycle.* (2014) 13:2821–6. doi: 10.4161/15384101.2014.949085
39. Bhalla S, Gordon LI. Functional characterization of NAD dependent deacetylases SIRT1 and SIRT2 in B-cell chronic lymphocytic leukemia (CLL). *Cancer Biol Ther.* (2016) 17:300–9. doi: 10.1080/15384047.2016.1139246
40. Ceballos MP, Decándido G, Quiroga AD, Comanzo CG, Livore VI, Lorenzetti F, et al. Inhibition of sirtuins 1 and 2 impairs cell survival and migration and modulates the expression of P-glycoprotein and MRP3 in hepatocellular carcinoma cell lines. *Toxicol Lett.* (2018) 289:63–74. doi: 10.1016/j.toxlet.2018.03.011
41. Kuo LJ, Yang L-X. γ -H2AX - a novel biomarker for DNA double-strand breaks. *In Vivo.* (2008) 22:305–9.
42. Wang R-H, Sengupta K, Li C, Kim H-S, Cao L, Xiao C, et al. Impaired DNA damage response, genome instability, and tumorigenesis in SIRT1 mutant mice. *Cancer Cell.* (2008) 14:312–23. doi: 10.1016/j.ccr.2008.09.001
43. Madabushi A, Hwang B-J, Jin J, Lu A-L. Histone deacetylase SIRT1 modulates and deacetylates DNA base excision repair enzyme thymine DNA glycosylase. *Biochem J.* (2013) 456:89–98. doi: 10.1042/BJ20130670
44. Jang J, Huh YJ, Cho H-J, Lee B, Park J, Hwang D-Y, et al. SIRT1 enhances the survival of human embryonic stem cells by promoting DNA repair. *Stem Cell Rep.* (2017) 9:629–41. doi: 10.1016/j.stemcr.2017.06.001
45. Jarrett SG, Carter KM, Bautista RM, He D, Wang C, D'Orazio JA. Sirtuin 1-mediated deacetylation of XPA DNA repair protein enhances its interaction with ATR protein and promotes cAMP-induced DNA repair of UV damage. *J Biol Chem.* (2018) 293:19025–37. doi: 10.1074/jbc.RA118.003940
46. Yu W, Li L, Wang G, Zhang W, Xu J, Liang A. KU70 Inhibition impairs both non-homologous end joining and homologous recombination DNA damage repair through SHP-1 induced dephosphorylation of SIRT1 in adult T-cell leukemia-lymphoma cells. *Cell Physiol Biochem.* (2018) 49:2111–23. doi: 10.1159/000493815
47. Alves-Fernandes DK, Jasiulionis MG. The role of SIRT1 on DNA damage response and epigenetic alterations in cancer. *Int J Mol Sci.* (2019) 20:3153. doi: 10.3390/ijms2013153
48. Asaka R, Miyamoto T, Yamada Y, Ando H, Mvunta DH, Kobara H, et al. Sirtuin 1 promotes the growth and cisplatin resistance of endometrial carcinoma cells: a novel therapeutic target. *Lab Invest.* (2015) 95:1363–73. doi: 10.1038/labinvest.2015.119
49. Napper AD, Hixon J, McDonagh T, Keavey K, Pons J-F, Barker J, et al. Discovery of indoles as potent and selective inhibitors of the deacetylase SIRT1. *J Med Chem.* (2005) 48:8045–54. doi: 10.1021/jm050522v
50. Trapp J, Meier R, Hongwiset D, Kassack MU, Sippl W, Jung M. Structure-activity studies on suramin analogues as inhibitors of NAD⁺-dependent histone deacetylases (sirtuins). *ChemMedChem.* (2007) 2:1419–31. doi: 10.1002/cmdc.200700003
51. Zhou Z, Ma T, Zhu Q, Xu Y, Zha X. Recent advances in inhibitors of sirtuin1/2: an update and perspective. *Future Med Chem.* (2018) 10:907–34. doi: 10.4155/fmc-2017-0207

52. Pagans S, Pedal A, North BJ, Kaehlcke K, Marshall BL, Dorr A, et al. SIRT1 regulates HIV transcription via tat deacetylation. *PLoS Biol.* (2005) 3:0210–20. doi: 10.1371/journal.pbio.0030041
53. Ismail, Kuthati B, Thalari G, Bommarapu V, Mulakayala C, Chitta SK, et al. Synthesis of novel spiro[pyrazolo[4,3-d]pyrimidinones and spiro[benzo[4,5]thieno[2,3-d]pyrimidine-2,3'-indoline]-2',4(3H)-diones and their evaluation for anticancer activity. *Bioorg Med Chem Lett.* (2017) 27:1446–50. doi: 10.1016/j.bmcl.2017.01.088
54. Schiedel M, Herp D, Hammelmann S, Swyter S, Lehotzky A, Robaa D, et al. Chemically induced degradation of sirtuin 2 (Sirt2) by a proteolysis targeting chimera (PROTAC) based on sirtuin rearranging ligands (SirReals). *J Med Chem.* (2018) 61:482–91. doi: 10.1021/acs.jmedchem.6b01872
55. Laemmli UK. Cleavage of structural proteins during the assembly of the head of bacteriophage T4. *Nature.* (1970) 227:680–5. doi: 10.1038/227680a0
56. Smith PK, Krohn RI, Hermanson GT, Mallia AK, Gartner FH, Provenzano MD, et al. Measurement of protein using bicinchoninic acid. *Anal Biochem.* (1985) 150:76–85. doi: 10.1016/0003-2697(85)90442-7
57. Heltweg B, Trapp J, Jung M. *In vitro* assays for the determination of histone deacetylase activity. *Methods.* (2005) 36:332–7. doi: 10.1016/j.jymeth.2005.03.003
58. Maurer B, Rumpf T, Scharfe M, Stolfa DA, Schmitt ML, He W, et al. Inhibitors of the NAD⁺-dependent protein desuccinylase and demalonylase sirt5. *ACS Med Chem Lett.* (2012) 3:1050–3. doi: 10.1021/ml3002709
59. Swyter S, Schiedel M, Monaldi D, Sippl W, Lehotzky A, Rumpf T, et al. New chemical tools for probing activity and inhibition of the NAD⁺-dependent lysine deacylase sirtuin 2. *Philos Trans R Soc.* (2018) 373:20170083. doi: 10.1098/rstb.2017.0083
60. Niesen FH, Berglund H, Vedadi M. The use of differential scanning fluorimetry to detect ligand interactions that promote protein stability. *Nat Protoc.* (2007) 2:2212–21. doi: 10.1038/nprot.2007.321
61. Ekkebus R, van Kasteren SI, Kulathu Y, Scholten A, Berlin I, Geurink PP, et al. On terminal alkynes that can react with active-site cysteine nucleophiles in proteases. *J Am Chem Soc.* (2013) 135:2867–70. doi: 10.1021/ja309802n
62. Rumpf T, Schiedel M, Karaman B, Roessler C, North BJ, Lehotzky A, et al. Selective Sirt2 inhibition by ligand-induced rearrangement of the active site. *Nat Commun.* (2015) 6:6263. doi: 10.1038/ncomms7263
63. Dignam JD, Lebovitz RM, Roeder RG. Accurate transcription initiation by RNA polymerase II in a soluble extract from isolated mammalian nuclei. *Nucleic Acids Res.* (1983) 11:1475–89. doi: 10.1093/nar/11.5.1475
64. Zhao X, Allison D, Condon B, Zhang F, Gheyi T, Zhang A, et al. The 2.5 Å crystal structure of the SIRT1 catalytic domain bound to nicotinamide adenine dinucleotide (NAD⁺) and an indole (EX527 analogue) reveals a novel mechanism of histone deacetylase inhibition. *J Med Chem.* (2013) 56:963–9. doi: 10.1021/jm301431y
65. Wang J, Wolf RM, Caldwell JW, Kollman PA, Case DA. Development and testing of a general amber force field. *J Comput Chem.* (2004) 25:1157–74. doi: 10.1002/jcc.20035
66. Jakalian A, Jack DB, Bayly CI. Fast, efficient generation of high-quality atomic charges. AM1-BCC model: II. Parameterization and validation. *J Comput Chem.* (2002) 23:1623–41. doi: 10.1002/jcc.10128
67. Jones G, Willett P, Glen RC, Leach AR, Taylor R. Development and validation of a genetic algorithm for flexible docking11 edited by F. E Cohen *J Mol Biol.* (1997) 267:727–48. doi: 10.1006/jmbi.1996.0897
68. Ho E, Clarke JD, Dashwood RH. Dietary sulforaphane, a histone deacetylase inhibitor for cancer prevention. *J Nutr.* (2009) 139:2393–6. doi: 10.3945/jn.109.113332
69. Amerik AY, Hochstrasser M. Mechanism and function of deubiquitinating enzymes. *Biochim Biophys Acta Mol Cell Res.* (2004) 1695:189–207. doi: 10.1016/j.bbamcr.2004.10.003
70. Altun M, Kramer HB, Willems LI, McDermott JL, Leach CA, Goldenberg SJ, et al. Activity-based chemical proteomics accelerates inhibitor development for deubiquitylating enzymes. *Chem Biol.* (2011) 18:1401–12. doi: 10.1016/j.chembiol.2011.08.018
71. Seiberlich V, Goldbaum O, Zhukareva V, Richter-Landsberg C. The small molecule inhibitor PR-619 of deubiquitinating enzymes affects the microtubule network and causes protein aggregate formation in neural cells: implications for neurodegenerative diseases. *Biochim Biophys Acta Mol Cell Res.* (2012) 1823:2057–68. doi: 10.1016/j.bbamcr.2012.04.011
72. Milne JC, Denu JM. The Sirtuin family: therapeutic targets to treat diseases of aging. *Curr Opin Chem Biol.* (2008) 12:11–7. doi: 10.1016/j.cbpa.2008.01.019
73. Weber PC, Salemme FR. Applications of calorimetric methods to drug discovery and the study of protein interactions. *Curr Opin Struct Biol.* (2003) 13:115–21. doi: 10.1016/S0959-440X(03)0003-4
74. Cimpmperman P, Baranauskiene L, Jachimovičiute S, Jachno J, Torresan J, Michailoviene V, et al. A quantitative model of thermal stabilization and destabilization of proteins by ligands. *Biophys J.* (2008) 95:3222–31. doi: 10.1529/biophysj.108.134973
75. Simeonov A. Recent developments in the use of differential scanning fluorometry in protein and small molecule discovery and characterization. *Expert Opin Drug Discov.* (2013) 8:1071–82. doi: 10.1517/17460441.2013.806479
76. Garbett NC, Chaires JB. Thermodynamic studies for drug design and screening. *Expert Opin Drug Discov.* (2012) 7:299–314. doi: 10.1517/17460441.2012.666235
77. Parenti MD, Bruzzone S, Nencioni A, Del Rio A. Selectivity hot-spots of sirtuin catalytic cores. *Mol Biosyst.* (2015) 11:2263–72. doi: 10.1039/C5MB00205B
78. Slichenmyer WJ, Rowinsky EK, Donehower RC, Kaufmann SH. The current status of camptothecin analogues as antitumor agents. *J Natl Cancer Inst.* (1993) 85:271–91. doi: 10.1093/jnci/85.4.271
79. Ryckewaert L, Sacconnay L, Carrupt P-A, Nurisso A, Simões-Pires C. Non-specific SIRT inhibition as a mechanism for the cytotoxicity of ginkgolic acids and urushiols. *Toxicol Lett.* (2014) 229:374–80. doi: 10.1016/j.toxlet.2014.07.002
80. Kim H, Jo A, Choi S-S, Nam H, Byun WG, Bae H, et al. Rational design and synthesis of reversible covalent PPAR γ antagonistic ligands inhibiting Ser273 phosphorylation. *Asian J Org Chem.* (2019) 8:1698–706. doi: 10.1002/ajoc.201800668

Conflict of Interest: The authors declare that the research was conducted in the absence of any commercial or financial relationships that could be construed as a potential conflict of interest.

Copyright © 2020 Wössner, Alhalabi, González, Swyter, Gan, Schmidtkunz, Zhang, Vaquero, Ovaa, Einsle, Sippl and Jung. This is an open-access article distributed under the terms of the Creative Commons Attribution License (CC BY). The use, distribution or reproduction in other forums is permitted, provided the original author(s) and the copyright owner(s) are credited and that the original publication in this journal is cited, in accordance with accepted academic practice. No use, distribution or reproduction is permitted which does not comply with these terms.

4.3. Manuscript 3: Potent and Selective Inhibitors of Human Sirtuin 5.

D., Kalbas, S., Liebscher, T., Nowak, M., Meleshin, M., Pannek, C., Popp,

Z., Alhalabi, F., Bordusa, W., Sippl, C., Steegborn, M., Schutkowski.

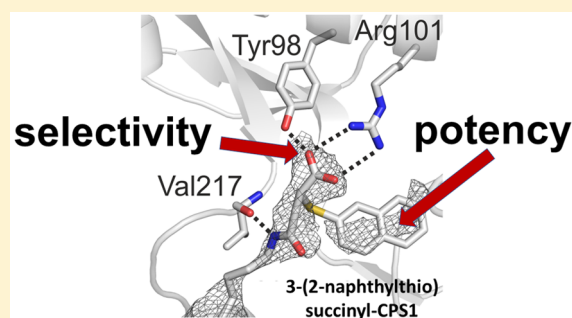
Journal of medicinal chemistry. 61, 2460–2471 (2018).

Potent and Selective Inhibitors of Human Sirtuin 5

Diana Kalbas,^{†,||} Sandra Liebscher,^{‡,||} Theresa Nowak,^{§,||} Marat Meleshin,[†] Martin Pannek,[⊥] Corinna Popp,[†] Zayan Alhalabi,[§] Frank Bordusa,[‡] Wolfgang Sippl,[§] Clemens Steegborn,[⊥] and Mike Schutkowski^{*,†,Ⓜ}[†]Department of Enzymology, Institute of Biochemistry and Biotechnology, Martin-Luther-University Halle-Wittenberg, 06120 Halle/Saale, Germany[‡]Department of Natural Product Biochemistry, Institute of Biochemistry and Biotechnology, Martin-Luther-University Halle-Wittenberg, 06120 Halle/Saale, Germany[§]Department of Medical Chemistry, Institute of Pharmacy, Martin-Luther-University Halle-Wittenberg, 06120 Halle/Saale, Germany[⊥]Department of Biochemistry, University of Bayreuth, 95447 Bayreuth, Germany

Supporting Information

ABSTRACT: Sirtuins are protein deacylases that regulate metabolism and stress responses and are implicated in aging-related diseases. Modulators of the human sirtuins Sirt1–7 are sought as chemical tools and potential therapeutics, e.g., for cancer. Selective and potent inhibitors are available for Sirt2, but selective inhibitors for Sirt5 with K_i values in the low nanomolar range are lacking. We synthesized and screened 3-arythiosuccinylated and 3-benzylthiosuccinylated peptide derivatives yielding Sirt5 inhibitors with low-nanomolar K_i values. A biotinylated derivative with this scaffold represents an affinity probe for human Sirt5 that is able to selectively extract this enzyme out of complex biological samples like cell lysates. Crystal structures of Sirt5/inhibitor complexes reveal that the compounds bind in an unexpected manner to the active site of Sirt5.



INTRODUCTION

Sirtuins (Sirt) represent an evolutionarily conserved family of NAD^+ -dependent lysine deacylases. Seven sirtuin isoforms have been identified in mammals, Sirt1 to Sirt7, which differ in their biochemical activities and subcellular localization. Sirt1 and Sirt2 are localized in the nucleus and cytoplasm, Sirt3–5 are mitochondrial enzymes, and Sirt6 and Sirt7 are localized exclusively in the nucleus. Sirtuins catalyze different lysine deacylation reactions, including removal of fatty acid modifications (Sirt1–6),¹ decrotonylation (Sirt1–3),² and removal of 3-hydroxy-3-methylglutaryl and lipoyl residues (Sirt4),³ but only Sirt5 possesses a strong desuccinylase, demalonylase, and deglutarylase activity *in vitro* and *in vivo*.⁴ The removal of negatively charged acyl moieties by Sirt5 results in up to 1000-fold higher catalytic activities compared to the respective deacetylation reaction.^{4c}

The role of Sirt5 in metabolic pathways like glycolysis, tricarboxylic acid cycle, fatty acid oxidation, ammonia detoxification, reactive oxygen defense, or apoptosis makes this enzyme an interesting target for drug development.^{4b,5} Deregulation or noncontrolled activation of Sirt5 is involved in several human diseases, including cancer, Alzheimer's disease, and Parkinson's disease.⁶ Inhibition of Sirt5 resulted in suppressed tumor cell proliferation caused by increased succinylation of lysine residue 498 in pyruvate kinase M2.^{6a}

Recently, it was shown that Sirt5-mediated desuccinylase activity is involved in pro-inflammatory response of macrophages by changing pyruvate kinase M2 enzymatic activity.⁷ Moreover, Sirt5 is overexpressed in human non-small-cell lung cancer, and this overexpression is correlated with poor prognosis.⁸ Effectors of Sirt5 activity are therefore needed as potential therapeutics and as chemical probes to investigate Sirt5 function in more detail. Here we present the development of selective and potent Sirt5 inhibitors with K_i values in the low nanomolar range.

RESULTS AND DISCUSSION

The 3-phenylsuccinyl moiety on a lysine side chain represents a specific Sirt5 inhibitor which acts by blocking the NAD^+ binding pocket.^{4c} Compound I (Figure 1) is one of the most effective and selective Sirt5 inhibitors with a K_i value of 4.3 μM . Other reported Sirt5 inhibitors are shown in Figure 1, but selectivity has not been determined for all of them. Inspection of the crystal structure of zebrafish Sirt5 (zSirt5) in complex with the structurally similar 3-phenylsuccinyl-carbamoyl phosphate synthetase (CPS1)-derived peptide (47; PDB ID 4UTV) revealed that the phenyl ring on the succinyl residue

Received: November 22, 2017

Published: March 1, 2018

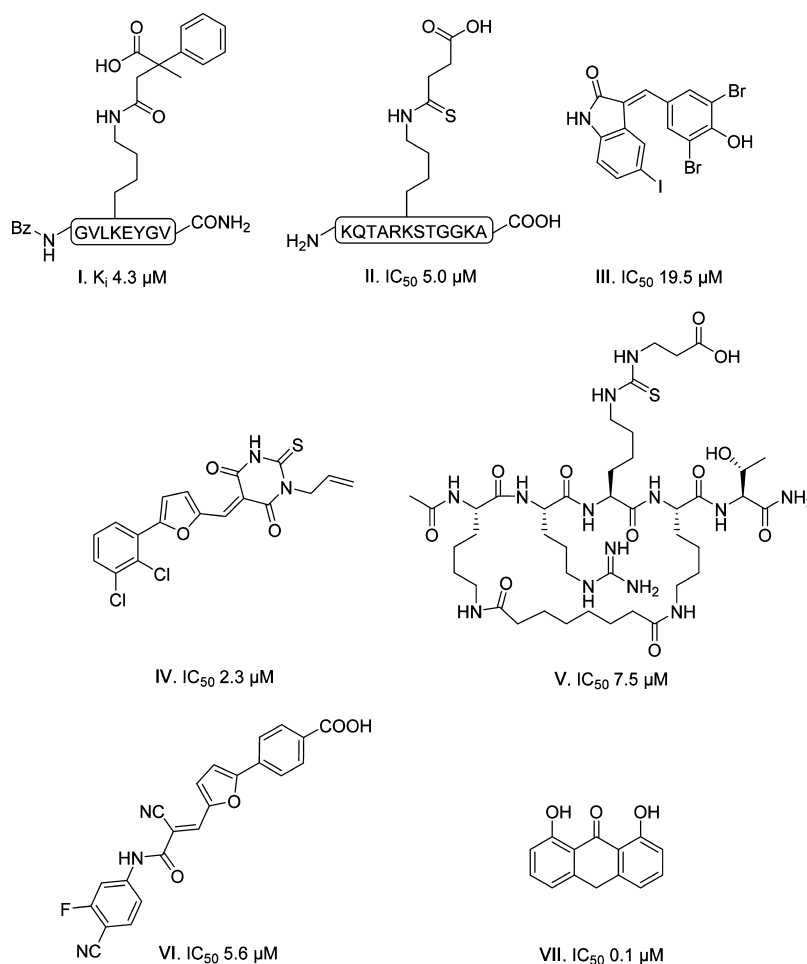


Figure 1. Reported Sirt5 inhibitors: **I**,^{4c} **II**,⁹ **III**,¹⁰ **IV**,¹¹ **V**,¹² **VI**,¹³ **VII**.¹⁴

points to the nicotinamide binding pocket (C-pocket) but is not able to reach the C-pocket.^{4c} Therefore, we started to analyze a 3-benzylsuccinyl derivative of CPS1 peptide, resulting in **1** (Table 1) with a K_i value of 263 ± 48 nM (Table S1). Reaction of substituted succinic anhydrides with the lysine side chain represents a convenient route to 3-alkyl(aryl)succinyl peptide derivatives.^{4c} However, because of limited access to such reagents and unsatisfactory regioselectivity of the reaction (often 2-substituted regioisomers are formed by alternative opening of the anhydride), we investigated another way to substitute succinyl peptides. Maleamic acid derivatives react with thiols, affording 2-(alkylthio)succinamic acid as the sole product.¹⁵ Because a large number of thiols are available commercially and respective Michael addition can be performed directly on the solid support, this method was chosen for the preparation of a library of 3-substituted succinyl-CPS1 peptides (Scheme 1). Treatment of resin-bound maleylated peptides with a thiol in the presence of tertiary base afforded expected diastereomeric mixtures of 3-substituted target peptides along with minor amounts of 2-substituted regioisomers. Treatment with trifluoroacetic acid at room temperature yielded four diastereomers/regioisomers. Surprisingly, reaction products were easily separated with HPLC, enabling convenient and simultaneous route to both (*S*)-3- and (*R*)-3-(alkyl(aryl)thio)succinyl-CPS1 peptide derivatives (2-substituted derivatives were formed in minor amounts and were not isolated). For convenience, we denote inseparable

equal mixtures of diastereomers as a number **N**, and fast- and slow-eluting diastereomers as **N.1** and **N.2**, respectively.

Using this reaction, we systematically optimized the acyl residue of the CPS1-derived peptide inhibitor (Table 1), resulting in a K_i value of 7 nM for **35.2** (Table S1). Compound **2** showed a K_i value similar to that of **1**. Nevertheless, we were able to demonstrate that the slower-migrating diastereomer, due to the substitution at position 3 of the succinyl residue **2.2**, is a more efficient inhibitor for Sirt5, with a K_i value of 135 nM. Insertion of one, two, or three methylene groups between the sulfur and the phenyl ring, resulting in **15**, **27**, and **32**, respectively, did not improve the inhibition constants. Additionally, replacement of the phenyl ring by heterocycles (see **28–31**) yielded inhibitors with K_i values between 3.5 and 11 μM . To analyze Sirt5/inhibitor interaction details, we solved crystal structures of **15**, respectively **2**, in complex with zSirt5 (Figure 2 and Table S2) and compared them with the previously solved structure of zSirt5/47^{4c} (PDB ID 4UTV). Surprisingly, the substituents at position 3 of the succinyl group occupy different binding pockets (Figure 2). The benzyl group of **15** is oriented similar to the phenyl ring of **1**, toward the C-pocket, and reaches deeper into this pocket yet still cannot fill it completely. In contrast, the phenyl group of **2** is positioned toward a hydrophobic patch formed by Ala78 and Phe219 and opened through rearrangements of the cofactor binding loop. Apparently, both sites can provide interactions for tight binding and potent inhibition. To explore the binding pocket of the phenyl ring of compound **2** in more detail, we generated all

Table 1. Chemical Structures of Succinyl-CPS1-Derived Peptide Inhibitors (Bz-GVLK(X)EYGV-NH₂)

X = CC(=O)C(R)C(=O)O

R*				
IC ₅₀ (nM)				
1 1122.0 ± 168.4	8.1 1606.9 ± 164.3 8.2 45.9 ± 11.3	15.1 644.1 ± 112.5 15.2 335.7 ± 39.7	22.1 2202.7 ± 245.7 22.2 803.5 ± 110.3	29 13243.9 ± 1931.5
2.1 1798.8 ± 200.4 2.2 273.5 ± 31.	9.1 2013.7 ± 586.7 9.2 176.6 ± 20.7	16.1 352.4 ± 48.2 16.2 533.3 ± 105.2	23.1 1148.2 ± 131.7 23.2 1124.6 ± 141.0	30 6966.3 ± 1261.6
3.1 3097.4 ± 361.4 3.2 857.0 ± 93.6	10.1 647.1 ± 73.2 10.2 86.1 ± 10.5	17.1 2673.0 ± 405.9 17.2 2710.2 ± 421.3	24.1 431.5 ± 57.0 24.2 543.3 ± 28.5	31.1 18492.7 ± 3575.3 31.2 8749.8 ± 1989.4
4.1 1383.6 ± 215.3 4.2 119.9 ± 7.4	11.1 12502.6 ± 2812.5 11.2 576.8 ± 77.9	18.1 1020.9 ± 169.4 18.2 893.3 ± 142.6	25.1 779.8 ± 40.0 25.2 739.6 ± 37.9	32.1 2060.6 ± 251.9 32.2 1129.8 ± 188.1
5.1 1614.4 ± 187.1 5.2 101.9 ± 9.5	12.1 1258.9 ± 153.2 12.2 46.1 ± 4.5	19.1 1235.9 ± 171.0 19.2 792.5 ± 92.8	26.1 631.0 ± 91.2 26.2 5200.0 ± 640.4	33.1 1181.0 ± 312.8 33.2 30.3 ± 3.5
6.1 3388.4 ± 410.6 6.2 714.5 ± 105.7	13.1 9078.2 ± 745.2 13.2 325.8 ± 42.9	20.1 4027.2 ± 445.4 20.2 3732.5 ± 489.9	27.1 591.6 ± 68.0 27.2 2741.6 ± 350.5	34.1 2196.2 ± 612 34.2 95.0 ± 14.2
7.1 1977.0 ± 251.1 7.2 295.1 ± 39.1	14.1 > 14000** 14.2 > 4000**	21.1 1111.7 ± 120.8 21.2 1047.1 ± 103.9	28 22803.4 ± 4586.4	35.1 207 ± 21.1 35.2 15.4 ± 9.5

*Hereinafter an equal mixture of diastereomers is denoted as N, with N.1 the fast- and N.2 the slow-eluting diastereomer. **Cannot be determined more precisely because of solubility problems.

possible monochloro- and dichloro-substituted compounds, resulting in 3–5 and 6–11, respectively. Substitution in the *o*-position seems not to be beneficial (Table 1) because it could lead to steric clash with the protein (Figure 2), but replacement of hydrogen by chlorine in the *m*- or *p*-position yielded inhibitors with K_i values between 50 and 60 nM for the better binding diastereomer. This improvement in binding is maybe caused by beneficial interactions with Sirt5 residues Phe66 and Arg67 (Figure 2). Chloro substitution in both the *p*- and *m*-positions led to 8, with a K_i value of 23 nM for 8.2. Flexible docking of 8.2 into the crystal structure of zSirt5 cocrystallized

with 2 showed that the dichlorophenyl ring fits perfectly into the hydrophobic pocket formed between Arg67 and Phe219 (Figure S25). Combined *m*- and *p*-substitution using methyl (12) and methoxy (13) moieties resulted in similar Sirt5 affinities. Inspired by this substitution pattern, we created 3-(2-naphthylthio)succinyl derivative 33.2, which represents the most efficient Sirt5 inhibitor with the 3-(arylthio)succinyl scaffold (IC_{50} value = 40 nM). Moreover, 33.2 is selective for Sirt5, evidenced by the fact that no effect on catalysis mediated by Sirt1, Sirt2, Sirt3, or Sirt6 could be detected with concentration of 33.2 up to 50 μ M (Figure S22). When the

Scheme 2. Synthesis of (S)-3-(Alkylthio/arylthio)succinyl Derivatives from (S)-Malic Acid

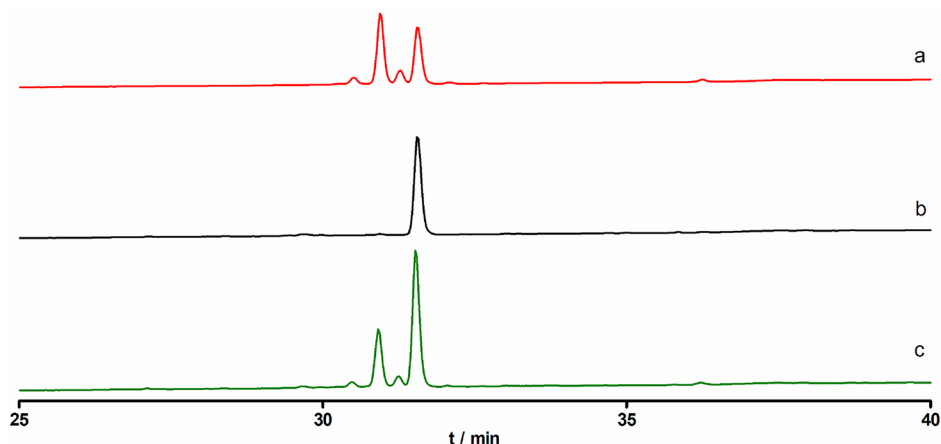
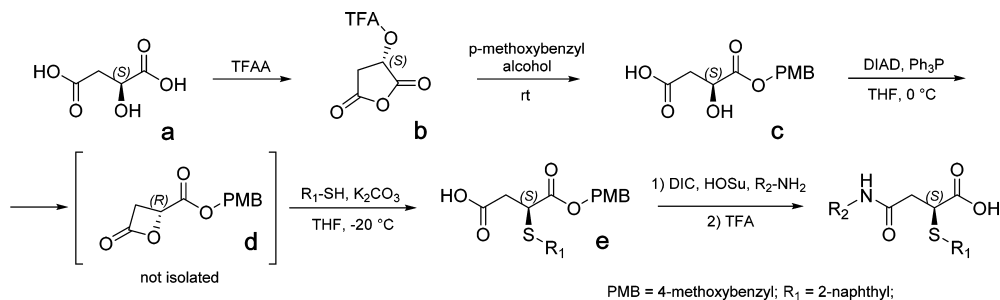


Figure 3. HPLC profiles of 33: (a) derived by Michael addition of 2-naphthalenethiol to maleyl-CPS1; (b) 33.2 prepared by coupling of (S)-2-(2-naphthylthio)succinic acid-1-(4-methoxybenzyl) ester to the CPS1-peptide (Scheme 2); and (c) mixed sample containing (a) and (b).

Table 3. Chemical Structures of Biotinylated Peptides 39 and 39.2

Structure	IC ₅₀ (nM)
	39 91.1 ± 14.1
	39.2 19.1 ± 14.1

with TFA led to a single diastereomer according to HPLC. Figure 3 shows the HPLC chromatogram of crude reaction product 33 using the Michael addition reaction. The two minor peaks are the two 2-substituted succinyl derivatives, and the two major peaks are the 3-substituted arylthiosuccinyl derivatives 33.1 and 33.2. The migration time of the reaction product derived from e shown in Scheme 2 is comparable to that of 33.2, enabling assignment of 33.2 to the (S)-3-(2-naphthylthio)succinyl derivative. Additionally, spiking the reaction mixture of the Michael reaction with the product of the stereocontrolled synthesis resulted in an increase of the area of the signal caused by 33.2 (see Figure 3c). Encouraged by the unique selectivity of the potent inhibition of Sirt5 by 33.2, we decided to develop an affinity probe for human Sirt5. Analysis of crystal structures of 15 and 2 in complex with zSirt5 (Figure 2) uncovered no interaction of the N-terminal benzoyl residue with the enzyme. Therefore, we replaced the benzoyl moiety in

33 by a spacer molecule and a biotinyl residue (compound 39), enabling immobilization on (strept)avidin-coated surfaces (Table 3). Mixture of 3-substituted diastereomers (compound 39) generated by Michael addition reaction yielded an inhibitor with a K_i value of 83.2 ± 15.4 nM, but stereoisomer 39.2, synthesized according to the method shown in Scheme 2, is a more effective Sirt5 inhibitor, with a K_i value of 13.6 ± 3.8 nM. The inhibition is in both cases competitive regarding the peptide substrate (Figure 4). To analyze our Sirt5 affinity probe in more detail, we used real-time, label-free surface plasmon resonance (SPR) measurements to investigate the interaction of surface-bound inhibitor and human Sirt5 (Figure 5). Biotinylated peptide derivative 39.2 was immobilized on a streptavidin-coated SPR sensorchip. Sirt5 binds to immobilized 39.2 in a dose-dependent manner (Figure 5a). Rate constants $k_{on} = (1.3 \pm 1.0) \times 10^{-6} \text{ M}^{-1} \text{ s}^{-1}$ and $k_{off} = (1.5 \pm 0.6) \times 10^{-4} \text{ M}^{-1} \text{ s}^{-1}$ result in a K_D value of about 0.12 nM. Binding was

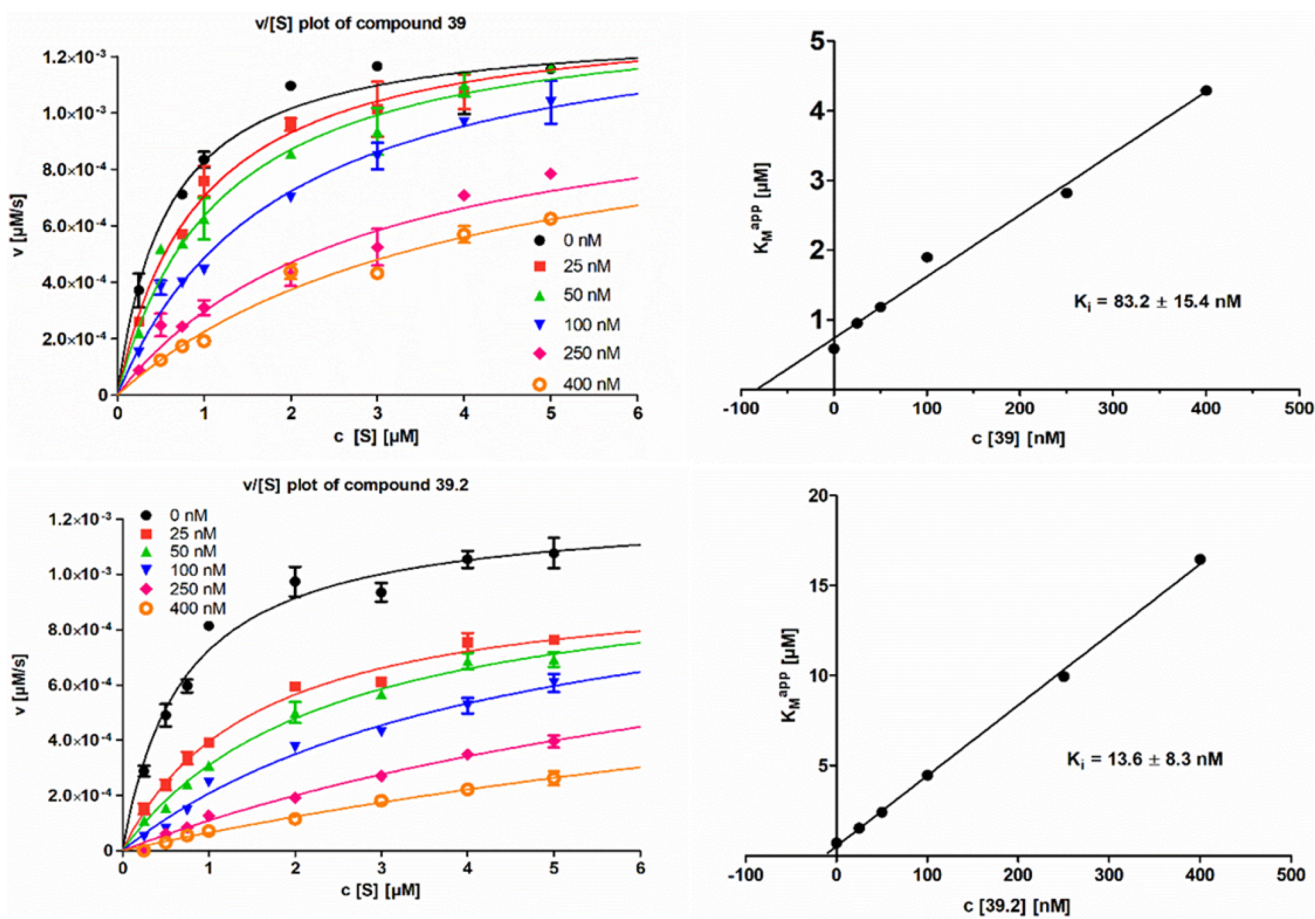


Figure 4. $v/[S]$ plots and fitting curves for compounds 39 and 39.2 generated using human Sirt5 in the presence of 500 μM NAD^+ cosubstrate.

linear up to 100 nM, representing the evaluation range for the rate constants ($R^2 = 0.9971$; Figure S22). This interaction seems to be very specific for Sirt5 because all other human sirtuin isoforms showed negligible K_D values (Figure 5b). The higher affinity of 39.2 for the active site of Sirt5 in the SPR experiment as compared to the kinetic measurements could be explained by the immobilization of the inhibitor leading to an avidity effect. However, in the presence of non-biotinylated inhibitor 33.2, Sirt5 was unable to bind to surface-bound 39.2 (Figure 5c), indicating the expected peptide–substrate competitive binding mode. Consistently, reduced but detectable binding was observed in the presence of 19.2, an inhibitor with a K_i value of 714 nM, or in the presence of succinylated CPS1-derived substrate peptide, demonstrating that surface-bound 39.2 competes with the substrate peptide. Analyzing interaction details of 33.2 with Sirt5 by solving a zSirt5/33.2 crystal structure (Figure 6, Figure S24, Table S2) revealed a surprising binding mode. Although it was based on *m*- and *p*-modified 2, the substituent of 33.2 occupies the C-pocket. Its bulky aromatic system fills much of the pocket yet remains flexible, as indicated by fragmented electron density and higher *B* factors. Further modifications that exploit polar groups, such as an addition at position 8 of the naphthyl moiety for beneficial interaction with Asp139 (Figure 2), might be a route for even further increased potency. Nevertheless, our data demonstrate that the combination of a succinyl scaffold for Sirt5 selectivity and a 3-(2-naphthyl)succinyl modification for potency yields compounds that bind Sirt5 tightly and specifically. We reversed the assembly by regioselective

immobilization of biotinylated Sirt5 to a streptavidin-coated sensorchip. Sirt5 was biotinylated at the N-terminus by the trypsiligase method.¹⁷ For that purpose, we elongated Sirt5 with *StrepII*-tagged Tyr-Arg-His tripeptide at the N-terminus. This introduces a recognition sequence for trypsiligase which cleaves the Tyr-Arg bond and transfers a biotinyl-Gly to the Arg residue, resulting in a Sirt5 variant with biotinyl-Gly-Arg-His at the N-terminus (Figure S19d). Biotinylated Sirt5 showed similar enzymatic activity compared to the enzyme without modification (Figure S20b). Treatment of the immobilized Sirt5 with 33.2 showed a very fast association and hardly detectable dissociation (Figure 5d), resulting in an estimated K_D value of about 10 pM. We were not able to remove bound inhibitor by extensive washing of the sensorchip (several days).

To test the suitability of 39.2 for pull-down experiments using more complex biological samples, we immobilized 39.2 on streptavidin-coated agarose beads and loaded the beads with *E. coli* BL21 (DE3) lysate expressing Sirt5. There was no Sirt5 detected in the flow-through using SDS-PAGE analysis. Extensive washings removed a lot of different proteins but not Sirt5 (Figure 7a). Virtually pure Sirt5 could be eluted using 200 mM sodium hydroxide. ESI-MS analysis of the elution fraction yielded a protein with a molecular mass of 30.798 Da (Figure 7b), which matches the calculated mass of 30.796 Da. Lysates of *E. coli* expressing either Sirt2 or Sirt3 were used for similar pull-down experiments. There was no capture of these two sirtuins by 39.2 detectable, as demonstrated by the empty elution fraction lanes (Figure S18a,b). Additionally, an equimolar mixture of Sirt2, Sirt3, and Sirt5 was applied to

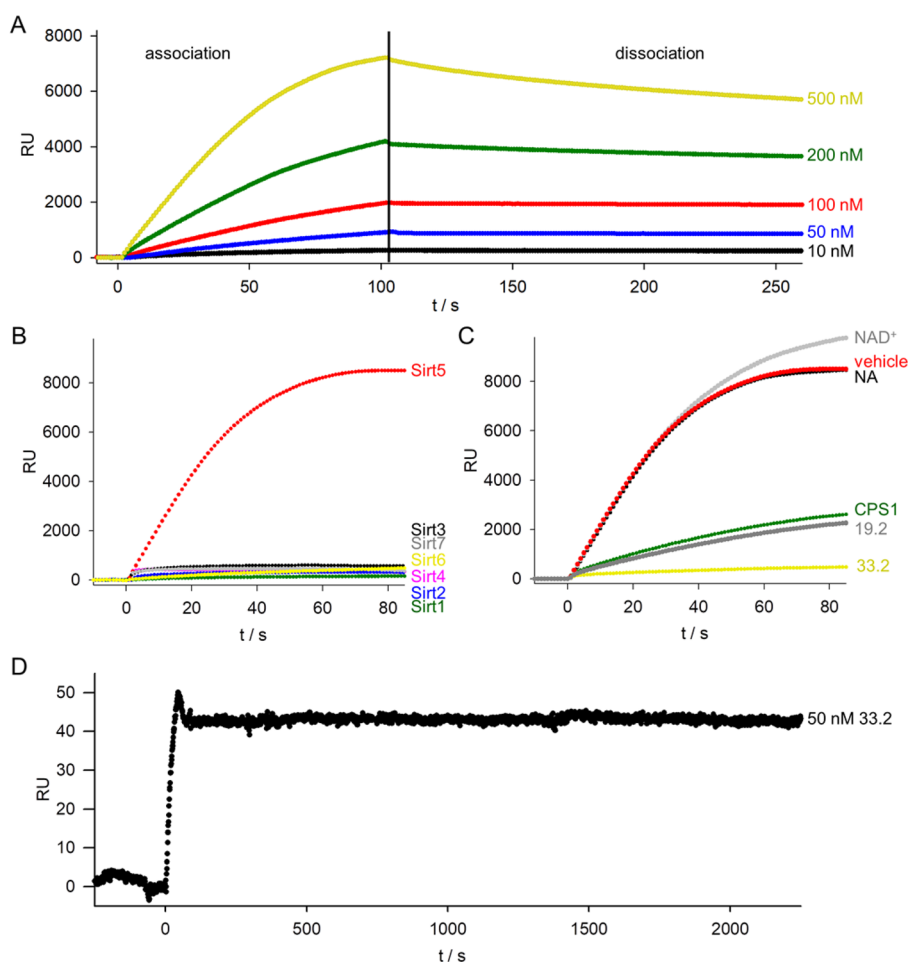


Figure 5. Biophysical characterization of compounds **33.2** and **39.2** by surface plasmon resonance spectroscopy. (a) SPR sensorgrams demonstrating binding of Sirt5 to immobilized **39.2**. (b) Association phase of sensorgrams representing binding of different sirtuin isoforms ($1 \mu\text{M}$) to immobilized **39.2**. (c) Association phase of SPR sensorgrams representing binding of Sirt5 to the immobilized inhibitor in the presence of CPS1-derived peptide substrate with succinyl residue on the lysine side chain ($2 \mu\text{M}$) or inhibitors **33.2** ($2 \mu\text{M}$) and **6.2** ($2 \mu\text{M}$); vehicle is PBS buffer. (d) Binding of compound **33.2** to immobilized, biotinylated Sirt5. Regioselective biotinylation of the N-terminus of Sirt5 was performed via trypsilgase reaction¹⁷ (Figure S20).

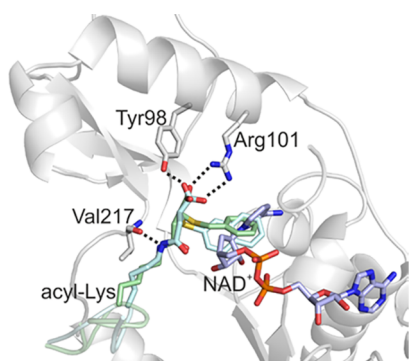


Figure 6. Comparison of the binding modes of **33.2** and **15** (in the Sirt5 active site). The zSirt5 complex with **33.2** (PDB ID 6FLG, cyan) was overlaid with the **15** complex (PDB ID 6FKY, ligand shown in green; one enantiomer omitted for clarity) and a Sirt5/NAD⁺ complex (PDB ID 4G1C) that indicates the C-pocket. NAD⁺ (light blue) was modeled from a Sirt5/peptide/NAD⁺ complex. The protein is only shown for zSirt5/**33.2**, and dotted lines indicate polar interactions to the acyl group.

the inhibitor matrix and analyzed via SDS-PAGE (Figure S18c). Sirt2 and Sirt3 were exclusively detected in the flow-through

and the wash fractions. Protein-containing elution fractions were analyzed using ESI-MS, and eluted protein was clearly identified as Sirt5 (Figure S18d).

CONCLUSIONS

For development of more drug-like Sirt5 inhibitors, we started to analyze the contribution of the peptide backbone to the affinity of (*S*)-3-(2-naphthylthio)succinyl derivatives. We shortened the peptide sequence to a tripeptide and generated **40.2** (see Table 4) using enantiomerically pure precursor **e**. This tripeptide binds 6-fold less strongly to Sirt5 as compared to **39.2**, but still with sub-micromolar inhibitory activity. Generation of an α -acetylated lysine amide, acylated with the (*S*)-3-(2-naphthylthio)succinyl moiety at the ϵ -amino group, resulted in **41**, showing a K_i value of $7 \mu\text{M}$, which is about 40-fold higher than the K_i value for **40.2**, yet close to those of the most potent Sirt5 selective inhibitors known so far. The peptide part of the peptidic inhibitors thus contributes to affinity and potency, but omitting these contributions from our inhibitors with optimized acyl moieties still allows for tight binding. Further shortening by formal removal of the acetylated glycine amide part of **41** yielded **42**, which binds about 20-fold less effectively to Sirt5 as compared to **41**. Replacement of the

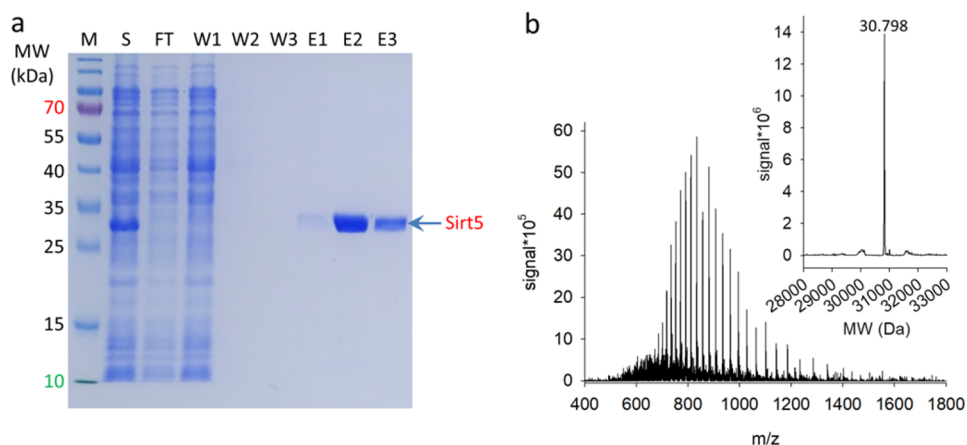


Figure 7. Immobilized **39.2** captures Sirt5 out of *E. coli* lysate. (a) SDS-PAGE analysis (Coomassie staining) of **39.2** bound to streptavidin-coated agarose interacting with *E. coli* BL21 (DE3) lysate expressing Sirt5. Exclusively Sirt5 was eluted from the matrix by addition of 200 mM NaOH. Abbreviations: S, supernatant after cell rupture; FT, flow-through; W, wash fractions; E, elution fractions. (b) ESI-MS analysis of the elution fraction E2; $M_{\text{calc}} = 30.796$ Da, $M_{\text{found}} = 30.798$ Da.

Table 4. Chemical Structures of Tripeptide and Small Molecules

Structure	IC ₅₀ (nM)
	40 1075.4 ± 117.7
	43 157200 ± 18900
	IV 25200 ± 2700
	40.2 350.4 ± 20.6
	44 90000 ± 12500
	VII 453400 ± 37600
	41 7400 ± 750
	45 124000 ± 17200
	42 154000 ± 19300
	46 72560 ± 9300

butylamide part in **42** by anilides (**43** and **44**) and benzamide (**45**) is well tolerated, resulting in similar IC₅₀ values, indicating potential for further improvement of this compound moiety through focused library screens or structure-based design. Replacement of the methyl group in **42** by a phenyl ring (**46**) already improves the IC₅₀ value more than 2-fold, and our

structural data provide a basis for further optimizing this compound part to obtain potencies comparable to that of **41** or even better without having the peptide backbone, which is unfavorable for drug applications. For comparison, we analyzed known small-molecule inhibitors **IV** and **VII** (Table 4) using similar assay conditions. In our hands these compounds

showed much weaker affinity to SIRT5 in comparison to published values.^{11,14} Collectively, these results show that the (S)-3-(2-naphthylthio)succinylamide scaffold represents a useful starting point for systematic development of small molecules that potently and selectively target Sirt5.

In this study we developed a peptide-based selective Sirt5 affinity probe by optimizing the acyl moiety in a systematic manner. Probe design was guided by analysis of a known crystal structure of Sirt5 in complex with 47 and crystal structures solved in this study. The developed affinity probe 39.2 is able to bind to Sirt5 in different matrixes and environments, accompanied by excellent selectivity and inhibitory activity. The high potency is caused by slow dissociation rate and fast association of the inhibitor–enzyme complex, making this probe to a multifunctional tool for investigation of Sirt5 biology at a new level.

EXPERIMENTAL SECTION

Chemicals and General Methods. Solutions of 0.1% trifluoroacetic acid (TFA) in H₂O (solvent A) and 0.1% TFA in acetonitrile (solvent B) were used as mobile phase for HPLC measurements. For sample analysis, an Agilent 1100 HPLC with a quaternary pump, a well-plate autosampler, and a variable-wavelength detector was used. Separations were performed on a Phenomenex Kinetex XB C-18 column (2.6 μ m, 3.0 \times 50 mm) with a linear gradient from 25 to 55% solvent B in 4 min at a flow rate of 0.6 mL min⁻¹. The compounds were detected at 260 nm. A Shimadzu LC system with a Phenomenex Kinetex 5 μ m XB-C18 column (250 \times 21.1 mm, 100 Å) was used for purification of peptides. The preparative separations were performed with a linear gradient from 25 to 90% solvent B in 80 min at a flow rate of 15 mL min⁻¹. The eluting compounds were detected at 220 and 260 nm. UPLC-MS analysis was performed using a Waters Acquity UPLC-MS system (Milford, USA) with a Waters Acquity UPLC-MS-BEH C18 column (1.7 μ m, 2.1 \times 50 mm; 30 Å). Data analysis was performed using Waters MassLynx software. NMR spectroscopy was carried out using a Varian Gemini 2000 spectrometer and deuterated chloroform or deuterated dimethyl sulfoxide (DMSO). All chemicals were purchased from Sigma-Aldrich if not stated otherwise.

Solid-Phase Peptide Synthesis. The peptide derivatives Bz-GVLK(Ns)EYGV-NH₂ and Ac-LK(Ns)A-NH₂ were synthesized on an MBHA Rink amide resin with a loading density of 0.59 mmol/g (IRIS Biotech), using standard Fmoc-based solid-phase peptide synthesis. At first the resin was treated with DMF for 20 min. Next, 4 equiv of Fmoc-protected amino acid derivatives (Anaspec) was activated with 4 equiv of HBTU and 8 equiv of DIPEA in DMF and was coupled for at least 1 h. Afterward the Fmoc deprotection was performed two times for 10 min with 20% piperidine in DMF followed by washing with DMF for 5 min, five times. Finally, the amino group of glycine was modified with 4 equiv of benzoic acid and 8 equiv of DIPEA in DMF or 4 equiv of acetic anhydride and 8 equiv of DIPEA in DMF for 30 min. The lysine to be modified was used as the ϵ -nosyl (Ns, 2-nitrobenzenesulfonyl)-protected derivative, allowing a selective on-resin modification of the lysine side chain. This derivative, Fmoc-Lys(Ns)-OH, was prepared as described elsewhere.²⁰ The nosyl protecting group was removed by using 5 equiv of thiophenol and 5 equiv of DBU in DMF for 90 min, two times. The free lysine side chain was modified with 4 equiv of maleic anhydride and 8 equiv of DIPEA in DMF for 4 h, followed by washing with DMF. Afterward a Michael addition reaction was performed with 4 equiv of mercapto derivative (2–13, 15–35, 39, 40) and 8 equiv DIPEA in DMF overnight. After sequential washing with DMF, DCM, methanol, and again with DCM for 4 min, five times, each peptide was cleaved from the resin using TFA–water solution (95:5 v/v) for 1 h, two times. The TFA was evaporated, and the peptide was dissolved in acetic acid. After purification by reversed-phase HPLC, collected fractions were analyzed with HPLC-MS and checked for purity. The purity was above 95% for all peptides (Figure S26–S105). The fractions containing target peptide were lyophilized.

(S)-2-Hydroxysuccinic Acid 1-(4-Methoxybenzyl) Ester (c). First, 3.2 g (15 mmol, 1 equiv) of (S)-2-trifluoroacetoxysuccinic anhydride (b), prepared from (S)-malic acid using a known method,¹⁸ was mixed with 9.3 mL (75 mmol, 5 equiv) of 4-methoxybenzyl alcohol, and the reaction mixture was stirred overnight. The resulting oil was dissolved in 50 mL of ethyl acetate (EtOAc) and extracted several times with saturated NaHCO₃ solution. The combined aqueous phases were washed with EtOAc and acidified with diluted HCl solution. The mixture was extracted with DCM, and the organic phase was washed with water, dried over Na₂SO₄, and evaporated, affording 3.16 g of crude ester. Recrystallization from 14 mL of EtOAc–petroleum ether mixture (1:1) yielded 2.2 g of pure compound.

¹H NMR (300 MHz, DMSO-*d*₆): δ 7.29 (d, *J* = 8.7 Hz, 2H), 6.91 (d, *J* = 8.7 Hz, 2H), 5.03 (s, 2H), 4.34 (dd, *J* = 7.5, 5.1 Hz, 1H), 3.73 (s, 3H), 2.61 (dd, *J* = 15.8, 5.1 Hz, 1H), 2.52–2.40 (m, 1H).

(S)-2-(2-Naphthylthio)succinic Acid 1-(4-Methoxybenzyl) Ester (e). First, 508.5 mg (2 mmol) of 1-(4-methoxybenzyl) malate and 525 mg (2 mmol) of Ph₃P were dissolved in 9 mL of dry tetrahydrofuran (THF), and the flask was cooled with an ice–water bath. To this mixture was added 393 μ L (404 mg, 2 mmol) of diisopropyl azodicarboxylate in 2 mL of THF dropwise over 5 min. The reaction mixture was stirred overnight at room temperature. The next day the yellow solution was cooled to –15 $^{\circ}$ C with an ice–salt mixture, and 320 mg of crystalline 2-naphthalenethiol (2 mmol) was added, followed by 276 mg (2 mmol) of solid K₂CO₃. After 20 min the cooling bath was removed, and the mixture was stirred at room temperature for 1 h. The product was isolated with acid–base extraction as described in the previous procedure, to yield 0.53 g of crude product, which contains around 25% of starting material. Recrystallization from methanol can be used for further purification.

¹H NMR (300 MHz, DMSO-*d*₆): δ 7.98–7.78 (m, 4H), 7.59–7.43 (m, 3H), 7.06 (d, *J* = 8.7 Hz, 2H), 6.75 (d, *J* = 8.7 Hz, 2H), 4.96 (dd, *J* = 28.2, 12.1 Hz, 2H), 4.15 (dd, *J* = 8.6, 6.6 Hz, 1H), 3.70 (s, 3H), 2.77 (dd, *J* = 7.6, 2.0 Hz, 2H).

General Procedure for the Synthesis of Maleamic Acid Derivatives 41–46. To the solution containing 20 mg (0.05 mmol) of (S)-2-(2-naphthylthio)succinic acid 1-(4-methoxybenzyl) ester and 7 mg (0.06 mmol) of *N*-hydroxysuccinimide (HOSu) in 500 μ L of dry THF was added 9 μ L (0.06 mmol) of *N,N'*-diisopropylcarbodiimide. After 30 min, 2 equiv (0.1 mmol) of the appropriate amino derivative was added. The progress of the reaction was monitored by TLC or HPLC. In the case of aromatic amines, longer reaction times and addition of 2 equiv of triethylamine were necessary to achieve satisfactory yields. After completion of the reaction, THF was evaporated, and the residue was redissolved in 500 μ L of TFA–water (95:5 v/v) solution and left for 30 min. The reaction solution was then concentrated *in vacuo*, and the residue was purified by RP-HPLC. The fractions containing target product were lyophilized, affording pure compound.

Synthesis of 2-Methyl-2-(2-naphthylthio)succinic Anhydride. This compound was prepared according to the method described for preparation of 2-methyl-2-(4-chlorophenylthio)succinic anhydride.¹⁹ Briefly, 1.12 g (10 mmol) of citraconic anhydride and 1.6 g (10 mmol) of 2-naphthalenethiol were mixed with 1 mL of toluene, and 4 μ L of triethylamine was added. The mixture was stirred and heated at 70–80 $^{\circ}$ C for 1 h. Volatiles were removed *in vacuo*, and the residue was purified by flash chromatography. Additional recrystallization from petroleum ether–EtOAc (3:1 v/v) solution gave pure material.

¹H NMR (700 MHz, CDCl₃): 8.08 (d, *J* = 1.9 Hz, 1H), 7.88–7.82 (m, 3H), 7.59–7.51 (m, 3H), 3.14 (d, *J* = 18.8 Hz, 1H), 3.07 (d, *J* = 18.8 Hz, 1H), 1.70 (s, 3H).

Fluorescence Inhibition Assay. The inhibitory activity of all compounds was measured in black low-binding 96-well microtiter plates, and each well contained 0.025–5 μ M substrate Abz-GVLK(glutaryl)AY(NO₂)GV-NH₂, 500 μ M NAD⁺, 500 nM trypsin, 10 nM SIRT5, 5% DMSO, and 0.01–20 μ M inhibitor (compounds 1–46) in assay buffer. The assay buffer contained 20 mM Tris, 150 mM NaCl, and 5 mM MgCl₂ at pH 7.8. The reaction mixture without enzymes was incubated for 5 min at 37 $^{\circ}$ C, followed by pipetting

trypsin and further incubation for 5 min at 37 °C. After addition of SIRT5, the measurements started, and the fluorescence was measured at an excitation wavelength of 320 nm and emission wavelength of 420 nm. The measurements were carried out in a plate reader (TECAN) and in a double determination.²⁰ IC₅₀ values were obtained with 0.03 μM substrate, and the resulting data were fitted by log(inhibitor) vs normalized response equation:

$$Y = \frac{100}{(1 + 10^{(X - \log IC_{50})})} \quad (1)$$

HPLC Assay. Reaction mixtures contained 0 μM or 50 μM inhibitor, 500 μM NAD⁺, 5% DMSO, 0.1 μM SIRT1, 2, 3, 5, or 6, and 50 μM Bz-GVLK(acetyl)EYGV-NH₂ for SIRT1–3, Bz-GVLK(succinyl)EYGV-NH₂ for SIRT5, and Ac-EALPKK(myristoyl)TGG-NH₂ for SIRT6 in assay buffer. The reactions were performed at 37 °C for 6 min (SIRT6), 8 min (SIRT1–3), or 10 min (SIRT5). After these time points, reaction was stopped with TFA–water solution (1:9 v/v), and samples were analyzed by HPLC. The stability of compounds 1–46 was determined by incubating 50 μM inhibitor in assay buffer at 37 °C for 24 h and measuring by HPLC. All measurements were carried out in duplicate.

Cloning, Expression, and Purification of Recombinant Proteins. Human Sirt5 was cloned with N-terminal StrepII-tag into pET-21a(+) vector. Sirt2_{43–356} and Sirt3_{114–380} were cloned with N-terminal StrepII-tag into pET-28a(+)-vector. All proteins were expressed using *E. coli* BL21 (DE3) in LB media supplemented with ampicillin or kanamycin, respectively. Overexpression was induced by the addition of IPTG (1 mM final concentration) at an OD₆₀₀ of 0.6. Cells were harvested, resuspended in lysis buffer (100 mM Tris-HCl, 250 mM NaCl, 10 mM DTT, 1 mM EDTA, pH 8.0), and lysed by sonification. Supernatant after centrifugation was loaded onto a StrepTrap column (GE Healthcare, Uppsala, Sweden). The loaded column was intensively washed before elution with 5 mM desthiobiotin in 100 mM Tris, 250 mM NaCl, pH 8.0. Sirt5-containing fractions were concentrated and further purified using a Superdex 75 5/150 gel filtration column (GE Healthcare). Expression of Sirt4 was performed using the IMPACT system (NEB, Frankfurt am Main, Germany). The corresponding gene was cloned into pTWIN2 via *SapI/PstI* and transformed in *E. coli* ER2566 (NEB). Overexpression was induced by the addition of IPTG (0.5 mM final concentration) at an OD₆₀₀ of 0.6 at 16 °C for 12 h. Chitin binding-domain-mediated affinity chromatography was performed as described in the supplier's manual. Enzymatic activity of the expressed Sirtuin isoforms was determined as described previously.¹⁷ Biotinylation of Sirt5 was conducted via trypsinoligase using biotinyl-4-guanidino-phenyl ester as described previously.¹⁷

Real-Time Biomolecular Interaction Analysis. Surface plasmon resonance spectroscopy was performed on a BIAcore X instrument (BIAcore, Uppsala, Sweden). Biotinylated inhibitor 39.2 (100 μM in PBS) was immobilized on an SAHC 200 M sensorchip (Xantec, Düsseldorf, Germany). Sirt5 was injected in a dilution series using PBS (4 mM KH₂PO₄, 16 mM Na₂HPO₄, 115 mM NaCl, pH 7.4) as running buffer. Vice versa, N-terminal biotinylated Sirt5 was immobilized on a second streptavidin-coated sensorchip, resulting in a surface density of approximately 1800 response units (RU), and 50 nM 39.2 in PBS was injected. Each complex formation was observed at a continuous flow rate of 30 μL/min. Kinetic parameters were determined by fitting the data to the 1:1 Langmuir binding model with the BIAevaluation software (BIAcore). After each measurement the inhibitor matrix was regenerated by injection of 100 μL of NaOH (200 mM).

Affinity Pull-Down Experiments. A 0.5 mL bed-volume of streptavidin-conjugated agarose (Sigma-Aldrich, Munich, Germany) was applied to a gravity column and equilibrated with 5 CV PBS. Agarose beads were loaded with the biotinylated inhibitor 39.2 (100 μM in PBS). After 30 min incubation, agarose was washed with 10 CV PBST (4 mM KH₂PO₄, 16 mM Na₂HPO₄, 115 mM NaCl, 0.05% Tween, pH 7.4). As protein samples, pellets of 20 mL induced *E. coli* BL21 (DE3) cells expressing the respective Sirt isoform were

resuspended in 100 mM Tris, 250 mM NaCl, 1 mM EDTA, 10 mM DTT, pH 8.0, and lysed by sonification. After removal of cell debris, supernatant was applied to the inhibitor matrix. Conjugated agarose beads were washed three times with 3 CV PBST. Bound protein was eluted by the addition of 200 mM NaOH. Elution fractions were analyzed by SDS-PAGE and LC-MS.

Crystal Structure Analyses. zSirt5 protein was purified by Co-Talon affinity chromatography, TEV proteolysis, reverse affinity chromatography, and gel filtration as reported, with the modification that 0.5 mM TCEP was added to the gel filtration buffer. For crystallization, zSirt5 (10 mg/mL) was mixed with 1 mM inhibitory peptide (20 mM stock in DMSO) and incubated on ice for 30 min. Complexes were crystallized in 2 μL sitting-drop vapor diffusion experiments at 20 °C using 0.1 M HEPES, pH 7.5, 20% PEG3350 as reservoir solution. After 2–4 days, crystals were transferred to a cryo-protection solution composed of reservoir and ligand supplemented with 25% glycerol. Crystals were shock-frozen and diffraction data collected at 100 K at BESSY II beamline MX14.1 (operated by the Helmholtz-Zentrum, Berlin, Germany) with a Pilatus 6 M detector (Dectris, Baden, Switzerland). Indexing, scaling, and merging were done in XDS,²¹ and structures were solved by molecular replacement with search model PDB 4UTV (zSirt5/47). Refinement was done with Refmac5,²² and manual modeling as well as structure validation were done with Coot.²³ Geometry parameters for the modified lysines were generated using PRODRG.²⁴

Computational Methods. The molecular structures of all peptides described in the present work were generated using the MOE 2014.09 program.²⁵ The initial conformations resulted from energy minimization using the Amber12:EHT force field as implemented in MOE. The crystal structure of zSirt5 in complex with peptides 2.2 and 15.2 were considered for the flexible docking study. For the subsequent docking studies, all water and ligand molecules were removed, and the structure was protonated and minimized using the Amber12:EHT force field.

All docking studies were carried out using the GOLD5.2 docking program (Cambridge Crystallographic Data Centre, Cambridge, UK) in exhaustive sampling mode.²⁶ The binding cavity was defined by the cocrystallized peptide. To guide the search process, the position of the cocrystallized succinyl-lysine of the peptides was used as a scaffold constraint. Using Goldscore as fitness function, the cocrystallized peptide was correctly docked into the zSirt5 catalytic site, with RMSD values of 1.25 Å (2.2) and 1.41 Å (15.2).

All tested peptides were docked in both crystal structures, and 100 docking poses were stored. The resulting poses were rescored using the Amber12:EHT force field and the MM-GB/SA approach. Partial charges were fixed using the MOE Protonate3D tool according to the used force field, followed by a short minimization. An in-house script for rescoring the zSirt5–ligand complexes and calculating the binding free energies was applied for the docking poses of ligands. During complex minimization, heavy atoms of protein were tethered with a deviation of 0.5 Å (force constant (3/2)kT/(0.5)²). Complexes that showed the most favorable MM-GB/SA energy were selected and visually analyzed using the MOE program.

■ ASSOCIATED CONTENT

Supporting Information

The Supporting Information is available free of charge on the ACS Publications website at DOI: 10.1021/acs.jmedchem.7b01648.

Detailed description of peptide synthesis including LC-MS runs for each derivative and NMR data for selected compounds, results of kinetic measurements, experimental details of crystallization, and SPR experiments, including Tables S1 and S2 and Figures S1–S108 (PDF)

Molecular formula strings (CSV)

AUTHOR INFORMATION

Corresponding Author

*E-mail: mike.schutkowski@biochemtech.uni-halle.de.

ORCID

Wolfgang Sippl: 0000-0002-5985-9261

Mike Schutkowski: 0000-0003-0919-7076

Author Contributions

[†]D.K., S.L., and T.N. contributed equally.

Notes

The authors declare no competing financial interest.

ACKNOWLEDGMENTS

We thank Oberfrankenstiftung (grant 04115 to C.S.) for financial support. Prof. Thomas Kieffhaber is gratefully acknowledged for providing access to HPLC-MS-equipment, Marvin Neuholz for the determination of IC₅₀ value of **1**, and Helga Ungar for technical assistance during determination of IC₅₀ values. We thank BESSY (operated by HZI Berlin, Germany) for synchrotron beamtime and experimental support.

ABBREVIATIONS USED

CPS1, carbamoyl phosphate synthetase 1; DIAD, diisopropyl azodicarboxylate; DIC, diisopropylcarbodiimide; DIPEA, diisopropylethylamine; EtOAc, ethyl acetate; HBTU, (2-(1H-benzotriazol-1-yl)-1,1,3,3-tetramethyluronium hexafluorophosphate; HOSu, N-hydroxysuccinimide; Ph₃P, triphenylphosphine; MBHA, 4-methylbenzhydrylamine; ϵ -nosyl, 2-nitrobenzenesulfonyl; Sirt, Sirtuin; TCEP, tris(2-carboxyethyl)phosphine; TEV, tobacco etch virus

REFERENCES

- (1) (a) Feldman, J. L.; Baeza, J.; Denu, J. M. Activation of the protein deacetylase SIRT6 by long-chain fatty acids and widespread deacetylation by mammalian sirtuins. *J. Biol. Chem.* **2013**, *288* (43), 31350–31356. (b) Feldman, J. L.; Dittenhafer-Reed, K. E.; Kudo, N.; Thelen, J. N.; Ito, A.; Yoshida, M.; Denu, J. M. Kinetic and structural basis for acyl-group selectivity and NAD(+) dependence in sirtuin-catalyzed deacetylation. *Biochemistry* **2015**, *54* (19), 3037–3050.
- (2) Bao, X.; Wang, Y.; Li, X.; Li, X. M.; Liu, Z.; Yang, T.; Wong, C. F.; Zhang, J.; Hao, Q.; Li, X. D. Identification of ‘erasers’ for lysine crotonylated histone marks using a chemical proteomics approach. *eLife* **2014**, *3*, e02999.
- (3) (a) Anderson, K. A.; Huynh, F. K.; Fisher-Wellman, K.; Stuart, J. D.; Peterson, B. S.; Douros, J. D.; Wagner, G. R.; Thompson, J. W.; Madsen, A. S.; Green, M. F.; Sivley, R. M.; Ilkayeva, O. R.; Stevens, R. D.; Backos, D. S.; Capra, J. A.; Olsen, C. A.; Campbell, J. E.; Muoio, D. M.; Grimsrud, P. A.; Hirschey, M. D. SIRT4 Is a lysine deacetylase that controls leucine metabolism and insulin secretion. *Cell Metab.* **2017**, *25* (4), 838–855. (b) Mathias, R. A.; Greco, T. M.; Oberstein, A.; Budayeva, H. G.; Chakrabarti, R.; Rowland, E. A.; Kang, Y.; Shenk, T.; Cristea, I. M. Sirtuin 4 is a lipamidase regulating pyruvate dehydrogenase complex activity. *Cell* **2014**, *159* (7), 1615–1625. (c) Pannek, M.; Simic, Z.; Fuszard, M.; Meleshin, M.; Rotili, D.; Mai, A.; Schutkowski, M.; Steegborn, C. Crystal structures of the mitochondrial deacetylase Sirtuin 4 reveal isoform-specific acyl recognition and regulation features. *Nat. Commun.* **2017**, *8* (1), 1513.
- (4) (a) Du, J.; Zhou, Y.; Su, X.; Yu, J. J.; Khan, S.; Jiang, H.; Kim, J.; Woo, J.; Kim, J. H.; Choi, B. H.; He, B.; Chen, W.; Zhang, S.; Cerione, R. A.; Auwerx, J.; Hao, Q.; Lin, H. Sirt5 is a NAD-dependent protein lysine demalonylase and desuccinylase. *Science* **2011**, *334* (6057), 806–809. (b) Tan, M.; Peng, C.; Anderson, K. A.; Chhoy, P.; Xie, Z.; Dai, L.; Park, J.; Chen, Y.; Huang, H.; Zhang, Y.; Ro, J.; Wagner, G. R.; Green, M. F.; Madsen, A. S.; Schmiesing, J.; Peterson, B. S.; Xu, G.;

Ilkayeva, O. R.; Muehlbauer, M. J.; Braulke, T.; Muhlhausen, C.; Backos, D. S.; Olsen, C. A.; McGuire, P. J.; Pletcher, S. D.; Lombard, D. B.; Hirschey, M. D.; Zhao, Y. Lysine glutarylation is a protein posttranslational modification regulated by SIRT5. *Cell Metab.* **2014**, *19* (4), 605–617. (c) Roessler, C.; Nowak, T.; Pannek, M.; Gertz, M.; Nguyen, G. T.; Scharfe, M.; Born, I.; Sippl, W.; Steegborn, C.; Schutkowski, M. Chemical probing of the human sirtuin 5 active site reveals its substrate acyl specificity and peptide-based inhibitors. *Angew. Chem., Int. Ed.* **2014**, *53* (40), 10728–10732.

(5) (a) Nishida, Y.; Rardin, M. J.; Carrico, C.; He, W.; Sahu, A. K.; Gut, P.; Najjar, R.; Fitch, M.; Hellerstein, M.; Gibson, B. W.; Verdin, E. SIRT5 Regulates both cytosolic and mitochondrial protein malonylation with glycolysis as a major target. *Mol. Cell* **2015**, *59* (2), 321–332. (b) Lin, Z. F.; Xu, H. B.; Wang, J. Y.; Lin, Q.; Ruan, Z.; Liu, F. B.; Jin, W.; Huang, H. H.; Chen, X. SIRT5 desuccinylates and activates SOD1 to eliminate ROS. *Biochem. Biophys. Res. Commun.* **2013**, *441* (1), 191–195.

(6) (a) Xiangyun, Y.; Xiaomin, N.; Linping, G.; Yunhua, X.; Ziming, L.; Yongfeng, Y.; Zhiwei, C.; Shun, L. Desuccinylation of pyruvate kinase M2 by SIRT5 contributes to antioxidant response and tumor growth. *Oncotarget* **2017**, *8* (4), 6984–6993. (b) Lutz, M. L.; Milenkovic, I.; Regelsberger, G.; Kovacs, G. G. Distinct patterns of sirtuin expression during progression of Alzheimer’s disease. *NeuroMol. Med.* **2014**, *16* (2), 405–414. (c) Liu, L.; Peritore, C.; Ginsberg, J.; Shih, J.; Arun, S.; Donmez, G. Protective role of SIRT5 against motor deficit and dopaminergic degeneration in MPTP-induced mice model of Parkinson’s disease. *Behav. Brain Res.* **2015**, *281*, 215–221.

(7) Wang, F.; Wang, K.; Xu, W.; Zhao, S.; Ye, D.; Wang, Y.; Xu, Y.; Zhou, L.; Chu, Y.; Zhang, C.; Qin, X.; Yang, P.; Yu, H. SIRT5 Desuccinylates and activates pyruvate kinase M2 to block macrophage IL-1 β production and to prevent DSS-induced colitis in mice. *Cell Rep.* **2017**, *19* (11), 2331–2344.

(8) Lu, W.; Zuo, Y.; Feng, Y.; Zhang, M. SIRT5 facilitates cancer cell growth and drug resistance in non-small cell lung cancer. *Tumor Biol.* **2014**, *35* (11), 10699–10705.

(9) He, B.; Du, J.; Lin, H. Thiosuccinyl peptides as Sirt5-specific inhibitors. *J. Am. Chem. Soc.* **2012**, *134* (4), 1922–1925.

(10) Suenkel, B.; Fischer, F.; Steegborn, C. Inhibition of the human deacetylase Sirtuin 5 by the indole GWS074. *Bioorg. Med. Chem. Lett.* **2013**, *23* (1), 143–146.

(11) Maurer, B.; Rumpf, T.; Scharfe, M.; Stofa, D. A.; Schmitt, M. L.; He, W.; Verdin, E.; Sippl, W.; Jung, M. Inhibitors of the NAD(+)-dependent protein desuccinylase and demalonylase Sirt5. *ACS Med. Chem. Lett.* **2012**, *3* (12), 1050–1053.

(12) Liu, J.; Huang, Y.; Zheng, W. A selective cyclic peptidic human SIRT5 inhibitor. *Molecules* **2016**, *21* (9), 1217–1229.

(13) Liu, S.; Ji, S.; Yu, Z. J.; Wang, H. L.; Cheng, X.; Li, W. J.; Jing, L.; Yu, Y.; Chen, Q.; Yang, L. L.; Li, G. B.; Wu, Y. Structure-based discovery of new selective small-molecule sirtuin 5 inhibitors. *Chem. Biol. Drug Des.* **2018**, *91* (1), 257–268.

(14) Guetschow, E. D.; Kumar, S.; Lombard, D. B.; Kennedy, R. T. Identification of sirtuin 5 inhibitors by ultrafast microchip electrophoresis using nanoliter volume samples. *Anal. Bioanal. Chem.* **2016**, *408* (3), 721–731.

(15) Augustin, M.; Mueller, W. Umsetzung von N-Maleyl-amino-säuren mit Nucleophilen. *Z. Chem.* **1985**, *25* (2), 61–62.

(16) Miller, M. J.; Bajwa, J. S.; Mattingly, P. G.; Peterson, K. Enantioselective syntheses of 3-substituted 4-(alkoxycarbonyl)-2-azetidinones from malic acid. *J. Org. Chem.* **1982**, *47* (25), 4928–4933.

(17) Liebscher, S.; Schopf, M.; Aumuller, T.; Sharkhuukhen, A.; Pech, A.; Hoss, E.; Parthier, C.; Jahreis, G.; Stubbs, M. T.; Bordusa, F. N-terminal protein modification by substrate-activated reverse proteolysis. *Angew. Chem., Int. Ed.* **2014**, *53* (11), 3024–3028.

(18) Miller, M. J.; Bajwa, J. S.; Mattingly, P. G.; Peterson, K. Base-catalyzed addition of thiols to α/β -unsaturated anhydrides. *J. Org. Chem.* **1982**, *47* (25), 4928–4933.

(19) Zienty, F. B.; Vineyard, B. D.; Schlepplnik, A. A. Base-catalyzed addition of thiols to α/β -unsaturated anhydrides. *J. Org. Chem.* **1962**, *27* (9), 3140–3146.

(20) Schuster, S.; Roessler, C.; Meleshin, M.; Zimmermann, P.; Simic, Z.; Kambach, C.; Schiene-Fischer, C.; Steegborn, C.; Hottiger, M. O.; Schutkowski, M. A continuous sirtuin activity assay without any coupling to enzymatic or chemical reactions. *Sci. Rep.* **2016**, *6*, 22643–33655.

(21) Kabsch, W. XDS. *Acta Crystallogr., Sect. D: Biol. Crystallogr.* **2010**, *66*, 125–132.

(22) Vagin, A. A.; Steiner, R. S.; Lebedev, A. A.; Potterton, L.; McNicholas, S.; Long, F.; Murshudov, G. N. REFMAC5 dictionary: organisation of prior chemical knowledge and guidelines for its use. *Acta Crystallogr., Sect. D: Biol. Crystallogr.* **2004**, *60*, 2284–2295.

(23) Emsley, P.; Lohkamp, B.; Scott, W. G.; Cowtan, K. Features and development of Coot. *Acta Crystallogr., Sect. D: Biol. Crystallogr.* **2010**, *66*, 486–501.

(24) Schüttelkopf, A. W.; van Aalten, D. M. F. PRODRG: a tool for high-throughput crystallography of protein-ligand complexes. *Acta Crystallogr., Sect. D: Biol. Crystallogr.* **2004**, *60*, 1355–1363.

(25) Chemical Computing Group. *Molecular Operating Environment (MOE)*, 2014.09; Chemical Computing Group Inc.: Montreal, Canada, 2014.

(26) Jones, G.; Willett, P.; Glen, R. C.; Leach, A. R.; Taylor, R. J. *Mol. Biol.* **1997**, *267*, 727–748.

4.4. Manuscript 4: Identification of Bichalcones as Sirtuin Inhibitors by Virtual Screening and *In Vitro* Testing.

B., Karaman, **Z., Alhalabi**, S., Swyter, S., Mihigo, K., Marobela, M., Jung, W., Sippl and F., Ntie-Kang.
Molecules. 23 (2018).

Article

Identification of Bichalcones as Sirtuin Inhibitors by Virtual Screening and In Vitro Testing

Berin Karaman ^{1,2,†}, Zayan Alhalabi ^{1,†} , Sören Swyter ³, Shetonde O. Mihigo ⁴,
Kerstin Andrae-Marobela ⁵, Manfred Jung ³ , Wolfgang Sippl ¹  and Fidele Ntie-Kang ^{1,6,*} 

¹ Department of Pharmaceutical Chemistry, Martin-Luther University of Halle-Wittenberg, Wolfgang-Langenbeck-Str. 4, 06120 Halle (Saale), Germany; karaman.berin@gmail.com (B.K.); zayan82at@hotmail.com (Z.A.); wolfgang.sippl@pharmazie.uni-halle.de (W.S.)

² Department of Pharmaceutical Chemistry, Faculty of Pharmacy, Biruni University, Istanbul 34010, Turkey

³ Institute of Pharmaceutical Sciences, Albert-Ludwigs-University of Freiburg, Albertstr. 25, 79104 Freiburg im Breisgau, Germany; soeren.swyter@pharmazie.uni-freiburg.de (S.S.); manfred.jung@pharmazie.uni-freiburg.de (M.J.)

⁴ Department of Chemistry, University of Kinshasa, Kinshasa P.O. Box 190 XI, Congo; smihigo@yahoo.com

⁵ Department of Biological Sciences, Faculty of Science, University of Botswana, Block 235, Private Bag, Gaborone 0022, Botswana; k_marobela@yahoo.com

⁶ Department of Chemistry, University of Buea, P.O. Box 63, Buea 00237, Cameroon

* Correspondence: ntiékfidele@gmail.com; Tel.: +237-685-625-811

† These authors contributed equally to this work.

Received: 23 January 2018; Accepted: 10 February 2018; Published: 14 February 2018

Abstract: Sirtuins are nicotinamide adenine dinucleotide (NAD⁺)-dependent class III histone deacetylases, which have been linked to the pathogenesis of numerous diseases, including HIV, metabolic disorders, neurodegeneration and cancer. Docking of the virtual pan-African natural products library (p-ANAPL), followed by in vitro testing, resulted in the identification of two inhibitors of sirtuin 1, 2 and 3 (sirt1–3). Two bichalcones, known as rhuschalcone IV (**8**) and an analogue of rhuschalcone I (**9**), previously isolated from the medicinal plant *Rhus pyroides*, were shown to be active in the in vitro assay. The rhuschalcone I analogue (**9**) showed the best activity against sirt1, with an IC₅₀ value of 40.8 μM. Based on the docking experiments, suggestions for improving the biological activities of the newly identified hit compounds have been provided.

Keywords: bichalcones; sirtuin inhibitors; virtual screening

1. Introduction

In the last few decades, natural products (NPs) or natural product derivatives have spurred great interest as re-fashionable sources for developing therapeutic agents against human diseases [1,2]. However, the isolation of NPs, the synthesis of their analogues and manufacturing them in larger quantities are major challenges that pharmaceutical companies face today [1–3]. Moreover, evaluating the potential of NPs using high throughput screening (HTS) techniques remains problematic [1,4]. Although, combinatorial chemistry is still used to generate large compound libraries for HTS campaigns, a detailed analysis of approved drugs from 1981 to 2014 showed that only two combinatorial chemistry-derived drugs were approved; sorafenib, approved by the Food and Drug Administration (FDA) in 2005 and ataluren, approved by the European Medicines Agency (EMA) in 2014 [5]. Moreover, it was observed that among all the new therapeutic agents approved during the first 15 years of the 21st Century, about 34% of were either NPs or NP-derived compounds [5].

It had been shown that natural products from African botanical sources possess a unique and broad chemical space, with biological and drug-like properties exploitable in the field of drug

discovery [6–9]. Docking and pharmacophore-based virtual screening (VS) campaigns conducted, for example, against a few selected known anti-cancer drug targets revealed the presence of potential anticancer agents within the newly developed AfroCancer database [6,7]. The efforts of the pan-African Natural Products Library (p-ANAPL) consortium were aimed at collecting physical samples of NPs at a central location, which could then be directly available for screening purposes [10]. Owing to the small quantities of the isolated samples, an efficient approach for the management of the p-ANAPL library has been to only test samples of *in silico* hits from virtual screening. A previous successful campaign, which combined pharmacophore-based virtual screening and *in vitro* testing of this compound library, had led to the identification of boldine and ixoratannin as anti-HIV-1 compounds [11]. These findings have prompted the search for potential inhibitors of sirtuins by *in silico* screening of the p-ANAPL library.

Recently, virtual screening for the identification of sirtuin inhibitors and modulators has received great interest [12–20]. Sirtuins are nicotinamide adenine dinucleotide (NAD⁺)-dependent class III histone deacetylases which have been linked to the pathogenesis of numerous diseases like HIV, metabolic disorders, neurodegeneration (including Alzheimer's disease and Parkinson's disease) and cancer [21–28]. Since the p-ANAPL library consists of compounds with a broad range of already reported activities, for example, antibacterial, antiviral, anticancer and anti-inflammatory properties [10], this collection represents a good starting point to search for novel inhibitors or modulators of sirtuins. Sirtuins share a highly conserved catalytic core composed of two sub domains; a large NAD⁺ binding domain (Rossmann fold) and a smaller domain generated by two insertions in the NAD⁺ binding domain, together with a helical module and a zinc-binding module [29,30].

In the last two decades, several sirt1 and sirt2 crystal structures have been solved in both apo and holo forms [31–43]. Ternary structures of sirt1 and sirt2 in complex with cofactor analogues, peptide-based and structurally diverse inhibitors revealed a high conformational flexibility in the catalytic pocket, especially in the extended C-pocket region. Thus, the experimentally known structures provide a good coverage of the conformational space of the catalytic pockets of sirt1 and 2 for a target-based vs. campaign.

In the present work, we used several of the reported crystal structures of sirt1 and sirt2 to virtually screen the p-ANAPL compound collection. The consideration of different protein conformations should increase the chance to identify novel active compounds. Several X-ray structures of sirt1 exist in the Protein Data Bank (PDB), notably co-crystallized with small molecule activators and inhibitors [44]. Sirt2 is also available in complex with a macrocyclic peptide [41], a thiomristoyl-lysine peptide [39], the cofactors ADP ribose and nicotinamide [40], the inhibitor SirReal2 [40] and the indole derivative EX-243 [38]. These crystal structures were considered for screening.

2. Results

2.1. Docking Results

Docking of the p-ANAPL virtual compound collection, followed by selecting 5% of the top-ranked poses (using GoldScore) yielded 22 hits for the substrate pocket of sirt1 (PDB ID: 4ZZJ) [45]. From the 22 hits, 5 compounds with sufficient quantities for bioassays were further retained for testing (Figure S1, Supplementary Materials). In a similar fashion, 5% of the top-ranked compounds were selected from docking experiments carried out onto the peptide (PDB IDs: 4R8M and 4L3O), the C (PDB ID: 4RMH) and the extended C (PDB ID: 5D7P) pockets of sirt2. The combined hit lists of sirt1 and sirt2 gave 13 compounds after the removal of duplicates and compounds forming unfavorable conformations within the respective binding sites (Figure S1, Supplementary Materials). Among the 13 retained compounds, only 7 had sufficient amounts within the p-ANAPL collection (>1 mg) for the screening assays. All 7 selected compounds (**1**, **2**, **8–10**, **12** and **13**, Figure 1) were tested in the assays against sirt1, 2 and 3. The entire virtual screening process for sirt1 and sirt2 has been summarised in Figure S2 (Supplementary Materials).

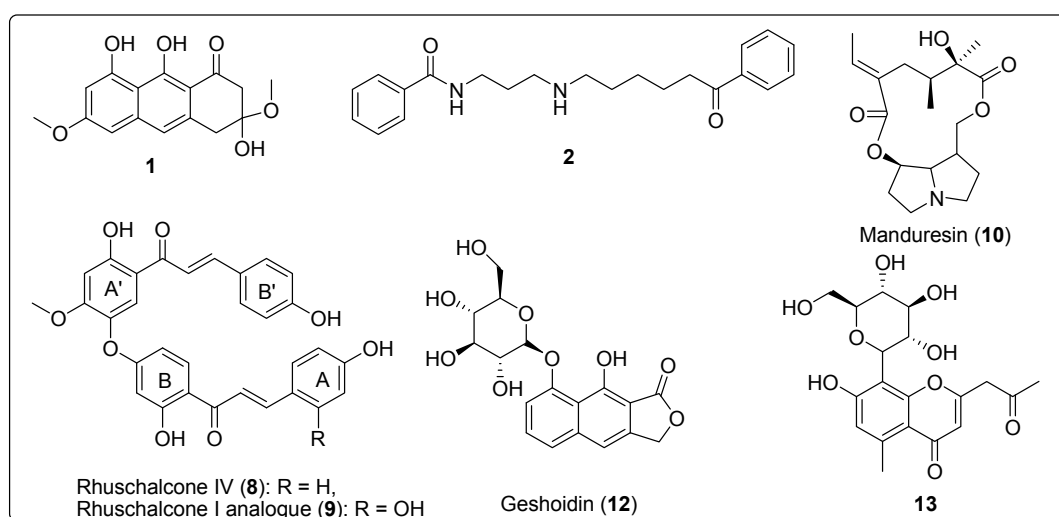


Figure 1. Compounds tested against sirt1, 2 and 3.

2.2. In Vitro Activities

Among the selected compounds, **1**, **10**, and **13** showed no inhibitory activities against sirt1, 2, and 3 at 50 μM concentration (Table 1), while inhibition could not be determined for compounds **1** and **12**. Meanwhile, compounds **8** and **9** showed moderate inhibitory effects against both sirt1 (**8**; $\text{IC}_{50} = 46.7 \pm 6.0$, **9**; $\text{IC}_{50} = 40.8 \pm 8.5$) and sirt2 (**8**; $\text{IC}_{50} = 48.5 \pm 39.5$, **9**; $\text{IC}_{50} = 44.8 \pm 5.1$) compared to the standard sirtuin inhibitors nicotinamide (NA) and EX-527 (Selisistat). Nevertheless, sirt3 was only slightly affected at a 50 μM concentration by compounds **8** and **9**. Moreover, none of the tested hits showed any PAINS alerts.

Table 1. IC_{50} or percentage inhibitions at 50% of tested pan-African Natural Products Library (p-ANAPL) compounds against sirt1, 2 and 3.

Compound Number	Sirt 1 (μM)	Sirt 2 (μM)	Sirt 3 (μM or % Inhibition)
1 ^b	n.d. ^c	n.d. ^c	n.d. ^c
2	n.i. ^a	n.i. ^a	n.i. ^a
8	46.7 ± 6.0	48.5 ± 39.5	38%
9	40.8 ± 8.5	44.8 ± 5.1	23%
10	n.i. ^a	n.i. ^a	n.i. ^a
12 ^b	n.d.	n.d.	n.d.
13	n.i. ^a	n.i. ^a	n.i. ^a
NA	142.4 ± 9.1	49.8 ± 4.6	67.9 ± 3.3
EX-527	1.4 ± 0.1	10.6 ± 1.1	19%

^a n.i. = no inhibition (<10%). ^b autofluorescence. ^c n.d. = not detectable. Note that activity was not detectable due to the autofluorescence. NA = nicotinamide, EX-527 = sirt inhibitor in clinical trials.

3. Discussion

The identified actives are an analogue of rhuschalcone I, along with and rhuschalcone IV. These compounds have been previously isolated from the twigs [46] and root bark [47] of *Rhus pyroides* Burch (Anacardiaceae), respectively. *R. pyroides* is a well known medicinal plant which is widely distributed in Eastern Botswana. This plant is also known to be the sources of several O-linked and C-C coupled bichalcones (Figure 2) and biflavonoids, some of which have been obtained by total synthesis [48–52]. The bichalcones and their analogues are known to possess cytotoxic [47], antiprotozoal [48,49] and carbonic anhydrase inhibitory [50] activities. Meanwhile, biflavones from this plant, e.g., agathisflavone and amentoflavone have shown an affinity for the GABA_A/benzodiazepine receptor [51].

It could be further proposed that analogues of the bichalcones (e.g., the O-linked littorachalcone or verbecharcone, verbenachalcone and rhuschalcones II and III, together with the C-C linked rhuschalcones V and VI, Figure 2) be tested for sirt1, 2 and 3 inhibition. Also, the binding of these compounds in the extended C pocket could be tested in fluorescence assays. It could be suggested that, unlike the rhuschalcones, both C-C and C-O linked non-symmetrical bichalcones be also be synthesized and tested against the sirtuins, with the view of investigating potential selectivities against the isoforms. Besides, chalcones have previously shown deacetylase inhibitory properties against sirt1 and hindered cell growth in HEK293T cells [53].

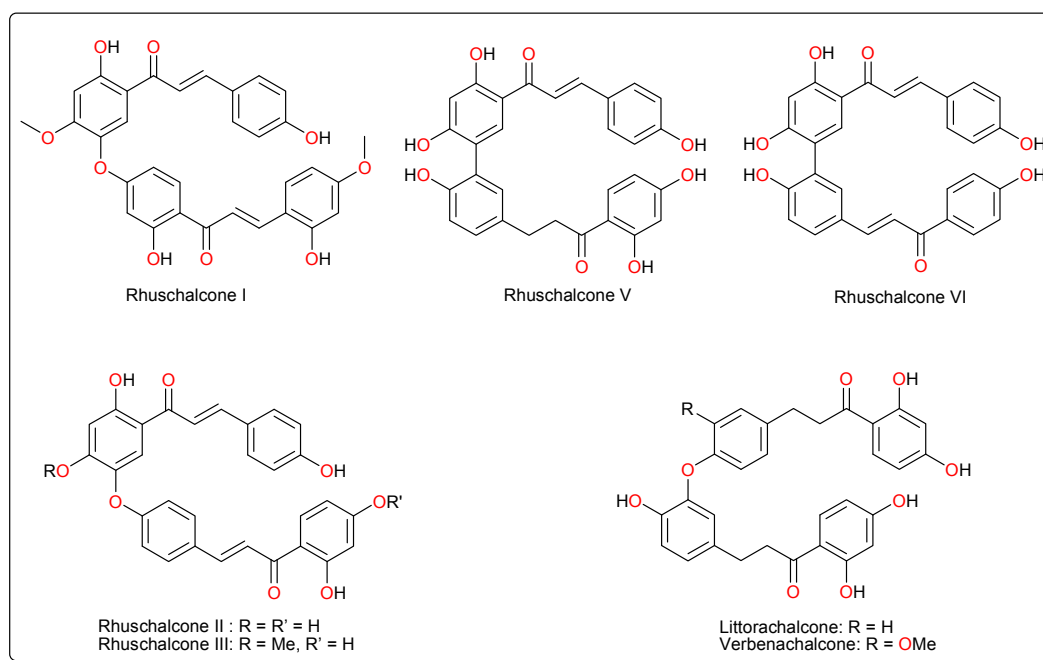


Figure 2. Untested bichalcones from *Rhus* species.

In order to rationalize the interaction of the identified hits in our study, all docking poses for sirt1 (PDB ID: 4ZZJ) and sirt2 (PDB ID: 4R8M and PDB ID: 5D7P) were analyzed using the Molecular Operating Environment (MOE) program [54]. Docking to sirt1 suggested two possible binding modes for the most active hits, compounds **8** and **9** (Figure 3a and Figure S3). The most favourable (top score) binding mode was observed in the peptide binding pocket, where the hydroxyl group on the ring A of compound **9** interacts with the backbone of the residue Gly415. A similar interaction was also observed for the co-crystallized peptide substrate [45]. Moreover, the hydroxyl groups on the ring A' of two active compounds made additional H-bonds with the backbone carbonyl group of Gln345 residue. Although compound **8** does not show H-bonding with Asp348, we assume both compounds have the same binding mode, since the experimentally measured inhibitory potencies are very close in all three assays. Moreover, an H-bond interaction was formed between the hydroxyl group of ring B' of compound **9** and the side chain of the residue Asp348. With regard to binding to the sirt2 peptide pocket, H-bonds were observed between the hydroxyl groups in ring A of the actives and the O atom of Val233 in the protein backbone (Figure 3b).

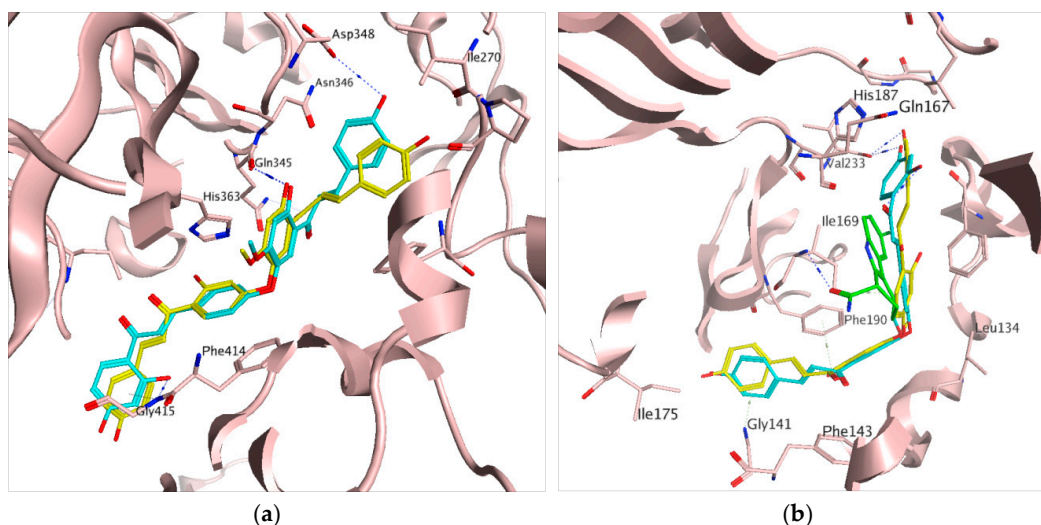


Figure 3. Predicted common binding mode of active compounds in the peptide binding pockets of (a) sirt1 (PDB ID: 4ZZJ) and (b) sirt2 (PDB ID: 4R8M). In both cases, compound 8 in yellow, compound 9 in cyan, hydrogen bonds drawn as dashed lines, while EX-243 is shown in green on subfigure (b).

The same interactions were observed for the myristol peptide as well in the X-ray structure of Sirt2, but not with the indole derivative EX-243 (Figure 3b). Within the sirt2 extended C pocket (Figure S4), the hydroxyl groups of the B' ring of the actives interact with His187 via the co-crystallized water molecule HOH676. Meanwhile, the hydroxyl groups of ring A interact with the O atom of Asp 170 in the backbone and the carbonyl groups (near the ring A') interact with the side chain of Ile232 (Figure S4). Binding in the peptide pockets of both sirt1 and sirt2 is driven by hydrophobic interactions rather than by H-bonding, explaining the similar activities against both sirtuin isoforms.

4. Materials and Methods

4.1. Database Preparation

Ligand preparation of the 463 natural compounds in the p-ANAPL database was carried out using the LigPrep module in Schrödinger [55]. 10 low energy conformers were generated for each molecule using the Merck Molecular Forcefield 94 version (MMFF94) [56] implemented in MOE [54] for minimization. Pan-Assay Interference (PAIN) filters were applied using Schrödinger's Canvas tool [57] and the CbLigand web server [58].

4.2. Protein Preparation

All protein X-ray structures were retrieved from the PDB [59]. Protein preparation of the different crystal structures of human sirt1 (PDB IDs: 4I5I [44], and 4ZZJ [45]), was carried out as detailed in the Supplementary Material, while the sirt2 protein structures were prepared as previously described [36] (details in Supplementary Materials). The docking procedure was performed using GOLD program (The Cambridge Crystallographic Data Centre, CCDC, Cambridge, UK) [60–62], preceded by preparation of the ligands using the LigPrep (Schrödinger, LLC, New York, NY, USA, 2014) [55] tool in Maestro (Schrödinger, LLC, New York, NY, USA, 2014) [61]. Hydrogen atoms were added to the ligand molecules, followed by minimization, using the MMFFs force field in Maestro [63]. The crystal structure in complex with NAD⁺ (PDB ID: 4I5I), along with the crystal structure co-crystallized with the acetyl lysine peptide (PDB ID: 4ZZJ), were used in the study. The protein structures were protonated and minimized, using the Amber 99SB force field, implemented in MOE [54].

4.3. Docking, Scoring and Hit Selection

All water molecules, the cofactor and the peptide were removed. The location of the native ligand (NAD⁺ or peptide) was used to define the docking site, where all protein residues within 6 Å from any heavy atom of the respective ligands were considered as part of the binding site. GoldScore was used as the fitness function to score all docking poses. All docking poses were analyzed by visual inspection and some compounds were chosen to be tested by *in vitro* assays, following a protocol to be given later. In the next step, ligands were docked into the substrate-binding pocket of human sirt1 and sirt2. This was carried out using two different docking programs (Gold [60–62] and Maestro [63]). The resulting docking poses were stored. The selection of compounds for testing was carried out by examining protein-ligand interactions in the derived docking poses. In the crystal structures of sirt1 it was shown that substrates make H-bond interactions with the backbone of a conserved valine residue (sirt1 numbering Val412), which is crucial for the correct orientation of the acyl-lysine in the active site [44]. In case of sirt2, the binding interactions of the native ligands including both the peptide substrates, the cofactor fragments and the co-crystallized inhibitors with the protein were first examined [31–43]. In the hit selection process, special importance was given to compounds interacting with residues Phe234, Phe235, Phe190 and Glu237 in the catalytic pocket. Seven compounds (1, 2, 8–10, 12 and 13, Figure 1) were identified as hits and retained for testing. All molecules, except the zinc ion (Zn²⁺), were removed from the structures prior to docking. Structural bridging water molecules (where mentioned), were included in the binding site of the protein structures before docking. Docking studies were performed using the Glide program (Schrödinger Suite 2012-5.8) [64,65]. The dockings were done using Glide high-throughput virtual screening (HTVS) mode, treating ligands flexibly. 10 docking poses were calculated for each conformer. Only the top-ranked poses were retained for each compound for each docking run. Docking poses retrieved for the top-ranked 20 compounds (~5% of the whole database) were visually analyzed, the hits being retained based on observed protein-ligand interactions within the target site. In sorting ligand poses by observed protein-ligand interactions, the emphasis was laid on ligand poses with putative interactions within the cofactor (NAD⁺) and peptide binding pockets.

4.4. *In Vitro* Assay

Human sirt1_{133–747} was expressed as a GST-tagged enzyme and purified as described previously [66]. Human sirt2_{56–356} and sirt3_{118–395} were expressed as an N-terminally His₆-tagged enzyme and purified as described previously. The identity and purity of the produced enzymes were verified using SDS-PAGE [67]. Protein concentration was determined by the Bradford assay [68]. Deacetylase activity of sirtuin isoforms was NAD⁺-dependent and could be inhibited by nicotinamide. Compound samples were provided from the p-ANAPL compound collection in Botswana, which has been stored below 0 °C. The inhibitory activity against hSirt1, hSirt2 and hSirt3 was determined by a histone deacetylase assay, previously established [69], with further details provided in the Supplementary Material. Human sirt1_{133–747}, sirt2_{25–389} or human sirt3_{118–395} were mixed with the assay buffer (50 mM Tris, 137 mM NaCl, 2.7 mM KCl, pH 8.0), NAD⁺ (final assay concentration 500 μM), the substrate Z-(Ac)Lys-AMC, also termed ZMAL (final assay concentration 10.5 μM). The inhibitor was dissolved in DMSO at various concentrations or DMSO as a control (final DMSO concentration 5% (*v/v*)). Total substrate conversion of controls was driven to about 15–30% to assure initial state conditions. The assay was carried out in 96-well plates with a reaction volume of 60 μL per well. All determinations were performed in triplicates. After an incubation for 4 h at 37 °C and 140 rpm, deacetylation was stopped by addition of 60 μL of a solution containing trypsin and nicotinamide (50 mM Tris, 100 mM NaCl, 6.7% (*v/v*) DMSO, trypsin 16.5 U/μL, 8 mM nicotinamide, pH 8.0). The microplate was further incubated for 20 min at 37 °C and 140 rpm. Finally, fluorescence intensity was measured in a microplate reader (BMG Polarstar, λ_{ex} 390 nm, λ_{em} 460 nm). All compounds were pre-tested on auto-fluorescence, amino-methylcoumarin (AMC) quenching, and trypsin inhibition under assay conditions. Rates of inhibition were calculated by using the controls, containing no inhibitor, as a reference. GraphPad Prism software, version 5 (La Jolla, CA, USA) was

employed to determine IC₅₀ values. Nicotinamide (as a pan-inhibitor) and EX527 (a sirt inhibitor in clinical trials) were included as controls.

5. Conclusions

In the present work, target-based virtual screening was combined with experimental testing in order to identify novel modulators of sirt1 and sirt2 within the p-ANAPL database. Molecular docking studies on available sirt1 and sirt2 crystal structures resulted in two sirt1 and sirt2 inhibitors with moderate inhibitory effect. Although the bichalcones **8** and **9** have been known to possess other biological activities [47–52], it is as yet unclear if their cytotoxicities are related to their abilities to inhibit sirtuins. However, natural product libraries like the p-ANAPL and the newly developed NANPDB [70] libraries could be good sources to search for modulators of sirtuins with novel scaffolds.

Supplementary Materials: The following are available online. Figure S1: 13 selected compounds on the hit list: black (>1 mg), red (tested negative) green (active); Figure S2: Complete workflow of the in silico and in vitro screening processes; Figure S3: Predicted common binding mode of active compounds in the peptide binding pockets of Sirt2 (PDB ID: 4R8M): compound **8** in yellow, compound **9** in cyan, hydrogen bonds drawn as dashed lines; Figure S4: Predicted common binding mode of active compounds in the extended C pocket of Sirt2 (left: PDB ID: 5D7P) and the pocket surface is colored according to hydrophobic (green) and hydrophilic (pink) regions Sirt2 (right). Compound **8** in yellow, compound **9** in cyan, hydrogen bonds drawn as dashed lines; Figure S5: Predicted common binding mode of active compounds in the peptide binding pocket of sirt1 (PDB ID: 4ZZJ), with compound **8** shown in yellow, compound **9** in cyan, hydrogen bonds are drawn as dashed lines and EX-243 in green; Protein Preparation Protocols and detailed in vitro assay description.

Acknowledgments: Z.A. is currently a doctoral candidate financed by the German Academic Exchange Services (DAAD), Germany. F.N.-K. acknowledges a Georg Forster fellowship from the Alexander von Humboldt Foundation, Germany. The Jung and Sippl group thank the German Research Foundation (DFG, within RTG1976, Ju295/14-1 and Si868/15-1) for support. The authors acknowledge the technical support of Conrad V. Simoben.

Author Contributions: F.N.-K., W.S., K.A.-M. and M.J. conceived and designed the experiments; B.K., Z.A., S.S., S.O.M. and F.N.-K. performed the experiments; B.K., Z.A., S.S., S.O.M. and F.N.-K. analyzed the data; W.S., S.O.M., K.A.-M. and M.J. contributed reagents/materials/analysis tools; B.K., Z.A. and F.N.-K. wrote the paper. All authors approved the final submission.

Conflicts of Interest: The authors declare no conflict of interest.

References

1. Harvey, A.L.; Edrada-Ebel, R.; Quinn, R.J. The re-emergence of natural products for drug discovery in the genomics era. *Nat. Rev. Drug Discov.* **2015**, *14*, 111–129. [[CrossRef](#)] [[PubMed](#)]
2. Rodrigues, T.; Reker, D.; Schneider, P.; Schneider, G. Counting on natural products for drug design. *Nat. Chem.* **2016**, *8*, 531–541. [[CrossRef](#)] [[PubMed](#)]
3. Mishra, B.B.; Tiwari, V.K. Natural products: An evolving role in future drug discovery. *Eur. J. Med. Chem.* **2011**, *46*, 4769–4807. [[CrossRef](#)] [[PubMed](#)]
4. Harvey, A.L. Natural products as a screening resource. *Curr. Opin. Chem. Biol.* **2007**, *11*, 480–484. [[CrossRef](#)] [[PubMed](#)]
5. Newman, D.J.; Cragg, G.M. Natural products as sources of new drugs from 1981 to 2014. *J. Nat. Prod.* **2016**, *79*, 629–661. [[CrossRef](#)] [[PubMed](#)]
6. Ntie-Kang, F.; Nwodo, J.N.; Ibezim, A.; Simoben, C.V.; Karaman, B.; Ngwa, V.F.; Sippl, W.; Adikwu, M.U.; Mbaze, L.M. Molecular modeling of potential anticancer agents from African medicinal plants. *J. Chem. Inf. Model.* **2014**, *54*, 2433–2450. [[CrossRef](#)] [[PubMed](#)]
7. Ntie-Kang, F.; Simoben, C.V.; Karaman, B.; Ngwa, V.F.; Judson, P.N.; Sippl, W.; Mbaze, L.M. Pharmacophore modeling and in silico toxicity assessment of potential anticancer agents from African medicinal plants. *Drug Des. Dev. Ther.* **2016**, *10*, 2137–2154. [[CrossRef](#)] [[PubMed](#)]
8. Ntie-Kang, F.; Zofou, D.; Babiaka, S.B.; Meudom, R.; Scharfe, M.; Lifongo, L.L.; Mbah, J.A.; Mbaze, L.M.; Sippl, W.; Efange, S.M.N. AfroDb: A select highly potent and diverse natural product library from African medicinal plants. *PLoS ONE* **2013**, *8*, e78085. [[CrossRef](#)] [[PubMed](#)]

9. Zofou, D.; Ntie-Kang, F.; Sippl, W.; Efange, S.M.N. Bioactive natural products derived from the Central African flora against neglected tropical diseases and HIV. *Nat. Prod. Rep.* **2013**, *30*, 1098–1120. [[CrossRef](#)] [[PubMed](#)]
10. Ntie-Kang, F.; Onguéné, P.A.; Fotso, G.W.; Andrae-Marobela, K.; Bezabih, M.; Ndom, J.C.; Ngadjui, B.T.; Ogundaini, A.O.; Abegaz, B.M.; Meva'a, L.M. Virtualizing the p-ANAPL library: A step towards drug discovery from African medicinal plants. *PLoS ONE* **2014**, *9*, e90655. [[CrossRef](#)] [[PubMed](#)]
11. Tietjen, I.; Ntie-Kang, F.; Mwimanzi, P.; Onguéné, P.A.; Scull, M.A.; Idowu, T.O.; Ogundaini, A.O.; Meva'a, L.M.; Abegaz, B.M.; Rice, C.M.; et al. Screening of the pan-African natural product library identifies ixoratannin A-2 and boldine as novel HIV-1 inhibitors. *PLoS ONE* **2015**, *10*, e0121099. [[CrossRef](#)] [[PubMed](#)]
12. Park, J.B. Finding potent sirt inhibitor in coffee: Isolation, confirmation and synthesis of javamide-II (*N*-caffeoyltryptophan) as sirt1/2 inhibitor. *PLoS ONE* **2016**, *11*, e0150392. [[CrossRef](#)] [[PubMed](#)]
13. Kokkonen, P.; Kokkola, T.; Suuronen, T.; Poso, A.; Jarho, E.; Lahtela-Kakkonen, M. Virtual screening approach of sirtuin inhibitors results in two new scaffolds. *Eur. J. Pharm. Sci.* **2015**, *76*, 27–32. [[CrossRef](#)] [[PubMed](#)]
14. Salo, H.S.; Laitinen, T.; Poso, A.; Jarho, E.; Lahtela-Kakkonen, M. Identification of novel Sirt3 inhibitor scaffolds by virtual screening. *Bioorg. Med. Chem. Lett.* **2013**, *23*, 2990–2995. [[CrossRef](#)] [[PubMed](#)]
15. Sacconay, L.; Angleviel, M.; Randazzo, G.M.; Queiroz, M.M.; Queiroz, E.F.; Wolfender, J.L.; Carrupt, P.A.; Nurisso, A. Computational studies on sirtuins from *Trypanosoma cruzi*: Structures, conformations and interactions with phytochemicals. *PLoS Negl. Trop. Dis.* **2014**, *8*, e2689. [[CrossRef](#)] [[PubMed](#)]
16. Sun, Y.; Zhou, H.; Zhu, H.; Leung, S.W. Ligand-based virtual screening and inductive learning for identification of Sirt1 inhibitors in natural products. *Sci. Rep.* **2016**, *6*, 19312. [[CrossRef](#)] [[PubMed](#)]
17. Sacconay, L.; Ryckewaert, L.; Randazzo, G.M.; Petit, C.; Passos Cdos, S.; Jachno, J.; Michailoviené, V.; Zubriené, A.; Matulis, D.; Carrupt, P.A.; et al. 5-Benzylidene-hydantoin is a new scaffold for Sirt inhibition: From virtual screening to activity assays. *Eur. J. Pharm. Sci.* **2016**, *85*, 59–67. [[CrossRef](#)] [[PubMed](#)]
18. Liu, S.; Ji, S.; Yu, Z.Y.; Wang, H.L.; Cheng, X.; Li, W.J.; Jing, L.; Yu, Y.; Chen, Q.; Yang, L.L.; et al. Structure-based discovery of new selective small-molecule sirtuin 5 inhibitors. *Chem. Biol. Drug Des.* **2017**, *91*, 257–268. [[CrossRef](#)] [[PubMed](#)]
19. Padmanabhan, B.; Ramu, M.; Mathur, S.; Unni, S.; Thiyagarajan, S. Identification of new inhibitors for human sirt1: An in-silico approach. *Med. Chem.* **2016**, *12*, 347–361. [[CrossRef](#)] [[PubMed](#)]
20. Pulla, V.K.; Sriram, D.S.; Viswanadha, S.; Sriram, D.; Yogeewari, P. Energy-based pharmacophore and three-dimensional quantitative structure-activity relationship (3D-QSAR) modeling combined with virtual screening to identify novel small-molecule inhibitors of silent mating-type information regulation 2 homologue 1 (sirt1). *J. Chem. Inf. Model.* **2016**, *56*, 173–187. [[CrossRef](#)] [[PubMed](#)]
21. Haigis, M.C.; Sinclair, D.A. Mammalian sirtuins: Biological insights and disease relevance. *Annu. Rev. Pathol.* **2010**, *5*, 253–295. [[CrossRef](#)] [[PubMed](#)]
22. Howitz, K.T.; Bitterman, K.J.; Cohen, H.Y.; Lamming, D.W.; Lavu, S.; Wood, J.G.; Zipkin, R.E.; Chung, P.; Kisielewski, A.; Zhang, L.L.; et al. Small molecule activators of sirtuins extend *Saccharomyces cerevisiae* lifespan. *Nature* **2003**, *425*, 191–196. [[CrossRef](#)] [[PubMed](#)]
23. Feige, J.N.; Lagouge, M.; Canto, C.; Strehle, A.; Houten, S.M.; Milne, J.C.; Lambert, P.D.; Matak, C.; Elliott, P.J.; Auwerx, J. Specific Sirt1 activation mimics low energy levels and protects against diet-induced metabolic disorders by enhancing fat oxidation. *Cell Metab.* **2008**, *8*, 347–358. [[CrossRef](#)] [[PubMed](#)]
24. Gallí, M.; van Gool, F.; Leo, O. Sirtuins and inflammation: Friends or foes? *Biochem. Pharmacol.* **2011**, *81*, 569–576. [[CrossRef](#)] [[PubMed](#)]
25. Vachharajani, V.T.; Liu, T.; Wang, X.; Hoth, J.J.; Yoza, B.K.; McCall, C.E. Sirtuins link inflammation and metabolism. *J. Immunol. Res.* **2016**, *2016*, 8167273. [[CrossRef](#)] [[PubMed](#)]
26. Outeiro, T.F.; Kontopoulos, E.; Altmann, S.M.; Kufareva, I.; Strathearn, K.E.; Amore, A.M.; Volk, C.B.; Maxwell, M.M.; Rochet, J.C.; McLean, P.J.; et al. Sirtuin 2 inhibitors rescue alpha-synuclein-mediated toxicity in models of Parkinson's disease. *Science* **2007**, *317*, 516–519. [[CrossRef](#)] [[PubMed](#)]
27. Luthi-Carter, R.; Taylor, D.M.; Pallos, J.; Lambert, E.; Amore, A.; Parker, A.; Moffitt, H.; Smith, D.L.; Runne, H.; Gokce, O.; et al. Sirt2 inhibition achieves neuroprotection by decreasing sterol biosynthesis. *Proc. Natl. Acad. Sci. USA* **2010**, *107*, 7927–7932. [[CrossRef](#)] [[PubMed](#)]
28. Hu, J.; Jing, H.; Lin, H. Sirtuin inhibitors as anticancer agents. *Future Med. Chem.* **2014**, *6*, 945–966. [[CrossRef](#)] [[PubMed](#)]
29. Li, X. Sirt1 and energy metabolism. *Acta Biochim. Biophys. Sin.* **2013**, *45*, 51–60. [[CrossRef](#)] [[PubMed](#)]

30. Davenport, A.M.; Huber, F.M.; Hoelz, A. Structural and functional analysis of human Sirt1. *J. Mol. Biol.* **2014**, *426*, 526–541. [[CrossRef](#)] [[PubMed](#)]
31. Jin, J.; He, B.; Zhang, X.; Lin, H.; Wang, Y. Sirt2 reverses 4-oxononanoyl lysine modification on histones. *J. Am. Chem. Soc.* **2016**, *138*, 12304–12307. [[CrossRef](#)] [[PubMed](#)]
32. Moniot, S.; Forgione, M.; Lucidi, A.; Hailu, G.S.; Nebbioso, A.; Carafa, V.; Baratta, F.; Altucci, L.; Giacché, N.; Passeri, D.; et al. Development of 1,2,4-oxadiazoles as potent and selective inhibitors of the human deacetylase sirtuin 2: Structure-activity relationship, X-ray crystal structure, and anticancer activity. *J. Med. Chem.* **2017**, *60*, 2344–2360. [[CrossRef](#)] [[PubMed](#)]
33. Sundriyal, S.; Moniot, S.; Mahmud, Z.; Yao, S.; Di Fruscia, P.; Reynolds, C.R.; Dexter, D.T.; Sternberg, M.J.; Lam, E.W.; Steegborn, C.; et al. Thienopyrimidinone based sirtuin-2 (sirt2)-selective inhibitors bind in the ligand induced selectivity pocket. *J. Med. Chem.* **2017**, *60*, 1928–1945. [[CrossRef](#)] [[PubMed](#)]
34. Knyphausen, P.; de Boor, S.; Kuhlmann, N.; Scislawski, L.; Extra, A.; Baldus, L.; Schacherl, M.; Baumann, U.; Neundorff, I.; Lammers, M. Insights into lysine deacetylation of natively folded substrate proteins by sirtuins. *J. Biol. Chem.* **2016**, *291*, 14677–14694. [[CrossRef](#)] [[PubMed](#)]
35. Schiedel, M.; Rumpf, T.; Karaman, B.; Lehotzky, A.; Gerhardt, S.; Ovádi, J.; Sippl, W.; Einsle, O.; Jung, M. Structure-based development of an affinity probe for sirtuin2. *Angew. Chem. Int. Ed. Engl.* **2016**, *55*, 2252–2256. [[CrossRef](#)] [[PubMed](#)]
36. Schiedel, M.; Rumpf, T.; Karaman, B.; Lehotzky, A.; Oláh, J.; Gerhardt, S.; Ovádi, J.; Sippl, W.; Einsle, O.; Jung, M. Aminothiazoles as potent and selective sirt2 inhibitors: A structure-activity relationship study. *J. Med. Chem.* **2016**, *59*, 1599–1612. [[CrossRef](#)] [[PubMed](#)]
37. Feldman, J.L.; Dittenhafer-Reed, K.E.; Kudo, N.; Thelen, J.N.; Ito, A.; Yoshida, M.; Denu, J.M. Kinetic and structural basis for acyl-group selectivity and NAD⁽⁺⁾ dependence in sirtuin-catalyzed deacetylation. *Biochemistry* **2015**, *54*, 3037–3050. [[CrossRef](#)] [[PubMed](#)]
38. Rumpf, T.; Gerhardt, S.; Einsle, O.; Jung, M. Seeding for sirtuins: Microseed matrix seeding to obtain crystals of human Sirt3 and Sirt2 suitable for soaking. *Acta Crystallogr. F Struct. Biol. Commun.* **2015**, *71*, 1498–1510. [[CrossRef](#)] [[PubMed](#)]
39. Teng, Y.B.; Jing, H.; Aramsangtienchai, P.; He, B.; Khan, S.; Hu, J.; Lin, H.; Hao, Q. Efficient demyristoylase activity of Sirt2 revealed by kinetic and structural studies. *Sci. Rep.* **2015**, *5*, 8529. [[CrossRef](#)] [[PubMed](#)]
40. Rumpf, T.; Schiedel, M.; Karaman, B.; Roessler, C.; North, B.J.; Lehotzky, A.; Oláh, J.; Ladwein, K.I.; Schmidtkunz, K.; Gajer, M.; et al. Selective Sirt2 inhibition by ligand-induced rearrangement of the active site. *Nat. Commun.* **2015**, *6*, 6263. [[CrossRef](#)] [[PubMed](#)]
41. Yamagata, K.; Goto, Y.; Nishimasu, H.; Morimoto, J.; Ishitani, R.; Dohmae, N.; Takeda, N.; Nagai, R.; Komuro, I.; Suga, H.; et al. Structural basis for potent inhibition of Sirt2 deacetylase by a macrocyclic peptide inducing dynamic structural change. *Structure* **2014**, *22*, 345–352. [[CrossRef](#)] [[PubMed](#)]
42. Moniot, S.; Schutkowski, M.; Steegborn, C. Crystal structure analysis of human Sirt2 and its ADP-ribose complex. *J. Struct. Biol.* **2013**, *182*, 136–143. [[CrossRef](#)] [[PubMed](#)]
43. Finnin, M.S.; Donigian, J.R.; Pavletich, N.P. Structure of the histone deacetylase Sirt2. *Nat. Struct. Biol.* **2001**, *8*, 621–625. [[CrossRef](#)] [[PubMed](#)]
44. Zhao, X.; Allison, D.; Condon, B.; Zhang, F.; Gheyi, T.; Zhang, A.; Ashok, S.; Russell, M.; MacEwan, I.; Qian, Y.; et al. The 2.5 Å crystal structure of the Sirt1 catalytic domain bound to nicotinamide adenine dinucleotide (NAD⁺) and an indole (EX527 analogue) reveals a novel mechanism of histone deacetylase inhibition. *J. Med. Chem.* **2013**, *56*, 963–969. [[CrossRef](#)] [[PubMed](#)]
45. Dai, H.; Case, A.W.; Riera, T.V.; Considine, T.; Lee, J.E.; Hamuro, Y.; Zhao, H.; Jiang, Y.; Sweitzer, S.M.; Pietrak, B.; et al. Crystallographic structure of a small molecule Sirt1 activator-enzyme complex. *Nat. Commun.* **2015**, *6*, 7645. [[CrossRef](#)] [[PubMed](#)]
46. Masesane, I.B.; Yeboah, S.O.; Liebscher, J.; Mügge, C.; Abegaz, B.M. A bichalcone from the twigs of *Rhus pyroides*. *Phytochemistry* **2000**, *53*, 1005–1008. [[CrossRef](#)]
47. Mdee, L.K.; Yeboah, S.O.; Abegaz, B.M. Rhuschalcones II-VI, five new bichalcones from the root bark of *Rhus pyroides*. *J. Nat. Prod.* **2003**, *66*, 599–604. [[CrossRef](#)] [[PubMed](#)]
48. Shetonde, O.; Mdee, L.; Bezibih, M.; Mammo, W.; Abegaz, B. The characterization, total synthesis and antiprotozoal activities of novel bichalcones from *Rhus pyroides*. *Planta Med.* **2009**, *75*, SL11. [[CrossRef](#)]

49. Mihigo, S.O.; Mammo, W.; Bezabih, M.; Andrae-Marobela, K.; Abegaz, B.M. Total synthesis, antiprotozoal and cytotoxicity activities of rhuschalcone VI and analogs. *Bioorg. Med. Chem.* **2010**, *18*, 2464–2473. [[CrossRef](#)] [[PubMed](#)]
50. Arslan, T.; Çelik, G.; Çelik, H.; Sentürk, M.; Yayli, N.; Ekinçi, D. Synthesis and biological evaluation of novel bischalcone derivatives as carbonic anhydrase inhibitors. *Arch. Pharm. Chem. Life Sci.* **2016**, *349*, 741–748. [[CrossRef](#)] [[PubMed](#)]
51. Svenningsen, A.B.; Madsen, K.D.; Liljefors, T.; Stafford, G.I.; van Staden, J.; Jäger, A.K. Biflavones from *Rhus* species with affinity for the GABA_A/benzodiazepine receptor. *J. Ethnopharmacol.* **2006**, *103*, 276–280. [[CrossRef](#)] [[PubMed](#)]
52. Zhang, Y.; Chen, Y.; Yang, Y.; Guan, X. The synthesis of bichalcone rhuschalcone I. *Chin. J. Appl. Chem.* **2011**, *28*, 652–656.
53. Kahyo, T.; Ichikawa, S.; Hatanaka, T.; Yamada, M.K.; Setou, M. A novel chalcone polyphenol inhibits the deacetylase activity of Sirt1 and cell growth in HEK293T cells. *J. Pharmacol. Sci.* **2008**, *108*, 364–371. [[CrossRef](#)] [[PubMed](#)]
54. *Molecular Operating Environment*, version 2014; Chemical Computing Group Inc.: Montreal, QC, Canada, 2014.
55. *LigPrep Software*; Version 2; LLC: New York, NY, USA, 2011.
56. Halgren, T.A. Merck molecular forcefield. *J. Comput. Chem.* **1996**, *17*, 490–641. [[CrossRef](#)]
57. *Canvas, Schrödinger*, version 3.1.011; LLC: New York, NY, USA, 2017.
58. Baell, J.B.; Holloway, G.A. New substructure filters for removal of Pan Assay Interference Compounds (PAINS) from screening libraries and for their exclusion in bioassays. *J. Med. Chem.* **2010**, *53*, 2719–2740. [[CrossRef](#)] [[PubMed](#)]
59. Berman, H.M.; Westbrook, J.; Feng, Z.; Gilliland, G.; Bhat, T.N.; Weissig, H.; Shindyalov, I.N.; Bourne, P.E. The Protein Data Bank. *Nucleic Acids Res.* **2000**, *28*, 235–242. [[CrossRef](#)] [[PubMed](#)]
60. Jones, G.; Willett, P.; Glen, R.C.; Leach, A.R.; Taylor, R. Development and validation of a genetic algorithm for flexible docking. *J. Mol. Biol.* **1997**, *267*, 727–748. [[CrossRef](#)] [[PubMed](#)]
61. Jones, G.; Willett, P.; Glen, R.C. Molecular recognition of receptor sites using a genetic algorithm with a description of desolvation. *J. Mol. Biol.* **1995**, *245*, 43–53. [[CrossRef](#)]
62. Verdonk, M.L.; Cole, J.C.; Hartshorn, M.J.; Murray, C.W.; Taylor, R.D. Improved protein-ligand docking using GOLD. *Proteins* **2003**, *52*, 609–623. [[CrossRef](#)] [[PubMed](#)]
63. *Maestro*; Version 9.2; LLC: New York, NY, USA, 2011.
64. *Glideprogram (Schrödinger Suite 2012-5.8)*, version 5.8; Schrodinger: New York, NY, USA, 2012.
65. Friesner, R.A.; Banks, J.L.; Murphy, R.B.; Halgren, T.A.; Klicic, J.J.; Mainz, D.T.; Repasky, M.P.; Knoll, E.H.; Shelley, M.; Perry, J.K.; et al. Glide: A new approach for rapid, accurate docking and scoring. 1. Method and assessment of docking accuracy. *J. Med. Chem.* **2004**, *47*, 1739–1749. [[CrossRef](#)] [[PubMed](#)]
66. Schiedel, M.; Herp, D.; Hammelmann, S.; Swyter, S.; Lehotzky, A.; Robaa, D.; Oláh, J.; Ovádi, J.; Sippl, W.; Jung, M. Chemically induced degradation of sirtuin 2 (sirt2) by a proteolysis targeting chimera (PROTAC) based on sirtuin rearranging ligands (SirReals). *J. Med. Chem.* **2018**, *61*, 482–491. [[CrossRef](#)] [[PubMed](#)]
67. Laemmli, U.K. Cleavage of structural proteins during the assembly of the head of bacteriophage T4. *Nature* **1970**, *227*, 680–685. [[CrossRef](#)] [[PubMed](#)]
68. Bradford, M.M. A rapid and sensitive method for the quantitation of microgram quantities of protein utilizing the principle of protein-dye binding. *Anal. Biochem.* **1976**, *72*, 248–254. [[CrossRef](#)]
69. Heltweg, B.; Trapp, J.; Jung, M. In vitro assays for the determination of histone deacetylase activity. *Methods* **2005**, *36*, 332–337. [[CrossRef](#)] [[PubMed](#)]
70. Ntie-Kang, F.; Telukunta, K.K.; Döring, K.; Simoben, C.V.; Moumbock, A.F.; Malange, Y.I.; Njume, L.E.; Yong, J.N.; Sippl, W.; Günther, S. NANPDB: A resource for natural products from Northern African sources. *J. Nat. Prod.* **2017**, *80*, 2067–2076. [[CrossRef](#)] [[PubMed](#)]

Sample Availability: Samples of the compounds **8** and **9** are available from the authors.



© 2018 by the authors. Licensee MDPI, Basel, Switzerland. This article is an open access article distributed under the terms and conditions of the Creative Commons Attribution (CC BY) license (<http://creativecommons.org/licenses/by/4.0/>).

**4.5. Manuscript 5: Three-Component Aminoalkylations
Yielding Dihydronaphthoxazine-Based Sirtuin
Inhibitors: Scaffold Modification and Exploration of
Space for Polar Side-Chains.**

S., Vojacek, K., Beese, Z., Alhalabi, S., Swyter, A., Bodtke, C., Schulzke,
M., Jung, W., Sippl, and A., Link.
Archiv der Pharmazie. 350 (2017).

Full Paper

Three-Component Aminoalkylations Yielding Dihydronaphthoxazine-Based Sirtuin Inhibitors: Scaffold Modification and Exploration of Space for Polar Side-Chains

Steffen Vojacek¹, Katja Beese¹, Zayan Alhalabi², Sören Swyter³, Anja Bodtke¹, Carola Schulzke⁴, Manfred Jung³, Wolfgang Sippl², and Andreas Link ¹

¹ Institute of Pharmacy, University of Greifswald, Greifswald, Germany

² Institute of Pharmacy, Martin Luther University of Halle-Wittenberg, Halle/Saale, Germany

³ Institute of Pharmaceutical Sciences, University of Freiburg, Freiburg, Germany

⁴ Institute of Biochemistry, University of Greifswald, Greifswald, Germany

Nonpolar derivatives of heterocyclic aromatic screening hits like the non-selective sirtuin inhibitor splitomicin tend to be poorly soluble in biological fluids. Unlike sp^3 -rich natural products, flat aromatic compounds are prone to stacking and often difficult to optimize into leads with activity in cellular systems. The aim of this work was to identify anchor points for the introduction of sp^3 -rich fragments with polar functional groups into the newly discovered active ($IC_{50} = 5 \mu M$) but nonpolar scaffold 1,2-dihydro-3H-naphth[1,2-e][1,3]oxazine-3-thione by a molecular modeling approach. Docking studies were conducted with structural data from crystallized human SIRT2 enzyme. Subsequent evaluation of the *in silico* hypotheses through synthesis and biological evaluation of the designed structures was accomplished with the aim to discover new SIRT2 inhibitors with improved aqueous solubility. Derivatives of 8-bromo-1,2-dihydro-3H-naphth[1,2-e][1,3]oxazine-3-thione N-alkylated with a hydrophilic morpholino-alkyl chain at the thiocarbamate group intended for binding in the acetyl-lysine pocket of the enzyme appeared to be promising. Both the sulfur of the thiocarbamate and the bromo substituent were assumed to result in favorable hydrophobic interactions and the basic morpholino-nitrogen was predicted to build a hydrogen bond with the backbone Ile196. While the brominated scaffold showed moderately improved activity ($IC_{50} = 1.8 \mu M$), none of the new compounds displayed submicromolar activity. Synthesis and characterization of the new compounds are reported and the possible reasons for the outcome are discussed.

Keywords: Docking studies / Enzyme inhibitors / Epigenetics / Mannich reaction / Sirtuins

Received: March 20, 2017; Revised: April 10, 2017; Accepted: April 17, 2017

DOI 10.1002/ardp.201700097



Additional supporting information may be found in the online version of this article at the publisher's web-site.

Introduction

Human sirtuin-2 (SIRT2) is a ubiquitously expressed class III histone deacetylase (HDAC). HDACs of this class require

nicotinamide adenine dinucleotide (NAD^+) for deacetylation of substrates [1]. In spite of the name histone deacetylases, sirtuins deacylate various other proteins than histones [2]. In the case of SIRT2, important substrates are transcription factors (FOXO1 [3] and FOXO3a [4]), α -tubulin [5], and glucose-6-phosphate dehydrogenase (G6PD) [6].

Even though the role of SIRT2 as a drug target is far from being settled, a recent study revealed that regulation of G6PD acetylation by SIRT2 is involved in the metabolic reprogramming of acute myeloid leukemia (AML) cells. Inhibition of SIRT2 through small-molecules or genetic

Correspondence: Prof. Andreas Link, Institute of Pharmacy, University of Greifswald, Friedrich-Ludwig-Jahn-Str. 17, 17487 Greifswald, Germany.

E-mail: link@uni-greifswald.de

Fax: +49 3834 4204895

ablation seems beneficial for the treatment of a number of neurodegenerative diseases and AML. The molecular basis for interference with leukemia cell proliferation is based upon the pronounced dependence on the oxidative branch of the pentose phosphate pathway (PPP) in these malignant cells. The first and rate-limiting enzyme of the PPP is G6PD. It has been reported, that SIRT2 is overexpressed in clinical AML samples, while acetylation at lysine 403 of G6PD is downregulated and G6PD catalytic activity is increased in comparison to normal controls. Because SIRT2 deacetylates G6PD at K403, it promotes production of NADPH. Pharmacological inhibition of SIRT2 thus leads to reduced cell proliferation of leukemia cells, leaving normal hematopoietic stem and progenitor cells unaffected. For this and other reasons, SIRT2 may serve as a promising target for further therapeutic investigations [6].

Results and discussion

The non-selective sirtuin inhibitor splitomicin [7] (**1**) is a screening hit that was used as starting point for hit-to-lead optimization seeking novel chemotypes inhibiting SIRT2. Splitomicin (**1**) is a fragment-like, flat molecule with $M_r < 200$. The hydrolysis-sensitive lactone is inactive in cellular systems and was analyzed in structure–activity studies, resulting in β -phenyl-8-bromo derivatives such as compound **2** that shows a manifest improvement in terms of stability and target inhibition (Fig. 1). Because docking studies as well as biological tests with recombinant human SIRT2 indicated that the (*R*)-1-phenyl splitomicin derivative **3R** was markedly more active than its (*S*)-enantiomer **3S**, the individual investigation of enantiomers was regarded mandatory in order to obtain valid SAR data within this series of compounds [8].

Replacement of the hydrogen-bond acceptor oxygen atom of the lactone series by a nitrogen atom resulted in non-hydrolysable, biologically active lactames such as **4**. Again, separation of enantiomers was necessary in order to investigate the activity of the racemic mixture in more depth. In a different approach toward less hydrolysable analogs we made use of a variant of the Betti reaction [1], a classical three-component reaction. Instead of aromatic amines, urea or thiourea were reacted with suitable β -naphthols and aromatic aldehydes. In an operationally simple one-pot reaction, we were able to obtain compounds such as **5** and **6** in racemic form. While both of these new splitomicin analogs displayed the desired activity against the target enzyme in low micromolar concentrations in a trypsin-coupled homogeneous assay ($IC_{50} = 2.6 \pm 0.3 \mu M$ for **5** and $IC_{50} = 6.7 \pm 0.9 \mu M$ for **6**), the molecules still require laborious chiral separation and are characterized by pronounced lipophilicity. In order to tackle both of these issues at the same time, we designed achiral naphtho[1,3]oxazin-2-one **7** and naphtho[1,3]oxazine-2-thione **8** derivatives (Fig. 1) and synthesized these two compound series via solvent-free one-pot syntheses.

While these molecular frameworks are closely related to **3** in terms of hydrogen-bond-acceptor properties, the carbamate and thiocarbamate structures are much less sensitive to hydrolysis than the lactone ring of splitomicin (**1**). The shift of the substituent from the benzylic carbon atom to the nitrogen atom resulted in a still non-flat pattern but without the formation of a chiral center. The exchange of aromatic substituents in position R^2 for aliphatic side-chains with polar hetero atoms as solubility enhancing motifs was intended to cure the problems associated with poor solubility.

We started our docking study using hSIRT2 in complex with the inhibitor EX-243 ((1*S*)-6-chloro-2,3,4,9-tetrahydro-1*H*-carbazole-1-carboxamide, PDB ID 5D7P). Interestingly, two inhibitor molecules are interacting in the C- and extended-C

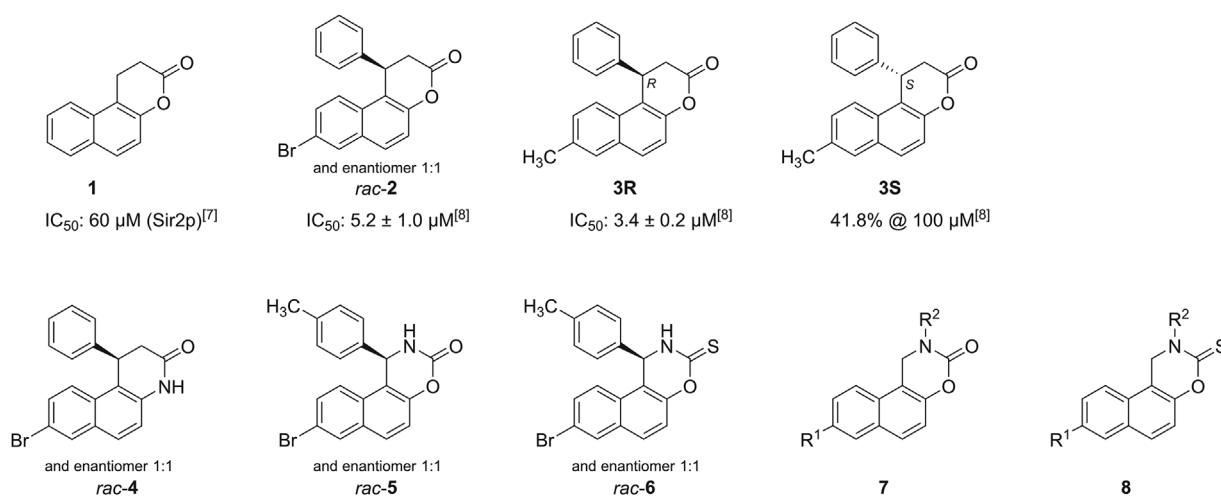


Figure 1. Splitomicin (**1**), hydrolysable derivatives (**2–3**) and less hydrolysable analogs (**4–8**).

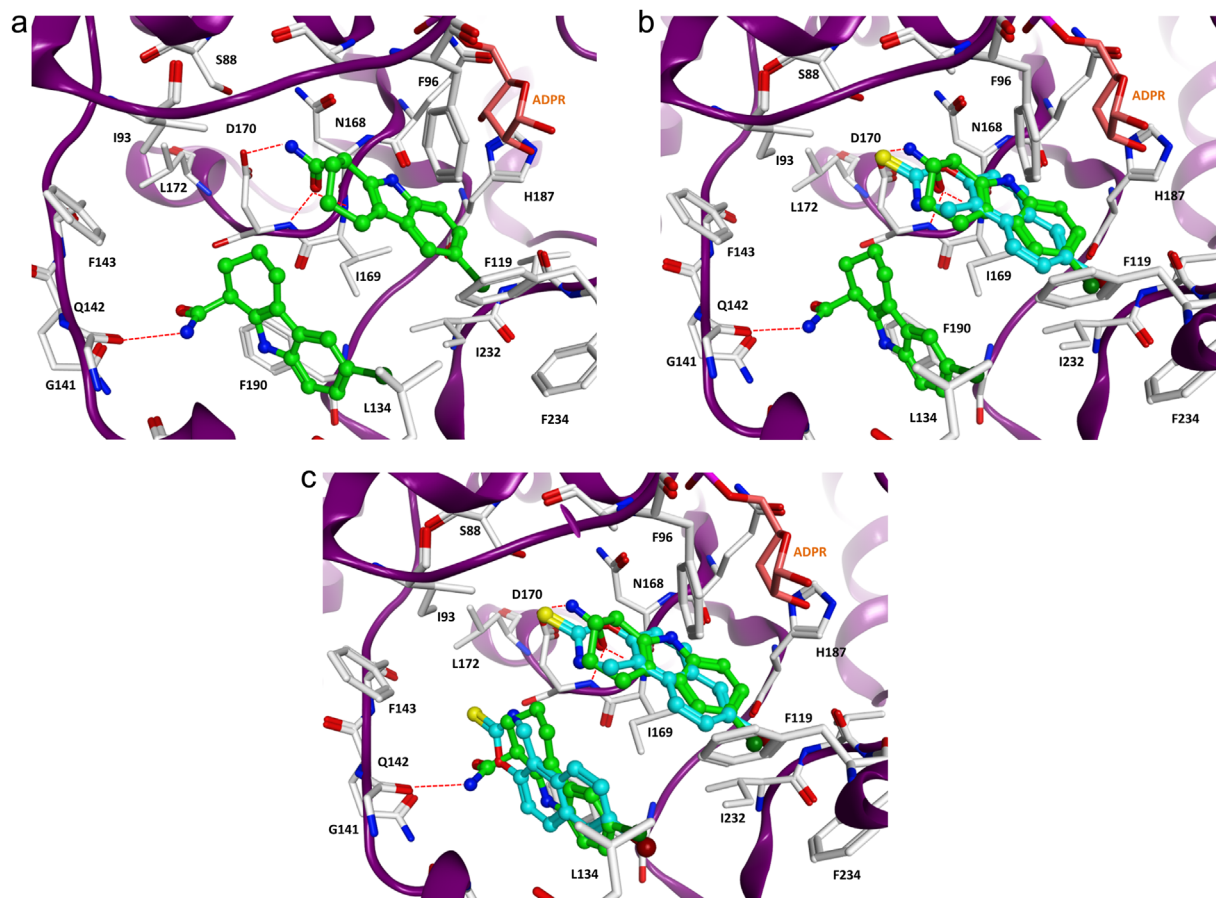


Figure 2. (a) Crystal structure of hSIRT2 complexed with the potent inhibitor EX-243 (green carbon atoms). Two inhibitor molecules are observed in the crystal structure, one bound to the nicotinamide site and one bound in the extended-C site of hSIRT2. Hydrogen bonds are shown as dashed lines. The co-crystallized ADPR molecule is colored in salmon. (b) Top-ranked docking solution for **8b** (cyan carbon atoms) in comparison to the co-crystallized inhibitor EX-243 (same coloring scheme as in a). (c) Docking solutions for **8b** (cyan carbon atoms) in comparison to the co-crystallized inhibitor EX-243 (same coloring scheme as in b).

site of hSIRT2 [9] (Fig. 2a). The docked 1,2-dihydro-3H-naphth[1,2-e][1,3]oxazine-3-thiones **8a** and **8b** were found to interact similarly as observed for EX-243 (Fig. 2b). The sulfur atom of the thiocarbamate makes favorable hydrophobic interactions with Ile193 that might explain the loss of activity for the more polar carbamate derivatives. Moreover, the 8-bromo substituent indicated good hydrophobic interactions with the enzyme (Phe119, Leu134, Ile232). The tricyclic moieties of both inhibitors are nicely superimposed. We also observed that as in case of EX-243 (PDB ID 5D7P) and CHIC35 (PDB ID 5D7Q) two inhibitor molecules of **8a** and **8b** can be bound simultaneously in the hSIRT2 pocket. The top-ranked docking solution is found for the nicotinamide binding site whereas the second molecule interacts at the extended C-site. The high structural similarity to the co-crystallized EX-243 is obvious (Fig. 2c).

In case of the substituted derivatives, the hydrophilic morpholino-alkyl-chain in position R² was proposed to bind at

the exit of the acetyl-lysine pocket of the enzyme (Fig. 3) where the second inhibitor molecule of EX-243 is bound in the hSIRT2 crystal structure.

Our initial synthetic strategy to access the target compound was to prepare an unsubstituted naphthoxazine thione (e.g., **8a**) with subsequent alkylation of the nitrogen atom. Key reaction of this approach was the formation of an electrophilic aromatic quinone methide *in situ* and subsequent oxazinthione-ring closure employing inorganic potassium thiocyanate [10].

Dimethylmethylidene ammonium iodide, a dimethylaminomethylation agent known as Eschenmoser's salt, was reacted with 2-naphthol under basic conditions, resulting in the formation of the corresponding Mannich bases **9** and **10**, respectively (Scheme 1). Using Eschenmoser's salt, superior regioselectivity and predominating mono-substitution compared to the classical Mannich reaction with formaldehyde and dimethyl amine, was anticipated [11]. In the next step, the

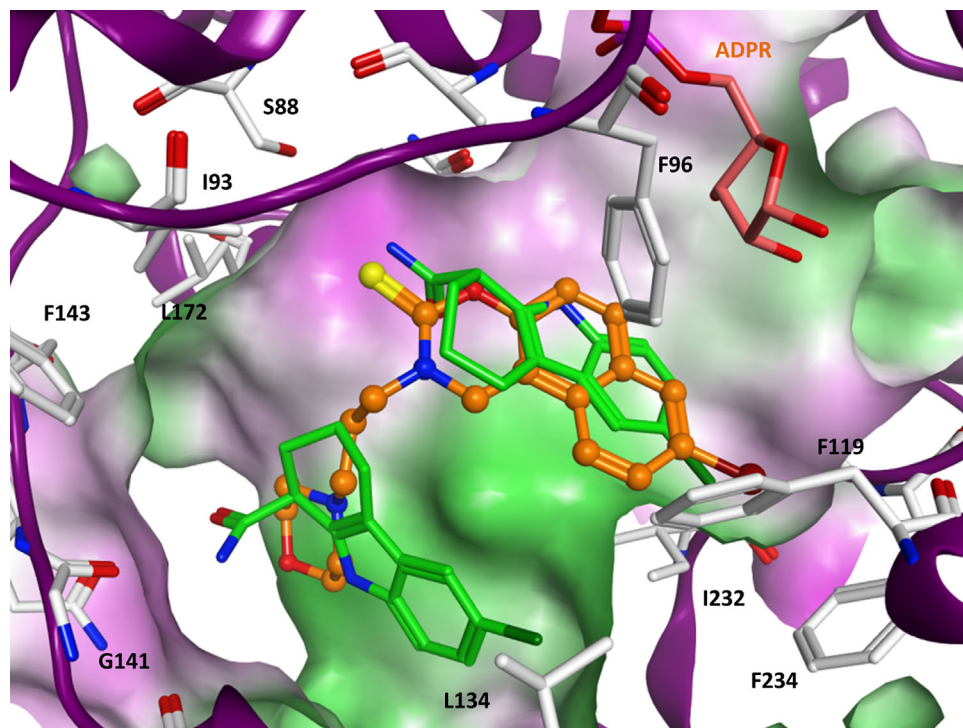
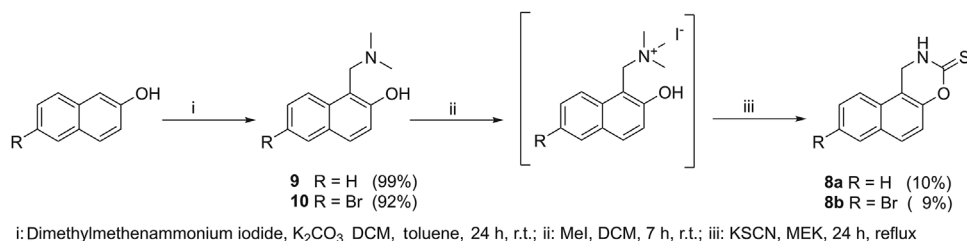


Figure 3. Docking result for the substituted derivative **8d** (orange carbon atoms). The two cocrystallized inhibitor molecules of EX-243 are shown as green sticks. The molecular surface of the binding pocket is displayed and colored according to the hydrophobicity (polar regions are colored magenta, hydrophobic regions are colored green).

resulting Mannich product was exhaustively alkylated with methyl iodide, and subsequently reacted with potassium thiocyanate [10]. Despite repeated attempts to purify the quaternized intermediate resulting from exhaustive alkylation by established procedures, we were unable to obtain the ammonium salts in pure form. While the progress of the reaction could be deduced from the precipitation observed, purification of the precipitate was neither possible via silica gel chromatography on normal nor on reversed phase, because of compound polarity. On normal silica gel phases, the compounds could not be eluted, because of the very strong interactions with the stationary phase. Quite to the contrary, preparative endcapped RP-18 HPLC columns were

unsuitable, because of very weak retention of the compounds. Due to a lack of thermal- and photo-stability of the quaternary products, recrystallization was not effective, either. So the intermediate was collected by filtration, washed, dried, and used without further purifications for the next step. A mechanistic reason for the failure to isolate the quaternary compounds can be attributed to the possible formation of quinone methide species. Most probably, highly reactive and short-lived quinone methide intermediates were generated. While these quinone methides formed *in situ* were too unstable to be isolated, they could efficiently be trapped by reaction with thiocyanate ions to yield the desired isolated products [12]. In addition to analytical characterization by



Scheme 1. First synthetic strategy. Dimethylaminomethylation followed by exhaustive methylation and subsequent thiocarbonylation.

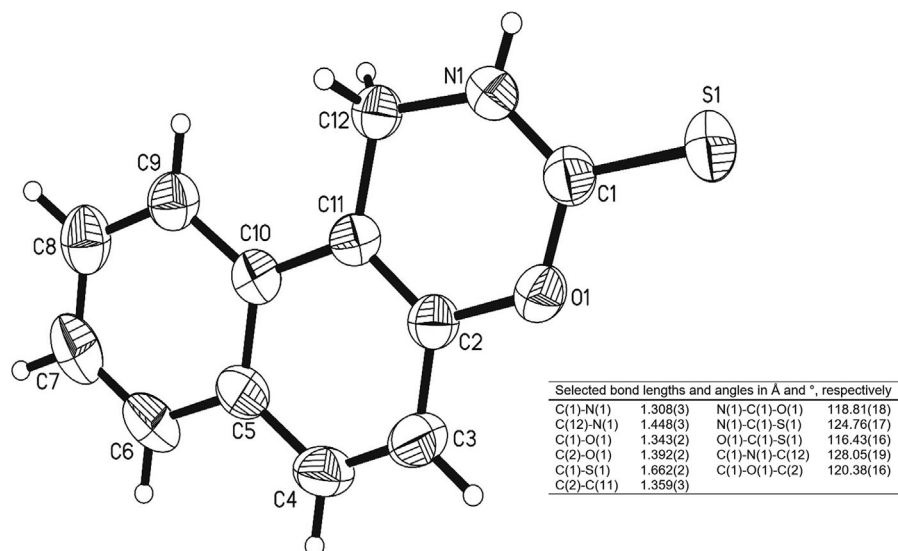


Figure 4. X-ray crystallography confirmed structure of compound **8a**. Ellipsoids are shown at the 50% probability level.

NMR and MS spectroscopy, the formation of the desired product **8a** was confirmed by X-ray crystallography (Fig. 4). The ring system under investigation contains a thiocarbamate with an exocyclic carbon sulfur double bond $\text{ROC}(=\text{S})\text{NR}_2$, which can be called *O*-organyl thiocarbamate or thionourthane in order to indicate the difference to another isomeric thiocarbamate, with an exocyclic carbonyl group $\text{RSC}(=\text{O})\text{NR}_2$, which could be called an *S*-organyl thiocarbamate or thiolurethane.

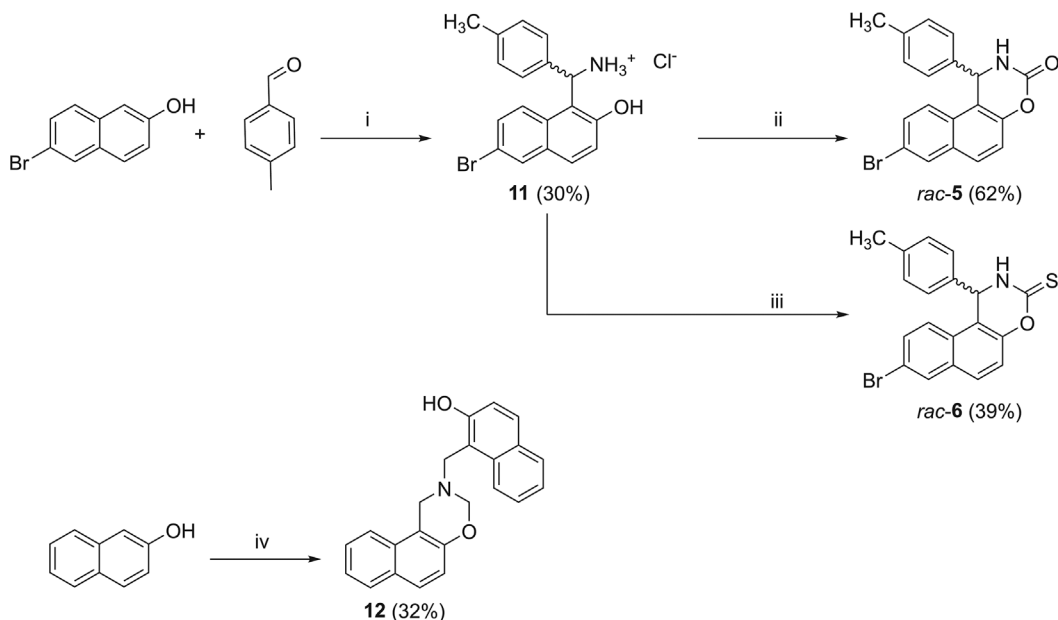
Because of the modest overall yield of the 1,2-dihydro-3*H*-naphth[1,2-*e*][1,3]oxazine-3-thiones **8a** and **8b** of not more than 10% (Scheme 1), an alternative route to the desired test compounds **8d** was investigated. In contrast to the strategy described above, we pursued a synthesis with 1-aminomethyl-2-naphthols as intermediates. It was known from the synthesis of **6**, that there are a number of suitable reagents, for instance thiophosgene [13], 1,1'-thiocarbonyldiimidazole [14] or carbon disulfide [15] available that are suited to transform the synthesized intermediate aminomethyl-2-naphthols into the desired heterocyclic carbamates **7** and thiocarbamates **8**.

The electrophilic aromatic substitution of an *in situ* formed benzaldimine with 2-naphthol was described by Betti even before the related 3-component reaction was reported by Mannich [16]. In a typical 3-component Betti reaction, 2-naphthol reacts in the presence of an ammonia source with benzaldehyde derivatives to give 1,3-diphenyl-2,3-dihydro-1*H*-naphth-[1,2-*e*][1,3]-oxazines. After hydrolysis of the intermediately formed *N,O*-acetals, the racemic Betti bases **11** with primary amino groups are formed (Scheme 2) [17]. Cyclization of compounds of type **11** yielded compounds **5** and **6**. To our understanding this 3-component aminoalkylation reaction can be interpreted as a Mannich reaction in the broadest sense, or with respect to the historical chronology, vice versa. However, despite mechanistic

similarities, Mannich and Betti reactions differ by the use of a secondary amine in place of ammonia and an enolizable CH-acidic compound instead of an electron-rich 2-naphthol [18]. In certain cases, however, for instance in the synthesis of the alkaloid gramine by aminomethylation of indole, it could be argued that this atypical Mannich reaction could as well or even better be classified as atypical Betti reaction [19].

In order to synthesize compounds of classes **7** and **8**, benzaldehyde had to be replaced by paraformaldehyde in order to obtain 1-aminomethyl-2-naphthols with two benzylic protons as intermediates under comparable 3-component Betti reaction conditions. However, in our case this did not result in the anticipated formation of primary amines, but yielded the bis-Betti-product **12**. The attempted hydrolysis of the *N,O*-acetals **12** would not cleave the C–N single bond to the required primary amines. Thus the 1-aminomethyl-2-naphthol intermediate **17** was synthesized by reaction of 2-naphthol with methenamine in the presence of acetic acid with subsequent hydrolysis [20]. This so-called Duff reaction can be regarded as related or similar to the observation published by Mannich and Krösche [18], that methenamine reacted in acidic solution with antipyrine, an electron-rich aromatic drug, which led Mannich to the development of the synthetic use of this phenomenon. Whereas the unwanted reaction of methenamine and antipyrine results in an aminomethylene bonded trimeric pyrazolone compound [21], in the Duff reaction the bis-naphthol-derivative **13** (respectively, **14**) with an iminomethyl group is formed.

In the first step of this reaction, protonated methenamine, acting as an electrophile, forms the aminomethyl group as condensation product with naphthol. Remarkably, in the course of the reaction methenamine acts as an oxidizing agent, as well [22]. The *N,N*-acetal-carbon of methenamine is reduced to methylamine, meanwhile the compound is



i: NH_4HCO_2 , solvent free, 15 min, 110°C ; 2: H_2O , HCl , 2 h, reflux; ii: CDI, THF, 10 min, μw 100°C ; iii: TCDI, THF, 10 min, μw 100°C ; iv: NH_4HCO_2 , paraformaldehyde, DMF, 20 min, 120°C

Scheme 2. Synthetic strategy. Betti reaction employing paraformaldehyde instead of the benzaldehyde derivative.

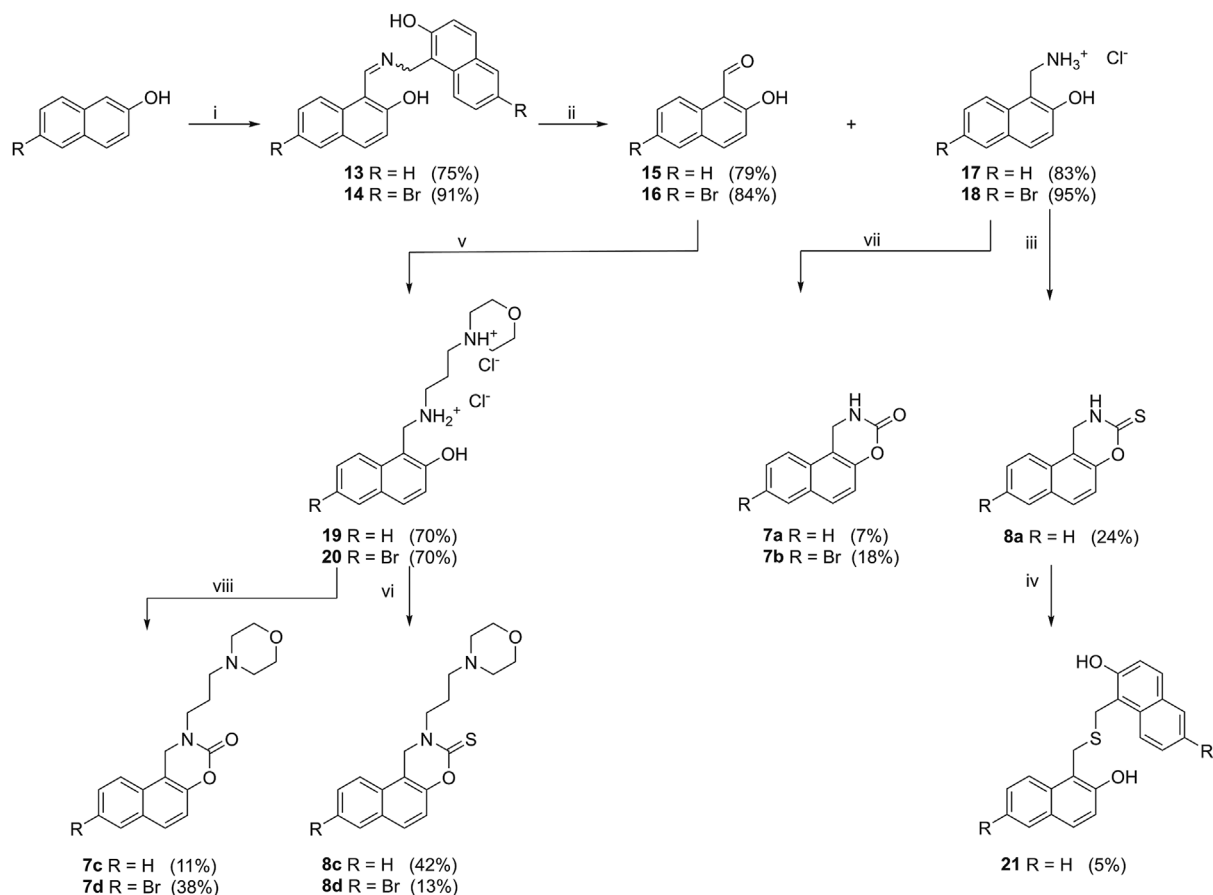
oxidized to an imine [23]. In the next step, the imine concurrently reacts with another methanal molecule and a second molecule naphthol to form the anticipated dimer. Hydrolysis of this intermediate results in two different naphthol derivatives: the primary amine and the aldehyde (Scheme 3). Consequently, the Duff synthesis suffers from the fact, that only half of the starting 2-naphthol can be converted into the aldehyde. On the other hand, it is reported that the yield of the respective aldehyde could be improved by hydrolysis of the intermediate imine **13** in aqueous acetic acid. One hydrolysis product, the primary amine, becomes oxidized by remaining methenamine yielding 1-iminomethyl-2-naphthol which is hydrolyzed to the aldehyde, directly. Although the drawback of the Duff reaction to yield the aldehyde in only 50% could thus be overcome by the above operation [23], we pursued an alternate synthesis employing the Gattermann–Adams reaction (Scheme 4) [24]. Hence, the 2-naphthol derivative was stirred with zinc cyanide in diethyl ether. Subsequent treatment with hydrochloric acid gas released zinc chloride and likewise HCN, which was protonated to form the intermediate iminium ion. Additionally, the zinc ions catalyzed due to their Lewis acid character the aromatic substitution of the electrophilic iminium yielding more than 85% of the aldehyde (based on recovered starting material).

In the second step, formation of the 1,2-dihydro-3*H*-naphth[1,2-*e*][1,3]oxazine-3-thione ring was envisioned. In order to achieve this goal, the thiocarbamate synthesis using carbon disulfide under basic conditions seemed to be the most promising strategy. The 1-aminomethyl-2-naphthol reacted

with CS_2 in basified methanol to a dithiocarbamate anion. The following addition of hydrogen peroxide caused the ring closure reaction to the thiocarbamate, presumably via an isothiocyanate intermediate [15]. Most likely, an intermediary dithiocarbamate disulfide [25] species emerged and subsequently disintegrated by ring closure reaction to the cyclic thiocarbamate.

In an analogous approach reported by Keck et al. [15], 2-hydroxymethyl aniline derivatives treated with one equivalent of triethylamine, three equivalents of carbon disulfide and two equivalents of hydrogen peroxide for disintegration yielded the inverse thionourea in 78% yield. Under the same conditions but starting from aminomethyl-naphthol instead of 2-hydroxymethyl aniline, we were only able to gain the desired product in 24% yield despite performing several attempts. Possibly, the reason for the much lower yield in our case compared to the inverse oxazine-thione is the dissimilarity in acidity of the different starting materials. In contrast to the weakly basic aniline derivative with only one nucleophilic center employed by Keck et al. [15], 1-aminomethyl-naphth-2-ol possesses two potentially nucleophilic groups, a basic aliphatic amino group and a phenolic OH-group. Most likely in our hands the phenol was partly deprotonated, thus forming a strong nucleophile giving rise to the formation of xanthates as side-products and hampering the ring closure reaction.

Once the envisioned thiocarbamate was synthesized in moderate yield, the derivatization was to be conducted with a strong base and subsequent addition of an alkyl halide in a

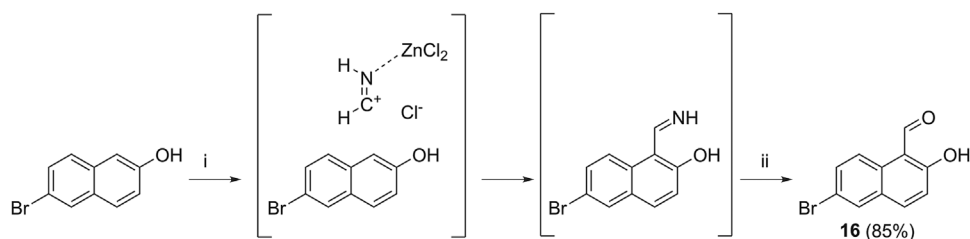


i: Methanamine, AcOH, 1 h, 100°C; ii: EtOH, H₂O, HCl, 2 h, reflux; iii: CS₂, NEt₃, MeOH, 1 h, r.t.; H₂O₂, 1 h; iv: NEt₃, THF, ethyl-3-bromopropionate, 0°C → r.t.; v: 3-morpholino-propylamine, MeOH, 2 h, r.t.; NaBH₄, 1 h, r.t.; HCl; vi: thiophosgene, NEt₃, DCM, 3 h, 0°C → r.t.; vii: TEA, 4-nitrophenyl chloroformate, dioxane, 10 min, r.t.; viii: phosgene, TEA, toluene/water, **7c**: 6 h, r.t.; **7d**: 4 h, r.t. (**7d** was isolated as HCl salt)

Scheme 3. Third synthetic strategy. Duff reaction with different attempts toward derivatization.

third step [26]. In order to deprotonate the N–H group, triethylamine was added [27]. Despite cooling or changes in solvent properties, the addition of the alkyl halide (e.g., chloride, iodide, or bromide) caused decomposition of the thiocarbamate in all attempts. Most of the degradation

products emerged as amorphous solid, insoluble in common solvents like DMSO or DMF. Therefore only the supernatant could be purified, yielding 5.5% of the 1,1'-[thiobis(methylene)]bis(naphthalen-2-ol) as yellowish crystals. The isolated by-product indicated that once the sulfur was



i: Zn(CN)₂, HCl, DEE, 2 h, r.t.; ii: H₂O, reflux

Scheme 4. Alternative synthesis route. Gattermann–Adams reaction.

alkylated, the sulfonium ion forced the cleavage to occur. Probably, a thiocyanate derivative was eliminated, yielding a naphthoquinone methide. The intermediate quinone methide as a strong nucleophile could react with another thiocarbamate as sulfur donating molecule. Eventually an intramolecular rearrangement caused the connection to the accessible thiomethyl-naphthol as nucleophile with subsequent elimination of a cyano-group containing molecule, explaining the formation of a thioether.

The rearrangement of substituted thiourea derivatives via methyl mercaptan elimination is described in the literature [28]. According to these reports, the methyl iodide reacts with the sulfur atom of thiourea derivatives. Upon basification, methyl mercaptan can be eliminated. Depending on the nucleophile, the compounds under investigation rearrange to cyclic isourea [13] or guanidine derivatives [29], respectively. Although the transformations discussed here are aimed at the formation of thionouretanes, from our preliminary observations together with the knowledge available from reports on thiourea rearrangement reactions, we draw the conclusion, that a different route toward these thiocarbamate derivatives had to be pursued. Based on our analysis of this problem, derivatization of carbamates appeared more suitable than alkylation of thiocarbonyl containing compounds. Thus, step three was reformed and divided into the synthesis of substituted carbamates and an additional step four, where the oxo groups should be exchanged for a thiono group with the help of Lawesson's reagent [30].

The conceptual basis for the intended carbamylation was the successful model reaction of **17** and **18** with 1-chloro-1-(4-nitrophenyl)formate (NPCF) in dioxane yielding **7a** and **8a**, respectively [31]. This transformation had allowed us to avoid highly toxic and hazardous reagents such as phosgene. On the other hand, the reaction produced only small amounts of the desired product, e.g., **7a** in 7% yield (Scheme 3). Hence, further experiments like derivatization or thionylation of **7a**, could not be pursued due to a lack of material.

Because the ring closure reaction of the 1-aminomethyl-2-naphthol to the thiocarbamate was effective but derivatization failed, and the alternative carbamylation route suffers from poor yields, synthetic access was attempted via derivatization of the 2-hydroxy-naphth-1-yl-methanal **15** using a modified reductive amination [32] with subsequent thiocarbamylation of the secondary amine. The aldehyde **15** was stirred with 3-morpholinopropan-1-amine in methanolic solution to form a yellowish imine. After a short reaction time, the reducing agent sodium borohydride was added [32].

Addition of solid borohydride in portions to the cooled solution led to a sluggish reaction with the formation of multiple by-products lowering yield and thwarting purification. With the aim of improving the outcome of this reaction, NaBH₄ was dissolved in a small amount of water and added as aqueous solution. After extraction and subsequent addition of HCl gas, the secondary amine could thus be obtained as its hydrochloride salt in almost 70% yield.

In the next step, thiophosgene was used to acquire the desired cyclic thiocarbamate in dichloromethane in good yields using triethylamine to neutralize released HCl. Alternatively, 1,1'-thiocarbonyldiimidazole (TCDI) was used as solid reactant. Advantageously, besides the low toxicity of TCDI, the released imidazole molecules made the addition of triethylamine unnecessary.

Overall, the synthesis of new test compounds with naphthoxazinethione scaffold and a hydrophilic side chain intended as water-soluble SIRT2 inhibitors was conducted and reactions were optimized. Key of the most suitable reaction was the formation of 2-hydroxy-1-naphthaldehyde by the Duff reaction, yielding more than 75% product referring to the use of two equivalents of 2-naphthol. Although the Gattermann–Adams reaction led to even higher yields (based on recovered starting material) of aldehyde **15** compared to the Duff synthesis, the Duff reaction using comparatively cheap and non-hazardous methenamine was advantageous with respect to improved safety, reduced expenditure and lower costs.

The following reductive amination was performed by combining both the formation of the imine and the reduction with sodium borohydride in one pot. The secondary amines **19** and **20** were gained as HCl-salt by treatment of extracted organic phases with hydrochloric acid gas. The conversion to the thionocarbamates was realized by the addition of thiophosgene and an auxiliary base. Compound **8c** was also synthesized from **19** by an alternative route using TCDI. Advantageously, the synthesis could be conducted without adding further bases, because released imidazole accepts protons from the hydrochloride salt **19**.

The 4-step synthesis for the bromo-substituted product **8d** could be achieved in a satisfactory overall yield of 26.6% using TCDI as ring closure reagent.

Selected compounds were tested for inhibition of human NAD-dependent deacetylase hSIRT2 in a fluorescence assay, with IC₅₀ determined for the best inhibitors (Table 1, Fig. 5) [33]. Unexpectedly the thionocarbamates **8c** and **8d**, the most promising compounds revealed by prior docking studies on hSIRT2, showed only moderate inhibition. To the contrary, both the non-derivatized naphtho[1,3]oxazine-2-thione **8a** and its bromo derivative **8b** exhibited good inhibition. An explanation for the only moderate inhibition of **8c/8d** is the high hydrophobicity of the extended C-site (Leu138, Ile169, Phe190, Leu206). We calculated the hydrophobic interaction between a methyl probe and the extended C-site using the GRID approach [34]. The hydrophobicity of the extended-C site is also favorable for the binding of the lipophilic myristoyl chain of a substrate peptide (PDB ID 4Y6L) [35] (Fig. 6a and b).

The results of the biochemical assay revealed that both small molecules inhibited the enzyme with IC₅₀ values of 5.0 and 1.8 μM, respectively. Apparently, the hydrophilic sp³-rich side chain elongations hinder binding in the catalytic cleft, which was not expected from the anticipated docking pose. Nevertheless, the sulfur appeared to be important for

Table 1. Biological test data of some selected compounds against hSIRT2 in an assay with a fluorescence-labeled *N*-acetyl-lysine derivative (ZMAL) [36] trypsin-coupled homogeneous assay.

Entry	IC ₅₀ or percentual inhibition of hSirt2
Nicotinamide ^{a)}	49.8 ± 4.6 μM
<i>rac</i> -5	2.6 ± 0.3 μM
<i>rac</i> -6	6.7 ± 0.9 μM
7a	n.i. ^{b)} @ 25 μM
7b	n.i. @ 25 μM
7c	n.i. @ 25 μM
7d	n.s. ^{c)}
8a	5.0 ± 0.4 μM
8b	1.8 ± 0.3 μM
8c	11% @ 25 μM
8d	n.i. @ 25 μM
19	33% @ 25 μM
20	33% @ 25 μM
22	n.i.% @ 25 μM
23	19% @ 25 μM

^{a)}Nicotinamide is shown as a reference inhibitor. ^{b)} n.i. = no inhibition (<10% inhibition). ^{c)} n.s. = not sufficiently soluble in DMSO.

inhibition whereas the oxo-derivatives, e.g., **7a** and **7b** showed no inhibition under the same conditions. Most likely the more space-filling and lipophilic sulfur-containing compounds could fit more suitably in the binding pocket with increased efficacy by interacting with Ile93 which is mainly driven by van-der-Waals interaction. In addition, the sulfur atom is known to be much more polarizable than the oxygen atom, which may account for the observed differences of closely related analogs as well.

Interestingly the amino-naphthol derivatives **19** and **20** appeared to be also moderate inhibitors of Sirt2. Possibly

these derivatives with potential chelating properties were able to complex the allosteric zinc ion of the enzyme forcing a change in conformation resulting in decreasing its efficacy.

Conclusion

The synthesis of 1,2-dihydro-3*H*-naphth[1,2-*e*][1,3]oxazine-3-thiones **8** intended as intermediate led to the discovery of achiral splitomicin analogs with improved stability and significant biological activity. The most active new compound was the brominated scaffold 8-bromo-1,2-dihydro-3*H*-naphth[1,2-*e*][1,3]oxazine-3-thione **8b** [IC₅₀ = 1.8 μM]. Because these novel scaffolds for diversity showed promising results, the designed *N*-alkylated derivatives with a hydrophilic morpholino-alkyl chain at the thiocarbamate that appeared to be promising were synthesized and tested. A thorough investigation of classical chemical name reactions was necessary in order to obtain the test candidates in practical yields for biological evaluation. While the predicted favorable hydrophobic interactions of the sulfur of the thiocarbamate and the bromo substituent resulted in the good activity of **8b**, the anticipated hydrogen bond of the basic morpholino-nitrogen with the backbone Ile196 did not, most likely due to the high hydrophobicity of this region. Soaking experiments with **8b** should give further insights and guide the way for an alternative position for the connection of additional binding motifs necessary for improved solubility and affinity.

Experimental

Chemistry

General remarks

All chemicals and solvents were purchased from commercial suppliers and used without further purification. Melting

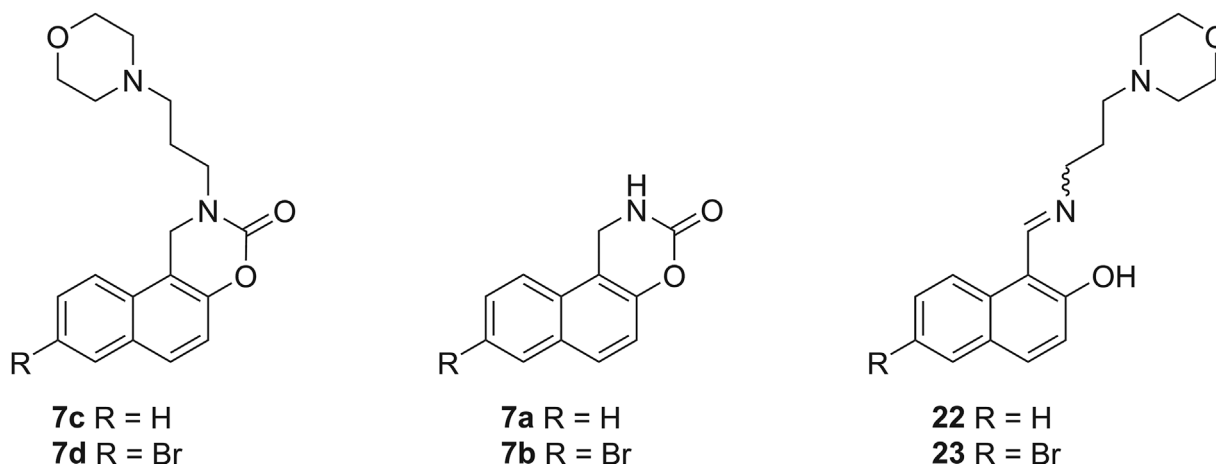


Figure 5. Additional target compounds which were tested in the biological assay.

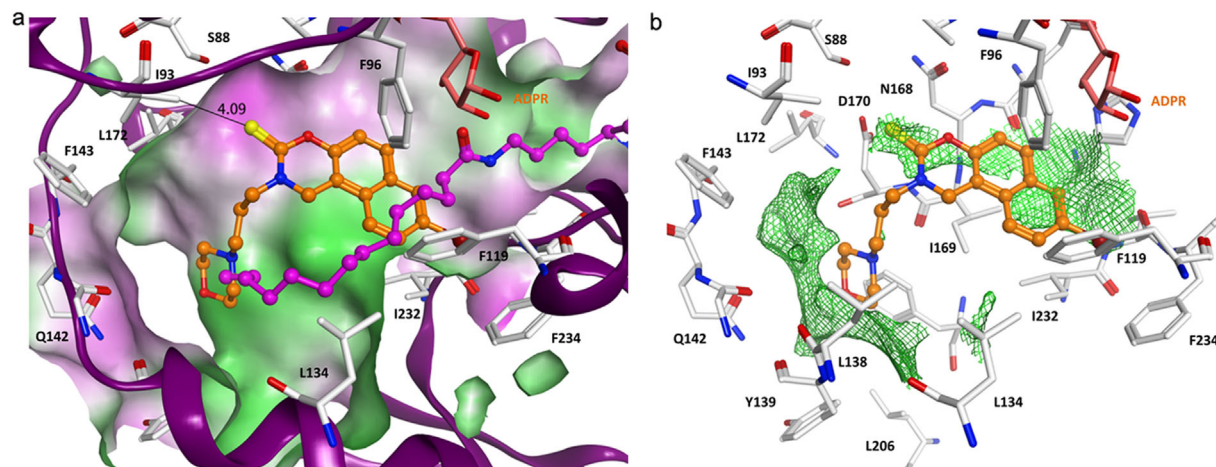


Figure 6. (a) Docking result of compound **8d** (orange carbon atoms) in comparison to the co-crystallized myristoyl-lysine peptide (magenta carbon atoms) which was found to be a substrate of hSIRT2 (PDB ID 4 × 3O). The distance between the thione sulfur and Ile93 is given in Å (same coloring scheme as in Fig. 3). (b) Hydrophobic interaction calculated for the extended C-site (shown as green contour plot, C3 probe, contour level -2.2 kcal/mol) (same coloring scheme as in panel a).

points were determined with a Büchi “Schmelzpunkt M-565” apparatus and are uncorrected. Microwave-assisted synthesis was performed using a microwave synthesis reactor Monowave 300 (“closed vessel” mode, G30-vials: 20 mL total capacity vessel, temperature control via IR sensor) from Anton Paar, while stirring at 600 rpm. NMR spectroscopic measurements were recorded with a Bruker Biospin Avance III Ultrashield 400 instrument (^1H : 400.2 MHz, ^{13}C : 100.6 MHz). Samples were dissolved in deuterated solvents, and chemical shifts (δ) in ^1H and ^{13}C NMR spectra are given in parts per million (ppm) with tetramethylsilane (TMS) signals as reference. Abbreviations are defined as follows: s=singlet, d=doublet, t=triplet, q=quartet. Mid-infrared spectra were recorded on an ALPHA FT-IR instrument from Bruker Optics with diamond ATR accessory. Elemental analyses (C, H, N, and S) were carried out with an Elementar Vario micro elemental analyzer. TLC was performed using pre-coated aluminum foil sheets silica gel 60 F354 provided by Merck. Flash chromatography and medium pressure liquid chromatography (MPLC) were performed using silica gel 60 (particle size 50–100 μm , 140–270 mesh provided by Macherey-Nagel) with Büchi devices C-630, C-601, C-615, and C-660 (column length 40 cm, column diameter 3.5 cm). High performance liquid chromatography (HPLC) was performed using Shimadzu devices CBM-20A, LC-20A P, SIL-20A, and FRC-10A with a SPD 20A UV-Vis detector and LiChrospher100 RP-18 end-capped (250 × 25 mm) HPLC columns.

The NMR spectra as well as the InChI codes of the investigated compounds together with some biological activity data are provided as Supporting Information.

Computational methods

3D structures of all compounds under study were generated from SMILES strings, and a subsequent energy minimization

was carried out using the MMFF94x force field implemented in Molecular Operating Environment System (MOE) 2012.10 (Chemical Computing Group, Montreal, Canada). All compounds were used in their neutral form. A maximum of 100 conformations were generated for each ligand using the Conformational Search module implemented in MOE.

Sirt2 protein structures in complex with small molecule inhibitors were downloaded from the Protein Data Bank (PDB ID 5D7P and 5D7Q) [9]. Currently there are 21 crystal structures of human Sirt2 stored in the PDB. We took the protein structures cocrystallized with inhibitors structurally similar to the compounds under study. All protein structures were prepared by using the Structure Preparation module in MOE. Hydrogen atoms were added, for titratable amino acids the protonation state was calculated using the Protonate 3D module in MOE. Protein structure was energy minimized using the AMBER99 force field [37] using a tethering force constant of $(3/2) kT/2$ ($\sigma = 0.5 \text{ \AA}$) for all atoms during the minimization. AM1-BCC charges [38] were used for ligands. All molecules except the zinc ion were removed from the structures.

Protein-ligand docking was performed using program GOLD 5.2 [39]. Phe96 was used to define the size of the grid box (15 \AA radius). The ligand was treated as flexible and 20 docking poses were calculated for each inhibitor. All other options were left at their default values. The top-ranked pose from each docking run was included in the final analysis and viewed graphically together with the protein structure using the program. Using the docking setup, the two cocrystallized inhibitors EX-243 and CHIR35 could be correctly docked into its crystal structure with RMSD values below 0.8 \AA (PDB ID, 5D7P, and 5D7Q).

The hydrophobic interaction at the extended C-site was calculated using the GRID approach [34] implemented in the

MOE program. The interaction was calculated for the region around the docked inhibitor **8d** using the hydrophobic methyl probe (C3) and was contoured at an interaction energy level of -2.2 kcal/mol. The protein structure PDB ID 5D7P was used for the calculation.

Binding free energies for the inhibitors under study were calculated using the top-ranked docking poses. Structurally conserved water molecules included for docking studies were maintained during the geometry optimization of the complexes. The protein–inhibitor complexes were energy minimized using the AMBER PFROSST force field and the GBSA solvation model implemented in MOE 2012.10.

X-ray crystallography

A suitable single crystal of compound **8a** was mounted on a thin glass fiber coated with paraffin oil. X-ray single-crystal structural data were collected at room temperature using a STOE-IPDS 2T diffractometer equipped with a normal-focus, 2.4 kW, sealed-tube X-ray source with graphite-monochromated Mo K_{α} radiation ($\lambda = 0.71073$ Å). The program XArea was used for integration of diffraction profiles; a numerical absorption correction was applied with the programs X-Shape and X-Red32; all from STOE © 2010. The structure was solved by SIR92 [40] and refined by full-matrix least-squares methods using SHELXL-2013 [41]. The non-hydrogen atoms were refined anisotropically. The hydrogen atoms were refined isotropically on calculated positions using a riding model with their Uiso values constrained to 1.2 Ueq of their pivot atoms. All calculations were carried out using SHELXL-2013 and the WinGX system, Ver1.70.01.61. Basic crystallographic data and structure refinement parameters are summarized in Table 2. Crystallographic data have been deposited with the Cambridge Crystallographic Data Centre with deposition number CCDC 1538210. Copies of the data can be obtained free of charge by contacting the CCDC via e-mail: deposit@ccdc.cam.ac.uk or its webpage <https://www.ccdc.cam.ac.uk/>.

8-Bromo-1-(p-tolyl)-1,2-dihydro-3H-naphtho[1,2-e][1,3]-oxazin-3-one (rac-5)

To a suspension of **11** (0.57 g, 1.5 mmol) in 10 mL tetrahydrofuran, carbonyl diimidazole (0.24 g, 1.5 mmol, 1.0 equiv.) was added in a G30 vial. The vial cap was closed and the vial was placed in the reaction chamber of the microwave reactor. The reaction was conducted at 250 W maximum to reach the reaction temperature of 100°C. Reaction temperature was held at 100°C for 10 min. Afterwards the solvent was evaporated and residue was crystallized from ethyl acetate/*n*-hexane, yielding compound *rac*-5 as colorless needles. Yield: 0.34 g (62.3%); mp: 200.5°C; $^1\text{H-NMR}$ (DMSO- d_6 , 400 MHz): $\delta = 2.23$ (s, 3H, C(14)H₃), 6.16 (s, 1H, C(9)H), 7.13 (d, 2H, C(12)H, C(12')H, $J = 8.0$ Hz), 7.18 (d, 2H, C(11)H, C(11')H, $J = 8.0$ Hz), 7.44 (d, 1H, C(3)H, $J = 8.8$ Hz), 7.59 (d, 1H, C(7)H, $J = 9.2$ Hz), 7.75 (d, 1H, C(8)H, $J = 9.2$ Hz), 7.98 (d, 1H, C(4)H, $J = 8.8$ Hz), 8.24 (s, 1H, C(5)H), 8.86 (s, 1H, NH) ppm; $^{13}\text{C-NMR}$ (DMSO- d_6 , 100 MHz): $\delta = 20.6$ (C14), 53.3 (C9), 114.5 (C1), 118.2 (C6), 118.2 (C3), 125.4 (C8), 126.8 (C11, C11'), 127.6 (C8a), 129.4 (C4), 129.5

Table 2. Crystal data and structure refinement parameters for **8a**.

Parameters	8a
Formula	C ₁₂ H ₉ NOS
Formula weight	215.26
Crystal system	Monoclinic
Space group	$P2_1/n$
Z	4
<i>a</i> , Å	5.0351 (10)
<i>b</i> , Å	10.062 (2)
<i>c</i> , Å	19.736 (4)
β , deg	90.10 (3)
<i>V</i> , Å ³	999.9 (3)
<i>T</i> , K	293 (2)
$\lambda(\text{MoK}_{\alpha})$, Å	0.71073
μ , mm ⁻¹	0.291
<i>D</i> _{calcd} , g/cm ³	1.430
<i>F</i> (000)	448
Collected reflections	9967
Unique reflections	2690
<i>R</i> _{int}	0.0840
GOF on <i>F</i> ²	0.971
<i>R</i> ₁ ^a , <i>R</i> _w ^b [<i>I</i> > 2σ (<i>I</i>)]	0.0467, 0.1067
<i>R</i> ₁ , <i>R</i> _w (all data)	0.1004, 0.1307
$\Delta\rho$ max/min (e Å ⁻³)	0.260, -0.204

$$^a) R_1 = \frac{\sum ||F_o| - |F_c||}{\sum |F_o|} \quad ^b) R_w = \left[\frac{\sum \{w(F_o^2 - F_c^2)^2\}}{\sum \{w(F_o^2)^2\}} \right]^{1/2}$$

(C12, C12'), 130.1 (C7), 130.4 (C5), 131.7 (C4a), 137.4 (C13), 139.7 (C10), 147.7 (C2), 149.0 (C15) ppm; FT-IR ($\bar{\nu}$): 3149 cm⁻¹ (m), 1747 cm⁻¹ (s), 1582 cm⁻¹ (m), 1499 cm⁻¹ (m), 1219 cm⁻¹ (s), 1109 cm⁻¹ (m); HRMS (ESI): found 368.0273, calcd. for C₁₉H₁₄NO₂Br [M+H]⁺ *m/z* = 368.0281.

8-Bromo-1-(p-tolyl)-1,2-dihydro-3H-naphth[1,2-e][1,3]-oxazine-3-thione (rac-6)

To a suspension of **11** (0.20 g, 0.5 mmol) in 10 mL tetrahydrofuran, 1,1'-thiocarbonyldiimidazole (0.13 g, 0.74 mmol, 1.4 equiv.) was added in a G30 vial. The vial cap was closed and the vial was placed in the reaction chamber of the microwave reactor. The reaction was conducted at 250 W maximum to reach the reaction temperature of 100°C within 5 min and temperature was held for 10 min. Afterwards the solvent was evaporated and residue was purified by column chromatography (*n*-hexane/ethyl acetate/acetic acid; 10:10:1). Product was crystallized from ethyl acetate/*n*-hexane, yielding compound as colorless needles. Yield: 0.08 g (38.6%); mp: 207.5°C; $^1\text{H-NMR}$ (DMSO- d_6 , 400 MHz): $\delta = 2.23$ (s, 3H, C(14)H₃), 6.20 (s, 1H, C(9)H), 7.14 (d, 2H, C(12)H, C(12')H, $J = 8.8$ Hz), 7.17 (d, 2H, C(11)H, C(11')H, $J = 8.8$ Hz), 7.53 (d, 1H, C(3)H, $J = 8.8$ Hz), 7.61 (d, 1H, C(7)H, $J = 8.8$ Hz), 7.74 (d, 1H, C(8)H, $J = 8.8$ Hz), 8.02 (d, 1H, C(4)H, $J = 9.2$ Hz), 8.28 (s, 1H, C(5)H), 11.11 (s, 1H, NH) ppm; $^{13}\text{C-NMR}$ (DMSO- d_6 , 100 MHz): $\delta = 20.6$ (C14), 53.5 (C9), 119.8 (C1), 117.5 (C3), 118.7 (C6), 125.4 (C8), 127.2 (C11, C11'), 127.3 (C8a), 129.5 (C12, C12'), 129.8 (C4), 130.3 (C7), 130.5 (C5), 132.2

(C4a), 137.8 (C13), 138.3 (C10), 146.3 (C2), 180.0 (C15) ppm; FT-IR (ν): 3198 cm^{-1} (m), 1584 cm^{-1} (m), 1496 cm^{-1} (s), 1145 cm^{-1} (s), 1081 cm^{-1} (m); HRMS (ESI): found 384.0066, calcd. for $\text{C}_{19}\text{H}_{14}\text{NOSBr}$ $[\text{M}+\text{H}]^+$ $m/z = 384.0052$.

1,2-Dihydro-3H-naphtho[1,2-e][1,3]oxazin-3-one (7a)

To a solution of **17** (2.26 g, 10.8 mmol) in dioxane (20 mL) was added triethylamine (1.65 mL, 1.20 g, 11.8 mmol, 1.1 equiv.) while stirring under nitrogen atmosphere at room temperature. Subsequently, 4-nitrophenyl chloroformate (1.94 g, 9.6 mmol, 1.0 equiv.) pre-dispersed in dioxane (10 mL) was added dropwise. After addition was complete, the reaction was stirred for further 10 min and then solid was collected by filtration. Solid was dissolved in 50 mL dichloromethane and extracted 3 times with 30 mL ammonia-ammonium chloride buffer (pH 9). Addition of 5 mL acetic acid to organic phase caused a precipitation. Solid was recrystallized from toluene yielding product as white needle-shaped crystals. Yield: 0.138 g (7.2%); mp: 193.7°C (degrad.); $^1\text{H-NMR}$ (DMSO- d_6 , 400 MHz): $\delta = 4.80$ (s, 2H, C(9)H₂), 7.23 (d, 1H, C(3)H, $J = 9.2$ Hz), 7.52 (t, 1H, C(6)H, $J = 7.6$ Hz), 7.60 (t, 1H, C(7)H, $J = 7.6$ Hz), 7.75 (d, 1H, C(8)H, $J = 8.2$ Hz), 7.91 (d, 1H, C(4)H, $J = 9.2$ Hz), 7.96 (d, 1H, C(5)H, $J = 8.0$ Hz), 8.23 (s, 1H, N(10)H) ppm; $^{13}\text{C-NMR}$ (DMSO- d_6 , 100 MHz): $\delta = 39.9$ (C9), 110.0 (C1), 116.6 (C3), 122.4 (C8), 125.1 (C6), 127.3 (C7), 128.4 (C5), 129.1 (C8a), 129.3 (C4), 129.9 (C4a), 147.0 (C2), 149.4 (C19) ppm; FT-IR (ν): 3241 cm^{-1} (w), 3150 cm^{-1} (w), 1732 cm^{-1} (s), 1634 cm^{-1} (w), 1380 cm^{-1} (m), 1215 cm^{-1} (m), 1171 cm^{-1} (s), 743 cm^{-1} (s); $\text{C}_{12}\text{H}_9\text{NO}_2$ (199.06): calcd.: C, 72.35; H, 4.55; N, 7.03; found C, 72.54; H, 4.32; N, 7.41 [28].

8-Bromo-1,2-dihydro-3H-naphtho[1,2-e][1,3]oxazin-3-one (7b)

To a solution of **18** (1.13 g, 3.91 mmol) in dioxane (30 mL) was added triethylamine (2.44 mL, 1.77 g, 17.5 mmol, 4.5 equiv.) while stirring under nitrogen atmosphere at room temperature. Further 20 mL dioxane and 10 mL dimethylformamide were added because of poor solubility. Subsequently, 4-nitrophenyl chloroformate (0.75 g, 3.7 mmol, 1.0 equiv.) pre-dispersed in dioxane (10 mL) was added dropwise. After addition was complete, the reaction mixture was stirred for a further 10 min at room temperature and then heated up to reflux for 1 h. While heating reaction color had changed to orange. After reaction was stirred for further 10 h at room temperature, dioxane was removed in rotary evaporator. A solid precipitated when 30 mL dichloromethane and 30 mL aqueous sodium carbonate solution (8%) were added to oily residue. The solid was collected by filtration off and was recrystallized from toluene yielding product as beige needle-shaped crystals. Yield: 0.183 g (17.8%); mp: 231.9°C (degrad.); $^1\text{H-NMR}$ (DMSO- d_6 , 400 MHz): $\delta = 4.78$ (s, 2H, C(9)H₂), 7.29 (d, 1H, C(3)H, $J = 9.2$ Hz), 7.68–7.73 (m, 2H, C(7,8)H), 7.91 (d, 1H, C(4)H, $J = 8.8$ Hz), 8.24 (s, 1H, C(5)H), 8.25 (s, 1H, N(10)H) ppm; $^{13}\text{C-NMR}$ (DMSO- d_6 , 100 MHz): $\delta = 39.8$ (C9), 110.5 (C1), 118.0 (C3), 118.2 (C6), 124.9 (C8), 127.8 (C8a), 128.6 (C4), 130.1 (C7), 130.2 (C5), 131.2 (C4a), 147.4 (C2), 149.2 (C19) ppm; FT-IR (ν):

3234 cm^{-1} (w), 3117 cm^{-1} (w), 2956 cm^{-1} (w), 1726 cm^{-1} (s), 1498 cm^{-1} (m), 1220 cm^{-1} (m), 808 cm^{-1} (s); $\text{C}_{12}\text{H}_8\text{BrNO}_2$ (276.97): calcd.: C, 51.83; H, 2.90; N, 5.04; found C, 51.82; H, 2.78; N, 5.43 [42].

2-(3-Morpholinopropyl)-1,2-dihydro-3H-naphtho[1,2-e][1,3]oxazin-3-one (7c)

To an emulsion of **19** (1.12 g, 3.0 mmol) in 40 mL toluene/water (1:1) was added triethylamine (2.51 mL, 1.82 g, 18.0 mmol) while stirring under argon atmosphere. To the ice-cooled reaction mixture, a 20% solution of phosgene in toluene (2.33 mL, 4.5 mmol) was added. Reaction was stirred for 6 h at room temperature and quenched by addition of ethyl acetate (40 mL) and 0.1 M hydrochloric acid solution (40 mL). The phases were separated and the organic phase was dried with sodium sulfate and concentrated *in vacuo*. Meanwhile, the aqueous phase was pH-adjusted to pH 9 with sodium carbonate and extracted with ethyl acetate (3 \times 50 mL). Ethyl acetate phase was dried with sodium sulfate and hydrochloric acid gas was injected. The solid formed was collected by filtration, dissolved in 50 mL 1 M sodium hydroxide solution and extracted with ethyl acetate (3 \times 50 mL). Organic phase was dried over sodium sulfate and concentrated *in vacuo*. Both residues were combined, purified by column chromatography (diethyl ether/isopropanol/ammonia, 10:3:0.1) and recrystallized from ethyl acetate/isopropanol (5:1) yielding product as colorless crystals. Yield: 0.11 g (11.0%); mp: 98.5°C; $^1\text{H-NMR}$ (DMSO- d_6 , 400 MHz): $\delta = 1.83$ –1.90 (m, 2H, C(12)H₂), 2.35 (t, 6H, C(13,15,18)H₂, $J = 6.8$ Hz), 3.50–3.54 (m, 6H, C(11,16,17)H₂), 4.93 (s, 2H, C(9)H₂), 7.24 (d, 1H, C(3)H, $J = 9.2$ Hz), 7.52 (t, 1H, C(6)H, $J = 7.6$ Hz), 7.63 (t, 1H, C(7)H, $J = 7.6$ Hz), 7.80 (d, 1H, C(8)H, $J = 8.0$ Hz), 7.92 (d, 1H, C(4)H, $J = 8.8$ Hz), 7.97 (d, 1H, C(5)H, $J = 8.0$ Hz) ppm; $^{13}\text{C-NMR}$ (DMSO- d_6 , 100 MHz): $\delta = 22.8$ (C12), 45.5 (C9), 47.3 (C11), 53.3 (C15,18), 55.5 (C13), 66.1 (C16,17), 110.3 (C1), 116.3 (C3), 122.4 (C8), 125.1 (C6), 127.3 (C7), 128.5 (C5), 128.9 (C8a), 129.3 (C4), 129.8 (C4), 129.8 (C4a), 146.6 (C2), 149.1 (C19) ppm; FT-IR (ν): 3083 cm^{-1} (w), 2947 cm^{-1} (w), 1699 cm^{-1} (m), 1225 cm^{-1} (m), 822 cm^{-1} (m), 744 cm^{-1} (m); HRMS (ESI): found 327.1703, calcd. for $\text{C}_{19}\text{H}_{22}\text{N}_2\text{O}_3$ $[\text{M}+\text{H}]^+$ $m/z = 327.1703$.

8-Bromo-2-(3-morpholinopropyl)-1,2-dihydro-3H-naphtho[1,2-e][1,3]oxazin-3-one (7d)

To an emulsion of **20** (0.45 g, 1.0 mmol) in 40 mL toluene/water (1:1) was added triethylamine (0.84 mL, 0.61 g, 6.0 mmol) while stirring under argon atmosphere. To the ice-cooled reaction mixture, a 20% solution of phosgene in toluene (0.77 mL, 1.5 mmol) was added and reaction was stirred for 4 h at room temperature. The emerged product as white solid was collected by filtration. More product was obtained by addition of 0.1 N hydrochloric acid solution (40 mL) to filtrate and following filtration. Then filtrate was pH adjusted to pH 11 and subsequently extracted with ethyl acetate (40 mL). Organic phase was dried with sodium sulfate and hydrochloric acid gas was injected. The emerged

white solid was collected by filtration. The solids were combined yielding product as white crystals. Yield: 0.17 g (38.4%); mp: 257.9°C (degrad.); ¹H-NMR (DMSO-d₆, 400 MHz): δ = 1.82–1.89 (m, 2H, C(12)H₂), 2.35 (t, 6H, C(13,15,18)H₂, J = 6.8 Hz), 3.50–3.53 (m, 6H, C(11,16,17)H₂), 7.29 (d, 1H, C(3)H, J = 8.8 Hz), 4.91 (s, 2H, C(9)H₂), 7.43 (d, 1H, C(7)H, J = 9.2 Hz), 7.76 (d, 1H, C(8)H, J = 8.8 Hz), 7.91 (d, 1H, C(4)H, J = 8.8 Hz), 8.26 (s, 1H, C(5)H) ppm; ¹³C-NMR (DMSO-d₆, 100 MHz): δ = 22.7 (C12), 45.4 (C9), 47.4 (C11), 53.3 (C15,18), 55.6 (C13), 66.2 (C16,17), 110.8 (C1), 117.6 (C3), 118.2 (C6), 124.8 (C8), 127.6 (C8a), 128.7 (C4), 130.1 (C7), 130.1 (C7), 130.3 (C5), 131.2 (C4a), 147.0 (C2), 148.9 (C19) ppm; FT-IR (ν): 3075 cm⁻¹ (w), 2981 cm⁻¹ (w), 2548 cm⁻¹ (w), 2468 cm⁻¹ (w), 1716 cm⁻¹ (m), 1108 cm⁻¹ (m), 821 cm⁻¹ (w); HRMS (ESI): found 405.0808, calcd. for C₁₉H₂₁BrN₂O₃ [M+H]⁺ m/z = 405.0808.

1,2-Dihydro-3H-naphth[1,2-e][1,3]oxazine-3-thione (8a)

A suspension of **17** (3.13 g, 15.0 mmol) in methanol (40 mL) was stirred at room temperature. Successively triethylamine (3.1 mL, 2.25 g, 22.5 mmol, 1.5 equiv.) and carbon disulfide (2.72 mL, 3.43 g, 45.0 mmol, 3.0 equiv.) were added. The pale yellow solution was stirred for 1 h at room temperature. Via dropping funnel hydrogen peroxide (6.0 mL, 58.7 mmol, 3.9 equiv.) was added in such a manner as the solution boiled slightly. After addition was completed, the solution was allowed cooling to room temperature. After 1 h the formed precipitate was collected by filtration and washed with methanol (3 × 20 mL). Colorless solid was used in next step without further purification. Yield: 0.789 g (24.4%); mp: 181°C (degrad.); ¹H-NMR (DMSO-d₆, 400 MHz): δ = 4.80 (s, 2H, C(9)H₂), 7.32 (d, 1H, C(3)H, J = 8.8 Hz), 7.55 (t, 1H, C(6)H, J = 7.6 Hz), 7.63 (t, 1H, C(7)H, J = 7.6 Hz), 7.75 (d, 1H, C(8)H, J = 8.0 Hz), 7.96 (d, 1H, C(4)H, J = 8.8 Hz), 7.99 (d, 1H, C(5)H, J = 8.8 Hz), 10.54 (s, 1H, N(10)H) ppm; ¹³C-NMR (DMSO-d₆, 100 MHz): δ = 40.06 (C9), 109.4 (C1), 116.0 (C3), 122.6 (C8), 125.6 (C6), 127.5 (C7), 128.5 (C5), 128.9 (C8a), 129.6 (C4), 130.4 (C4a), 145.3 (C2), 180.9 (C19) ppm; FT-IR (ν): 3164 cm⁻¹ (w), 3085 cm⁻¹ (w), 2993 cm⁻¹ (w), 1636 cm⁻¹ (w), 1580 cm⁻¹ (m), 1175 cm⁻¹ (s), 1149 cm⁻¹ (s), 806 cm⁻¹ (s), 746 cm⁻¹ (s). Product was confirmed by X-ray crystallography.

Alternative synthesis of 1,2-dihydro-3H-naphth[1,2-e][1,3]oxazine-3-thione (8a)

To a solution of **9** (1.71 g, 8.5 mmol) in dichloromethane (35 mL) was added methyl iodide (1.59 mL, 3.61 g, 25.4 mmol, 3.0 equiv.). After 7 h stirring at room temperature, the solid was collected by filtration and washed with dichloromethane (2 × 50 mL). Solid was used directly in the crude form for next step. So a suspension of crude intermediate product (1.722 g, 5.0 mmol) and potassium thiocyanate (0.99 g, 10.3 mmol) in butanone (50 mL) was heated to reflux. After 24 h, reaction mixture was allowed to cool down to room temperature and solvent was removed in rotary evaporator. Afterwards 100 mL 0.25 M aqueous hydrochloric acid solution was added and solid was collected by filtration. Crude product was washed with acetone (2 × 20 mL), H₂O (2 × 50 mL), methanol

(2 × 50 mL) and was recrystallized from ethyl acetate, yielding product **8a** as colorless crystals. Yield: 0.18 g (9.8%); mp: 181°C (decomp.); ¹H-NMR (DMSO-d₆, 400 MHz): δ = 4.80 (s, 2H, C(9)H₂), 7.32 (d, 1H, C(3)H, J = 8.8 Hz), 7.55 (t, 1H, C(6)H, J = 7.6 Hz), 7.63 (t, 1H, C(7)H, J = 7.6 Hz), 7.74 (d, 1H, C(8)H, J = 8.4 Hz), 7.95 (d, 1H, C(4)H, J = 9.2 Hz), 7.98 (d, 1H, C(5)H, J = 8.0 Hz), 10.56 (s, 1H, N(10)H) ppm; ¹³C-NMR (DMSO-d₆, 100 MHz): δ = 40.1 (C9), 109.4 (C1), 116.0 (C3), 122.6 (C8), 125.6 (C6), 127.5 (C7), 128.5 (C5), 128.9 (C8a), 129.6 (C4), 130.4 (C4a), 145.3 (C2), 180.9 (C19) ppm; FT-IR (ν): 3164 cm⁻¹ (w), 3085 cm⁻¹ (w), 2993 cm⁻¹ (w), 1636 cm⁻¹ (w), 1580 cm⁻¹ (m), 1175 cm⁻¹ (s), 1149 cm⁻¹ (s), 806 cm⁻¹ (s), 746 cm⁻¹ (s). Product confirmed by X-ray crystallography.

8-Bromo-1,2-dihydro-3H-naphth[1,2-e][1,3]oxazine-3-thione (8b)

To a solution of **10** (3.08 g, 11.0 mmol) in dichloromethane (20 mL) was added methyl iodide (2.06 mL, 4.68 g, 33.0 mmol, 3.0 equiv.). After 7 h stirring at room temperature the solid was collected by filtration and washed with dichloromethane (2 × 50 mL). Solid was used directly in the crude form for next step. So a suspension of crude intermediate product (2.988 g, 7.1 mmol) and potassium thiocyanate (1.37 g, 14.1 mmol) in butanone (60 mL) was heated to reflux. After 24 h, reaction mixture was allowed to cool down to room temperature. Afterwards 10 mL 1 M aqueous hydrochloric acid solution were added and solid was collected by filtration. Crude product was washed with acetone (2 × 20 mL), H₂O (2 × 50 mL), methanol (2 × 50 mL) and was recrystallized from ethyl acetate, yielding product **8b** as colorless crystals. Yield: 0.31 g (9.4%); mp: 255°C (decomp.); ¹H-NMR (DMSO-d₆, 400 MHz): δ = 4.79 (s, 2H, C(9)H₂), 7.38 (d, 1H, C(3)H, J = 8.8 Hz), 7.72 (m, 2H, C(4)H, C(8)H), 7.95 (d, 1H, C(7)H, J = 9.2 Hz), 8.28 (s, 1H, C(5)H), 10.58 (s, 1H, NH) ppm; ¹³C-NMR (DMSO-d₆, 100 MHz): δ = 40.1 (C9), 110.0 (C1), 117.4 (C3), 118.7 (C6), 125.0 (C8), 127.6 (C8a), 128.9 (C7), 130.3 (C4, C5), 131.7 (C4a), 145.6 (C2), 180.7 (C=S) ppm; FT-IR (ν): 3343 cm⁻¹ (m), 3065 cm⁻¹ (w), 1635 cm⁻¹ (m), 1502 cm⁻¹ (s), 1173 cm⁻¹ (s), 1139 cm⁻¹ (s); HRMS (ESI): found 293.9569, calcd. for C₁₂H₈BrNOS [M+H]⁺ m/z = 293.9583.

2-(3-Morpholinopropyl)-1,2-dihydro-3H-naphth[1,2-e][1,3]oxazine-3-thione (8c)

To a suspension of **19** (0.75 g, 2.0 mmol) in dichloromethane (40 mL) triethylamine (1.39 mL, 1.01 g, 10.0 mmol) was added under argon atmosphere. While stirring in an ice bath, thiophosgene (0.25 mL, 0.37 g, 3.0 mmol) dissolved in 10 mL dichloromethane was added dropwise. After addition was complete, ice bath was removed and reaction was stirred for 2 h at room temperature. Reaction mixture was extracted with water (2 × 20 mL) and finally organic phase was extracted with 0.5 N hydrochloric acid (20 mL). Dichloromethane phase was dried with anhydrous sodium sulfate and concentrated *in vacuo*. Residue was diluted in less dichloromethane and extracted with aqueous sodium hydroxide solution (2 × 10 mL). Organic phase was dried with

sodium sulfate and concentrated *in vacuo*. Solid residue was recrystallized from ethyl acetate/isopropanol (5:1) yielding pale brownish crystals. Yield: 0.32 g (42.3%); mp: 144°C; ¹H-NMR (DMSO-*d*₆, 400 MHz): δ = 1.99–2.07 (m, 2H, C(12)H₂), 2.35–2.41 (m, 6H, C(13,15,18)H₂), 3.48 (t, 4H, C(16,17)H₂, *J* = 4.6 Hz), 4.03 (t, 2H, C(11)H₂, *J* = 7.2 Hz), 4.54 (s, 2H, C(9)H₂), 7.32 (d, 1H, C(3)H, *J* = 9.2 Hz), 7.56 (t, 1H, C(6)H, *J* = 7.6 Hz), 7.65 (t, 1H, C(7)H, *J* = 7.6 Hz), 7.82 (d, 1H, C(8)H, *J* = 8.0 Hz), 7.96 (d, 1H, C(4)H, *J* = 8.8 Hz), 7.99 (d, 1H, C(5)H, *J* = 8.0 Hz) ppm; ¹³C-NMR (DMSO-*d*₆, 100 MHz): δ = 21.3 (C12), 46.3 (C9), 53.2 (C15,18), 53.9 (C11), 55.4 (C13), 66.1 (C16,17), 110.2 (C1), 115.5 (C3), 115.5 (C3), 122.4 (C8), 125.6 (C6), 127.5 (C7), 128.6 (C8a,5), 129.6 (C4), 130.3 (C4a), 144.8 (C2), 179.9 (C19) ppm; FT-IR (ν): 3054 cm⁻¹ (w), 2976 cm⁻¹ (w), 1200 cm⁻¹ (m), 1110 cm⁻¹ (s), 811 cm⁻¹ (m), 745 cm⁻¹ (m); HRMS (ESI): found 343.1475, calcd. for C₁₉H₂₂N₂O₂S [M+H]⁺ *m/z* = 343.1475.

Alternative synthesis of 2-(3-morpholinopropyl)-1,2-dihydro-3H-naphth[1,2-*e*][1,3]oxazine-3-thione (8c)

To a suspension of **19** (1.12 g, 3.0 mmol) in tetrahydrofuran (10 mL) was added 1,1'-thiocarbonyldiimidazole (0.54 g, 3.0 mmol) pre-dissolved in 5 mL tetrahydrofuran while stirring under argon atmosphere. Reaction mixture was stirred 43 h at room temperature, and then solvent was removed in rotary evaporator. Aqueous sodium hydroxide solution (50 mL, 1 N) was added to residue and solution was extracted with ethyl acetate (3 × 50 mL). Organic phases were combined and washed with water (2 × 30 mL). Ethyl acetate phase was dried over anhydrous sodium sulfate and concentrated *in vacuo*. Residue was recrystallized from ethyl acetate/isopropanol (5:1) yielding desired product as pale brownish crystals. Yield: 0.52 g (50.0%); mp: 144°C; ¹H-NMR (DMSO-*d*₆, 400 MHz): δ = 1.99–2.07 (m, 2H, C(12)H₂), 2.35–2.41 (m, 6H, C(13,15,18)H₂), 3.48 (t, 4H, C(16,17)H₂, *J* = 4.6 Hz), 4.03 (t, 2H, C(11)H₂, *J* = 7.2 Hz), 4.54 (s, 2H, C(9)H₂), 7.32 (d, 1H, C(3)H, *J* = 9.2 Hz), 7.56 (t, 1H, C(6)H, *J* = 7.6 Hz), 7.65 (t, 1H, C(7)H, *J* = 7.6 Hz), 7.82 (d, 1H, C(8)H, *J* = 8.0 Hz), 7.96 (d, 1H, C(4)H, *J* = 8.8 Hz), 7.99 (d, 1H, C(5)H, *J* = 8.0 Hz) ppm; ¹³C-NMR (DMSO-*d*₆, 100 MHz): δ = 21.3 (C12), 46.3 (C9), 53.2 (C15,18), 53.9 (C11), 55.4 (C13), 66.1 (C16,17), 110.2 (C1), 115.5 (C3), 115.5 (C3), 122.4 (C8), 125.6 (C6), 127.5 (C7), 128.6 (C8a,5), 129.6 (C4), 130.3 (C4a), 144.8 (C2), 179.9 (C19) ppm; FT-IR (ν): 3054 cm⁻¹ (w), 2976 cm⁻¹ (w), 1200 cm⁻¹ (m), 1110 cm⁻¹ (s), 811 cm⁻¹ (s), 745 cm⁻¹ (s).

8-Bromo-2-(3-morpholinopropyl)-1,2-dihydro-3H-naphth[1,2-*e*][1,3]oxazine-3-thione (8d)

To a suspension of **20** (0.90 g, 2.0 mmol) in dichloromethane (15 mL), triethylamine (1.39 mL, 1.01 g, 10.0 mmol) was added under argon atmosphere. While stirring in an ice bath, thiophosgene (0.25 mL, 0.37 g, 3.0 mmol) dissolved in 10 mL dichloromethane was added dropwise. After addition was complete, ice bath was removed and reaction was stirred for 3 h at room temperature. Reaction mixture was extracted with water (2 × 20 mL) and afterwards organic phase was extracted with 0.5 M hydrochloric acid (20 mL). Finally the

dichloromethane phase was extracted with aqueous sodium hydroxide solution (2 × 10 mL), dried with anhydrous sodium sulfate and concentrated *in vacuo*. Residue was purified with column chromatography (diethyl ether/isopropanol/25% ammonia solution, 10:3:0.1) yielding product as pale brownish platelets. Yield: 0.11 g (12.9%); mp: 167°C (degrad.); ¹H-NMR (DMSO-*d*₆, 400 MHz): δ = 1.99–2.06 (m, 2H, C(12)H₂), 2.35–2.41 (m, 6H, C(13,15,18)H₂), 3.47 (t, 4H, C(16,17)H₂, *J* = 4.4 Hz), 4.01 (t, 2H, C(11)H₂, *J* = 7.4 Hz), 5.07 (s, 2H, C(9)H₂), 7.38 (d, 1H, C(3)H, *J* = 8.8 Hz), 7.78 (s, 1H, C(7,8)H), 7.95 (d, 1H, C(4)H, *J* = 8.8 Hz), 8.30 (s, 1H, C(5)H) ppm; ¹³C-NMR (DMSO-*d*₆, 100 MHz): δ = 21.3 (C12), 46.1 (C9), 53.2 (C15,18), 54.0 (C11), 55.4 (C13), 66.1 (C16,17), 110.7 (C1), 116.9 (C3), 118.7 (C6), 124.8 (C8), 127.3 (C8a), 128.9 (C4), 130.3 (C7), 130.4 (C5), 131.6 (C4a), 145.1 (C2), 179.7 (C19) ppm; FT-IR (ν): 3068 cm⁻¹ (w), 2950 cm⁻¹ (w), 1536 cm⁻¹ (m), 1353 cm⁻¹ (m), 1204 cm⁻¹ (m), 1109 cm⁻¹ (m), 808 cm⁻¹ (m); HRMS (ESI): found 443.0399, calcd. for C₁₉H₂₁BrN₂O₂S [M+Na]⁺ *m/z* = 443.0399.

1-[(Dimethylamino)methyl]naphthalen-2-ol (9)

To a suspension of 2-naphthol (5.85 g, 40.2 mmol), dimethylmethylideneammonium iodide (97%, 7.58 g, 39.7 mmol, 1.0 equiv.) and potassium carbonate (8.31 g, 60.1 mmol, 1.5 equiv.) in toluene (20 mL) was added 30 mL dichloromethane. After stirring for 24 h at room temperature, the reaction mixture was extracted with 3 × 60 mL 1 M aqueous hydrochloric acid solution. Phases were separated and potassium carbonate was added to the aqueous phase adjusting the pH to 8, whereby product precipitation emerged. The aqueous phase was stored at 5°C for 5 h and the white solid was collected by filtration, yielding **9** as white crystals. Yield: 7.98 g (98.7%); mp: 74.5°C; ¹H-NMR (DMSO-*d*₆, 400 MHz): δ = 3.98 (s, 2H, C(9)H₂), 7.06 (d, 1H, C(3)H, *J* = 8.8 Hz), 7.27 (t, 1H, C(6)H, *J* = 8.0 Hz), 7.43 (t, 1H, C(7)H, *J* = 8.4 Hz), 7.70 (d, 1H, C(8)H, *J* = 8.8 Hz), 7.77 (d, 1H, C(4)H, *J* = 8.0 Hz), 7.94 (d, 1H, C(5)H, *J* = 8.4 Hz) ppm; ¹³C-NMR (DMSO-*d*₆, 100 MHz): δ = 44.3 (N(CH₃)₂), 55.4 (C9), 113.0 (C8a), 118.5 (C3), 122.2 (C5, C6), 126.1 (C7), 127.9 (C1), 128.3 (C4), 128.7 (C8), 132.9 (C4a), 155.4 (C2) ppm; FT-IR (ν): 3380 cm⁻¹ (w), 3006 cm⁻¹ (w), 2950 cm⁻¹ (w), 1626 cm⁻¹ (s), 1439 cm⁻¹ (m), 1322 cm⁻¹ (m), 1245 cm⁻¹ (s); HRMS (ESI): found 202.1226, calcd. for C₁₃H₁₅NO [M+H]⁺ *m/z* = 202.1226 [12].

6-Bromo-1-[(dimethylamino)methyl]naphthalen-2-ol (10)

To a suspension of 6-bromo-2-naphthol (9.20 g, 40.0 mmol), dimethylmethylideneammonium iodide (97%, 7.62 g, 40.0 mmol, 1.0 equiv.) and potassium carbonate (8.30 g, 60.0 mmol, 1.5 equiv.) in toluene (30 mL) was added 20 mL dichloromethane. The suspension was stirred 16 h at room temperature. Product was gained as a solid by filtering the reaction mixture. In addition 0.2 M hydrochloric acid solution (50 mL) was added to the filtrate. Phases were separated and 2.0 g potassium carbonate was added to the aqueous phase, whereby product **10** emerged as a voluminous precipitate. Solids were combined and washed with water (3 × 50 mL) yielding **10** as colorless solid. Yield: 10.35 g

(92.4%); mp: 178°C; ¹H-NMR (DMSO-d₆, 400 MHz): δ = 2.28 (s, 6H, N(CH₃)₂), 3.96 (s, 2H, C(9)H₂), 7.12 (d, 1H, C(3)H, J = 8.8 Hz), 7.53 (d, 1H, C(4)H, J = 9.2 Hz), 7.71 (d, 1H, C(8)H, J = 8.8 Hz), 7.91 (d, 1H, C(9)H, J = 8.8 Hz), 8.04 (s, 1H, C(6)H), 11.33 (s, 1H, OH) ppm; ¹³C-NMR (DMSO-d₆, 100 MHz): δ = 44.3 (N(CH₃)₂), 55.0 (C9), 113.5 (C1), 115.0 (C6), 119.7 (C3), 124.9 (C8), 128.0 (C7), 128.8 (C4), 129.3 (C4a), 129.9 (C5), 131.7 (C8a), 155.7 (C2) ppm; FT-IR (ν̄): 3195 cm⁻¹ (m), 3036 cm⁻¹ (w), 2955 cm⁻¹ (w), 1357 cm⁻¹ (m), 1270 cm⁻¹ (s); HRMS (ESI): found 280.0332, calcd. for C₁₃H₁₄BrNO [M+H]⁺ m/z = 280.0332.

(6-Bromo-2-hydroxynaphthalen-1-yl)(p-tolyl)-methanaminium chloride (11)

To a flask containing 6-bromo-2-naphthol (2.23 g, 10.0 mmol) and ammonium formate (1.1 g, 22.3 mmol, 2.2 equiv.) was added 4-methylbenzaldehyde (3.36 mL, 2.40 g, 2.0 equiv). Reaction mixture was heated to 110°C for 15 min and was allowed to cool down to room temperature. To the solid residue 50 mL water and 2 mL HCl (36%) were added and the slurry was heated for 2 h to 100°C. The solid was collected by filtration and was subsequently diluted again in 50 mL water and 1 mL H₂SO₄ (96%) and then heated for 15 h to 70°C. Slurry was stored at 5°C for 1 h. Solid was collected by filtration and was refluxed in ethyl acetate. The product was collected by filtration of hot slurry. Procedure was repeated for the insoluble precipitate yielding product as colorless crystals. Yield: 1.15 g (30.4%); mp: 188°C (degrad.); ¹H-NMR (DMSO-d₆, 400 MHz): δ = 2.26 (s, 3H, C(14)H₃), 6.20 (s, 1H, C(9)H), 7.16 (d, 2H, C(12)H, C(12')H, J = 8.0 Hz), 7.37 (d, 2H, C(11)H, C(11')H, J = 8.4 Hz), 7.52 (d, 1H, C(3)H, J = 8.8 Hz), 7.56 (d, 1H, C(7)H, J = 8.8 Hz), 7.87 (d, 1H, C(4)H, J = 8.8 Hz), 7.97 (d, 1H, C(8)H, J = 9.2 Hz), 8.14 (s, 1H, C(5)H), 8.91 (s, 3H, N⁺H₃), 11.22 (s, 1H, OH) ppm; ¹³C-NMR (DMSO-d₆, 100 MHz): δ = 20.6 (C14), 50.5 (C9), 114.3 (C1), 115.7 (C6), 119.9 (C3), 124.4 (C8), 127.1 (C11, 11'), 129.0 (C12, 12'), 129.4 (C4a), 129.7 (C4), 129.8 (C7), 130.4 (C5), 130.5 (C8a), 134.3 (C13), 137.4 (C10), 154.3 (C2) ppm; FT-IR (ν̄): 3059 cm⁻¹ (m), 2903 cm⁻¹ (m), 1517 cm⁻¹ (s), 1503 cm⁻¹ (s), 1273 cm⁻¹ (s), 455 cm⁻¹ (s); HRMS (ESI): found 325.0209, calcd. for C₁₈H₁₃OBr [M+H]⁺ m/z = 325.0223.

1-([1H-Naphtho[1,2-e][1,3]oxazin-2(3H)-yl]methyl)-naphthalen-2-ol (12)

A suspension of 2-naphthol (7.26 g, 50.4 mmol), paraformaldehyde (3.07 g, 102.1 mmol, 2.0 equiv.) and ammonium formate (4.98 g, 78.9 mmol, 1.5 equiv.) in dimethylformamide (30 mL) was heated to 120°C for 20 min. Within 15 min mixture turned into a homogeneous yellow solution. Then reaction mixture was allowed to cool down to room temperature and was poured into 600 mL water. The mixture was stored 1 h at 5°C and precipitate was collected by filtration. The collected solid was recrystallized from ethanol, yielding product **12** as pale pink needle-shaped crystals. Yield: 2.76 g (32.1%); mp: 162°C; ¹H-NMR (DMSO-d₆, 400 MHz): δ = 4.25 (s, 2H, C(9)H₂), 4.35 (s, 2H, C(9')H₂), 5.02 (s, 2H, C(10)H₂), 7.11 (d, 1H, C(3)H, J = 8.8 Hz), 7.15 (d, 1H, C(3')H, J = 8.8 Hz), 7.30 (t, 1H, C(6')H, J = 7.6 Hz), 7.36 (t, 1H, C(6)H, J = 7.6 Hz), 7.44 (m, 2H, C(7)H, C

(7')H), 7.78 (d, 1H, C(8')H, J = 8.4 Hz), 7.74 (dd, 2H, C(4')H, C(4)H, J = 8.8 Hz), 7.79 (d, 1H, C(5')H, J = 8.0 Hz), 7.84 (d, 1H, C(5)H, J = 8.0 Hz), 8.06 (d, 1H, C(8)H, J = 8.4 Hz), 9.63 (s, 1H, OH) ppm; ¹³C-NMR (DMSO-d₆, 100 MHz): δ = 45.1 (C9'), 46.0 (C9), 82.0 (C10), 112.4 (C1), 114.7 (C1'), 118.0 (3'), 118.4 (C3), 121.3 (C8), 122.4 (C6), 123.2 (C6'), 123.7 (C8'), 126.1 (C7'), 126.4 (C7), 127.6 (C4), 128.1 (C5'), 128.2 (C4a), 128.3 (C5), 129.1 (C4a'), 131.7 (C8a), 134.0 (C8a'), 151.5 (C2), 153.8 (C2') ppm; FT-IR (ν̄): 3059 cm⁻¹ (w), 2996 cm⁻¹ (w), 1593 cm⁻¹ (m), 1213 cm⁻¹ (s), 807 cm⁻¹ (s); HRMS (ESI): found 342.1491, calcd. for C₂₃H₁₉NO₂ [M+H]⁺ m/z = 342.1489.

1-(((E)-(2-Hydroxynaphthalen-1-yl)methyl)imino)methyl)-naphthalen-2-ol (13)

General procedure: To a mixture of 2-naphthol (10.0 g, 69.4 mmol) and methenamine (10.0 g, 71.3 mmol) acetic acid (40 mL) was added. The suspension was stirred at 100°C for 1 h. The yellow precipitate formed was collected by filtration and washed with ethanol (3 × 20 mL). The amorphous yellow solid was used in the next step without further purification. Yield: 8.55 g (75.3%); mp: 211°C (degrad.); ¹H-NMR (DMSO-d₆, 400 MHz): δ = 5.28 (s, 2H, C(11)H₂), 6.63 (d, 1H, C(3)H, J = 9.6 Hz), 7.19 (t, 1H, C(6)H, J = 8.0 Hz), 7.29 (d, 1H, C(14)H, J = 8.8 Hz), 7.34 (t, 1H, C(17)H, J = 8.0 Hz), 7.46 (t, 1H, C(7)H, J = 7.6 Hz), 7.55 (t, 1H, C(18)H, J = 7.6 Hz), 7.61 (d, 1H, C(5)H, J = 8.0 Hz), 7.68 (d, 1H, C(4)H, J = 9.6 Hz), 7.87–7.83 (2d, 2H, C(15, 16)H), 8.09 (d, 1H, C(8)H, J = 8.4 Hz), 8.22 (d, 1H, C(19)H, J = 8.4 Hz), 9.39 (d, 1H, C(9)H, J = 10.4 Hz), 14.27 (s, 1H, =N⁺(10)H), 10.34 (s, 1H, OH) ppm; ¹³C-NMR (DMSO-d₆, 100 MHz): δ = 44.8 (C11), 105.5 (C1), 113.8 (C12), 118.0 (C14), 118.2 (C8), 122.1 (C19), 122.1 (C6), 122.8 (C17), 125.1 (C4a), 125.5 (C3), 127.0 (C18), 127.9 (C7), 128.1 (C15a), 128.6 (C16), 128.9 (C5), 130.0 (C15), 132.7 (C19a), 134.3 (C8a), 137.0 (C4), 153.8 (C13), 158.3 (C9), 177.3 (C2) ppm; FT-IR (ν̄): 3050 cm⁻¹ (w, ν_{C-H}, unsat.), 2957 cm⁻¹ (w, ν_{C-H}, sat.), 2497 cm⁻¹ (w, ν_{O-H}), 1639 cm⁻¹ (s, ν_{C=N}); HRMS (ESI): found 328.1332, calcd. for C₂₂H₁₇NO [M+H]⁺ m/z = 328.1332 [43].

6-Bromo-1-(((6-bromo-2-hydroxynaphthalen-1-yl)-methyl)imino)methyl)naphthalen-2-ol (14)

To a mixture of 6-bromo-naphth-2-ol (15.9 g, 71.3 mmol) and methenamine (10.0 g, 71.3 mmol) acetic acid (40 mL) was added. The suspension was stirred at 100°C for 2 h. The yellow precipitate formed was collected by filtration and washed with acetic acid (2 × 20 mL) and finally with hot ethanol (3 × 30 mL). The amorphous yellow solid was used in the next step without further purification. Yield: 15.72 g (90.7%); mp: 222°C (degrad.); ¹H-NMR (DMSO-d₆, 400 MHz): δ = 5.25 (s, 2H, C(11)H₂), 6.67 (d, 1H, C(3)H, J = 9.2 Hz), 7.32 (d, 1H, C(14)H, J = 8.8 Hz), 7.58 (d, 1H, C(18)H, J = 8.8 Hz), 7.64 (d, 1H, C(7)H, J = 8.8 Hz), 7.68 (d, 1H, C(4)H, J = 9.2 Hz), 7.83 (d, 1H, C(15)H, J = 8.8 Hz), 7.87 (s, 1H, C(5)H), 8.04 (d, 1H, C(8)H, J = 9.2 Hz), 8.13 (s, 1H, C(16)H), 8.19 (d, 1H, C(19)H, J = 9.2 Hz), 9.39 (s, 1H, C(9)H), 10.55 (s, 1H, OH), 14.23 (s, 1H, =N⁺(10)H) ppm; ¹³C-NMR (DMSO-d₆, 100 MHz): δ = 44.7 (C11), 105.3 (C1), 114.1 (C12), 114.4 (C6), 115.6 (C17), 119.2 (C14), 120.6 (C8), 124.6 (C19), 126.7 (C4a), 126.9 (C3), 129.3 (C15), 129.4

(C15a), 129.8 (C7), 130.3 (C16,C18), 133.2 (C8a), 136.0 (C4), 154.3 (C13), 130.6 (C5), 131.3 (C19a), 158.6 (C9), 177.5 (C2) ppm; FT-IR (ν): 3052 cm^{-1} (w), 2582 cm^{-1} (m), 1627 cm^{-1} (s), 1534 cm^{-1} (w), 1494 cm^{-1} (s), 1345 cm^{-1} (s), 1165 cm^{-1} (s), 804 cm^{-1} (s); HRMS (ESI): found 481.9401, calcd. for $\text{C}_{22}\text{H}_{15}\text{NO}_2\text{Br}_2$ $[\text{M}-\text{H}]^-$ $m/z = 481.9397$.

2-Hydroxy-1-naphthaldehyde (15)

To a suspension of **13** (12.07 g, 36.85 mmol) in ethanol (200 mL) was added 6 N hydrochloric acid (40 mL) via dropping funnel with continuous stirring. After adding was completed, mixture was refluxed for 2 h. Subsequently suspension was cooled down on an ice bath. Solid was filtered off. Hereafter cold water (400 mL) was added to filtrate, whereby a yellow precipitate was formed immediately. Suspension was stored at 5°C for 2 h and then precipitate was collected by filtration. A pale yellow solid was obtained by recrystallization in 2-propanol. Yield: 5.03 g (79.3%); mp: 82°C (degrad.). Spectroscopic data were consistent with those reported in the literature [44].

6-Bromo-2-hydroxy-1-naphthaldehyde (16)

To a suspension of **14** (12.20 g, 25.0 mmol) in ethanol (150 mL) was added 6 N hydrochloric acid (37.5 mL) via dropping funnel with continuous stirring. After adding was completed, mixture was refluxed for 2.5 h. Subsequently suspension was cooled down on an ice bath. Solid was filtered off. Hereinafter cold water (300 mL) was added to filtrate, whereby a bluish precipitate was formed immediately. Suspension was stored at 5°C for 2 h and then precipitate was collected by filtration. Solid was dissolved in diethyl ether (100 mL), insoluble materials were collected by filtration. Filtrate was dried with sodium sulfate and evaporated to dryness, by means of a rotary evaporator. Yield was improved by extracting hydrolysis filtrate with diethyl ether (3 \times 30 mL). Organic phase was filtered and desiccated with sodium sulfate and evaporated to dryness, by means of a rotary evaporator. Yielding product as yellow crystals. Yield: 5.30 g (83.9%); mp: 150°C (degrad.); $^1\text{H-NMR}$ (DMSO- d_6 , 400 MHz): $\delta = 7.31$ (d, 1H, C(3)H, $J = 9.2$ Hz), 7.73 (d, 1H, C(7)H, $J = 9.2$ Hz), 8.11 (d, 1H, C(4)H, $J = 8.8$ Hz), 8.17 (s, 1H, C(5)H), 8.93 (d, 1H, C(8)H, $J = 9.2$ Hz), 10.77 (s, 1H, C(9)H), 11.91 (s, 1H, OH) ppm; $^{13}\text{C-NMR}$ (DMSO- d_6 , 100 MHz): $\delta = 112.6$ (C1), 116.9 (C6), 120.1 (C3), 125.0 (C8), 129.0 (C4a), 130.2 (C8a), 130.5 (C5), 131.9 (C7), 137.2 (C4), 164.1 (C2), 192.1 (C9) ppm; FT-IR (ν): 2983 cm^{-1} (w), 1630 cm^{-1} (m), 1458 cm^{-1} (m), 1302 cm^{-1} (m), 1163 cm^{-1} (m), 809 cm^{-1} (m); HRMS (ESI): found 248.9565, calcd. for $\text{C}_{11}\text{H}_7\text{O}_2\text{Br}$ $[\text{M}-\text{H}]^-$ $m/z = 248$.

Alternative synthesis of 6-bromo-2-hydroxy-1-naphthaldehyde (16)

To a suspension of 6-bromo-naphthol (30.78 g, 138.0 mmol) and zinc cyanide (20.76 g, 176.8 mmol) in 150 mL diethyl ether was injected continuously hydrochloride acid gas at room temperature. After 2 h, yellowish solid was collected by filtration and was refluxed two times in 250 mL water. The insoluble solid was refluxed in 240 mL water/methanol (4:1)

and was collected by filtration, yielding product as yellow solid. The filtrates were allowed to cool to 5°C and formed precipitations were combined recovering 22.98 g starting material 6-bromo-2-naphthol. Yield: 7.49 g (21.6%, 85.3% based on recovered starting material); mp: 150°C (degrad.). Spectroscopic data were consistent with those reported in literature.

(2-Hydroxynaphthalen-1-yl)methanaminium chloride (17)

To a suspension of **13** (12.07 g, 36.85 mmol) in ethanol (200 mL) was added dropwise 6 M hydrochloric acid (40 mL) with stirring. After addition was completed, mixture was refluxed for 2 h. Subsequently, the suspension was cooled down on an ice bath. The precipitate was collected by filtration and was washed thoroughly with cold ethanol (3 \times 20 mL). A colorless solid was recrystallized from 2-propanol. Yield: 6.43 g (83.2%); mp: 207°C (degrad.); $^1\text{H-NMR}$ (DMSO- d_6 , 400 MHz): $\delta = 4.39$ (s, 2H, C(9)H₂), 7.33–7.40 (m, 2H, C(3, 6)H), 7.53 (t, 1H, C(7)H, $J = 7.6$ Hz), 7.85 (d, 2H, C(5, 4)H, $J = 8.8$ Hz), 8.03 (d, 1H, C(8)H, $J = 8.4$ Hz), 8.25 (s, 3H, N(10)H₃), 10.71 (s, 1H, OH) ppm; $^{13}\text{C-NMR}$ (DMSO- d_6 , 100 MHz): $\delta = 32.7$ (C9), 111.0 (C1), 118.0 (C3), 122.4 (C8), 122.8 (C6), 126.9 (C7), 127.9 (C4a), 128.5 (C5), 130.6 (C4), 132.7 (C8a), 154.6 (C2) ppm; FT-IR (ν): 3020 cm^{-1} (m), 2923 cm^{-1} (m), 1597 cm^{-1} (m), 1517 cm^{-1} (m), 1286 cm^{-1} (s), 813 cm^{-1} (s), 746 cm^{-1} (s); HRMS (ESI): found 174.0913, calcd. for $\text{C}_{11}\text{H}_{12}\text{NO}$ $[\text{M}]^+$ $m/z = 174.0913$ [45].

(6-Bromo-2-hydroxynaphthalen-1-yl)methanaminium chloride (18)

To a suspension of **14** (12.20 g, 25.0 mmol) in ethanol (150 mL) was added 6 M hydrochloric acid (37.5 mL) via dropping funnel with continuous stirring. After addition was completed, the mixture was refluxed for 2.5 h. Subsequently the resulting suspension was cooled down on an ice bath for 2 h. Formed solid was collected by filtration and was washed with hot ethanol (2 \times 20 mL). Yield was improved by treatment of filtrate with cold water (300 mL), whereby a bluish precipitate was formed immediately. Suspension was stored at 5°C for 2 h and then bluish precipitate was collected by filtration. The solid was dissolved in diethyl ether (100 mL), thereby an insoluble solid was collected by filtration and washed with ethanol (2 \times 20 mL). Both the solid of the hydrolysis and the diethyl ether precipitate were combined yielding product as pale yellow crystals. Yield: 6.91 g (95.2%); mp: 223°C (degrad.); $^1\text{H-NMR}$ (DMSO- d_6 , 400 MHz): $\delta = 4.37$ (s, 2H, C(9)H₂), 7.41 (d, 1H, C(3)H, $J = 8.8$ Hz), 7.63 (d, 1H, C(7)H, $J = 9.2$ Hz), 7.86 (d, 1H, C(4)H, $J = 9.2$ Hz), 8.01 (d, 1H, C(8)H, $J = 9.2$ Hz), 8.12 (s, 1H, C(5)H), 8.20 (s, 3H, N⁺(10)H₃), 10.85 (s, 1H, OH) ppm; $^{13}\text{C-NMR}$ (DMSO- d_6 , 100 MHz): $\delta = 32.7$ (C9), 111.4 (C1), 115.6 (C6), 119.1 (C3), 125.0 (C8), 129.1 (C4a), 129.5 (C7), 129.9 (C4), 130.1 (C5), 131.4 (C8a), 155.1 (C2) ppm; FT-IR (ν): 3198 cm^{-1} (m), 3022 cm^{-1} (m), 2925 cm^{-1} (m), 1578 cm^{-1} (m), 1496 cm^{-1} (s), 1271 cm^{-1} (s), 1053 cm^{-1} (w), 879 cm^{-1} (s), 811 cm^{-1} (s); HRMS (ESI): found 252.0019, calcd. for $\text{C}_{11}\text{H}_{11}\text{BrNO}$ $[\text{M}]^+$ $m/z = 252.0019$ [45].

4-(3-[(2-Hydroxynaphthalen-1-yl)methyl]ammonio}propyl)morpholin-4-ium chloride (19)

To a solution of **15** (3.44 g, 20.0 mmol) in methanol (50 mL) 3-(morpholino-4-yl)propan-1-amine (2.90 g, 20.1 mmol) was added under a nitrogen atmosphere. After 3 h stirring at room temperature, mixture was cooled in an ice-bath. Afterwards sodium borohydride (1.51 g, 39.9 mmol) pre-dissolved in 20 mL water was added. After removing the ice-bath, solution was stirred 1 h at room temperature. Reaction was quenched by slow addition of 4 M hydrochloric acid (25 mL). After addition was completed, methanol was removed by means of a rotary evaporator and aqueous residue was extracted with diethyl ether (3 × 30 mL). Subsequently aqueous phase was extracted with ethyl acetate (3 × 50 mL) after pH-adjustment to pH 7–8 with ammonium chloride and sodium carbonate. Immediately aqueous phase was adjusted to pH 9 with sodium hydroxide and extracted again with ethyl acetate (3 × 50 mL). Both organic phases were dried with anhydrous sodium sulfate and then hydrochloric acid gas was introduced. The resulting precipitate was collected by filtration after storage at –20°C for 12 h. Solid was recrystallized from ethyl acetate/methanol/isopropanol yielding product as pale rose crystals. Yield: 5.19 g (69.7%); mp: 169°C (degrad.); ¹H-NMR (DMSO-d₆, 400 MHz): δ = 2.20–2.27 (m, 2H, C(12)H₂), 3.03–3.19 (m, 6H, C(11,13,15/18)H₂), 3.36 (s, 2H, C(15/18)H), 3.85–3.97 (m, 4H, C(16,17)H₂), 4.54 (s, 2H, C(9)H₂), 7.36 (t, 1H, C(6)H, *J* = 7.4 Hz), 7.44 (d, 1H, C(3)H, *J* = 8.8 Hz), 7.54 (t, 1H, C(7)H, *J* = 7.6 Hz), 7.89 (d, 1H, C(4)H, *J* = 9.2 Hz), 8.12 (d, 1H, C(8)H, *J* = 8.4 Hz), 9.14 (s, 1H, N⁺(10)H₂), 10.87 (s, 1H, OH), 11.70 (s, 1H, N⁺(14)H) ppm; ¹³C-NMR (DMSO-d₆, 100 MHz): δ = 19.6 (C12), 40.7 (C9), 44.3 (C11), 50.9 (C15,18), 53.0 (C13), 109.0 (C1), 117.9 (C3), 122.6 (C8), 122.9 (C6), 127.0 (C7), 127.9 (C4a), 128.5 (C5), 131.1 (C4), 133.0 (C8a), 155.3 (C2) ppm; FT-IR (ν̄): 3429 cm⁻¹ (w), 3358 cm⁻¹ (w), 3135 cm⁻¹ (w), 2934 cm⁻¹ (w), 2590 cm⁻¹ (w), 1626 cm⁻¹ (w), 1264 cm⁻¹ (m), 1136 cm⁻¹ (w), 819 cm⁻¹ (m), 751 cm⁻¹ (m); HRMS (ESI): found 371.1299, calcd. for C₁₈H₂₆Cl₂N₂O₂ [M–H][–] *m/z* = 371.1299.

4-(3-[(6-Bromo-2-hydroxynaphthalen-1-yl)methyl]ammonio}propyl)morpholin-4-ium chloride (20)

To a solution of **18** (2.51 g, 10.0 mmol) in methanol (50 mL) 3-(morpholino-4-yl)propan-1-amine (2.90 g, 20.1 mmol) was added under a nitrogen atmosphere. After 2 h stirring at room temperature, mixture was cooled in an ice-bath. Afterwards sodium borohydride (1.0 g, 26.4 mmol) pre-dissolved in 20 mL water was added. After removing the ice-bath, solution was stirred 1 h at room temperature. Reaction was quenched by slow addition of 4 M hydrochloric acid (30 mL). After addition was completed, methanol was removed on a rotary evaporator and aqueous residue was extracted with diethyl ether (3 × 30 mL). Subsequently, aqueous phase was extracted with ethyl acetate (3 × 50 mL) after pH-adjustment to pH 7–8 with sodium carbonate. Immediately aqueous phase was adjusted to pH 9 with ammonia and sodium carbonate and extracted again with

ethyl acetate (3 × 50 mL). Both organic phases were dried with anhydrous sodium sulfate and then hydrochloric acid gas was introduced. The resulting precipitate was collected by filtration after storage at –20°C for 12 h. Solid was recrystallized from ethyl acetate/methanol/isopropanol yielding product as pale rose crystals. Yield: 3.16 g (69.9%); mp: 184°C (degrad.); ¹H-NMR (DMSO-d₆, 400 MHz): δ = 2.21–2.26 (m, 2H, C(12)H₂), 3.05–3.18 (m, 6H, C(11,13,15/18)H₂), 3.37 (s, 2H, C(15/18)H), 3.85–3.97 (m, 4H, C(16,17)H₂), 4.52 (s, 2H, C(9)H₂), 7.47 (d, 1H, C(3)H, *J* = 8.8 Hz), 7.63 (d, 1H, C(7)H, *J* = 8.8 Hz), 7.89 (d, 1H, C(4)H, *J* = 8.8 Hz), 8.11 (d, 1H, C(8)H, *J* = 9.2 Hz), 9.13 (s, 1H, N⁺(10)H₂), 11.03 (s, 1H, OH), 11.62 (s, 1H, N⁺(14)H) ppm; ¹³C-NMR (DMSO-d₆, 100 MHz): δ = 19.6 (C12), 40.6 (C9), 44.3 (C11), 50.9 (C15,18), 53.0 (C13), 63.0 (C16,17), 109.5 (C1), 115.7 (C6), 119.1 (C6), 125.3 (C8), 129.2 (C4a), 129.6 (C7), 130.1 (C5), 130.4 (C4), 131.7 (C8a), 155.7 (C2) ppm; FT-IR (ν̄): 3444 cm⁻¹ (w), 3058 cm⁻¹ (w), 2935 cm⁻¹ (w), 2465 cm⁻¹ (w), 1595 cm⁻¹ (w), 1269 cm⁻¹ (m), 1087 cm⁻¹ (m), 816 cm⁻¹ (s); HRMS (ESI): found 449.0404, calcd. for C₁₈H₂₅BrCl₂N₂O₂ [M–H][–] *m/z* = 449.0404.

1,1'-[Thiobis(methylene)]bis(naphthalen-2-ol) (21)

To a suspension of **8a** (1.076 g, 5.0 mmol) in 30 mL dry tetrahydrofuran was added triethylamine (1.50 mL, 1.10 g, 10.8 mmol, 2.2 equiv.). After 25 min stirring under nitrogen atmosphere, ethyl-3-bromopropionate (0.64 mL, 0.90 g, 5.0 mmol, 1.0 equiv.) was added to the yellowish solution at room temperature. Within few minutes the reaction mixture became turbid. After 9 days stirring at room temperature (TLC indicated that after 30 min the reaction was ended, composition does not change within the long reaction time) the insoluble solid was filtered off. To the filtrate 10 mL *n*-hexane was added. The slurry was stored at –20°C for 10 h. The flaky precipitation was collected by filtration and was subsequently purified by column chromatography (*n*-hexane/ethyl acetate/acetic acid; 10:5:1) yielding product as colorless crystals. Crystallization for X-ray diffraction measurement was conducted via vapor diffusion with a solution of the product in dichloromethane in *n*-hexane atmosphere. Yield: 0.10 g (5.5%); mp: 255°C (decomp.); ¹H-NMR (DMSO-d₆, 400 MHz): δ = 4.29 (s, 4H, C(9)H₂, C(9')H₂), 7.17 (d, 2H, C(3)H, C(3')H, *J* = 9.2 Hz), 7.25 (t, 2H, C(6)H, C(6')H, *J* = 8.0 Hz), 7.31 (t, 2H, C(7)H, C(7')H, *J* = 8.0 Hz), 7.38 (d, 2H, C(4)H, C(4')H, *J* = 8.8 Hz), 7.76 (d, 4H, C(5)H, C(8)H, C(5')H, C(8')H, *J* = 9.2 Hz), 9.66 (s, 2H, OH) ppm; ¹³C-NMR (DMSO-d₆, 100 MHz): δ = 26.3 (C9,9'), 115.2 (C1,1'), 117.9 (C3,3'), 122.4 (C6,6'), 123.0 (C8,8'), 126.0 (7,7'), 128.2 (C4a, C4a'), 128.2 (C5, C5'), 128.4 (C4, C4'), 132.8 (C8a, C8a'), 152.8 (C2, C2') ppm; FT-IR (ν̄): 3526 cm⁻¹ (w), 3056 cm⁻¹ (w), 1626 cm⁻¹ (m), 1356 cm⁻¹ (m), 1213 cm⁻¹ (m), 809 cm⁻¹ (s). Product structure was confirmed by X-ray crystallography.

Biochemistry

Expression and purification of recombinant protein

The expression and purification of Sirt2_{56–356} was performed as described previously with minor modifications [46]. The enzyme was resuspended in lysis buffer (25 mM KH₂PO₄,

25 mM NaH₂PO₄, 400 mM NaCl, 5% (v/v) glycerol, 5 mM 2-mercaptoethanol, pH 8.0) and finally purified with a Superdex S75 26/60 gel filtration column (25 mM Hepes, 200 mM NaCl, 5% (v/v) glycerol, pH 8.0). Via SDS-PAGE the identity and purity of the produced enzymes was verified [47] and the protein concentration was determined by Bradford assay [48]. The catalytic reaction of hSirt2 was dependent on NAD⁺ and was able to inhibit by nicotinamide.

Biochemical assay

For the activity testing of hSirt2 an established high-throughput (96-well plate) fluorescence-based assay was used [33]. hSirt2_{56–356} was added to a solution of NAD⁺ (final assay concentration 500 μM), the substrate Z-(Ac)Lys-AMC (ZMAL, final assay concentration 10.5 μM), DMSO as a control or the inhibitor in several concentrations dissolved in DMSO (final DMSO concentration 5% (v/v)), filled up with assay buffer (50 mM Tris, 137 mM NaCl, 2.7 mM KCl, pH 8.0) to 60 μL. The enzyme concentration was adjusted to a final substrate conversion of 15–30% to stay in a linear range. The incubation time was 4 h at 37°C and 150 rpm. The catalytic reaction was stopped by adding 60 μL of a developer solution (50 mM Tris, 100 mM NaCl, 6.7% (v/v) DMSO, trypsin 16.5 U/μL, 8 mM nicotinamide, pH 8.0) and incubated 20 min at 37°C and 150 rpm. Fluorescence intensity was measured in a microplate reader (BMG Polarstar, λ_{ex} = 390 nm, λ_{em} = 460 nm). All compounds were pretested on auto-fluorescence, aminomethylcoumarin (AMC) quenching, and trypsin inhibition under assay conditions. No interferences were observed. The inhibitory effect was determined by using the DMSO-controls as a reference. Graphpad Prism software (La Jolla, CA) was used to calculate IC₅₀ values.

The Jung group thanks the Deutsche Forschungsgemeinschaft (DFG, within GRK1976) for support.

Author contributions

S.V. and K.B. synthesized, purified, and isolated new compounds. A.B. performed structure elucidation by NMR and accurate mass analysis. Z.A.H. and W.S. carried out docking experiments, C.S. accomplished X-ray crystallographic structure determination, S.S. and M.J. performed the biological evaluation; W.S. and A.L. designed the study and wrote the manuscript together with S.V.

The authors have declared no conflict of interest.

References

- [1] A. A. Sauve, I. Celic, J. Avalos, H. Deng, J. D. Boeke, V. L. Schramm, *Biochemistry* **2001**, *40*, 15456–15463.
- [2] I. Carnevale, L. Pellegrini, P. D'Aquila, S. Saladini, E. Lococo, L. Polletta, E. Vernucci, E. Foglio,

- S. Coppola, L. Sansone, G. Passarino, D. Bellizzi, M. A. Russo, M. Fini, M. Tafani, *J. Cell. Physiol.* **2017**, *232*, 1835–1844.
- [3] E. Jing, S. Gesta, C. Ronald Kahn, *Cell Metab.* **2007**, *6*, 105–114.
- [4] F. Wang, M. Nguyen, F.X. -F. Qin, Q. Tong, *Aging Cell* **2007**, *6*, 505–514.
- [5] Y. K. Yoon, T. S. Choon, *Arch. Pharm.* **2016**, *349*, 1–8.
- [6] S.-N. Xu, T.-S. Wang, X. Li, Y.-P. Wang, *Sci. Rep.* **2016**, *6*, 32734.
- [7] A. Bedalov, T. Gatabonton, W. P. Irvine, D. E. Gottschling, J. A. Simon, *Proc. Natl. Acad. Sci. U.S.A.* **2001**, *98*, 15113–15118.
- [8] R. C. Neugebauer, U. Uchiechowska, R. Meier, H. Hruba, V. Valkov, E. Verdin, W. Sippl, M. Jung, *J. Med. Chem.* **2008**, *51*, 1203–1213.
- [9] T. Rumpf, S. Gerhardt, O. Einsle, M. Jung, *Acta Crystallogr. F* **2015**, *71*, 1498–1510.
- [10] J. Arct, E. Jakubska, G. Olszewska, *Synthesis* **1977**, *1977*, 314–315.
- [11] A. Pochini, G. Puglia, R. Ungaro, *Synthesis* **1983**, *1983*, 906–907.
- [12] A. Blade-Font, T. de Mas Rocabayera, *J. Chem. Soc., Perkin Trans.* **1982**, *1*, 841–848.
- [13] M. Heydenreich, A. Koch, I. Szatmari, F. Fülöp, E. Kleinpeter, *Tetrahedron* **2008**, *64*, 7378–7385.
- [14] T. Meyer, D. Geffken, *Pharmazie* **2003**, *59*, 593–596.
- [15] D. Keck, S. Vanderheiden, S. Bräse, *Eur. J. Org. Chem.* **2006**, *2006*, 4916–4923.
- [16] C. Cardellicchio, M. A. M. Capozzi, F. Naso, *Tetrahedron-Asymmetry* **2010**, *21*, 507–517.
- [17] D. Tóth, I. Szatmári, F. Fülöp, *Eur. J. Org. Chem.* **2006**, *2006*, 4664–4669.
- [18] S. B. Sapkal, K. F. Shelke, A. H. Kategaonkar, M. S. Shingare, *Green Chem. Lett. Rev.* **2009**, *2*, 57–60.
- [19] J.-T. Li, S.-F. Sun, M.-X. Sun, *Ultrason. Sonochem.* **2011**, *18*, 42–44.
- [20] J. C. Duff, E. J. Bills, *J. Chem. Soc.* **1934**, *282*, 1305–1308.
- [21] C. Mannich, W. Krösche, *Arch. Pharm.* **1912**, *250*, 647–667.
- [22] I. S. Belostotskaya, N. L. Komissarova, T. I. Prokof'eva, L. N. Kurkovskaya, V. B. Vol'eva, *Russ. J. Org. Chem.* **2005**, *41*, 703–706.
- [23] Y. Ogata, A. Kawasaki, F. Sugiura, *Tetrahedron* **1968**, *24*, 5001–5010.
- [24] S. K. Grover, A. C. Jain, T. R. Seshadri, *J. Indian Chem. Soc.* **1962**, *39*, 301–305.
- [25] D. Li, Y. Shu, P. Li, W. Zhang, H. Ni, Y. Cao, *Med. Chem. Res.* **2013**, *22*, 3119–3125.
- [26] J. Girniene, S. Tardy, A. Tatibouët, A. Sačkus, P. Rollin, *Tetrahedron Lett.* **2004**, *45*, 6443–6446.
- [27] Y. Nagao, K. Inoue, M. Yamaki, M. Shiro, S. Takagi, E. Fujita, *Chem. Pharm. Bull.* **1988**, *36*, 4293–4300.
- [28] I. Szatmári, A. Hetényi, L. Lázár, F. Fülöp, *Heterocycl. Chem.* **2004**, *41*, 367–373.
- [29] C. L. Perrin, D. B. Young, *J. Am. Chem. Soc.* **2001**, *123*, 4446–4450.

- [30] M. P. Cava, M. I. Levinson, *Tetrahedron* **1985**, *41*, 5061–5087.
- [31] J. Mindl, O. Hrabik, V. Sterba, J. Kavalek, *Collect. Czech. Chem. Commun.* **2000**, *65*, 1262–1272.
- [32] N. Philippe, F. Denivet, J.-L. Vasse, J. Sopkova-de Olivera Santos, V. Levacher, G. Dupas, *Tetrahedron* **2003**, *59*, 8049–8056.
- [33] B. Heltweg, J. Trapp, M. Jung, *Methods* **2005**, *36*, 332–337.
- [34] P. J. Goodford, *J. Med. Chem.* **1985**, *28*, 849–857.
- [35] J. L. Feldman, K. E. Dittenhafer-Reed, N. Kudo, J. N. Thelen, A. Ito, M. Yoshida, J. M. Denu, *Biochemistry* **2015**, *54*, 3037–3050.
- [36] B. Heltweg, F. Dequiedt, E. Verdin, M. Jung, *Anal. Biochem.* **2003**, *319*, 42–48.
- [37] J. Wang, R. M. Wolf, J. W. Caldwell, P. A. Kollman, D. A. Case, *J. Comput. Chem.* **2004**, *25*, 1157–1174.
- [38] A. Jakalian, D. B. Jack, C. I. Bayly, *J. Comput. Chem.* **2002**, *23*, 1623–1641.
- [39] G. Jones, P. Willett, R. C. Glen, A. R. Leach, R. Taylor, *J. Mol. Biol.* **1997**, *267*, 727–748.
- [40] A. Altomare, G. Cascarano, C. Giacovazzo, A. Guagliardi, *J. Appl. Crystallogr.* **1993**, *26*, 343–350.
- [41] G. Sheldrick, *Acta Crystallogr. Sect. A* **2008**, *64*, 112–122.
- [42] R. D. Haworth, R. MacGillivray, D. H. Peacock, *J. Chem. Soc.* **1952**, *541*, 2857–2858.
- [43] W. J. Burke, M. J. Kolbezen, R. J. Reynolds, G. A. Short, *J. Am. Chem. Soc.* **1956**, *78*, 805–808.
- [44] Y. Wang, M. Wang, Y. Wang, Y. Chen, L. Sun, *Synth. Commun.* **2011**, *41*, 1381–1393.
- [45] R. D. Haworth, R. MacGillivray, D. H. Peacock, *J. Chem. Soc.* **1950**, *309*, 1493–1498.
- [46] T. Rumpf, M. Schiedel, B. Karaman, C. Roessler, B. J. North, A. Lehotzky, J. Oláh, K. I. Ladwein, K. Schmidtkunz, M. Gajer, M. Pannek, C. Steegborn, D. A. Sinclair, S. Gerhardt, J. Ovádi, M. Schutkowski, W. Sippl, O. Einsle, M. Jung, *Nat. Commun.* **2015**, *6*, 6263.
- [47] U. K. Laemmli, *Nature* **1970**, *227*, 680–685.
- [48] M. M. Bradford, *Anal. Biochem.* **1976**, *72*, 248–254.

4.6. Manuscript 6: Virtual screening and identification of specific inhibitors for the mitochondrial deacylase Sirtuin 4

Pannek, M., Alhalabi, Z., Robaa, D., Rotili, D., Weyand, M., Mai, A., Sippl, W., Steegborn, S.

(in preparation 2020)

Virtual screening and identification of specific inhibitors for the mitochondrial deacylase Sirtuin 4

Abstract

Sirtuins are NAD⁺-dependent protein lysine deacylases implicate in aging processes and aging-related diseases. Mammalian sirtuin isoform 4 (Sirt4) is located in mitochondria and hydrolyses protein lysine hydroxymethylglutarylations and related acylations. It acts as a regulator of fatty acid metabolism, insulin release, and apoptosis, and it is a potential drug target for treating cancer and metabolic diseases. In this work, the first potent, Sirt4 selective small molecule inhibitors were identified by virtual screening. Testing top candidates from docking results revealed two novel series of inhibitors. Our results thus provide the first lead compounds for further development of Sirt4-specific inhibitors as experimental tools.

1. Introduction

Sirt4 localizes in mitochondria of human and mouse cells in the mitochondrial matrix. Sirt4 interacts with insulin-degrading enzyme and suppresses the insulin secretion. It was shown that Sirt4 could inhibit glutamate dehydrogenase (GDH), which regulates the usage of amino acids in energy production and promote the metabolism of glutamate and glutamine. Sirt4 functions as a tumor suppressor by suppressing glutamine metabolism and promoting genomic stability. Sirt4 represses mitochondrial glutamine metabolism in response to DNA damage. Since glutamine is critical for the G1 to S-phase cell cycle progression, Sirt4 indirectly regulates the cell cycle, allowing for accurate DNA repair and maintenance of genomic stability [1, 2]. Sirt4 does not have detectable NAD⁺-dependent deacetylase activity towards sirtuin targets, but it has strong NAD⁺-dependent mono-ADP-ribosylation activity. The catalytic efficiency of Sirt4 for lipoyl and biotinyl lysine modifications is superior to its deacetylation activity [3, 4, 5]. Moreover, Sirt4 catalyzes the removal of 3-hydroxy-3-methylglutaryl (HMG) from lysine residues of target proteins [6].

2. Homology models of human Sirt4

Prediction of protein structures is one of the challenging procedures in molecular modeling since there is no crystal structure for Sirt4; therefore, predicted homology models of Sirt4 were generated.

We searched first for the sequence of human Sirt4 (hSirt4) in UniProt entry ID: **Q9Y6E7**, residues 29-314. Then the template selection was done using HHblits - Homology detection by iterative HMM-HMM comparison technique [7], which identified Sirt5 PDB code: **3RIY** (identity: 28%) and bacterial sirtuin Sir2 Af1Tm PDB code: **2H59** (identity: 30%) as the best templates. The sequence alignment was done using MOE [8]; 20 homology models were generated using Modeller program version 9.11 [9]. The model with the lowest value of Dope (Discrete Optimized Protein Energy) score was chosen and analyzed in Procheck program [10]. The residues located in the most favorable regions were 82.8% for HM1 (template: **3RIY**) and 84.5% for HM2 (template: **3RIY, 2H59**).

The gap in the loop that exists in the zinc-binding domain was modeled using a loop refinement script in Modeller program. The Root-mean-square deviations (RMSD) of the protein atom backbone and the cofactor binding pocket between the template and the homology models were less than 2, as shown in **Figure 1, 2**.

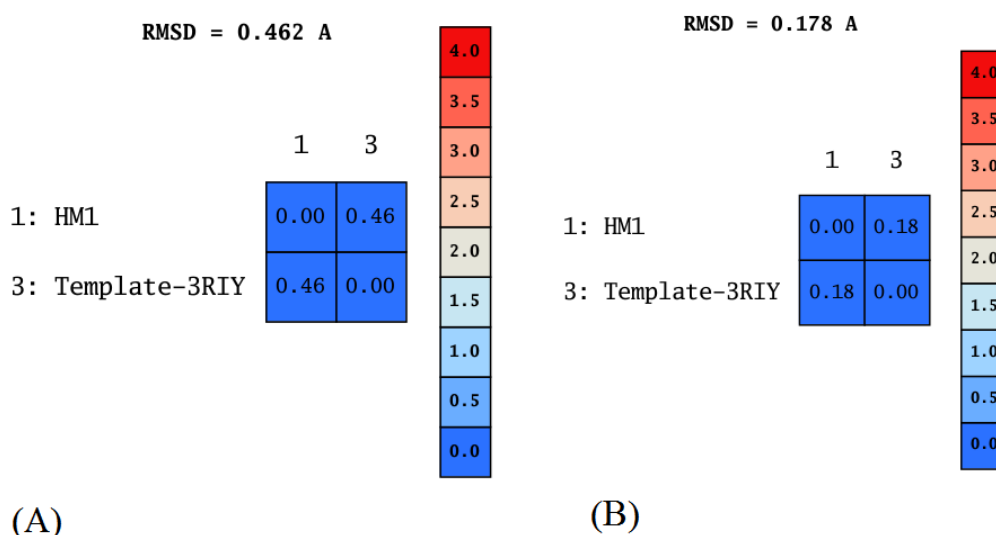


Figure 1: RMSD between HM1 and the template, protein backbone (A), and peptide binding pocket (B).

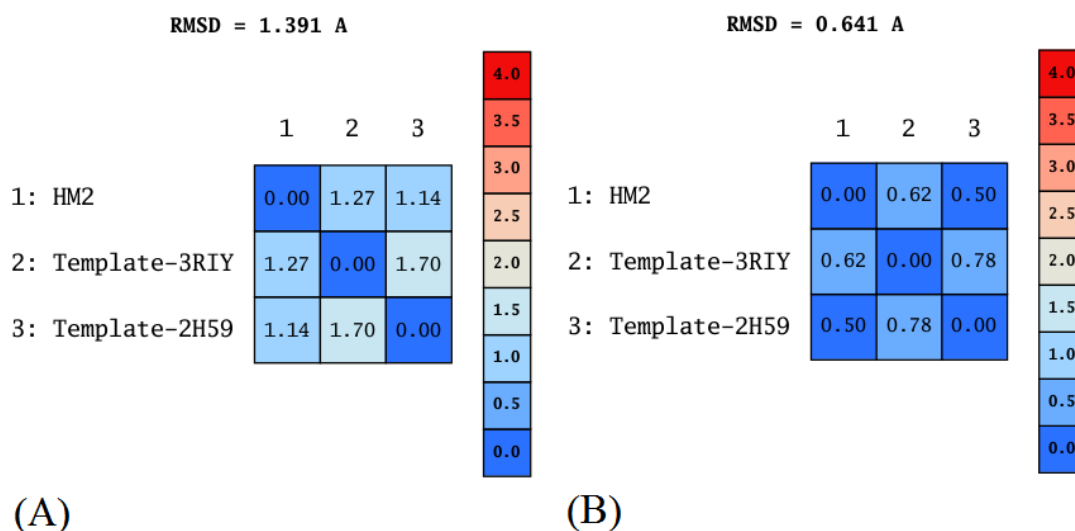


Figure 2: RMSD between HM2 and the templates, protein backbone (A), and peptide binding pocket (B).

3. Virtual screening of Sirt4 inhibitors

Since no inhibitor is known so far for Sirt4, a virtual screening was done in order to find novel Sirt4 inhibitors. The virtual screening was carried out using the following setup.

Docking calculations were done using Glide (Schrödinger Suite v2012-5.8; Schrödinger LLC, New York City, NY), which has performed well in previous sirtuin docking studies [11, 12, 13]. A homology model for human Sirt4 was generated with MOE (Molecular Operating Environment, Version 2014.09; Chemical Computing Group Inc., Montreal, Canada) using Sirt4 from *Xenopus tropicalis* (PDB ID: **5OJN**) as the template [14]. The sequence alignment was done using MOE. It shows for the catalytic core (hSirt4: 32–312; XSirt4: 31–314) a sequence similarity of 81%. Hydrogen atoms were added to the homology model and for titratable amino acids. The protonation state was calculated using the protonate 3D module in MOE. The phenol oxygen of Tyr105 (hSirt4) was defined as the center of the substrate-binding site with a 12 Å radius.

Ligprep (Schrödinger Suite v2012-5.8) was used to convert a virtual library of 1.3 million compounds (diverse_targeted_screening_compounds) from Princeton BioMolecular Research, Inc. (Princeton, NJ, USA) to the 3D structures. All tautomeric forms and stereoisomers were generated with Epik (2,608,137 structures, protonation states at pH

7.3 ± 0.2). The resulting library was docked to the hSirt4 substrate-binding pocket with Glide HTVS, and the top 10% scoring compounds were redocked with Glide SP, ten docking poses were stored for each compound. All docking poses of top-ranked (1000 compounds) were rescored using the MM-GB/SA protocol implemented in MOE 2014.09. The AMBER force field [15] and the GB/SA method implemented in MOE 2014.09 was used to relax the protein-inhibitor complexes. During the minimization step, the protein backbone atoms were tethered using a force constant of (3/2) kT / 2 ($\sigma = 0.5$ Å). Complexes showing favorable binding free energy values were visually analyzed, and 62 compounds were cherry-picked for in vitro testing.

Filtering the final dataset for PAINS was performed using PAINS1, PAINS2, and PAINS3 filters, as implemented in Schrödinger's Canvas program. None of the selected compounds was flagged as PAINS. In total, 62 compounds were tested against hSirt4 by the research group of Prof. Steegborn at Bayreuth University.

Among the tested virtual screening hits, 20 compounds were found to show at least 50% of inhibition using in vitro assay, the IC₅₀ values were determined for nine inhibitors. The best hits showed an IC₅₀ value of around 50 µM (**Table 1**). Two compounds were identified **OSSK_979070** (**Figure 3**), which contains benzimidazole and sulfanilamide, and **OSSK_671780** (**Figure 3**), which contains a pyrimidone ring as a promising starting point for further chemical optimization.

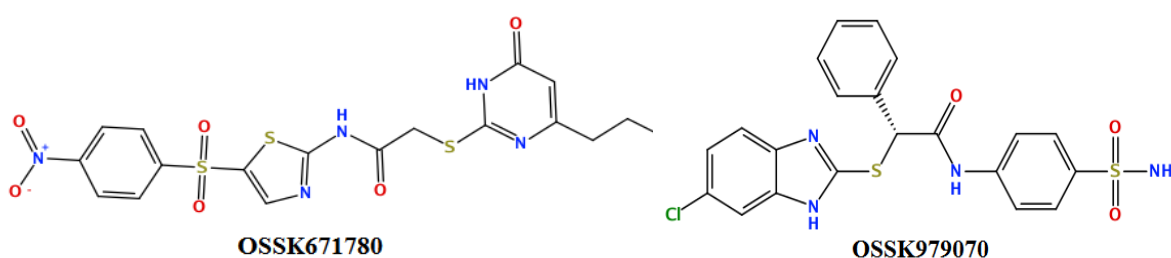


Figure 3: 2D structures of hSirt4 inhibitors.

Analyzing the docking poses of the most active VS hits indicated that they fill the substrate-binding pocket of hSirt4 (**Figure 4a, 4b, 4c**). Two chemical scaffolds (**OSSK_979070** and **OSSK_671780**) were identified as promising starting points for chemical optimization. One type contains a para-carbamoylbenzenesulfonamide (**OSSK_979070**, **OSSK_766801**, and **OSSK_990343**), which appears to form a hydrogen

bond to the backbone carbonyl of D236 (**Figure 4a**). The phenyl groups of the compounds could interact with H161 and V232. Both residues are conserved among sirtuins and also involved in substrate interactions, and the modeled binding pose would suggest a substrate competitive inhibition mechanism. The benzimidazole/benzthiazole of the inhibitors forms T-stacking interaction with F233, whereas the phenyl ring is protruding into the nicotinamide binding pocket (observed for both enantiomeric forms).

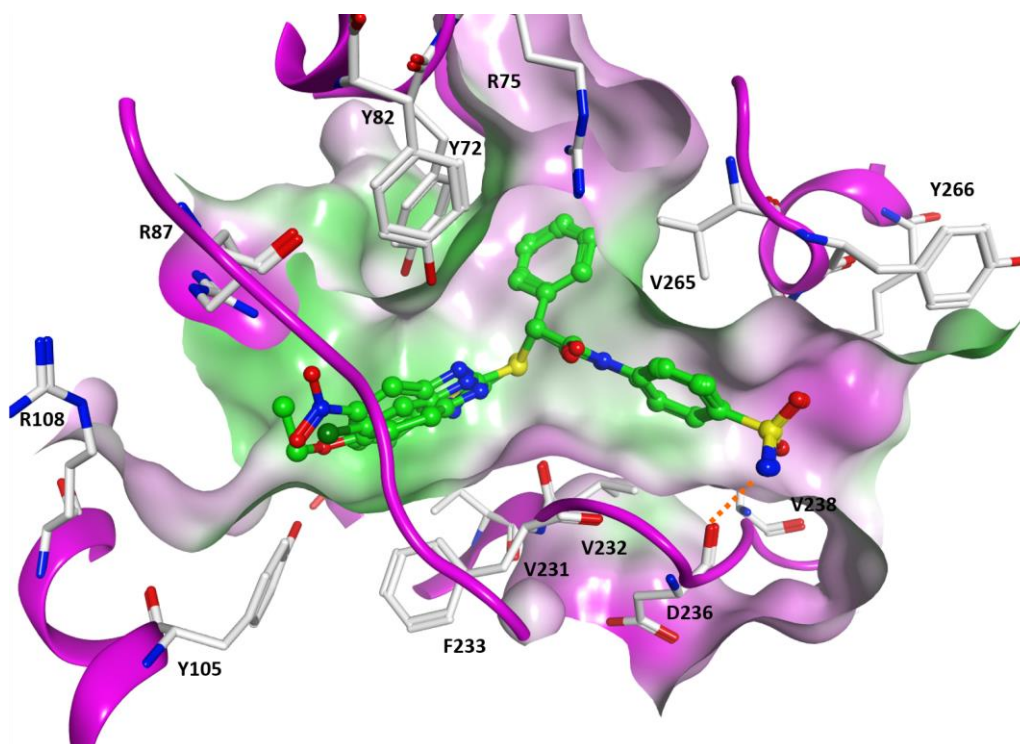


Figure 4a: Predicted docking pose of the structurally similar OSSK_979070, OSSK_766801, and OSSK_990343 in the peptide-binding pocket of hSirt4 homology model (magenta ribbon). The molecular surface of the pocket is colored according to the hydrophobicity (green = hydrophobic, magenta = polar).

Compounds of the second type of hits contain a central N-1, 3-thiazol-2-ylformamide that is substituted on both sites (**OSSK_671780** and **OSSK_531891**). The amide group is donating a hydrogen bond to the backbone carbonyl of V232, whereas the thiazole ring is interacting with H161 (**Figure 4b, 4c**). In addition, the active hits contain a 2-sulfanylpyrimidin-4-ol ring that is showing T-stacking interactions with F233 in the hSirt4-acyl pocket. In case of **OSSK_671780**, a further hydrogen bond is observed between the sulfonamide group and the backbone NH of S267.

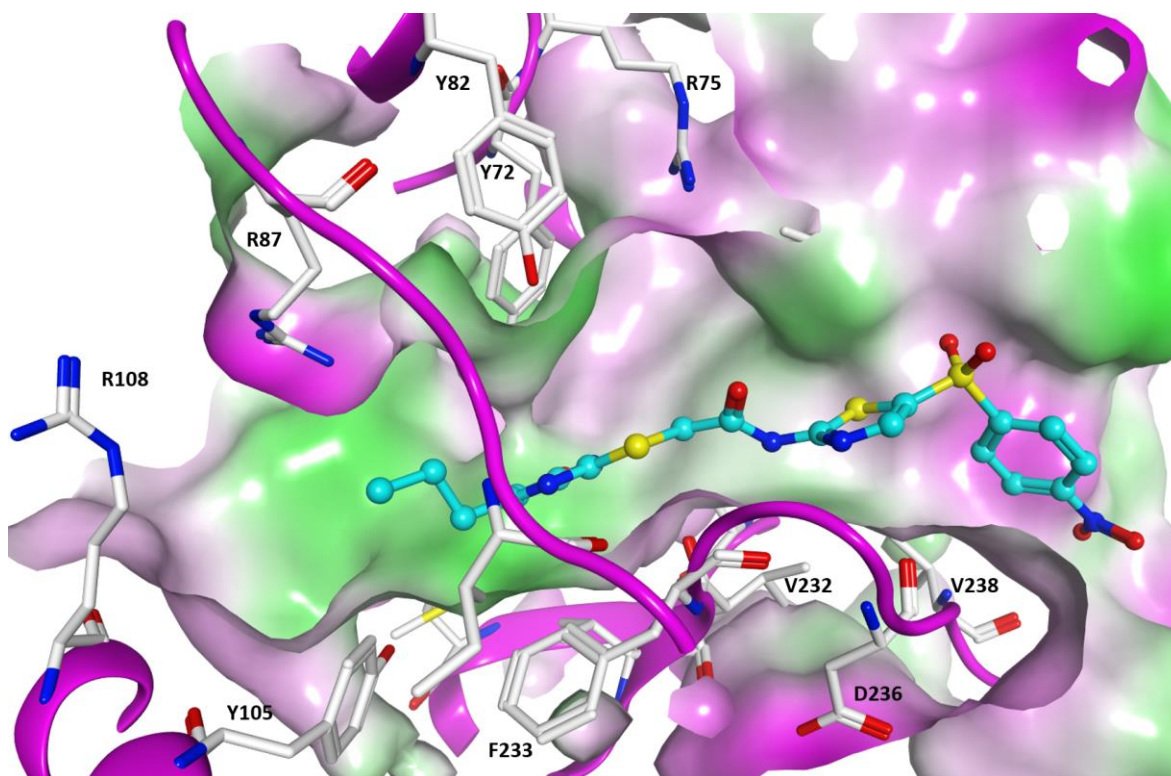


Figure 4b: Predicted docking pose of the VS hits **OSSK_671780** in the peptide-binding pocket of hSirt4 homology model. The molecular surface of the pocket is colored according to the hydrophobicity (green = hydrophobic, magenta = polar).

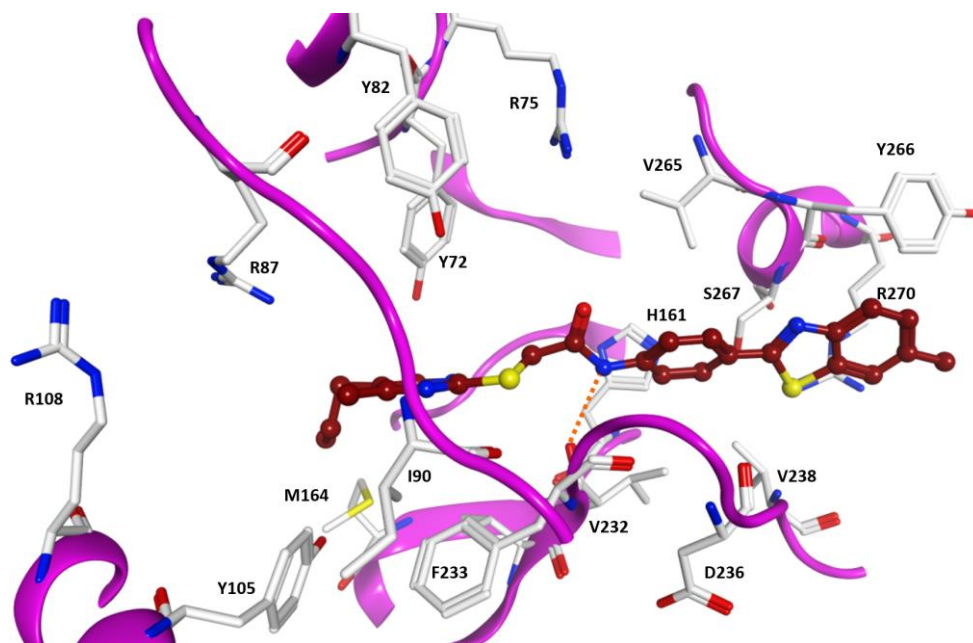


Figure 4c: Predicted docking pose of the VS hit OSSK_531891 in the peptide-binding pocket of hSirt4 homology model (cyan ribbon).

Table 1: Percentage of inhibition and IC₅₀ values of the VS hits for hSirt4.

Princeton ID	%Activity 100 mM	IC ₅₀ Sirt4 μM	E GBSA kcal/mol	Glidescore SP
OSSK_480394	90		-57,8	-6,89
OSSK_979070	70	48	-61,7	-5,83
OSSK_766801	73	54	-53,8	-5,36
OSSK_671780	88	77	-53,0	-5,99
OSSK_531891	79	85	-56,7	-7,78
OSSL_117187	75		-56,5	-6,38
OSSL_266012	48	107	-57,3	-6,86
OSSK_990343	60	117	-58,9	-6,11
OSSK_706267	71	122	-49,1	-6,36
OSSK_221646	60	420	-48,5	-6,50
OSSK_671862	80	455	-49,4	-7,10
OSSK_026091	60		-48,0	-5,60
OSSL_117254	60		-57,0	-8,51
OSSK_360152	60		-48,0	-7,14
OSSL_125753	60		-53,8	-7,04
OSSK_510319	60		-53,1	-7,71
OSSL_318655	58		-58,0	-5,42
OSSK_627999	51		-53,7	-7,03
OSSK_671345	51		-50,6	-5,87
OSSK_763561	47		-48,8	-6,72

OSSK_763565	46		-51,8	-6,96
OSSK_766801	45		-54,9	-6,04
OSSK_763562	42		-57,2	-6,33
OSSK_978369	40		-47,7	-7,47
OSSK_980849	40		-40,1	-5,89
OSSK_659424	40		-48,7	-5,84
OSSK_571792	40		-42,6	-6,29
OSSK_713772	40		-50,7	-6,62
OSSK_515470	38		-55,6	-6,77
OSSK_763567	37		-43,1	-7,13
OSSK_511579	37		-47,6	-5,88
OSSK_766803	33		-58,6	-6,78
OSSK_471253	30		-50,3	-6,65
OSSK_362013	27		-44,1	-6,68
OSSK_818973	24		-41,9	-7,09
OSSK_999387	21		-44,4	-6,39
OSSK_921921	20		-51,2	-6,43
OSSK_280440	20		-42,7	-5,72
OSSK_925126	20		-42,8	-6,69
OSSL_280987	20		-47,3	-8,16
OSSK_407712	20		-46,2	-6,02
OSSK_452333	20		-65,2	-7,10
OSSK_735818	20		-40,5	-7,47
OSSL_011334	20		-51,6	-6,53
OSSK_321995	19		-45,0	-6,48
OSSK_999416	19		-45,1	-5,95
OSSK_671785	18		-38,4	-6,09
OSSK_763564	16		-48,4	-6,15
OSSK_490855	10		-48,1	-5,46
OSSK_206176	9		-40,3	-6,58
OSSK_530294	5		-44,9	-5,19
OSSL_009878	3		-43,2	-5,74
OSSL_112932	2		-43,4	-6,27
OSSK_393678	0		-42,3	-5,91
OSSK_363499	0		-40,6	-6,62
OSSK_628038	0		-41,7	-5,83
OSSK_539021	0		-48,2	-5,00
OSSK_776865	0		-40,5	-6,84
OSSL_259361	0		-40,4	-5,58
OSSK_937818	0		-49,6	-6,72
OSSL_136829	0		-42,0	-5,57
OSSK_965398	0		-48,6	-5,47

4. In vitro Assay

Peptide- and FdL-based activity assays

The coupled continuous assay was performed [16]. In brief, assays were performed with 5 μM hSirt4 or 5 μM XSirt4 in 20 mM sodium phosphate buffer pH 7.8, 10% DMSO, 3.3 mM α -ketoglutarate, 0.2 mM NADPH, 0.05 mg/ml nicotinamidase, 2 U/ml GDH, and 500 μM substrate peptide and 2 mM NAD^+ . Reactions were incubated at room temperature in microtiter plates for one hour, and the absorption at 340 nm was monitored in a LAMBDA Scan plate reader (MWG Biotech).

The fluorescence-based “FdL” assay was done in 25 mM Tris/HCl pH 7.5, 150 mM NaCl using 1 μM hSirt4, 500 μM fluo-HMG-Lys substrate, and 500 μM NAD^+ . After 20 min at 37°C, 2 mM NAM, and 10 mg/ml trypsin in assay buffer was added 1:1, and samples were incubated at room temperature for 45 min. Fluorescence was detected with excitation wavelength 365 nm and emission wavelength 465 nm using a FluoDia T70 (PTI Technologies). Assays with hSirt1, hSirt2, hSirt3, and hSirt5 were performed with the same concentration of NAD^+ , but FdL substrate concentrations were adapted to the KM for each Sirtuin/substrate pair: 50, 200, 40, and 300 μM FdL1, respectively, for hSirt1, hSirt2, hSirt3 and hSirt6; and 40 μM succ-FdL5 for hSirt5. Reaction times were decreased to 7 min for all sirtuins except hSirt6, for which reaction time was elongated to 30 min.

5. Crystal structure of Sirt4

At the end of 2017, *Xenopus* Sirt4 crystal structures (XSirt4) PDB codes: **5OJ7** and **5OJN** bound to APR (Adenosine Diphosphate Ribose) were solved by our project partner at the University of Bayreuth (Prof. Dr. C. Steegborn) [14]. **Figure 5** shows the crystal structure PDB code: **5OJN**, which has an accessible substrate-binding pocket, whereas the peptide pocket in **5OJ7** is partially blocked by Sirt4 loop. The novel X-ray structure was compared with our previously generated Sirt4 homology models. The models show a good overall agreement in the catalytic binding site with the crystal structure. Thus, the RMSD values in the peptide-binding pocket between the crystal structure and the previous homology models are less than 1.

The XSirt4 overall structure shows Rossmann-fold domain and smaller Zn^{2+} binding module. The active-site is located in between them. The six-stranded β -sheet of the

Rossmann-fold domain provides a place for the APR. It was shown that the APR induced closed conformation and stabilized the protein.

Comparing the crystal structure of XSirt4 PDB code: **5OJ7** to other sirtuin isoforms reveals a special extended loop in the Zn²⁺ binding domain between $\alpha 8$ and $\alpha 9$. The loop is located deep into the catalytic core close to the active site or the peptide-binding pocket.

The crystal structure of XSirt4 was superimposed with the crystal structure of Sirt5 and Sirt3 using MOE program. The peptide binding pocket of XSirt4 is similar to the Sirt5 peptide binding pocket (RMSD is 0.8), whereas the RMSD between the peptide-binding pocket of Sirt4 and Sirt3 is 1.3. The residue ASP201 in **5OJ7** is located near the peptide-binding pocket of XSirt4. The backbone of Thr231 in XSirt4 can interact with the substrate, as can be seen in **Figure 6**, which shows the peptide-binding pocket of Sirt4 and Sirt5.

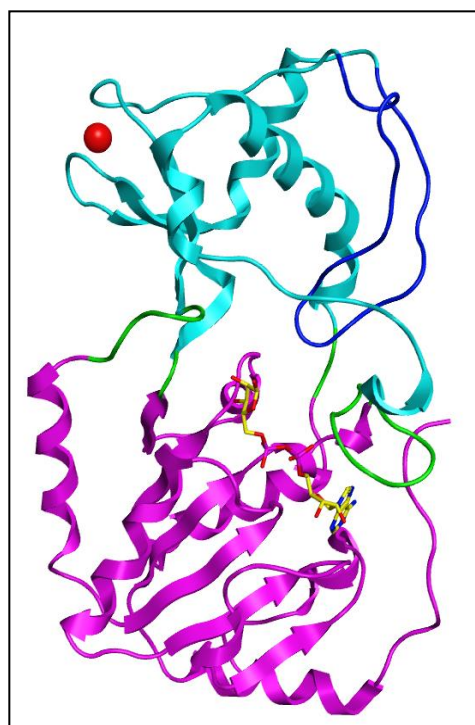


Figure 5: Crystal structure of Sirt4 PDB code: 5OJ7 is shown in cartoon representation. Rossmann-fold domain is in magenta. The zinc-binding domain is in cyan, and zinc ion is shown in red color. The extended loop is in dark blue, APR in yellow, the connecting loops are in green.

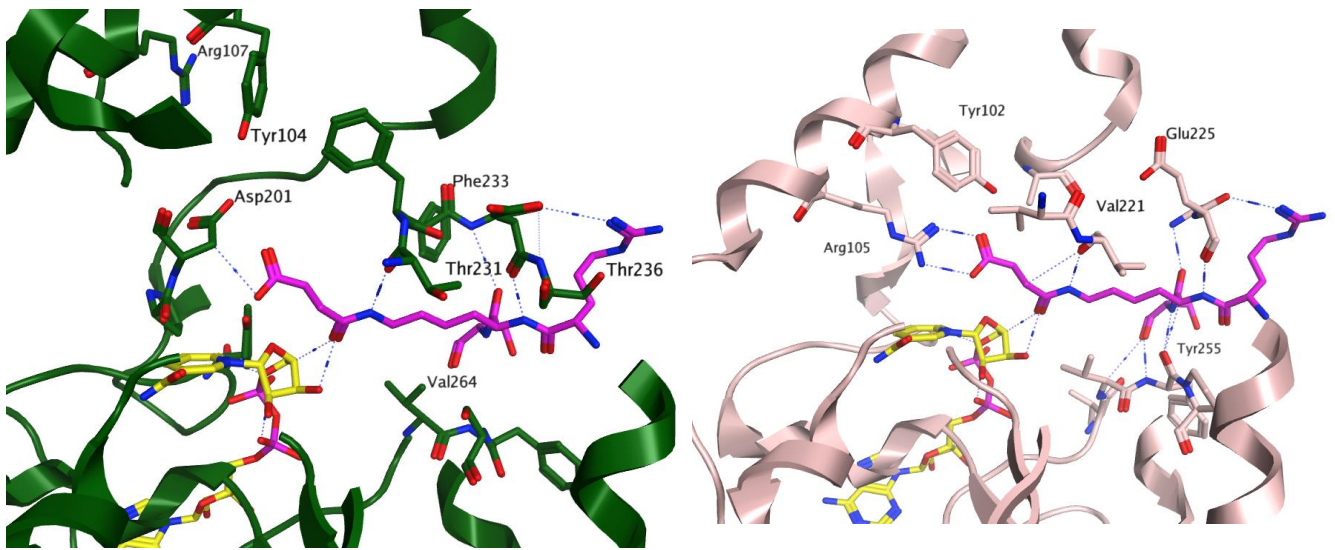


Figure 6: Peptide binding pocket of the crystal structure of Sirt4 (PDB code: 5OJN) (left figure with green ribbon) and Sirt5 (PDB code: 3RIY) (right figure with pink ribbon), APR is in yellow, succinyl lysine peptide is in magenta.

Based on the new XSirt4 crystal structures PDB code: **5OJ7**, **5OJN**, new Sirt4 human homology models HM3, HM5, respectively, were generated. The RMSD values between these homology models and the crystal structures of Sirt4 are less than 1.

Additionally, HM4 was generated using two templates: Sirt5 PDB code: **3RIY** and XSirt4 PDB code: **5OJ7**, the RMSD values of the peptide-binding pocket between HM4 and the templates **3RIY**, **5OJ7** were 1.1, 0.8 respectively, whereas the RMSD values of the protein backbone between HM4 and the templates **5OJ7**, **3RIY** were 1.03, 4.8 respectively.

The five hSirt4 homology models were superimposed using MOE program. The RMSD in the peptide-binding pocket is 2.3 **Figure 7**.

Since the template of HM1, HM2 is Sirt5. Thus, both homology models don't have the extension loop that is close to the active site. Moreover, the overall structure of HM1 is similar to HM2 (RMSD is 1.5). Whereas the structure of HM3 is similar to the structure HM4 (RMSD is 1.6), they both have the extension Sirt4 loop close to the active site. HM5 has an accessible peptide binding pocket, but it is not blocked by Sirt4 loop. The superimposition of the homology models is shown in **Figure 8**.

RMSD = 2.362 A

		1	3	6	8	10	
1:	HM1	0.00	1.55	1.76	2.75	2.41	4.0
3:	HM2	1.55	0.00	2.43	3.23	2.77	3.5
6:	HM4	1.76	2.43	0.00	1.66	1.95	3.0
8:	HM3	2.75	3.23	1.66	0.00	2.50	2.5
10:	HM5	2.41	2.77	1.95	2.50	0.00	2.0

Figure 7: RMSD of the peptide-binding pocket between hSirt4 homology.

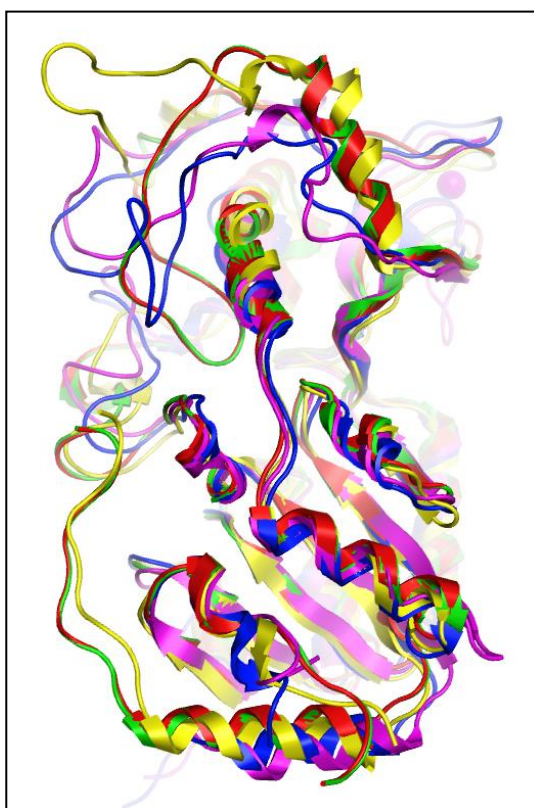


Figure 8: Superimposition of the homology models of hSirt4: HM1 in magenta color, HM2 in blue color, HM3 in red color, HM4 in green color, HM5 in yellow color.

6. Validation of docking

The crystal structures of Sirt4 in complex with APR was taken from the Protein Data Bank (PDB code: **5OJN**, **5OJ7**). All the water molecules were removed. The structures were then protonated and minimized using Amber 99SB force field implemented in MOE. The ligand (APR) preparation was achieved by using MOE. The ligand was protonated at PH=7, followed by a minimization using the Merck Molecular Force Field 94 (MMFF94). Several scoring functions, namely Gold score, Chem score, Chem PLP and ASP available in GOLD 5.2 [17], and XP, SP scores implemented in Glide [18], were used. The APR was re-docked into the XSirt4 cofactor binding pocket, and the binding site was defined by the co-crystallized APR, including all amino acid residues within a distance of 6Å.

The accuracy of the docking programs was tested by observing the ability of the docking score to reproduce the binding mode of the APR. Therefore the root-mean-square deviation (RMSD) values between the experimental binding mode and the docked poses were evaluated. Twenty solutions were generated, and the RMSD values for the three top-ranked were calculated in MOE using APR as a reference (**Table 2**). Importantly, both Gold Score and Glide XP were able to reproduce the experimental binding mode of the docked ligand. Moreover, the RMSD values of the top score poses were below 1Å, Gold Score, and Glide-XP were therefore used for all the following docking processes.

Table 2: RMSD values between the docking poses of the APR and the experimental binding modes observed in the crystal structures.

PDB code	Gold Score	Gold PLP	Gold Chem	Gold Asp	Glide-XP	Glide-SP
5OJ7	0.6	1.2	12.06	12.22	0.9	1.8
	0.5	1.0	12.14	11.77	-	2.4
	0.7	0.9	12.34	12.12	-	2.3
5OJN	0.9	1.3	1.3	1.5	0.8	0.9
	0.7	4.6	12.9	12.5	-	1.9
	1.0	1.7	12.7	12.3	-	1.5

7. MD simulation of Sirt4

7.1. MD simulation of HM1

In order to study the stability of the Sirt4, MD simulations were carried out on Sirt4 homology model HM1 in complex with different substrates such as lipoyl and succinyl lysine using AMBER 12 and AMBER 2003 force field. The RMSD of the protein backbone atoms and the studied substrates were calculated and plotted. VMD (Visual Molecular Dynamics) was used to analyze the RMSD and the trajectories [19]. The Xmgrace plotting tool was used to plot the RMSD data.

MD simulations of Sirt5 crystal structures have also been performed and compared with the MD simulation results of Sirt4. The RMSD of the protein backbone atoms and the studied substrates were calculated and plotted. The RMSD plots of HM1 showed no significant increase in deviation until the completion of 15 ns. The residues of the HM1 substrate-binding pocket showed RMSD values between 1.0-1.3 Å with lipoyl lysine peptide and 2.0-2.2 Å with succinyl lysine peptide. Thus the substrate-binding pocket of hSirt4 with lipoyl substrate is more stable than with the succinyl substrate. Moreover, Sirt5 peptide-binding pocket is more stable than the peptide-binding pocket of hSirt4 (HM1) **Figure 9**.

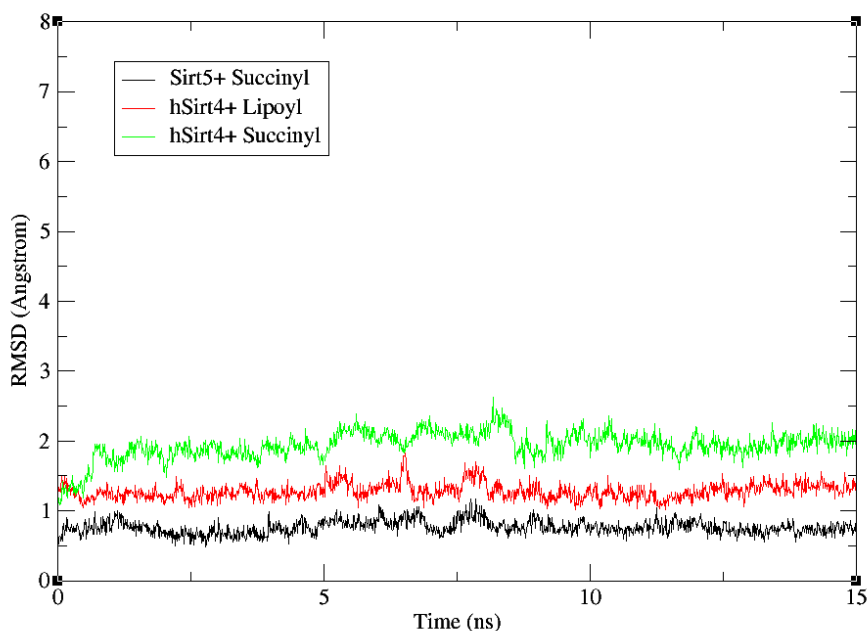


Figure 9: RMSD of backbone atoms of the substrate-binding pocket of Sirt5 (PDB: 3RIY) and hSirt4 (HM1).

7.2. MD simulation of HM3

HM3 bound to APR was simulated for 40 ns using AMBER 12 and AMBER 2003 force field. The RMSD of the protein backbone atoms was calculated and plotted. The structure of HM3 and APR were found to be highly stable during 40 ns MD. In addition, the RMSD values are below 2 (**Figure 10**).

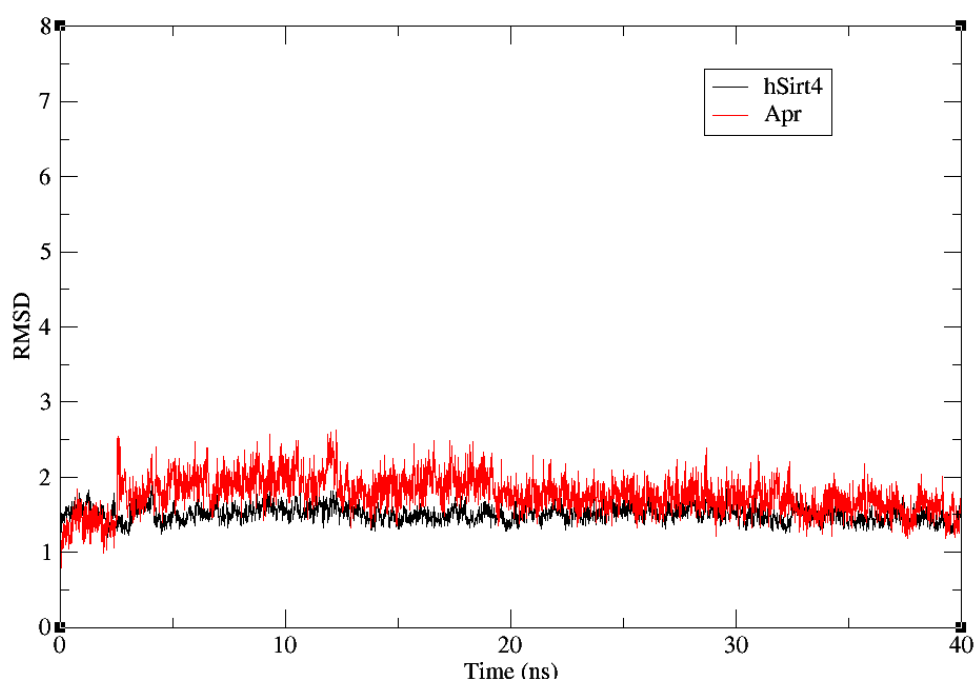


Figure 10: RMSD plot of the backbone atoms of HM3 (black), APR (red).

7.3. MD simulation of Sirt4 crystal structure (XSirt4)

Several substrates such as lipoyl, hydroxymethylglutaryl (HMG) lysine were docked into the peptide-binding pocket of XSirt4 (PDB code: **5OJ7**). MD simulations were carried out on the complex of XSirt4 with the substrates. **Figure 11, 12** shows the binding modes of XSirt4 with HMG and lipoyl after 20 ns MD simulation. It was observed that the interactions between the key residues Gly234, Asp235, Thr231, and the substrates (lipoyl, HMG) were maintained during the MD simulation. Moreover, the residues of the XSirt4 substrate-binding pocket with the studied substrates were stable during the MD simulation. Thus the RMSD values are less than 2 (**Figure 13**).

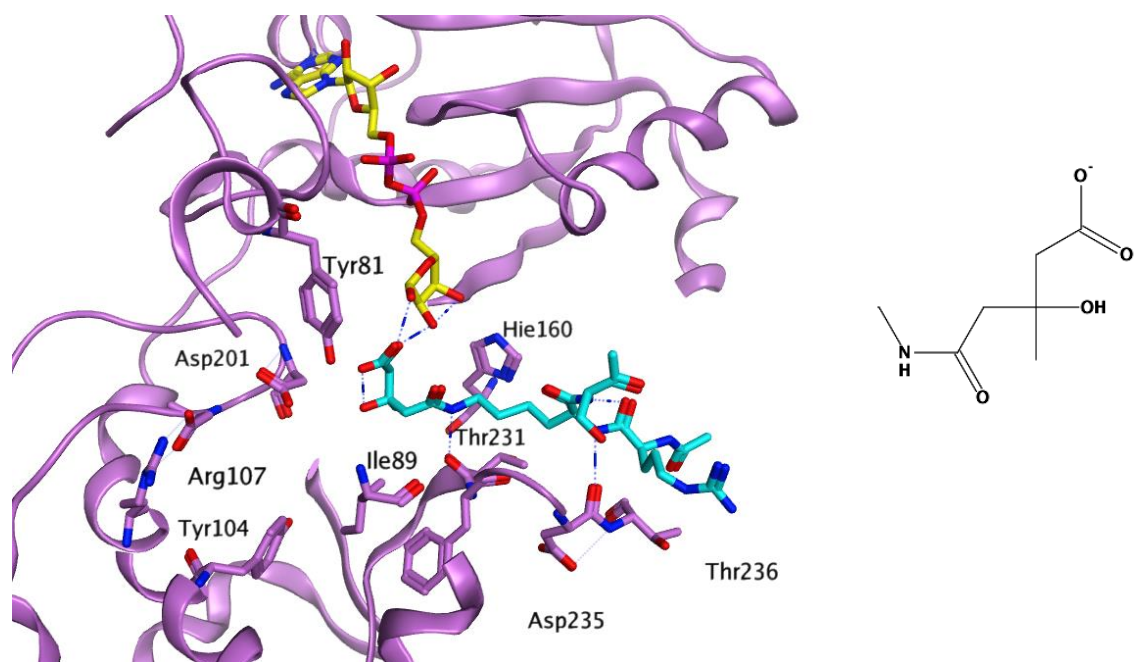


Figure 11: Putative binding mode of HMG substrate (cyan color) with XSirt4 after 20 ns MD simulation.

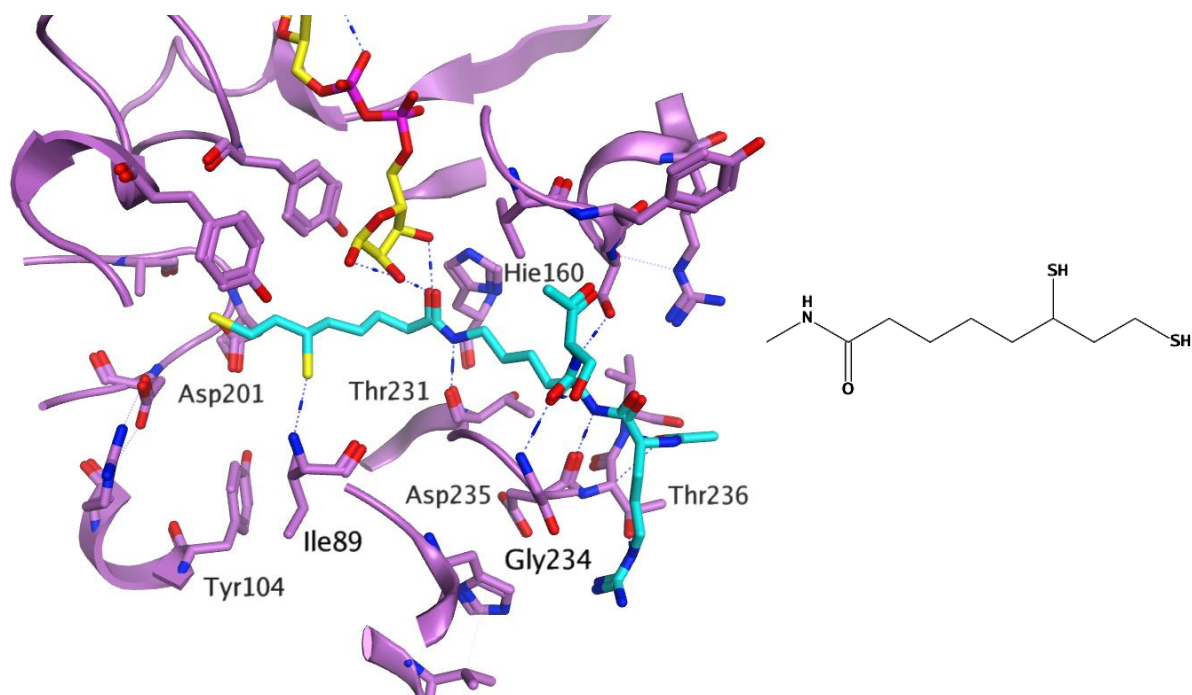


Figure 12: Putative binding mode of lipoyl substrate (blue color) with XSirt4 after 20 ns MD simulation.

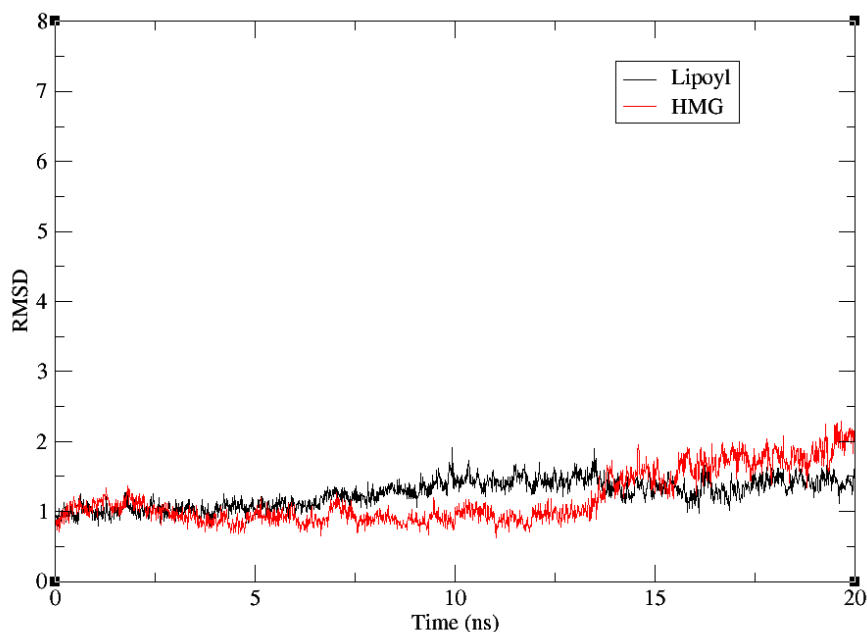


Figure 13: Root-mean-square deviations (RMSD) of the backbone atoms of the substrate-binding pocket of XSirt4 with lipoyl in black, XSirt4 with HMG in red.

8. Conformational changes of XSirt4 and hSirt4

To study the conformational dynamics and the motion of Sirt4, we should first simulate the protein by MD simulation, then a cluster analysis of molecular simulation trajectories can be done. XSirt4 (PDB code: **5OJ7**) and HMG were simulated for 80 ns by accelerated MD simulation using AMBER 12 (APR was kept inside the APR-binding pocket). The simulation was also done on XSirt4 without the substrate, and the results were compared with the results of the MD simulation of XSirt4 with a substrate. Besides, HM3 was also simulated with the most active VS hit.

The effect of an inhibitor or a substrate on the structure of Sirt4 was investigated. Average fluctuation values for individual amino acid residues were calculated during the MD simulations. The stability and the fluctuations of a protein during the simulations were confirmed by the root-mean-square deviation (RMSD) and root-mean-square fluctuation (RMSF) of the protein C α -analysis, respectively.

In order to reduce the number of MD snapshots, clustering was done. Since we will focus on the dynamics of the peptide-binding pocket, we used the atoms around the peptide-binding pocket in the clustering process. We applied the average linkage clustering algorithm to the snapshots from the MD simulation using Cpptraj from Amber Tools 16.

It was shown that the substrate HMG stabilizes the residues of the peptide-binding pocket of XSirt4. Thus, the RMSD of the peptide pocket residues is less than 2 **Figure 14**.

Based on RMSF results (**Figure 15**), the most flexible residues which contribute to the structure motion of XSirt4 are the residues of the numbers: 37-74, 135-166, and 201-220, whereas the flexible residues in hSirt4 are 37-72 and 154-171. Additionally, it was shown that the residues 201-220, which refer to the Sirt4 loop, are more flexible in XSirt4 than in hSirt4 **Figure 16**. The flexible residues contribute in α -helix: $\alpha 9$, $\alpha 7$, $\alpha 2$, and β -strands: $\beta 1$, $\beta 2$, $\beta 3$ of the protein; these helices and strands region refer to the Sirt4 loop and parts of Rossmann-fold domain as shown in **Figure 17**.

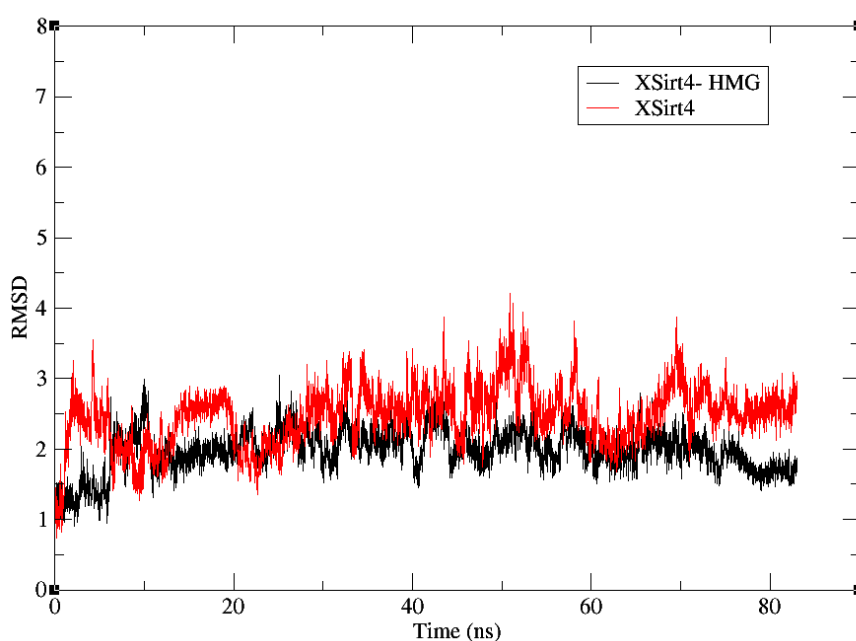


Figure 14: RMSD of C α atoms of the XSirt4 peptide-binding pocket in the substrate (HMG) bound form and substrate-free forms.

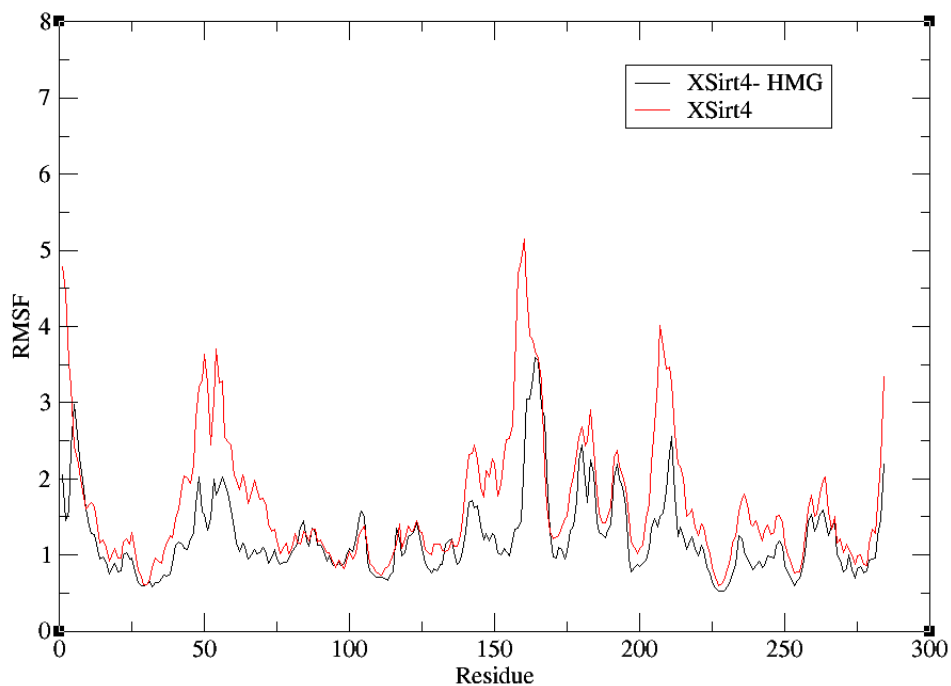


Figure 15: RMSF values of C α atoms versus residue numbers during 80 ns MD simulations, fluctuations of the XSirt4 HMG bound- and HMG-free forms.

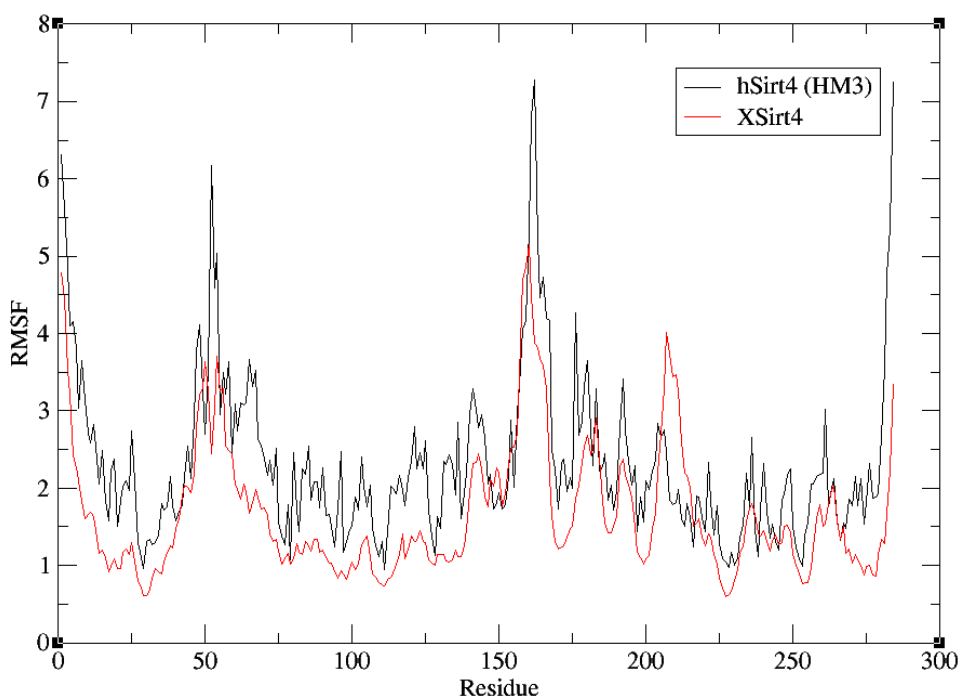


Figure 16: RMSF values of C α atoms versus residue numbers during 80 ns MD simulations, fluctuations are compared between XSirt4 crystal structure and HM3.

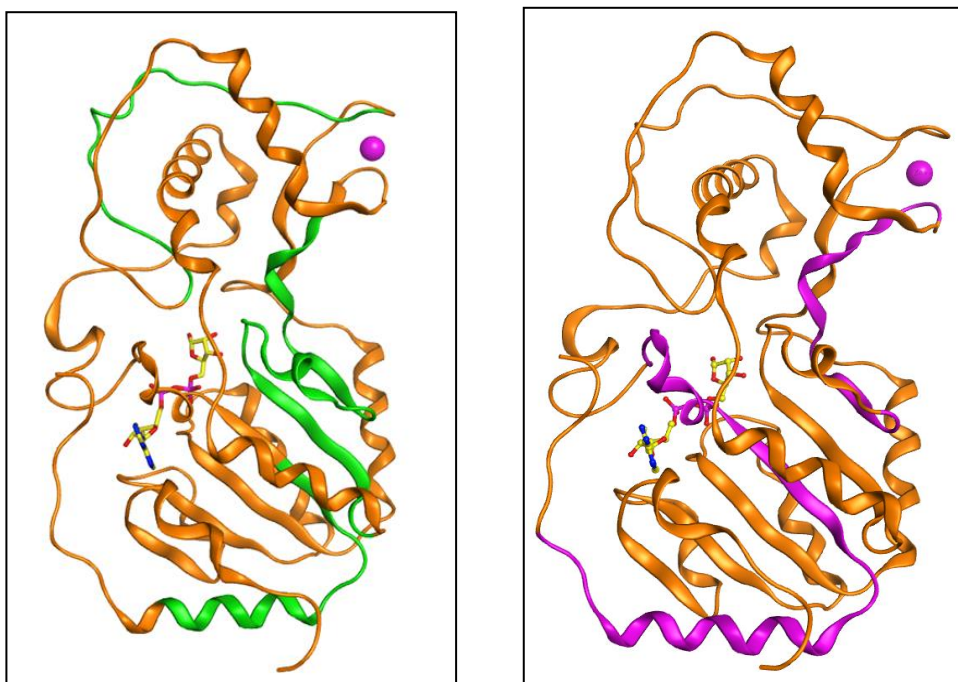


Figure 17: The flexible parts of XSirt4 (green color) and hSirt4 (magenta color).

9. Predicting of XSirt4 apo form

Since no apo-form structure has been proposed so far for Sirt4, a predicted Sirt4 apo form was generated. Hierarchical clustering was done for MD trajectories, which resulted from the previous 80 ns accelerated MD simulation that was done on XSirt4. Consequently, three cluster representative structures were obtained.

A blast search was done using XSirt4 sequence to search for a structure that is similar to XSirt4. As a result, the apo structure of Sirt3 PDB code: **5D7N** was found with identity 30.4. We superimposed this structure with the representative structures from clustering groups. The RMSD was calculated using MOE. One structure from the cluster representative structures was similar to Sirt3 apo structure with RMSD 1.87. Since the overall structure of Sirt4 is similar to Sirt3 (the RMSD of the protein backbone was 2.3), thus we considered this apo conformation form as Sirt4 apo form (**Figure 18**), the RMSD between the predicted Sirt4 apo form and XSirt4 is 2.73. **Figure 19** shows the peptide-binding pocket of the predicted Sirt4 apo form and XSirt4.

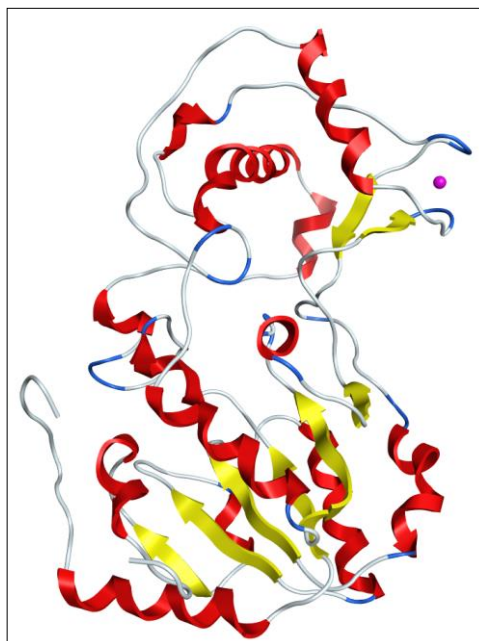


Figure 18: Predicted Sirt4 apo form; β strands are colored yellow, α helix are red, and loops are white, zinc atom in magenta color.

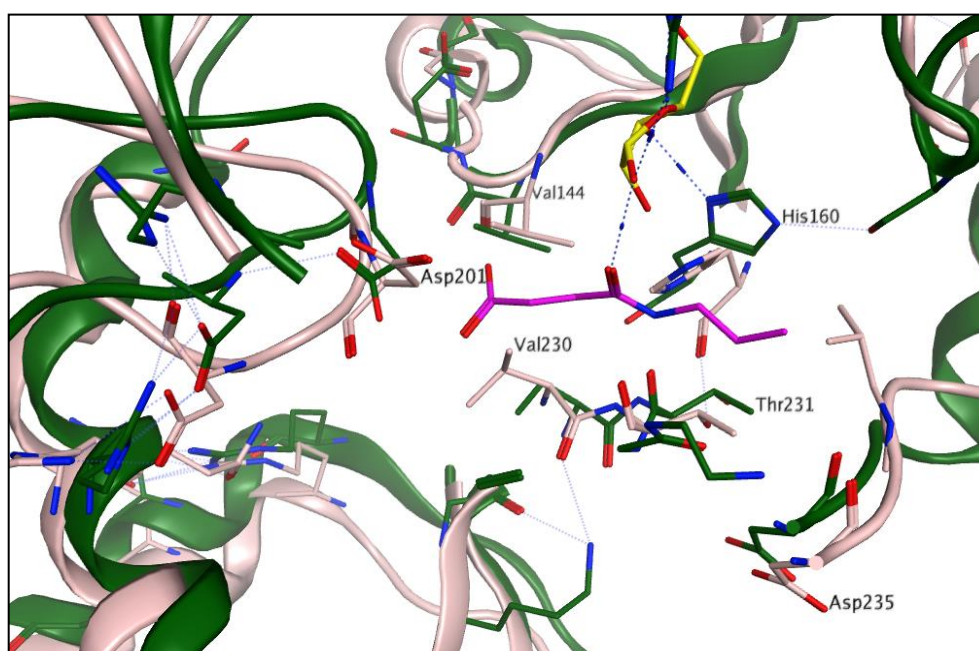


Figure 19: Peptide binding pocket of the predicted Sirt4 apo form (pink color) and XSirt4 (green color), the peptide is shown in magenta color.

10. Conclusions

The following conclusions can be made:

- Five homology models of hSirt4 were generated using different templates, and the stability of the structures was studied using MD simulation.
- MD simulation of Sirt5 crystal structure was performed and compared with the Sirt4 MD simulation results. It was shown that the substrate-binding pocket of hSirt4 with lipoyl substrate is more stable than hSirt4 with succinyl substrate. In addition, Sirt5 peptide-binding pocket is more stable than the peptide-binding pocket of hSirt4 (HM1).
- Virtual screening for novel hSirt4 inhibitors was carried out using Glide program and resulted in proposals for in vitro testing. Based on docking studies employed in this study, a plausible binding mode for novel hSirt4 inhibitors has been established. Besides, models and inhibitors found during this work provide a promising starting point for discovering new Sirt4 inhibitors.
- This study provides information and mechanistic details of the conformational changes in Sirt4 induced by substrates and inhibitor. The conformational dynamics of XSirt4 with hydroxymethylglutaryl (HMG) were studied. Thus, HMG was docked into the peptide pocket of XSirt4 crystal structure. Accelerated MD simulation was done on both the complex of XSirt4 crystal structure with the substrate HMG and the complex of hSirt4 with the most active compound to study the conformational changes of the protein upon ligand binding. The RMSD plots indicate that the XSirt4 bound to HMG is more stable than the XSirt4 form without the substrate. Hence, the substrate HMG stabilizes the residues of the peptide-binding pocket of XSirt4. Besides, the flexible helices and strands region refer to the Sirt4 extended loop and parts of Rossmann-fold domain.
- Since no apo-form from Sirt4 structure model has been proposed so far, Sirt4 apo form was established in this study and analyzed using MD simulation studies.

References

- [1] Vatrinet R, Iommarini L, et al., Targeting respiratory complex I to prevent the Warburg effect, *the International Journal of Biochemistry & Cell Biology* 63, (2015), 41-45.
- [2] Jeong SM, Xiao C, Finley LW, et al., SIRT4 has tumor-suppressive activity and regulates the cellular metabolic response to DNA damage by inhibiting mitochondrial glutamate metabolism. *Cancer Cell* 23(4), (2013), 450–463.
- [3] Rommel M, Todd G, et al., Sirtuin 4 Is a Lipoamidase Regulating Pyruvate Dehydrogenase Complex Activity, *Cell* 159, (2014), 1615–1625.
- [4] Shih J and Donmez G, Mitochondrial Sirtuins as Therapeutic Targets for Age-Related Disorders, *Genes & Cancer* 4 (3-4), (2013), 91 –96.
- [5] Parihar P, Solanki I et al., Mitochondrial sirtuins: Emerging roles in metabolic regulations, energy homeostasis, and diseases, *Experimental Gerontology* 61, (2015), 130- 141.
- [6] K. A. Anderson et al., SIRT4 Is a Lysine Deacylase that Controls Leucine Metabolism and Insulin Secretion. *Cell metabolism*. 25, 838-855, (2017), 838-855.
- [7] Remmert, Michael et al., HHblits: Lightning-fast iterative protein sequence searching by HMM-HMM alignment. *Nature methods*. 9. (2011), 173-5.
- [8] MOE brochure, Chemical Computing Group Inc. & Ryoka Systems Inc, (2014).
- [9] Eswar N, Webb B, Marti-Renom MA, et al. Comparative protein structure modeling using Modeller. *Curr Protoc Bioinformatics*, (2006), 5-6.
- [10] R. A. Laskowski, M. W. MacArthur, D. S. Moss, J. M. Thornton, PROCHECK: a program to check the stereochemical quality of protein structures. *J Appl Crystallogr*. 26, (1993), 283–291.
- [11] Swyter S, Schiedel M, Monaldi D, et al. New chemical tools for probing activity and inhibition of the NAD⁺-dependent lysine deacylase sirtuin 2. *Philos Trans R Soc Lond B Biol Sci*. 373, (2018).
- [12] Schiedel M, Rumpf T, Karaman B, et al. Structure-Based Development of an Affinity Probe for Sirtuin 2. *Angew Chem Int Ed Engl*. 55(6), (2016), 2252-2256.
- [13] Rumpf T, Schiedel M, Karaman B, et al. Selective Sirt2 inhibition by ligand-induced rearrangement of the active site. *Nat Commun*. 6, (2015).
- [14] Pannek, M., Simic, Z., Fuszard, M. et al. Crystal structures of the mitochondrial deacylase Sirtuin 4 reveal isoform-specific acyl recognition and regulation features. *Nat*

Commun 8, (2017), 1-13.

[15] Wang, J. et al. Development and testing of a general amber force field. *Journal of computational chemistry* 25 (9) (2004), 1157-74.

[16] Smith BC, Hallows WC, Denu JM. A continuous microplate assay for sirtuins and nicotinamide-producing enzymes. *Anal Biochem*, 394(1), (2009), 101-109.

[17] Verdonk M et al., Improved protein-ligand docking using GOLD, *J Protein* 1; 52 (4), (2003), 609-23.

[18] Halgren T et al. Glide: A new approach for rapid, accurate docking and scoring. Method and assessment of docking accuracy. *J. Med. Chem.*, 47, (2004), 1739-1749.

[19] Humphrey W, Dalke A, Schulten K, VMD: Visual molecular dynamics *Journal of Molecular Graphics* 14, (1996), 33-38.

4.7. Manuscript 7: Unexpected AChE inhibitory activity of (2E) α , β unsaturated fatty acids.

A., Loesche, J., Wiemann, Z., Alhalabi, J., Karasch, W., Sippl, R., Csuk.

Bioorganic & medicinal chemistry letters. 28, 3315–3319 (2018).



Unexpected AChE inhibitory activity of (2E) α,β -unsaturated fatty acids

Anne Loesche^a, Jana Wiemann^a, Zayan Al Halabi^b, Julia Karasch^a, Wolfgang Sippl^b, René Csuk^{a,*}

^a Martin-Luther-University Halle-Wittenberg, Organic Chemistry, Kurt-Mothes-Str. 2, D-06120 Halle (Saale), Germany

^b Martin-Luther-University Halle-Wittenberg, Institute of Pharmacy, Wolfgang-Langenbeck-Str. 4, D-06120 Halle (Saale), Germany

ARTICLE INFO

Keywords:

Fatty acid derivatives
Acetylcholinesterase
Butyrylcholinesterase
Alzheimer's disease

ABSTRACT

A small library of (E) α,β -unsaturated fatty acids was prepared, and 20 different saturated and mono-unsaturated fatty acids differing in chain length were subjected to Ellman's assays to determine their ability to act as inhibitors for AChE or BChE. While the compounds were only very weak inhibitors of BChE, seven molecules were inhibitors of AChE holding $IC_{50} = 4.3\text{--}12.8\ \mu\text{M}$ with three of them as significant inhibitors of this enzyme. The results have shown *trans* 2-mono-unsaturated fatty acids are better inhibitors for AChE than their saturated analogs. Furthermore, the screening results indicate that the chain length is crucial for obtaining an inhibitory efficacy. The best results were obtained for (2E) eicosenoic acid (14) showing inhibition constants $K_i = 1.51 \pm 0.09\ \mu\text{M}$ and $K_i' = 7.15 \pm 0.55\ \mu\text{M}$. All tested compounds were mixed-type inhibitors with a dominating competitive part. Molecular modelling calculations indicate a different binding mode of active/inactive compounds for the enzymes AChE and BChE.

The lifespan of people has increased dramatically over the last decades as a result of modern and better medical care through better medicines and improved living conditions.¹ However, the latter have also led to a sharp increase in the number of people suffering from civilization diseases, especially in Europe, the Americas and parts of Asia.² The prolonged life expectancy also increased the proportion of people badly affected by diseases that are currently incurable or difficult to cure, among them neurodegenerative diseases such as Alzheimer's disease (AD).^{3,4} It is interesting in this context that the proportion of people suffering from certain diseases varies from region to region. In particular, the number of people afflicted with cardiovascular diseases is significantly reduced in Mediterranean countries.^{5,6} Over a longer period of time, this phenomenon was explained either by the French paradox (increased uptake of resveratrol, for example by increased consumption of red wine) or by eating a Mediterranean diet. Recent research shows, however, that the French paradox does not seem to be valid, and that an increased uptake of resveratrol does not adequately explain the prolonged life expectancy.⁷ Mediterranean diet is characterized by a high content of unsaturated fatty acids resulting from the almost exclusive use of olive oil.⁸ Circulating fatty acids are associated with a multitude of chronic diseases. In continuation of our earlier studies on the cure or at least alleviation of AD we became interested in the search and development of inhibitors of the enzymes acetylcholinesterase (AChE) and butyrylcholinesterase (BChE). We are aware that cholinesterase inhibitors are not suited to cure AD,^{9,10} but

these compounds are able to slow down the progression of the disease and restore part of the patient's quality of life for a longer period of time.^{11,12} Individual observations from the use of vegetable oils indicate that certain fatty acids could possibly act as inhibitors of the cholinesterases (ChE).^{13,14} As a consequence, we became particularly interested in the potential of this class of compounds as to whether long-chain fatty acids (or derivatives thereof) could serve as potential inhibitors of ChE.^{6,15} This is supported by the findings of a prospective study in non-decent older persons, which showed that an increased uptake of mono-unsaturated fatty acids and poly-unsaturated fatty acids is associated with a slowed cognitive decline.¹⁶ The increased consumption of olive oil, which is very rich in mono-unsaturated fatty acids, is considered a trademark of traditional Mediterranean diet.¹⁷ The free fatty acids mainly found in olive oil are palmitic acid (C16:0), palmitoleic acid (C16:1), stearic acid (C18:0), oleic acid (C18:1), linoleic acid (C18:2), linolenic acid (18:3), and eicosanoic acid (C20:0). The composition of the fatty acids can vary according to the growing area and the type of olives. Studies of Scarmeas et al. showed that compliance with a Mediterranean diet is associated with a lower risk of developing the symptoms of AD.¹⁸ Martinez-Lapiscina et al. also showed in a clinical study that patients on a diet rich in olive oil showed better cognitive functions than patients on a control diet.¹⁹ In addition to olive oil, plant extracts (with a higher content of unsaturated fatty acids and mono-unsaturated *cis* configured fatty acids) were also tested positively for their inhibitory properties for ChE.^{20–22} We were

* Corresponding author.

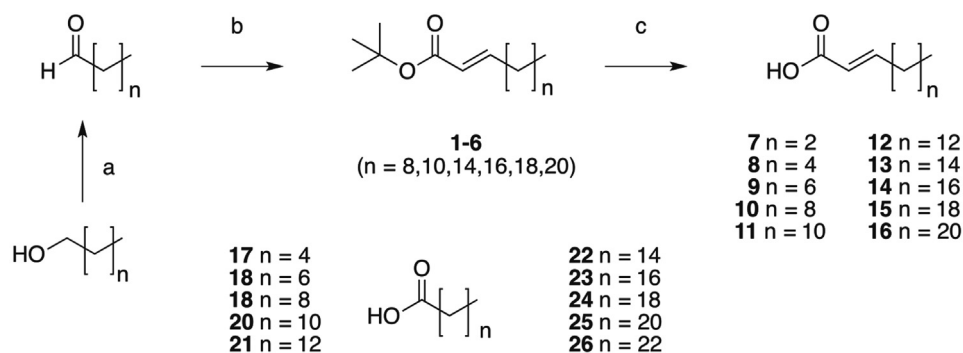
E-mail address: rene.csuk@chemie.uni-halle.de (R. Csuk).

<https://doi.org/10.1016/j.bmcl.2018.09.013>

Received 25 July 2018; Received in revised form 7 September 2018; Accepted 10 September 2018

Available online 11 September 2018

0960-894X/© 2018 Elsevier Ltd. All rights reserved.



Scheme 1. Structure and synthesis of *trans*-mono-unsaturated fatty acid esters **1–6** and of carboxylic acids **7–16** as well as of saturated fatty acids **17–26**: a) eicosanol/docosanol, Celite[®], PCC, DCM, 0 °C, 1 h, →r.t.; b) *tert*-butoxycarbonylmethylene-triphenylphosphorane, DCM, r.t., 12 h; c) TFA, DCM, 0 °C →r.t., 1 h.

Table 1

Relative inhibition (in %), inhibitory activity (IC_{50} in μM) and inhibitory constants (K_i and K_i' in μM) for galantamine hydrobromide (**GH**) and compounds **7–26** determined in Ellman's assay employing acetylcholinesterase (AChE, from *Electrophorus electricus*) and butyrylcholinesterase (BChE, from equine serum). Each experiment was performed at least in triplicate.

Compounds	AChE			BChE
	inhibition (%) ^a	IC_{50} (μM)	K_i (μM) [K_i' (μM)] (type of inhibition)	inhibition (%) ^a
GH	90.30 ± 0.08	1.23 ± 0.07	0.37 ± 0.14 (<i>competitive</i>)	56.32 ± 1.02
7	14.42 ± 0.79			5.91 ± 1.09
8	14.77 ± 0.77			6.00 ± 1.43
9	13.29 ± 0.62			7.72 ± 2.36
10	19.41 ± 1.03			3.91 ± 1.24
11	15.78 ± 0.87			4.18 ± 0.76
12	73.58 ± 0.42	7.90 ± 0.63		4.33 ± 1.09
13	89.64 ± 0.25	4.30 ± 0.54	3.21 ± 0.18 [5.51 ± 0.18] (<i>mixed-type</i>)	8.01 ± 0.74
14	94.92 ± 0.04	5.00 ± 0.34	1.51 ± 0.09 [7.15 ± 0.55] (<i>mixed-type</i>)	7.69 ± 0.91
15	40.74 ± 1.02	11.72 ± 0.71		13.33 ± 1.41
16	n.sol.			n.sol.
17	11.39 ± 0.64			4.87 ± 0.77
18	9.49 ± 1.00			3.49 ± 0.84
19	15.74 ± 1.49			9.91 ± 3.42
20	13.76 ± 0.59			3.29 ± 1.33
21	23.69 ± 0.50			2.71 ± 0.83
22	43.63 ± 2.25	10.15 ± 1.60		3.55 ± 1.02
23	78.35 ± 0.99	7.50 ± 0.92	4.40 ± 0.25 [3.62 ± 0.06] (<i>mixed-type</i>)	3.84 ± 0.80
24	33.93 ± 0.41	12.80 ± 1.31		4.67 ± 1.24
25	23.26 ± 1.02	n.sol.		4.24 ± 1.03
26	n.sol.			n.sol.

^a Percent inhibition was determined at 10 M concentration; n.sol. stands for non-soluble under the conditions of the assay; mean ± SD.

therefore interested in the potency and selectivity of *trans* configured fatty acids as possible ChE inhibitors. Therefore, a series of *trans* 2-mono-unsaturated fatty acids differing in chain length was prepared and screened for their potential to act as inhibitors of AChE and/or BChE.

Our synthetic approach for the synthesis of *trans* 2-mono-unsaturated fatty acids is depicted in Scheme 1. Six different (*E*) α,β -unsaturated fatty acid *tert*-butyl esters **1–6** were used as starting materials for the straightforward synthesis of the fatty acids **10–16**.

Thus, *tert*-butyl esters **1–6** were synthesized by Wittig reactions in DCM at room temperature starting from commercially available aldehydes of different chain lengths and (*tert*-butoxycarbonylmethylene) triphenylphosphorane (**1–4**).²³ The synthesis of long-chain esters **5** and **6** started from 1-eicosanol and 1-docosanol, respectively. These alcohols were oxidized to aldehydes using PCC in dry DCM.²⁴ The esters were obtained in 72–99% yields, and the removal of the *tert*-butyl group was performed in almost quantitative yields with TFA in DCM.²⁵

Compound **1–16** were analyzed in detail by several spectroscopic techniques. Thus, *tert*-butylesters **1–6** showed in the ¹H NMR spectra

the signal for the *tert*-butyl group a δ = 1.48 ppm; in the ¹³C NMR spectra chemical shifts of δ = 28.0–28.3 ppm (methyl) and δ = 80.1 ppm ($C_{\text{quart.}}$) were found, respectively. As exemplified for **10**, acids **7–16** are characterized in their ¹H NMR spectra by the presence of two signals at δ = 7.09 (3-H) and 5.82 (2-H). The coupling constant ³ $J_{\text{H,H}}$ = 15.6 Hz indicates the presence of a (*2E*) configuration.

The potential of an enzyme inhibitor to decrease the activity of an enzyme is often associated with its more often less perfect fit into the enzyme's active site.²⁶ Therefore, we investigated the effect of an increasing chain length in acids **7–16**; the influence of the double bond was investigated by comparative screening saturated fatty acids **17–24**. Due to the high degree of homology between the amino acid sequences of different AChE and the similarity in the active site, the enzymes generally show similarity in their interaction with substrates and inhibitors. Due to the high price for human AChE and the poor availability of human BChE, we decided to carry out first experiments with AChE from electric eel and BChE from equine serum. Pre-screening of the *trans*-configured fatty acids **7–16** using AChE (from electric eel, *Electrophorus electricus*) showed four compounds as inhibitors while all

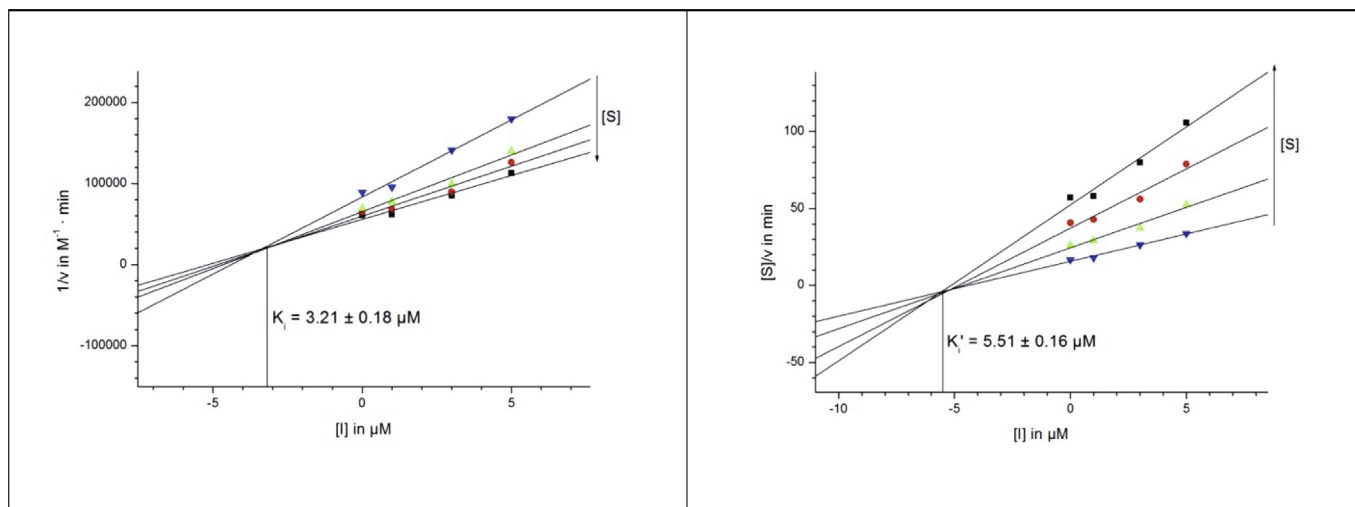


Fig. 1. Dixon (left) and Cornish-Bowden (right) plot for 13.

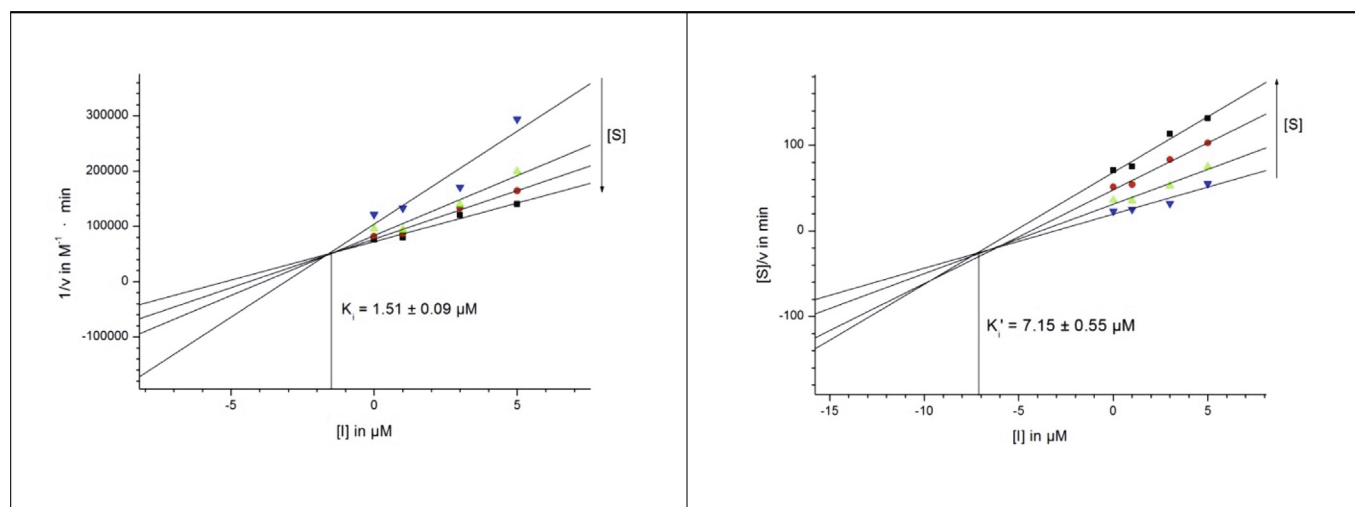


Fig. 2. Dixon (left) and Cornish-Bowden (right) plot for 14.

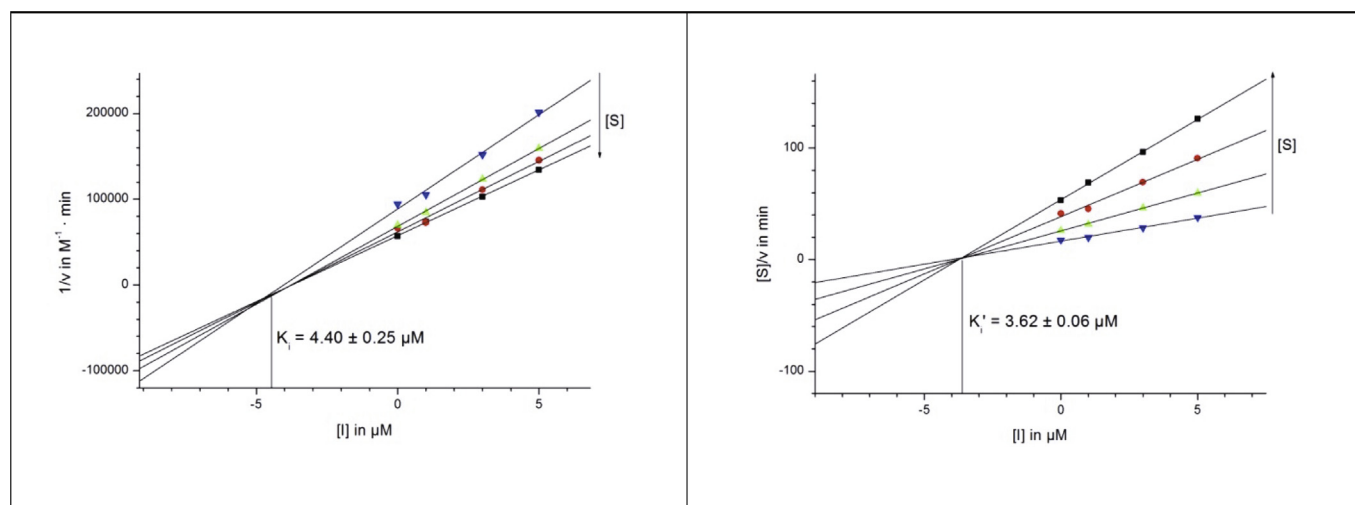


Fig. 3. Dixon (left) and Cornish-Bowden (right) plot for 23.

of these acids are very weak inhibitors of BChE (from equine serum). For the latter, at 10 M concentration the percentage of inhibition was always less than 15%. The results of this screening experiments

applying Ellman's colorimetric assay are compiled in Table 1.²⁷ Galantamine hydrobromide (GH), one of the gold standard drugs to treat the symptoms of AD was used for comparison. The inhibition constants

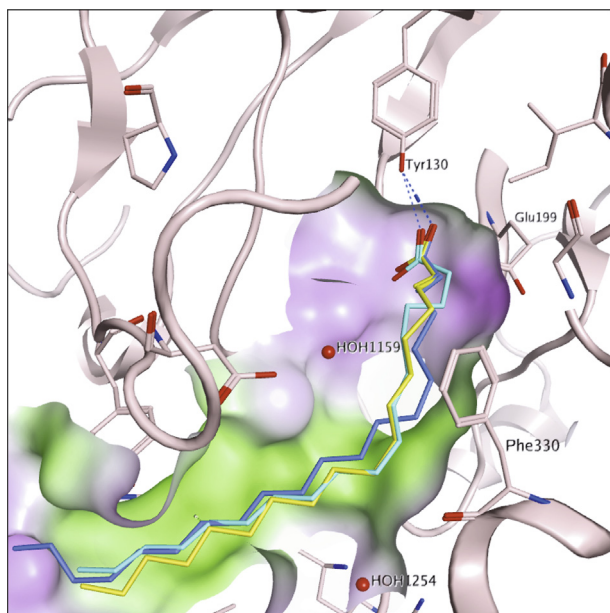


Fig. 4. Predicted common binding mode of the active compounds (compound 13 in yellow, compound 23 in light blue, compound 14 in dark blue) in the binding pocket of AChE (PDB code: 1EVE); hydrogen bonds were drawn as dashed lines, and the binding pocket is colored according to hydrophobic (green) and hydrophilic (pink) regions.

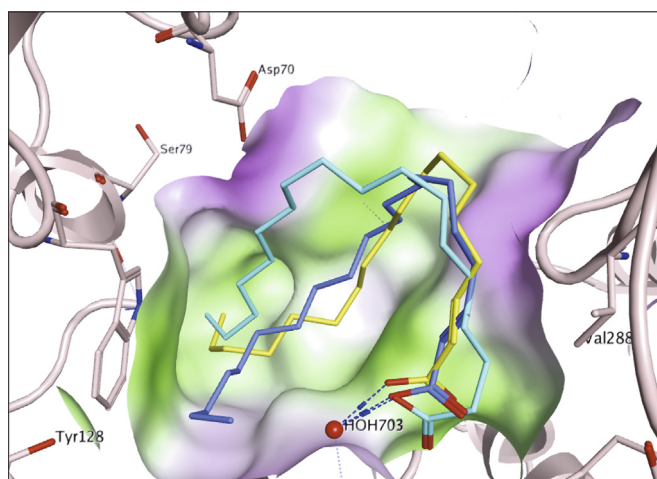


Fig. 5. Predicted common binding mode of the active compounds (compound 13 in yellow, compound 23 in light blue, compound 14 in dark blue) in the binding pocket of the horse BChE homology model; hydrogen bonds were drawn as dashed lines, and the binding pocket is colored according to hydrophobic (green) and hydrophilic (pink) regions.

K_i (competitive part) and K_i' (uncompetitive part) as well as the type of inhibition was determined using Dixon,²⁸ Cornish-Bowden²⁹ and Lineweaver-Burk plots for those compounds showing the highest rate of inhibition in the preliminary screening (Figs. 1–3).³⁰

These experiments showed 13 as a good mixed-type inhibitor for AChE with $K_i = 3.21 \pm 0.18$ M and $K_i' = 5.51 \pm 0.18$ M with $IC_{50} = 4.30 \pm 0.54$ M. Even better results were obtained for chain extended acid 14 as the most active compound of this series. This compound inhibits AChE as a mixed-type inhibitor ($K_i = 1.51 \pm 0.09$ M, $K_i' = 7.15 \pm 0.55$ M) with the competitive part of the inhibition being predominant. This indicates that 14 deploys its inhibitory activity predominantly by binding to the free enzyme rather than by binding to the enzyme-substrate complex. The half maximal inhibitory concentration of 14 is $IC_{50} = 5.00 \pm 0.34$ M. For

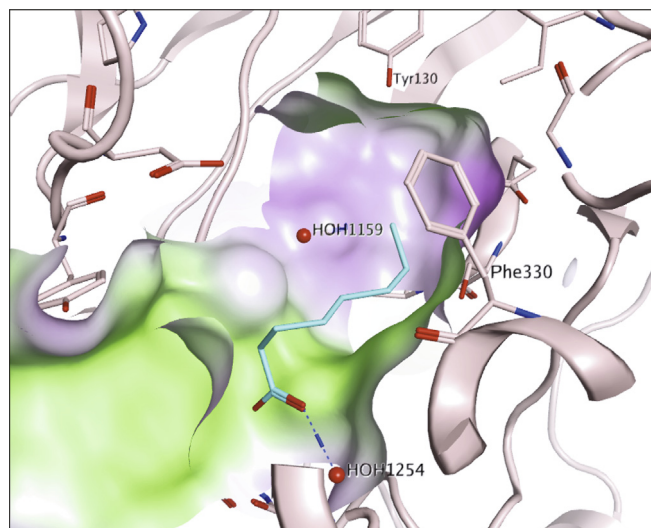


Fig. 6. Predicted common binding mode of an inactive compound (compound 18 in light blue) in the binding pocket of AChE (PDB code: 1EVE); hydrogen bonds were drawn as dashed lines, and the binding pocket is colored according to hydrophobic (green) and hydrophilic (pink) regions.

comparison, standard GH (as a competitive inhibitor) holds a $K_i = 0.37 \pm 0.14$ and an $IC_{50} = 1.23 \pm 0.07$ M. With exception of 23 ($K_i = 4.40 \pm 0.25$ M, $K_i' = 3.62 \pm 0.06$ M; $IC_{50} = 7.50 \pm 0.92$ M), none of the saturated fatty acids showed any significant activity for AChE. Extra experiments using variable substrate/inhibitor concentrations should the compounds as reversible inhibitors (Fig. 3).

Some molecular modelling calculations were performed to get deeper insights in the mode of action of these inhibitors (details are found in the supplementary part). As a result, a common binding mode of the active compound 13, 14 and 23 was found inasmuch as these compounds interact with the side chain of Tyr130 in AChE (PDB code: 1EVE).

The screening of the compounds showed the selectivity of these compounds being higher for AChE than for BChE. It seems probable that the α,β -unsaturated fatty acids interact with the residue Tyr 130 in the AChE binding pocket and could fit very well into the AChE hydrophobic binding pocket, too. Moreover, the carboxyl groups of the compounds fit reasonably into the hydrophilic part of the pocket whereas for BChE the inhibitors interact with the water molecule HOH 703 (Figs. 4 and 5).

The molecular modelling calculations also revealed that the inactive compounds (as exemplified for 18) interact in a different way since they interact with the water molecule HOH 1254 in AChE (Fig. 6).

In conclusion, we report the synthesis of a small series of (*E*) α,β -unsaturated fatty acids; 20 different saturated and mono-unsaturated fatty acids differing in chain length were subjected to Ellman's assays to determine their ability to act as inhibitors for AChE or BChE. The compounds were only weak inhibitors of BChE but seven molecules were inhibitors of AChE holding $IC_{50} = 4.3$ to 12.8 M. Extra assays revealed three of them as significant inhibitors of this enzyme. The results have shown *trans* 2-mono-unsaturated fatty acids are better inhibitors for AChE than their saturated analogs. Thus, octadecanoic acid (23) was the most active saturated fatty acid holding inhibition constants $K_i = 4.40 \pm 0.25$ M and $K_i' = 3.62 \pm 0.06$ M. For comparison, for analog 13 inhibition constants $K_i = 3.21 \pm 0.18$ and $K_i' = 5.51 \pm 0.18$ M have been determined. Furthermore, the screening results indicate that the chain length is crucial for obtaining an inhibitory efficacy. The best results were obtained for 14, a chain-extended eicosenoic acid showing inhibition constants $K_i = 1.51 \pm 0.09$ M and $K_i' = 7.15 \pm 0.55$ M. All tested compounds were mixed-type inhibitors with a dominating competitive part.

Molecular modelling calculations indicate a different binding mode of active/inactive compounds for the enzymes AChE and BChE. Our results may contribute to a stronger and more intensive investigation of the role of fatty acid derivatives in the therapy of chronic diseases or the relief of its symptoms. The inhibitor concentrations are partly in those concentration ranges that were also measured in the plasma of adults.³¹

Acknowledgments

We like to thank Dr. D. Ströhl and his team for the NMR spectra, Dr. R. Kluge for the ESI-MS and ASAP-MS spectra, B.Sc. V. Simon for taking the IR and UV/Vis spectra as well as Mrs. S. Fülle for supporting the synthesis and B.Sc. S. Ludwig for the micro-analyses. Financial support by ScienceCampus Halle WCH (W13004216 to R.C.) is gratefully acknowledged.

Appendix A. Supplementary data

Supplementary data to this article can be found online at <https://doi.org/10.1016/j.bmcl.2018.09.013>.

References

1. www.ourworldindata.org/life-expectancy.html; last accessed: 25.07.18.
2. Sharma M, Majumdar PK. Occupational lifestyle diseases: an emerging issue. *Indian J Occup Environ Med.* 2009;13:109–112.
3. Whiteford HA, Degenhardt L, Rehm J, et al. Global burden of disease attributable to mental and substance use disorders: findings from the Global Burden of Disease Study 2010. *Lancet.* 2013;382:1575–1586.
4. Alzheimer A. Über eine eigenartige Erkrankung der Hirnrinde. *Allg Z Psychiatr Psych-gerichtl Med.* 1907;64:146–148.
5. Dangour AD, Whitehouse PJ, Rafferty K, et al. B-Vitamins and fatty acids in the prevention and treatment of Alzheimer's disease and dementia: a systematic review. *J Alzheimer's Dis.* 2010;22:205–224.
6. Menotti A, Puddu PE. Coronary heart disease differences across Europe: a contribution from the Seven Countries Study. *J Cardiovasc Med.* 2013;14:767–772.
7. Semba RD, Ferrucci L, Bartali B, et al. Resveratrol levels and all-cause mortality in older community-dwelling adults. *JAMA Intern Med.* 2014;174:1077–1084.
8. Sofi F, Macchi C, Casini A. Mediterranean diet and minimizing neurodegeneration. *Curr Nutr Rep.* 2013;2:75–80.
9. Anand P, Singh B. A review on cholinesterase inhibitors for Alzheimer's disease. *Arch Pharm Res.* 2013;36:375–399.
10. Zemek F, Drtinova L, Nepovimova E, et al. Outcomes of Alzheimer's disease therapy with acetylcholinesterase inhibitors and memantine. *Expert Opin Drug Saf.* 2014;13:759–774.
11. Quintero-Flórez A, Sinausia Nieva L, Sánchez-Ortiz A, Beltrán G, Perona JS. The fatty acid composition of virgin olive oil from different cultivars is determinant for foam cell formation by macrophages. *J Agr Food Chem.* 2015;63:6731–6738.
12. Gila A, Jiménez A, Beltrán G, Romero A. Correlation of fatty acid composition of virgin olive oil with thermal and physical properties: Correlation of fatty acid composition of virgin olive oil. *Eur J Lipid Sci Technol.* 2015;117:366–376.
13. Logroscino G, Marder K, Cote L, Tang M-X, Shea S, Mayeux R. Dietary lipids and antioxidants in Parkinson's disease: a population-based, case-control study. *Ann Neurol.* 1996;39:89–94.
14. Sofi F, Macchi C, Abbate R, Gensini GF, Casini A. Effectiveness of the mediterranean diet: can it help delay or prevent Alzheimer's disease? *J Alzheimer's Dis.* 2010;20:795–801.
15. Dangour AD, Whitehouse K, Fau PJ, Rafferty SA, Fau Rafferty K, Mitchell L, Fau Mitchell Sa, Smith S Smith, Fau L, Hawkesworth B, Fau Hawkesworth S, Vellas B. B-vitamins and fatty acids in the prevention and treatment of Alzheimer's disease and dementia: a systematic review. *J Alzheimer's Dis.* 2010;22:205–224.
16. Solfrizzi V, Colacicco AM, D'Introno A, et al. Dietary intake of unsaturated fatty acids and age-related cognitive decline: A 8.5-year follow-up of the Italian longitudinal study on aging. *Neurobiol Aging.* 2006;27:1694–1704.
17. Solfrizzi V, Frisardi V, Seripa D, et al. Mediterranean diet in predementia and dementia syndromes. *Curr Alzheimer Res.* 2011;8:520–542.
18. Scarmeas N, Stern Y, Mayeux R, Luchsinger JA. Mediterranean diet, alzheimer disease, and vascular mediation. *Arch Neurol.* 2006;63:1709.
19. Martinez-Lapiscina EH, Clavero P, Toledo E, et al. Virgin olive oil supplementation and long-term cognition: the Predimed-Navarra randomized, trial. *J Nutr Health Aging.* 2013;17:544–552.
20. Morganstern I, Ye Z, Liang S, Fagan S, Leibowitz SF. Involvement of cholinergic mechanisms in the behavioral effects of dietary fat consumption. *Brain Res.* 2012;1470:24–34.
21. Tel G, Öztürk M, Duru ME, Doğan B, Harmandar M. Fatty acid composition, antioxidant, anticholinesterase and tyrosinase inhibitory activities of four serratula species from anatolia. *Rec Nat Prod.* 2013;7(2):86–95.
22. Itriago CV, Melo Filho AA, Ribeiro PRE, Melo ACGR, Takahashi JA, Ferraz VP, Mozambique DMS, Santos RC. Inhibition of acetylcholinesterase and fatty acid composition in theobroma grandiflorum seeds, orbital. *Electron J Chem.* 2017;9. <https://doi.org/10.17807/orbital.v0i0.894>.
23. Seto Y, Takahashi K, Matsuura H, et al. Novel Cyclic Peptide, Epichlicin, from the Endophytic Fungus, Epichloe typhina. *Biosci Biotechn Biochem.* 2007;71:1470–1475.
24. Vijai Kumar Reddy T, Jyotsna A, Prabhavathi Devi BLA, Prasad RBN, Poornachandra Y, Ganesh Kumar C. Total synthesis and in vitro bioevaluation of clavaminols A, C, H & deacetyl clavaminol H as potential chemotherapeutic and antibiofilm agents. *Eur J Med Chem.* 2016;120:86–96.
25. Castellano S, Milite C, Feoli A, et al. Inside Cover: Identification of Structural Features of 2-Alkylidene-1,3-Dicarbonyl Derivatives that Induce Inhibition and/or Activation of Histone Acetyltransferases KAT3B/p300 and KAT2B/PCAF. *ChemMedChem.* 2015;10 2–2.
26. Kubinyi H. Structure-based design of enzyme inhibitors and receptor ligands. *Curr Opin Drug Discov Dev.* 1998;1:4–15.
27. Loesche A, Wiese J, Sommerwerk S, Simon V, Brandt W, Csuk R. Repurposing N, N'-bis-(arylamidino)-1,4-piperazinedicarboxamides: an unexpected class of potent inhibitors of cholinesterases. *Eur J Med Chem.* 2017;125:430–434.
28. Dixon M. The determination of enzyme inhibitor constants. *Biochem J.* 1953;55:170–171.
29. Cornish-Bowden A. A simple graphical method for determining the inhibition constants of mixed, uncompetitive and non-competitive inhibitors. *Biochem J.* 1974;137:143–144.
30. Lineweaver H, Burk D. The Determination of Enzyme Dissociation Constants. *J Am Chem Soc.* 1934;56:658–666.
31. Abdelmagid SA, Clarke SE, Nielsen DE, Badawi A, El-Sohemy A, Munch DM, Ma DWL. Comprehensive profiling of plasma fatty acid concentrations in young healthy canadian adults. *Plos One.* 2015;10. <https://doi.org/10.1371/journal.pone.0116195>.

4.8. Manuscript 8: Ursolic and oleanolic acid derivatives with cholinesterase inhibiting potential.

A., Loesche, A., Köwitsch, S., Lucas, Z., Alhalabi, W., Sippl, A., Harrasi,
R., Csuk.

Bioorganic chemistry. 85, 23–32 (2019).



Ursolic and oleanolic acid derivatives with cholinesterase inhibiting potential

Anne Loesche^a, Alexander Köwitsch^a, Susana D. Lucas^b, Zayan Al-Halabi^c, Wolfgang Sippl^c, Ahmed Al-Harrasi^d, René Csuk^{a,*}

^a Martin-Luther-University Halle-Wittenberg, Organic Chemistry, Kurt-Mothes-Str. 2, D-06120 Halle (Saale), Germany

^b Universidade de Lisboa, Faculdade de Farmácia, Instituto de Investigação do Medicamento (iMed.Ulisboa), Av. Prof. Gama Pinto, 1649-003 Lisboa, Portugal

^c Martin-Luther-University Halle-Wittenberg, Institute of Pharmacy, Wolfgang-Langenbeck-Str. 4, D-06120 Halle (Saale), Germany

^d University of Nizwa, Chair of Oman's Medicinal Plants and Marine Natural Products, PO Box 33, Birkat Al-Mauz, Nizwa, Oman

ABSTRACT

Triterpenoids are in the focus of scientific interest, and they were evaluated for many pharmacological applications among them their ability to act as inhibitors of cholinesterases. These inhibitors are still of interest as drugs that improve the life quality of patients suffering from age-related dementia illnesses especially of Alzheimer's disease. Herein, we prepared several derivatives of ursolic and oleanolic acid and screened them in Ellman's assays for their ability to inhibit acetylcholinesterase and/or butyrylcholinesterase, and for each of the active compounds the type of inhibition was determined. As a result, several compounds were shown as good inhibitors for acetylcholinesterase and butyrylcholinesterase even in a micromolar range. An ursolic acid derived hydroxyl-propinyl derivative **10** was a competitive inhibitor for butyrylcholinesterase with an inhibition constant of $K_i = 4.29 \mu\text{M}$, and therefore being twice as active as gold standard galantamine hydrobromide. The best inhibitor for acetylcholinesterase, however, was 2-methyl-3-oxo-methyl-ursolate (**18**), acting as a mixed-type inhibitor showing $K_i = 1.72 \mu\text{M}$ and $K_i' = 1.28 \mu\text{M}$, respectively.

1. Introduction

Spending their last days on earth having already lost many cognitive functions remains a major fear of elderly people. Although during the last century their lifespans increased, the so-called "old-age diseases" became more and more important. Alzheimer's disease (AD) besides cancer, strokes, heart attacks and dementia diseases became the most important diseases of the 21st century; these diseases cause the highest death rates. Nowadays, one person in 200 suffers from any kind of dementia, and this number is expected to double within the next 30 years [1,2]. Therefore, the scientific and economic interest remains unbroken, and the research for a better understanding of dementia and possible treatments especially of AD have been in progress for decades.

The large number of patients suffering from AD makes this disease of special interest within the field of dementia diseases. Many theories regarding the causes of these diseases were postulated, resulting in some therapeutic concepts. One of the most often followed ideas is the β -amyloid hypothesis basing essentially on the neurotoxic effect of β -amyloid plaques inside the human brain having been formed by the action of α -, β - and γ -secretases [3,4]. However, about 30 percent of middle-aged people have AD-equal amounts of these plaques but without suffering from AD [5,6]. In addition, several therapies basing on this theory failed to increase the cognitive abilities [7–10] by

decreasing the β -amyloid plaque's concentration. Other therapeutic targets refer, for example, to inflammatory processes or mitochondrial disorder of the τ -protein [11–13].

Another concept relies on the neurotransmitter acetylcholine (ACh) since its concentration seems reduced during AD; AD typical symptoms such as amnesia or behavioral disorders [14–17] have been credited to a lowered concentration of ACh. Usually, the cleavage of this neurotransmitter is performed by the hydrolase acetylcholinesterase (AChE, E.C. 3.1.1.7) but another enzyme, butyrylcholinesterase (BChE, E.C. 3.1.1.8), seems also important for controlling the concentration of ACh in different tissues of an organism including the brain. It was assumed that BChE is able to compensate a lack of AChE activity [18,19]. Furthermore, the AChE/BChE ratio in the brain alters from 0.2 in healthy brains to 11 during advanced AD [14,20,21]. Thus, both enzymes represent interesting targets for potential AD cures or – at least – as tools for a deeper insight into AD's pathology.

Triterpenes represent a group of pharmacologically active substances having already been tested for cholinergic activities [22–24]. Triterpenes holding hopyl [25], lanostyl [26] or lupyl [27] skeletons have been targets in recent studies. Also, pentacyclic triterpenic acids and compounds derived thereof showed an inhibitory potential for AChE in micromolar range [28]. Especially several subgroups of α - and β -amyrins were most effective inhibitors for this cholinesterase.

* Corresponding author.

<https://doi.org/10.1016/j.bioorg.2018.12.013>

Received 26 October 2018; Received in revised form 3 December 2018; Accepted 10 December 2018

Available online 15 December 2018

0045-2068/ © 2018 Elsevier Inc. All rights reserved.

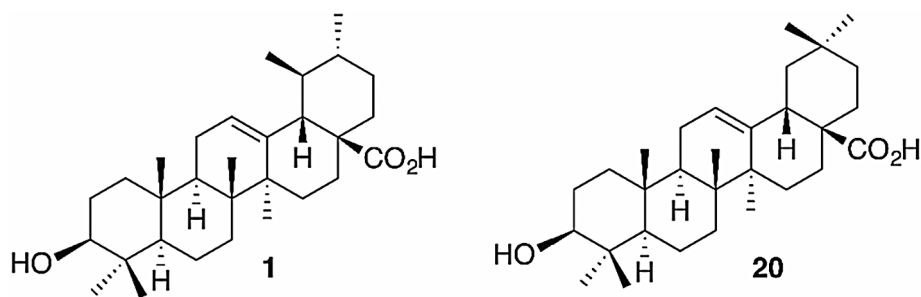


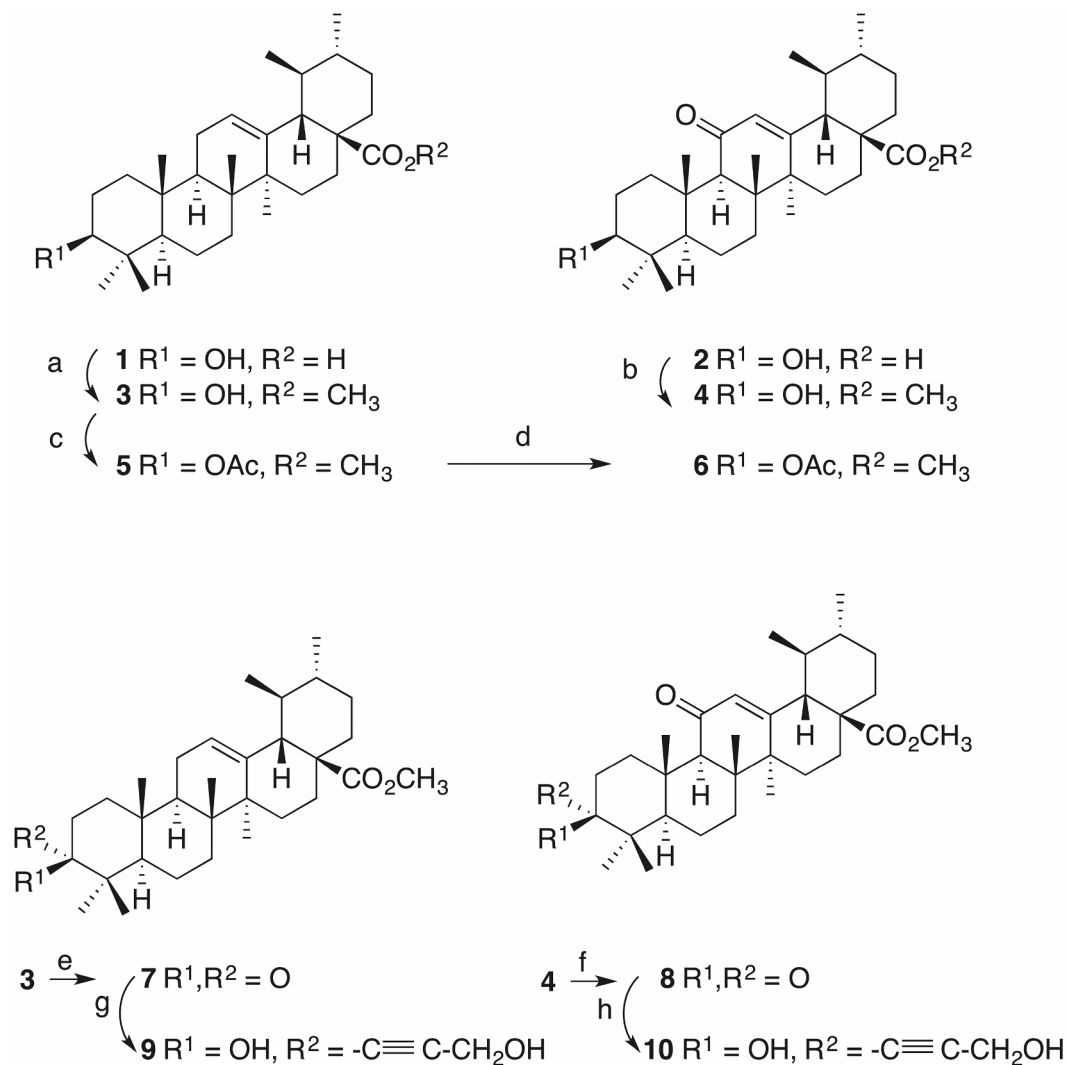
Fig. 1. Structure of ursolic acid (1) and oleanolic acid (20).

Furthermore, AChE inhibition has been found for derivatives of oleanolic acid [29–32], ursolic acid [33] as well as of glycyrrhetic acid [34] or platanic acid derived compounds [35]. Therefore, we decided to synthesize and to test several ursolic and oleanolic acid (Fig. 1) derived compounds in Ellman's assays for their ability to act as inhibitors of AChE as well as of BChE and to obtain inhibitory constants (K_i and K_i').

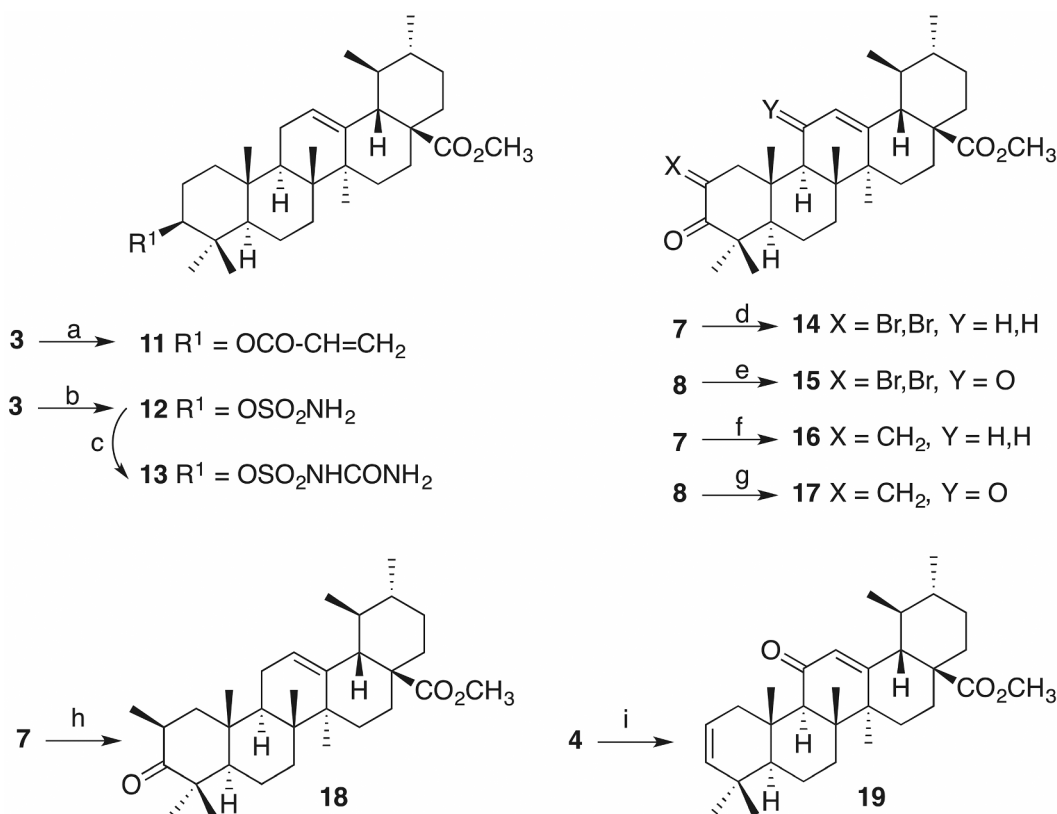
2. Results and discussion

2.1. Chemistry

Reaction of ursolic acid (1, Scheme 1) or of its 11-oxo analogue 2 [36] with methyl iodide in the presence of potassium carbonate gave esters 3 and 4 in good yields. These esters served as valuable starting



Scheme 1. Synthesis of ursolic acid (1) derived compounds 2–10: (a) K_2CO_3 , MeI, DMF, 12 h, 25 °C, 78%; (b) K_2CO_3 , MeI, DMF, 12 h, 25 °C, 82%; (c) Ac_2O , TEA, DCM, 12 h, 25 °C, 87%; (d) $\text{Na}_2\text{Cr}_2\text{O}_7$ AcOH, NHS, acetone, 2 d, 40 °C, 65%; (e) CrO_3 , H_2SO_4 , acetone, 1 h, 25 °C, 88%; (f) CrO_3 , H_2SO_4 , acetone, 1 h, 25 °C, 88%; (g) LDA, THF, $-78^\circ\text{C} \rightarrow 25^\circ\text{C}$, 53%; (h) LDA, THF, $-78^\circ\text{C} \rightarrow 25^\circ\text{C}$, 63%.



Scheme 2. Synthesis of compounds 11–19: (a) TEA, acryloyl chloride, DMAP, CHCl_3 , 30 min, 25 °C, 45%; (b) NaH, THF, 0 °C → 25 °C, 30 min then sulfamoyl chloride, THF, 5 d, 25 °C, 69%; (c) NaH, THF, 0 °C → 25 °C, 30 min then CDI, NH_3 , THF, 3 h, 25 °C, 95%; (d) Br_2 , AcOH, 15 min, 25 °C, 80%; (e) Br_2 , AcOH, 15 min, 25 °C, 93%; (f) K_2CO_3 , paraformaldehyde, DMF, 1 h, 90 °C, 45%; (g) K_2CO_3 , paraformaldehyde, DMF, 1 h, 90 °C, 44%; (h) LDA, MeI, THF, -78 °C → 25 °C, 71%; (i) 3,3-dimethylglutarimide, PPh_3 , DEAD, THF, 12 h, 0 °C, 93%.

materials for the syntheses to follow. Acetylation of **3** or **4** with acetic anhydride and triethylamine in dry DCM furnished acetates **5** and **6**, respectively. Jones oxidation of **3** or **4** gave 3-oxo compounds **7** and **8**. Their reaction with lithium diisopropylamide in THF followed by adding 2-propyn-1-ol yielded 3-hydroxyprop-1-ynyl derivatives **9** and **10**, respectively. Compound **9** is characterized in its ^{13}C NMR spectrum by the presence of the alkynyl carbons detected at $\delta = 88.9$ and 83.7 ppm. The ^1H NMR chemical shift of 33-H was determined at $\delta = 4.26$ ppm.

The 3-O-acryloyl derivative **11** (Scheme 2) was obtained from the reaction of **3** with acryloyl chloride in the presence of triethylamine and catalytic amounts of DMAP. Reaction of **3** with sodium hydride and sulfamoyl chloride in THF gave **12** which was converted into the corresponding carbamoylsulfamate **13** using sodium hydride, 1,1'-carbonyldiimidazole and a saturated solution of ammonia. Products dibrominated at position C-2 were obtained from the 3-oxo esters **7** and **8**. Thus, **7** or **8** was allowed to react with bromine in glacial acetic acid, and compounds **14** and **15** were obtained.

Reaction of **7** and **8** with paraformaldehyde in DMF under basic conditions gave the 2-methylenated derivatives **16** and **17**, respectively. Compound **16** is characterized in its ^1H NMR spectrum by the presence of a methylene group resulting in signals at $\delta = 5.93$ ppm and 5.07 ppm (for **17**: $\delta_{\text{H}} = 5.95$ and 5.18 ppm, respectively). In the ^{13}C NMR spectrum signals at $\delta = 141.9$ and 123.6 ppm (for **17**: $\delta_{\text{C}} = 141.8$ and 124.1 ppm) were assigned to this group. Treatment of **7** with LDA and iodomethane in dry THF yielded compound **18**. Compound **19** holding a double bond in ring A was synthesized as previously reported [37].

Following the procedures given for the synthesis of the derivatives of ursolic acid, starting from oleanolic acid (**20**) and 11-oxo-oleanolic acid **21** [38] the corresponding methyl esters **22** and **23** were prepared

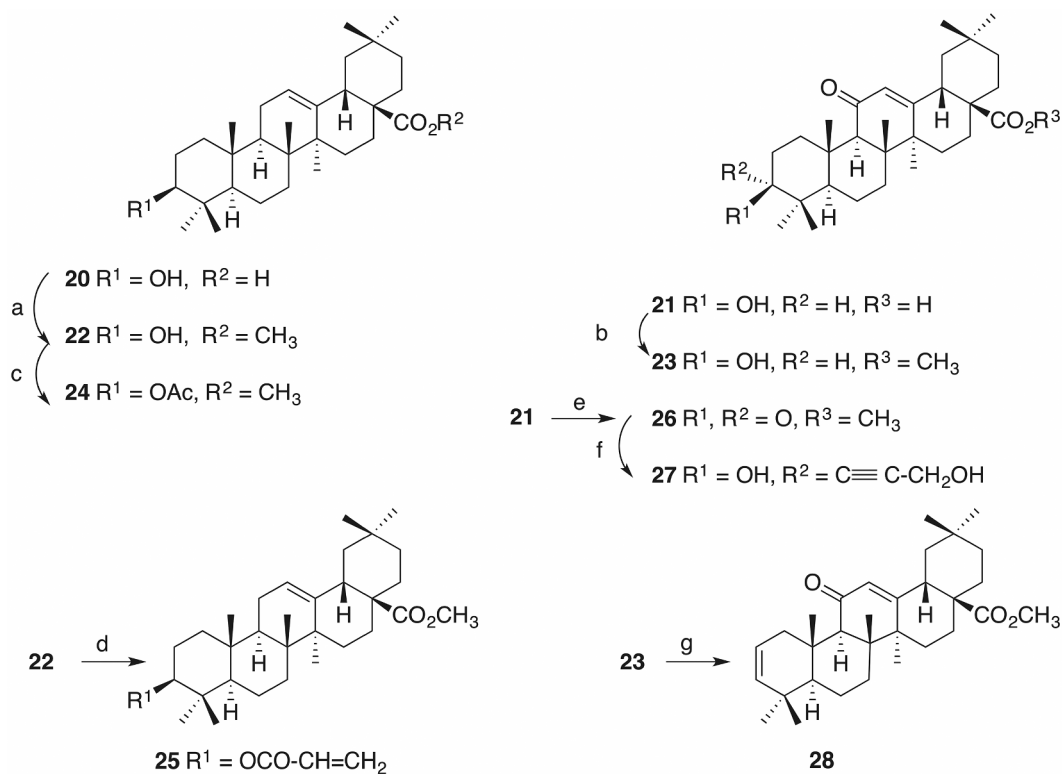
(Scheme 3). Acetylation of **22** afforded **24**; from the reaction of **22** with acryloyl chloride/trimethylamine/DMAP acryloylated **25** was obtained in 63% isolated yield. The olefinic protons of this compound were detected in the ^1H NMR spectrum at $\delta = 6.30$, 6.04 and 5.73 ppm, respectively.

Oxidation of **21** gave a 3,11-dioxo-oleanoate **26** whose reaction with LDA and 2-propyn-1-ol afforded **27** in 52% yield. Reaction of **23** with triphenylphosphane, 3,3-dimethylglutarmide and diethyl azodicarboxylate in THF gave 87% of a 2,12-diene **28**. Sulfamoylated **29** was prepared from **22** (Scheme 4) according to our previously published procedure [39]; this compound was further transformed into carbamoylsulfamated **30**. The diene **28** served as a starting material for the synthesis of the 1,9-endoperoxide **31** and epoxide **32**, respectively [34]. Bromination of **32** gave **33** whose Jones-oxidation furnished **34**.

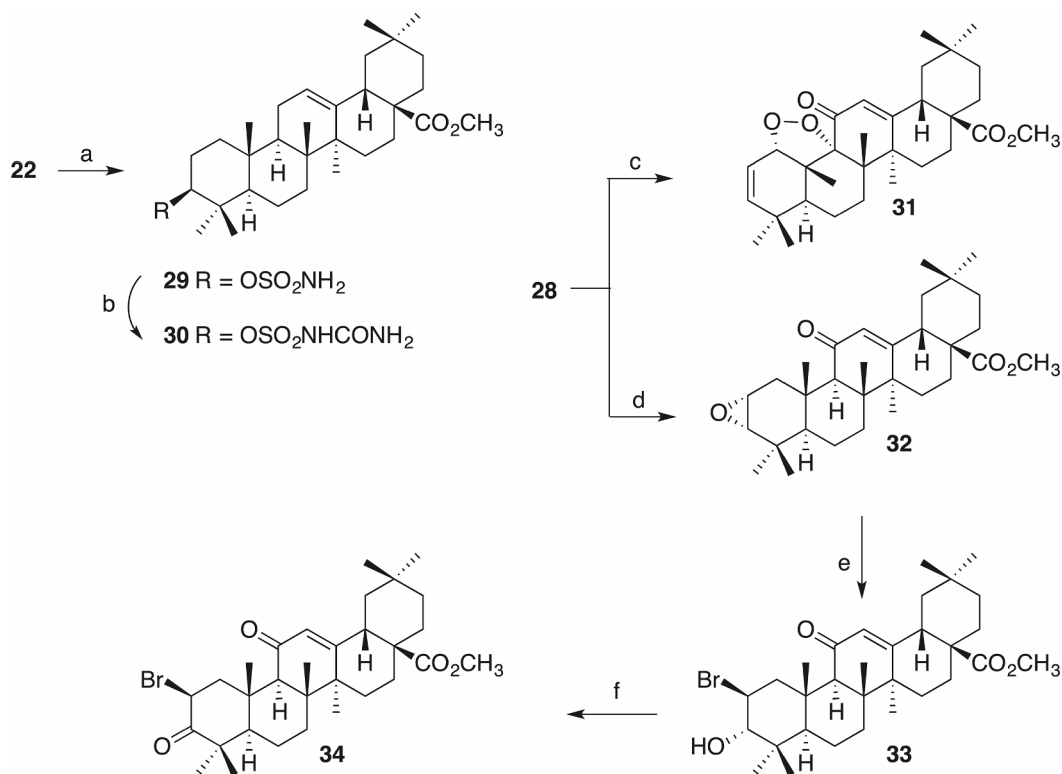
2.2. Biology

Compounds **1–34** and galantamine hydrobromide (GH, as a standard) were subjected to Ellman's assays to measure their ability to inhibit the enzymes acetylcholinesterase (from *Electrophorus electricus*, electric eel) and butyrylcholinesterase (from equine serum). Cholinesterases from different species are very similar. Due to these large and functional conservations, AChE from the electric eel, and BChE from equine serum can be used as suitable models for the corresponding enzymes from humans. As a result, while most of the compounds inhibited AChE, only two compounds displayed a significant activity for BChE; several compounds were insoluble under the conditions of the assay. The results from these assays are compiled in Table 1.

For the parent triterpenic acids inhibition constants for AChE in low micromolar magnitude were measured. Thus, ursolic acid (**1**) gave a



Scheme 3. Synthesis of 21–28: (a) K_2CO_3 , MeBr, DMF, 18 h, 25 °C, 88%; (b) K_2CO_3 , MeBr, DMF, 18 h, 25 °C, 90%; (c) Ac_2O , TEA, DCM, 12 h, 25 °C, 95%; (d) TEA, acryloyl chloride, DMAP, CHCl_3 , 30 min, 25 °C, 63%; (e) CrO_3 , H_2SO_4 , acetone, 1 h, 25 °C, 75%; (f) LDA, THF, $-78^\circ\text{C} \rightarrow 25^\circ\text{C}$, 52%; (g) 3,3-dimethylglutarimide, PPh_3 , DEAD, THF, 12 h, 0 °C, 96%.



Scheme 4. Synthesis of 29–34: (a) NaH, THF, $0^\circ\text{C} \rightarrow 25^\circ\text{C}$, 30 min then sulfamoyl chloride, THF, 5 d, 25 °C, 70%; (b) NaH, THF, $0^\circ\text{C} \rightarrow 25^\circ\text{C}$, 30 min then CDI, NH_3 , THF, 3 h, 25 °C, 96%; (c) $\text{Na}_2\text{Cr}_2\text{O}_7$, AcOH, NHS, acetone, 2 d, 40 °C, 46%; (d) *m*-CPBA, MeCl, 2 d, 25 °C, 55%; (e) HBr, THF, 10 min, 10 °C, 77%; (f) CrO_3 , H_2SO_4 , acetone, 30 min, 25 °C, 53%.

Table 1

Inhibitory constants for galantamine hydrobromide ($K_i = \text{AChE}: 0.54 \pm 0.01 \mu\text{M}$; $\text{BChE}: K_i = 9.37 \pm 0.67 \mu\text{M}$) as a standard and compounds 1–34 (except insoluble and inactive ones) using Ellman's assay employing AChE (electric eel) and BChE (equine serum); four different substrate concentrations and four different inhibitor concentrations were used; K_i and K_i' are reported in μM ; mean \pm SE; inactive means less than 30% inhibition at $50 \mu\text{M}$ concentration.

Compound	AChE		BChE		Compound	AChE		BChE	
	K_i (μM)	$[K_i'$ (μM)]	K_i (μM)	$[K_i'$ (μM)]		K_i (μM)	$[K_i'$ (μM)]	K_i (μM)	$[K_i'$ (μM)]
1 (UA)	8.54 ± 1.33	$[38.16 \pm 3.28]$	(Mixed type)	inactive	20 (OA)	11.62 ± 2.82	(competitive)	inactive	
2	7.48 ± 0.53	$[17.40 \pm 0.63]$	(Mixed type)	inactive	21	4.22 ± 0.68	$[12.24 \pm 0.85]$	(Mixed type)	inactive
3	9.48 ± 0.98	$[45.90 \pm 0.81]$	(Mixed type)	inactive	22	3.46 ± 0.56	$[49.11 \pm 7.28]$	(Mixed type)	inactive
10	inactive			4.29 ± 0.29	27	inactive			24.35 ± 9.07
12	7.39 ± 1.51	$[11.1 \pm 1.37]$	(Mixed type)	inactive	28	6.26 ± 2.71	$[15.06 \pm 2.00]$	(Mixed type)	inactive
14	11.50 ± 1.75	$[35.83 \pm 1.21]$	(Mixed type)	inactive	29	6.37 ± 0.26	$[26.69 \pm 0.18]$	(Mixed type)	inactive
16	20.73 ± 0.17	$[12.42 \pm 1.33]$	(Mixed type)	inactive	31	17.01 ± 1.02	$[36.51 \pm 4.25]$	(Mixed type)	inactive
18	1.72 ± 0.24	$[1.28 \pm 0.05]$	(Mixed type)	inactive	32	21.89 ± 5.93	$[21.53 \pm 3.57]$	(Mixed type)	inactive
19	4.43 ± 0.46	$[5.26 \pm 1.04]$	(Mixed type)	inactive	34	12.88 ± 0.77	$[14.58 \pm 0.92]$	(Mixed type)	inactive

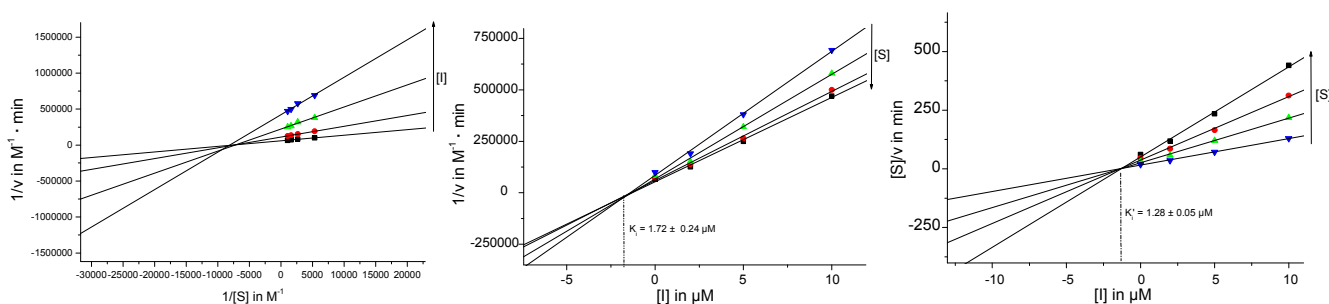


Fig. 2. Lineweaver-Burk (left), Dixon (middle) and Cornish-Bowden (right) plots for mixed-type inhibitor 18.

mixed-type inhibition ($K_i = 8.54 \pm 1.33 \mu\text{M}$, $K_i' = 38.16 \pm 3.28 \mu\text{M}$) while for oleanolic acid (20) a competitive inhibition ($K_i = 11.62 \pm 2.82 \mu\text{M}$) was found. Inhibition of both compounds, however, was lower than the inhibition measured for standard galantamine hydrobromide (GH, $K_i = 0.54 \pm 0.01 \mu\text{M}$). Esterification of 1 had no significant impact on the ability to act as an inhibitor, and the inhibition constants of 3 were similar to those of parent ursolic acid. Interestingly, the methyl ester of oleanolic acid 22 was a mixed-type inhibitor, and elimination of HO-C(3) provided compounds with rather lower K_i values. Furthermore, introduction of a 2-methyl-3-oxo-moiety increased the inhibition potential, and inhibition constants of $K_i = 1.72 \pm 0.24 \mu\text{M}$ and $K_i' = 1.28 \pm 0.05 \mu\text{M}$ were determined for 18. Finally, introduction of a 3-hydroxyprop-1-ynyl moiety provided a selective BChE inhibitor; thus, ursolic acid derived 10 ($K_i = 4.29 \pm 0.29 \mu\text{M}$, competitive inhibitor) was twice as active as galantamine hydrochloride (See Fig. 2).

2.3. Docking

Molecular modeling is a valuable tool to rationalize different biological outcomes from closely related compounds. Therefore, we used GOLD 5.2 docking software [40] to evaluate the preferred poses of some of the synthesized compounds in the active site of the targeted enzymes AChE and BChE. Compound 18 being the most active compound towards AChE showed a preferential U-shape pose facing the active site Ser203. This led to an acceptable positioning for subsequent ester hydrolysis and hence to an inactivation of the enzyme. Docking of several UA derived compounds revealed that their preferential pose did not allow the entrance into the AChE gorge and thus there was no inhibition of the targeted esterase. From the results of the biological assay it was known that the selectivity of the inhibitors to AChE is higher than to BChE. This can probably be explained by the fact that the inhibitors interact with the residues Phe 330, Trp 279, Tyr 121 in the AChE binding pocket via pi-pi interactions whereas the corresponding

residues in BChE (Ala 328, Val 277, Gln 119) cannot. The active compounds could fit reasonably into the AChE hydrophobic binding pocket. In addition, the carboxyl groups of the compounds fit very well into the hydrophilic part of the pocket (See Fig. 3).

3. Conclusions

Several derivatives of ursolic and oleanolic acid varying in their substitution pattern were synthesized in this study and screened for their inhibitory potential for the enzymes AChE and BChE applying Ellman's assays. The inhibition constants and the type of inhibition were determined for each compound. While parent ursolic acid gave inhibition constants of about $10 \mu\text{M}$ for AChE, no inhibition for BChE was detected. However, several compounds showed a higher inhibition for AChE and two compounds inhibited BChE even in micromolar magnitude. The results obtained in the biological assay can be explained by appropriate molecular modelling calculations.

4. Experimental

4.1. Chemistry

4.1.1. General

Reagents were bought from commercial suppliers without any further purification. Instrumental analysis was performed as previously reported [42]. The purity of the compounds was checked by HPLC, and found to $> 96\%$.

4.2. Syntheses

4.2.1. β -Hydroxy-urs-12-en-28-oic acid (ursolic acid, 1)

This compound was commercially obtained from Betulinines (Střbrná Skalice, Czech Republic) and used as received.

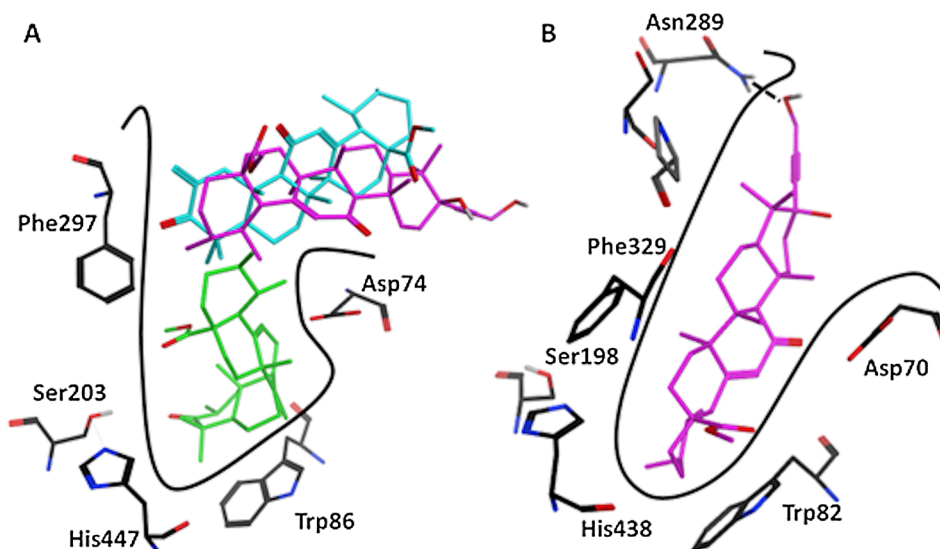


Fig. 3. Docked poses at the AChE and BChE active sites calculated with GOLD 5.2 [37]. (A) AChE: compounds 18 (green), 17 (cyan) and 10 (pink); (B) BChE, compound 10 (pink). Pictures made with MOE2014 software [41].

4.2.2. Methyl 3 β -hydroxy-urs-12-en-28-oate (3)

This compound was synthesized according to literature from **1** [39]; m.p. 165–167 °C; $[\alpha]_D = +68^\circ$ ($c = 0.53$, CHCl_3); MS (ESI): m/z (%) = 471.2 ($[\text{M}+\text{H}]^+$, 80), 493.4 ($[\text{M}+\text{Na}]^+$, 100).

4.2.3. Methyl 3 β -hydroxy-11-oxo-urs-12-en-28-oate (4)

Esterification [39] of **2** [36] gave compound **4**; m.p. 132–135 °C; $[\alpha]_D = +87^\circ$ ($c = 3.0$, CHCl_3); MS (ESI): m/z (%) = 485.5 ($[\text{M}+\text{H}]^+$, 100), 507.5 ($[\text{M}+\text{Na}]^+$, 50).

4.2.4. Methyl 3 β -acetyloxy-urs-12-en-28-oate (5)

This compound was synthesized by acetylation of **3** [42]; m.p. 243–246 °C; $[\alpha]_D = 64.7^\circ$ ($c = 0.30$, CHCl_3); MS (ESI): m/z (%) = 513.2 ($[\text{M}+\text{H}]^+$, 40), 535.5 ($[\text{M}+\text{Na}]^+$, 100).

4.2.5. Methyl 3 β -acetyloxy-11-oxo-urs-12-en-28-oate (6)

Compound **5** (480 mg, 0.94 mmol) was dissolved in acetone (50 mL) and glacial acetic acid (5 mL). *N*-hydroxysuccinimide (1.20 g, 10.43 mmol) and potassium dichromate (1.05 g, 3.56 mmol) were added. After 2 days of continuous stirring at 40 °C, solutions of saturated potassium bisulfite solution and saturated sodium bicarbonate were added. The aqueous solution was extracted with dichloromethane (4 \times 50 mL); the combined organic layers were washed with water (20 mL) and brine (20 mL), dried (Na_2SO_4) and evaporated to dryness. The residue was subjected to column chromatography (silica gel, hexanes/ethyl acetate, 8:2) to afford **6** (0.32 g, 65%) as a colorless solid; m.p. 245–250 °C (lit.: 235 °C [43]; $R_f = 0.66$ (chloroform/diethyl ether, 95:5); $[\alpha]_D = +75^\circ$ ($c = 3.3$, CHCl_3); UV–Vis (methanol): λ_{max} (log ϵ) = 274 nm (4.21); IR (KBr): $\nu = 3441\text{br}$, 2971s, 2875m, 1731s, 1655s, 1620w, 1459m, 1427w, 1396m, 1371m, 1319m, 1307m, 1272m, 1239s, 1202m, 1142m, 1116m, 1101w, 1088w, 1028m, 1002m, 983m cm^{-1} ; ^1H NMR (500 MHz, CDCl_3): $\delta = 5.58$ (s, 1H, H-12), 4.51 (dd, 1H, $J = 11.6$, 4.6 Hz, H-3), 3.59 (s, 3H, OMe), 2.77 (d, 1H, $J = 13.8$ Hz, H-1), 2.40 (d, 1H, $J = 11.3$ Hz, H-18), 2.30 (s, 1H, H-9), 2.11–2.01 (m, 1H, H-16), 2.03 (s, 3H, Ac), 1.81–1.50 (m, 10H, H-2, H-6, H-7, H-15, H-16', H-21, H-22), 1.44–1.20 (m, 4H, H-7', H-19, H-15', H-21'), 1.28 (s, 3H, H-27), 1.13 (s, 3H, H-25), 1.10–1.01 (m, 2H, H-1', H-20), 0.95 (d, 3H, $J = 6.4$ Hz, H-30), 0.89 (s, 3H, H-26), 0.86 (d, 3H, $J = 6.1$ Hz, H-29), 0.85 (s, 3H, H-24), 0.85 (s, 3H, H-23), 0.76 (d, 1H, $J = 11.4$ Hz, H-5) ppm; ^{13}C NMR (125 MHz, CDCl_3): $\delta = 199.6$ (C-11), 177.1 (C-28), 170.9 (Ac), 162.8 (C-13), 130.6 (C-12), 80.6 (C-3), 61.3 (C-9), 55.0 (C-5), 52.7 (C-18), 51.8 (OMe), 47.6 (C-17), 44.6 (C-8), 43.7 (C-14), 38.8

(C-4), 38.6 (C-19), 38.5 (C-20), 38.0 (C-1), 37.0 (C-10), 35.9 (C-22), 32.9 (C-7), 30.3 (C-21), 28.3 (C-15), 28.0 (C-23), 23.9 (C-16), 23.5 (C-2), 21.3 (Ac), 21.0 (C-27), 20.9 (C-30), 18.8 (C-26), 17.3 (C-6), 17.1 (C-29), 16.7 (C-24), 16.2 (C-25) ppm; MS (ESI): m/z (%) = 527.5 ($[\text{M}+\text{H}]^+$, 85), 549.5 ($[\text{M}+\text{Na}]^+$, 100); anal. calcd. for $\text{C}_{33}\text{H}_{50}\text{O}_5$ (526.75): C, 75.25; H, 9.57; found: C, 75.07; H, 9.74.

4.2.6. Methyl 3-oxo-urs-12-en-28-oate (7)

This compound was synthesized according to literature from **3** [44]; m.p. 193–195 °C; $[\alpha]_D = +90^\circ$ ($c = 5.90$, CHCl_3); MS (ESI): m/z (%) = 496.3 ($[\text{M}+\text{H}]^+$, 75), 523.0 ($[\text{M}+\text{Na}+\text{MeOH}]^+$, 100).

4.2.7. Methyl 3,11-dioxo-urs-12-en-28-oate (8)

This amorphous compound was synthesized according to literature from **4** [44]; $[\alpha]_D = +108^\circ$ ($c = 4.80$, CHCl_3); MS (ESI): m/z (%) = 483.5 ($[\text{M}+\text{H}]^+$, 100).

4.2.8. Methyl 3 β -hydroxy-3 α -hydroxy-1-propynyl-urs-12-en-28-oate (9)

To a freshly prepared solution of lithium diisopropylamide [made from diisopropylamine (605 mg, 5.99 mmol) and *n*-butyllithium (1.6 M in hexane, 3.78 mL, 6.05 mmol) in dry THF (20 mL)] at -78°C , 2-propyn-1-ol (223 mg, 4 mmol) in dry THF (4 mL) was added, and the mixture was stirred for 30 min. Compound **7** (360 mg, 0.74 mmol) in dry THF (5 mL) was added dropwise, and the mixture was allowed to warm to room temperature. Usual aqueous workup followed by column chromatography (silica gel, hexanes/ethyl acetate, 7:3) gave **9** (207 mg, 53%) as an amorphous solid; $R_f = 0.35$ (hexanes/ethyl acetate, 7:3); $[\alpha]_D = 32^\circ$ ($c = 3.0$, CHCl_3); UV–Vis (methanol): λ_{max} (log ϵ) = 213 nm (3.86); IR (KBr): $\nu = 3433\text{br}$, 2948s, 2870m, 1725m, 1455m, 1388m, 1308w, 1231m, 1200w, 1144w, 1114w, 1076w, 1033m, 994m cm^{-1} ; ^1H NMR (500 MHz, CDCl_3): $\delta = 5.19$ (m, 1H, H-12), 4.26 (s, 2H), 3.54 (s, 3H, OMe), 2.17 (d, 1H, H-18, $J = 11.0$ Hz), 1.97–1.83 (m, 4H, H-11, H-11', H-16, H-2), 1.70 (ddd, 1H, H-15, $J = 13.8$, 13.8, 4.6 Hz), 1.63–1.57 (m, 3H, H-22, H-16', H-2'), 1.55–1.47 (m, 3H, H-9, H-22', H-1), 1.45–1.39 (m, 3H, H-6, H-21, H-7), 1.32–1.18 (m, 5H, H-19, H-6', H-1', H-7', H-21'), 1.06 (d, 1H, H-5, $J = 11.0$ Hz), 1.03–0.92 (m, 2H, H-15', H-20), 1.02 (s, 3H, H-27), 0.98 (s, 3H, H-23), 0.87 (d, 3H, H-30, $J = 5.6$ Hz), 0.86 (s, 3H, H-25), 0.81 (s, 3H, H-24), 0.80 (d, 3H, H-29, $J = 6.0$ Hz), 0.67 (s, 3H, H-26) ppm; ^{13}C NMR (125 MHz, CDCl_3): $\delta = 178.0$ (C-28), 138.1 (C-13), 125.5 (C-12), 88.9 (C-31, $\text{C}\equiv\text{C}$), 83.7 (C-32, $\text{C}\equiv\text{C}$), 75.8 (C-3), 53.1 (C-5), 52.8 (C-18), 51.4 (OMe), 51.2 (C-33, $\text{H}_2\text{C-O}$), 48.1 (C-17), 47.6 (C-9), 41.9 (C-14), 41.4 (C-4), 39.4 (C8),

39.0 (C-19), 38.8 (C-20), 37.8 (C-1), 36.9 (C-10), 36.6 (C-22), 32.8 (C-7), 32.4 (C-2), 30.6 (C-21), 28.0 (C-15), 25.8 (C-23), 24.2 (C-16), 23.7 (C-27), 23.3 (C-11), 21.1 (C-30), 18.5 (C-6), 17.8 (C-24), 17.0 (C-29), 16.8 (C-26), 15.7 (C-25) ppm; MS (ESI): m/z (%) = 547.5 ([M+Na]⁺, 100); anal. calcd. for C₃₄H₅₂O₄ (524.77): C, 77.82; H, 9.99; found: C, 77.52; H 10.19.

4.2.9. Methyl 3β-hydroxy-3α-hydroxy-1-propynyl-11-oxo-urs-12-en-28-oate (10)

Following procedure described for the synthesis of **9**, compound **10** (282 mg, 63%) was obtained as an amorphous solid from the reaction of **8** (400 mg, 0.83 mmol) followed by column chromatography (silica gel, hexanes/ethyl acetate, 7:3); R_f = 0.54 (hexanes/ethyl acetate, 1:1); $[\alpha]_D = 66^\circ$ (c = 3.5, CHCl₃); UV–Vis (MeOH): λ_{max} (log ϵ) = 269 nm (4.04); IR (KBr): ν = 3432br, 2950s, 2871m, 1728s, 1661s, 1457m, 1388w, 1323w, 1272w, 1231w, 1202m, 1167w, 1145w, 1112w, 1083w, 1036m, 993m cm⁻¹; ¹H NMR (500 MHz, CDCl₃): δ = 5.59 (s, 1H, H-12), 4.29 (s, 2H), 3.59 (s, 3H, OMe), 2.75 (dd, 1H, H-1, J = 14.0, 2.8 Hz), 2.40 (d, 1H, H-18, J = 11.9 Hz), 2.34 (s, 1H, H-9), 2.09–1.95 (m, 2H, H-2, H-16), 1.81–1.71 (m, 3H, H-16', H-22, H-15), 1.68–1.49 (m, 5H, H-2', H-7, H-22', H-6, H-21), 1.43–1.34 (m, 5H, H-19, H-7', H-16', H-1', H-15', H-21'), 1.30 (s, 3H, H-27), 1.11 (s, 3H, H-25), 1.08–1.00 (m, 2H, H-5, H-20), 1.03 (s, 3H, H-23), 0.95 (d, 3H, H-30, J = 6.4 Hz), 0.89 (s, 3H, H-26), 0.87 (s, 3H, H-24), 0.85 (d, 3H, H-29, J = 6.7 Hz) ppm; ¹³C NMR (125 MHz, CDCl₃): δ = 199.8 (C-11), 177.2 (C=28), 162.9 (C-13), 130.6 (C-12), 88.9 (C-31, C≡C), 83.7 (C-32, C≡C), 75.5 (C-3), 61.5 (C-9), 52.8 (C-5), 52.7 (C-18), 51.8 (OMe), 51.1 (C-33, H₂C-O), 47.6 (C-17), 44.6 (C-8), 43.6 (C-14), 41.5 (C-4), 38.6 (C-19), 38.5 (C-20), 38.3 (C-1), 37.1 (C-10), 36.0 (C-22), 32.9 (C-7), 32.5 (C-2), 30.3 (C-21), 28.4 (C-15), 25.9 (C-23), 23.9 (C-16), 21.0 (C-27), 20.9 (C-30), 18.8 (C-26), 17.8 (C-24), 17.7 (C-6), 17.0 (C-29), 16.5 (C-25) ppm; MS (ESI): m/z (%) = 539.5 ([M+H]⁺, 100); anal. calcd. for C₃₄H₅₀O₅ (538.76): C, 75.80; H, 9.35; found: C, 75.63; H, 9.51.

4.2.10. Methyl 3β-acryloyloxy-urs-12-en-28-oate (11)

Compound **3** (233 mg, 0.49 mmol) was dissolved in dry chloroform (30 mL), triethylamine (184 mg, 1.81 mmol), acryloyl chloride (113 mg, 1.25 mmol) and catalytic amounts of 4-dimethylaminopyridine were added successively. After 30 min of continuous stirring, water (40 mL) was added, and the layers were separated. The aqueous solution was extracted with chloroform (2 × 30 mL); the combined organic layers were washed with water (20 mL) and brine (20 mL), dried (Na₂SO₄) and evaporated to dryness. The residue was subjected to column chromatography (silica gel, hexanes/ethyl acetate, 9:1) to afford **11** (115 mg, 45%) as an amorphous solid; R_f = 0.78 (hexanes/ethyl acetate, 8:2); $[\alpha]_D = 67^\circ$ (c = 5.0, CHCl₃); UV–Vis (methanol): λ_{max} (log ϵ) = 221 nm (4.19); IR (KBr): ν = 2935s, 2872s, 1728s, 1634m, 1456m, 1409m, 1390w, 1370w, 1295m, 1272w, 1225m, 1204s, 1187s, 1146m, 1114w, 1034w, 1012w cm⁻¹; ¹H NMR (500 MHz, CDCl₃): δ = 6.36 (dd, 1H, acryloyl, J = 17.2, 1.5 Hz), 6.10 (dd, 1H, acryloyl, J = 17.2, 10.4 Hz), 5.79 (dd, 1H, acryloyl, J = 10.6, 1.5 Hz), 5.23 (m, 1H, H-12), 4.56 (dd, 1H, H-3, J = 9.8, 7.3 Hz), 3.59 (s, 3H, OMe), 2.22 (d, 1H, H-18, J = 11.0 Hz), 1.99 (ddd, 1H, H-16, J = 13.6, 13.4, 4.8 Hz), 1.91 (d, 1H, H-11, J = 3.7 Hz), 1.89 (d, 1H, H-11', J = 3.7 Hz), 1.76 (ddd, 1H, H-15, J = 13.9, 13.6, 4.8 Hz), 1.69–1.56 (m, 6H, H-22, H-22', H-1, H-16', H-2, H-2'), 1.54–1.44 (m, 4H, H-9, H-6, H-21, H-7), 1.37–1.23 (m, 4H, H-19, H-6', H-7', H-21), 1.12–1.03 (m, 2H, H-15', H-1'), 1.06 (s, 3H, H-27), 0.97–0.91 (m, 1H, H-20), 0.94 (s, 3H, H-25), 0.93 (d, 3H, H-30, J = 6.2 Hz), 0.89–0.83 (m, 1H, H-5), 0.88 (s, 3H, H-23), 0.87 (s, 3H, H-26), 0.85 (d, 3H, H-29, J = 6.6 Hz), 0.74 (s, 3H, H-24) ppm; ¹³C NMR (125 MHz, CDCl₃): δ = 178.0 (C-28), 166.0 (C-31), 138.1 (C-13), 130.0 (C-33, H₂C=CH), 129.1 (C-32, HC=CH₂), 125.4 (C-12), 81.0 (C-3, HC-O), 55.3 (C-5), 52.9 (C-18), 51.4 (OMe), 48.0 (C-17), 47.5 (C-9), 42.0 (C-14), 39.5 (C-8), 39.0 (C-19), 38.8 (C-20), 38.2 (C-1), 37.8 (C-4), 36.8 (C-22), 36.6 (C-10), 32.9 (C-7), 30.6 (C-21), 28.1 (C-23), 28.0 (C-15), 24.2 (C-16), 23.6 (C-27), 23.5 (C-2),

23.3 (C-11), 21.1 (C-30), 18.2 (C-6), 17.0 (C-29), 16.9 (C-24), 16.7 (C-26), 15.4 (C-25) ppm; MS (ESI): m/z (%) = 525.3 ([M+H]⁺, 60), 547.3 ([M+Na]⁺, 100); anal. calcd. for C₃₄H₅₂O₄ (524.77): C, 77.82; H, 9.99; found: C, 77.66; H, 10.15.

4.2.11. Methyl 3β-[(aminosulfonyl)oxy]-urs-12-en-28-oate (12)

This compound was synthesized from **3** as previously reported [39]; m.p. 115–118 °C; $[\alpha]_D = +62.10^\circ$ (c = 0.32, CHCl₃); MS (ESI): m/z (%) = 548.3 ([M-H]⁻, 90), 1097.1 ([2M-H]⁻, 100).

4.2.12. Methyl 3β-[[[(aminocarbonyl)amino]sulfonyl]oxy]-urs-12-en-28-oate (13)

This compound was synthesized from **12** as previously reported [45]; m.p. 49–53 °C; $[\alpha]_D = +81.4^\circ$ (c = 0.3, CHCl₃); MS (ESI): m/z (%) = 591.5 ([M-H]⁻, 32), 1183.1 ([2M-H]⁻, 31).

4.2.13. Methyl 2,2-dibromo-3-oxo-urs-12-en-28-oate (14)

This amorphous compound was synthesized from **7** as previously reported [44]; $[\alpha]_D = +43^\circ$ (c = 5.70, CHCl₃); MS (ESI): m/z (%) = 647.1 ([M (2 × ⁷⁹Br) + Na]⁺, 56), 649.2 ([M (⁷⁹Br, ⁸¹Br) + Na]⁺, 100), 651.2 ([M (2 × ⁸¹Br) + Na]⁺, 46).

4.2.14. Methyl 2,2-dibromo-3,11-dioxo-urs-12-en-28-oate (15)

This compound was synthesized from **8** as previously reported [41]; m.p. 225–227 °C; $[\alpha]_D = +48^\circ$ (c = 5.90, CHCl₃); MS (ESI): m/z (%) = 639.3 ([M (2 × ⁷⁹Br) + H]⁺, 23), 641.3 ([M (⁷⁹Br, ⁸¹Br) + H]⁺, 51), 643.3 ([M (2 × ⁸¹Br) + H]⁺, 27), 661.1 ([M (2 × ⁷⁹Br) + Na]⁺, 46), 663.1 ([M (⁷⁹Br, ⁸¹Br) + Na]⁺, 100), 665.0 ([M (2 × ⁸¹Br) + Na]⁺, 52).

4.2.15. Methyl 2-methylene-3-oxo-urs-12-en-28-oate (16)

This amorphous compound was synthesized from **7** as previously reported [44]; $[\alpha]_D = +100^\circ$ (c = 3.20, CHCl₃); MS (ESI): m/z (%) = 481.1 ([M+H]⁺, 100).

4.2.16. Methyl 2-methylene-3,11-dioxo-urs-12-en-28-oate (17)

This compound was synthesized from **8** as previously reported [44]; m.p. 219–222 °C; $[\alpha]_D = +126^\circ$ (c = 4.40, CHCl₃); MS (ESI): m/z (%) = 495.5 ([M+H]⁺, 100).

4.2.17. Methyl 2β-methyl-3-oxo-urs-12-en-28-oate (18)

To a solution of lithium diisopropylamide [prepared from diisopropylamine (85 mg, 0.84 mmol) and *n*-butyllithium (1.6 M in hexane, 0.60 mL, 0.96 mmol) in dry THF (10 mL)] at –78 °C methyl 3-oxo-urs-12-en-28-oate (300 mg, 0.64 mmol) in dry THF (5 mL) was added followed by iodomethane (200 mg, 1.41 mmol) in dry THF (3 mL) after additional 30 min. The mixture was allowed to reach room temperature, and water (30 mL) was added. Usual aqueous work-up and extraction with dichloromethane (3 × 20 mL) followed by column chromatography (silica gel, hexanes/ethyl acetate, 9:1) afforded **18** (220 mg, 71%) as an amorphous solid; R_f = 0.4 (hexanes/ethyl acetate, 9:1); $[\alpha]_D = 49^\circ$ (c = 2.0; CHCl₃); UV–Vis (MeOH): λ_{max} (log ϵ) = 216 nm (3.80); IR (KBr): ν = 3440br, 2929s, 1725m, 1704m, 1654w, 1456w, 1388w, 1230w, 1200w, 1146w cm⁻¹; ¹H NMR (500 MHz, CDCl₃): δ = 5.24 (m, 1H, H-12), 3.60 (s, 3H, OMe), 2.77–2.71 (m, 1H, H-2), 2.21 (d, 1H, H-18, J = 11.3 Hz), 2.02–1.89 (m, 4H, H-11, H-11', H-16, H-1), 1.75 (ddd, 1H, H-15, J = 13.8, 13.8, 4.6 Hz), 1.69–1.62 (m, 2H, H-22, H-16'), 1.56 (ddd, 1H, H-22', J = 13.4, 13.4, 4.0 Hz), 1.52–1.41 (m, 5H, H-6, H-6', H-21, H-7, H-9), 1.35–1.22 (m, 3H, H-19, H-7', H-21'), 1.19 (s, 3H, H-31), 1.12 (d, 1H, H-5, J = 12.2 Hz), 1.08–1.01 (m, 2H, H-15', H-1'), 1.05 (s, 3H, H-23), 1.04 (s, 3H, H-27), 1.03 (s, 3H, H-24), 1.00–0.95 (m, 1H, H-20), 0.99 (s, 3H, H-25), 0.91 (d, 3H, H-30, J = 6.1 Hz), 0.83 (d, 3H, H-29, J = 6.4 Hz), 0.78 (s, 3H, H-26) ppm; ¹³C NMR (125 MHz, CDCl₃): δ = 218.0 (C-3), 177.9 (C-28), 138.3 (C-13), 125.2 (C-12), 57.2 (C-5), 52.8 (C-18), 51.4 (OMe), 49.5 (C-1), 48.0 (C-17), 48.0 (C-4), 47.0 (C-9), 42.0 (C-14), 39.5

(C-8), 38.9 (C-19), 38.8 (C-20), 37.2 (C-10), 36.6 (C-22), 36.4 (C-2), 32.7 (C-7), 30.6 (C-21), 28.0 (C-15), 25.4 (C-23), 24.1 (C-16), 23.5 (C-27), 23.4 (C-11), 22.0 (C-24), 21.1 (C-30), 19.3 (C-6), 17.0 (C-29), 16.9 (C-26), 15.5 (C-25), 15.5 (C-31) ppm; MS (ESI): m/z (%) = 483.3 ([M + H]⁺, 65), 537.0 ([M + Na + MeOH]⁺, 100); anal. calcd. for C₃₂H₅₀O₃ (482.74): C, 79.62; H, 10.44; found: C 79.51; H, 10.58.

4.2.18. Methyl 11-oxo-urs-2,12-dien-28-oate (19)

This compound was synthesized from **4** as previously reported [37]; m.p. 179–187 °C; [α]_D = +141° (c = 1.8, CHCl₃); MS (ESI): m/z (%) = 467.5 ([M + H]⁺, 100), 489.5 [M + Na]⁺, 30).

4.2.19. 3β-Hydroxy-olean-12-en-28-oic acid (oleanolic acid, 20)

This compound was commercially obtained from Betulinines (Střbrná Skalice, Czech Republic) and used as received.

4.2.20. Methyl 3β-hydroxy-olean-12-en-28-oate (22)

This compound was synthesized from **20** as previously reported [42]; m.p. 198–200 °C; [α]_D = +70° (c = 0.43, CHCl₃); MS (ESI): m/z (%) = 493.5 ([M + Na]⁺, 100).

4.2.21. Methyl 3β-hydroxy-11-oxo-olean-12-en-28-oate (23)

Esterification of **21** as previously reported [42] gave **21** as a colorless solid; m.p. 184–188 °C; [α]_D = +82° (c = 0.14, CHCl₃); MS (ESI): m/z (%) = 485.6 ([M + H]⁺, 100), 507.5 [M + Na]⁺, 35).

4.2.22. Methyl 3β-acetyloxy-olean-12-en-28-oate (24)

The acetylation of **22** using acetic anhydride gave **24** [37]; m.p. 219–221 °C 224–225 °C; [α]_D = +69.3° (c = 3.8, CHCl₃); MS (ESI): m/z (%) = 535.5 ([M + Na]⁺, 100).

4.2.23. Methyl 3β-acryloyloxy-olean-12-en-28-oate (25)

Following the procedure given for the synthesis of **11**, from **22** (198 mg, 0.42 mmol) and acryloyl chloride followed by chromatography (silica gel, chloroform/diethyl ether, 98:2) **25** (138 mg, 63%) was obtained as a colorless solid; m.p. 227–233 °C; R_F = 0.62 (hexanes/ethyl acetate, 9:1); [α]_D = 70° (c = 4.2, CHCl₃); UV-Vis (MeOH): λ_{max} (log ε) = 219 nm (4.28); IR (KBr): ν = 3425br, 2940s, 2862m, 1722s, 1471m, 1404m, 1388w, 1363w, 1272m, 1240w, 1204m, 1191s, 1163m, 1124w, 1096w, 1046m, 1014w cm⁻¹; ¹H NMR (500 MHz, CDCl₃): δ = 6.30 (dd, 1H, acryloyl, J = 17.4, 1.5 Hz), 6.04 (dd, 1H, acryloyl, J = 17.2, 10.6 Hz), 5.73 (dd, 1H, acryloyl, J = 10.7, 1.5 Hz), 5.21 (m, 1H, H-12), 4.50 (dd, 1H, H-3, J = 8.6, 7.3 Hz), 3.56 (s, 3H, OMe), 2.82 (dd, 1H, H-18, J = 13.8, 4.2 Hz), 1.90 (ddd, 1H, H-16, J = 14.4, 14.5, 4.0 Hz), 1.85–1.80 (m, 2H, H-11, H-11'), 1.65–1.42 (m, 11H, H-9, H-1, H-19, H-6, H-7, H-15, H-22, H-22', H-16', H-2, H-2'), 1.39–1.09 (m, 4H, H-6', H-21, H-21', H-7', H-19'), 1.07 (s, 3H, H-27), 1.02–0.96 (m, 2H, H-15', H-1'), 0.88 (s, 3H, H-25), 0.86 (s, 3H, H-30), 0.84–0.77 (m, 1H, H-5), 0.83 (s, 3H, H-29), 0.83 (s, 3H, H-26), 0.81 (s, 3H, H-23), 0.66 (s, 3H, H-24) ppm; ¹³C NMR (125 MHz, CDCl₃): δ = 178.2 (C-28), 166.0 (C-31), 143.8 (C-13), 130.0 (C-33, H₂C = C), 129.9 (C-32), 122.2 (C-12), 81.1 (C-3, HC-O), 55.3 (C-5), 51.5 (OMe), 47.4 (C-9), 46.7 (C-17), 45.8 (C-19), 41.6 (C-14), 41.2 (C-18), 39.3 (C-8), 38.1 (C-1), 37.8 (C-4), 36.9 (C-10), 33.8 (C-21), 33.1 (C-29), 32.6 (C-7), 32.3 (C-22), 30.7 (C-20), 28.0 (C-23), 27.6 (C-15), 25.8 (C-27), 23.5 (C-30), 23.4 (C-11), 23.4 (C-2), 23.0 (C-16), 18.2 (C-6), 16.7 (C-24), 16.6 (C-26), 15.3 (C-25) ppm; MS (ESI): m/z (%) = 547.3 ([M + Na]⁺, 100); anal. calcd. for C₃₄H₅₂O₄ (524.77): C, 77.82; H, 9.99; found: C, 77.64; H, 10.13.

4.2.24. Methyl 3,11-dioxo-olean-12-en-28-oate (26)

This amorphous compound was synthesized from **21** as previously reported [44]; [α]_D = +119° (c = 3.30, CHCl₃); MS (ESI): m/z (%) = 483.5 ([M + H]⁺, 100).

4.2.25. Methyl 3β-hydroxy-3α-(3-hydroxy-1-propynyl)-11-oxo-olean-12-en-28-oate (27)

As described for **10**, compound **27** was obtained from methyl 3,11-dioxo-olean-12-en-28-oate (**26**, 300 mg, 0.62 mmol) as an amorphous solid (175 mg, 52%); R_F = 0.54 (hexanes/ethyl acetate, 1:1); [α]_D = 42° (c = 4.4, CHCl₃); UV-Vis (MeOH): λ_{max} (log ε) = 269 nm (4.02); IR (KBr): ν = 3423br, 2950s, 2867m, 1727s, 1655s, 1464m, 1385s, 1366w, 1328w, 1264m, 1206m, 1163w, 1081w, 1036m, 994w cm⁻¹; ¹H NMR (500 MHz, CDCl₃): δ = 5.62 (s, 1H, H-12), 4.27 (s, 2H), 3.61 (s, 3H, OMe), 2.98 (dd, 2H, H-18, J = 13.4, 3.7 Hz), 2.77 (dd, 1H, H-1, J = 13.4, 3.7 Hz), 2.36 (s, 1H, H-9), 2.07–1.94 (m, 2H, H-2, H-16), 1.75–1.56 (m, 7H, H-19, H-16', H-2, H-7, H-15, H-22, H-22'), 1.54–1.49 (m, 1H, H-6), 1.41–1.27 (m, 4H, H-1', H-7', H-21, H-6'), 1.37 (s, 3H, H-27), 1.26–1.15 (m, 4H, H-5, H-19', H-21', H-15'), 1.09 (s, 3H, H-25), 1.03 (s, 3H, H-23), 0.91 (s, 3H, H-30), 0.91 (s, 3H, H-29), 0.88 (s, 3H, H-26), 0.86 (s, 3H, H-24) ppm; ¹³C NMR (125 MHz, CDCl₃): δ = 200.4 (C-11), 177.5 (C-28), 168.8 (C-13), 127.7 (C-12), 88.9 (C-31, C≡C), 83.7 (C-32, C≡C), 75.5 (C-3), 61.9 (C-9), 52.7 (C-5), 51.9 (OMe), 51.0 (C-33), 46.2 (C-17), 45.0 (C-14), 44.3 (C-19), 43.4 (C-8), 41.6 (C-18), 41.6 (C-4), 38.2 (C-1), 37.2 (C-10), 33.7 (C-21), 32.8 (C-29), 32.7 (C-7), 32.5 (C-2), 31.6 (C-22), 30.6 (C-20), 27.7 (C-15), 25.9 (C-23), 23.6 (C-27), 23.4 (C-30), 22.9 (C-16), 18.9 (C-26), 17.7 (C-24), 17.6 (C-6), 16.5 (C-25) ppm; MS (ESI): m/z (%) = 539.5 ([M + H]⁺, 100); anal. calcd. for C₃₄H₅₀O₅ (538.76): C, 75.80; H, 9.35; found: C, 75.56; H, 9.51.

4.2.26. Methyl 11-oxo-olean-2,12-dien-28-oate (28)

This compound was synthesized according to literature from **23** [37]; m.p. 177–183 °C; [α]_D = +147° (c = 1.5, CHCl₃); MS (ESI): m/z (%) = 467.5 ([M + H]⁺, 100).

4.2.27. Methyl 3β-[(aminosulfonyl)oxy]-olean-12-en-28-oate (29)

As described for **12**, compound **29** was obtained from **22** [39]; m.p. 128–129 °C; [α]_D = 73.69° (c = 0.3, CHCl₃); MS (ESI): m/z (%) = 548.3 ([M-H]⁻, 96), 1098.2 ([2M-H]⁻, 100).

4.2.28. Methyl 3β-[[[(aminocarbonyl)amino]sulfonyl]oxy]-olean-12-en-28-oate (30)

As described for **13**, this compound was obtained from **29** [45]; m.p. 77–82 °C; [α]_D = +79.2° (c = 0.28, CHCl₃); MS (ESI): m/z (%) = 91.5 ([M-H]⁻, 95), 1183.1 ([2M-H]⁻, 97).

4.2.29. Methyl 2,3-dihydro-1α,9α-peroxo-11-oxo-olean-12-en-28-oate (31)

This compound was synthesized according to literature from **28**; [37]; m.p. 160–165 °C; [α]_D = -19° (c = 1.7, CHCl₃); MS (ESI): m/z (%) = 497.4 ([M + H]⁺, 25), 519.6 ([M + Na]⁺, 100).

4.2.30. Methyl 3α-epoxy-11-oxo-olean-12-en-28-oate (32)

To a mixture of **28** (391 mg, 0.84 mmol) in DCM (40 mL) *m*-CPBA (550 mg, 3.19 mmol) was added, and the mixture was stirred at 25 °C for 2 h. Cold saturated solution of sodium bicarbonate (100 mL) was added, and the reaction mixture was extracted with DCM (2 × 100 mL). The solvent was evaporated under diminished pressure. The residue was subjected to chromatography (silica gel, hexane/ethyl acetate, 9:1) to afford **32** (227 mg, 55%) as an colorless solid; m.p. 205–207 °C; R_F = 0.60 (hexanes/ethyl acetate, 4:1); [α]_D = +70° (c = 3.1, CHCl₃); UV-Vis (methanol): λ_{max} (log ε) = 269 nm (4.00); IR (KBr): ν = 3424br, 2948s, 1720s, 1653s, 1576m, 1461m, 1438m, 1387m, 1366m, 1329m, 1308m, 1259m, 1236m, 1214m, 1169m, 1129w, 1064w, 1012w cm⁻¹; ¹H NMR (500 MHz, CDCl₃): δ = 5.64 (s, 1H, H-12), 3.62 (s, 3H, OMe), 3.21–3.14 (m, 2H, H-2, H-1), 2.99 (dd, 1H, J = 13.8, 3.7 Hz, H-18), 3.05 (dd, 1H, J = 17.8, 5.9 Hz, H-1'), 2.80 (d, 1H, J = 3.7 Hz, H-3), 2.28 (s, 1H, H-9), 2.02 (ddd, 1H, J = 13.8, 13.8, 4.3 Hz, H-16), 1.74–1.66 (m, 2H, H-16', H-22), 1.64–1.51 (m, 5H, H-6H-7, H-15, H-19, H-22'), 1.49–1.20 (m, 6H, H-6', H-7', H-15', H-19', H-21), 1.29 (s, 3H, H-27), 1.10 (s, 3H, H-25), 1.08 (s, 3H, H-23), 1.01 (s, 3H, H-26), 0.96–0.90 (m,

1H, H-5), 0.92 (s, 3H, H-30), 0.91 (s, 3H, H-29), 0.87 (s, 3H, H-24) ppm; ¹³C NMR (125 MHz, CDCl₃): δ = 199.9 (C11), 177.5 (C-28), 169.1 (C-13), 127.8 (C-12), 61.3 (C-3), 60.4 (C-9), 52.6 (C-2, HC-O), 51.8 (OMe), 46.6 (C-5), 46.2 (C-17), 44.8 (C-14), 44.2 (C-19), 43.5 (C-8), 41.6 (C-18), 40.6 (C-1), 36.1 (C-4), 33.7 (C-21), 32.8 (C-29), 32.6 (C-10), 32.0 (C-7), 31.5 (C-22), 30.6 (C-20), 28.2 (C-23), 27.7 (C-15), 23.4 (C-27), 23.4 (C-26), 22.9 (C-16), 22.0 (C-30), 18.2 (C-25), 18.1 (C-24), 17.8 (C-6) ppm; MS (ESI): *m/z* (%) = 483.5 ([M+H]⁺, 100); anal. calcd. for C₃₁H₄₆O₄ (482.69): C, 77.14; H, 9.61; found: C, 76.91; H, 9.72.

4.2.31. Methyl 2β-bromo-3α-hydroxy-11-oxo-olean-12-en-28-oate (33)

To a solution of **32** (95 mg, 0.20 mmol) in THF (10 mL), HBr (47%, 100 mg) was added dropwise at 10 °C. After stirring for 10 min, the solvent was removed *in vacuo*, water (10 mL) was added, and the reaction mixture was extracted with DCM (2 × 20 mL). Chromatographic purification (silica gel, hexane/ethyl acetate, 4:1) gave **33** (85 mg, 77%) as an amorphous solid; *R_F* = 0.50 (hexanes/ethyl acetate, 4:1); [α]_D²⁰ = +102° (*c* = 4.2, CHCl₃); UV-Vis (MeOH): λ_{max} (log ε) = 268 nm (4.08); IR (KBr): ν = 3447*br*, 2949*s*, 2869*m*, 1727*s*, 1657*s*, 1463*m*, 1388*m*, 1367*m*, 1329*w*, 1304*w*, 1262*m*, 1210*m*, 1164*m*, 1104*w*, 1080*w*, 1052*w*, 1032*w*, 1009*w*, 757*m* cm⁻¹; ¹H NMR (500 MHz, CDCl₃): δ = 5.61 (s, 1H, H-12), 4.23 (ddd, 1H, *J* = 11.9, 8.9, 7.9 Hz, H-2), 3.80 (d, 1H, *J* = 12.2 Hz, H-3), 3.56 (s, 3H, OMe), 2.96 (dd, 1H, *J* = 13.7, 4.3 Hz, H-18), 2.79 (dd, 1H, *J* = 15.3, 11.0 Hz, H-1), 2.43 (s, 1H, H-9), 2.19 (dd, 1H, *J* = 15.3, 7.9 Hz, H-1'), 1.97 (ddd, 1H, *J* = 13.7, 13.7, 4.3 Hz, H-16), 1.70–1.61 (*m*, 2H, H-16', H-22), 1.60–1.50 (*m*, 4H, H-7, H-15, H-19, H-22'), 1.45–1.39 (*m*, 2H, H-6), 1.31–1.11 (*m*, 5H, H-7', H-15', H-19'H-21), 1.28 (s, 3H, H-27), 1.21 (s, 3H, H-25), 1.02–0.96 (*m*, 1H, H-5), 1.00 (s, 3H, H-24), 0.88 (s, 3H, H-23), 0.87 (s, 3H, H-30), 0.87 (s, 3H, H-29), 0.80 (s, 3H, H-26) ppm; ¹³C NMR (125 MHz, CDCl₃): δ = 198.7 (C-11), 177.4 (C-28), 169.6 (C-13), 127.6 (C-12), 76.2 (C-2), 62.9 (C-9), 58.7 (C-3), 52.4 (C-1), 51.9 (OMe), 50.5 (C-5), 46.1 (C-17), 44.8 (C-14), 44.3 (C-19), 43.6 (C-8), 41.6 (C-18), 39.2 (C-4), 39.0 (C-10), 33.7 (C-21), 32.8 (C-29), 31.7 (C-7), 31.6 (C-22), 30.7 (C-20), 27.7 (C-15), 23.6 (C-27), 23.4 (C-23), 23.4 (C-24), 23.0 (C-30), 22.8 (C-16), 21.9 (C-25), 19.1 (C-6), 18.5 (C-26) ppm; MS (ESI): *m/z* (%) = 585.2 ([M(⁷⁹Br) + Na]⁺, 94), 587.2 ([M(⁸¹Br) + Na]⁺, 100); anal. calcd. for C₃₁H₄₇BrO₄ (563.61): C, 66.06; H, 8.41; found: C, 65.83; H, 8.62.

4.2.32. Methyl 2β-bromo-3,11-dioxo-olean-12-en-28-oate (34)

To a solution of **33** (84 mg, 0.15 mmol) in acetone (10 mL) at 0 °C CrO₃ (40 mg, 0.40 mmol) in sulfuric acid (2 M, 0.28 mL) was added. The mixture was stirred for 30 min and then evaporated to dryness. Saturated potassium disulfite solution (10 mL) and saturated sodium bicarbonate solution (10 mL) were added, and the mixture was extracted with DCM (2 × 20 mL). The combined organic layers were washed with brine (10 mL), dried (Na₂SO₄, 10 mL), filtered and evaporated to dryness. The residue was subjected to column chromatography (silica gel, hexane/ethyl acetate, 4:1) to yield **34** (45 mg, 53%) as a colorless solid; m.p. 221–223 °C; *R_F* = 0.36 (hexane/ethyl acetate, 4:1); [α]_D²⁰ = +121° (*c* = 5.1, CHCl₃); UV-Vis (methanol): λ_{max} (log ε) = 269 nm (4.08); IR (KBr): ν = 2950*s*, 2868*m*, 1728*s*, 1659*s*, 1461*m*, 1388*m*, 1366*w*, 1329*w*, 1262*w*, 1190*w*, 1163*m*, 1125*w*, 1062*w*, 1012*w* cm⁻¹; ¹H NMR (500 MHz, CDCl₃): δ = 5.70 (s, 1H, H-12), 5.05 (dd, 1H, *J* = 10.4, 10.4 Hz, H-2), 3.62 (s, 3H, OMe), 3.04 (dd, 1H, *J* = 13.4, 4.3 Hz, H-18), 2.89 (dd, 1H, *J* = 14.7, 10.4 Hz, H-1), 2.59 (s, 1H, H-9), 2.53 (dd, 1H, *J* = 15.0, 11.0 Hz, H-1'), 2.06 (ddd, 1H, *J* = 14.4, 13.6, 4.8 Hz, H-16), 1.74–1.47 (*m*, 9H, H-5, H-6, H-7, H-15, H-16', H-19, H-22), 1.41–1.33 (*m*, 2H, H-7', H-21), 1.38 (s, 3H, H-27), 1.25–1.09 (*m*, 3H, H-15', H-19', H-21'), 1.15 (s, 3H, H-25), 1.13 (s, 3H, H-23), 1.04 (s, 3H, H-26), 0.93 (s, 3H, H-30), 0.93 (s, 3H, H-29), 0.87 (s, 3H, H-24) ppm; ¹³C NMR (125 MHz, CDCl₃): δ = 208.6 (C-3), 198.1 (C-11), 177.3 (C-28), 169.8 (C-13), 127.5 (C-12), 65.8 (C-9), 54.2 (C-1, CH₂), 52.2 (C-5), 51.9 (OMe), 51.0 (C-2, HC-Br), 47.5 (C-4), 46.1 (C-17), 44.6 (C-14), 44.3 (C-19), 43.7 (C-8), 41.6 (C-18), 38.5 (C-10), 33.6 (C-21), 32.3 (C-29), 31.5 (C-7), 31.5 (C-22), 30.7 (C-20), 29.3 (C-23), 27.8 (C-15), 23.6

(C-27), 23.4 (C-30), 22.8 (C-16), 20.0 (C-25), 19.1 (C-6), 19.0 (C-26), 18.1 (C-24) ppm; MS (ESI): *m/z* (%) = 561.4 ([M(⁷⁹Br) + H]⁺, 93), 563.4 ([M(⁸¹Br) + H]⁺, 100), 583.3 ([M(⁷⁹Br) + Na]⁺, 34), 585.2 ([M(⁸¹Br) + Na]⁺, 40); anal. calcd. for C₃₁H₄₅BrO₄ (561.59): C, 66.30; H, 8.08; found: C, 66.11; H, 8.26.

4.3. Enzymatic studies

4.3.1. Spectrometer and chemicals

The Ellman assays were performed as previously described [35] using a TECAN SpectraFluorPlus working in the kinetic mode and measuring the absorbance at λ = 415 nm was used for the enzymatic studies. Acetylcholinesterase (from *Electrophorus electricus*), 5,5'-dithiobis-(2-nitrobenzoic acid) (DTNB) and acetylthiocholine iodide were purchased from Fluka. Butyrylcholinesterase (from equine serum) was purchased from Sigma, and butyrylthiocholine iodide was bought from Aldrich. Details can be found in the Supplementary Material.

5. Modelling

A detailed description can be found in the Supplementary Material.

Acknowledgements

The authors like to thank Dr. Ralph Kluge for ESI-MS and Dr. Dieter Ströhl and his team for the NMR measurements. The IR and optical rotations were measured by Mrs. U. Lammel, MSc. J. Wiese and B.Sc. V. Simon. We like to thank Dr. St. Schwarz for his help in the screening. Support by the “ScienceCampus Halle WCH (W13004216 to RC)” is gratefully recognized.

Appendix A. Supplementary material

Supplementary data to this article can be found online at <https://doi.org/10.1016/j.bioorg.2018.12.013>.

References

- [1] World health organization and alzheimer's disease international. Dementia: A public health priority. Organization, W.H., Ed. Geneva; 2012.
- [2] C. Ballard, S. Gauthier, A. Corbett, C. Brayne, D. Aarsland, E. Jones, Alzheimer's disease, *Lancet* 377 (2011) 1019–1031.
- [3] J. Hardy, D. Allsop, Amyloid deposition as the central event in the etiology of Alzheimer's disease, *Trends Pharmacol. Sci.* 12 (1991) 383–388.
- [4] T. Polvikoski, R. Sulkava, M. Haltia, K. Kainulainen, A. Vuorio, A. Verkkoniemi, L. Niinisto, P. Halonen, K. Kontula, Apolipoprotein-e, dementia, and cortical deposition of beta-amyloid protein, *New Engl. J. Med.* 333 (1995) 1242–1247.
- [5] B.E. Tomlinson, G. Blessed, M. Roth, Observations on the brains of demented old people, *J. Neurol. Sci.* 11 (1970) 205–242.
- [6] D.W. Dickson, H.A. Crystal, L.A. Mattiace, D.M. Masur, A.D. Blau, P. Davies, S.H. Yen, M.K. Aronson, Identification of normal and pathological aging in prospectively studied nondemented elderly humans, *Neurobiol. Aging* 13 (1992) 179–189.
- [7] K. Iqbal, I. Grundke-Iqbal, Alzheimer's disease, a multifactorial disorder seeking multitherapies, *Alzheimers Dement.* 6 (2010) 420–424.
- [8] S. Gilman, M. Koller, R.S. Black, L. Jenkins, S.G. Griffith, N.C. Fox, L. Eisner, L. Kirby, M.B. Rovira, F. Forette, J.-M. Orgogozo, Clinical effects of a beta immunization (an1792) in patients with ad in an interrupted trial, *Neurology* 64 (2005) 1553–1562.
- [9] D. Boche, J. Donald, S. Love, S. Harris, J.W. Neal, C. Holmes, J.A.R. Nicoll, Reduction of aggregated tau in neuronal processes but not in the cell bodies after a beta 42 immunisation in Alzheimer's disease, *Acta Neuropathol.* 120 (2010) 13–20.
- [10] J.O. Rinne, D.J. Brooks, M.N. Rossor, N.C. Fox, R. Bullock, W.E. Klunk, C.A. Mathis, K. Blennow, J. Barakos, A.A. Okello, Rodriguez Martinez, S. de Liano, E. Liu, M. Koller, K.M. Gregg, D. Schenk, R. Black, M. Grundmann, C-11-pib pet assessment of change in fibrillar amyloid-beta load in patients with alzheimer's disease treated with bapineuzumab: a phase 2, double-blind, placebo-controlled, ascending-dose study, *Lancet Neurol.* 9 (2010) 363–372.
- [11] C. Behl, Brain aging and late-onset alzheimer's disease: Many open questions, *Int. Psychogeriatr.* 24 (2012) S3–S9.
- [12] D. Galimberti, E. Scarpini, Treatment of alzheimer's disease: symptomatic and disease-modifying approaches, *Curr. Aging Sci.* 3 (2010) 46–56.
- [13] K. Iqbal, F. Liu, C.X. Gong, Alzheimer disease therapeutics: focus on the disease and not just plaques and tangles, *Biochem. Pharmacol.* 88 (2014) 631–639.

- [14] E.K. Perry, R.H. Perry, G. Blessed, B.E. Tomlinson, Changes in brain cholinesterases in senile dementia of alzheimer type, *Neuropath. Appl. Neuro.* 4 (1978) 273–277.
- [15] P.J. Whitehouse, D.L. Price, A.W. Clark, J.T. Coyle, M.R. DeLong, Alzheimer-disease - evidence for selective loss of cholinergic neurons in the nucleus basalis, *Ann. Neurol.* 10 (1981) 122–126.
- [16] R.T. Bartus, R.L. Dean, B. Beer, A.S. Lipka, The cholinergic hypothesis of geriatric memory dysfunction, *Science* 217 (1982) 408–417.
- [17] J.T. Coyle, D.L. Price, M.R. DeLong, Alzheimers-disease - a disorder of cortical cholinergic innervation, *Science* 219 (1983) 1184–1190.
- [18] E. Giacobini, Cholinesterases and cholinesterase inhibitors, Martin Dunitz, London, 2000, pp. 181–226.
- [19] M.M. Mesulam, A. Guillozet, P. Shaw, A. Levey, E.G. Duysen, O. Lockridge, Acetylcholinesterase knockouts establish central cholinergic pathways and can use butyrylcholinesterase to hydrolyze acetylcholine, *Neuroscience* 110 (2002) 627–639.
- [20] A. Ciro, J. Park, G. Burkhard, N. Yan, C. Geula, Biochemical differentiation of cholinesterases from normal and alzheimer's disease cortex, *Curr. Alzheimer Res.* 9 (2012) 138–143.
- [21] N.H. Greig, T. Utsuki, D.K. Ingram, Y. Wang, G. Pepeu, C. Scali, Q.S. Yu, J. Mamczarz, H.W. Holloway, T. Giordano, D. Chen, K. Furukawa, K. Sambamurti, A. Bossi, D.K. Lahiri, Selective butyrylcholinesterase inhibition elevates brain acetylcholine, augments learning and lowers alzheimer beta-amyloid peptide in rodent, *Proc. Natl. Acad. Sci. USA* 102 (2005) 17213–17218.
- [22] K.-Y. Yoo, S.-Y. Park, Terpenoids as potential anti Alzheimer's disease therapeutics, *Molecules* 17 (2012) 3524–3538.
- [23] R. Tundis, M. Bones, F. Menichini, M.R. Loizzo, Recent knowledge on medicinal plants as source of cholinesterase inhibitors for the treatment of dementia, *Min. Rev. Med. Chem.* 16 (2016) 605–618.
- [24] A.A. Shah, T.A. Dar, P.A. Dar, S.A. Ganje, M.A. Kamal, A current perspective on the inhibition of cholinesterases by natural and synthetic inhibitors, *Curr. Drug Metab.* 18 (2017) 96–111.
- [25] G.F. Sousa, L.P. Duarte, A.F.C. Alcantara, G.D.F. Silva, S.A. Vieira, R.R. Silva, D.M. Oliveira, J.A. Takahashi, New triterpenes from maytenus robusta: structural elucidation based on nmr experimental data and theoretical calculations, *Molecules* 17 (2012) 13439–13456.
- [26] I. Lee, B. Ahn, J. Choi, M. Hattori, B. Min, K. Bae, Selective cholinesterase inhibition by lanostane triterpenes from fruiting bodies of ganoderma lucidum, *Bioorg. Med. Chem. Lett.* 21 (2011) 6603–6607.
- [27] N. Riaz, M.A. Naveed, M. Saleem, B. Jabeen, M. Ashraf, S.A. Ejaz, A. Jabbar, I. Ahmed, Cholinesterase inhibitory constituents from ficus bengalensis, *J. Asian Nat. Prod. Res.* 14 (2012) 1149–1155.
- [28] S. Mehmood, N. Riaz, S.A. Nawaz, N. Afza, A. Malik, M.I. Choudhary, New butyrylcholinesterase inhibitory triterpenes from salvia santolinifolia, *Arch. Pharm. Res.* 29 (2006) 195–198.
- [29] B. Culhaoğlu, G. Yapar, T. Dirmenci, G. Topcu, Bioactive constituents of Salvia Chrysophylla Stapf, *Nat. Prod. Res.* 27 (2013) 438–447.
- [30] A. Yilmaz, P. Caglar, T. Dirmenci, N. Goren, G. Topcu, A novel isopimarane diterpenoid with acetylcholinesterase inhibitory activity from nepeta sorgerae, an endemic species to the nemrut mountain, *Nat. Prod. Commun.* 7 (2012) 693–696.
- [31] J.H. Lee, K.T. Lee, J.H. Yang, N.I. Baek, D.K. Kim, Acetylcholinesterase inhibitors from the twigs of vaccinium oldhami miquel, *Arch. Pharm. Res.* 27 (2004) 53–56.
- [32] I.H. Jung, S.E. Jang, E.H. Joh, J. Chung, M.J. Han, D.H. Kim, Lancemaside A isolated from codonopsis lanceolata and its metabolite echinocystic acid ameliorate scopolamine-induced memory and learning deficits in mice, *Phytomedicine: Int. J. Phytother. Phytopharm.* 20 (2012) 84–88.
- [33] Y.K. Chung, H.J. Heo, E.K. Kim, H.K. Kim, T.L. Huh, Y. Lim, S.K. Kim, D.H. Shin, Inhibitory effect of ursolic acid purified from origanum majorana l on the acetylcholinesterase, *Mol. Cells* 11 (2001) 137–143.
- [34] S. Schwarz, S.D. Lucas, S. Sommerwerk, R. Csuk, Amino derivatives of glycyrrhetic acid as potential inhibitors of cholinesterases, *Bioorg. Med. Chem.* 22 (2014) 3370–3378.
- [35] L. Heller, M. Kahnt, A. Loesche, P. Grabandt, S. Schwarz, W. Brandt, R. Csuk, Amino derivatives of platanic acid act as selective and potent inhibitors of butyrylcholinesterase, *Eur. J. Med. Chem.* 126 (2017) 652–668.
- [36] S.Y. Ryu, C.-K. Lee, J.W. Ahn, S.H. Lee, O.P. Zee, Antiviral activity of triterpenoid derivatives, *Arch. Pharmacol. Res.* 16 (1993) 339–342.
- [37] A. Niesen, A. Barthel, R. Kluge, A. Köwitsch, D. Ströhl, S. Schwarz, R. Csuk, Antitumoractive endoperoxides from triterpenes, *Arch. Pharm.* 342 (2009) 569–576.
- [38] Y. Zhang, J. Li, J. Zhao, S. Wang, Y. Pan, K. Tanaka, S. Kadota, Synthesis and activity of oleanolic acid derivatives, a novel class of inhibitors of osteoclast formation, *Bioorg. Med. Chem. Lett.* 15 (2005) 1629–1632.
- [39] S. Schwarz, S. Sommerwerk, S.D. Lucas, L. Heller, R. Csuk, Sulfamates of methyl triterpenoates are effective and competitive inhibitors of carbonic anhydrase II, *Eur. J. Med. Chem.* 86 (2014) 95–102.
- [40] Cambridge Crystallographic Data Centre; GOLD, Version 5.2; Cambridge, U.K., < www.ccdc.cam.ac.uk/products/gold_suite > .
- [41] Chemical Computing Group: Montreal, C., MOE 2014, Molecular Operating Environment; Montreal, Canada 2014, < www.Chemcomp.Com > .
- [42] B. Siewert, J. Wiemann, A. Köwitsch, R. Csuk, The chemical and biological potential of C ring modified triterpenoids, *Eur. J. Med. Chem.* 72 (2014) 84–101.
- [43] P.L. Majumder, A. Bagchi, Oxidative transformations of triterpenoids of the ursane and oleanane skeleta with hydrogen peroxide. Introduction of 11,12 double bond and 13(28)oxide moiety in the ursane system, *Tetrahedron* 39 (1983) 649–655.
- [44] L. Heller, S. Schwarz, V. Verl, A. Köwitsch, B. Siewert, R. Csuk, Incorporation of a Michael acceptor enhances the antitumor activity of triterpenoic acids, *Eur. J. Med. Chem.* 101 (2015) 391–399.
- [45] S. Sommerwerk, L. Heller, R. Csuk, Synthesis and cytotoxic activity of pentacyclic triterpenoid sulfamates, *Arch. Pharm.* 348 (2015) 46–54.

5. Summary of the Results

5. Summary of the Results

Sirtuins and cholinesterases represent two promising therapeutic targets investigated in this study. Consequently, searching for sirtuin and cholinesterase inhibitors is of great interest in the scientific community. In order to identify novel chemotypes of inhibitors and to understand the binding mode of these novel compounds, various computer-aided molecular design methods were applied in the current thesis. Based on the observed results obtained in this work, the following summaries can be made.

5.1. Developing selective Sirt1 inhibitors and investigating their inhibition in some cancer cell lines

Up to now, selisistat (**EX-527**) is the only small molecule inhibitor of Sirt1 in clinical trials. It reached phase III clinical trials for the treatment of Huntington's disease.

In this work (186), a virtual screening based on a previously collected library of putative sirtuin inhibitors was done using several crystal structures of Sirt1. Phenylthiocyanate compounds were proved to inhibit Sirt1 selectively. The first hypothesis based on the docking study was a covalent binding of the thiocyanate group to a cysteine in the NAD⁺ binding pocket. However, in several biological experiments, the thiocyanate inhibitors were found to be reversible binders and, in agreement with the docking results, NAD⁺ competitive inhibitors. The cellular assay confirmed that the thiocyanate inhibitors induce tumor suppressor protein (p53) acetylation, which leads to inhibition of the proliferation and death of cells. Additionally, colony-forming capacities of human cervical cancer cells are inhibited by these inhibitors. Moreover, the inhibitors reduced the level of phosphorylation of the DNA damage sensor Histone Family Member X (H2AX). Thus, DNA damage will be decreased.

The docking was done to predict the binding modes of the compounds. The binding mode postulated that the phenyl thiocyanate moiety is located in the adenine pocket and is making a hydrogen bond to the backbone NH of Cys482.

All the active compounds exhibit high selectivity for Sirt1 over Sirt2, Sirt3, and Sirt5.

Since thiocyanate acts as a chelating group, this makes the thiocyanate inhibitors candidates for ion-dependent enzyme inhibition, such as zinc-dependent histone deacetylases (HDACs). Therefore, the selectivity of the compounds was also tested against the zinc-

dependent deacetylases HDAC1, HDAC6. The compounds showed no inhibition against HDAC1, whereas some compounds **S1th 10**, **12**, and **13** showed a very weak inhibition against HDAC6. Furthermore, the selectivity was also tested against deubiquitinases (DUBs) since DUBs are inhibited by thiocyanates; this can occur by the binding of the compounds with cysteine residues in the active site of DUBs (187). Interestingly, the inhibitors showed no inhibition against DUBs.

The most active compounds **S1th 13** (IC_{50} : $5.2 \pm 1.0 \mu M$) and **S1th 3** (IC_{50} : $2.8 \pm 0.5 \mu M$) are shown in **Figure 9**. The docking showed that these two compounds interact with Asp272 by hydrogen bonds. **Figure10** reveals the binding modes of these compounds.

The inactive compounds exhibited a similar binding mode, but without interactions in the adenine pocket.

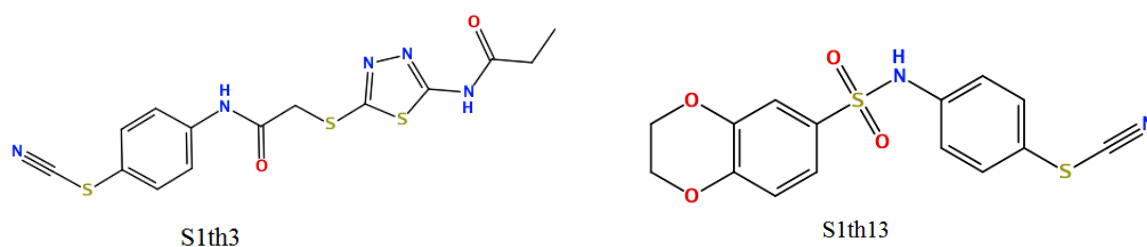


Figure 9: 2D structures of the compounds S1th3, S1th13.

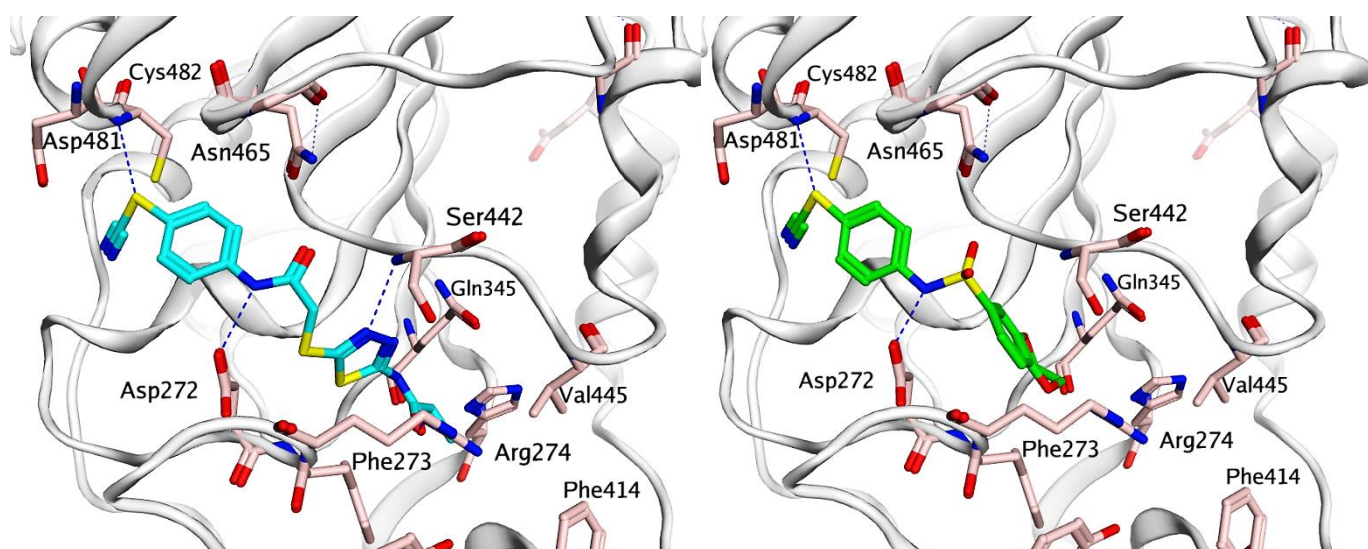


Figure 10: Docking poses obtained for S1th 3 (colored cyan) and S1th 13 (colored green) in Sirt1 NAD⁺ binding pocket. Hydrogen bonds are shown as dashed lines.

5.2. Identification of potent and selective Sirt5 inhibitors

In this work (48), modifications of the lysine side chain of a carbamoyl phosphate synthetase 1 (CPS1) derived peptide substrate were studied. The moiety of 3-phenylsuccinyl on a lysine side chain represents a specific inhibitor of Sirt5, which works by blocking the NAD⁺ binding pocket. Thus, the succinylated CPS1 peptide was used as a scaffold to target the Sirt5 specific Tyr/Arg motif. This motif is an important hotspot for Sirt5 selectivity between the mammalian sirtuins. Consequently, different succinyl-CPS1-derived peptide inhibitors with the activity of nanomolecular range were synthesized in the group of Prof. Mike Schutkowski and identified as Sirt5 inhibitors.

The probe design was guided by the analysis of the crystal structure of PDB ID: 4UTV and the two crystal structures that were solved in this study (PDB ID: 6FLG and PDB ID: 6FKY). The analysis of the crystal structure of zebrafish Sirt5 (zSirt5) with the 3-phenylsuccinyl-carbamoyl phosphate synthetase (CPS1)-derived peptide (compound **47**) PDB ID: 4UTV showed that the phenyl ring of this compound blocks the NAD⁺ binding pocket and points towards the C-pocket, but it cannot reach it.

Several peptidic inhibitors were discovered, such as 3-(2-naphthylthio) succinyl derivative compound **33**. It is the most selective and efficient Sirt5 selective inhibitor with the (IC₅₀: 40 nM). Analyzing the interaction of **33** with zebrafish Sirt5 (zSirt5) in the solved crystal structure PDB ID: 6FLG revealed that the bulky aromatic substituent of **33** occupies the C-pocket.

The investigation of the crystal structure PDB ID: 6FKY, which is also solved in this work, shows that the benzyl group of **15** is oriented toward the C pocket and extends deeper into this pocket but cannot fill it completely. Interestingly, there is no interaction between the N-terminal benzoyl residue and zSirt5.

The peptidic part of the inhibitors was truncated in order to improve the cellular permeability of the compounds. It was shown that the peptide part of the inhibitors is responsible for the potency and affinity of the inhibitors to Sirt5. Nevertheless, the omission of peptide additions and moving to tripeptide compounds will keep the activity of the compounds.

The crystal structures of zSirt5 with the compounds **33** and **15** are shown in **Figure 11**.

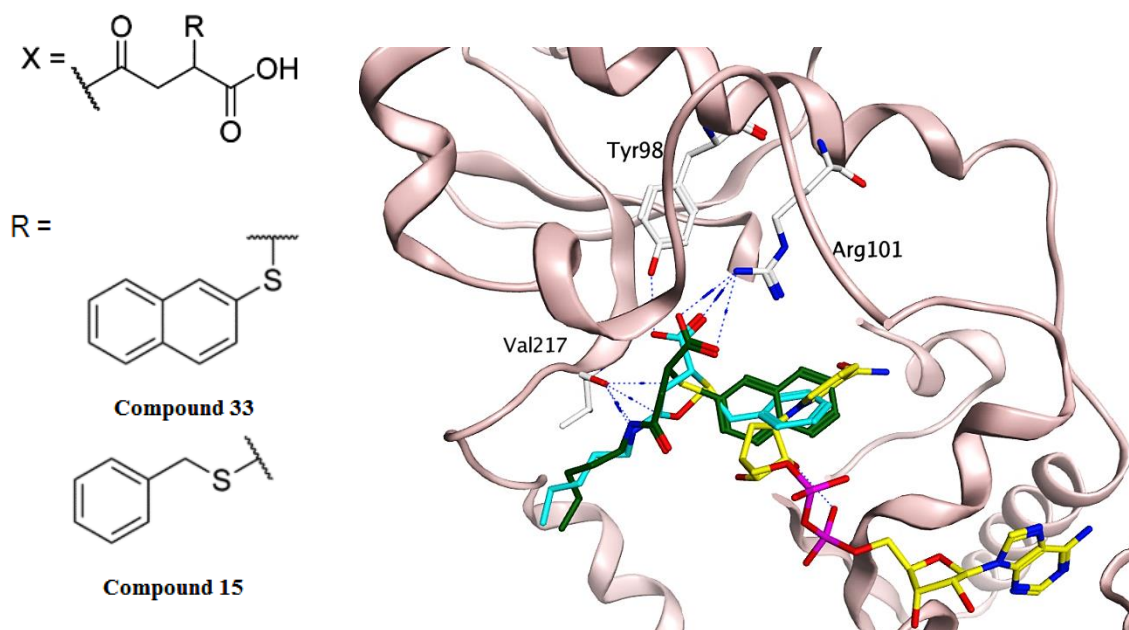


Figure 11: The chemical Structures of succinyl-CPS1-derived peptide inhibitors (Bz GVLK(X) EYGV-NH₂) and the binding modes of compounds 33 and 15. The crystal structure of zSirt5 with 33 (PDB ID: 6FLG, the ligand is shown in green) was overlaid with the crystal structure of zSirt5, and 15 (PDB ID: 6FKY, the ligand is shown in blue), NAD⁺ (yellow) was modeled from PDB ID: 4G1C.

5.3. Identification of sirtuin inhibitors from natural products using virtual screening of the p-ANAPL library

Pan-African natural products library (P-ANAPL) library consists mostly of drug-like compounds with a broad range of reported activities as antibacterial, antiviral, anti-cancer, and anti-inflammatory properties (188). This library represents a good starting point to search for novel modulators of sirtuin. Most of the natural products from African botanical sources have a unique and broad chemical space with drug-like properties (189).

In the present work (190), high-throughput virtual screening (HTVS) was done to virtually screen the p-ANAPL compound data using several Sirt1 and Sirt2 crystal structures.

Docking of p-ANAPL library (463 compounds) into Sirt1 Sirt2 Sirt3 was done. Visual inspection was done on all the docking poses, followed by *in vitro* testing. Consequently, two moderately active compounds, which are rhuschalcone IV (**compound 8**) and an analogue of rhuschalcone I (**compound 9** Figure 12), were identified as sirtuin inhibitors (the IC₅₀ value of **compound 8** is 46.7 μM for Sirt1, and 48.5 for Sirt2, the IC₅₀ value of

compound 9 is 40.8 μM for Sirt1, and 44.8 for Sirt2). Both **compounds 8** and **9** were isolated from the medicinal plant *Rhus pyroides* Burch (*Anacardiaceae*), which has a wealthy source of several O-linked and C-C coupled bichalcones (191).

The most favorable binding mode of the two compounds in Sirt1 was noticed in the peptide-binding pocket; here, the hydroxyl groups on the ring A' of the compounds showed H-bonds with the backbone carbonyl group of the residue Gln345. **Figure 13** shows the possible binding modes of the active compounds in Sirt1 peptide-binding pocket

The two compounds can also interact in the extended C pocket of Sirt2; in this pocket, the hydroxyl groups in the ring B' of the compounds interact with His187 via the water molecule HOH676. Additionally, the hydroxyl groups of ring A interact with the O atom of the backbone of Asp 170. The binding modes of the actives in the Sirt2 extended C-pocket is shown in **Figure 13**.

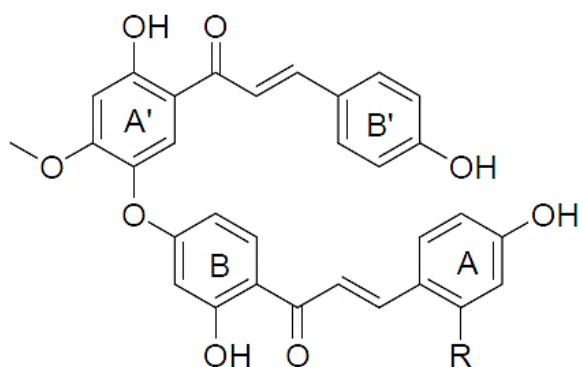


Figure 12: 2D structure of Rhuschalcone IV (8): R = H, Rhuschalcone I analogue (9): R = OH

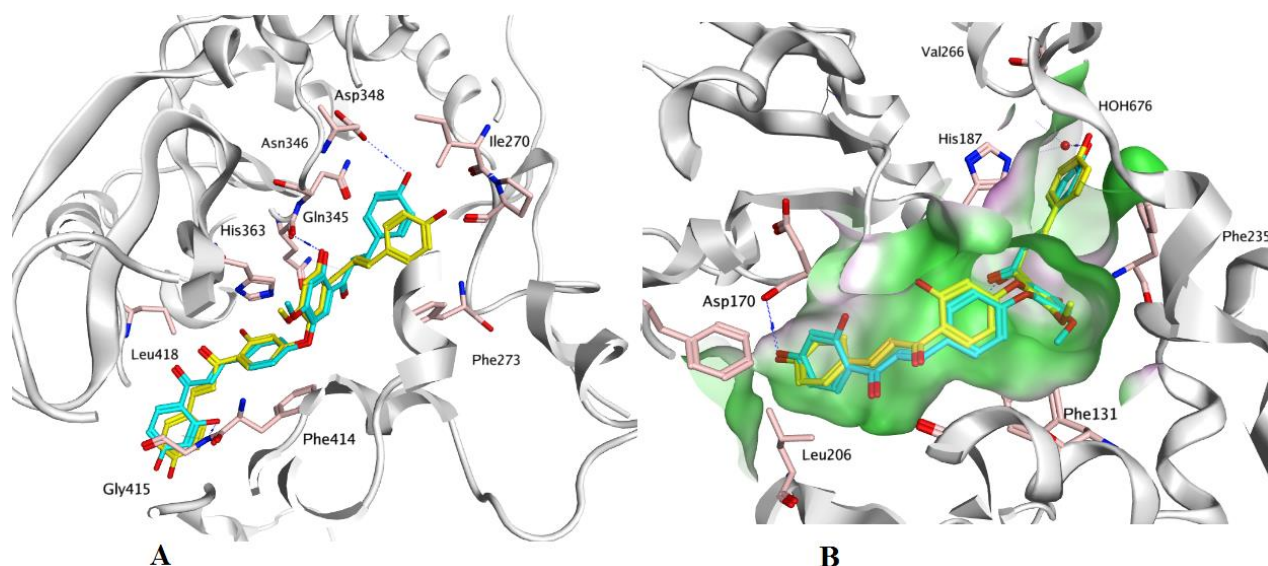


Figure 13: The possible binding modes of the natural product inhibitors in Sirt1 peptide pocket (PDB code: 4ZZJ) (A), and in Sirt2 extended C-pocket (PDB code: 5D7P) (B), the binding pocket is colored according to hydrophilic (pink) and hydrophobic (green) regions.

5.4. Hit identification and lead optimization for Sirt2

Splitomicin, is a non - selective sirtuin inhibitor. It is poorly soluble in water and biological fluids. Thus this work (192) aimed to modify the nonpolar splitomicin derivative scaffold 1,2- dihydro-3*H*-naphth[1,2-*e*][1,3]oxazine-3-thione with polar functional groups to get novel Sirt2 inhibitors with improved aqueous solubility. In order to identify where to modify the compounds, structure-based modeling was carried out.

N-alkylated derivatives with a hydrophilic morpholino-alkyl chain at the thiocarbamate were proposed, synthesized, and tested *in vitro* against several sirtuins. Unfortunately, in most cases adding the polar substituents resulted in a decreased inhibitory activity.

Interestingly, the most active compound was the brominated compound **8b** (IC₅₀ = 1.8 μM).

Figure 14 shows the chemical structure of the compound **8b**. Docking was performed to predict the possible binding mode of the inhibitors. Two molecules of compound **8b** can interact at the same time in the nicotinamide binding pocket and extended C-pocket. The best-ranked docking solution was obtained for the nicotinamide binding pocket, whereas the second molecule interacts at the extended C-pocket (**Figure 14**).

It was shown that the hydrophobic interactions of the sulfur of the thiocarbamate of the compound with Sirt2, as well as the bromo substituent led to the good inhibitory activity of

the compound **8b**. This compound can be used as a starting point to search for new inhibitors with improved aqueous solubility and affinity to Sirt2.

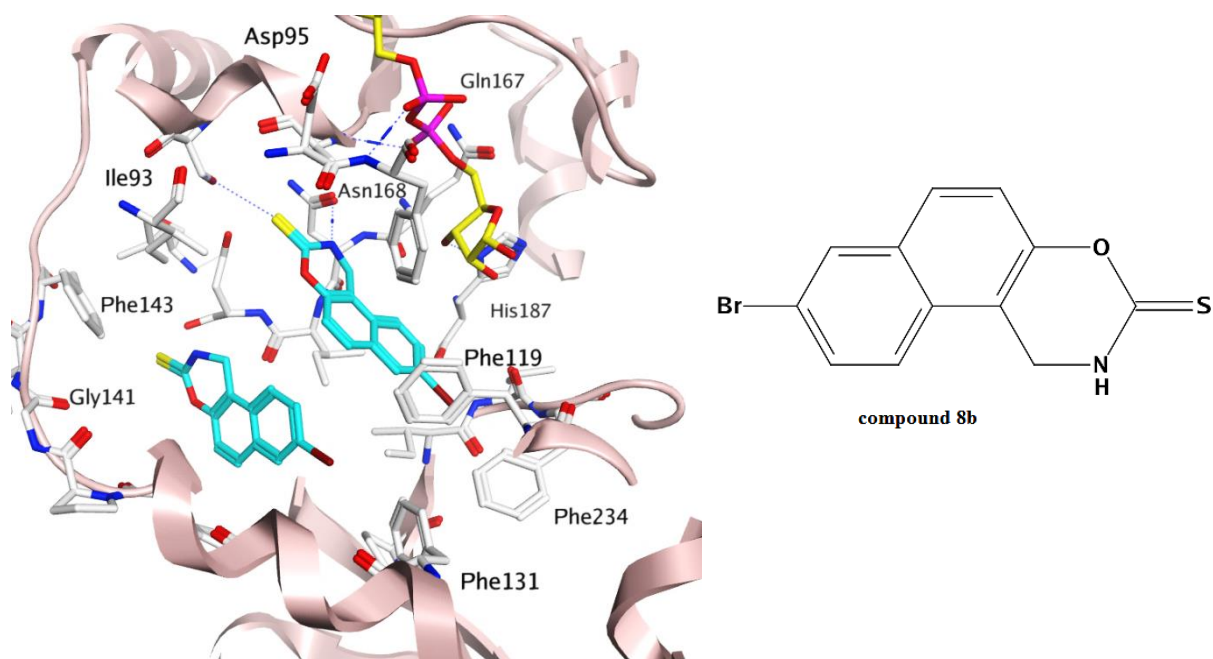


Figure 14: The crystal structure of hSirt2 with the compound **8b**, two inhibitor molecules are shown, the hydrogen bonds are depicted as dashed lines. ADPR molecule is colored in yellow.

5.5. Virtual screening and identification of specific inhibitors for the mitochondrial deacylase Sirtuin 4

In this work, we described how the first potent human Sirt4-selective small molecule inhibitors were discovered using a combination of virtual screening and *in vitro* testing. Structure-based virtual screening was done using the available X-ray crystal structure from *Xenopus tropicalis* Sirt4 and a human Sirt4 (hSirt4) homology model. Consequently, two chemical scaffolds (examples **OSSK_979070** and **OSSK_671780**, **Figure 15**) were identified. They represent promising starting points for chemical optimization to get lead compounds. The first scaffold contains para-carbamoylbenzenesulfonamide (e.g. compound **OSSK_979070**). The binding mode of this compound showed that the phenyl group of the compound could interact with His161 and Val232 in the substrate pocket of Sirt4. Both residues are conserved among sirtuins; these residues are involved in substrate interactions. The modeled binding pose would suggest a substrate competitive inhibition mechanism. Compounds of the second type of hits include a central N-1,3-thiazol-2-ylformamide that is substituted on both sites (e.g. **OSSK_671780**). The amide group of

this compound is donating a hydrogen bond to the backbone carbonyl of Val232, whereas the thiazole ring is interacting with His161 (**Figure 16**). Additionally, the active hits contain a 2-sulfanylpurimidin-4-ol ring, which shows T-stacking interactions with Phe233 in the Sirt4-acyl pocket.

HMG was docked into the peptide pocket of XSirt4 crystal structure and accelerated MD simulation was done on the complex of XSirt4 crystal structure with the substrate HMG as well as the complex of hSirt4 with the most selective compound to study the conformational changes of the protein upon ligand binding. The RMSD plots indicate that XSirt4 bound to HMG is more stable than XSirt4 form without a bound substrate. Hence, the substrate HMG stabilizes the residues of the peptide-binding pocket of XSirt4. Furthermore, hSirt4 apo form was predicted in this study and used for docking studies.

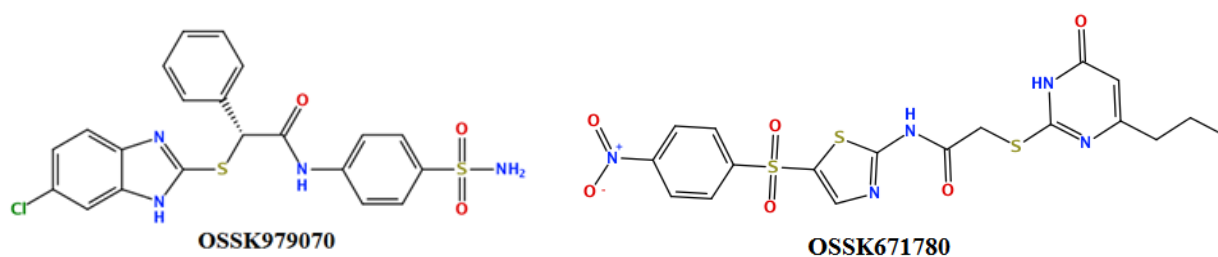


Figure 15: 2D structure of the compounds OSSK_979070 and OSSK_671780.

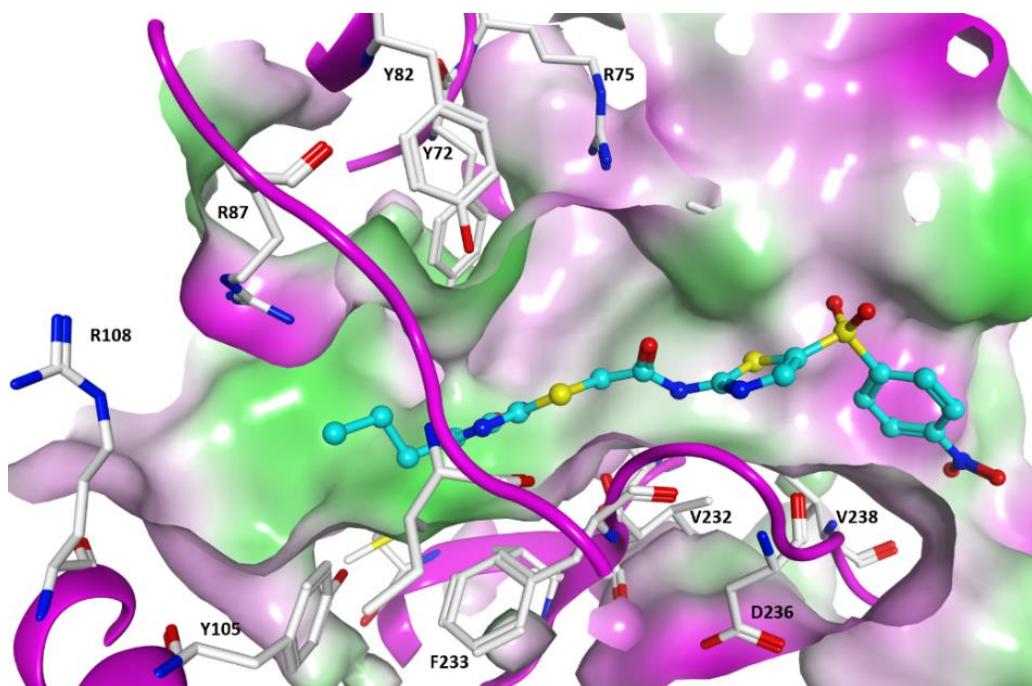


Figure 16: Predicted docking pose of the VS hits OSSK_671780 in the peptide-binding pocket of the homology model of hSirt4 (magenta ribbon). The molecular surface of the pocket is colored according to the hydrophobicity (green = hydrophobic, magenta = polar).

5.6. Discovering novel acetylcholinesterase (AChE) and butyrylcholinesterase (BChE) inhibitors

Acetylcholinesterase (AChE) and butyrylcholinesterase (BChE) inhibitors are of great interest because they improve the life quality of patients with age-related dementia, especially Alzheimer's disease.

In this work (193), seven molecules from (2E) α , β -unsaturated fatty acids differing in chain length were discovered as inhibitors of AChE with IC_{50} = 4.3 to 12.8 μ M.

The results showed that the trans-2-mono-unsaturated fatty acids are better AChE inhibitors than their saturated analogs, and the chain length of the compound is important to get the inhibition effect. The most active compounds are compounds **13**, **14**, and **23**. The best results were obtained for the unsaturated compound (2E) eicosenoic acid (compound **14**) (n= 16) with $K_i = 1.51 \pm 0.09$ μ M for AChE.

The docking studies were done on horse BChE homology model and the crystal structure of AChE in complex with donepezil. The common binding mode of the active compounds revealed that they interact with the residue Tyr 130 in the AChE binding pocket and could fit very well with their hydrophobic tails into the AChE hydrophobic pocket. At the same

time, the carboxyl groups of the compounds fit reasonably into the hydrophilic part of the pocket. **Figure 17** shows the 2D structures and the binding modes of the active compounds with the crystal structure of AChE.

Further, another group of pharmacologically active substances (triterpenes) has been tested in this work (194). They were evaluated for the cholinergic activities. Consequently, several derivatives of ursolic and oleanolic acid were discovered as inhibitors for AChE. The most active inhibitor for acetylcholinesterase was 2-methyl-3-oxo-methyl-ursolate (compound **18**) with an inhibition constant of $K_i = 1.72 \pm 0.24 \mu\text{m}$ for AChE. Importantly, 3-hydroxyprop-1-ynyl methyl-ursolate (compound **10**) was a selective inhibitor for butyrylcholinesterase with an inhibition constant of $K_i = 4.29 \pm 0.29 \mu\text{m}$ for BChE. **Figure 18** shows the chemical structures of the compounds **18, 10**.

We docked the inhibitors to assess the preferred poses of the compounds in the active site of the AChE and BChE. Notably, compound **18** showed U shape in AChE binding pocket. It was shown that the selectivity for AChE could be explained by the fact that the inhibitors interact with the residues Phe 330, Trp 279, Tyr 121 in the AChE binding pocket, whereas the corresponding residues in BChE (Ala 328, Val 277, Gln 119) don't make interactions with the inhibitors.

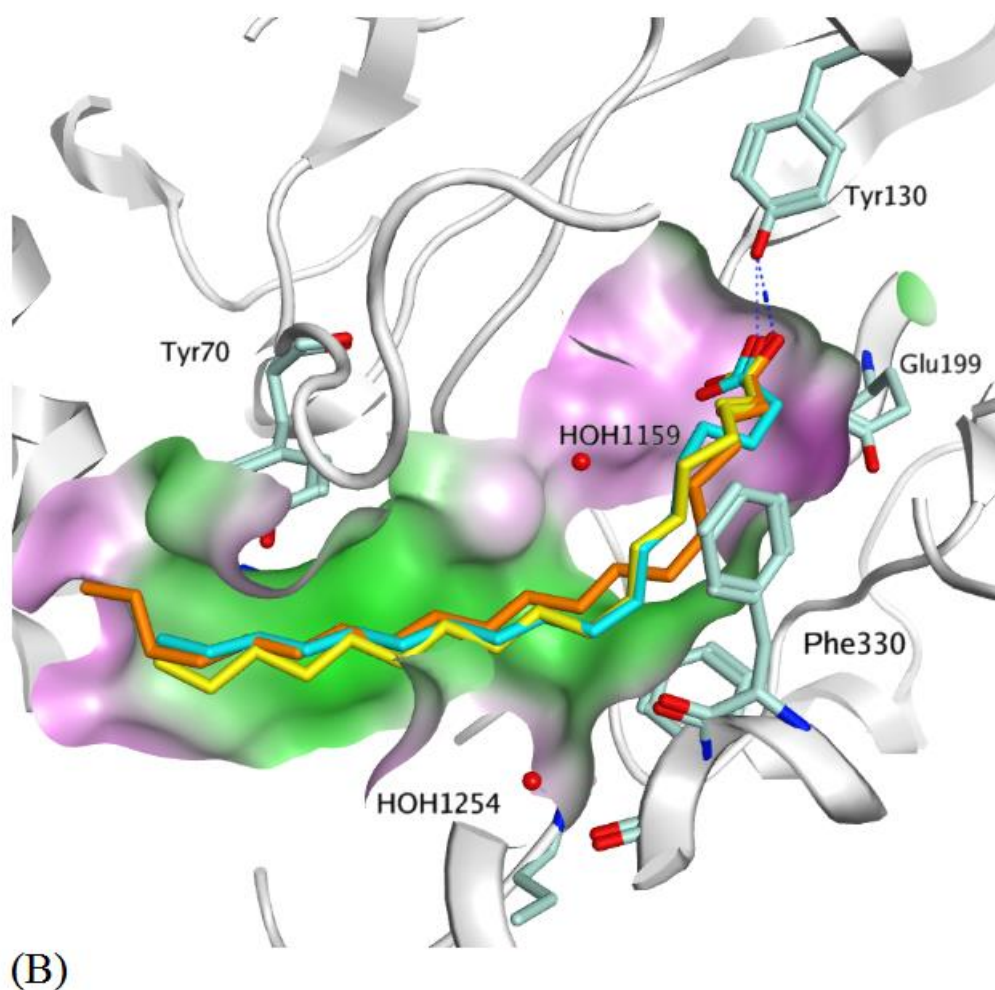
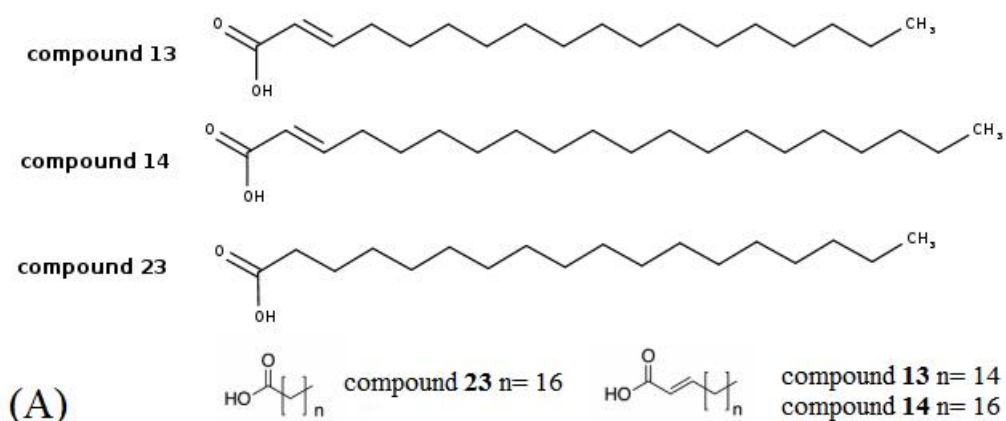
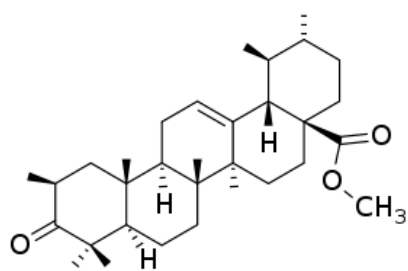
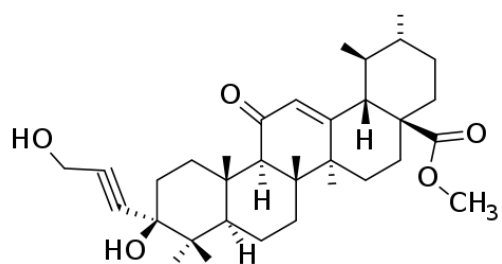


Figure 17: (A): The 2D structures of AChE inhibitors, (B): Predicted common binding mode of AChE inhibitors from fatty acids with the crystal structure of AChE (PDB code: 1EVE). Compound 13 in yellow, compound 14 in orange, compound 23 in light blue. Hydrogen bonds were drawn as dashed lines. The binding pocket is colored according to hydrophobic (green) and hydrophilic (pink) regions.



Compound 18



Compound 10

Figure 18: The 2D chemical structures of the cholinesterase inhibitors (compounds 18, 10).

6. Conclusion

Computational methods are considered as efficient methods to design selective inhibitors. Hence, computational methods were used in this work to identify novel hits for sirtuins and cholinesterase.

The molecular docking studies that were carried out in this work predicted the binding modes of the discovered compounds. Furthermore, homology modeling using several programs was utilized to generate 3D structures for sirtuins and cholinesterases. *In vitro* testing was performed to assess the activities of the compounds using different *in vitro* assays. Thus, the incorporation of *in silico* and *in vitro* methods was established as an ideal approach to accelerate the discovery of novel inhibitors.

The first part of the work was focused on searching for new and selective sirtuin inhibitors. In this part, the results can be summarized as follows:

- Molecular docking and virtual screening procedures were applied in order to search for Sirt1 novel inhibitors. As a result, thiocyanate compounds were found to inhibit Sirt1 selectively. The most active compounds are **S1th 13** (IC_{50} : $5.2 \pm 1.0 \mu\text{M}$) and **S1th 3** (IC_{50} : $2.8 \pm 0.5 \mu\text{M}$). All of the inhibitors show high selectivity for Sirt1 over Sirt2, Sirt3, Sirt5, HDAC1, HDAC6, and other possible off-targets such as deubiquitinases (DUBs). Interestingly, in contrast to the reported Sirt1 inhibitors, which are all substrate competitive or mixed-type inhibitors, the thiocyanates represent reversible NAD^+ -competitive inhibitors. The cellular assay showed that these inhibitors induce tumor suppressor protein (p53) acetylation; additionally, they induce cell death and inhibit cell proliferation. Moreover, the inhibitors inhibit the colony-forming abilities of human cervical cancer cells. Hence, these promising inhibitors can play a role in cancer therapy.
- The succinylated CPS1 peptide was used as a scaffold to target Sirt5 Tyr/Arg motif, which is an essential hotspot for Sirt5 selectivity among the mammalian sirtuins. The computational studies were used to rationalize the binding mode of the studied inhibitors. The structure-activity relationship of this series of highly active and selective peptide-based Sirt5 inhibitors was described. Interestingly, structural differences of the studied stereoisomers could explain their different inhibitory activities. The most active Sirt5 inhibitor has an IC_{50} of 40 nM, and this compound shows high selectivity for Sirt5.

- Due to the vital role of natural products in drug discovery, virtual screening (VS) was performed to virtually screen the natural products from the African botanical p-ANAPL library in order to search for novel sirtuins inhibitors. Virtual screening and docking of this library led to the identification of two moderately active bichalcones compounds from the medicinal plant *Rhus pyroides*. They are inhibitors for Sirt1 and Sirt2 (the IC₅₀ value of **compound 8** is 46.7 μM for Sirt1, and 48.5 for Sirt2, the IC₅₀ value of **compound 9** is 40.8 μM for Sirt1, and 44.8 for Sirt2).
- New derivatives derived from the known inhibitor spiltomicin with improved aqueous solubility were found. Molecular docking studies were performed in order to understand the binding modes of these inhibitors. The most active compound is **8b**, which has IC₅₀ = 1.8 μM. Importantly, the hydrophobic interactions of the sulfur of the thiocarbamate of this compound with Sirt2, and its bromo substituent contributed to its good activity. This compound could be a starting point to discover more potent Sirt2 inhibitors.
- To date, Sirt4 is the least characterized member of human mitochondrial sirtuins. Sirt4 has been identified as a potential target to support cancer therapy. The first crystal structure of Sirt4 was discovered in 2017, and until now, no inhibitors for Sirt4 have been found. Computational methods such as structure-based virtual screening were performed, and as a consequence, novel selective Sirt4 inhibitors were found. This study also provides information and mechanistic details of the conformational changes in Sirt4 induced by substrates and inhibitor. MD simulation was done, and the stability of the homology models was studied. The conformational dynamics of XSirt4 with HMG were studied. The RMSD plots indicate that the structure of XSirt4 bound to HMG is more stable than the structure of XSirt4 form without the substrate. Interestingly, the apo-form structure model of Sirt4 has also been proposed.

The second part of this work used computational methods to study the binding mode of novel inhibitors for acetylcholinesterase and butyrylcholinesterase. Such inhibitors are necessary to improve the life quality of patients suffering from age-related dementia illnesses, especially Alzheimer's disease. Two groups were tested for their inhibitory effect against cholinesterase: the first group is fatty acids, and the second group is triterpenes. The following conclusion can be made:

- Seven molecules from (2E) α , β -unsaturated fatty acids were identified by the collaborators as inhibitors of AChE with IC_{50} = 4.3 to 12.8 μ M. The most active compounds **13**, **14**, and **23** were found to inhibit AChE. Furthermore, the screening results revealed that the chain length is critical in achieving the inhibition. Moreover, the unsaturated fatty acids showed better activity than saturated ones. Docking the compounds was helpful to understand the binding mode and to explain the high activity of compound **14** (unsaturated, n= 16), which shows inhibition constant $K_i = 1.51 \pm 0.09 \mu$ M for AChE.
- Several compounds from ursolic and oleanolic acid derivatives were found to inhibit cholinesterase. Consequently, compound **18** (2-methyl-3- oxo-methyl-ursolate, $K_i = 1.72 \pm 0.24 \mu$ M for AChE) was discovered as a selective inhibitor of AChE and was analyzed using docking studies. In addition, the hydroxy-propinyl derivative compound **10** (3-hydroxyprop-1-ynyl methyl-ursolate, $K_i = 4.29 \pm 0.29 \mu$ M for BChE) was provided as a selective butyrylcholinesterase inhibitor and was also included in the computational study. Different binding modes were obtained and could be used to rationalize the biological activities.

To conclude, the process of drug design is a challenging, expensive, and time-consuming process. Therefore, CADD methods, which are effective and essential tools in the drug development procedure, have been used in our study to develop sirtuins and cholinesterase inhibitors. These methods reduce the numbers of compounds necessary for the screening and the numbers of compounds that should be synthesized and tested *in vitro*. Hence, many compounds that are predicted to be inactive can be avoided, and the compounds that are predicted to be active can be selected. Additionally, the filters such as PAINS are also useful to narrow the chemical space and to decrease the numbers of potential inhibitors for biological testing. As a consequence, the time and expense involved in the drug development process can be reduced.

Within this work, molecular docking studies provided a better understanding of the interactions between the protein and the ligands. In addition, the binding modes of the inhibitors are well predicted, and the molecular structures of the protein targets are well analyzed. Thus, the modeled binding poses would suggest that the inhibitors are well accommodated into either a peptide-binding pocket or NAD^+ binding pocket of sirtuins.

This depends on the shape of the compounds and the important interactions of compounds with the key residues existing in the binding site that allow specific and good occupation into the binding pocket.

However, it is sometimes difficult to balance accuracy and speed when using CAAD methods. The flexibility of the receptor and the accurate estimation of the binding affinities of the protein-ligand complexes are still big challenges for the docking and virtual screening process. In order to decrease these problems, validation of the docking program was performed, and several additional techniques were applied to the docking poses, for example, molecular mechanics/generalized born (Poisson–Boltzmann) surface area (MM/PB(GB)SA simulation).

Interestingly, the homology modeling approach used in this study was useful to predict the structure of the target protein of Sirt4. Good accuracy was observed, and only some flexible loop regions were not correctly modeled.

Finally, since ligand is thought to interact with some protein conformations but not others, the docking into a rigid protein structure can be therefore misleading, and the chosen conformation may not be representative for a conformation that is suitable for ligand binding. Accordingly, conformational sampling is necessary in order to give a series of snapshots that can be used instead of a single structure. Therefore, molecular dynamics simulation techniques were utilized. They are useful tools to evaluate the conformational space of the protein, study the stability of the protein structures, and to predict the apo conformation when it is missing.

The techniques and protocols applied in this work are supported and validated experimentally by several collaborations. Without experimental validation, computer-based models represent only hypotheses, so it was of utmost importance to validate the *in silico* results in the case of virtual screening hits as well as for proposed modified inhibitors. Especially in case of Sirt4, resolving the crystal structure showed the good accuracy of the applied approach and was extremely helpful in the development of small-molecule inhibitors.

7. References

1. C. H. Arrowsmith, C. Bountra, P. V. Fish, K. Lee, M. Schapira, Epigenetic protein families: a new frontier for drug discovery. *Nature reviews. Drug discovery*. **11**, 384–400 (2012), doi:10.1038/nrd3674.
2. L. Simó-Riudalbas, M. Esteller, Targeting the histone orthography of cancer: drugs for writers, erasers and readers. *British journal of pharmacology*. **172**, 2716–2732 (2015), doi:10.1111/bph.12844.
3. T. G. Gillette, J. A. Hill, Readers, writers, and erasers: chromatin as the whiteboard of heart disease. *Circulation research*. **116**, 1245–1253 (2015), doi:10.1161/CIRCRESAHA.116.303630.
4. I. Ali, R. J. Conrad, E. Verdin, M. Ott, Lysine Acetylation Goes Global: From Epigenetics to Metabolism and Therapeutics. *Chemical reviews*. **118**, 1216–1252 (2018), doi:10.1021/acs.chemrev.7b00181.
5. A. Ganesan, Epigenetic drug discovery: a success story for cofactor interference. *Philosophical transactions of the Royal Society of London. Series B, Biological sciences*. **373** (2018), doi:10.1098/rstb.2017.0069.
6. P. Parihar, I. Solanki, M. L. Mansuri, M. S. Parihar, Mitochondrial sirtuins: emerging roles in metabolic regulations, energy homeostasis and diseases. *Experimental gerontology*. **61**, 130–141 (2015), doi:10.1016/j.exger.2014.12.004.
7. M. D. Parenti, S. Bruzzone, A. Nencioni, A. Del Rio, Selectivity hot-spots of sirtuin catalytic cores. *Molecular bioSystems*. **11**, 2263–2272 (2015), doi:10.1039/c5mb00205b.
8. D. Rauh *et al.*, An acetylome peptide microarray reveals specificities and deacetylation substrates for all human sirtuin isoforms. *Nature communications*. **4**, 2327 (2013), doi:10.1038/ncomms3327.
9. S. Michan, D. Sinclair, Sirtuins in mammals: insights into their biological function. *The Biochemical journal*. **404**, 1–13 (2007), doi:10.1042/BJ20070140.
10. J. Hu, H. Jing, H. Lin, Sirtuin inhibitors as anticancer agents. *Future medicinal chemistry*. **6**, 945–966 (2014), doi:10.4155/fmc.14.44.
11. K. Huber, G. Superti-Furga, After the grape rush: sirtuins as epigenetic drug targets in neurodegenerative disorders. *Bioorganic & medicinal chemistry*. **19**, 3616–3624 (2011), doi:10.1016/j.bmc.2011.01.018.
12. A. Vaquero, The conserved role of sirtuins in chromatin regulation. *The International journal of developmental biology*. **53**, 303–322 (2009), doi:10.1387/ijdb.082675av.
13. L. Simó-Riudalbas, M. Esteller, Targeting the histone orthography of cancer: drugs for writers, erasers and readers. *British journal of pharmacology*. **172**, 2716–2732 (2015), doi:10.1111/bph.12844.
14. A. A. Sauve, Sirtuin chemical mechanisms. *Biochimica et biophysica acta*. **1804**, 1591–1603 (2010), doi:10.1016/j.bbapap.2010.01.021.
15. E. Fiorino *et al.*, The sirtuin class of histone deacetylases: regulation and roles in lipid metabolism. *IUBMB life*. **66**, 89–99 (2014), doi:10.1002/iub.1246.
16. H. Jing, H. Lin, Sirtuins in epigenetic regulation. *Chemical reviews*. **115**, 2350–2375 (2015), doi:10.1021/cr500457h.

17. Y. Jiang, J. Liu, Di Chen, L. Yan, W. Zheng, Sirtuin Inhibition: Strategies, Inhibitors, and Therapeutic Potential. *Trends in pharmacological sciences*. **38**, 459–472 (2017), doi:10.1016/j.tips.2017.01.009.
18. M. C. Haigis *et al.*, SIRT4 inhibits glutamate dehydrogenase and opposes the effects of calorie restriction in pancreatic beta cells. *cell*. **126**, 941–954 (2006), doi:10.1016/j.cell.2006.06.057.
19. G. Liszt, E. Ford, M. Kurtev, L. Guarente, Mouse Sir2 homolog SIRT6 is a nuclear ADP-ribosyltransferase. *The Journal of biological chemistry*. **280**, 21313–21320 (2005), doi:10.1074/jbc.M413296200.
20. K. A. Anderson *et al.*, SIRT4 Is a Lysine Deacylase that Controls Leucine Metabolism and Insulin Secretion. *Cell metabolism*. **25**, 838-855.e15 (2017), doi:10.1016/j.cmet.2017.03.003.
21. J. Du *et al.*, Sirt5 is a NAD-dependent protein lysine demalonylase and desuccinylase. *Science (New York, N.Y.)*. **334**, 806–809 (2011), doi:10.1126/science.1207861.
22. H. Jiang *et al.*, SIRT6 regulates TNF- α secretion through hydrolysis of long-chain fatty acyl lysine. *Nature*. **496**, 110–113 (2013), doi:10.1038/nature12038.
23. Y.-B. Teng *et al.*, Efficient demyristoylase activity of SIRT2 revealed by kinetic and structural studies. *Scientific reports*. **5**, 8529 (2015), doi:10.1038/srep08529.
24. J. Jin, B. He, X. Zhang, H. Lin, Y. Wang, SIRT2 Reverses 4-Oxononanoyl Lysine Modification on Histones. *Journal of the American Chemical Society*. **138**, 12304–12307 (2016), doi:10.1021/jacs.6b04977.
25. B. D. Sanders, B. Jackson, R. Marmorstein, Structural basis for sirtuin function: what we know and what we don't. *Biochimica et biophysica acta*. **1804**, 1604–1616 (2010), doi:10.1016/j.bbapap.2009.09.009.
26. Min Jinrong, Landry Joseph, Sternglanz Rolf, Xu Rui-Ming, Crystal Structure of a SIR2 Homolog-NAD Complex. *cell*. **105**, 269–279 (2001), doi:10.1016/S0092-8674(01)00317-8.
27. T. Rumpf *et al.*, Selective Sirt2 inhibition by ligand-induced rearrangement of the active site. *Nature communications*. **6**, 6263 (2015), doi:10.1038/ncomms7263.
28. H. M. Berman *et al.*, The Protein Data Bank. *Nucleic acids research*. **28**, 235–242 (2000), doi:10.1093/nar/28.1.235.
29. A. Schuetz *et al.*, Structural basis of inhibition of the human NAD⁺-dependent deacetylase SIRT5 by suramin. *Structure (London, England : 1993)*. **15**, 377–389 (2007), doi:10.1016/j.str.2007.02.002.
30. M. Pannek *et al.*, Crystal structures of the mitochondrial deacylase Sirtuin 4 reveal isoform-specific acyl recognition and regulation features. *Nature communications*. **8**, 1513 (2017), doi:10.1038/s41467-017-01701-2.
31. M. Schutkowski, F. Fischer, C. Roessler, C. Steegborn, New assays and approaches for discovery and design of Sirtuin modulators. *Expert opinion on drug discovery*. **9**, 183–199 (2014), doi:10.1517/17460441.2014.875526.
32. M. Gertz, C. Steegborn, Using mitochondrial sirtuins as drug targets: disease implications and available compounds. *Cellular and molecular life sciences : CMLS*. **73**, 2871–2896 (2016), doi:10.1007/s00018-016-2180-7.
33. S. Moniot, M. Schutkowski, C. Steegborn, Crystal structure analysis of human Sirt2 and its ADP-ribose complex. *Journal of structural biology*. **182**, 136–143 (2013), doi:10.1016/j.jsb.2013.02.012.

34. A. M. Davenport, F. M. Huber, A. Hoelz, Structural and functional analysis of human SIRT1. *Journal of Molecular Biology*. **426**, 526–541 (2014), doi:10.1016/j.jmb.2013.10.009.
35. L. Jin *et al.*, Crystal structures of human SIRT3 displaying substrate-induced conformational changes. *The Journal of biological chemistry*. **284**, 24394–24405 (2009), doi:10.1074/jbc.M109.014928.
36. Y. Zhou *et al.*, The bicyclic intermediate structure provides insights into the desuccinylation mechanism of human sirtuin 5 (SIRT5). *The Journal of biological chemistry*. **287**, 28307–28314 (2012), doi:10.1074/jbc.M112.384511.
37. B. Chen *et al.*, The chemical biology of sirtuins. *Chemical Society reviews*. **44**, 5246–5264 (2015), doi:10.1039/c4cs00373j.
38. M. Pan, H. Yuan, M. Brent, E. C. Ding, R. Marmorstein, SIRT1 contains N- and C-terminal regions that potentiate deacetylase activity. *The Journal of biological chemistry*. **287**, 2468–2476 (2012), doi:10.1074/jbc.M111.285031.
39. X. Ke, L. Shen, Molecular targeted therapy of cancer: The progress and future prospect. *Frontiers in Laboratory Medicine*. **1**, 69–75 (2017), doi:10.1016/j.flm.2017.06.001.
40. S. M. Jeong, M. C. Haigis, Sirtuins in Cancer: a Balancing Act between Genome Stability and Metabolism. *Molecules and cells*. **38**, 750–758 (2015), doi:10.14348/molcells.2015.0167.
41. S.-i. Imai, C. Armstrong, M. Kaerberlein, Transcriptional silencing and longevity protein Sir2 is an NAD-dependent histone deacetylase. *Nature*. **403**, 795–800 (2000), doi:10.1038/35001622.
42. A. Chalkiadaki, L. Guarente, The multifaceted functions of sirtuins in cancer. *Nature reviews. Cancer*. **15**, 608–624 (2015), doi:10.1038/nrc3985.
43. L. Bosch-Presegué, A. Vaquero, The dual role of sirtuins in cancer. *Genes & cancer*. **2**, 648–662 (2011), doi:10.1177/1947601911417862.
44. M. Schiedel, D. Robaa, T. Rumpf, W. Sippl, M. Jung, The Current State of NAD⁺ - Dependent Histone Deacetylases (Sirtuins) as Novel Therapeutic Targets. *Medicinal research reviews*. **38**, 147–200 (2018), doi:10.1002/med.21436.
45. T. Kozako *et al.*, Anticancer agents targeted to sirtuins. *Molecules (Basel, Switzerland)*. **19**, 20295–20313 (2014), doi:10.3390/molecules191220295.
46. M. Roth, W. Y. Chen, Sorting out functions of sirtuins in cancer. *Oncogene*. **33**, 1609–1620 (2014), doi:10.1038/onc.2013.120.
47. C. Roessler *et al.*, Chemical probing of the human sirtuin 5 active site reveals its substrate acyl specificity and peptide-based inhibitors. *Angewandte Chemie (International ed. in English)*. **53**, 10728–10732 (2014), doi:10.1002/anie.201402679.
48. D. Kalbas *et al.*, Potent and Selective Inhibitors of Human Sirtuin 5. *Journal of medicinal chemistry*. **61**, 2460–2471 (2018), doi:10.1021/acs.jmedchem.7b01648.
49. L. Yang *et al.*, Sirtuin 5: a review of structure, known inhibitors and clues for developing new inhibitors. *Science China. Life sciences*. **60**, 249–256 (2017), doi:10.1007/s11427-016-0060-7.
50. B. Suenkel, F. Fischer, C. Steegborn, Inhibition of the human deacetylase Sirtuin 5 by the indole GW5074. *Bioorganic & medicinal chemistry letters*. **23**, 143–146 (2013), doi:10.1016/j.bmcl.2012.10.136.

51. Villalona-Calero MA et al., Phase I study of low-dose suramin as a chemosensitizer in patients with advanced non-small cell lung cancer. *Clinical Cancer Research*. **9**, 3303–3311 (2003).
52. M. Muscolini et al., SIRT1 Modulates the Sensitivity of Prostate Cancer Cells to Vesicular Stomatitis Virus Oncolysis. *Journal of virology*. **93** (2019), doi:10.1128/JVI.00626-19.
53. S. Lain et al., Discovery, in vivo activity, and mechanism of action of a small-molecule p53 activator. *Cancer cell*. **13**, 454–463 (2008), doi:10.1016/j.ccr.2008.03.004.
54. A. R. McCarthy et al., Synthesis and biological characterisation of sirtuin inhibitors based on the tenovins. *Bioorganic & medicinal chemistry*. **20**, 1779–1793 (2012), doi:10.1016/j.bmc.2012.01.001.
55. M. Gertz et al., Ex-527 inhibits Sirtuins by exploiting their unique NAD⁺-dependent deacetylation mechanism. *Proceedings of the National Academy of Sciences of the United States of America*. **110**, E2772–81 (2013), doi:10.1073/pnas.1303628110.
56. X. He et al., SIRT2 activity is required for the survival of C6 glioma cells. *Biochemical and biophysical research communications*. **417**, 468–472 (2012), doi:10.1016/j.bbrc.2011.11.141.
57. H. Dai, D. A. Sinclair, J. L. Ellis, C. Steegborn, Sirtuin activators and inhibitors: Promises, achievements, and challenges. *Pharmacology & therapeutics*. **188**, 140–154 (2018), doi:10.1016/j.pharmthera.2018.03.004.
58. L. Quinti et al., SIRT2- and NRF2-Targeting Thiazole-Containing Compound with Therapeutic Activity in Huntington's Disease Models. *Cell chemical biology*. **23**, 849–861 (2016), doi:10.1016/j.chembiol.2016.05.015.
59. A. Bedalov, T. Gatabont, W. P. Irvine, D. E. Gottschling, J. A. Simon, Identification of a small molecule inhibitor of Sir2p. *Proceedings of the National Academy of Sciences of the United States of America*. **98**, 15113–15118 (2001), doi:10.1073/pnas.261574398.
60. R. C. Neugebauer et al., Structure-activity studies on splitomicin derivatives as sirtuin inhibitors and computational prediction of binding mode. *Journal of medicinal chemistry*. **51**, 1203–1213 (2008), doi:10.1021/jm700972e.
61. H. Ota et al., Sirt1 inhibitor, Sirtinol, induces senescence-like growth arrest with attenuated Ras-MAPK signaling in human cancer cells. *Oncogene*. **25**, 176–185 (2006), doi:10.1038/sj.onc.1209049.
62. J. Wang et al., Sirtinol, a class III HDAC inhibitor, induces apoptotic and autophagic cell death in MCF-7 human breast cancer cells. *International journal of oncology*. **41**, 1101–1109 (2012), doi:10.3892/ijo.2012.1534.
63. B. Heltweg et al., Antitumor activity of a small-molecule inhibitor of human silent information regulator 2 enzymes. *Cancer research*. **66**, 4368–4377 (2006), doi:10.1158/0008-5472.CAN-05-3617.
64. E. Lara et al., Salermide, a Sirtuin inhibitor with a strong cancer-specific proapoptotic effect. *Oncogene*. **28**, 1168 (2009), doi:10.1038/onc.2009.1.
65. J. George, N. Ahmad, Mitochondrial Sirtuins in Cancer: Emerging Roles and Therapeutic Potential. *Cancer research*. **76**, 2500–2506 (2016), doi:10.1158/0008-5472.CAN-15-2733.

66. H.-S. Kim *et al.*, SIRT3 is a mitochondria-localized tumor suppressor required for maintenance of mitochondrial integrity and metabolism during stress. *Cancer cell*. **17**, 41–52 (2010), doi:10.1016/j.ccr.2009.11.023.
67. Alhazzazi, Turki Y *et al.*, A Novel Sirtuin-3 Inhibitor, LC-0296, Inhibits Cell Survival and Proliferation, and Promotes Apoptosis of Head and Neck Cancer Cells. *Anticancer Res*. **36**, 49–60 (2016).
68. C. Sebastián *et al.*, The histone deacetylase SIRT6 is a tumor suppressor that controls cancer metabolism. *cell*. **151**, 1185–1199 (2012), doi:10.1016/j.cell.2012.10.047.
69. V. Heger *et al.*, Quercetin based derivatives as sirtuin inhibitors. *Biomedicine & pharmacotherapy = Biomedecine & pharmacotherapie*. **111**, 1326–1333 (2019), doi:10.1016/j.biopha.2019.01.035.
70. Z. Li, B. Bridges, J. Olson, S. A. Weinman, The interaction between acetylation and serine-574 phosphorylation regulates the apoptotic function of FOXO3. *Oncogene*. **36**, 1887–1898 (2017), doi:10.1038/onc.2016.359.
71. Y. Mo *et al.*, SIRT7 deacetylates DDB1 and suppresses the activity of the CRL4 E3 ligase complexes. *The FEBS journal*. **284**, 3619–3636 (2017), doi:10.1111/febs.14259.
72. S. Li, B. Wu, W. Zheng, Cyclic tripeptide-based potent human SIRT7 inhibitors. *Bioorganic & medicinal chemistry letters*. **29**, 461–465 (2019), doi:10.1016/j.bmcl.2018.12.023.
73. M. Gertz *et al.*, A molecular mechanism for direct sirtuin activation by resveratrol. *PLoS one*. **7**, e49761 (2012), doi:10.1371/journal.pone.0049761.
74. H. Yuan, L. Su, W. Y. Chen, The emerging and diverse roles of sirtuins in cancer: a clinical perspective. *OncoTargets and therapy*. **6**, 1399–1416 (2013), doi:10.2147/OTT.S37750.
75. I. Wessler, C. J. Kirkpatrick, Acetylcholine beyond neurons: the non-neuronal cholinergic system in humans. *British journal of pharmacology*. **154**, 1558–1571 (2008), doi:10.1038/bjp.2008.185.
76. P. Anand, B. Singh, A review on cholinesterase inhibitors for Alzheimer's disease. *Archives of pharmacal research*. **36**, 375–399 (2013), doi:10.1007/s12272-013-0036-3.
77. N. H. Greig *et al.*, A new therapeutic target in Alzheimer's disease treatment: attention to butyrylcholinesterase. *Current medical research and opinion*. **17**, 159–165 (2001), doi:10.1185/0300799039117057.
78. Mirjana B. *et al.*, Acetylcholinesterase Inhibitors: Pharmacology and Toxicology. *Current Neuropharmacology*. **11**, 315–335 (2013), doi:10.2174/1570159X11311030006.
79. Y. Nicolet, O. Lockridge, P. Masson, J. C. Fontecilla-Camps, F. Nachon, Crystal structure of human butyrylcholinesterase and of its complexes with substrate and products. *The Journal of biological chemistry*. **278**, 41141–41147 (2003), doi:10.1074/jbc.M210241200.
80. J. L. Sussman *et al.*, Atomic structure of acetylcholinesterase from *Torpedo californica*: a prototypic acetylcholine-binding protein. *Science (New York, N.Y.)*. **253**, 872–879 (1991), doi:10.1126/science.1678899.
81. M. Bajda *et al.*, Structure-based search for new inhibitors of cholinesterases. *International journal of molecular sciences*. **14**, 5608–5632 (2013), doi:10.3390/ijms14035608.

82. T. Lazarevic-Pasti, A. Leskovac, T. Momic, S. Petrovic, V. Vasic, Modulators of Acetylcholinesterase Activity: From Alzheimer's Disease to Anti-Cancer Drugs. *Current medicinal chemistry*. **24**, 3283–3309 (2017), doi:10.2174/0929867324666170705123509.
83. M. Pohanka, Cholinesterases, a target of pharmacology and toxicology. *Biomedical papers of the Medical Faculty of the University Palacky, Olomouc, Czechoslovakia*. **155**, 219–229 (2011), doi:10.5507/bp.2011.036.
84. J. L. Johnson, B. Cusack, M. P. Davies, A. Fauq, T. L. Rosenberry, Unmasking tandem site interaction in human acetylcholinesterase. Substrate activation with a cationic acetanilide substrate. *Biochemistry*. **42**, 5438–5452 (2003), doi:10.1021/bi027065u.
85. A. Bosak *et al.*, Peripheral site and acyl pocket define selective inhibition of mouse butyrylcholinesterase by two biscarbamates. *Archives of biochemistry and biophysics*. **529**, 140–145 (2013), doi:10.1016/j.abb.2012.11.012.
86. A. Bosak *et al.*, Design and evaluation of selective butyrylcholinesterase inhibitors based on Cinchona alkaloid scaffold. *PloS one*. **13**, e0205193 (2018), doi:10.1371/journal.pone.0205193.
87. L. Pezzementi, F. Nachon, A. Chatonnet, Evolution of acetylcholinesterase and butyrylcholinesterase in the vertebrates: an atypical butyrylcholinesterase from the Medaka *Oryzias latipes*. *PloS one*. **6**, e17396 (2011), doi:10.1371/journal.pone.0017396.
88. G. Kryger, I. Silman, J. L. Sussman, Structure of acetylcholinesterase complexed with E2020 (Aricept®): implications for the design of new anti-Alzheimer drugs. *Structure (London, England : 1993)*. **7**, 297–307 (1999), doi:10.1016/S0969-2126(99)80040-9.
89. I. Silman, J. L. Sussman, Recent developments in structural studies on acetylcholinesterase. *Journal of neurochemistry*. **142 Suppl 2**, 19–25 (2017), doi:10.1111/jnc.13992.
90. H. Dvir, I. Silman, M. Harel, T. L. Rosenberry, J. L. Sussman, Acetylcholinesterase: from 3D structure to function. *Chemico-biological interactions*. **187**, 10–22 (2010), doi:10.1016/j.cbi.2010.01.042.
91. D. Grisaru *et al.*, Structural roles of acetylcholinesterase variants in biology and pathology. *Biochemistry*. **264**, 672–686 (1999), doi:10.1046/j.1432-1327.1999.00693.x.
92. S. Shaikh *et al.*, Current acetylcholinesterase-inhibitors: a neuroinformatics perspective. *CNS & neurological disorders drug targets*. **13**, 391–401 (2014), doi:10.2174/18715273113126660166.
93. S. Darvesh, D. A. Hopkins, C. Geula, Neurobiology of butyrylcholinesterase. *Nature reviews. Neuroscience*. **4**, 131–138 (2003), doi:10.1038/nrn1035.
94. M. Mehta, A. Adem, M. Sabbagh, New acetylcholinesterase inhibitors for Alzheimer's disease. *International journal of Alzheimer's disease*. **2012**, 1–8 (2012), doi:10.1155/2012/728983.
95. B. Zhao, S. M. Moochhala, S.-Y. Tham, Biologically active components of Physostigma venenosum. *Journal of chromatography. B, Analytical technologies in the biomedical and life sciences*. **812**, 183–192 (2004), doi:10.1016/j.jchromb.2004.08.031.
96. J. Corey-Bloom, R. Anand, and J. Veach, A randomized trial evaluating the efficacy and safety of ENA 713 (rivastigmine tartrate), a new acetylcholinesterase inhibitor, in

- patients with mild to moderately severe Alzheimer's disease. *International journal of Ger.* **1**, 55–65 (1998).
97. M. I. Fernández-Bachiller *et al.*, Novel tacrine-8-hydroxyquinoline hybrids as multifunctional agents for the treatment of Alzheimer's disease, with neuroprotective, cholinergic, antioxidant, and copper-complexing properties. *Journal of medicinal chemistry*. **53**, 4927–4937 (2010), doi:10.1021/jm100329q.
 98. S. Rogers, R. Doody, R. Mohs, Donepezil improves cognition and global function in Alzheimer Disease. *Arch Intern Med.* **158**, 1021–1031 (1998), doi:10.1001/archinte.158.9.1021.
 99. T. Zhang *et al.*, Donepezil attenuates high glucose-accelerated senescence in human umbilical vein endothelial cells through SIRT1 activation. *Cell stress & chaperones*. **20**, 787–792 (2015), doi:10.1007/s12192-015-0601-4.
 100. M. Heinrich, H. Lee Teoh, Galanthamine from snowdrop--the development of a modern drug against Alzheimer's disease from local Caucasian knowledge. *Journal of ethnopharmacology*. **92**, 147–162 (2004), doi:10.1016/j.jep.2004.02.012.
 101. J. Klein, Phenserine. *Expert opinion on investigational drugs*. **16**, 1087–1097 (2007), doi:10.1517/13543784.16.7.1087.
 102. C. Bartolucci *et al.*, Structural determinants of Torpedo californica acetylcholinesterase inhibition by the novel and orally active carbamate based anti-alzheimer drug ganstigmine (CHF-2819). *Journal of medicinal chemistry*. **49**, 5051–5058 (2006), doi:10.1021/jm060293s.
 103. H. Dvir, H. L. Jiang, D. M. Wong, M. Harel, M. Chetrit, X. C. He, G. Y. Jin, G. L. Yu, X. C. Tang, I. Silman, D. L. Bai, and J. L. Sussman, X-ray Structures of Torpedo californica Acetylcholinesterase Complexed with (+)-Huperzine A and (-)-Huperzine B: Structural Evidence for an Active Site Rearrangement. *Biochemistry*. **41**, 10810–10818 (2002), doi:10.1021/bi020151+.
 104. T. C. Dos Santos, T. M. Gomes, B. A. S. Pinto, A. L. Camara, A. M. d. A. Paes, Naturally Occurring Acetylcholinesterase Inhibitors and Their Potential Use for Alzheimer's Disease Therapy. *Frontiers in pharmacology*. **9**, 1192 (2018), doi:10.3389/fphar.2018.01192.
 105. N. E. Labrou, Ed., *Targeting Enzymes for Pharmaceutical Development, Methods and Protocols* (Springer US; Imprint: Humana, New York, NY, ed. 1, 2020).
 106. A. Castro, A. Martinez, Peripheral and dual binding site acetylcholinesterase inhibitors: implications in treatment of Alzheimer's disease. *Mini reviews in medicinal chemistry*. **1**, 267–272 (2001), doi:10.2174/1389557013406864.
 107. G. V. de Ferrari *et al.*, A structural motif of acetylcholinesterase that promotes amyloid beta-peptide fibril formation. *Biochemistry*. **40**, 10447–10457 (2001), doi:10.1021/bi0101392.
 108. M. Mehta, A. Adem, M. Sabbagh, New acetylcholinesterase inhibitors for Alzheimer's disease. *International journal of Alzheimer's disease*. **2012**, 728983 (2012), doi:10.1155/2012/728983.
 109. C.-S. Jiang *et al.*, Discovery of New Selective Butyrylcholinesterase (BChE) Inhibitors with Anti-A β Aggregation Activity: Structure-Based Virtual Screening, Hit Optimization and Biological Evaluation. *Molecules (Basel, Switzerland)*. **24** (2019), doi:10.3390/molecules24142568.

110. U. Kořak *et al.*, Development of an in-vivo active reversible butyrylcholinesterase inhibitor. *Scientific reports*. **6**, 39495 (2016), doi:10.1038/srep39495.
111. L. Jing *et al.*, Contemporary medicinal-chemistry strategies for the discovery of selective butyrylcholinesterase inhibitors. *Drug discovery today*. **24**, 629–635 (2019), doi:10.1016/j.drudis.2018.11.012.
112. S. Agatonovic-Kustrin, C. Kettle, D. W. Morton, A molecular approach in drug development for Alzheimer's disease. *Biomedicine & pharmacotherapy = Biomedecine & pharmacotherapie*. **106**, 553–565 (2018), doi:10.1016/j.biopha.2018.06.147.
113. W. Qin *et al.*, Neuronal SIRT1 activation as a novel mechanism underlying the prevention of Alzheimer disease amyloid neuropathology by calorie restriction. *The Journal of biological chemistry*. **281**, 21745–21754 (2006), doi:10.1074/jbc.M602909200.
114. R. Lalla, G. Donmez, The role of sirtuins in Alzheimer's disease. *Frontiers in aging neuroscience*. **5**, 16 (2013), doi:10.3389/fnagi.2013.00016.
115. P. D. Lyne, Structure-based virtual screening: an overview. *Drug discovery today*. **7**, 1047–1055 (2002), doi:10.1016/S1359-6446(02)02483-2.
116. S. J. Y. Macalino, V. Gosu, S. Hong, S. Choi, Role of computer-aided drug design in modern drug discovery. *Archives of pharmacal research*. **38**, 1686–1701 (2015), doi:10.1007/s12272-015-0640-5.
117. S. Ghosh, A. Nie, J. An, Z. Huang, Structure-based virtual screening of chemical libraries for drug discovery. *Current opinion in chemical biology*. **10**, 194–202 (2006), doi:10.1016/j.cbpa.2006.04.002.
118. W. Lu, R. Zhang, H. Jiang, H. Zhang, C. Luo, Computer-Aided Drug Design in Epigenetics. *Frontiers in chemistry*. **6**, 57 (2018), doi:10.3389/fchem.2018.00057.
119. M. Bajda *et al.*, Structure-based search for new inhibitors of cholinesterases. *International journal of molecular sciences*. **14**, 5608–5632 (2013), doi:10.3390/ijms14035608.
120. P. Kokkonen *et al.*, Virtual screening approach of sirtuin inhibitors results in two new scaffolds. *European journal of pharmaceutical sciences : official journal of the European Federation for Pharmaceutical Sciences*. **76**, 27–32 (2015), doi:10.1016/j.ejps.2015.04.025.
121. S. Chiba *et al.*, A prospective compound screening contest identified broader inhibitors for Sirtuin 1. *Scientific reports*. **9**, 19585 (2019), doi:10.1038/s41598-019-55069-y.
122. D. G. I. Kingston, Modern natural products drug discovery and its relevance to biodiversity conservation. *Journal of natural products*. **74**, 496–511 (2011), doi:10.1021/np100550t.
123. M. Feher, J. M. Schmidt, Property distributions: differences between drugs, natural products, and molecules from combinatorial chemistry. *Journal of chemical information and computer sciences*. **43**, 218–227 (2003), doi:10.1021/ci0200467.
124. A. L. Demain, P. Vaishnav, Natural products for cancer chemotherapy. *Microbial biotechnology*. **4**, 687–699 (2011), doi:10.1111/j.1751-7915.2010.00221.x.
125. A. L. Harvey, Natural products in drug discovery. *Drug discovery today*. **13**, 894–901 (2008), doi:10.1016/j.drudis.2008.07.004.
126. B. Karaman Mayack, W. Sippl, F. Ntie-Kang, Natural Products as Modulators of Sirtuins. *molecules*. **25**, 1–29 (2020), doi:10.3390/molecules25143287.

127. M. Lahlou, The Success of Natural Products in Drug Discovery. *PP*. **04**, 17–31 (2013), doi:10.4236/pp.2013.43A003.
128. G. M. Cragg, D. J. Newman, Plants as a source of anti-cancer agents. *Journal of ethnopharmacology*. **100**, 72–79 (2005), doi:10.1016/j.jep.2005.05.011.
129. P. Williams, A. Sorribas, M.-J. R. Howes, Natural products as a source of Alzheimer's drug leads. *Natural product reports*. **28**, 48–77 (2011), doi:10.1039/c0np00027b.
130. B. A. Q. Gomes *et al.*, Neuroprotective Mechanisms of Resveratrol in Alzheimer's Disease: Role of SIRT1. *Oxidative medicine and cellular longevity*. **2018**, 8152373 (2018), doi:10.1155/2018/8152373.
131. M. T. Borra, B. C. Smith, J. M. Denu, Mechanism of human SIRT1 activation by resveratrol. *The Journal of biological chemistry*. **280**, 17187–17195 (2005), doi:10.1074/jbc.M501250200.
132. T. Jayasena *et al.*, The role of polyphenols in the modulation of sirtuins and other pathways involved in Alzheimer's disease. *Ageing research reviews*. **12**, 867–883 (2013), doi:10.1016/j.arr.2013.06.003.
133. T. Kahyo, S. Ichikawa, T. Hatanaka, M. K. Yamada, M. Setou, A novel chalcone polyphenol inhibits the deacetylase activity of SIRT1 and cell growth in HEK293T cells. *Journal of pharmacological sciences*. **108**, 364–371 (2008), doi:10.1254/jphs.08203fp.
134. E. Zendedel, A. E. Butler, S. L. Atkin, A. Sahebkar, Impact of curcumin on sirtuins: A review. *Journal of cellular biochemistry*. **119**, 10291–10300 (2018), doi:10.1002/jcb.27371.
135. J. M. Barbosa Filho *et al.*, Natural products inhibitors of the enzyme acetylcholinesterase. *Rev. bras. farmacogn.* **16**, 258–285 (2006), doi:10.1590/S0102-695X2006000200021.
136. A. P. Murray, M. B. Faraoni, M. J. Castro, N. P. Alza, V. Cavallaro, Natural AChE Inhibitors from Plants and their Contribution to Alzheimer's Disease Therapy. *Current Neuropharmacology*. **11**, 388–413 (20), doi:10.2174/1570159X11311040004.
137. K. Dastmalchi *et al.*, Acetylcholinesterase inhibitory guided fractionation of *Melissa officinalis* L. *Bioorganic & medicinal chemistry*. **17**, 867–871 (2009), doi:10.1016/j.bmc.2008.11.034.
138. D. Kaufmann, A. Kaur Dogra, A. Tahrani, F. Herrmann, M. Wink, Extracts from Traditional Chinese Medicinal Plants Inhibit Acetylcholinesterase, a Known Alzheimer's Disease Target. *Molecules (Basel, Switzerland)*. **21** (2016), doi:10.3390/molecules21091161.
139. H. Khan, Marya, S. Amin, M. A. Kamal, S. Patel, Flavonoids as acetylcholinesterase inhibitors: Current therapeutic standing and future prospects. *Biomedicine & pharmacotherapy = Biomedecine & pharmacotherapie*. **101**, 860–870 (2018), doi:10.1016/j.biopha.2018.03.007.
140. M. Baig, Computer Aided Drug Design: Success and Limitations. *Current pharmaceutical design*. **22**, 572–581 (2016), doi:10.2174/1381612822666151125000550.
141. G. Klebe, Virtual ligand screening: strategies, perspectives and limitations. *Drug discovery today*. **11**, 580–594 (2006), doi:10.1016/j.drudis.2006.05.012.

142. K. L. Damm-Ganamet *et al.*, Accelerating Lead Identification by High Throughput Virtual Screening: Prospective Case Studies from the Pharmaceutical Industry. *Journal of chemical information and modeling*. **59**, 2046–2062 (2019), doi:10.1021/acs.jcim.8b00941.
143. D. E. Clark, What has virtual screening ever done for drug discovery? *Expert opinion on drug discovery*. **3**, 841–851 (2008), doi:10.1517/17460441.3.8.841.
144. T. Cheng, Q. Li, Z. Zhou, Y. Wang, S. H. Bryant, Structure-based virtual screening for drug discovery: a problem-centric review. *The AAPS journal*. **14**, 133–141 (2012), doi:10.1208/s12248-012-9322-0.
145. S. Kar, K. Roy, How far can virtual screening take us in drug discovery? *Expert opinion on drug discovery*. **8**, 245–261 (2013), doi:10.1517/17460441.2013.761204.
146. T. I. Oprea, H. Matter, Integrating virtual screening in lead discovery. *Current opinion in chemical biology*. **8**, 349–358 (2004), doi:10.1016/j.cbpa.2004.06.008.
147. A. Gimeno *et al.*, The Light and Dark Sides of Virtual Screening: What Is There to Know? *International journal of molecular sciences*. **20** (2019), doi:10.3390/ijms20061375.
148. J. B. Baell, G. A. Holloway, New substructure filters for removal of pan assay interference compounds (PAINS) from screening libraries and for their exclusion in bioassays. *Journal of medicinal chemistry*. **53**, 2719–2740 (2010), doi:10.1021/jm901137j.
149. J. L. Dahlin, M. A. Walters, How to Triage PAINS-Full Research. *Assay and drug development technologies*. **14**, 168–174 (2016), doi:10.1089/adt.2015.674.
150. C. A. Lipinski, Lead- and drug-like compounds: the rule-of-five revolution. *Drug Discovery Today: Technologies*. **1**, 337–341 (2004), doi:10.1016/j.ddtec.2004.11.007.
151. C. A. Lipinski, F. Lombardo, B. W. Dominy, P. J. Feeney, Experimental and computational approaches to estimate solubility and permeability in drug discovery and development settings IPII of original article: S0169-409X(96)00423-1. The article was originally published in *Advanced Drug Delivery Reviews* 23 (1997) 3–25.1. *Advanced Drug Delivery Reviews*. **46**, 3–26 (2001), doi:10.1016/S0169-409X(00)00129-0.
152. F. Ban *et al.*, Best Practices of Computer-Aided Drug Discovery: Lessons Learned from the Development of a Preclinical Candidate for Prostate Cancer with a New Mechanism of Action. *Journal of chemical information and modeling*. **57**, 1018–1028 (2017), doi:10.1021/acs.jcim.7b00137.
153. L. Pinzi, G. Rastelli, Molecular Docking: Shifting Paradigms in Drug Discovery. *International journal of molecular sciences*. **20** (2019), doi:10.3390/ijms20184331.
154. R. A. Friesner *et al.*, Glide: a new approach for rapid, accurate docking and scoring. 1. Method and assessment of docking accuracy. *Journal of medicinal chemistry*. **47**, 1739–1749 (2004), doi:10.1021/jm0306430.
155. G. Jones, P. Willett, R. C. Glen, A. R. Leach, R. Taylor, Development and validation of a genetic algorithm for flexible docking. *Journal of Molecular Biology*. **267**, 727–748 (1997), doi:10.1006/jmbi.1996.0897.
156. A. Baldi, Computational approaches for drug design and discovery: An overview. *Syst Rev Pharm*. **1**, 99 (2010), doi:10.4103/0975-8453.59519.
157. S. Vilar, G. Cozza, S. Moro, Medicinal chemistry and the molecular operating environment (MOE): application of QSAR and molecular docking to drug discovery.

- Current topics in medicinal chemistry.* **8**, 1555–1572 (2008), doi:10.2174/156802608786786624.
158. P. Labute, Protonate3D: assignment of ionization states and hydrogen coordinates to macromolecular structures. *Proteins.* **75**, 187–205 (2009), doi:10.1002/prot.22234.
159. Molecular Operating Environment, version 2014; Chemical Computing Group Inc.: Montreal, QC, Canada, 2014.
160. V. Hornak *et al.*, Comparison of multiple Amber force fields and development of improved protein backbone parameters. *Proteins.* **65**, 712–725 (2006), doi:10.1002/prot.21123.
161. M. J. Hartshorn *et al.*, Diverse, high-quality test set for the validation of protein-ligand docking performance. *Journal of medicinal chemistry.* **50**, 726–741 (2007), doi:10.1021/jm061277y.
162. S. Genheden, U. Ryde, The MM/PBSA and MM/GBSA methods to estimate ligand-binding affinities. *Expert opinion on drug discovery.* **10**, 449–461 (2015), doi:10.1517/17460441.2015.1032936.
163. T. A. Halgren *et al.*, Glide: a new approach for rapid, accurate docking and scoring. 2. Enrichment factors in database screening. *Journal of medicinal chemistry.* **47**, 1750–1759 (2004), doi:10.1021/jm030644s.
164. R. A. Friesner *et al.*, Extra precision glide: docking and scoring incorporating a model of hydrophobic enclosure for protein-ligand complexes. *Journal of medicinal chemistry.* **49**, 6177–6196 (2006), doi:10.1021/jm051256o.
165. M. L. Verdonk *et al.*, Modeling water molecules in protein-ligand docking using GOLD. *Journal of medicinal chemistry.* **48**, 6504–6515 (2005), doi:10.1021/jm050543p.
166. LigPrep Software; Version 2; LLC: New York, NY, USA, 2011.
167. J. L. Banks *et al.*, Integrated Modeling Program, Applied Chemical Theory (IMPACT). *Journal of computational chemistry.* **26**, 1752–1780 (2005), doi:10.1002/jcc.20292.
168. P. C. D. Hawkins, A. G. Skillman, G. L. Warren, B. A. Ellingson, M. T. Stahl, Conformer generation with OMEGA: algorithm and validation using high quality structures from the Protein Databank and Cambridge Structural Database. *Journal of chemical information and modeling.* **50**, 572–584 (2010), doi:10.1021/ci100031x.
169. S. Kalyaanamoorthy, Y.-P. P. Chen, Modelling and enhanced molecular dynamics to steer structure-based drug discovery. *Progress in biophysics and molecular biology.* **114**, 123–136 (2014), doi:10.1016/j.pbiomolbio.2013.06.004.
170. M. T. Muhammed, E. Aki-Yalcin, Homology modeling in drug discovery: Overview, current applications, and future perspectives. *Chemical biology & drug design.* **93**, 12–20 (2019), doi:10.1111/cbdd.13388.
171. A. Šali, T. L. Blundell, Comparative Protein Modelling by Satisfaction of Spatial Restraints. *Journal of Molecular Biology.* **234**, 779–815 (1993), doi:10.1006/jmbi.1993.1626.
172. B. Webb, A. Sali, Comparative Protein Structure Modeling Using MODELLER. *Current protocols in bioinformatics.* **54**, 5.6.1-5.6.37 (2016), doi:10.1002/cpbi.3.
173. A. Nayeem, D. Sitkoff, S. Krystek, A comparative study of available software for high-accuracy homology modeling: from sequence alignments to structural models.

- Protein science : a publication of the Protein Society.* **15**, 808–824 (2006), doi:10.1110/ps.051892906.
174. R. A. Laskowski, M. W. MacArthur, D. S. Moss, J. M. Thornton, PROCHECK: a program to check the stereochemical quality of protein structures. *J Appl Crystallogr.* **26**, 283–291 (1993), doi:10.1107/S0021889892009944.
175. Activities at the Universal Protein Resource (UniProt). *Nucleic acids research.* **42**, D191-8 (2014), doi:10.1093/nar/gkt1140.
176. S. F. Altschul, W. Gish, W. Miller, E. W. Myers, D. J. Lipman, Basic local alignment search tool. *Journal of Molecular Biology.* **215**, 403–410 (1990), doi:10.1016/S0022-2836(05)80360-2.
177. M.-Y. Shen, A. Sali, Statistical potential for assessment and prediction of protein structures. *Protein science : a publication of the Protein Society.* **15**, 2507–2524 (2006), doi:10.1110/ps.062416606.
178. S. A. Hollingsworth, R. O. Dror, Molecular Dynamics Simulation for All. *Neuron.* **99**, 1129–1143 (2018), doi:10.1016/j.neuron.2018.08.011.
179. Y. Wang, C. B. Harrison, K. Schulten, J. A. McCammon, Implementation of Accelerated Molecular Dynamics in NAMD. *Computational science & discovery.* **4** (2011), doi:10.1088/1749-4699/4/1/015002.
180. J. Wang, R. M. Wolf, J. W. Caldwell, P. A. Kollman, D. A. Case, Development and testing of a general amber force field. *Journal of computational chemistry.* **25**, 1157–1174 (2004), doi:10.1002/jcc.20035.
181. B. Heltweg, J. Trapp, M. Jung, In vitro assays for the determination of histone deacetylase activity. *Methods (San Diego, Calif.).* **36**, 332–337 (2005), doi:10.1016/j.ymeth.2005.03.003.
182. B. C. Smith, W. C. Hallows, J. M. Denu, A continuous microplate assay for sirtuins and nicotinamide-producing enzymes. *Analytical biochemistry.* **394**, 101–109 (2009), doi:10.1016/j.ab.2009.07.019.
183. L. Heller *et al.*, Amino derivatives of platanic acid act as selective and potent inhibitors of butyrylcholinesterase. *European journal of medicinal chemistry.* **126**, 652–668 (2017), doi:10.1016/j.ejmech.2016.11.056.
184. R.-H. Wang *et al.*, Impaired DNA damage response, genome instability, and tumorigenesis in SIRT1 mutant mice. *Cancer cell.* **14**, 312–323 (2008), doi:10.1016/j.ccr.2008.09.001.
185. R. Ekkebus *et al.*, On terminal alkynes that can react with active-site cysteine nucleophiles in proteases. *Journal of the American Chemical Society.* **135**, 2867–2870 (2013), doi:10.1021/ja309802n.
186. N. Wössner *et al.*, Sirtuin 1 Inhibiting Thiocyanates (S1th)-A New Class of Isotype Selective Inhibitors of NAD⁺ Dependent Lysine Deacetylases. *Frontiers in oncology.* **10**, 657 (2020), doi:10.3389/fonc.2020.00657.
187. A. Y. Amerik, M. Hochstrasser, Mechanism and function of deubiquitinating enzymes. *Biochimica et biophysica acta.* **1695**, 189–207 (2004), doi:10.1016/j.bbamcr.2004.10.003.
188. F. Ntie-Kang *et al.*, Virtualizing the p-ANAPL library: a step towards drug discovery from African medicinal plants. *PloS one.* **9**, e90655 (2014), doi:10.1371/journal.pone.0090655.

189. F. Ntie-Kang *et al.*, AfroDb: a select highly potent and diverse natural product library from African medicinal plants. *PloS one.* **8**, e78085 (2013), doi:10.1371/journal.pone.0078085.
190. B. Karaman *et al.*, Identification of Bichalcones as Sirtuin Inhibitors by Virtual Screening and In Vitro Testing. *Molecules (Basel, Switzerland).* **23** (2018), doi:10.3390/molecules23020416.
191. O. Shetonde *et al.*, The characterization, total synthesis and antiprotozoal activities of novel bichalcones from *Rhus pyroides*. *Planta Med.* **75** (2009), doi:10.1055/s-0029-1234266.
192. S. Vojacek *et al.*, Three-Component Aminoalkylations Yielding Dihydronaphthoxazine-Based Sirtuin Inhibitors: Scaffold Modification and Exploration of Space for Polar Side-Chains. *Archiv der Pharmazie.* **350** (2017), doi:10.1002/ardp.201700097.
193. A. Loesche *et al.*, Unexpected AChE inhibitory activity of (2E) α,β -unsaturated fatty acids. *Bioorganic & medicinal chemistry letters.* **28**, 3315–3319 (2018), doi:10.1016/j.bmcl.2018.09.013.
194. A. Loesche *et al.*, Ursolic and oleanolic acid derivatives with cholinesterase inhibiting potential. *Bioorganic chemistry.* **85**, 23–32 (2019), doi:10.1016/j.bioorg.2018.12.013.

8. Appendix

(Declaration of Authorship)

Selbstständigkeitserklärung

Hiermit erkläre ich, dass ich die vorliegende Dissertationsschrift selbständig und ohne fremde Hilfe angefertigt, keine anderen als die angegebenen Quellen und Hilfsmittel benutzt und die aus ihnen wörtlich oder inhaltlich entnommenen Stellen als solche kenntlich gemacht habe.

Die Arbeit wurde ausschließlich der Mathematisch-Naturwissenschaftlichen Fakultät I der Martin-Luther-Universität Halle-Wittenberg vorgelegt und an keiner anderen Universität oder Hochschule weder im In- und Ausland zur Erlangung des Doktorgrades eingereicht.
Halle (Saale), den 01.09. 2020

Zayan Alhalabi

Curriculum Vitae (CV)

Name & Surname: Zayan Alhalabi

E-Mail: Zayan82at@hotmail.com

Zayan.alhalabi@student.uni-halle.de

Gender: Female

Place of Birth: Damascus- Syria.

Date of Birth: 15.1. 1982

Birthplace: Damascus -Syria

Citizenship: Syrien

Academic Qualifications:

- (2017) Staatexam 3 (Approbation als Apotheker) Martin luther university (MLU).
- (2015) Diploma in Pharmaceutical Sciences (drug design), Institute of Pharmacy, Martin Luther University (MLU).
- (2012) Master in Pharmaceutical Sciences, thesis: " Development of an analytical method for assay of Antiprotozoal derivative from imidazole in pharmaceutical preparations" department of Pharmaceutical chemistry and drug control, Damascus University
- (2006) Diploma in Pharmaceutical Sciences (drug control), Damascus University.
- (2005) Bachelor in Pharmacy& Pharmaceutical Chemistry, College of Pharmacy, Damascus University.

Scientific Activities:

- (2005-2011) Research assistant at the Institute of Pharmacy in Pharmaceuticals and Pharmaceutical Chemistry Department Faculty of Pharmacy, Damascus University.

Publication List

- Pannek, M., **Alhalabi, Z.**, Robaa, D., Rotili, D., Weyand, M., Mai, A., Sippl, W., Steegborn, S., Virtual screening and identification of specific inhibitors for the mitochondrial deacylase Sirtuin 4 (2020) (in preparation).
- Wössner, N., **Alhalabi, Z.**, Nieto, J., Swyter, S., Gan, J., Schmidtkunz, K., Zhang, L., Vaquero, A., Ovaa, H., Einsle, O., Sippl, W., Jung, M., Sirtuin 1 Inhibiting Thiocyanates (S1th)-A New Class of Isotype Selective Inhibitors of NAD⁺ Dependent Lysine Deacetylases. *Frontiers in oncology*. **10**, 657 (2020).
- Simon, R.P., Robaa, D., **Alhalabi, Z.**, Sippl, W., Jung, M., KATching-Up on Small Molecule Modulators of Lysine Acetyltransferases. *Journal of medicinal chemistry*. **59**, 1249–1270 (2016).
- Loesche, A., Köwitsch, A., Lucas, S., **Alhalabi, Z.**, Sippl, W., Al-Harrasi, A., Csuk, R., Ursolic and oleanolic acid derivatives with cholinesterase inhibiting potential. *Bioorganic chemistry*. **85**, 23–32 (2019).
- Loesche, A., Wiemann, J., **Alhalabi, Z.**, Karasch, J., Sippl, W., Csuk, R., Unexpected AChE inhibitory activity of (2E) α,β -unsaturated fatty acids. *Bioorganic & medicinal chemistry letters*. **28**, 3315–3319 (2018).
- Karaman, B., **Alhalabi, Z.***, Swyter, S., Mihigo, S., Marobela, K., Jung, M., Sippl, W., Ntie, F., Identification of Bichalcones as Sirtuin Inhibitors by Virtual Screening and In Vitro Testing. *Molecules (Basel, Switzerland)*. **23**, (2018).
- Kalbas, D., Liebscher, S., Nowak, T., Meleshin, M., Pannek, M., Popp, C., **Alhalabi, Z.**, Bordusa, F., Sippl, W., Steegborn C., Schutkowski, M., Potent and Selective Inhibitors of Human Sirtuin 5. *Journal of medicinal chemistry*. **61**, 2460–2471 (2018).
- Vojacek, S., Beese, K., **Alhalabi, Z.**, Swyter, S., Bodtke, A., Schulzke, C. Jung, M. Sippl, W., Link, A. *Arch Pharm (Weinheim)*. 2017 Jul;350(7)., Three-Component Aminoalkylations Yielding Dihydronaphthoxazine-Based Sirtuin Inhibitors: Scaffold Modification and Exploration of Space for Polar Side-Chains. *Archiv der Pharmazie*. **350**, (2017).
- **Alhalabi, Z.**, A.Al-khayat, S. Haidar, Separation And Assay Of Antiprotozoal Imidazole Derivatives (Metronidazole, Tinidazole And Secnidazole) By RP-HPLC, *J.International Journal of Pharmaceutical Sciences Review and Research*, (2012).

Posters

- D. Kalbas, S.Liebscher, T.Nowak, M.Meleshin, M. Pannek, C.Popp, **Z. Alhalabi**, F. Bordusa, W.Sipl, C.Steegborn and M.Schutkowski, Natural product sirtuin inhibitors: Identification of bichalcones as by virtual screening and in vitro testing, Frontiers in Medicinal Chemistry 11-14 March 2018, Jena, Germany.
- **Alhalabi Z**, Nowak T, Schutkowski M, Sippl W, Discovery and optimization of Novel Sirt5 inhibitors: Molecular docking, virtual screening and molecular dynamics simulations, 8th Summer School Medicinal Chemistry, 21– 23. 09. 2016, Regensburg, Germany.
- **Alhalabi Z**, Sippl W. Homology Modeling and Molecular Dynamics Simulations of Sirtuin 4. Central German Meeting on Bioinformatics 2015, 26-27 August, Halle/Saale, Germany.
- **Alhalabi Z**, Sippl W. Homology modeling, molecular dynamics and virtual screening of the mitochondrial sirtuins Sirt4 And Sirt5, 11th German Conference on Chemoinformatics 2015, 8 – 10 November, Fulda, Germany.

Scholarships and Awards:

- German Academic Exchange Service (DAAD) Scholarship for Doctora Student 01.10.2013-01.10.2017.
- Ph.D scholarship for women (MLU) 01.10.2017-01.10.2018

Language

English (very good Toefl certificate 2013)

German (Good, ZD certificate 2012), C1 level

Arabic (native)

Address: Germany, Halle Saale.

